ISSN 2188-5001

MATERIALS DESIGN AND
CHARACTERIZATION LABORATORY

SUPERCOMPUTER CENTER

ACTIVITY REPORT
2017

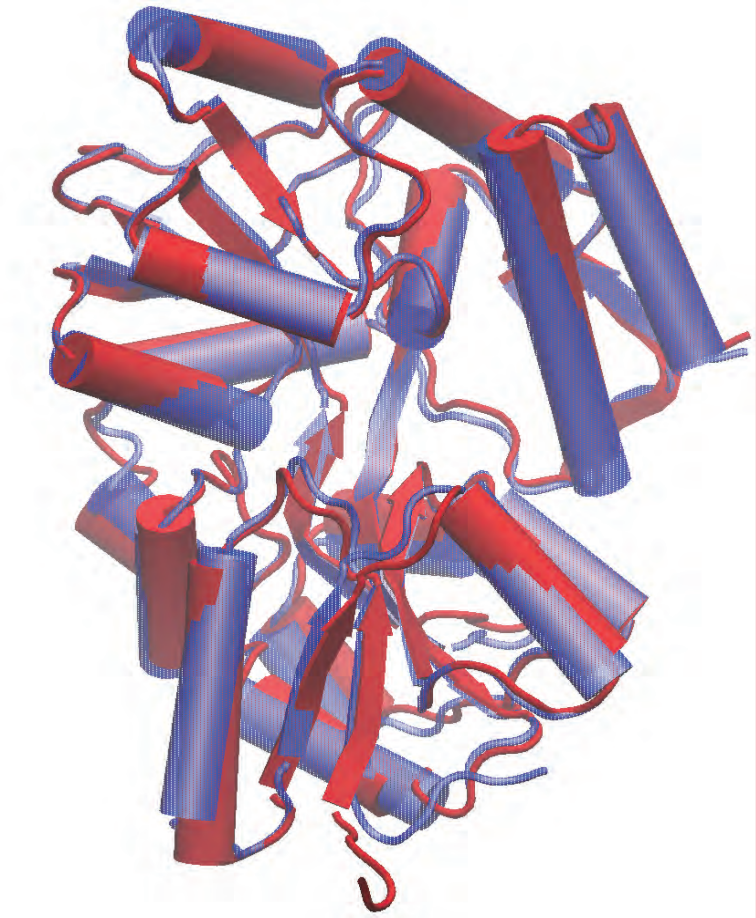

INSTITUTE FOR SOLID STATE PHYSICS
THE UNIVERSITY OF TOKYO

Materials Design and Characterization Laboratory (MDCL)

The MDCL was established as the third research facility of the Institute for Solid State Physics (ISSP) when the latter was reorganized in May 1996. Its aim is to promote material science with an emphasis on the “DSC cycle”, where DSC stands for design, synthesis and characterization, three processes for developing new materials.

The MDCL consists of two sections, Materials Design (MD) section and Materials Synthesis and Characterization (MSC) section. The Supercomputer Center of the ISSP (SCC-ISSP) is placed in the MD section, while in the MSC section there are seven laboratories for joint use; Materials Synthesis Laboratory, Chemical Analysis Laboratory, X-ray Diffraction Laboratory, Electron Microscope Laboratory, Electromagnetic Measurement Laboratory, Spectroscopy Laboratory, and High-Pressure Synthesis Laboratory.

Almost all the facilities of the MDCL are open to scientists in Japan through the User Programs conducted by two steering committees of the MDCL. One is the steering committee of the SCC-ISSP, under which the Supercomputer Project Advisory Committee is placed for reviewing proposals. The other is the steering committee of the MSC facilities. More than half of the members of these committees are from the outside of ISSP.

PREFACE

The Supercomputer Center (SCC) is a part of the Materials Design and Characterization Laboratory (MDCL) of ISSP. Its mission is to serve the whole community of computational condensed-matter physics of Japan providing it with high performance computing environment. In particular, the SCC selectively promotes and supports large-scale computations. For this purpose, the SCC invites proposals for supercomputer-aided research projects and hosts the Steering Committee, as mentioned below, that evaluates the proposals.

The ISSP supercomputer system consists of two subsystems: System B, which is intended for more nodes with relatively loose connections. In July, 2015, the SCC replaced the two supercomputer subsystems (SGI Altix ICE 8400EX and NEC SX-9) to one new system (System B, SGI ICE XA/UV hybrid system). The system B consists of 1584 CPU nodes, 288 ACC nodes, and 19 FAT nodes. The CPU node has 2 CPUs (Intel Xeon). The ACC node has 2CPUs (Intel Xeon) and 2GPUs (NVIDIA Tesla K40). The FAT node has 4CPUs (Intel Xeon) and large memory (1TB). The system B has totally 2.6 PFlops theoretical peak performance.
The new system C (HPE SGI 8600) was installed in January, 2018. It consists of 252 nodes, and each node has 2 CPUs (Intel Xeon) and 192 GB of memory. The system C has totally 774 TFlops.

The hardware administration is not the only function of the SCC. Since 2015, the SCC has started “Project for advancement of software usability in materials science”. In this project, for enhancing the usability of the ISSP supercomputer system, we perform some software-advancement activities such as implementing a new function to an existing code, releasing a private code on Web, and writing manuals. Two target programs were selected in fiscal year 2017 and developed software were released as DCore and HΦ 3.0. The SCC has also started a service for porting users’ materials science software to General Purpose GPUs (GPGPU) since 2015. Three programs were selected for the GPGPU porting in fiscal year 2017.

All staff members of university faculties or public research institutes in Japan are invited to propose research projects (called User Program). The proposals are evaluated by the Steering Committee of SCC. Pre-reviewing is done by the Supercomputer Project Advisory Committee. In fiscal year 2017, totally 267 projects were approved. The total points applied and approved are listed on Table. 1 below. Additionally, we supported post-K and other computational materials science projects through Supercomputing Consortium for Computational Materials Science (SCCMS).

The research projects are roughly classified into the following three (the number of projects approved):

First-Principles Calculation of Materials Properties (121)
Strongly Correlated Quantum Systems (29)
Cooperative Phenomena in Complex, Macroscopic Systems (117)

All the three involve both methodology of computation and its applications. The results of the projects are reported in 'Activity Report 2017' of the SCC. Every year 3-4 projects are selected for “invited papers” and published at the beginning of the Activity Report. In the Activity Report 2017, the following three invited papers are included:

" Development of open-source software HΦ",
Mitsuaki KAWAMURA, Takahiro MISAWA, Youhei YAMAJI, and Kazuyoshi YOSHIMI

"Monte Carlo study of Ising model with non-integer effective dimensions",
Synge TODO

"Recent Extensions and Applications of Parallel Cascade Selection Molecular Dynamics Simulations",
Ryuhei HARADA and Yasuteru SHIGETA

May 21, 2018

Naoki Kawashima
(Chairman of the steering committee, SCC, ISSP)

CONTENTS

PREFACE

1 OUTLINE 1

1.1 Supercomputer System 1
1.2 Project Proposals 1
1.3 Committees 3
1.4 Staff 6

2 STATISTICS OF SCHOOL YEAR 2017 7

2.1 System Statistics 7
2.2 Queue, Job, and User Statistics 8
2.3 Project for Advancement of Software Usability in Materials Science 9
2.4 GPGPU Support Service 10

3 RESEARCH REPORTS 12

3.1 Invited Articles 12
3.2 First-Principles Calculation of Material Properties 39
3.3 Strongly Correlated Quantum Systems 172
3.4 Cooperative Phenomena in Complex Macroscopic Systems 204
3.5 SCCMS Projects 322
3.6 Software Advancement Projects, GPGPU Implementation, and Workshop Support 345

4 PUBLICATION LIST 354

ISSP Joint Research Projects 355
SCCMS Projects 391
Doctor Theses 398
Master Theses 400

1 Outline

1.1 Supercomputer System

In SY2017, the ISSP supercomputer center provided users with System B - SGI ICE XA/UV hybrid system, which is a massively-parallel supercomputer with three types of compute nodes: 19 “Fat” nodes, 1584 “CPU” nodes, and 288 “ACC” nodes. “Fat” nodes are each comprised of four Intel Xeon E5-4627v3 CPUs (10 cores/CPU) and 1 TB of memory. “CPU” nodes have two Intel Xeon E5-2680v3 CPUs (12 cores/CPU) and 128 GB of memory. “ACC” nodes have two nVIDIA Tesla K40 GPUs in additon to two Xeon E5-2680v3 CPUs and 128 GB of memory. System B achieves 2.6 PFLOPS in theoretical peak performance with high power efficiency. The subsystem comprised of only CPU nodes ranks 61st on the November 2015 Top 500 List, which is a ranking based on total performance measured by the HPL benchmark. The subsystem of ACC nodes ranks 104th on the Top 500 List, and it also ranks 23rd on the Green 500 List, which is a ranking based on performance per watt of electrical power consumption. The compute nodes communicate to each other through FDR Infiniband. The Fat nodes are interconnected in fat tree topology, while the CPU and ACC nodes are connected in enhanced hypercube topology. System B entered official operation on Aug. 21, 2015.

The previous System C - FUJITSU PRIMEHPC FX10 ceased operation at the end of the previous school year. It has been replaced by the new System C - HPE SGI 8600 system, which entered official operation in April, 2018.

SY2017 was the third year of the operation of the current System B. For further details, please contact ISSP Supercomputer Center (SCC-ISSP).

[Correspondence: center@issp.u-tokyo.ac.jp]

1.2 Project Proposals

The ISSP supercomputer system provides computation resources for scientists working on condensed matter sciences in Japan. All scientific staff members (including post-docs) at universities or public research institutes in Japan can submit proposals for projects related to research activities on materials and condensed matter sciences. These proposals are peer-reviewed by the Advisory Committee members (see Sec. 1.3), and then the computation resources are allocated based on the review reports. The leader of an approved project can set up user accounts for collaborators. Other types of scientists, including graduate students, may also be added. Proposal submissions, peer-review processes, and user registration are all managed via a web system.

The computation resources are distributed in a unit called “point”, determined as a function of available CPU utilization time and consumed disk resources. There were calls for six classes of research projects in SY 2017. The number of projects and the total number of points that were applied for and approved in this school year are listed in Table 1.

Table 1: Classes of research projects in SY 2017

Class	Maximum Points		Application	# of Proj.	Total points			
					Applied		Approved	
	Sys–B	Sys–C			Sys–B	Sys–C	Sys–B	Sys–C
A	100	100	any time	12	1.2k	–	1.2k	–
B	1k	500	twice a year	62	56.9k	–	40.0k	–
C	10k	2.5k	twice a year	171	1433.8k	–	633.0k	–
D	10k	2.5k	any time	6	26.5k	–	24.5k	–
E	30k	2.5k	twice a year	16	474.0k	–	258.0k	–
S	–	–	twice a year	0	0	–	0	–
SCCMS				35	271.5k	–	271.5k	–
Total				302	2263.9k	–	1228.2k	–

- Class A is for trial use by new users; proposals for Class A projects are accepted throughout the year.

- Proposals for projects in Classes B (small), C (mid-size), E (large-scale), and S (exceptional) can be submitted twice a year. Approved projects in Classes A, B, C, and E continue to the end of the school year.

- In Class D, projects can be proposed on rapidly-developing studies that need to perform urgent and relatively large calculations. An approved project continues for 6 months from its approval.

- Class S is for projects that are considered extremely important for the field of condensed matter physics and requires extremely large-scale computation. The project may be carried out either by one research group or cooperatively by several investigators at different institutions. A project of this class should be applied with at least 10,000 points; there is no maximum. We require group leaders applying for Class S to give a presentation on the proposal to the Steering Committee of the SCC-ISSP. Class S projects are carried out within one year from its approval.

- Project leaders can apply for points so that the points for each system do not exceed the maximum point shown in this table.

- There was no official System C operation in SY2017.

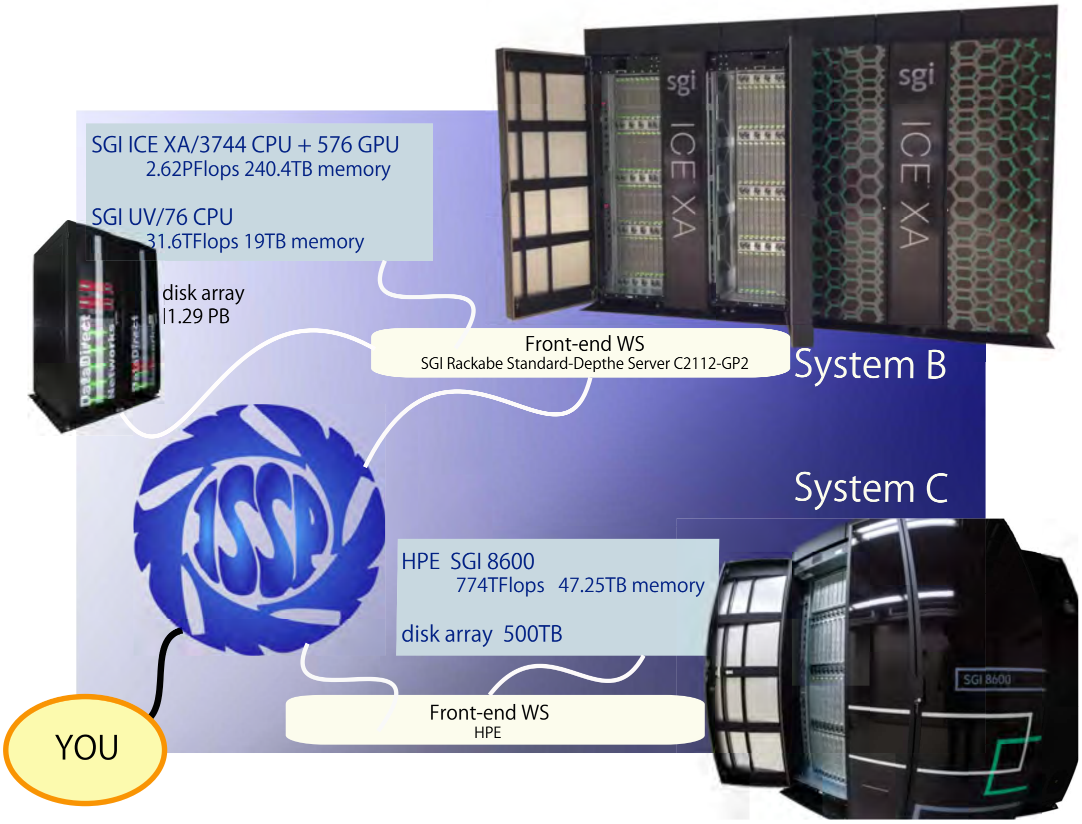

Figure 1: Supercomputer System at the SCC-ISSP

In addition, from SY 2016, ISSP Supercomputer is providing 20% of its computational resources for Supercomputing Consortium for Computational Materials Science (SCCMS), which aims at advancing parallel computations in condensed matter, molecular, and materials sciences on the 10-PFlops K Computer and the exascale post-K project. Computer time has also been alloted to Computational Materials Design (CMD) workshops, as well as for Science Camps held in ISSP for undergraduate students.

1.3 Committees

In order to fairly manage the projects and to smoothly determine the system operation policies, the Materials Design and Characterization Laboratory (MDCL) of the ISSP has organized the Steering Committee of the MDCL and the Steering Committee of the SCC-ISSP, under which the Supercomputer Project Advisory Committee (SPAC) is formed to review proposals. The members of the committees in SY 2016 were as follows:

Steering Committee of the MDCL

HIROI, Zenji	ISSP (Chair person)

KATO, Takeo	ISSP
KAWASHIMA, Naoki	ISSP
NOGUCHI, Hiroshi	ISSP
SUGINO, Osamu	ISSP
UWATOKO, Yoshiya	ISSP
KIMURA, Kaoru	Univ. of Tokyo
YOSHIMOTO, Yoshihide	Univ. of Tokyo
SAWA, Hiroshi	Nagoya Univ.
KAGEYAMA, Hiroshi	Kyoto Univ.
SUZUKI, Takafumi	Univ. of Hyogo
OKUMURA, Hisashi	NINS-RSCS
OTSUKI, Tomi	Sophia Univ.
TAKEDA Mahoto	Yokohama Natl. Univ.

Steering Committee of the SCC-ISSP

NOGUCHI, Hiroshi	ISSP (Chair person)
KAWASHIMA, Naoki	ISSP
OZAKI, Taisuke	ISSP
SUGINO, Osamu	ISSP
TSUNETSUGU, Hirokazu	ISSP
KATO, Takeo	ISSP
MASUDA, Takatsugu	ISSP
HIGUCHI, Yuji	ISSP
KASAMATSU, Shusuke	ISSP
MORITA, Satoshi	ISSP
WATANABE, Hiroshi	ISSP
HATANO, Naomichi	Univ. of Tokyo
IMADA, Masatoshi	Univ. of Tokyo
NAKAJIMA, Kengo	Univ. of Tokyo
TSUNEYUKI, Shinji	Univ. of Tokyo
YOSHIMOTO, Yoshihide	Univ. of Tokyo
KUBO, Momoji	Tohoku Univ.
MORIKAWA, Yoshitada	Osaka Univ.
OTSUKI, Tomi	Sophia Univ.
OKUMURA, Hisashi	NINS-RSCS
HOSHI, Takeo	Tottori Univ.
SUZUKI, Takafumi	Univ. of Hyogo
YATA, Hiroyuki	ISSP
FUKUDA, Takaki	ISSP

Supercomputer Project Advisory Committee

NOGUCHI, Hiroshi	ISSP (Chair person)
KATO, Takeo	ISSP

KAWASHIMA, Naoki	ISSP
OZAKI, Taisuke	ISSP
SUGINO, Osamu	ISSP
TSUNETSUGU, Hirokazu	ISSP
MASUDA, Takatsugu	ISSP
HIGUCHI, Yuji	ISSP
KASAMATSU, Shusuke	ISSP
MORITA, Satoshi	ISSP
WATANABE, Hiroshi	ISSP
HATANO, Naomichi	Univ. of Tokyo
HUKUSHIMA, Koji	Univ. of Tokyo
IKUHARA, Yuichi	Univ. of Tokyo
IMADA, Masatoshi	Univ. of Tokyo
IWATA, Jun-Ichi	Univ. of Tokyo
MIYASHITA, Seiji	Univ. of Tokyo
MOTOME, Yukitoshi	Univ. of Tokyo
NAKAJIMA, Kengo	Univ. of Tokyo
OGATA, Masao	Univ. of Tokyo
OSHIYAMA, Atsushi	Univ. of Tokyo
TODO, Synge	Univ. of Tokyo
TSUNEYUKI, Shinji	Univ. of Tokyo
WATANABE, Satoshi	Univ. of Tokyo
YOSHIMOTO, Yoshihide	Univ. of Tokyo
ARITA, Ryotaro	RIKEN-CEMS
NEMOTO, Koji	Hokkaido Univ.
AKAGI, Kazuto	Tohoku Univ.
KAWAKATSU, Toshihiro	Tohoku Univ.
KUBO, Momoji	Tohoku Univ.
SHIBATA, Naokazu	Tohoku Univ.
YANASE, Yoichi	Niigata Univ.
ISHIBASHI, Shoji	AIST
OTANI, Minoru	AIST
KOBAYASHI, Kazuaki	NIMS
TATEYAMA, Yoshitaka	NIMS
HATSUGAI, Yasuhiro	Univ. of Tsukuba
KOBAYASHI, Nobuhiko	Univ. of Tsukuba
OKADA, Susumu	Univ. of Tsukuba
ONO, Tomoya	Univ. of Tsukuba
YABANA, Kazuhiro	Univ. of Tsukuba
ODA, Tatsuki	Kanazawa Univ.
SAITO, Mineo	Kanazawa Univ.
HIDA, Kazuo	Saitama Univ.
NAKAYAMA, Takashi	Chiba Univ.
FURUKAWA, Nobuo	Aoyama Gakuin Univ.
MATSUKAWA, Hiroshi	Aoyama Gakuin Univ.

TAKANO, Hiroshi	Keio Univ.
YAMAUCHI, Jun	Keio Univ.
YASUOKA, Kenji	Keio Univ.
TOMITA, Yusuke	Shibaura Inst. Tech.
OTSUKI, Tomi	Sophia Univ.
OBATA, Shuji	Tokyo Denki Univ.
KITAO, Akio	Tokyo Tech.
TADA, Tomofumi	Tokyo Tech.
HOTTA, Takashi	Tokyo Metropolitan Univ.
TOHYAMA, Takami	Tokyo Univ. of Sci.
WATANABE, Kazuyuki	Tokyo Univ. of Sci.
HAGITA, Katsumi	National Defense Academy
KONTANI, Hiroshi	Nagoya Univ.
MASUBUCHI, Yuichi	Nagoya Univ.
SHIRAISHI, Kenji	Nagoya Univ.
TANAKA, Yukio	Nagoya Univ.
KAWAKAMI, Norio	Kyoto Univ.
KAWAMURA, Hikaru	Osaka Univ.
KIM, Kang	Osaka Univ.
KUROKI, Kazuhiko	Osaka Univ.
KUSAKABE, Koichi	Osaka Univ.
MORIKAWA, Yoshitada	Osaka Univ.
OGUCHI, Tamio	Osaka Univ.
SHIRAI, Koun	Osaka Univ.
YOSHINO, Hajime	Osaka Univ.
YUKAWA, Satoshi	Osaka Univ.
SAKAI, Toru	JAEA
SUGA, Seiichiro	Univ. of Hyogo
SUZUKI, Takafumi	Univ. of Hyogo
TATENO, Masaru	Univ. of Hyogo
HOSHI, Takeo	Tottori Univ.
YASUDA, Chitoshi	Univ. of the Ryukyus
OKUMURA, Hisashi	NINS-RSCS

1.4 Staff

The following staff members of the SCC-ISSP usually administrate the ISSP Supercomputer.

NOGUCHI, Hiroshi	Associate Professor (Chair person)
KAWASHIMA, Naoki	Professor
OZAKI, Taisuke	Professor
SUGINO, Osamu	Associate Professor
WATANABE, Hiroshi	Research Associate
KASAMATSU, Shusuke	Research Associate

HIGUCHI, Yuji	Research Associate
NOGUCHI, Yoshifumi	Research Associate
MORITA, Satoshi	Research Associate
YATA, Hiroyuki	Technical Associate
FUKUDA, Takaki	Technical Associate
ARAKI, Shigeyuki	Technical Associate

2 Statistics (School Year 2017)

2.1 System and User Statistics

In the following, we present statistics for operation time taken in the period from April 2017 to March 2018 (SY 2017). In Table 2, we show general statistics of the supercomputer system in SY 2017. The total number of compute nodes in System B is 1891. Consumed disk points amount to about 3% of the total consumed points in System B. Roughly 20% of the total points in System B were consumed by SCCMS projects. This means that about 20% of the total computational resources in this school year were actually used by SCCMS projects.

In the left column of Fig. 2, availabilities, utilization rates, and consumed points in System B are plotted for each month. Throughout the school year, the utilization rates were very high. exceeding 90% throughout most of the year.

The user statistics are shown in the right column of Fig. 2. The horizontal axis shows the rank of the user/group arranged in the descending order of the execution time (hour×nodes). The execution time of the user/group of the first rank is the longest. The vertical axis shows the sum of the execution time up to the rank. From the saturation points of the graphs, the number of "active" users of System B is around 300. The maximum ranks in the graphs correspond to the number of the users/groups that submitted at least one job.

Table 2: Overall statistics of SY 2017

	System B
total service time ($\times 10^3$ node·hours)	15814
number of executed jobs	665306
total consumed points ($\times 10^3$ point)	629
CPU points ($\times 10^3$ point)	613
disk points ($\times 10^3$ point)	16
total exec. time ($\times 10^3$ node·hours)	14399
availability	95.9%
utilization rate	91.1%

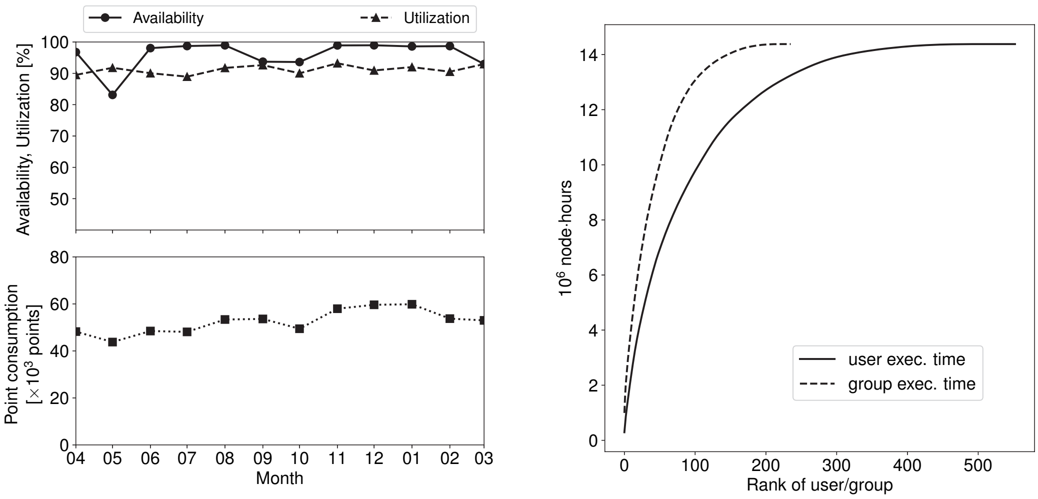

Figure 2: Left: Availabilities, utilization rates and point consumptions of each month during SY 2017. Right: User statistics. The horizontal axis shows the rank of the user/group arranged in the descending order of the execution time (hour×nodes). The vertical axis shows the sum of the execution time up to the rank.

2.2 Queue and Job Statistics

Queue structure of System B in SY2017 is shown in Table 3. In System B, users can choose from three types of compute nodes; jobs submitted to queues with “cpu”, “acc”, and “fat” at the end of their queue names are submitted to CPU, ACC, and Fat nodes, respectively. See Sec. 1.1 for a description of each type of compute node. The user then has to choose the queue according to the number of nodes to use and the duration of their calculation jobs. Queue names starting with “F” are for jobs taking 24 hours or less, while those starting with “L” can run much longer up to 120 hours. More nodes are allotted to “F” queues in order to maximize the turnaround time of user jobs. The queue names starting with “i” are used for interactive debugging of user programs and the elapsed time limit is 30 minutes. The number following “F”, “L”, or “i” correspond to the number of nodes that can be used by one user job.

To prevent overuse of the storage, points are charged also for usage of disk quota in the three systems, as shown in Table 4. Disk points are revised often for optimal usage of the resources by examining usage tendencies each year.

Although we do not mention here in detail, to promote utilization of the massively parallel supercomputer, background queues (“B4cpu”, “B36cpu”, “B144cpu”, “B18acc”, “B72acc”, and “B2fat”) which charge no points for the jobs have also been open in System B.

The number of jobs, average waiting time, and total execution time in each queue are shown in Table 5. In System B, a large portion of jobs have been executed

Table 3: Queue structures in SY 2017

System–B

queue name	Elapsed time limit (hr)	# of nodes /job	# of nodes /queue	Memory limit (GB)	job points /(node·day)
F4cpu	24	1–4	216	120/node	1
L4cpu	120	1–4	108	120/node	1
F36cpu	24	5–36	288	120/node	1
L36cpu	120	5–36	144	120/node	1
F144cpu	24	37–144	1008	120/node	1
L144cpu	120	37–144	144	120/node	1
i18cpu	0.5	1–18	72	120/node	1
F18acc	24	1–18	180 (108)*	120/node	2
L18acc	120	1–18	90 (54)*	120/node	2
F72acc	24	19–72	72 (144)*	120/node	2
i9acc	0.5	1–9	36	120/node	2
F2fat	24	1–2	17	1000/node	4
L2 fat	120	1–2	6	1000/node	4
i1fat	0.5	1	2	1000/node	4

* The number of nodes allocated to F18acc, L18acc, and F72acc queues were changed on Sept. 8. The number of allocated nodes before the change are given in parentheses.

in "F" queues. The largest amount of the execution time has been consumed in the large-scale "F144cpu" queue, but substantial number of jobs were run in every queue, suggesting that a wide variety of user needs are met by this queuing scheme. In most of these queues, the queue settings meet the user's tendencies in that the waiting times are on the order of the elapsed-time limit. The acc queues have relatively short waiting times, but we expect that to change as more users get accustomed to using GPGPUs.

2.3 Project for advancement of software usability in materials science

From SY 2015, the supercomputer center (SCC) has started "Project for advancement of software usability in materials science". In this project, for enhancing the usability of the supercomputer system in ISSP, we perform some software-advancement activity such as implementing a new function to an existing code, releasing a private code on Web, writing manuals. Target programs are publicly offered in December and selected in the review by the Steering Committee of SCC. The projects are carried out by the software development team composed of three members in ISSP. In SY 2017, two projects are selected as listed in Table 6.

Table 4: Disk points of System B

		point/day
System B	`/home`	$0.001 \times \theta(q - 300)$
	`/work`	$0.0001 \times \theta(q - 3000)$

* q is denoted in unit of GB.
* $\theta(x)$ is equal to the Heaviside step function $H(x)$ multiplied by x, i.e., $xH(x)$.

Table 5: Number of jobs, average waiting time, total execution time, and average number of used nodes per job in each queue.

System-B

queue	# of Jobs	Waiting Time (hour)	Exec. Time ($\times 10^3$ node·hour)	# of nodes
F4cpu	360588	36.05	1236.11	1.32
L4cpu	6087	38.66	508.93	1.76
F36cpu	25506	22.53	1425.45	12.86
L36cpu	972	91.16	731.55	16.33
F144cpu	11664	23.43	6963.52	85.27
L144cpu	176	154.74	883.50	118.64
i18cpu	82805	0.62	157.06	9.58
F18acc	39002	9.88	568.23	2.13
L18acc	2316	12.41	246.15	2.86
F72acc	1556	14.93	460.21	50.02
i9acc	8193	0.34	6.50	3.56
F2fat	7590	22.80	72.43	1.32
L2fat	546	46.75	21.91	1.20
i1fat	5238	0.19	0.85	1.00

2.4 GPGPU Support Service

As noted in Sec. 1.1, ACC nodes with graphics processing units (GPU) were introduced in System B in SY 2015. Since GPUs were introduced in the ISSP Supercomputer center for the first time, many programs developed or utilized by users of this center have not been implemented for GPU computing. To help users take advantage of GPUs, the supercomputer center has started a service for porting users' materials science software to General Purpose GPUs (GPGPU). After a call for proposals (which will usually be in December), target programs for the next school year are selected by the Steering Committee of SCC. The porting service is carried out on each program for about two months; the coding is performed by engineers from the computer vender suppling the ISSP supercomputer system, and ISSP staff oversee the progress of the project and manage necessary commu-

Table 6: List of Project for advancement of software usability in materials science for SY 2017.

Software	Project Proposer
Advancement of first-principles program based on dynamical mean-field theory for correlated electrons	Hiroshi Shinaoka Saitama University
Development of quantum lattice model simulator for integrating theoretical, experimental and data science approaches	Youhei Yamaji The University of Tokyo

Table 7: List of supported software and project proposers for the GPGPU support service for SY 2017.

Software	Project Proposer
Acceleration of large-scale coarse-grained molecular dynamics simulation by GPGPU and its application to polymers	Yuji Higuchi Tohoku University
GPGPU implementation of Fluid Particle Dynamics (FPD) method (RS-CPMD)	Kohei Takae The University of Tokyo
Implementation of GPGPU computing in full diagonalization for HΦ	Takahiro Misawa The University of Tokyo

nications with the proposer. Copyrights of the resulting software basically belong to the proposers, but the supported contents might be published under agreement with the proposer. In SY 2017, three projects are selected as listed in Table 7.

Acknowledgments

The staffs would like to thank Prof. Takafumi Suzuki (now at University of Hyogo) for developing WWW-based system (SCM: SuperComputer Management System) for management of project proposals, peer-review reports by the SPAC committee, and user accounts. We also thank Ms. Reiko Iwafune for creating and maintaining a new WWW page of the ISSP Supercomputer Center.

3 RESEARCH REPORTS

3.1 Invited Articles

Development of Open-Source Software HΦ 13

Mitsuaki KAWAMURA, Takahiro MISAWA, Youhei YAMAJI,
and Kazuyoshi YOSHIMI

Monte Carlo Study of Ising Model with Non-Integer Effective Dimensions 23

Synge TODO

Recent Extensions and Applications of Parallel Cascade Selection Molecular Dynamics Simulations 31

Ryuhei HARADA and Yasuteru SHIGETA

Development of open-source software $\mathcal{H}\Phi$

Mitsuaki Kawamura[a], Takahiro Misawa[a], Youhei Yamaji[b,c,d], Kazuyoshi Yoshimi[a]
[a] *Institute for Solid State Physics, University of Tokyo*
Kashiwa-no-ha, Kashiwa, Chiba 277-8581
[b] *Quantum-Phase Electronics Center (QPEC), The University of Tokyo*
Bunkyo-ku, Tokyo, 113-8656, Japan
[c] *Department of Applied Physics, The University of Tokyo*
Bunkyo-ku, Tokyo, 113-8656, Japan
[d] *JST, PRESTO*
Bunkyo-ku, Tokyo, 113-8656, Japan

Abstract

We overview “Project for advancement of software usability in materials science” (PASMS) managed by the center of the supercomputer at Institute for Solid State Physics (ISSP) in this activity report. In PASMS, we have supported the developments of the software packages that will be useful in a wide range of the condensed matter physics. In a part of the project, we have newly developed an open-source software package for the exact diagonalization $\mathcal{H}\Phi$. In this report, we focus on $\mathcal{H}\Phi$ and explain the basic properties including the user interfaces, the implemented modern algorithms, and the parallelization efficiency. We also show the applications of $\mathcal{H}\Phi$ to the frustrated Hubbard model and the Kitaev systems where the quantum spin liquids are expected to appear. The easy-to-use interface of $\mathcal{H}\Phi$ helps us to investigate these systems promptly by calculating the finite-temperature properties, low-energy excited state and the excitation spectrum of the quantum spin liquids. These applications show that $\mathcal{H}\Phi$ is a useful software package and has large spillover effects on the studies of condensed matter physics.

1 Introduction

From the 2015 fiscal year, the supercomputer center at ISSP has started PASMS [1]. In PASMS, we have developed new software packages, implemented new functions to existing software, and supported for releasing software packages. As shown in Table 1, in one fiscal year, two software packages were supported by this project. These developed software packages are released as open-source software packages and thus can be utilized by a wide range of scientists working in materials science including the non-experts of the computational materials science such as the experimentalists. Furthermore, users can easily use these software packages on the supercomputer at ISSP because they are pre-installed in the supercomputer at ISSP [2].

Fiscal year	Software	Main proposer
2015	$\mathcal{H}\Phi$[3]	Youhei Yamaji
2015	OpenMX[4]	Taisuke Ozaki
2016	mVMC[5]	Takahiro Misawa
2016	$K\omega$[6]	Takeo Hoshi
2017	$\mathcal{H}\Phi$[3]	Youhei Yamaji
2017	DCore[7]	Hiroshi Shinaoka

Table 1: List of software packages developed in “Project for advancement of software usability in materials science”.

In this activity report, we focus on a program package $\mathcal{H}\Phi$ [3, 8] newly developed by

PASMS. The core of $\mathcal{H}\Phi$ is numerical exact diagonalization for quantum lattice Hamiltonians. Before explaining the details of $\mathcal{H}\Phi$, we briefly summarize our motivation and aim for developing a new exact diagonalization package in this project. We note that there are several numerical diagonalization packages such as TITPACK [9], KOBEPACK [10] and SPINPACK [11]. Although these pioneering software packages are useful for treating conventional models such as the Heisenberg model and have been widely used for several decades in the community of the condensed matter physics, they are not suitable for the architecture of the modern supercomputers. For example, the distributed memory parallelization, is not supported in TITPACK and KOBEPACK. Although SPINPACK supports such parallelization, it does not support the general interactions that often appear in low-energy effective Hamiltonians for real materials. Moreover, the above packages do not support the modern algorithms such as the thermal pure quantum (TPQ) state approach [12, 13, 14, 15] for finite-temperature calculations, shifted Krylov subspace method [16, 17] for calculating the dynamical Green functions, and the locally optimal block preconditioned conjugate gradient (LOBPCG) method [18] for obtaining the many low-energy excited states at one calculation. Our aim of developing $\mathcal{H}\Phi$ is to provide a user-friendly, general-purpose, and parallelized diagonalization package that includes the above modern algorithms for the condensed matter community.

Here, in chronological order, we summarize the main functions/methods implemented in $\mathcal{H}\Phi$. In the 2015 fiscal year, we first implemented Lanczos and full diagonalization algorithms for obtaining the ground states and finite temperature calculations based on thermal pure quantum state approach [15]. We also designed a simple and flexible user interfaces that enable users to handle general interactions and also calculate physical quantities, such as internal energy, temperature dependence of specific heat, and charge/spin structure factors. In the 2016 fiscal year, the numericallibrary $K\omega$[6] was developed by collaborating with scientists in mathematical physics. This library provides large-scale parallel computing algorithms for sparse matrices based on the shifted Krylov subspace method. By using $K\omega$, we implemented the shifted bi-conjugate gradient (sBiCG) method [16, 17] in $\mathcal{H}\Phi$ to obtain the dynamical Green functions and the excitation spectrum. We also implemented the locally optimal block preconditioned conjugate gradient (LOBPCG) method [18]. By using the LOBPCG method, users can compute several low-energy eigenvalues and eigenvectors simultaneously in one calculation. Furthermore, in the 2017 fiscal year, the real-time evolution was implemented to investigate the nonequilibrium states of the quantum many-body systems.

In this report, we explain the basic properties of $\mathcal{H}\Phi$ and show several applications. The organization of this report is as follows: In Sec. 2, we detail the target models, numerical methods, and the calculation flow of $\mathcal{H}\Phi$. We also show benchmark results of the parallelization of $\mathcal{H}\Phi$ on SGI ICE XA (Sekirei) at ISSP. In Sec. 3, as the demonstration of numerical analyses of $\mathcal{H}\Phi$, we show the applications of $\mathcal{H}\Phi$ to the quantum spin liquids. In Sec. 4, we summarize this report.

2 Basic properties

2.1 Models

By using $\mathcal{H}\Phi$, users can treat the general Hamiltonians defined as

$$\hat{\mathcal{H}} = \hat{\mathcal{H}}_0 + \hat{\mathcal{H}}_\mathrm{I}, \tag{1}$$

$$\hat{\mathcal{H}}_0 = \sum_{ij} \sum_{\sigma_1,\sigma_2} t_{i\sigma_1 j\sigma_2} \hat{c}^\dagger_{i\sigma_1} \hat{c}_{j\sigma_2}, \tag{2}$$

$$\hat{\mathcal{H}}_\mathrm{I} = \sum_{i,j,k,l} \sum_{\sigma_1,\sigma_2,\sigma_3,\sigma_4} I_{i\sigma_1 j\sigma_2 k\sigma_3 l\sigma_4} \hat{c}^\dagger_{i\sigma_1} \hat{c}_{j\sigma_2} \hat{c}^\dagger_{k\sigma_3} \hat{c}_{l\sigma_4}, \tag{3}$$

where $\hat{c}^{\dagger}_{i\sigma}$ ($\hat{c}_{i\sigma}$) is the creation (the annihilation) operator of an electron at site-i with spin-σ, and $t_{ij\sigma_1\sigma_2}$ and $I_{ijkl\sigma_1\sigma_2\sigma_3\sigma_4}$ are the one-body potentials and two-body interactions, respectively. As an special case of the above general Hamiltonian, we can treat spin 1/2 localized spin systems and the Kondo systems, where the itinerant electrons couple with the spin 1/2 localized spins. $\mathcal{H}\Phi$ can also treat quantum spin systems with arbitrary spin whose amplitude s larger than 1/2, i.e, $S = 1, 3/2, 2, \ldots$ and mixed-spin systems.

2.2 Method

2.2.1 Eigenvectors by the Lanczos and the LOBPCG method

To obtain the eigenvalues and eigenvectors of the quantum lattice Hamiltonians, the Lanczos method [19] has been employed in the previous packages. In this method, we compute eigenvalues by diagonalizing the tri-diagonal matrix that is generated by multiplying the Hamiltonian to the initial vector. The Lanczos method, however, has two problems. One is that eigenvectors can not be obtained in a set of the Lanczos process. If we need eigenvectors, we must perform the same Lanczos process again. Moreover, generally, the obtained eigenvector is not accurate enough and we have to refine the obtained eigenvector with the inverse iteration method. The other problem is that the Lanczos method cannot compute the number of degeneracy in one calculation. To determine the degeneracy, it is necessary to perform the several Lanczos calculations for different initial vectors and orthogonalize the obtained eigenvectors. This redundancy is a main weak point in the Lanczos method.

To overcome this weak point, we employ LOBPCG method in $\mathcal{H}\Phi$ [18]. In this method, we obtain M eigenvectors from the subspace spanned by $3M$ vectors

$$\{\, |\,\Phi_1^{(i)}\rangle,\, |\,\Phi_2^{(i)}\rangle, \cdots,\, |\,\Phi_M^{(i)}\rangle \,\}, \tag{4}$$

$$\{\, |\,r_j^{(i)}\rangle = \hat{\mathcal{H}}\ |\,\Phi_j^{(i)}\rangle - \varepsilon_j^{(i)}\ |\,\Phi_j^{(i)}\rangle \,\}, \tag{5}$$

$$\{\, |\,\Phi_1^{(i-1)}\rangle,\, |\,\Phi_2^{(i-1)}\rangle, \cdots,\, |\,\Phi_M^{(i-1)}\rangle \,\}, \tag{6}$$

at each iteration, where $|\Phi_j^{(i)}\rangle$ is the jth eigenvector at the ith iteration and $\varepsilon_j^{(i)} = \langle\Phi_j^{(i)}|\hat{\mathcal{H}}|\Phi_j^{(i)}\rangle$. This method allows us to simultaneously obtain arbitrary number of excited states in one calculation. We will show an example of the calculation for the frustrated Hubbard model in Sec. 3.

2.2.2 Finite-temperature properties by the TPQ state

Recently, an efficient unbiased numerical method for calculating finite-temperature properties in quantum systems is proposed [15]. In this method, thermodynamic properties such as internal energy and the correlation functions are given as expectation values of *one* TPQ state for sufficiently large system sizes. This method enables us to calculate the finite-temperature properties *without* ensemble average and perform the unbiased finite-temperature calculations for a large system size to which full diagonalization method is almost inapplicable. We note that, the idea for calculating the finite-temperature properties without ensemble average were proposed in the pioneering works [12, 20, 21, 22]. In some of these papers, the finite-temperature observables were already calculated by replacing ensemble average with random sampling of wave functions.

We explain how to construct the TPQ state [15], which offers a simple way for finite-temperature calculations. Let $|\psi_0\rangle$ be a random initial vector. By operating $(l - \hat{\mathcal{H}}/N_{\rm s})^k$ (l is a constant, $N_{\rm s}$ represents the number of sites) to $|\psi_0\rangle$, we obtain the k-th TPQ states as

$$|\psi_k\rangle \equiv \frac{(l - \hat{\mathcal{H}}/N_{\rm s})\,|\psi_{k-1}\rangle}{|(l - \hat{\mathcal{H}}/N_{\rm s})\,|\psi_{k-1}\rangle\,|}. \tag{7}$$

From $|\psi_k\rangle$, we estimate the corresponding inverse temperature β_k as

$$\beta_k \sim \frac{2k/N_{\mathrm{s}}}{l - u_k}, \qquad u_k = \langle \psi_k | \hat{\mathcal{H}} | \psi_k \rangle / N_{\mathrm{s}}, \tag{8}$$

where u_k is the internal energy. Arbitrary local physical properties at β_k are also estimated as

$$\langle \hat{A} \rangle_{\beta_k} = \langle \psi_k | \hat{A} | \psi_k \rangle / N_{\mathrm{s}}. \tag{9}$$

In a finite-size system, a finite statistical fluctuation is caused by the choice of the initial random vector. To estimate the average value and the error of the physical properties, we perform some independent calculations by changing $|\psi_0\rangle$. Usually, we regard the standard deviations of the physical properties as the error bars.

2.2.3 Dynamical structure factors by the shifted Krylov method

In $\mathcal{H}\Phi$, users can calculate the dynamical correlation function defined as

$$G_{\alpha\beta}(\omega) = \langle \Phi_0 | \hat{A}_\alpha^\dagger (\omega - \hat{H})^{-1} \hat{A}_\beta | \Phi_0 \rangle, \tag{10}$$

where $|\Phi_0\rangle$ is the initial wavefunction, and $\hat{A}_\alpha$ and $\hat{A}_\beta$ are the excited operators. When $\alpha = \beta$, this quantity can be computed by the continued fraction algorithm and the elements of the tri-diagonal matrix obtained in the Lanczos method [19]. However, this conventional method is not applicable to the case that $\alpha \neq \beta$.

In $\mathcal{H}\Phi$, we employ the shifted Krylov method [17] which can compute both diagonal and off-diagonal dynamical correlation functions as follows:

$$|b_\beta\rangle = \hat{A}_\beta |\Phi_0\rangle \tag{11}$$

$$(\omega - \hat{\mathcal{H}}) |x_\beta(\omega)\rangle = |b_\beta\rangle \tag{12}$$

$$G_{\alpha\beta}(\omega) = \langle b_\alpha | x_\beta(\omega) \rangle. \tag{13}$$

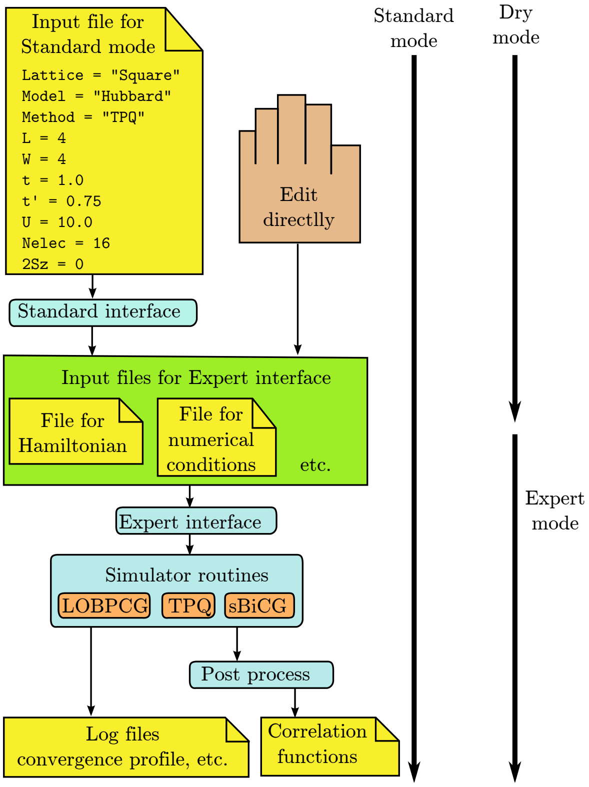

```
Lattice = "Square"
Model = "Hubbard"
Method = "TPQ"
L = 4
W = 4
t = 1.0
t' = 0.75
U = 10.0
Nelec = 16
2Sz = 0
```

Figure 1: Calculation flow of $\mathcal{H}\Phi$.

The series of the linear equations (12) can be solved simultaneously by using sBiCG method [16]. The sBiCG method is based on the shift invariance of the Krylov subspace, which is defined as

$$\mathcal{K}_n(\omega) = \{ |b_\beta\rangle, (\omega - \hat{\mathcal{H}}) |b_\beta\rangle, \ldots, (\omega - \hat{\mathcal{H}})^{n-1} |b_\beta\rangle \}. \tag{14}$$

Shift invariance means that spanned sub space by $\mathcal{K}_n(\omega)$ do not depend on ω, i.e., $\mathrm{span}\{\mathcal{K}_n(\omega)\} = \mathrm{span}\{\mathcal{K}_n(\omega')\}$. Due to the shift invariance, if we once obtain $G_{\alpha\beta}(\omega)$ for given ω, we can obtain the arbitrary $G_{\alpha\beta}(\omega')$ from $G_{\alpha\beta}(\omega)$. This means that the numerical cost of this method does not depend on the number of frequencies. This efficient method is implemented in $\mathcal{H}\Phi$ by using $K\omega$ library [6], which is also developed in this project.

2.3 Calculation flow and user interfaces

A typical calculation flow in $\mathcal{H}\Phi$ is shown in Fig. 1. If the target system is supported by Standard mode, only one input file is necessary for a calculation. For example, in the left top panel in Fig. 1, we show an example of input file for the TPQ calculation (`Method="TPQ"`) in the Hubbard model (`Model="Hubbard"`) on the square lattice (`Lattice="Square"`). In the input file, we set the nearest-neighbor hopping as `t=1`, the second nearest-neighbor hopping as `t’=0.75`, on-site Coulomb interaction as `U=10`, the width of cell as `W=4`, the length of cell as `L=4` (16 sites), number of electrons as `Nelec=16`, and the double of the total z component of spin as `2Sz=0`. From this file, $\mathcal{H}\Phi$ generates input files for Expert mode, which specify the Hamiltonian and the details of the numerical conditions. Then, $\mathcal{H}\Phi$ performs the TPQ calculations by reading these automatically generated input files. After the calculation, we can obtain the temperature dependence of the physical properties and the elapsed time in the generated log files. We can also plot the correlation function in the reciprocal space by using the utility tool to perform the Fourier transformation (Fourier tool).

If users want to compute more complicated system that is not supported in Standard mode, users should prepare the input files in Expert mode. Using Dry model is a convenient way for generating input files in Expert mode. By using the Dry mode, only the input files in Expert mode are generated without calculations. By editing the generated input files for the standard models, users can treat more general models in Expert mode.

2.4 Performance of parallelization

Here, we show benchmark result of the parallelization in $\mathcal{H}\Phi$. To examine the efficiency of the parallelization of $\mathcal{H}\Phi$, we carry out TPQ simulations for half-filled 18-site Hubbard model with $S_z = 0$ on the square lattice shown in the inset of Fig. 2 with varying numbers of threads and processes. In this system, the dimension of the Hilbert space is given by $({}_{18}C_9)^2 = 2,363,904,400$, where ${}_aC_b$ represents the binomial coefficient.

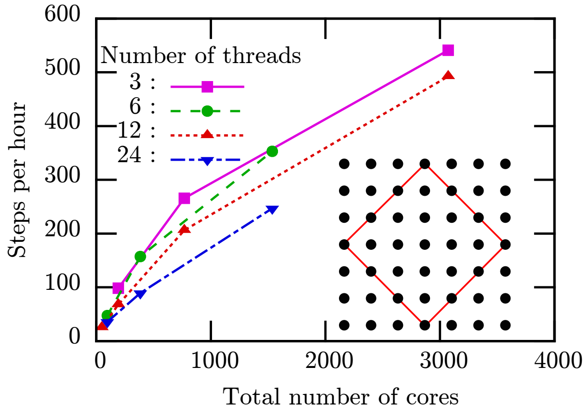

Figure 2: Speedup of TPQ calculations with hybrid parallelization by using up to 3,072 cores on Sekirei [8]. The squares, circles, upward triangles, and downward triangles represent the results with 3 threads, 6 threads, 12 threads, and 24 threads, respectively. The inset shows the shape of the 18-site cluster used in the benchmark calculations.

In Fig. 2, we show TPQ steps per hour up to 3,072 cores at SGI ICE XA (Sekirei) at ISSP. We can see significant acceleration caused by the increase of CPU cores. This acceleration is almost linear up to 192 cores, and is weakened as we further increase the number of cores. This weakening of the acceleration may come from the load imbalance in the S^z conserved simulation. This imbalance is expected to be solved by using randomly distributed memory parallelization [23].

3 Result

In this section, we show applications of $\mathcal{H}\Phi$ to the quantum spin liquids in the frustrated Hubbard model and the Kitaev systems.

3.1 Application to the frustrated Hubbard model

The Hubbard model with the next-nearest-neighbor (nnn) hopping t' on the square lattice [see, Fig. 3(a)] is a prototypical system for

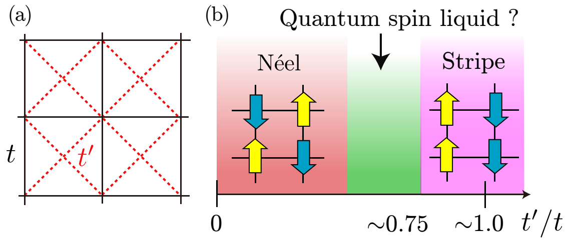

Figure 3: (a) Schematic picture for frustrated Hubbard model. (b) Schematic phase diagram for the frustrated Hubbard model in the strong coupling region.

studying the quantum spin liquids induced by the geometrical frustrations. In the following, we focus on half filling, i.e., the filling is given by $n = N_{\mathrm{s}}^{-1}\sum_{i\sigma}\langle c_{i\sigma}^{\dagger}c_{i\sigma}\rangle = 1$ ($N_{\mathrm{s}} = L \times L$ is the system size). To reduce the numerical cost, we only consider the total $S_{\mathrm{total}}^{z} = 0$ space, i.e., $S_{\mathrm{total}}^{z} = \sum_i S_i^z = 0$. We employ a $N_{\mathrm{s}} = 16 = 4 \times 4$ cluster with the periodic-periodic boundary condition and a $N_{\mathrm{s}} = 18 = 3\sqrt{2}\times 3\sqrt{2}$ cluster with antiperiodic-periodic boundary condition.

In the strong coupling region ($U/t >> 1$, where U is the on-site Coulomb integral), the nearest-neighbor (next-nearest-neighbor) superexchange interactions J_1 (J_2) are given by $J_1 = 4t^2/U$ ($J_2 = 4t'^2/U$). From this, in the strong coupling region, simple Néel magnetic order is expected to appear around $t' = 0$ and the stripe magnetic order is expected to appear around $t'/t = 1$ as shown in Fig. 3(b). In fact, highly-accurate numerical calculations at zero temperature have shown that the expected magnetic orders appear for both the t-t' Hubbard model [24, 25, 26] and the J_1-J_2 Heisenberg model [27, 28, 29, 30].

In the intermediate region where J_1 and J_2 competes, i.e., $J_2/J_1 \sim 0.5$ [27, 28, 29, 30] or $t'/t \sim 0.75$ [24, 25, 26], it has been proposed that the quantum spin liquid appears. In spite of the huge number of the ground-state calculations, finite-temperature properties have not been systematically studied so far due to the lack of the efficient numerical method. Because the errors of TPQ method are determined by the entropy [15, 31], the TPQ method is useful for studying the finite-temperature properties of the quantum spin liquids, where the entropy is expected to remain large. Although the applicable system sizes of the TPQ method are limited to small system sizes such as $N_{\mathrm{s}} = 16(4 \times 4)$ for the frustrated Hubbard model, we find the signature of the quantum spin liquid at the moderately high-temperature region where the finite-system size effects are small.

In Fig. 4(a), we show temperature dependence of the specific heat, which is defined as

$$C/N_{\mathrm{s}} = (\langle\hat{\mathcal{H}}^2\rangle - \langle\hat{\mathcal{H}}\rangle^2)/(N_{\mathrm{s}}T^2). \tag{15}$$

The high-temperature peaks ($T/t \sim 2$) in the specific heat are governed by the energy scale of U and do not depend on t'. In contrast to this, the low-temperature peaks are governed by the super exchange interactions and largely depend on t'. When the ground states are magnetically ordered state, i.e., Néel state ($t'/t = 0.5$) or stripe state ($t'/t = 1.0$), obvious low-temperature peaks exist while peak height is reduced for $t'/t = 0.75$ where the quantum spin liquid is expected to appear. This indicates that the entropy remains large around $t'/t = 0.75$.

We now examine the temperature dependence of the entropy, which is defined as

$$S(T)/N_{\mathrm{s}} = c\ln 2 - \frac{1}{N_{\mathrm{s}}}\int_{\infty}^{T}\frac{C}{TdT},$$
$$S_{\mathrm{norm}} = \frac{1}{c\ln 2}\frac{S(T)}{N_{\mathrm{s}}}. \tag{16}$$

Because we restrict the Hilbert space with the fixed particle number and $S_z = 0$, the normalization factors c appears in the definition of the entropy. The normalization factor is given by $c \sim 1.706$ for 16 sites. As shown in Fig. 4(b), we find that the entropy remains large at $t'/t = 0.75$ compared to the other t'.

Furthermore, we plot the t' dependence of the finite-temperature entropy in Fig. 4(c).

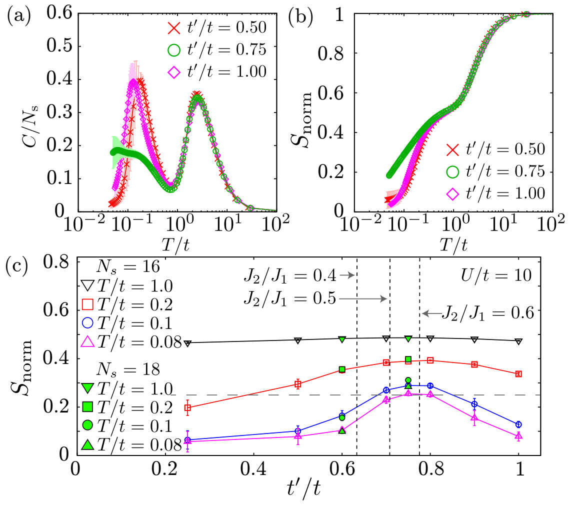

Figure 4: (a) Temperature dependence of the specific heat for $U/t = 10$. (b) Temperature dependence of the entropy for $U/t = 10$. (c) Frustration (t'/t) dependence of the entropy at fixed temperatures for $N_{\rm s} = 16$ and $N_{\rm s} = 18$. Around $t'/t \sim 0.75$, the entropy remains large at moderately high-temperature and shows a peak structure. The large remaining entropy is the signature of the quantum spin liquid.

As a result, we find that the entropy has peak structure, in the intermediate region ($t'/t \sim 0.75$) even at moderately high-temperature ($T/t \sim 0.1$). By calculating $N_{\rm s} = 18$ site cluster, we confirm that the finite-size effects are small at this temperature range. This large remaining entropy at moderately high-temperature ($T/t \sim 0.1$) offers an useful criterion whether the target systems have a chance to be quantum spin liquid or not.

By using LOBPCG method implemented in $\mathcal{H}\Phi$, it is possible to obtain the several low-energy exited states. In Fig. 5, we show an example of the LOBPCG calculations for the frustrated Hubbard model shown in the previous section. In the calculations, we obtain 16 lowest eigenvalues and eigenvectors simultaneously. We can see the degeneracy of the eigenvalues is large for $t'/t = 0.75$ and it is consistent with the large remaining entropy at finite temperatures.

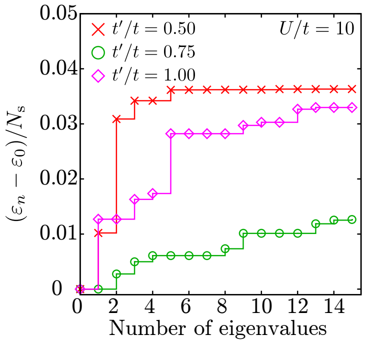

Figure 5: Eigenvalues obtained by the LOBPCG method for the frustrated Hubbard model. The n-th eigenvalues are denoted by ε_n (ε_0 represents the ground state energy).

3.2 Application to Kitaev systems

In this section, we show dynamical spin structure factors of the Kitaev model [32] and *ab initio* effective Hamiltonian of the related iridium oxide $\rm Na_2IrO_3$ [33] simulated by the sBiCG method. These systems show complicated spin excitation continua in contrast to spin wave spectra in typical magnets such as the Heisenberg model on a square lattice. In addition, the Kitaev model and the *ab initio* effective Hamiltonian show remarkably different convergences of the sBiCG method, which are quantified by the norm of the residual vectors in each sBiCG step.

The Kitaev model on the honeycomb structure is an exactly solvable quantum spin $S = 1/2$ system defined as

$$\hat{\mathcal{H}}_{\rm K} = \sum_{\langle i,j \rangle_x} K_x \hat{S}_i^x \hat{S}_j^x + \sum_{\langle i,j \rangle_y} K_y \hat{S}_i^y \hat{S}_j^y + \sum_{\langle i,j \rangle_z} K_z \hat{S}_i^z \hat{S}_j^z, \tag{17}$$

where $\langle i,j \rangle_\gamma$ ($\gamma = x, y, z$) represents a pair of the nearest neighbor sites along γ-bond illustrated in Fig. 6(a), and K_γ is a bond-direction dependent Ising coupling. The Kitaev model has attracted considerable attention due to its spin liquid ground state and the emergent fractionalization of spin degrees of freedom [32]. Due to the fractionalization, the dynamical spin structure factor of the Kitaev model shows excitation continuum.

Although the Kitaev model seems to be an artificial model and to be difficult to realize in real materials, Jackeli and Khaliullin proposed that low-energy physics of an iridium oxide $\mathrm{Na_2IrO_3}$ is described by the Kitaev model [33]. Even though the experimental observations reveal the magnetically ordered ground state of $\mathrm{Na_2IrO_3}$ [34], theoretical researchers tried to write down the effective Hamiltonian of the iridium oxides to figure out how to realize the *Kitaev materials*. One of the authors and his colleagues derived the *ab initio* Hamiltonian of $\mathrm{Na_2IrO_3}$ [35] and found that the dominant energy scale of the effective Hamiltonian is indeed given by the Kitaev's bond-dependent Ising couplings $K_x = K_y = -23.9$ meV and $K_z = -30.7$ meV while there are other small but finite couplings even in the nearest neighbor couplings. In addition, there are the second and third neighbor couplings (see the reference [35] for the details). Although the effective Hamiltonian shows the magnetically ordered ground state consistent with the experiments, it is expected that the signature of the fractionalization can be seen in the spin excitation.

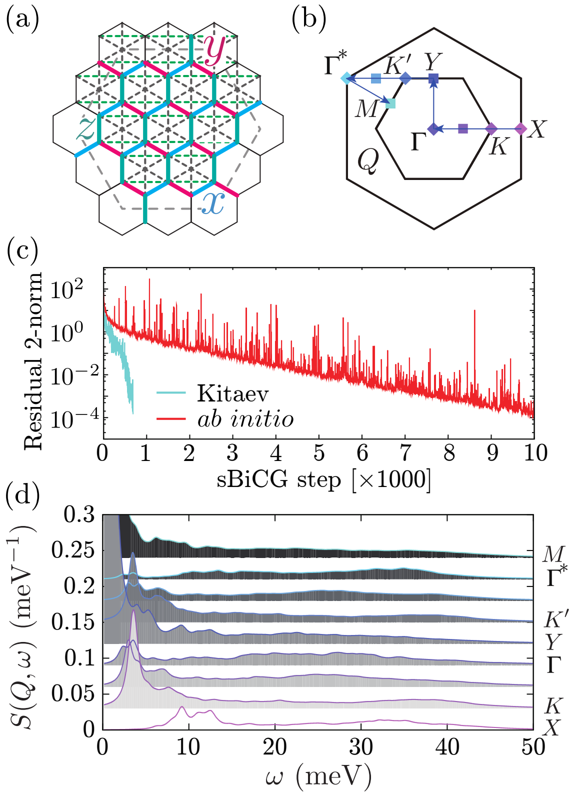

Figure 6: (a) 24 site cluster of the Kitaev and *ab initio* Hamiltonian. (b) Brillouin zone of honeycomb structure and symmetric momenta. (c) sBiCG step dependence of 2-norm of residual vectors for the Kitaev and *ab initio* Hamiltonian. (d) Dynamical spin structure factors of the *ab initio* Hamiltonian calculated by using sBiCG method.

To see the signature of the fractionalization we calculate the spin excitation by using the sBiCG method. The controlled convergence of the sBiCG enables us to examine the detailed spin excitation continuum obtained by calculating dynamical spin structure factor,

$$S(\vec{Q},\omega) = -\frac{1}{\pi}\mathrm{Im}\sum_{\gamma=x,y,z}\langle\Phi_0|\,\hat{S}^{\gamma}(\vec{Q})^{\dagger} \times(\omega+i\delta+\varepsilon_0-\hat{\mathcal{H}})^{-1}\hat{S}^{\gamma}(\vec{Q})\,|\Phi_0\rangle\,, \tag{18}$$

where the broadening factor is chosen as $\delta = |K_z|/100$ and $\hat{S}^{\gamma}(\vec{Q}) = N_{\mathrm{s}}^{-1/2}\sum_i \hat{S}_i^{\gamma} e^{i\vec{Q}\cdot\vec{r}_i}$. We choose $\vec{Q}$ along symmetry lines in the Brillouin zone shown in Fig. 6(b). First, the convergence of the sBiCG steps for excitation spectra is examined for the Kitaev model $\hat{\mathcal{H}}_{\mathrm{K}}$ and the *ab initio* Hamiltonian $\hat{\mathcal{H}}_{\mathrm{K}}+\hat{\mathcal{H}}'$, where $\hat{\mathcal{H}}'$ includes complicated interactions other than the Kitaev interactions. As shown in Fig. 6(c), the sBiCG step dependence of the 2-norm of the residual vector depends on the Hamiltonians. While the residual vector of the Kitaev model shows faster decay within thousand sBiCG steps, the residual vector of the *ab initio* Hamiltonian shows one order of magnitude slower convergence. The slower convergence may suggest larger density of states in the excitation spectrum. The significant dependence of the convergence on the Hamiltonians hampers *a priori* choice of number of the sBiCG steps. However, the sBiCG method enables us to control the convergence by examining the sBiCG step dependence of the residual vector.

Figure 6(d) shows detailed continuum in the spin excitation spectrum of Na_2IrO_3 obtained by sBiCG. The proximity of the Kitaev's spin liquid phase is evident in the excitation continuum up to 40 meV.

4 Summary

In this report, we first explained "Project for advancement of software usability in materials science"(PASMS) in Sec. 1. As one of the achievements in this project, we focused on an open-source software package for the exact diagonalization, $\mathcal{H}\Phi$ and explained the target models, algorithms, and usage of $\mathcal{H}\Phi$ in Sec. 2. In this section, we also showed that $\mathcal{H}\Phi$ has good parallelization efficiency on Sekirei at ISSP by seeing the drastically acceleration with the increase of CPU cores. In Sec. 3, we showed applications of $\mathcal{H}\Phi$ to the frustrated Hubbard models and the Kitaev models, both of which are candidates of quantum spin liquids. For the frustrated Hubbard model, we studied finite-temperature properties by the TPQ method, and found that an entropy at moderately high-temperature remains large around the quantum spin liquids. For the Kitaev systems, we studied dynamical spin structure factors by using the sBiCG method considering a simple Kitaev model and a low-energy effective Hamiltonian of Na_2IrO_3 obtained by downfolding using outputs of the first-principles calculation. By careful analysis, we concluded that the remnant of the continuous spin excitations observed in the Kitaev model still remains in a realistic model of Na_2IrO_3.

As demonstrated in these two applications, $\mathcal{H}\Phi$ provides a powerful tool for analyzing exotic phases in quantum many-body systems. To further improve the functionality of $\mathcal{H}\Phi$ and make the closer comparisons possible, we will implement algorithms for simulating finite-temperature spectra [36] and will combine data science approaches [37] in the near future. We believe that $\mathcal{H}\Phi$ is useful for a wide range of the scientists in the filed of condensed matter physics and will accelerate developing material designs by promoting close collaboration between theories and experiments.

Acknowledgment

This work was supported by Grant-in-Aid for Building of Consortia for the Development of Human Resources in Science and Technology from the MEXT of Japan. The numerical calculation of this work performed with the supercomputer in the Institute for Solid State Physics, The University of Tokyo. TM was supported by JSPS KAKENHI (Grant Nos. 16K17746 and 16H06345). YY was supported by PRESTO, JST (JPMJPR15NF). This work was also supported in part by MEXT as a social and scientific priority issue (Creation of new functional devices and high-performance materials to support next-generation industries) to be tackled by using post-K computer. The authors acknowledge Naoki Kawashima, Synge Todo, Takeo Hoshi, Tomohiro Sogabe, and Kota Ido for collaborations in developing $\mathcal{H}\Phi$.

References

[1] `http://www.issp.u-tokyo.ac.jp/supercom/softwaredev`

[2] `http://www.issp.u-tokyo.ac.jp/supercom/visitor/applications`

[3] `https://github.com/issp-center-dev/HPhi`

[4] `http://www.openmx-square.org`

[5] `https://github.com/issp-center-dev/mVMC`

[6] `https://github.com/issp-center-dev/Komega/releases`

[7] `https://github.com/issp-center-dev/DCore`

[8] M. Kawamura, K. Yoshimi, T. Misawa, Y. Yamaji, S. Todo, N. Kawashima, Comp. Phys. Commun. **217**, 180 (2017).

[9] `http://www.stat.phys.titech.ac.jp/~nishimori/titpack2_new/index-e.html`

[10] `http://quattro.phys.sci.kobe-u.ac.jp/Kobe_Pack/Kobe_Pack.html`

[11] `http://www-e.uni-magdeburg.de/jschulen/spin/`

[12] M. Imada, M. Takahashi, J. Phys. Soc. Jpn. **55**, 3354 (1986).

[13] J. Jaklič, P. Prelovšek, Phys. Rev. B **49**, 5065 (1994).

[14] A. Hams, H. De Raedt, Phys. Rev. E **62**, 4365 (2000).

[15] S. Sugiura, A. Shimizu, Phys. Rev. Lett. **108**, 240401 (2012).

[16] A. Frommer, Computing **70**, 87 (2003).

[17] S. Yamamoto, T. Sogabe, T. Hoshi, S.-L. Zhang, T. Fujiwara, J. Phys. Soc. Jpn. **77**, 114713 (2008).

[18] A. V. Knyazev, SIAM J. Sci. Comput. **23**, 517 (2001).

[19] E. Dagotto, Rev. Mod. Phys. **66**, 763 (1994).

[20] J. Jaklič, P. Prelovšek, Phys. Rev. B **49**, 5065 (1994).

[21] A. Hams, H. De Raedt, Phys. Rev. E **62**, 4365 (2000).

[22] S. Lloyd, arXiv:1307.0378.

[23] A. Wietek, A. M. Lauchli, arXiv:1804.05028.

[24] T. Kashima, M. Imada, J. Phys. Soc. Jpn. **70**, 3052 (2001).

[25] T. Mizusaki, M. Imada, Phys. Rev. B **74**, 014421 (2006).

[26] L. F. Tocchio, F. Becca, A. Parola, S. Sorella, Phys. Rev. B **78**, 041101 (2008).

[27] H.-C. Jiang, H. Yao, L. Balents, Phys. Rev. B **86**, 024424 (2012).

[28] W.-J. Hu, F. Becca, A. Parola, S. Sorella, Phys. Rev. B **88**, 060402 (2013).

[29] S.-S. Gong, W. Zhu, D. N. Sheng, O. I. Motrunich, M. P. A. Fisher, Phys. Rev. Lett. **113**, 027201 (2014).

[30] S. Morita, R. Kaneko, M. Imada, J. Phys. Soc. Jpn. **84**, 024720 (2015).

[31] S. Sugiura, A. Shimizu, Phys. Rev. Lett. **111**, 010401 (2013).

[32] A. Kitaev, Ann. Phys. **321**, 2 (2006).

[33] G. Jackeli, G. Khaliullin, Phys. Rev. Lett. **102**, 017205 (2009).

[34] F. Ye, S. Chi, H. Cao, B. C. Chakoumakos, J. A. Fernandez-Baca, R. Custelcean, T. F. Qi, O. B. Korneta, G. Cao, Phys. Rev. B **85**, 180403 (2012).

[35] Y. Yamaji, Y. Nomura, M. Kurita, R. Arita, M. Imada, Phys. Rev. Lett. **113**, 107201 (2014).

[36] Y. Yamaji, T. Suzuki, M. Kawamura, arXiv:1802.02854.

[37] R. Tamura, K. Hukushima, Phys. Rev. B **95**, 064407 (2017).

Monte Carlo study of Ising model with non-integer effective dimensions

Synge TODO
Department of Physics, University of Tokyo, Tokyo, 113-0033
Institute for Solid State Physics, University of Tokyo, Kashiwa, 277-8581

Abstract

We review recent advances in the Markov-chain Monte Carlo method, especially the irreversible kernel and the $O(N)$ method based on the geometric allocation technique. After the review of the MCMC, we present the results of our recent Monte Carlo simulation of the Ising model with long-range interaction as well as the correlated random-field Ising model, both of which exhibits critical behavior with non-integer effective dimensions depending on the decay exponent of the long-range interaction or the spatial correlation of the random field.

1 Introduction

Critical phenomena are classified into "universality classes" according to their critical exponents. In general, the critical exponents depend on only a few basic properties of the system, such as the dimensionality, symmetry of the order parameter, etc. However, the existence of long-range interaction (LRI) and/or randomness may change the critical behavior [1]. Various materials exhibit nontrivial phenomena, in which the long-range nature of the interactions, such as the dipole-dipole interaction and the RKKY interaction, plays an essential role. The randomness also causes various nontrivial behavior such as the spin-glass transition, slow dynamics, etc [2]. As for the critical behavior, they also alter the universality class. Interestingly, this change of universality can be interpreted as a continuous change of the effective dimension of the system as seen below.

If a spin system has LRI, all possible pairs of spins interact with each other. The simplest and most fundamental LRI is the algebraically decaying Ising interaction, $\sim r^{-(d+\sigma)}$, where d is the dimension of the lattice and σ is the decay exponent. For σ smaller than the lower critical decay exponent, $\sigma_{\rm L}$, the phase transition is expected to belong to the mean-field universality class. Especially, in the limit of $d + \sigma \to 0$, the system becomes equivalent to the fully connected Ising model. On the other hand, when σ becomes larger than the upper critical decay exponent, $\sigma_{\rm U}$, the nearest-neighbor interaction dominates and the transition belongs to the short-range universality class. In the intermediate regime, $\sigma_{\rm L} < \sigma < \sigma_{\rm U}$, the critical exponents vary continuously as σ changes (Fig. 1). For the d-dimensional LRI system, this continuous change of the critical exponents can be interpreted as a continuous change of the effective dimension between d and the upper critical dimension [3].

Similarly, the presence of randomness often changes the effective dimension of the system as well. The random-field Ising model (RFIM) is one of the representative random systems, which has randomly distributed external field [4]. In contrast to the LRI, however, the random field generally decreases the effective dimension. Especially, near the upper critical dimension, it is predicted that the critical behavior of the d-dimensional RFIM is the same as the pure system in $(d-2)$ dimen-

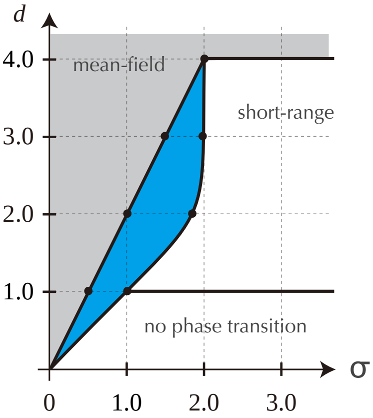

Figure 1: Schematic universality phase diagram of the Ising model with LRI. In the intermediate region, the effective dimension increases as σ decreases.

sions. This phenomena is called "dimensional reduction" [5]. Moreover, it is expected that the spatial correlation between random fields can further decrease the effective dimension. For the spatial correlation that decreases algebraically with exponent $d - \rho$, the renormalization group study predicts that the upper critical dimension D_{U} and the lower critical dimension D_{L} become as $D_{\mathrm{U}} = d_{\mathrm{U}} + \rho$ and $D_{\mathrm{L}} = d_{\mathrm{L}} + \rho$, respectively, for $\rho \geq 0$, where $d_{\mathrm{U}} = 6$ and $d_{\mathrm{L}} = 2$ are those for uncorrelated random field [6]. This means that the effective dimension D of the d-dimensional RFIM with correlation exponent ρ is given by $d - \rho$, if we interpolate the effective dimension linearly between the lower and upper critical dimensions.

In this article, after a brief review of recent advances in the Markov-chain Monte Carlo method, we will present our results of extensive Monte Carlo simulation on the spin systems with LRI and the spatially correlated RFIM.

2 Advances in Markov-chain Monte Carlo method

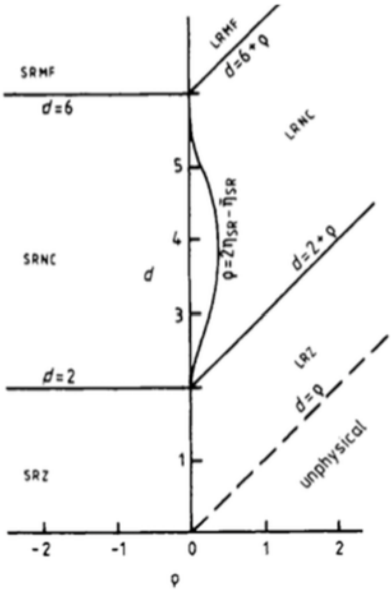

Figure 2: Schematic universality phase diagram of the $O(n)$ spin model with correlated random-field proposed (taken from Ref. [1]). For $\rho > 0$, the effective dimension decreases linearly as ρ increases.

The Markov-chain Monte Carlo (MCMC) method is one of the most powerful algorithms for numerical simulations in many research fields, such as the statistical physics, particle physics, chemistry, biology, informatics, finance, etc. In principle, the method can achieve statistically exact sampling asymptotically as long as the Markov chain satisfies the (total) balance and the ergodicity. Since the invention of the Metropolis algorithm in 1953, the detailed balance condition, a.k.a. reversibility, has been additionally imposed in most practical simulations as a sufficient condition for the total balance. Under the detailed balance condition, we enforce that every elementary transition should balance with its inverse process. Although a Markov chain satisfying the balance condition and ergodicity can generate random variables, or configurations, according to the target probability distribution, the MCMC method often suffers from strong correlation between successive samples in practice, which causes slow convergence and reduction in the effective number of samples. In other words, the strong autocorrelation may introduce systematic error as well as the increase of statistical error.

In generally, we should take the following five key points into account in order to achieve efficient MCMC sampling:

i) Representation (definition of "configurations").
ii) Choice of ensemble (weight of configurations).
iii) Generation of candidate configurations from the current configuration.
iv) Choice of transition kernel (probability), given a set of candidate configurations.
v) Algorithm for choosing a configuration according to transition probability.

From the viewpoint of the ergodicity, i), ii) and iii) are essential. In the quantum Monte Carlo method, for example, the non-local cluster update method [7], in which a world-line configuration is updated globally thorough a graph configuration, is often used. Another major technique is the worm algorithm [8, 9], where we introduce a pair of defects into the world-line configurations, to relax the strong restriction and recover the ergodicity. These techniques often reduce the correlation time drastically by orders of magnitude as well especially near the phase transition point.

More recently, from viewpoint iv), the importance of breaking the reversibility has been discussed intensively. In Ref. [9], we have shown that it is generally possible to construct an irreversible transition kernel by using the geometric allocation technique, and also that it can indeed reduce the auto-correlation drastically in many relevant cases by minimizing the rejection probability. The concept of breaking the reversibility can be applied not only to the elementary transition but also to the chain of events (or updates) [9, 10], where the global stochastic flow is introduced in the phase space and the Markov chain is further accelerated.

The technique of geometric allocation for the probability even improves the algorithm for choosing configuration [viewpoint v)]. Indeed, it is possible to draw a random number according to arbitrary probability distribution in a constant time by using Walker's method of aliases. This method, together with the space-time interchange technique, can reduce the computational time especially for the case where the number of candidates is large, such as models with LRI [11]. In the naive implementation of the Metropolis algorithm or the Swendsen-Wang algorithm, the total cost of one Monte Carlo step for N spins is proportional to N^2. However, since the interaction becomes weaker as the distance increases, one may reduce the computational cost from $O(N^2)$ to $O(N)$ without introducing any approximation [12]. The present $O(N)$ technique can be generalized to the quantum Monte Carlo method as well as the extended ensemble methods, such as the exchange Monte Carlo, multi-canonical method, and Wang-Landau sampling, etc.

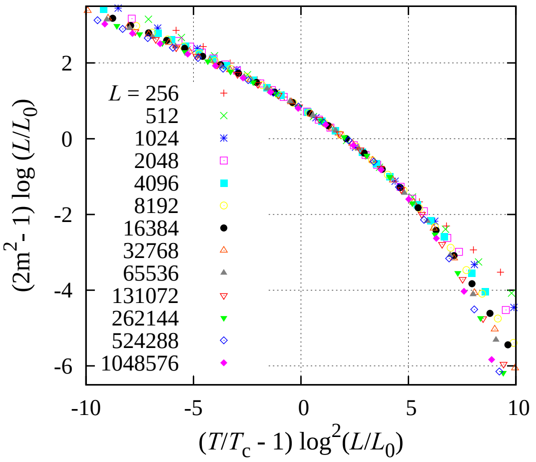

Figure 3: Scaling plot of the magnetization squared for the 1D transverse-field Ising model with $\sigma = 1$ and $\Gamma = 1$ (taken from Ref. [12]).

3 Ising model with long-range interaction

Transverse-field Ising model

In this section, we first consider the one-dimensional (1D) transverse-field Ising model, whose Hamiltonian is defined as

$$\mathcal{H} = -\sum_{i<j} J_{ij}\sigma_i^z\sigma_j^z - \sum_i \Gamma\sigma_i^x \qquad (1)$$

with

$$J_{ij} = r_{ij}^{-(1+\sigma)}. \qquad (2)$$

In the absence of the transverse field, Γ, this model reduces to the classical Ising chain. In the classical case, the lower and upper critical decay exponents are known as $\sigma_\mathrm{L} = \frac{1}{2}$ and $\sigma_\mathrm{U} = 1$, respectively. When $\sigma > \sigma_\mathrm{U}$, there is no finite-temperature phase transition.

At $\sigma = \sigma_\mathrm{U}$, however, it is known that the system exhibits a Kosterlitz-Thouless (KT) phase transition at a finite temperature [13]. This KT transition is expected to persist, as long as Γ is sufficiently small. In Fig. 3, the system size and the temperature dependence of the magnetization squared, m^2, is shown for the quantum case, $\Gamma = 1$. Surprisingly, all the data with different system sizes (from $L = 2^8$ to 2^{20}) collapse on a single curve, by rescaling the temperature and the magnetization squared as $(T/T_\mathrm{c})\log^2(L/L_0)$ and $(2m^2 - 1)\log(L/L_0)$, where T is the temperature, and T_c and L_0 are determined as 1.38460(25) and 0.26(10), respectively, by using the least-squares fitting. This logarithmic scaling behavior strongly suggests that the KT transition in the classical case is robust against the quantum fluctuation, though the transition temperature becomes lower [$T_\mathrm{c} = 1.52780(9)$ for $\Gamma = 0$].

At critical transverse field Γ_c, the finite-temperature KT transition vanishes, at which a quantum multicritical point emerges. By the finite-size scaling analysis, we evaluated as $\Gamma_\mathrm{c} \simeq 2.5236$, and found that the spin gap Δ and the susceptibility χ at Γ_c are scaled as $\Delta = L^{-z}f(L^zT)$ and $\chi = L^\gamma g(L^zT)$, respectively, with the dynamical exponent $z = 0.501$ and the exponent for the susceptibility $\gamma/\nu = 0.99$. These value are consistent with the predicted value $z = 0.5$ and $\gamma/\nu = 1$ by the renormalization group analysis [14].

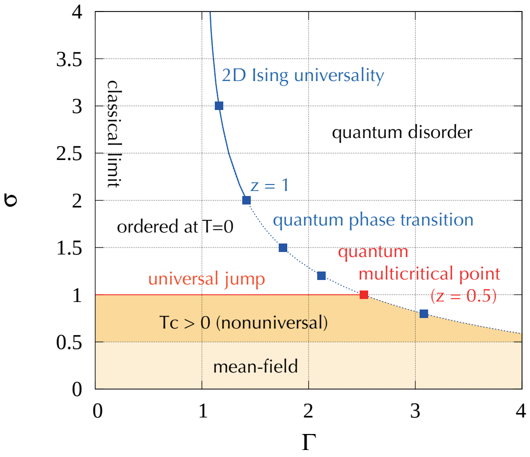

Figure 4: Ground-state phase diagram of the 1D transverse-field Ising model. In the shaded region, there occurs a finite-temperature transition.

In Fig. 4, we present the ground state phase diagram of the transverse field Ising model with LRI obtained by the quantum Monte Carlo simulation. In the limit of $\sigma = \infty$, the present model is reduced to the nearest neighbor Ising model, where the quantum phase transition of the classical two-dimensional (2D) Ising universality occurs at $\Gamma = 1$. As σ decreases, the critical transverse field increases. We found that, for $\sigma \geq 2$, the universality class of the quantum phase transition is the same as the 2D classical Ising universality, whereas the critical exponents, z and γ/ν, start to deviate continuously from the 2D classical Ising values for $\sigma < 2$.

Critical decay exponent in two dimensions

Nest, we discuss the classical 2D case ($d = 2$ and $\Gamma = 0$). While there is a consensus that $\sigma_\mathrm{L} = d/2 = 1$ in 2D, there still remain theoretical as well as numerical discussions about the upper critical decay exponent σ_U [15, 16, 17, 18, 19, 20, 21]. One of the largest difficulty in the numerical analysis of the present model is the large finite-size corrections to the scaling in the vicinity of the critical decay exponent. To overcome this problem,

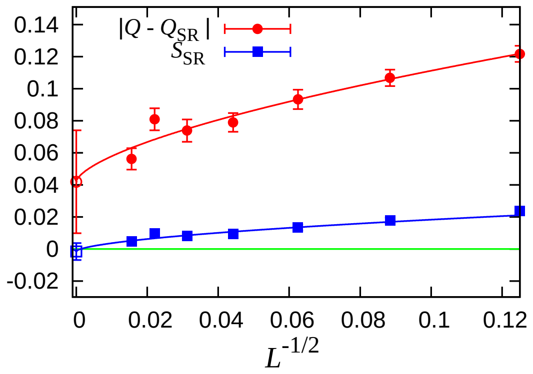

Figure 5: System-size dependence of the conventional Binder ratio Q and the self-combined Binder ratio $S_{\rm SR}$ at $\sigma = 7/4$. The solid lines denotes the result of least-squares fitting to $A + aL^{-b}$.

instead of the critical exponents, we use the value of the Binder ratio, $Q = \langle m^2 \rangle^2 / \langle m^4 \rangle$. The Binder ratio at the critical point, which is also referred to as the universal ratio, does not depend on the system size and takes a universal value, since it is the ratio of two physical quantities that have the same anomalous dimension. It can be calculated more accurately than the critical exponents, which leads to more reliable identification of the universality class [22].

In order to further suppress the finite-size corrections, we introduce another quantity, named the "self-combined Binder ratio",

$$S(T,L) = \frac{1}{Q_\infty} Q(T,L) + Q_\infty \frac{1}{Q(T,L)} - 2, \tag{3}$$

where Q_∞ denotes the universal ratio. This quantity is a linear combination of Q and Q^{-1}. It is easily seen that regardless of the form of the correction term in Q at the critical point, the leading correction of the universal ratio is removed automatically if Q_∞ is chosen as the exact universal ratio [23]. Indeed, we already know the precise value of the universal ratio for the mean-field universality and the 2D short-range Ising universality as $Q_{\rm MF} = 0.456947$ and $Q_{\rm SR} = 0.856216$, respectively [24, 25].

By using the $O(N)$ Swendsen-Wang cluster algorithm [12], we simulate the 2D Ising model up to $L = 4096$ for $\sigma = 0.8, 0.9, \cdots, 1.9, 2.0$ and perform the finite-size scaling analysis. In Fig. 5, we show the system-size dependence of the (standard) Binder ratio Q and the self-combined Binder ratio $S_{\rm SR}$ at $\sigma = 7/4$. For the definition of $S_{\rm SR}$, we use the universal ratio for the short-range Ising universality, $Q_{\rm SR} = 0.856216$. We observe that the self-combined Binder ratio converges rapidly to zero. This strongly supports that the assumed value for Q_∞ is correct, that is, $\sigma = 7/4$ belongs to the short-range universality. We also confirmed that the extrapolated value of $S_{\rm SR}$ grows as $\sim (7/4 - \sigma)^2$ for $\sigma < 7/4$. Thus, we conclude that the upper critical decay exponent is $\sigma_{\rm U} = 7/4$ for $d = 2$ [23].

On the other hand, the conventional Binder ratio Q is extrapolated to some different value from $Q_{\rm SR}$. This is due to the existence of strong (likely logarithmic) corrections at the critical decay exponent. We also confirmed that at $\sigma = 1$, $S_{\rm MF}$ converges to zero, whereas Q shows slow convergence.

4 Random-field Ising model with spatial correlation

Correlated random field

In this section, we discuss the dimensional reduction in the random-field Ising model with spatial correlation. We consider the Gaussian random fields with algebraically long-range correlation,

$$P(h_i) = \frac{1}{\sqrt{2\pi} h_R} \exp[-h_i^2 / 2h_R^2] \tag{4}$$

$$C_{ij} = \langle\!\langle h_i h_j \rangle\!\rangle = \begin{cases} h_R^2 & \text{for } i = j \\ a h_R^2 / r_{ij}^{d-\rho} & \text{otherwise,} \end{cases} \tag{5}$$

where $\langle\!\langle \cdot \rangle\!\rangle$ denotes the average over the random field realizations. The random-field generation is accomplished by the decomposition of $(L^d \times L^d)$ correlation matrix C. Let us consider the factorization of the positive definite

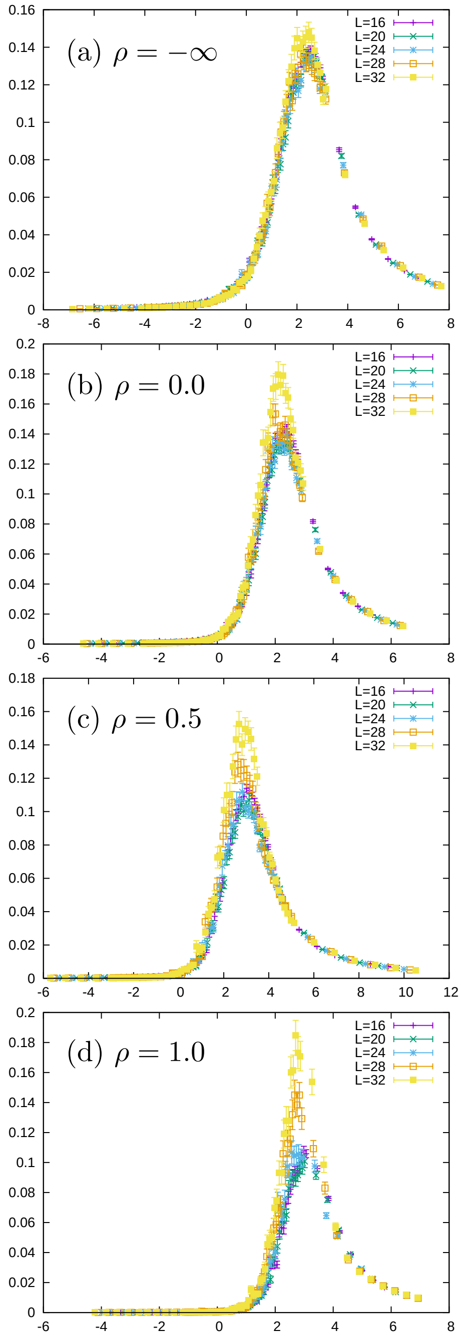

Figure 6: Scaling plot of the connected susceptibility of the 3D RFIM with (a) $\rho = -\infty$, (b) $\rho = 0.0$, (c) $\rho = 0.5$, and (d) $\rho = 1.0$.

symmetric matrix C into a matrix M and its transpose, $C = MM^T$. This factorization can be done by the Cholesky decomposition or the diagonalization. Once the matrix M is constructed, we can generate the correlated Gaussian random fields Y by multiplying the matrix M and a vector of independent standard Gaussian random numbers X as $Y = MX$. It is straightforward to confirm that the correlation between the components in Y is equal to C, i.e., $\langle\!\langle YY^T \rangle\!\rangle = C$. Note that the cost for the random field generation is proportional to L^{3d}. In this work, we use the parallel eigensolver via the Rokko Library [26] to generate 2^{20} samples of random field up to $L = 32$ and 14 for three-dimensional (3D) and four-dimensional (4D) cases, respectively.

Finite size scaling analysis

We calculated the specific heat, the connected and disconnected susceptibilities, the connected and disconnected Binder ratios, etc, by using the MCMC method. The connected and disconnected susceptibilities are defined by

$$\chi_{\rm con} = L^d \langle\!\langle\, \langle m^2 \rangle - \langle |m| \rangle^2 \,\rangle\!\rangle \qquad (6)$$

$$\chi_{\rm dis} = L^d [\langle\!\langle\, \langle |m| \rangle^2 \,\rangle\!\rangle - \langle\!\langle\, \langle |m| \rangle \,\rangle\!\rangle^2], \qquad (7)$$

respectively. The former represents the thermal fluctuations, whereas the latter does the random fluctuations. Accordingly, they are characterized by different critical exponents, γ and $\bar{\gamma}$, respectively.

In Fig. 6, we show the finite-size scaling plot of the connected susceptibility,

$$\chi_{\rm con} = L^{\gamma/\nu} \bar{\chi}_{\rm con}(L^{1/\nu}(T - T_{\rm c})) \qquad (8)$$

for the 3D RFIM with $\rho = -\infty$, 0.0, 0.5, and 1.0, from which the exponent γ and ν are estimated as listed in Table 1. We also performed similar analysis for the 4D RFIM with $\rho = -\infty$, 0.0, 0.5, 1.0, and 1.5. We found that the exponent γ increases gradually as ρ increases. This behavior is consistent with that the effective dimension decreases as ρ increases

Table 1: Critical exponents of the 3D and 4D RFIM obtained by the finite-size scaling analysis for the connected susceptibility.

d	ρ	T_{c}	ν	γ	D
3	$-\infty$	3.42(4)	1.4(2)	2.3(2)	1.3(1)
	0.0	3.55(6)	1.5(4)	2.5(7)	1.4(2)
	0.5	3.43(5)	1.5(3)	2.5(4)	0.8(3)
	1.0	3.17(9)	1.8(4)	3.0(2)	0.3(3)
4	$-\infty$	5.74(3)	0.8(1)	1.5(2)	2.0(2)
	0.0	5.82(6)	1.1(2)	2.1(3)	2.1(2)
	0.5	5.68(9)	1.3(3)	2.3(3)	1.7(2)
	1.0	5.5(2)	1.6(3)	2.6(4)	1.3(3)
	1.5	4.9(3)	2.3(6)	3.4(7)	1.0(1)

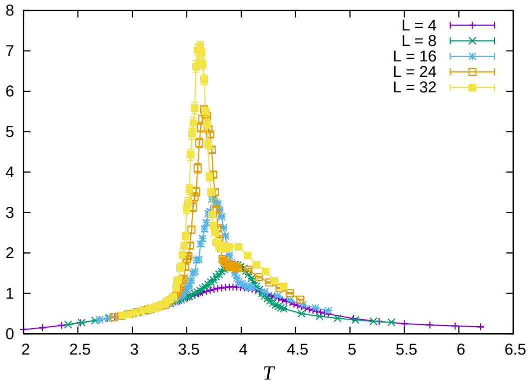

Figure 7: Temperature dependence of the specific heat of the 3D RFIM with $\rho = 0.5$. Growth of the second peak around $T \approx 4.0$ is clearly observed.

for $\rho \geq 0$ (cf. $\gamma = 1$, 1.2372, and 7/4 for the pure Ising model in four, three, and two dimensions, respectively). We observe the critical exponents for the 3D case with $\rho = 0.0$ agree with those for the 4D case with $\rho = 1.0$. This is again consistent with the previous theoretical prediction, $D = d - \rho$ at the upper and lower critical dimensions.

As seen clearly in Fig. 6, the finite-size scaling becomes worse as ρ increases. This might be due to the fact that the effective dimension approaches to the lower critical dimension, or becomes lower than that. Indeed, by using the scaling relation, $\eta = 2 - \gamma/\nu$ together with $D = d - \rho - 2 + \eta$, we can estimate the effective dimension of the criticality as presented in Table 1. The effective dimension is the same for $\rho = -\infty$ and 0.0, and starts to decrease both in the 3D and 4D cases as expected, and it becomes smaller than the lower critical dimension, $D = 1$, for 3D case with $\rho = 1.0$.

Finally, we mention the double peak structure of the specific heat. In Fig. 7, we show the temperature dependence of the specific heat of the 3D RFIM with $\rho = 0.5$. The sharper peak at lower temperature corresponds to the phase transition to the ordered phase. However, we observe that for sufficiently large ρ an extra peak appears at higher temperature. The weird double peak behavior may manifest another critical behavior at higher temperature [27], though we have no solid explanation for for the moment,

5 Summary

In this article, we have reviewed the recent advances in the Markov-chain Monte Carlo method, especially the irreversible kernel and the $O(N)$ method based on the geometric allocation technique. We present the results of our recent Monte Carlo study on the Ising model with long-range interaction as well as the correlated random-field Ising model, both of which exhibits critical behavior with non-integer effective dimensions depending on the decay exponent of the interaction or the spatial correlation of the random field. We established the upper and lower critical decay exponent for the 2D Ising model with LRI by using the $O(N)$ cluster Monte Carlo method together with the self-combined Binder ratio. For the correlated RFIM, we also observed that the effective dimension of the universality becomes small as the decay exponent increased. However, by the present accuracy of the MCMC simulation, we can not determine the critical decay exponent of the spatial correlation, at which the effective dimension becomes unity and thus the finite-temperature phase transition vanishes. This is due to the lack of efficient MCMC method for the system with random field. A further development of the MCMC technique for such systems with lower symmetry is strongly demanded.

Acknowledgment

The author acknowledge the collaboration with T. Horita and H. Suwa. The simulation code used in the present study has been developed on the ALPS Library [28, 29] and the Rokko Library [26].

References

[1] A. J. Bray: J. Phys. C **19** (1986) 6225.

[2] D. S. Fisher: Phys. Rev. Lett. **56** (1986) 416.

[3] M. E. Fisher, S.-K. Ma, and B. G. Nickel: Phys. Rev. Lett. **29** (1972) 917.

[4] Y. Imry and S. K. Ma: Phys. Rev. Lett. **35** (1975) 1399.

[5] A. Aharony, Y. Imry, and S. K. Ma: Phys. Rev. Lett. **37** (1976) 1364.

[6] M. Kardar, B. McClain, and C. Taylor: Phys. Rev. B **27** (1983) 5875.

[7] S. Todo: *Strongly Correlated Systems: Numerical Methods (Springer Series in Solid-State Sciences)*, ed. A. Avella and F. Mancini (Springer-Verlag, Berlin, 2013) pp. 153–184.

[8] O. F. Syljuasen and A. W. Sandvik: Phys. Rev. E **66** (2002) 046701.

[9] H. Suwa and S. Todo: Phys. Rev. Lett. **105** (2010) 120603.

[10] M. Michel, S. C. Kapfer, and W. Krauth: J. Chem. Phys. **140** (2014) 054116.

[11] S. Todo and H. Suwa: J. Phys.: Conf. Ser. **473** (2013) 012013.

[12] K. Fukui and S. Todo: J. Comp. Phys. **228** (2009) 2629.

[13] P. W. Anderson and G. Yuval: J. Phys. C **4** (1971) 607.

[14] A. Dutta and J. K. Bhattacharjee: Phys. Rev. B **64** (2001) 184106.

[15] J. Sak: Phys. Rev. B **8** (1973) 281.

[16] A. C. D. van Enter: Phys. Rev. B **26** (1982) 1336.

[17] E. Luijten and H. W. J. Blöte: Phys. Rev. Lett. **89** (2002) 025703.

[18] M. Picco: arXiv:1207.1018.

[19] T. Blanchard, M. Picco, and M. A. Rajabpour: Europhys. Lett. **101** (2013) 56003.

[20] M. C. Angelini, G. Parisi, and F. Ricci-Tersenghi: Phys. Rev. E **89** (2014) 062120.

[21] N. Defenu, A. Trombettoni, and A. Codello: Phys. Rev. E **92** (2015) 052113.

[22] S. Yasuda and S. Todo: Phys. Rev. E **88** (2013) 061301(R).

[23] T. Horita, H. Suwa, and S. Todo: Phys. Rev. E **95** (2017) 012143.

[24] E. Luijten and H. W. J. Blöte: Int. J. Mod. Phys. C **6** (1995) 359.

[25] G. Kamieniarz and H. W. J. Blöte: J. Phys. A: Math. Gen. **26** (1993) 201.

[26] https://github.com/t-sakashita/rokko/.

[27] R. Sacconi: J. Phys. A: Math. Gen. **31** (1997) 3751.

[28] B. Bauer, L. D. Carr, H. G. Evertz, A. Feiguin, J. Freire, S. Fuchs, L. Gamper, J. Gukelberger, E. Gull, S. Guertler, A. Hehn, R. Igarashi, S. V. Isakov, D. Koop, P. N. Ma, P. Mates, H. Matsuo, O. Parcollet, G. Pawlowski, J. D. Picon, L. Pollet, E. Santos, V. W. Scarola, U. Schollwöck, C. Silva, B. Surer, S. Todo, S. Trebst, M. Troyer, M. L. Wall, P. Werner, and S. Wessel: J. Stat. Mech.: Theo. Exp. (2011) P05001.

[29] http://alps.comp-phys.org/.

Recent Extensions and Applications of Parallel Cascade Selection Molecular Dynamics Simulations

Ryuhei HARADA and Yasuteru SHIGETA
Center for Computational Sciences, University of Tsukuba, 1-1-1 Tennodai, Tsukuba, Ibaraki 305-8577, Japan

1. Introduction

Proteins have incredibly complex structures and functions related to its structural dynamics, which are fundamental to various biological phenomena occurring *in vivo* such as molecular recognition, transport processes, enzymatic reactions, *etc*. Although more than 130,000 structures are currently stored in the Protein Data Bank (PDB), the direct measurement of structural changes, which are essential for a protein function, was quite limited in spite of the recent advances in single-molecule experiments. Alternatively, conventional molecular dynamics (CMD) are ways to reproduce biological phenomena *in silico*. However, it is often difficult for CMD to keep track with real biological phenomena owing to its accessible timescale. Thus, in order to theoretically observe large-scale structural changes such as protein folding and domain motion, extremely long-time dynamics [1-3], multi-canonical method [4-5], replica exchange method [6], metadynamics [7-9], temperature-accelerated MD method [10], *etc* were applied to overcome the timescale issue. However, they still need know-how for the individual problem and huge computer resources. Therefore, it is desirable to develop easier and automatic methods for transition pathway sampling of complicated systems such as proteins.

As a more straightforward and faster sampling method, we have proposed an efficient sampling method consisting of (1) an initial structure selection with high possibility of inducing structural changes and (2) structural resampling of initial structure based on short time MD. The key to this method is to select plausible initial structures from past trajectories. Once a transition path, which connects one stable structure to the other, is obtained, precise free energy analyses can be performed immediately. Therefore, this method might be more efficient than the other conformational sampling methods.

In this short review, the calculation schemes and several examples of structural changes of proteins are outlined (for details see the review paper [11]). In the following section, we explain the methodologies of our approach. Then, numerical results are discussed in Sec. 3. Concluding remarks are given in Sec. 4.

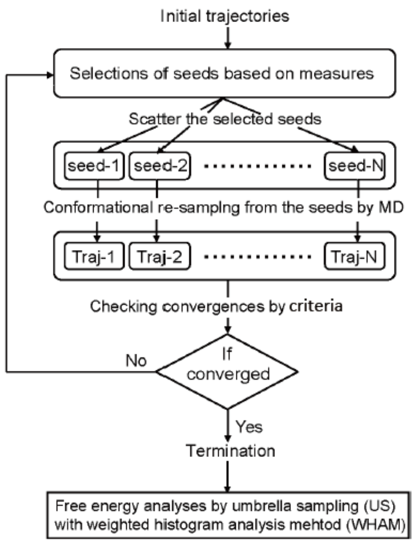

Figure 1. A flowchart of our conformational sampling scheme

2. Methodology

2.1. Basic Idea of Parallel Cascaed Selection Molecular Dymamics (PaCS-MD)

The method we have proposed is rather simple. The flowchart of the algorithm is shown in **Figure 1**. The calculation procedure of the structural sampling method is briefly described below.

I. Executing MD simulations from several selected initial structures ($n_{\mathrm{initial}} = N$) for a relatively short time with a canonical ensemble (*NVT* or *NPT*).

II. Ranking snapshots of each MD trajectory based on a predetermined rule (selection rule) for some measures.

III. Selecting the n_{initial} structures of the next cycle, where snapshots with higher rank are preferentially selected.

IV. Regenerating the initial velocities at the target temperature according to the Maxwell-Boltzmann distribution.

V. Repeating the cycles of (I) - (IV) until the distribution function along certain reaction coordinates does not change any more. Otherwise, the cycle ends when some of structures (or data) are sufficiently close to the target structure (or data).

VI. Applying the umbrella sampling (US) method [12-13] followed by the weighted histogram analysis method (WHAM) [14-15] to obtain free energy landscape projected onto reaction coordinates by referring a reactive trajectory obtained above. Markov State Model is also utilized to estimate free energy surfaces in terms of trajectories sampled by PaCS-MD.

The original methodology, i.e. PaCS-MD [16], ranks snapshots based on the similarity between the trajectory obtained from the short-time MD and the target structure (for example, root-mean square deviation (RMSD) between them). After determining the ranks, one selects the n_{initial} (typically 10 – 100) structures with higher rank as the initial structures of the next cycle and performs n_{initial} different short-time (typically 100 ps) MD simulations independently. By repeating the series of cycles, PaCS-MD generates closer structures to the target structure than those found in the previous cycle and occasionally induces structural transitions without using external perturbations.

2.2 Variants of PaCS-MD without using target structures

The disadvantage of the original PaCS-MD is to require the target state. To remove the drawback, we have developed several variants discussed below in detail. A conceptual difference from PaCS-MD is to use a different selection rule in each method, which has each advantage and disadvantage compared to PaCS-MD. Unlike PaCS-MD, its variants, i.e. fluctuation flooding method (FFM) [22], outlier flooding (OFLOOD) [24], structural dissimilarity sampling (SDS) [29] methods mentioned below, do not require a target (product) structure *a priori*, while these method take more cycles to find transition pathway than PaCS-MD does.

Dynamics of proteins involved in functional expression are often anisotropic, and certain vibrational modes with high anharmonicity are dominant. We consider that the anisotropy can be extracted by principal component analysis (PCA). We have developed FFM that efficiently induces structure transitions by assuming that protein structure with high structural fluctuation transits with high probability with structural re-sampling [22]. The basic concept of FFM is that the principal modes with large eigenvalues are chosen as reaction coordinates of a large amplitude motion and used for estimating measures. The snapshots with the maximum and minimum inner product values for the j-th principal component coordinates (PCj) and/or a multi-dimensinal PC vector space, which is obtained by PCA, are selected as the initial structures at the next cycle.

Metastable states exist in a high-dimensional subspace, where high density distributions appear during MD simulations and are detected as clusters, and transitions among different metastable states occur with large structural changes. Since the sparse distribution exists among clusters (sometimes between two clusters), a structure change is induced by intensively selecting structures with lower density distribution as the initials. Sparse distributions that do not belong to clusters are referred as "outliers" and can be detected using a hierarchical clustering method such as FlexDice [23]. Structural resampling intensively from the outliers of distribution is called as "OFLOOD” method [24], which promotes structural transformation efficiently in addition to its variants [24-28].

SDS, which realizes efficient structural sampling by repeating structural resampling, selects the initial structures so that the structural correlation with a structure (starting structure, mean structure, and so on) becomes as small as possible in the current cycle. This method is an effective technique when the target structure is unknown and a dissociation process of a molecular copmlex. For details of the calculation procedure, see the previous works [29-30].

2.3. Numerical Details

Initial structural data were taken from the PDB as the starting structures of PaCS-MD and its variants. After solvation with SPC/E or TIP3P water models and neutralization with counter ions, CMD simulations were performed under three-dimensional periodic boundary conditions using the Amber force field [31]. Water molecules were treated as rigid bodies with the SETTLE algorithm [32], while chemical bonds of the proteins were treated as rigid bodies with the LINCS algorithm [33]. To model the equilibrated systems, *NVT* simulations were first performed and followed by *NPT* simulations. *NVT* and *NPT* simulations were conducted with the modified Berendsen thermostat at 300 K [34] and the Parrinello-Rahman method at 1 bar and 300 K [35-36]. The equations of motion were integrated by the leapfrog method. The time step length was set to 2 fs. The cutoff value for Coulomb and van der Walls interactions was set to 10 Å. During conformational resampling, trajectories were recorded every 1 ps. For the PaCS-MD and its variant simulations, 10 or 100 different initial structures (n_{initial}) were simultaneously used for the efficient conformational sampling depending on the biological systems At every cycle, 100 ps short-time MD simulation with renewed velocity under *NVT* ensemble ($T = 300$ K) were launched until sufficient conformational sampling was accomplished. For the free energy analysis, 200 reference structures were randomly selected from the trajectories of FFM and the umbrella sampling for each reference structure was performed for 1ns and followed by WHAM to estimate the free energy landscape of T4L. All MD simulations were performed with the GPU version of the Gromacs 5.0.7 package [37].

3. Results and Discussion

3.1 Domain motion of T4L by FFM

As an example of FFM, we here explain results of an open-closed structure transition of T4L. The open structure of T4L (wild type) was chosen as a starting structure. In order to induce structural transition, we selected the first and second principal coordinates (PC_1 and PC_2) as the reaction coordinates. In order to obtain PCs, CMD (10 ns) from the open structure was performed *a priori*, then PCA was performed using the 10-ns trajectory. According to the accumulated contribution of principal modes (PMs), the open-closed conformational transition can be sufficiently described because

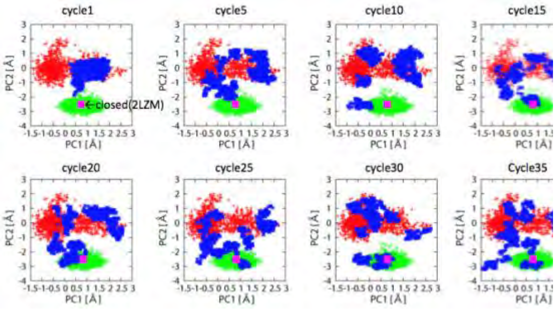

Figure 2: Conformational transition pathways from the open to the closed states of T4 lysozyme reproduced by FFM.

the top two PMs accounted for 80% or even more of the overall protein structure fluctuation. Here, we show the structural transition process from the open to closed structures of T4L reproduced by FFM [16]. **Figure 2** shows the accumulated distributions of trajectories projected onto a subspace spanned by PC_1 and PC_2. For comparison, we also depicted red points (green points) which show the projection of a conventional MD trajectory (10 ns) from the open structure (the closed structure). The projected points by FFM (blue points) expand to the periphery and reaches the closed structure (magenta) within about 15 cycles (several tens of ns). After 15th cycles, the accumulated trajectories travels all over regions in the subspace. As a comparative calculation, extremely long-time CMD simulation (1 μs) was started from the open structure. However, no open-close conformational transition was observed. After FFM, we estimated FEL onto the subspace as illustrated in **Fig. 3**, whose cost was 200 ns, indicating the efficient structure search and FEL analyses of FFM. According to this result, the free energy barrier and transition states are clearly found between two states.

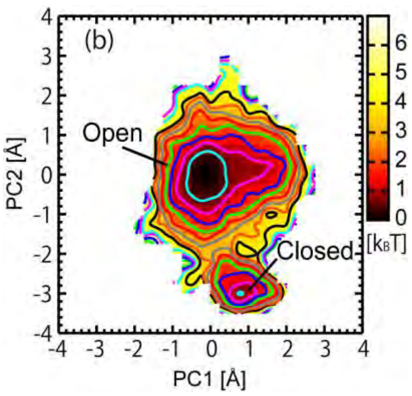

Figure 3: Conformational transition pathways from the open to the closed states of T4 lysozyme reproduced by FFM.

3.2 Protein folding pathway of Villin by OFLOOD method

As an application example of the OFLOOD method, we here show the protein folding process of the small protein Villin (35 residues). Partial RMSDs, helix 1 - helix 2 (segment A) and helix 2 - helix 3 (segment B), measured from the native structure were used as the reaction coordinates, which had been defined in the previous study [32]. After modeling the amino acid chain, structural sampling by the OFLOOD method with 100 seeds was repeated for 20 cycles, where the generalized Born and surface area (GB/SA) solvation model was adopted for the solvent around the Villin.

The projection of the trajectories generated by the OFLOOD method is shown in **Figure 4**. It is easily found that the outliers (black points) were located the edge of the distribution at each cycle and became broaden as cycles went by. It took about 10 cycles to reach the native structure of Villin highlited by a cross in **Figure 4**. The minimum C_α RMSD measured from the X-ray crystal structure after the end of 20 cycles was 0.60 Å, indicating that natural structure can be sampled by the OFLOOD method accurately. Furthermore, we also extracted a minor pathway (see right bottom of **Figure 4**) that could not be observed in the

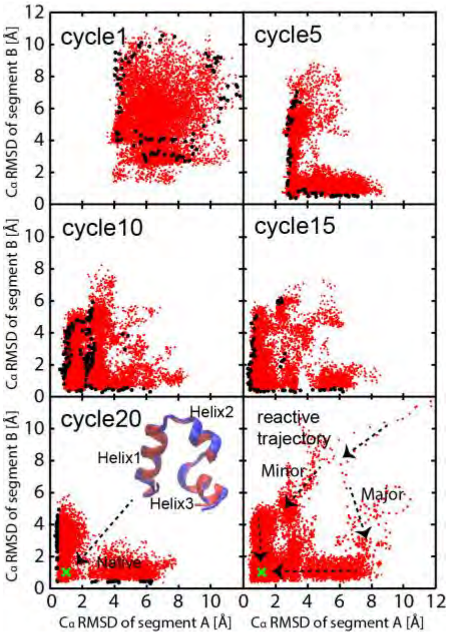

Figure 4. Major and minor folding pathways of Villin reproduced by OFLOOD method

previous study [4]. Concerning to the computational efficiency, the cumulative computation time to sample the native structure (C_α RMSD <1.0 Å) was 135.6 ns. We could extract the folding path very efficiently compared to the replica exchange MD (8 μs) [4]. Since computational cost required in our calculations was ns-order and the time-scale of the protein folding process is μs-order, the OFLOOD method is quite efficient for finding protein folding pathways.

3.3 Open-to-Closed structure transition pathway searches by SDS

To show the conformational sampling efficiency, SDS was applied to structural transition between two different states (open and closed states) of maltodextrin binding protein (MBP) in explicit water. MBP is a protein consisting of 370 residues and induces large-amplitude domain motions for ligand binding. In this example, apo-type simulations were considered. CMD simulation may be useful for reproducing the large-amplitude (open-closed) domain motions of MBP. However, we have not detected the structural transition at all, even if a long-time (1 μsec) simulation was perform starting from the open state. Instead we have performed SDS simulations for 50 cycles starting both from the apo-type closed and open states. As a result of the demonstration starting from the open (closed) structures, the minimum values of Cα RMSD measured from the X-ray crystal structure of closed (open) forms were 0.78 Å (0.89 Å) as illustrated in **Fig. 5**. The closest snapshots to the X-ray crystal structures sampled by the SDS simulations are overlapped

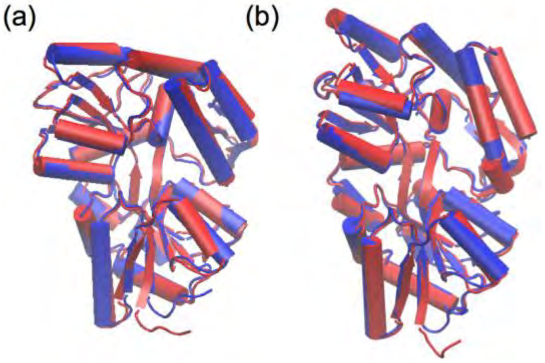

Figure 5: (a) Snapshot with the minimum value of RMSD (0.78 Å) measured from the closed state of MBP (red), which was sampled by SDS during the 50 cycles starting from the open state of MBP. (b) Snapshot with the minimum value of RMSD (0.89 Å) measured from the open state of MBP (red). Each snapshot is superimposed with the X-ray crystal structure (blue).

in **Figure 5(a)** and **5(b)**, indicating that SDS also induces the open-to-closed and its inverse conformational transitions quite efficiently and gave accurate structures without knowledge of the well-defined target structures.

4. Conclusion

In this review, we outline the PaCS-MD and its variants and show examples of their applications. If the reactant and the protein structure of the product are known, PaCS-MD can be applied to extract the path connecting the two end-point structures. On the other hand, FFM, OFLOOD, and SDS are applicable to extract transitional pathways starting from the protein structure of a given reactant without knowldge of any product. For example, FFM started with an open structure and derives an open-closed domain motion of T4L using ns-order simulation. OFLOOD also presumed Villin's folding pathways using ns-order simulations starting with fully extended structures. SDS generates both open-to-closed and closed-to-open structural transitions of MBP within 500 ns-order simulations. These types of methods may be convenient for predicting metastatic pathways or starting from a given reactant without knowledge of the reactants and finding the local/global energy minimum state of proteins , Which is one of the advantages of three-dimensional sampling.

Acknowledgement

This work was supported by Japan Society for the Promotion of Science (JSPS) KAKENHI Grant-in-Aid for Young Scientists (A) (No. JP16H06164), and by Grant-in-Aid for Scientific Research of the Innovative Areas (Nos. JP26102525, JP 26107004, and JP 26105012) from JSPS. The computations were performed using the RIKEN Integrated Cluster of Clusters (RICC), Super Computer Center of Institute of Solid State Physics, The University of Tokyo and COMA / HP-PACS at the CCS, University of Tsukuba.

References

[1] D.E. Shaw, *et al.*, *Commun. Acm.*, **51** (2008) 91.

[2] D.E. Shaw, *et al.*, *Science*, **330** (2010) 34.

[3] K. Lindorff-Larsen, S. Piana, R.O. Dror, D.E. Shaw, *Science*, **334** (2011) 517

[4] N. Nakajima, H. Nakamura, A. Kidera, *J. Phys. Chem. B*, **101** (1997) 817.

[5] U.H.E. Hansmann, Y. Okamoto, F. Eisenmenger, *Chem. Phys. Lett.* **259** (1996) 321.

[6] Y. Sugita, Y. Okamoto, *Chem. Phys. Lett.*, **314** (1999) 141.

[7] A. Laio, M. Parrinello, *Proc. Natl. Acad. Sci. U. S. A.* **99** (2002) 12562.

[8] A. Laio, F.L. Gervasio, *Rep. Prog. Phys.* **71** (2008) 126601.

[9] P. Raiteri, A. Laio, F.L. Gervasio, C. Micheletti, M. Parrinello, *J. Phys. Chem.*

B, **110** (2006) 3533.

[10] C.F. Abrams, E. Vanden-Eijnden, *Proc. Natl. Acad. Sci. U. S. A.* **107** (2010) 4961.

[11] R. Harada, Y. Takano, T. Baba, Y. Shigeta, *Phys. Chem. Chem. Phys.*, **17** (2015) 6155.

[12] G.M. Torrie, J.P. Valleau, *J. Comput. Phys.*, **23** (1977) 187.

[13] G.M. Torrie, J.P. Valleau, *J. Chem. Phys.*, **66** (1977)1402.

[14] A.M. Ferrenberg, R.H. Swendsen, *Phys. Rev. Lett.*, **63** (1989) 1195.

[15] M. Souaille, B. Roux, *Comput. Phys. Commun.*, **135** (2001) 40.

[16] R. Harada, A. Kitao, *J. Chem. Phys.*, **139** (2013) 035103.

[17] R. Harada, A. Kitao, *J. Chem. Theory Comput.*, **11** (2015) 5493.

[18] R. Harada, Y. Shigeta, *J. Comput. Chem.*, **38**, 2671, (2017).

[19] R. Harada, Y. Shigeta, *Bull. Chem. Soc. Jpn.*, **90** (2017) 1236.

[20] R. Harada, Y. Shigeta, *Chem. Lett.*, **46** (2017) 862.

[21] R. Harada, Y. Shigeta, *Mol. Simul.*, **44** (2017) 206.

[22] R. Harada, Y. Takano, Y. Shigeta, *J. Chem. Phys.*, **140** (2014) 125103.

[23] T. Nkamura, Y. Kamidoi, N. Wakabayashi, N. Yoshida, *IPSJ J. Database*, **46** (2005) 40.

[24] R. Harada, T. Nakamura, Y. Takano, Y. Shigeta, *J. Comput. Chem.*, **36** (2015) 97.

[25] R. Harada, T. Nakamura, Y. Shigeta, *Chem. Phys. Lett.*, **639** (2015) 269.

[26] R. Harada, T. Nakamura, Y. Shigeta, *J. Comput. Chem.*, **37** (2016) 724.

[27] R. Harada, T. Nakamura, Y. Shigeta, *Bull. Chem. Soc. Jpn.*, **89** (2016) 1361.

[28] R. Harada, Y. Takano, Y. Shigeta, *J. Comput. Chem.*, **38** (2017) 790.

[29] R. Harada, Y. Shigeta, *J. Comput. Chem.*, **38** (2017) 1921.

[30] R. Harada, Y. Shigeta, *Phys. Chem. Chem. Phys. acceped for publication* (2018).

[31] Y. Duan, *et al.*, *Comput. Chem.* **24** (2003) 1999.

[32] S.Miyamoto, P.A. Kollman, *J. Comput. Chem.* **13** (1992) 952.

[33] B. Hess, H. Bekker, H.J. Berendsen, J.G.E. Fraaije, *J. Comput. Chem.* **18** (1997) 1463.

[34] G. Bussi, D. Donadio, M. Parrinello, *J. Chem. Phys.* **126** (2007) 014101.

[35] S. Nose, M.L. Klein, *Mol. Phys.* **50** (1983) 1055.

[36] M. Parrinello, A. Rahman, *J. Appl. Phys.* **52** (1981) 7182.

[37] M.J. Abraham, D. van der Spoel, E. Lindahl, B. Hess, and the GROMACS development team, *GROMACS User Manual version 5.0.7*, www.gromacs.org (2015).

3.2 First-Principles Calculation of Material Properties

Atomic Structures and Electronic Properties of Hard- and Soft-Nanomaterials

Atsushi Oshiyama
Department of Applied Physics, The University of Tokyo
Hongo, Tokyo 113-8656

In the fiscal year of 2017, on the basis of the density-functional theory we have clarified 1) roles of stacking faults in electronic properties at SiC/SiO_2 interfaces[1], 2) physical and chemical origins of the electron states at the Fermi level and the disappearance of so called Dirac states in silicene on Ag substrate using our newly developed unfolding technique2, 3, and 3) the atom-scale mechanism of the atom manipulation by using AFM tip on Si (111) surface[4]. In the following, I explain the first issue.

An intrinsic interface state controlled by atomic stacking sequence at SiC/SiO_2

To realize energy-saving society, highly efficient power devices are necessary. SiC has been recognized to be suitable for such purpose due to its prominent material properties. SiC-MOSFET devices are indeed available commercially. However, they still face a severe problem that the electron mobility is far from the theoretical values due to the huge density of interface levels at the SiC/SiO_2 interface. In particular, energy levels appearing in the gap within the range of 0.3 eV below the conduction band minimum (CBM) are known to cause the substantial reduction of the electron mobility.

SiC is a tetrahedrally bonded semiconductor in which atomic bilayers consisting of Si and C atoms are stacked along the bond direction. Different stacking sequences lead to polytypes. Figure shows three typical SiC polytypes, 2H, 3C, and 4H structures. The most frequently obtained structure is the 4H-structure whose stacking sequence is depicted as ABCB. Although the local atomic structures of polytypes are identical to each other, their electronic properties, in particular, the band gaps, are known to differ from one to another. As we have clarified [PRL, 112, 136403 (2014)], this is due to the interesting character of the CBM: i.e., the wavefunction of the CBM is not distributed around the atomic sites but is extended or floats in the interstitial structural channels generally existing in the tetrahedrally bonded structures. This *floating* nature renders the energy level of the CBM being strongly affected by the length of the internal structural channel which is peculiar to each polytype.

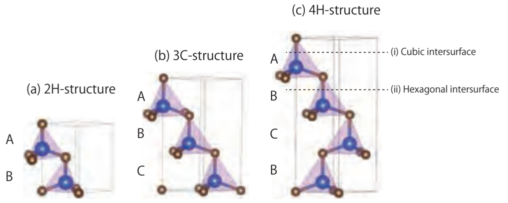

Figure 1: Atomic structures of (a) 2H-SiC, (b) 3C-SiC, and (c) 4H-SiC polytypes. Different stacking sequences of atomic bilayers are depicted by the letters, A, B and C. In (c), two dotted lines show (i) the cubic and (ii) the hexagonal surface planes. When SiO_2 films contact with the SiC substrate at the position (i) or (ii), we call it the cubic or the hexagonal interface.

Considering the layer-by-layer oxidation of 4H-SiC (0001) surface, only two types of the stacking termination at the interface are possible. Those correspond to the two interface planes shown by the dotted lines in Figure (c): One is a cubic interface [BCBA-stack/SiO_2 as shown in Figures (c) and (a)], and the other is a hexagonal interface [ABCB-stack/SiO_2 as in Figures (c) and (b)]. In addition to those interfaces, we here consider a stacking-fault interface, where the topmost stacking sequence in the hexagonal interface ABCB is changed to be ABCA, forming the ABCA-stack/SiO_2 shown in Figure (c). As deduced from the *floating* nature explained above, the variation of the stacking sequence near the interface leads to the variation of the channel length there and hereby varies the energy level of the CBM at the interface.

Figure is the calculated Local density of states (LDOS) for the three interfaces. Importantly, in the energy region near the CBM, the LDOS at the interface is sensitive to the atomic stacking

(a) Cubic stacking

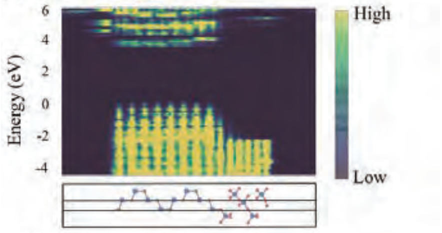

(b) Hexagonal stacking

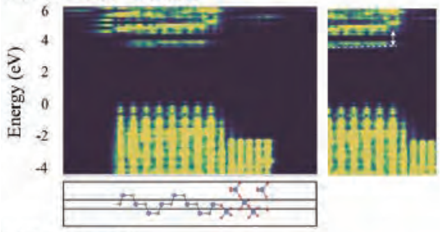

(c) Stacking fault

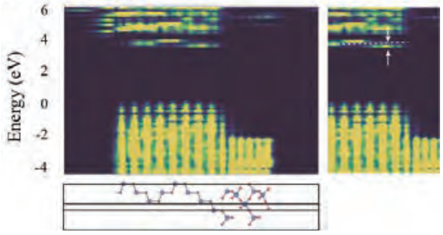

Figure 2: Calculated LDOS by the HSE functional for the cubic (a), the hexagonal (b), and the stacking-fault (c) interfaces. The left and right sides correspond to the SiC and SiO_2 regions.

at the interface. Comparing Figures (a) and (b), we have found that the hexagonal-stacking interface (ABCB-stack/SiO_2) induces an interface state located about 1.2 eV above the bulk CBM. This interface state is caused by the quantum confinement of the bulk CBM state in the shorter interstitial channel near the interface. Furthermore, in the stacking-fault interface (ABCA-stack/SiO_2), an interface state caused by the modulation of the length of the interstitial channel is located at 0.3 eV below the bulk CBM [Figure (c)]. This interface state induces not a single level but a band as observed in Figure (c). The width of the band is due to the kinetic energy dispersion in the lateral plane of the interface state. This unequivocally clarifies that the stacking difference near the interface changes the interface properties considerably.

Imperfection of atomic stacking is commonly observed in tetrahedrally bonded semiconductors. This planar imperfection has been thought to play a minor role in electronic structure. However, we have found, for the SiC(0001) surface or the interface, that this stacking sequence determines the length of the internal channel and thus induces interface states near CBM, which are strong candidates for the mobility killer, not yet identified before, in the performance of MOSFET devices. Importantly, the mechanism for the appearance of those interface states is the intrinsic *floating* nature of the conduction electrons in SiC. In contrast, the channel lengths are infinite in 3C-SiC. This fact means that the channel structure modification at interface can not be seen in 3C-SiC. Therefore, the interface states induced by stacking near the interface is not expected in 3C-SiC. Another noteworthy thing in 4H-SiC is non-polar surfaces such as $(11\bar{2}0)$- or $(1\bar{1}00)$-face. In actual SiC-MOSFET devices, non-polar surfaces In SiC MOSFET, non-polar surfaces such as $(11\bar{2}0)$- or $(1\bar{1}00)$-face are occasionally used for the device fabrication. In those non-polar surfaces, the lengths of the channels are infinite, thus being independent of the bilayer stacking along the (0001) direction. Hence, the interface state near the CBM is not expected to emerge by the stacking modulation on the non-polar surface. From this viewpoint, the $(11\bar{2}0)$ and $(1\bar{1}00)$ surfaces are expected to have advantages than the (0001) surface to fabricate high-performance SiC devices.

Related Publuications

1. Y.-i. Matsushita and A. Oshiyama, Nano Lett. **17**, 6458 (2017).
2. J.-I. Iwata, Y.-i. Matsushita, H. Nishi, Z.-X. Guo, and A. Oshiyama, Phys. Rev B **96**, 235442 (2017).
3. Y.-i. Matsushita, H. Nishi, J.-i. Iwata, T. Kosugi and A. Oshiyama, Phys. Rev. Materials **2**, 010801 (R) (2018).
4. B. Enkhtaivan, Y. Sugimoto and A. Oshiyama, Phys. Rev. B **96**, 155417 (2017).

Analyses on atomic structure, magnetism, and electronic structure in spintronics materials and molecular magnets

Tatsuki ODA[1,2], Mega CHRISTIVANA[2], Tomosato KANAGAWA[2], Indra PARDEDE[2],
Nurul IKHSAN[2], Hasan Al RASYID[2], Masao OBATA[2]
[1]*Institute of Science and Engineering, Kanazawa University, Kanazawa, Ishikawa 920-1192*
[2]*Graduate School of Natural Science and Technology, Kanazawa University, Kanazawa, Ishikawa, 920-1192*

We studied the several topics involved with this project; magnetic anisotropy and its electric field (EF) effect in the thin film related with spintronic devices. We also developed a method of van der Waals density functional (vdW-DF) approach for magnetic systems. These investigations have been done by employing the home-made density functional code, which has run efficiently in the architectures in Systems B in ISSP.

Magnetic anisotropy and electric field effect

Magnetic anisotropy energy (MAE) and its EF effect were investigated in the slab system of V/Fe/MgO by using first-principles calculation.

Such system keeps the Fe/MgO interface and was reported as a system with a large voltage-control magnetic anisotropy (VCMA) coefficient. We estimated MAEs and VCMA coefficient and analyzed the electronic structures in V/Fe/MgO slabs. As the results, we found the maximum perpendicular magnetic anisotropy energy of 1.5 mJ/m^2 and tends to decrease with the decreasing lattice constant. The EF control coefficient of MAE initially tends to increase to the reach maximum value 136 fJ/Vm with increasing the lattice constant, and then decreases to a negative value at the strain of 5.23% inducing with respect to the Fe lattice constant. This behavior may be addressed to the modulation of eigenstates of Fe minority d-orbital component at the interface near the Fermi level.

Van der Waals density functional approach

The vdW-DF approach is one of promising methods to overcome the problem that the density functional approach, such as local density approximation or generalized gradient approximation, cannot describe van der Waals (vdW) force properly. We have proposed the extension of vdW-DF to spin-polarized systems, vdW-DF-SGC (SGC stands for spin-polarization-dependent gradient correction), and demonstrated the usefulness. Another spin van der Waals method (svdW-DF) was developed in 2015. We found that the results of the svdW-DF is very similar to those of the vdW-DF-SGC by using the alpha solid oxygen.

We have extended the methods of vdW-DF to noncollinear magnetism. To demonstrate them, we have carried out the electronic structure calculation for the beta solid oxygen which has a spin configuration of 120 degree in the same oxygen layer. The results for the optimized crystal structure show an agreement with those obtained by experiments. We may study inadequate elements of vdW-DF to reproduce the structural properties in oxygen systems.

Analyses on atomic, magnetic, and electronic structures in high-performance spintronics materials and molecular magnets

Tatsuki ODA[1,2], Mega CHRISTIVANA[2], Tomosato KANAGAWA[2], Indra PARDEDE[2], Nurul IKHSAN[2], Hasan Al RASYID[2], Masao OBATA[2]

[1]*Institute of Science and Engineering, Kanazawa University, Kanazawa, Ishikawa 920-1192*

[2]*Graduate School of Natural Science and Technology, Kanazawa University, Kanazawa, Ishikawa, 920-1192*

We studied the several topics involved with this project; magnetic anisotropy and its electric field (EF) effect in the thin film related with spintronic devices and ferrimagnetic spinels. These investigations have been done by employing the home-made density functional code, which has run efficiently in the architectures in Systems B in ISSP. Additionally, we used a code of quasiparticle self-consistent GW method (QSGW) developed by Kotani et al.[1].

Magnetic anisotropy and electric field effect

Magnetic anisotropy energy (MAE) and its EF effect were investigated in the slab system of Cr/[CrFe]/Fe/MgO by using first-principles calculation. We estimated MAEs and voltage-control magnetic anisotropy (VCMA) coefficient (γ) and analyzed the electronic structures. We observe that the perpendicular magnetic anisotropy energy (PMAE) is enhanced when introducing Fe/Cr interchanges, compared with the system without interchange. This is related to the significant orbital reconstruction in electronic structure of Fe at the interface as a proximity effect of Cr. In this system, the enhanced PMAE can be achieved by both expansive and compressive strains. These behaviors are related to the oscillation position of d-orbital states near the Fermi level with magnetic quantum number $|m|=1$ and $|m|=2$. For the second one, we found that sign changes in γ are also induced by Fe/Cr interchanges and much enhanced at the compressive strain -3.1%, appearing with the minimum value of -170 fJ/Vm. The enhancement of γ is strongly related to the density of states (DOSs) in the vicinity of the Fermi level. Small modulation by EF in large DOS near and/or cross the Fermi level will increase or decrease the number of coupling states between occupied and unoccupied states. Hence, the PMAEs will significantly change, according to through the second order perturbation theory.

Nickel cobaltite spinels

Spinel compounds, AB_2X_4, could exhibit many different properties due to the choice of A, B and X atoms. The spinel compound $NiCo_2O_4$, which has a ferrimagnetic property, shows an interesting peculiar variation on its metallicity and magnetism, widely spanned from metallic-ferrrimagnetic until non-magnetic insulator. This unique properties of $NiCo_2O_4$ opens many possibilities for its application, i.e. as catalyst in oxygen reduction reaction, photonic devices, etc. To have better understanding and encourage efficient development process, we investigated electronic structures. We employed the density functional theory (DFT) and quasiparticle self-consistent GW method (QSGW) to elucidate electronic and magnetic properties of different types of $NiCo_2O_4$. The QSGW method is considered as one of post-DFT method that can better describe the properties of materials, due to its inclusion of many-body effects among electrons and the self-consistent treatment [1].

The QSGW shows a larger band gap on the majority spin state, compared to the GGA method. From its band structure, we found that NiCo2O4 has direct band gap around X point. This information might be important for experiment research to explore optical band gap properties from the angle-resolved photoemission spectroscopy (ARPES).

The discrepancies arose between both methods were also investigated, especially those on conduction band of majority-spin regarding hybridization of Ni e_g-orbital and that of octahedral Co. The band structure from the QSGW method have better agreement with the model proposed previously.

This information could be taken in making the model of interaction on $NiCo_2O_4$ surface.

[1] T. Kotani et al., PRL, **96**, (2006), 226402.

Large-scale device-material research by massively parallel electronic structure calculation and data science

Takeo Hoshi

Department of Applied Mathematics and Physics, Tottori University,
4-101 Koyama-Minami, Tottori 680-8550, Japan.

The present project was carried out for the joint research between electronic structure calculations and data science. Related mathematical studies and software development were also carried out. The main collaborators are Yusaku Yamamoto (U. Elec. Comm.), Koji Hukushima (U. Tokyo), Takatoshi Fujita (IMS), Hiroyuki Matsui (Yamagata U.), Toshio Hyodo and Ayahiko Ichimiya (KEK).

The large-scale electronic-state and transport calculations were carried out for flexible organic devices. As a main achievement, principal component analysis (PCA) was carried out so as to analyze large-scale electronic state calculation data for exploration of organic polymer device materials [1-3]. The method is given by the dimensional reduction of electronic wavefunctions, since the original data size is huge. The reduction is realized, when the participation ratio of wavefunctions, a measure of quantum localization, is chosen as the descriptor. The computation was carried out for electronic states for 40,000 samples of disordered organic polymers with 1,200 atoms by our large-scale electronic state calculation code ELSES (http://www.elses.jp/) on the K computer. As results, the polymer samples are classified into four groups correctly and the physical meaning of the principal components is clarified. The present method is general and forms a rigorous foundation of the data-driven material science. Numerical methods for large-scale electronic state calculations were developed for efficient contour integral [4], intermediate eigenpair computation [5], middleware for parallel eigenvalue computation with the performance prediction function by Bayesian inference [6]. In addition, preliminary researchs were carried out for large-scale exiton calculation of organic interface [7] and large-scale electronic state calculation of disordered pentacene thin film [8], the development of data analysis on positron diffraction experiment [9].

As mathematical studies, we developed a new preconditioner for the CG method which combines the block red-black ordering with relaxed modified incomplete Cholesky factorization. Numerical experiments on a multicore processor shows that the preconditioner is both effective and scalable [10]. We also developed a new algorithm for the nonlinear eigenvalue problem based on signed singular values [11].

References

[1] T. Hoshi, H. Imachi, K. Oohira, Y. Abe, and K. Hukushima, ‘Principal component analysis with electronic wavefunctions for exploration of organic polymer device materials’, International Meeting on High-Dimensional Data-Driven Science , Kyoto, 10-13. Sep. 2017

[2] T. Hoshi, H. Imachi, Y. Abe, K. Oohira, K. Hukusima, ‘Principal component analysis with large-scale electronic state calculation for ultra-flexible device materials’, Waseda U., 18th SIAM Conference on Parallel Processing for Scientific Computing (SIAM-PP18), 7-10, Mar. 2018.

[3] (Award) T. Hoshi, ‘Organic-device material research based on 100-nano-meter electronic structure calculation and data science’, Excellent achievement award of HPCI projects, 2. Nov., 2017.

[4] H. Kohashi, K. Sugita, M. Sugihara and T. Hoshi, ‘Efficient methods for computing integrals in electronic structure calculations’, JSIAM Letters 9, pp. 81-84 (2017)

[5] D. Lee, T. Hoshi, T. Sogabe, Y. Miyatake, S.-L. Zhang, ‘Solution of the k-th eigenvalue problem in large-scale electronic structure calculations’, submitted; Preprint (http://arxiv.org/abs/1710.05134).

[6] T. Hoshi, T. Fukumoto, T. Fukaya, Y. Yamamoto, ‘Analysis and prediction of the performance in generalized eigenvalue solvers on Oakforest-PACS’, International Workshop on Eigenvalue Problems: Algorithms; Software and Applications, in Petascale Computing (EPASA2018), 5-6, Mar. 2018.

[7] MD K. ALAM, T. Fujita, T. Hoshi, ‘Excited-state calculation for large size C60/Pentacene interface based on the fragment molecular orbital method’, Meeting of The Japan Society of Applied Physics, Hakata, 5-8, Sep 2017.

[8] T. Hoshi, Y. Abe, A. Kuwata, K. Kakuda, T. Fujita, H. Matsui, 'Large-scale electronic state calculation in disordered pentacene thin film', Meeting of The Japan Society of Applied Physics, Waseda U., 17-20, Mar. 2018 (Japanese)

[9] T. Hoshi, K. Tanaka, I. Mochizuki, T. Hyodo, A. Ichimiya, Y. Nakanishi, K. Hukushima, ‘Development of data analysis software for positron diffraction’, 2nd Workshop on Positron Diffraction, organized by T. Hyodo and T. Hoshi, KEK Tsukuba, 30. Mar. 2018. (Japanese)

[10] A. Shioya and Y. Yamamoto, 'The danger of combining block red–black ordering with modified incomplete factorizations and its remedy by perturbation or relaxation', Jpn. J. Ind. Appl. Math., 35, pp 195-216 (2018).

[11] K. Ooi, Y. Mizuno, T. Sogabe, Y. Yamamoto and S.-L. Zhang, 'Solution of a nonlinear eigenvalue problem using signed singular values', East Asian J. Appl. Math. 7, pp. 799 - 809 (2018).

Development of first-principles electronic-structure and transport calculation method based on real-space finite-difference approach

Tomoya ONO
Center for Computational Sciences, University of Tsukuba
Tennodai, Tsukuba, Ibaraki 305-8577

1 Introduction

Among the high-k materials, HfO_2 is one of the most intensively studied materials for the gate oxide of MOSFET because of its large dielectric constant, large band gap, and thermodynamic stability. The performance of such high-k-based MOSFETs depends on the interface state formed between the HfO_2 layer and Si substrate. Oxygen vacancies are generated in the HfO_2 layer, SiO_2 layer, and at HfO_2/SiO_2 interface. However, the relationship between the leakage current and oxygen vacancies in high-k gate stacks is not fully understood.

In this study, the leakage current through $HfO_2/SiO_2/Si(001)$ gate stacks are investigated by a first-principles calculation based on density functional theory (DFT).

2 Computational models and methods

Several studies on HfO_2-based gate stacks involving first-principles calculations have been performed using interface atomic structures consisting of crystalline SiO_2 and HfO_2. The monoclinic HfO_2 structure is widely employed for the computational models in first-principles calculations. In accordance with previous studies, the monoclinic HfO_2/β-cristobalite SiO_2/Si structure is employed for our computational model, as shown in Fig. 1. Following the study by Capron *et al.*,[1] oxygen vacancies are inserted by removing an O atom from the HfO_2 layer, HfO_2/SiO_2 interface plane, or SiO_2 interlayer and the doubly positively charged state is considered for the vacancy in the HfO_2 layer. The positions of oxygen vacancies are indicated by arrows in Fig. 1(b). The model without the O atom indicated by Ox is referred to as V_{Ox}.

To perform the electronic-structure and electron-conduction calculations, we employ first-principles calculation code RSPACE[2] based on DFT and real-space finite-difference method. The other computational details are explained in Ref. 3. The interface atomic structures in the scattering region are those obtained by the structural optimization. In our computational model for the electron-conduction calculation, a monoclinic HfO_2/β-cristobalite SiO_2/Si structure consisting of three molecular layers of HfO_2, two molecular layers of SiO_2, and eight atomic layers of Si is suspended between Al jellium electrodes.

3 Leakage current

The ratios of the leakage current are shown in in Table 1, where the leakage current of the interface without oxygen vacancies is set to 1. It is found that the leakage current is increased by the generation of oxygen vacancies in the HfO_2 layer. In the cases of V_{O1} and V_{O1}^{2+}, the leakage currents are 247 and 396 times that in the model before the generation of oxygen va-

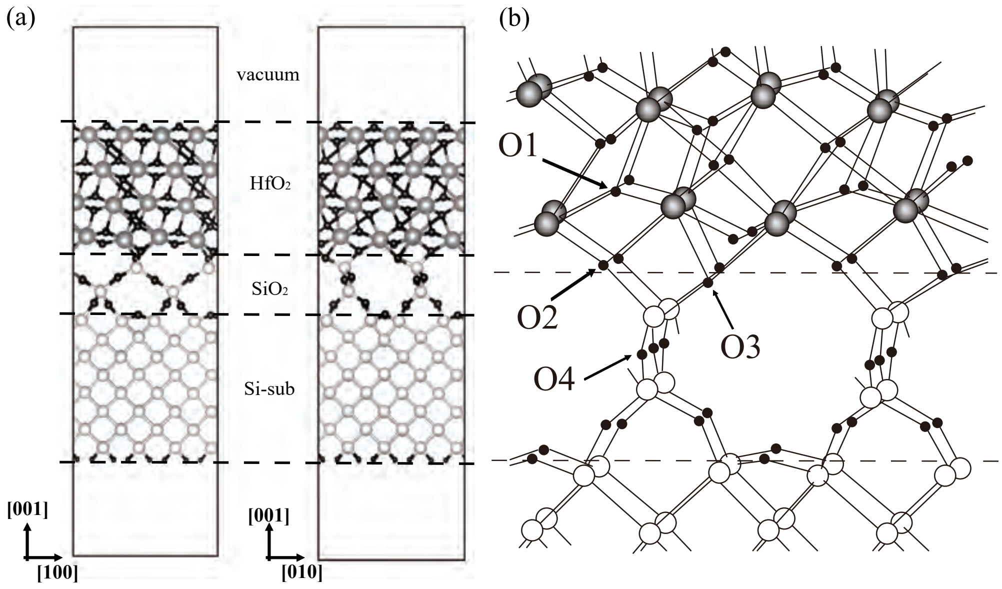

Figure 1: (a) Computational model of monoclinic HfO_2/β-cristobalite SiO_2/Si(001). Gray, black, white, and small black balls represent Hf, O, Si, and H atoms, respectively. (b) Enlarged view at the interface plane. Arrows represent O atoms that are removed. The model without an O atom at an Ox site is referred to as V_{Ox}. Figure is taken from Ref. 3.

Table 1: Ratios of leakage current for models with and without oxygen vacancies. Data are taken from Ref. 3.

Model	Current ratio
No oxygen vacancy	1.0
V_{O1}	247
V_{O2}	1.3
V_{O3}	3.6
V_{O4}	2.6
V_{O1}^{2+}	396

cancies, respectively. On the other hand, the amount of the leakage current is comparable when oxygen vacancies exist at the HfO_2/SiO_2 interface plane or in the SiO_2 interlayer. It is reported that charged oxygen vacancies appear in an n-type MOSFET under zero gate voltage stress or a p-type MOSFET under finite gate voltage stress. The ratio of the leakage current of V_{O1}^{2+} is larger than that of V_{O1}, however the effect of charged states is not significant compared with the position of the vacancies. It is reported by an experimental study that doubly charged oxygen vacancies are replaced by neutral oxygen vacancies by applying voltage stress and that the decrease in the leakage current is not large, a maximum of 30%, when the density of the doubly charged oxygen vacancies is decreased. Our result is consistent with this experimental result.

References

[1] N. Capron, P. Broqvist, and A. Pasquarello: Appl. Phys. Lett. **91** (2007) 192905.

[2] K. Hirose, T. Ono, Y. Fujimoto, and S. Tsukamoto: *First-Principles Calculations in Real-Space Formalism, Electronic Configurations and Transport Properties of Nanostructures* (Imperial College, London, 2005).

[3] K. Takagi and T. Ono: Jpn. J. Appl. Phys., in press.

Theoretical Analyses on Ionic Transport Properties, Electrical Properties and Interfacial Electronic States of Nanostructures

Satoshi WATANABE
Department of Materials Engineering, the University of Tokyo
7-3-1 Hongo, Bunkyo-ku, Tokyo, 113-8656

1 Introduction

Design and control of novel nanoscale information and energy devices require us to deepen our understanding on complicated situations and phenomena at nanoscale. Keeping this in minds, we have been performing atomic/electronic level simulations (mainly based on density functional theory (DFT)), taking various nanostructures as target systems. In the followings, some of our results in the fiscal year 2017 are described.

2 Development of neural network interatomic potentials to study ion diffusion in amorphous materials

Ion diffusion behaviors in amorphous materials play important role in several novel devices such as resistive memories. To clarify such behaviors, atomistic simulations based on density functional theory (DFT) are powerful, but they need heavy computation for amorphous materials. So we have tried to construct interatomic potentials for efficient prediction of ion diffusion behaviors using neural network (NN).

We adopted the high-dimensional NN potential proposed by Belher and Parrinello [1]. To obtain the data used for training NN, DFT calculations were performed using VASP package.

Firstly, we have constructed a NN potential for amorphous Li_3PO_4 [2, 3]. The average errors of the NN potential, compared with the DFT calculations, are 48 meV and 41 meV in calculating energy barriers of diffusion paths and diffusion activation energy, respectively. Moreover, the NN potential was applied to simulations using much larger supercell (about 1,000 atoms) than the cell used in the training (about 120 atoms). The Li diffusivity evaluated by molecular (MD) simulations with the large cell agrees well with the experimental observation.

Second, we have developed a NN potential to study Cu diffusion in amorphous AlO_x system with the wide range of variation in density (2.7-3.3 g/cm^3) and atomic composition (O/Al ratio of 1.0-1.5) [3]. The accuracy of the NN potential in energy prediction was about 14 meV/atom in the whole range of density and composition variation. Preliminary MD simulations show that the Cu diffusion activation energies decreased from 1.02 eV to 0.79 eV with the decrease of AlO_x density from 3.1 to 2.7 g/cm^3, while the variation of O/Al ratio does not affect the Cu diffusion activation energy significantly.

3 Li defect formation and interfacial structures of γ-Li_3PO_4/metal stacked systems

Recently, a novel memory device had been proposed using Au/Li_3PO_4/Li (or Ni/Li_3PO_4/Li) stacked structures, which exhibit two different voltage states by applying voltages [4].

Cyclic voltammetry and alternating current impedance spectroscopy measurements suggest different metal-Li_3PO_4 interface structures between the two states. Though it is speculated that the Li diffusion must be the key in the change of the interface structure, microscopic details of the two states was unknown. Therefore, we have investigated the Li vacancy and interstitial formation at the interface using DFT calculations and one-dimensional continuum-model calculations [5]. As the simulation models, we adopted Au(111)/γ-Li_3PO_4/Au(111) and Li(001)/γ-Li_3PO_4/Li(001). Formation energies calculated via DFT were used in the continuum-model calculations [6].

Our calculation results show that in the Au case within the realistic range of Li chemical potential, Li interstitials stay at the interface, while Li vacancies do not. On the other hand, the stability of the two Li defects depends on the Li chemical potential in the Li case. In both cases, the region where the Li defects accumulate is within 1 nm or less from the interface. On the basis of our results, we suggest that the interstitial Li-ions formed at few Å from the Au(111) interface and the Li-Au alloying play a central role in the switching of the novel memory device.

References

[1] J. Behler and M. Parrinello: Phys. Rev. Lett. **98** (2007) 146401.

[2] W. Li, Y. Ando, E. Minamitani and S. Watanabe: J. Chem. Phys. **147** (2017) 214106.

[3] W. Li, Doctoral thesis, The University of Tokyo (2017).

[4] I. Sugiyama, R. Shimizu, T. Suzuki, K. Yamamoto, H. Kawasoko, S. Shiraki and T. Hitosugi: APL Mater. **5** (2017) 046105.

[5] K. Shimizu, W.Liu, W. Li, S. Kasamatsu, Y. Ando, E. Minamitani and S. Watatanbe: in preparation.

[6] S. Kasamatsu, T. Tada and S. Watanabe: Solid State Ionics **183** (2011) 20.

First-Principles Study of Excited Electron Dynamics and Optical Responses of Nanostructures

Kazuyuki WATANABE, Yasumitsu SUZUKI,
Yoshihiro UEDA, Kazuki UCHIDA, Tomoki SHINOZAKI
Department of Physics, Tokyo University of Science
1-3 Kagurazaka, Shinjuku-ku, Tokyo 162-8601

In this project we investigated the following five topics this year. 1) Angle-resolved secondary electron emission from atomic sheets, 2) plasmon excitation and electron emission of a carbon nanotube, 3) exact time-dependent exchange-correlation potential in electron scattering processes, 4) positron-stimulated ion desorption from $TiO_2(110)$ surface, and 5) electron transmission through mono- and bilayer graphene.

1) *Angle-resolved secondary electron emission from atomic sheets* [1]: Angle-resolved secondary electron emission (ARSEE) spectra of atomic sheets have been considered to reflect the unoccupied energy bands of the targets. However, far less is known about the dynamics of electron excitation from the valence bands to the unoccupied bands upon electron impact, leading to emission into the vacuum. We kept track of the electrons excited to the unoccupied bands and emitted to the vacuum in real time, position space, and k-space simultaneously by our homemade time-dependent density-functional theory (TDDFT) code, KENS. Parallelized calculations have been performed using System B. We have demonstrated that the calculated ARSEE spectra capture the unoccupied band structure of the atomic sheets. The excitation dynamics that lead to SEE have also been revealed by the time-dependent Kohn-Sham decomposition scheme. In this study the mechanism for the experimentally observed ARSEE from atomic sheets was elucidated with respect to both energetics and the dynamical aspects of SEE.

2) *Plasmon excitation and electron emission of a carbon nanotube* [2]: We studied the properties of electron excitation and emission of a finite carbon nanotube (CNT) under a linearly polarized femtosecond laser using our homemade real-space TDDFT code, RENS. Parallelized calculations have been performed using System B. We found a plasmon resonance in the near-infrared region of the optical absorption spectrum that is highly sensitive to the laser polarization direction. The laser polarization direction dependence of the plasmon excitation obtained is consistent with the properties of polarized optical absorption observed in experiments. In electron emission that occurs subsequent to electronic excitation, the yield of emitted electrons also shows a laser polarization direction dependence, and the kinetic energy spectrum of the emitted electrons is broadened in the high-energy regime due to the electron acceleration caused by plasmon-induced electric-field enhancement. These findings are of crucial importance for understanding the laser-CNT interaction, which is a prerequisite for applications of CNTs in electron emitters, nanodevices, and optoelectronic components and sensors.

3)*Exact time-dependent exchange-correlation potential in electron scattering processes* [3]: We calculated the exact exchange-correlation potential of time-dependent density functional theory in one-dimensional electron scattering system, and identified crucial peak and valley structures. These structures are completely missed by adiabatic approximations that, consequently, significantly underestimate the scattering probability. We also showed that a recently proposed nonadiabatic approximation, v^s_{xc}, correctly capture the approach of the electron to the target when the initial Kohn-Sham state is chosen judiciously, and it is more accurate than standard adiabatic functionals but ultimately fails to accurately capture reflection. These results explain the underestimation of scattering probabilities in some recent studies on molecules and surfaces. Part of the computations that required a lot of memory were performed on System B.

4) *Positron-stimulated ion desorption from* TiO_2*(110) surface* [4]: This is a joint work with an experimental group. We studied the positron-stimulated O^+ ion desorption process from a TiO_2(110) surface. The measured data indicate that the O^+ ion yields depend on the positron incident energy in the energy range between 0.5 keV and 15 keV. This dependence is closely related to the fraction of positrons which diffuse back to the surface after thermalization in the bulk. We calculated the electron and positron work functions and positronium affinity at TiO_2(110) surface using two-component DFT implemented in ABINIT code. By comparing the calculated positron binding energy and work function, we showed that thermalized positrons which diffuse back to the surface can be trapped by the surface induced image potential. Based on the experimental and computational results, we concluded that the ion desorption via positron-stimulation occurs dominantly by the annihilation of surface-trapped positrons with core electrons of the topmost surface atoms. All calculations were performed with ABINIT code on System B.

5) *Electron transmission through mono- and bilayer graphene* [5]: This is also a joint work with an experimental group. The experimental group proposed a virtual substrate method to characterize nanomaterials without the influence of underlying substrate signals from four interrelated measurements. We calculated elastic transmission coefficient of mono- and bilayer graphene by real-time TDDFT simulation with RENS code, which well corresponded with the virtual substrate measurements. Based on the experimental and computational results, we concluded that the virtual substrate method represents a benchmark to provide free-standing nanomaterial information from measurements of substrate-supported samples. All TDDFT calculations were performed on System B.

References

[1] Y. Ueda, Y. Suzuki, and K. Watanabe, Phys. Rev. B **97**, 075406 (2018).

[2] K. Uchida and K. Watanabe, Phys. Rev. B **96**, 125419 (2017).

[3] Y. Suzuki, L. Lacombe, K. Watanabe, and N. T. Maitra, Phys. Rev. Lett. **119**, 263401 (2017).

[4] T. Yamashita, S. Hagiwara, T. Tachibana, K. Watanabe, and Y. Nagashima, Materials Research Express **4**, 116303 (2017).

[5] B. Da, J. Liu, M. Yamamoto, Y. Ueda, K. Watanabe, N. T. Cuong, S. Li, K. Tsukagoshi, H. Yoshikawa, H. Iwai, S. Tanuma, H. Guo, Z. Gao, X. Sun, and Z. Ding, Nat. Commun. **8**, 15629 (2017).

First-principels study of anomalous thermoelectric effect on magnetic materials

Fumiyuki ISHII, Susumu MINAMI, Teguh Budi PRAYITNO, Yo Pierre MIZUTA
Faculty of Mathematics and physics, Institute of Science and Engineering, Kanazawa University
Kanazawa, 920-1192, Japan

Anomalous transport properties originated in Berry curvature is one of the key ingredients of new thermoelectric(TE) materials. For example, the anomalous Nernst effect (ANE), which is induced by the anomalous Hall effect (AHE) is one of the TE phenomena caused by the Berry curvature. ANE and AHE are reported in various magnetic materials[1, 2] which are not only ferromagnetic but also antiferromagnetic. However the magnitude of anomalous Nernst coefficient is quite small to apply it for TE generation device.

Our aim is to find and design materials with large ANE and clarify the origin of large ANE system. We have investigated two kind of systems as follows based on first-principles calculations based on density functional theory (DFT) implemented in OpenMX code[3]. We have constructed maximally localized Wannier functions (MLWF) using Wannier90 code[4] and evaluated the transport properties within the semiclassical Boltzmann transport theory with relaxation time approximation.

Magnetic half-Heusler compounds CoMSb (M=V, Cr, Mn)

We focused on the half-Heusler compounds CoMSb (M=V, Cr, Mn) and calculated ANE systematically. Half-Heusler intermetallic compounds have a face-centered cubic crystal structure with chemical composition XYZ and space group $F\bar{4}3m$. CoVSb and CoMnSb are known as ferromagnetic compounds with Curie temperatures of 58K and 490K, respectively[5, 6].

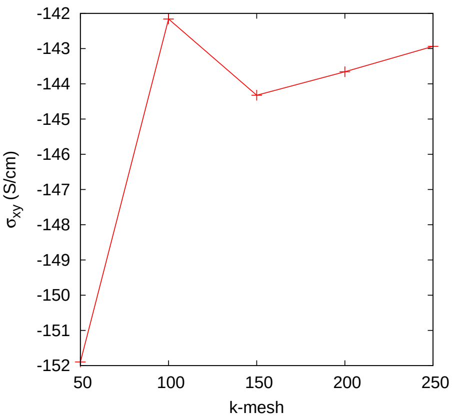

Figure 1: k-mesh dependence of anomalous Hall conductivity $\sigma_{xy}|_{T=0}$ for CoVSb at Fermi energy. σ_{xy} are calculated by using $k \times k \times k$ mesh in the Brillouin zone.

First, we checked the convergence of the anomalous Hall conductivity (AHC) in terms of k point sampling. Figure 1 shows k-mesh dependence of AHC σ_{xy} on CoVSb at Fermi energy. The evaluation of the AHC require a lot of k point sampling and it can be efficiently parallelized. We confirmed that over the 100 k-mesh is sufficient to obtain accurate results.

Figure 2 shows carrier concentration dependence of anomalous Nernst coefficient in CoMSb at 300K. Transport properties are calculated by using constant relaxation time approximation (τ = 3fs). The results show each materials have a peak of ANE near the Fermi energy. We also found that the peaks shift corresponding to the number of valence electron

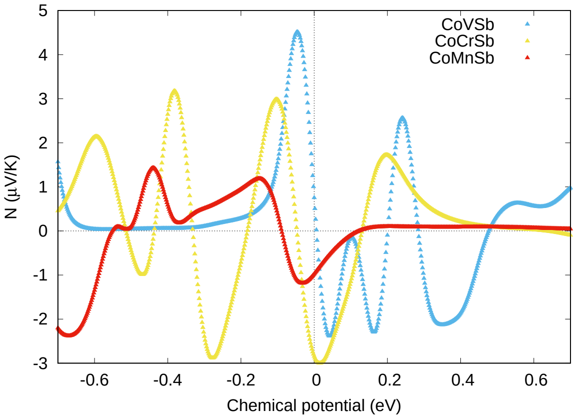

Figure 2: Anomalous Nernst coefficient at 300K. The Fermi energy is set to 0 eV.

of *M*. We investigated CoMnSb in details because of its applicability for an ANE-based TE module that can operate below room temperature. In conclusion, the origin of the large ANE on CoMnSb is the large Berry curvature on symmetry line of the Z-Uz in the Brillouin zone[7].

Topological half-Heusler compound YPtBi

We have calculated topological surface states for half-Heusler compounds YPtBi, which is known as a one of the topological semimetal by using band unfolding method. In this calculation, we used 46 atomic-layer slab model with a vacuum more than 15 Å. The calculation are considered three kind of terminated condition, namely the atom on the surface is Y, Bi, and Pt.

Figure 3 shows calculated surface state of Bi-terminated YPtBi. We obtained non-trivial topological surface sate around the Γ point and metallic surface state around the M point, which is correspond to the calculated and observed results[8].

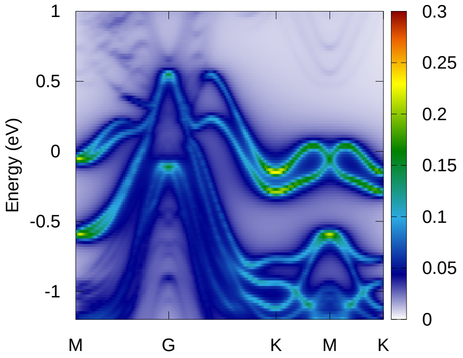

Figure 3: Calculated surface state of Bi-terminated YPtBi. The intensity spectra are calculated by projecting the band onto the 10 atomic-layer unit cell.

References

[1] K. Hasegawa, et al., Appl. Phys. Lett. **106** (2015) 252405.

[2] M. Ikhlas et al., Nat. Phys. **13** (2017) 1085.

[3] T. Ozaki et al., OpenMX, http://www.openmx-square.org.

[4] A. A. Mostofi et al., Comput. Phys. Commun. **178**, (2008) 685.

[5] M. Otto et al., J. Magn. Magn. Mater. **70** (1987)33.

[6] M. Terada et al., J. Phys. Soc. Jpn **32** (1972) 91.

[7] S. Minami, F, Ishii, Y. P. Mizuta, and M. Saito, arXiv:1804.00297.

[8] Z. K. Liu et al., Nat. Commun. **7** (2016) 12924.

First-principles calculations of spin textures at the surfaces and interfaces

Fumiyuki ISHII, Megumi SUGITA, Hikaru SAWAHATA,
Yo Pierre MIZUTA, Naoya YAMAGUCHI
Faculty of Mathematics and Physics, Institute of Science and Engineering, Kanazawa University
Kanazawa, 920-1192, Japan

We have studied the systems with special spin structures applicable to spintronics or thermoelectric conversion based on first-principles density functional calculations using OpenMX. This year, we focused on surfaces/interfaces with spin splittings such as Rashba spin splittings that can lead to spin-to-charge conversion (from a spin current to a charge current), and investigated topological insulators, and skyrmions. We also improved the code to calculate spin textures and enhanced the code of the band unfolding scheme in OpenMX to analyze spin textures for unfolded band structures.

Rashba Effect

Spin-to-charge conversion due to the Rashba effect, that is, the inverse Rashba-Edelstein effect (IREE) was observed in two-dimensional electron gas (2DEG) at various interfaces [1, 2]. The efficiency of IREE may become higher, as the Rashba coefficient, the strength of the Rashba effect, α_R is larger [1]. Therefore, the 2DEG with large spin splittings are promising candidates for such spintronic materials. The Rashba coefficient α_R can be controlled by a built-in electric field at surfaces and interfaces, i.e. electric polarization. For $SrTiO_3$, there is the strain-induced polarization, which can be controlled by the epitaxial strain [3].

In this project, we investigated the Rashba effect for interfaces between perovskite-type oxides ($PbTiO_3$, $BiAlO_3$) and noble metals (Cu, Ag, Au) and the effect of strain on $LaAlO_3/SrTiO_3$ interfaces and $SrTiO_3$ surfaces. For a tensile-strained $LaAlO_3/SrTiO_3$ interface, there is the strain dependence of the spin splitting (Fig. 1) and for the tensile strain of 5%, we found the persistent spin helix state, which has a long spin life time [4]. For a compressive-strained $SrTiO_3$ surface, we found the 2DEG with a Rashba spin splitting of $\alpha_R = 155.7$ meV·Å (Fig. 2) [5].

In order to investigate the Rashba effect at Bi_2O_3/M (M=Cu, Ag, Au) interfaces, we also calculated the electronic structures and spin textures for the realistic model (>100 atoms) and the simple model based on Bi/M (M=Cu, Ag, Au) surface alloy structures, as for an bismuth atom, an oxigen atom is located at a twofold bridge site randomly.

For the Bi/M-surface-alloy-based model, the system was modeled by using the supercell method, and thus we used the unfolding method to compare the calculated band structure with that for a $M(111)$ surface. Besides, we enhanced the unfolding scheme in OpenMX so that the spin components could be analyzed and we confirmed that there were spin splittings in the unfolded band structures.

Calculating fine spin textures or unfolding band structures along a **k**-path including many **k**-points, especially for the realistic system with the large number of atoms, requires large computational resources (e.g. memory) and we improved our calculation code of spin textures in terms of parallelization for **k**-points by changing the schemes and data structures from those for small computers to those for supercomputers. We investigated the trend of α_R of Bi_2O_3/M using the realistic model, and found the sign change of α_R between systems with different M. These results support the experiments and are published in a collaboration work with the experimental group [6].

Anomalous Nernst Effect

We focus on the anomalous Nernst effect (ANE), heat-to-electricity conversion in transverse direction, driven by an emergent magnetic field originating from spontaneous inhomogeneous magnetization. We have so far found from computations on some models that, in the so-called 2D skyrmion crystal (SkX) phase, where skyrmions are crystallized in two dimensions, the crystal-momentum component of effective magnetic field gives rise to the band structure that could generate large ANE when chemical potential is properly tuned[7]. Although this behavior was most clearly confirmed in the simplest model of square SkX with single s-orbital per site, our subsequent computations on more realistic models of transition-metal oxides also showed possible large ANE[8]. A sizable transverse thermoelectric coefficient is predicted to arise, by means of first-principles calculations, in a Skyrmion crystal assumed on EuO monolayer where carrier electrons are introduced upon a quantum anomalous Hall insulating phase of Chern number C = 2. This encourages future experiments to pursue such an effect.

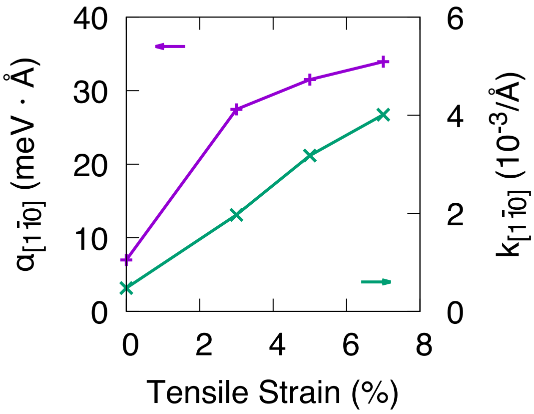

Figure 1: Strain dependence of the spin-orbit coefficient and the momentum offset along $[1\bar{1}0]$-direction in a $LaAlO_3/SrTiO_3$ interface.

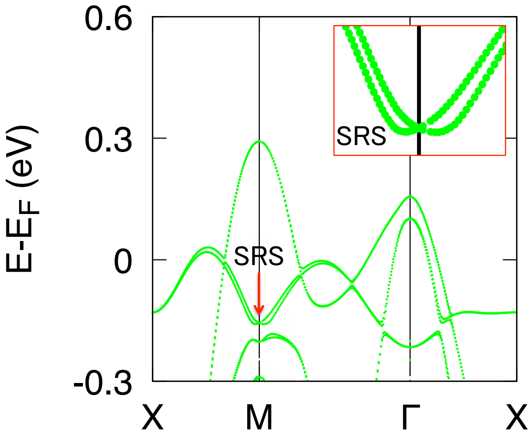

Figure 2: Surface-projected band structures for a strained $SrTiO_3$ surface. The inset shows the enlarged view for surface Rashba states.

References

[1] J. C. Rojas Sánchez et al., Nat. Commun. **4**, 2944 (2013).

[2] E. Lesne et al., Nat. Mater. **15**, 1261 (2016).

[3] J. H. Haeni et al., Nature **430**, 758 (2004).

[4] N. Yamaguchi and F. Ishii, Appl. Phys. Express **10**, 123003 (2017).

[5] N. Yamaguchi and F. Ishii, *submitted.*

[6] H. Tsai, S. Karube, K. Kondou, N. Yamaguchi, F. Ishii and Y. Otani, Sci. Rep. **8** 5564 (2018).

[7] Y. P. Mizuta and F. Ishii, Scientific Reports **6**, 28076 (2016).

[8] Y. P. Mizuta, H. Sawahata, and F. Ishii, arXiv:1803.08148.

Ab initio molecular dynamics simulation of graphene/ionic liquids interfaces

Tatsuhiko OHTO
Graduate School of Engineering Science,
Osaka University, 1-3 Machikaneyama, Toyonaka, Osaka 560-8531

Ab initio MD (AIMD) is a powerful tool to describe heterogeneous systems such as the water/solid interface, Although AIMD is computationally expensive, it describes electronic states beyond classical force fields,[1] which is important for interfaces. We calculated graphene/ionic liquid interfaces using the CP2K code [2].

We studied the interfacial structure of room temperature ionic liquids (RTILs).[3] RTIL interfaces controls many of the unique properties of RTILs, such as the high capacitance of RTILs and the efficiency of charge transport between RTILs and electrodes. RTILs have been experimentally shown to exhibit interfacial molecular layering structures over a 10 Å length scale. However, the driving force behind the formation of these layered structures has not been resolved. Here, we report *ab initio* molecular dynamics simulations of imidazolium RTIL/air interfaces along with force field molecular dynamics simulations. We find that the π+–π+ interaction of imidazolium cations enhances the layering structure of RTILs, despite the electrostatic repulsion. The length scales of the molecular layering at the RTIL/air and RTIL/graphene interfaces are very similar, manifesting the limited effect of the substrate on the interfacial organization of RTILs.

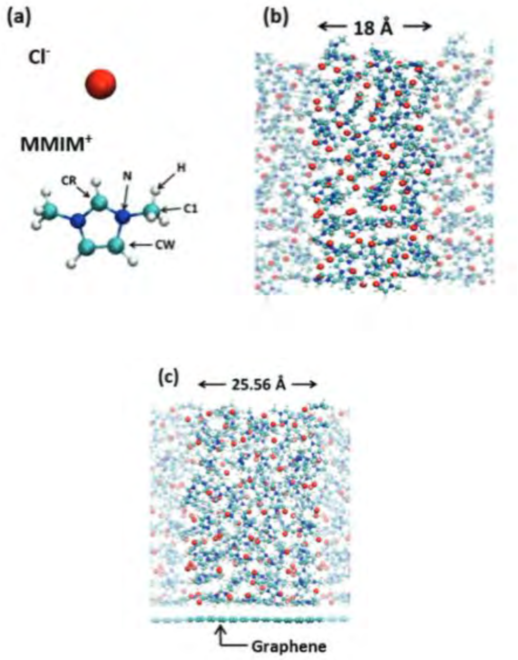

Fig. 1: Structures of RTIL, RTIL-air and RTIL-graphene interfaces.

References

[1] T. Ohto et al. Phys. Chem. Chem. Phys. **19**, 6909 (2017).

[2] The CP2K developers group, http://cp2k.berlios.de/

[3] T. Fujie et al. Phys. Chem. Chem. Phys. **19**, 2805 (2017)

Ab initio molecular dynamics simulation of doped-graphene/water interfaces

Tatsuhiko OHTO

Graduate School of Engineering Science,

Osaka University, 1-3 Machikaneyama, Toyonaka, Osaka 560-8531

Ab initio MD (AIMD) is a powerful tool to describe heterogeneous systems such as the water/solid interface, Although AIMD is computationally expensive, it describes electronic states beyond classical force fields,[1] which is important for interfaces.

We have simulated sum-frequency generation (SFG) spectra of isotopically diluted water at the water-graphene and water-hexagonal boron-nitride (hBN) sheet interfaces, using ab initio molecular dynamics simulations. The simulations themselves were performed using ISSP several years ago and recently we have submitted a paper.[2] A sharp 'dangling' O-D peak around ~2640 cm-1 appearing in both simulated SFG spectra evidences that both graphene and hBN are hydrophobic. The dangling O-D peak is 10 cm^{-1} red-shifted at the water-hBN interface relative to the peak at the water-graphene interfaces. This frequency difference manifests a stronger O-D…N intermolecular interaction between water and hBN than a O-D…C interaction between water and graphene.

To modify the hydrophobic interaction, we calculated doped-graphene water interfaces using the CP2K code [3]. We prepared 2 % B-doped, 2 % N-doped and 10 % N-doped graphene sheets. We tried to accumulate the 80 ps trajectory for each system and completed 50 % of AIMD runs. We will continue running the AIMD and analyze the results after completing the AIMD simulations.

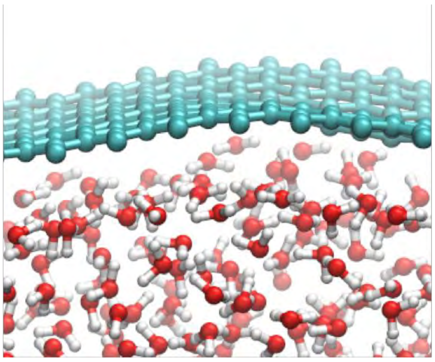

Fig. 1: Structures of the graphene-water interface.

References

[1] T. Ohto et al. Phys. Chem. Chem. Phys. **19**, 6909 (2017).

[2] T. Ohto et al. submitted.

[3] The CP2K developers group, http://cp2k.berlios.de/

Ab initio phonon calculations for $Ca_5Ir_3O_{12}$

Kazuma NAKAMURA
Quantum Physics Section, Kyushu Institute of Technology
1-1 Sensui-cho, Tobata, Kitakyushu, Fukuoka, 804-8550

The title compound has recently attracted attention as a thermoelectric material because it has a relatively high Seebeck coefficient. In this study, we report an ab initio study about electronic and phononic properties for $Ca_5Ir_3O_{12}$. In particular, we investigated the effect of spin-orbit interaction (SOI) on the low-energy properties [1].

Density functional calculations with plane-wave basis sets were performed using the xTAPP code [2], where the ultrasoft pseudopotential and the generalized gradient approximation (GGA) of the exchange correlation potential were employed. The cutoff energies in the wavefunction and charge densities were 64 and 256 Ry, respectively, and the SOI was explicitly considered. To study the effects of SOI, we performed the usual GGA calculation and compared it with the result including the SOI. Below, we refer to the former as GGA and to the latter as SO-GGA. The atomic and lattice parameters were optimized with an 8×8×8 k-point sampling, and we found that SO-GGA reproduces the experimental crystal structure quite well. The Fermi-surface calculations were performed with the dense 21×21×63 k-point sampling to obtain the detailed surface structure [3]. Phonon calculations were performed using 11×11×11 k-point sampling for a 1×1×3 supercell [4].

Figure 1(a) shows our calculated band structure. To see the SOI effect, the SO-GGA band (thick red curves) is compared with the GGA band (thin blue curves) in Fig. 1(b). An appreciable difference can be observed in the low-energy bands; the GGA result exhibits metallic bands, particularly along the L-M or H-K lines. When the SOI is switched on, the metallic bands are split and a pocket-like band structure appears. The gap size due to the SOI is about 0.3 eV, which is comparable to the valence bandwidth 0.5 eV.

Figures 1(c) and 1(d) show the Fermi surfaces based on the SO-GGA and GGA, respectively. We see that the GGA Fermi surface is contributed from the two bands (indicated in dark-blue and bright-red colors), while the SO-GGA Fermi surface is basically formed by the one band; the SOI makes the bright-red colored GGA Fermi surface disappear. In the SO-GGA Fermi surface, since the SOI resolves the band degeneracy, the Fermi surfaces are seemingly two (dark-blue and bright-blue colored surfaces); however, these two are originated from the same band. Also, in the SO-GGA Fermi surface, we see a sheet structure along the c*-axis (the Γ-A line), which indicates a nesting trend along this direction. We note that the SOI is relevant to the narrowing of the sheet separation between the blue colored Fermi surfaces.

Figures 2(a) and 2(b) are our calculated phonon dispersions with and without SOI, respectively, and Fig. 2(c) is a comparison of two densities of states. Considering the SOI, the density of state is blue shifted as a whole, and a gap is formed around 10 THz. We found that phonon frequencies at the Γ point are in a good agreement with the Raman measurement.

As another achievement, we have released a new software RESPACK [5] that is a

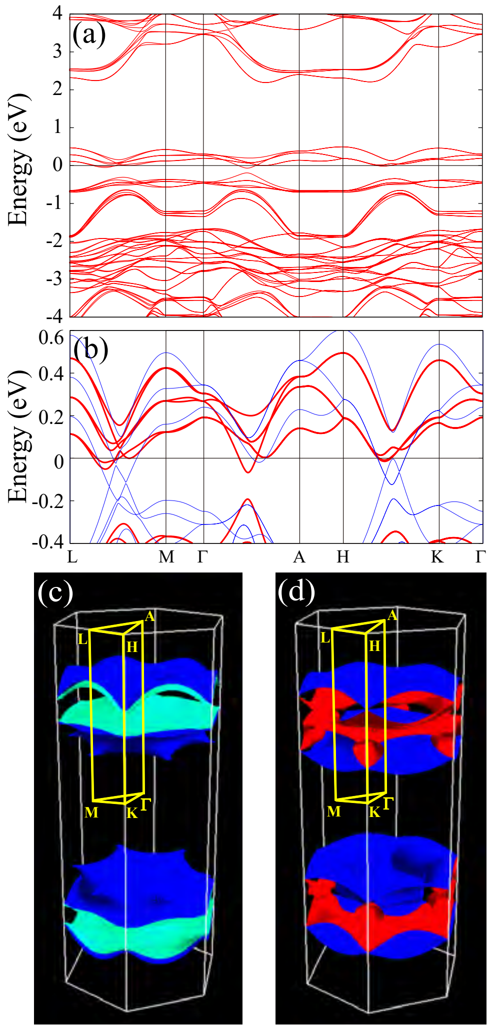

Figure 1: (Color online) (a) Ab initio electronic band structure considering the SOI in $Ca_5Ir_3O_{12}$. The energy zero is the Fermi level. (b) A zoom of the low-energy band structure, where the SO-GGA result (thick red curves) is compared with the usual GGA result (thin blue curve). (c) Calculated Fermi surface for SO-GGA and (d) GGA.

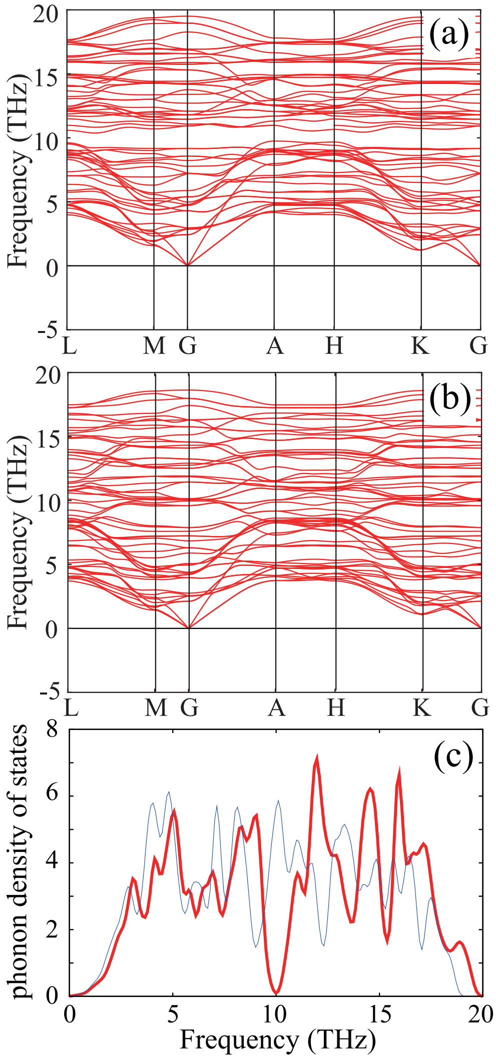

Figure 2: (Color online) (a) Ab initio phonon dispersion with the SOI in $Ca_5Ir_3O_{12}$. (b) The result without SOI. (c) Calculated phonon density of states, where the SO-GGA result (thick red curves) is compared with the usual GGA result (thin blue curve).

first-principles calculation program to evaluate the maximally localized Wannier functions, the RPA response functions, and frequency-dependent electronic interaction parameters.

References

[1] K. Matsuhira, K. Nakamura, Y. Yasukuni, Y. Yoshimoto, D. Hirai, Z. Hiroi: J. Phys. Soc. Jpn. **87** (2018) 013703.

[2] http://xtapp.cp.is.s.u-tokyo.ac.jp

[3] http://fermisurfer.osdn.jp

[4] https://atztogo.github.io/phonopy

[5] https://sites.google.com/view/kazuma7k6r

First-principles study of quantum transport in nanostructures

NOBUHIKO KOBAYASHI
Institute of Applied Physics, University of Tsukuba
1-1-1 Tennodai Tsukuba Ibaraki 305-8573

1 Introduction

An atomic-scale understanding of electron transport properties in materials is an important issue in materials science and nanotechnology. Theoretical investigations on transport properties are indispensable for the recent developments of high-performance electronic devices. Quantum nature is essential in nanoscale systems, and atomistic analysis based on detailed electronic states calculations are indispensable to discuss the transport property. In order to analyze transport properties, we have developed the nonequilibrium Green's function (NEGF) method, and the O(N) time dependent wave-packet diffusion (TD-WPD) method on the basis of the density functional theory (DFT). Using these methods, we have investigated charge, head and spin transport properties of materials. [1]

2 O(N) TD-WPD method and application to organic semiconductors

Organic semiconductors have attracted much attention for their applications to flexible, lightweight, and low-cost electronic devices. Organic semiconductors are crystals that are assemblies of π-conjugated molecules weakly bonded by van der Waals interactions, and single crystallization has been achieved, enhancing the mobility. It is now expected that the mechanism of carrier transport in organic semiconductors can be elucidated and that materials exhibiting high mobility can be developed by novel molecular synthesis.

We developed the O(N) TD-WPD method for the quantum transport calculation of huge systems of up to 100 million atoms a decade ago.We calculated the conductance and the mobility of the system with micron-order lengths at room temperature based on the Kubo-Greenwood formula. Using this method we can study the transport properties from diffusive to ballistic regimes including the effect of realistic electron-phonon scattering, and determine the mean free path and relaxation time from an atomistic viewpoint. We performed DFT calculations of electronic structures and interactions between molecules of single-crystal organic semiconductors including the effect of the van der Waals interaction, and applied the TD-WPD method to the analysis of transport properties of the organic semiconductors. We analyzed the transport properties of various organic semiconductors such as pentacene, rubrene, C8-BTBT, DNTT, and C10-DNBDT. We reveal the mobility and the temperature-dependent behavior from band-like to thermally activated behavior due to extrinsic disorder effects, which correspond to experimental observations.[2]

3 NEGF method and application to thermoelectricity

We have developed an efficient numerical calculation code for the ab-initio electron transport based on the DFT and NEGF formalism. We have applied the method to analyses of thermoelectricity of magnetic semiconductors.

Thermoelectric materials have attracted considerable attention from viewpoints not only of materials science but also of applications for energy harvesting by waste heat, and intensive works have been devoted to enhance conversion efficiency from thermal energy into

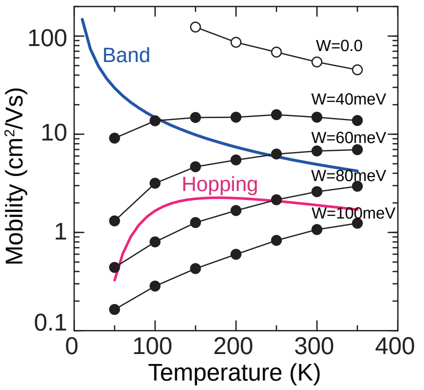

Figure 1: Calculated mobility of a pentacene single crystal along the a axis as a function of temperature for several magnitudes of static disorder W. [2]

electricity. The efficiency is expressed as a function of the figure of merit $ZT = \sigma S^2 T/\kappa$, where σ, S, κ and T are the electrical conductivity, the Seebeck coefficient, the thermal conductivity and the temperature, respectively, and the thermoelectric power factor is written as σS^2. Enhancement of thermoelectric efficiency is not an easy task since the Seebeck coefficient, the electrical conductivity, and the thermal conductivity are not independent of each other. There is the trade-off between σ and S, and materials with high electric conductivity tend to have high thermal conductivity.

We analyze the thermoelectric properties of a magnetic semiconductor CuFeS2 by NEGF-DFT. The electronic transport properties, Seebeck coefficient, and the figures of merit in doped compositions are estimated. The results show that they obtain their maximum values around the electronic band edge and suitable doping enhances the thermoelectric properties of CuFeS2. We theoretically demonstrate the enhancement in the figure of merit by doping, which is in agreement with experimental work, and show further enhancement by the optimized doping.[3, 4]

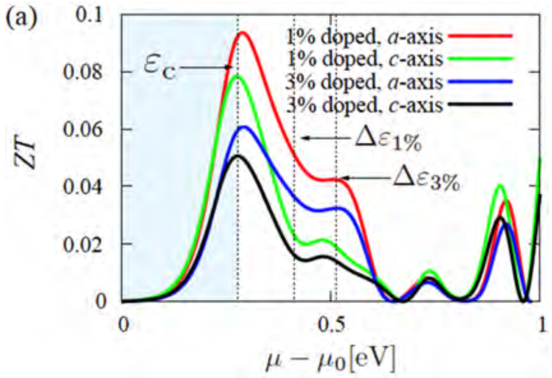

Figure 2: Figures of merit ZT of CuFeS2 as a function of the chemical potential at 300 K [4]

References

[1] N. Kobayashi, H. Ishii, K. Hirose, Jpn. J. Appl. Phys. (2018) in press.

[2] H.Ishii, N.Kobayashi, K.Hirose, Phys. Rev. B 95, 035433 (2017)

[3] H.Takaki, K.Kobayashi, M.Shimono, N.Kobayashi, K.Hirose, N.Tsujii, T.Mori, Appl. Phys. Lett. 110, 072107 (2017)

[4] H.Takaki, K.Kobayashi, M.Shimono, N.Kobayashi, K.Hirose, N.Tsujii, T.Mori, Materials Today Physics 3 85e92 (2017).

The Study on the Electronic State of Reduced Anatase TiO_2 Nanocrystal

Kenji YASUOKA

Department of Mechanical Engineering,

Keio University, Kohoku, Yokohama, Kanagawa 223-8522

TiO_2, a wide-gap semiconductor, have attracted considerable attention due to its potential applications as solar cell, photocatalysis and biocompatible materials.[1] Among three major polymorphs of TiO_2, rutile, anatase, and brookite, anatase is known to be the most favoured for photocatalytic reactions. Reactivity of anatase is known to be further enhanced by preparing it in a nanocrystalline structure. In the previous studies, both experimental and computational approach has been adopted clarify the underlying mechanism.[2] However the polaronic nature of excess electrons in TiO_2 made this difficult.

We have overcome this difficulty by adopting hybrid functional (HSE06) for exchange-correlation functional in density functional theory. More than 20 defect configurations were prepared and optimised using the HSE06 throughout the calculation. Adopting multi-leveled parallelisation, this calculation was performed on multiple computer nodes by taking advantages of the node-node data transmission technology such as the "enhanced hypercube" topology and 4× FDR InfiniBand 2× used in the System B.

As a result, different defect structure have shown different excess electron structures (Fig 1). These excess electrons formed polarons and created different band gap width according to their spatial distribution. This result indicates the possibility to tune the reactivity of TiO_2 nanocrystals through controlling the defect configurations.

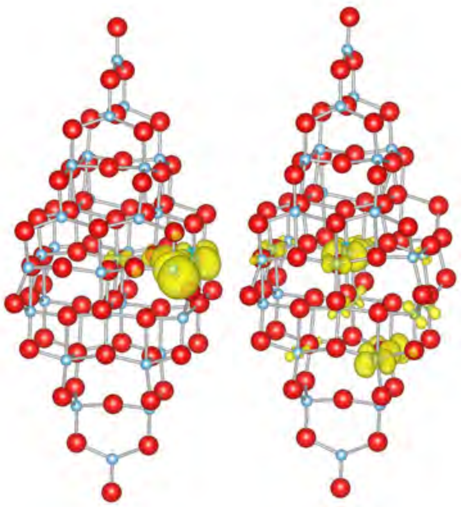

Fig. 1: Representative excess electron structures. (Left) Two excess electrons distributed in the close proximity (left) and apart (right) from each other.

References

[1] U. Diebold: Surf. Sci. Rep. **48** (2003) 53.

[2] K. Zhang and J. H. Park: J. Phys. Chem. Lett. **8** (2017) 199.

Structural transition analyses on nano- and bio-systems using dissimilarity

Yasuteru SHIGETA

Center for Computational Sciences,

University of Tsukuba,1-1-1 Tennodai, Tsukuba, Ibaraki 305-8577

Several biological functions, such as molecular recognition, enzyme catalysis, signal transduction, allosteric regulation, and protein folding, are strongly related to conformational changes of proteins. These conformational changes are induced as slow dynamics upon collective motions, including biologically relevant large-amplitude fluctuations of proteins. Although molecular dynamics (MD) simulation has become a powerful tool for extracting conformational transitions of proteins, it might still be difficult to reach time scales of the biological functions, because the accessible time scales of MD simulations are far from biological time scales, even if straightforward conventional MD (CMD) simulations using massively parallel computers are employed. Thus, it is desirable to develop efficient methods to achieve canonical ensembles with low computational costs.

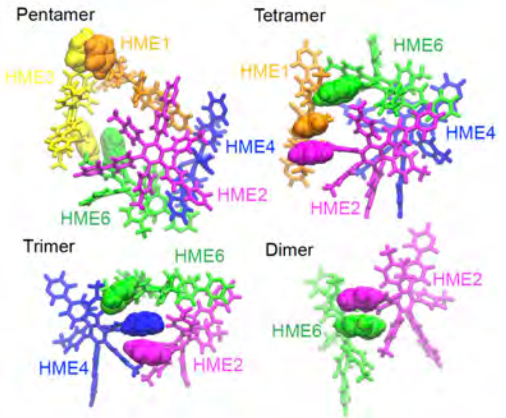

Figure 1. Representative oligomeric structures (**1**$_n$: n=2-5) during a dissociation pathway of nanocube (**1**$_6$) which consists of six gear-shaped amphiphile molecules (**1**).

For this aim, we have developed several enhanced conformational search techniques of biomolecules [1] and extended it to refer structural dissimilarity [2] to induce structural transitions of a given system by avoiding already sampled area. Our basic strategy is as follows: (i) selection of initial seeds (initial structures) for the conformational sampling in restarting MD simulations. Here, the seeds should be selected as candidates with the high potential to transit. (ii) Resampling from the selected seeds by initializing velocities in restarting short-time MD simulations [1]. A cycle of these simple protocols might drastically promote the conformational transitions of biomolecules.

By self-organization processes, six gear-shaped amphiphile molecules **(1)** form the hexameric structure of a nanocube (**1**$_6$) [3]. Structural dissimilarity sampling (SDS) simulations [2] of **1**$_6$ in a 25% aqueous methanol were conducted to extract dissociation pathway of $\mathbf{1}_6$ into monomers step-by-step as the reverse . Our MD study unveiled that a programed dynamic ordering exists in the dissociation processes of a nanocube. According to the dissociation processes, it is proposed that the triple π-stacking among three 3-pyridyl groups and CH-π or other hydrophobic interactions were sequentially formed at stable and transient oligomeric states in the self-organization processes, i.e. $\mathbf{1}_2$ (dimer), $\mathbf{1}_3$ (trimer), $\mathbf{1}_4$ (tetramer), and $\mathbf{1}_5$ (pentamer). By subsequent analyses on the stability of these oligomers, it was found that $\mathbf{1}_3$ and $\mathbf{1}_4$ are stable intermediate oligomers, whereas $\mathbf{1}_2$ or $\mathbf{1}_5$ are transient ones. Thus, the formations of $\mathbf{1}_3$ from three monomers and of $\mathbf{1}_6$ from $\mathbf{1}_4$ and two monomers via corresponding transients are time-consuming steps in forming the nanocube [4].

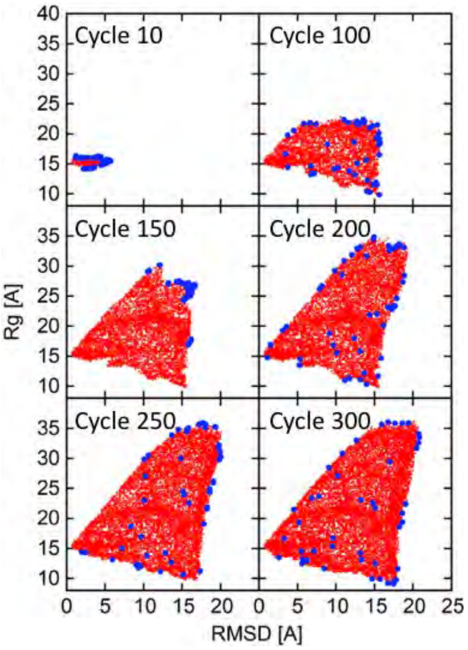

Figure 2 Accumulated trajectories mapped on to RMSD and R_g [Å] during dissimilarity sampling

We have also applied the dissimilarity sampling method to the dissociation of cytochrome *c* dimer [5]. As illustrated in Fig. 1, the sampled area spanned by root-mean-square deviation (RMSD) and a radius of gyration (R_g) spreads over. However, the dissociation of Cyt *c* dimer did not occur during 300 cycles. Although the sampled area were fully sampled as cycles of structure sampling went, our conformational sampling method fail to find the dissociation pathway of Cyt *c* dimer owing to improper choice of reaction coordinates (RCs). To remedy the drawback, we now try to choose the effective RCs automatically [6] to describe the dissociation pathway of Cyt *c* dimer.

References

[1] R. Harada, Y. Takano, T. Baba, Y. Shigeta: Phys. Chem. Chem. Phys. **17** (2015) 6155.

[2] R. Harada, Y. Shigeta: J. Chem. Theor. Compt. **13** (2017) 1411.

[3] S. Hiraoka, K. Harano, M. Shiro, M. Shionoya: *J. Am. Chem. Soc. 130 (***2008**) 14368.

[4] R. Harada, T. Mashiko, M. Tachikawa, S. Hiraoka, Y. Shigeta: Phys. Chem. Chem. Phys. in press.

[5] S. Hirota, Y. Hattori, S. Nagao, M. Taketa, H. Komori, H. Kamikubo, Z. Wang, I. Takahashi, S. Negi, Y. Sugiura, M. Kataoka, Y. Higuchi; *Proc. Nat. Acad. Sci. U.S.A.* **107** (2010)12854.

[6] R. Harada, Y. Shigeta: J. Chem. Theor. Compt. submitted.

First-Principles Calculation for Positron and Muon Experiments as Measurements of Crystals

Mineo SAITO

Institute of Science and Technology, Kanazawa University

Kakuma, Kanazawa, 920-1192 Japan

The spin-polarized positron annihilation technique is expected to be a useful tool to detect spin states in materials [1]. Analysis based on first-principles calculations is necessary to get useful information from experimental results. We study the positron annihilation in the Zn vacancy in ZnO that induces ferromagnetism.

We find that the vacancy has the C_{3v} symmetry and is spin polarized. The defect level E is found to be occupied by two electrons and we thus conclude that the electronic ground state belongs to $^3A_2$. Since the E state is partially occupied by electrons, the Jahn-Teller distortion of the E vibrational mode is expected to lower the symmetry and to lead to the spin singlet state. We however find that the Jahn-Teller energy is very small, thus the above mentioned spin triplet state is the most stable. The distance between nearest O atoms is found to be 3.60Å, which is much larger than the ideal one (3.31Å). This outward relaxation is expected to be the origin of the small Jahn-Teller effect and leads to the sp^2 like bond angle (117.3°). Therefore the spin density originates from the p-orbitals of O atoms as shown in Fig. 1. The calculated positron lifetimes for the majority (207ps) and minority (216ps) spins are found to be substantially different .

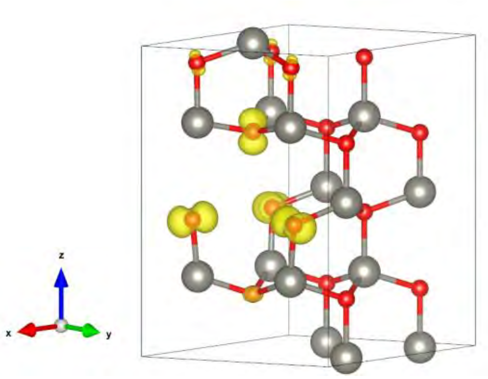

Fig. 1 Spin density of the Zn vacancy in ZnO.

We also study the Fermi contact term of muon in Si by using up to the 512 site supercell and find that a large unit supercell is necessary to obtain the converged result.

References

[1] M. Maekawa et al., Appl. Phys. Lett., 110, 172402 (2017).

Development and application of a new method for material structure prediction supported by experimental data

Shinji TSUNEYUKI

Department of Physics, School of Science,

The University of Tokyo, 7-3-1 Hongo, Bunkyo-Ku, Tokyo 113-0033

Institute for Solid State Physics,

The University of Tokyo, Kashiwa-no-ha, Kashiwa, Chiba 277-8581

Theoretical prediction of crystal structure from its chemical composition and physical conditions has been a long-standing problem of physical sciences [1]. There have been so many attempts in this direction and some of them have made a great success such as the prediction of high-temperature superconducting phases of sulfur hydride with the genetic algorithm [2] and the particle swarm optimization [3]. And yet the number of atoms in the unit cell reachable with these algorithms are limited, and we need to develop alternative approaches for theoretical prediction of new materials.

In this project, we are developing a method of structure prediction supported by experimental data. The method is designed to utilize powder diffraction data whose range of diffraction angle is limited by experimental setup or whose quality is insufficient for Rietveld analysis just like ultra-high-pressure experiments. In this method, instead of finding the global minimum of the multi-dimensional potential energy surface $E(\mathbf{R})$ as a function of the atomic positions $\mathbf{R}$, we define the effective potential $F(\mathbf{R})$ defined as the sum of $E(\mathbf{R})$ and a penalty function which increases when the simulated diffraction pattern deviates from the experimental one:

$$F(\mathbf{R}) = E(\mathbf{R}) + \alpha N(1-\lambda),$$

$$\lambda = \sum_{\theta_{\mathrm{obs}}} I(\theta_{\mathrm{obs}}) \Big/ \int I(\theta)d\theta.$$

Here, $I(\theta)$ is the diffraction intensity of the simulated crystal and so is a function of $\mathbf{R}$, N is the number of atoms in the simulation cell, and α is a control parameter. The sum and integral for so-called crystallinity λ are taken within the

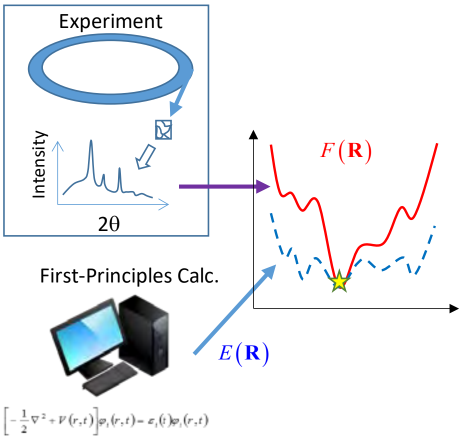

Fig.1 Schematic view of the data assimilation for the prediction of crystal structures with incomplete diffraction data.

range of the experimentally available diffraction angle θ, while θ_{obs} is the angle of each diffraction peak observed within the range. λ becomes unity when the simulated structure reproduces the experimentally observed diffraction data. The global minimum of $E(\mathbf{R})$ coincides with that of $F(\mathbf{R})$, while other local minima of $E(\mathbf{R})$ becomes less stable in $F(\mathbf{R})$ due to the penalty $\alpha N(1-\lambda)$ so that we can find the global minimum of $F(\mathbf{R})$ more easily.

We performed simulated annealing with the effective potential $F(\mathbf{R})$ for polymorphs of SiO_2 (low quartz, low cristobalite, coesite) and carbon (diamond, graphite) to find that each crystal structure can be obtained with high probability even if we use the diffraction data of a very limited range of $20° < \theta < 45°$ [4]. It should be noted that λ does not contain the information on the diffraction peak intensity except for the diffraction angle. It means that the method is robust against the noise and the preferred orientation effect which are often problematic when the sample for the diffractometry is small.

The present method is in a sense a realization of data assimilation in materials science. Data assimilation is often used in the simulation for the weather forecast, where the solution of the Navier-Stokes equation is adjusted to reproduce the temporal sequence of weather data at discrete observation points. In the present method, limited information on the diffraction angle helps the structure simulation. The same idea could be, in principle, applied to materials simulation with various experimental data such as the scanning tunneling microscope or the transmission electron microscope.

References

[1] J. Maddox, Nature 335, 201 (1988).

[2] D. Duan, Y. Liu, F. Tian, D. Li, X. Huang, Z. Zhao, H. Yu, B. Liu, W. Tian, and T. Cui, Sci. Rep. 4, 06968 (2014).

[3] Y. Li, J. Hao, H. Liu, Y. Li, and Y. Ma, J. Chem. Phys. 140, 174712 (2014).

[4] N. Tsujimoto, D. Adachi, R. Akashi, S. Todo and S. Tsuneyuki, to appear in Phys. Rev. Mat.

DFT studies on next-generation battery, solar cell and catalyst

Yoshitaka TATEYAMA

Center for Green Research on Energy and Environmental Materials (GREEN), National Institute for Materials Science (NIMS), 1-1 Namiki, Tsukuba, Ibaraki 305-0044; Elements Strategy Initiative for Catalysts & Batteries (ESICB), Kyoto University, Goryo-Ohara, Nishikyo-ku 615-8245.

We have addressed the mechanisms, and as well conducted materials search for next-generation batteries [1], solar cells [2] and catalysts [3], with cutting-edge DFT calculation techniques. In this report, we mainly describe the novel Na-excess cathodes for Na-ion batteries [1].

Increasing the capacity of Na ions batteries is a highly desired industrial goal. One possible way of achieving such an increase is evoking reversible oxygen redox that would add extra capacity to that of transition metal (TM) redox. To understand the atomistic origin of the O redox, we carried out a comprehensive density functional study of the electronic properties of the $R\bar{3}m$ Na_2RuO_3 (space group 166) and $R\bar{3}$ Na_1RuO_3 (space group 148) as shown in Figure 1. It was speculated that these compounds undergo reversible O redox which increases the capacity by 40% beyond the TM redox capacity to an impressive value of 180 mA.h/g. We then screened the full range of ternary $R\bar{3}$ compounds that consist of Na, O and *4d* transition metal (TM) elements in search for candidate compositions with higher electrochemical potential and larger capacity for sodium ion battery cathode applications.

Computationally, we treated the exchange-correlation functional with GGA+U formalism. U term was particularly fine-tuned to reproduce the electrochemical potential of Na extraction in the Na_xRuO_3 compound for which measurements exist. We found that U = 2 eV fulfils this criterion and moreover it produces an electronic structure that resembles the one obtained with higher level HSE03 functional.

We could reproduce theoretically the voltage plateaus detected in the Na_xRuO_3 cathode (x = 0.5–2) and demonstrate that O's significant participation in the redox reaction was the origin of the extra capacity that has been observed experimentally. We also found that O–O distance was maintained at ~2.5 Å during the desodiation process. Furthermore, our results regarding the survey of Na_1TMO3 compounds revealed that in descending order Na_1NbO_3, Na_1AgO_3, Na_1PdO_3 and Na_1RhO_3 had O populations of 4.94 e/O, 4.66 e/O, 2.10 e/O and 1.5 e/O near the Fermi level, respectively, all being higher than that of

Na_1RuO_3. Consequently, in all these compounds O’s participation in the redox mechanism is predicted to be more prominent. The case of Na_1NbO_3 is particularly interesting as its high capacity originates entirely from reversible O redox as Nb adopts d^0 configuration in this compound. Given the affordability of Nb metal and the robust stability of $R\bar{3}$ Na_1NbO_3 phase, we predict that Na_1NbO_3 is a prime candidate for Na ion battery applications.

In compounds with $R\bar{3}$ structure, the availability of O electrons for redox reaction originates from the local coordination environment. In these compounds, O ions are coordinated by two TM ions and two Na ions. Consequently, O under-coordination elevates some of un-hybridised or orphaned O *2p* states closer to the Fermi level and thus facilitates continuous O redox over a wide range of Na concentrations. Although this mechanism, to some extent, resembles the exclusive reversible O redox in 3d transition metal oxides, however, due to weaker localisation effects of *4d* transition metals, some TM–O hybridisation always exists. This hybridisation together with relatively large O–O separation prevents the detrimental O_2 evolution in these compounds.

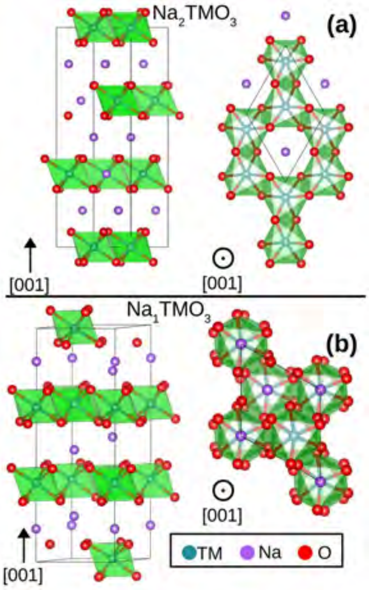

Fig. 1: The structures of surveyed Na_xTMO_3 Compounds. Space group 166 ($R\bar{3}m$) is presented in (a) while space group 148 ($R\bar{3}$) is presented in (b). Note the difference in Na content.

References

[1] M. H. N. Assadi, Masashi Okubo, Atsuo Yamada, Yoshitaka Tateyama, J. Mater. Chem. A 6, 3747-3753 (2018).

[2] Jun Haruyama, Keitato Sodeyama, Ikutaro Hamada, Liyuan Han, Yoshitaka Tateyama, J. Phys. Chem. Lett. 8, 5840-5847 (2017).

[3] Seiji Kasahara, Keisuke Natsui, Takeshi Watanabe, Yasuyuki Yokota, Yousoo Kim, Shota Iizuka, Yoshitaka Tateyama, Yasuaki Einaga, Anal. Chem. 89, 11341-11347 (2017).

.

Atomic structure and electromagnetic properties of oxide interfaces

Chunlin Chen[1], Deqiang Yin[1], Hongping Li[1], Kazutoshi Inoue[1], Yuichi Ikuhara[1,2]
[1]*Advanced Institute for Materials Research, Tohoku University, Sendai, Miyagi, 980-8577*
[2]*Institute of Engineering Innovation, The University of Tokyo, Yayoi, Tokyo, 113-8656*

Clarifying how the atomic structure of interfaces/boundaries in materials affects the electronic and magnetic properties is of fundamental interest in materials science. By combining atomistic first-principles calculations with atomic-resolution transmission electron microscopy (TEM), we systematically investigated the atomic structure and electromagnetic property of the perovskite-related $Sr_nNb_nO_{3n+2}$ compounds [1] and Fe_3O_4 twin boundaries (TBs) [2]. We performed the density functional theory (DFT) calculations using the projector augmented wave (PAW) method as implemented within Vienna ab Initio Simulation Package (VASP) with the DFT+U formulation. The valence-electron wave functions were expanded in a plane wave basis with energies up to 400 eV. All of the atoms in the system were fully relaxed with the conjugate gradient algorithm until the magnitude of the Hellmann-Feynman force on each atom and the total energies converged to less than 0.05 eV/Å and 1.0×10^{-4} eV, respectively. The Brillouin zone integration was performed via the tetrahedron method with the Blöchl correction.

The physical origin has been unknown for the transition of electrical properties from the 3D isotropic conductivity in $SrNbO_3$ to the quasi-1D metallic conductivity in $Sr_nNb_nO_{3n+2}$. The generalized gradient approximation (GGA) within the Perdew and Wang (PW91) scheme was employed to describe the exchange-correlation functional with an $8\times6\times2$ Monkhorst-Pack k-point grid. The effective Hubbard parameter ($U_{\text{eff}} = 7.8$ eV) was used to consider the effect of the localization of Nb-4d electrons. We have demonstrated that the local electrical conductivity in the $Sr_nNb_nO_{3n+2}$ compounds directly depended on the configuration of the NbO_6 octahedra in local regions [1].

On the other hand, by combining atomistic spin-polarized first-principles calculations and atomic-resolution TEM with differential phase contrast imaging, we investigated the atomic and electronic structures of individual Fe_3O_4 TBs to systematically determine their magnetic couplings. The Perdew-Burke-Ernzerh GGA schemewas employed with an $7\times5\times1$ Monkhorst-Pack k-point grid. The effective Hubbard parameter ($U_{\text{eff}} = 3.8$ eV) was used. The magnetic coupling across the Fe_3O_4 TBs can be either antiferromagnetic or ferromagnetic, which directly depends on the TB atomic core structures and resultant electronic structures within a few atomic layers [2].

References

[1] C. Chen, D. Yin, K. Inoue, F. Lichtenberg, X. Ma, Y. Ikuhara, J. G. Bednorz: ACS Nano **11** (2017) 12519.

[2] C. Chen, H. Li, T. Seki, D. Yin, G. Sanchez-Santolino, K. Inoue, N. Shibata, Y. Ikuhara: ACS Nano **12** (2018) 2662.

Development & Application of Rational Drug Design using the Forth Innovation Methodology

Yuta Yamamoto[1], Shogo Nakano[2], and Hiroaki Tokiwa[1]
[1]Rikkyo University, 3-34-1 Nishi-Ikebukuro, Toshima, Tokyo 171-8501
[2]University of Shizuoka, 52-1 Yada, Suruga-ku, Shizuoka 422-8526

We have identified a short chain dehydrogenase like l-threonine 3-dehydrogenase (SDR-TDH) from metagenome data (mtTDH) by database mining based on the forth innovation methodology. Its enzymatic properties suggested that mtTDH has unique characteristics relative to other SDR-TDHs, including two mesophilic and thermophilic SDR-TDHs identified in this study. The activation energy of mtTDH was the lowest of those of the SDR-TDHs, indicating that it is a psychrophilic enzyme. Size-exclusion chromatography analysis revealed mtTDH is a monomer. We could also determine crystal structures of mtTDH in apo, binary, and two ternary complexes (L-Ser- and L-Thr-soaked forms) at resolutions of 1.25–1.9 Å.[1] *Ab initio* computational analysis using the fragment molecular orbital (FMO) calculations and the molecular dynamics (MD) simulation revealed the molecular mechanism of switching between the open and closed states induced by substrate binding and product release. We used the programs PAICS and AMBER14 for the FMO and MD calculations, respectively. Furthermore, six residues and two water molecules at the active site contributing to product release were assigned. The residues could be categorized into two groups on the basis of the enzymatic properties of their variants. The former group appeared to affect L-Thr dehydrogenation directly, because the K_{cat} value of their variants was >80-fold lower than that of wild-type mtTDH. On the other hand, the latter group contributes to switching between the open and closed states, which is important for the high substrate specificity of SDR-TDH for l-Thr: the K_{cat} and K_{m} toward L-Thr values of variants in these residues could not be determined because the initial velocity was unsaturated at high concentrations of L-Thr. On the basis of these findings, we proposed a product release mechanism for SDR-TDH associated with specific structural changes.

References

[1] T. Motoyama, S. Nakano, Y. Yamamoto, H. Tokiwa, Y. Asano, and S. Ito, *Biochemistry,* **56(43)**, 5758-5770 (2017)
DOI: 10.1021/acs.biochem.7b00832.

Development of High-performance Perfluoro Polymer Electret

Seonwoo KIM and Yuji SUZUKI

Department of Mechanical Engineering, The University of Tokyo
Hongo, Bunkyo-ku, Tokyo 113-8656

Electret is a dielectric with quasi-permanent charge. The charges trapped in proper electret materials can be stably stored and able to generate an external electrostatic field for tens of years. In recent years, a vibration-driven electret energy harvester attracts much attention, because it can convert ambient low-frequency vibration into electricity. High-performance electret materials have been desired, since the maximum power output of electret energy harvester is proportional to the electret surface potential squared [1]. Also, long-term stability of trapped charge determines the lifespan of the device. Although high-performance electrets have been reported in recent years [2], they are discovered from experimental trials, while its properties were unpredicted. In order to develop a new high-performance electret, it is necessary to understand underlying physics.

In the present study, we made numerical simulations to understand electron trapping phenomenon in polymer electrets using quantum mechanical analysis. An amorphous polymer electret CYTOP (AGC Co., Ltd) is mainly assumed, focusing on the electron trap site and the trap energy for different end groups.

Density functional theory with long-range correction (LC-DFT) calculation is adopted to analyze the electronic state of CYTOP molecules. The LC-BLYP density functional is used to solve Kohn-Sham equation with 6-31+g* basis sets. Three types of CYTOP with different end group are studied as shown in Fig. 1; CTL-S has trifluoromethyl end, CTL-A has carboxyl end, and CTL-M has amidosyl end. Conventionally-used bulk polymer electrets (PE, ETFE, PTFE) are also analyzed for comparison. Fig. 2 shows distribution of electrons trapped in electret tetramers. The electron trapped in PE does not lie on the structure, showing the molecule is electrophobic. On the other hand, clear electrophilicity can be found in fluorine-rich part of ETFE and PTFE. For CYTOP molecules, the trapped electron populates near

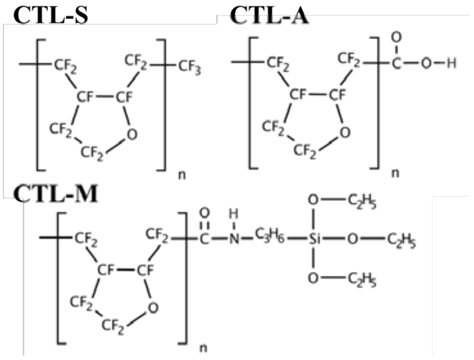

Fig 1. Chemical structure of CYTOP polymers

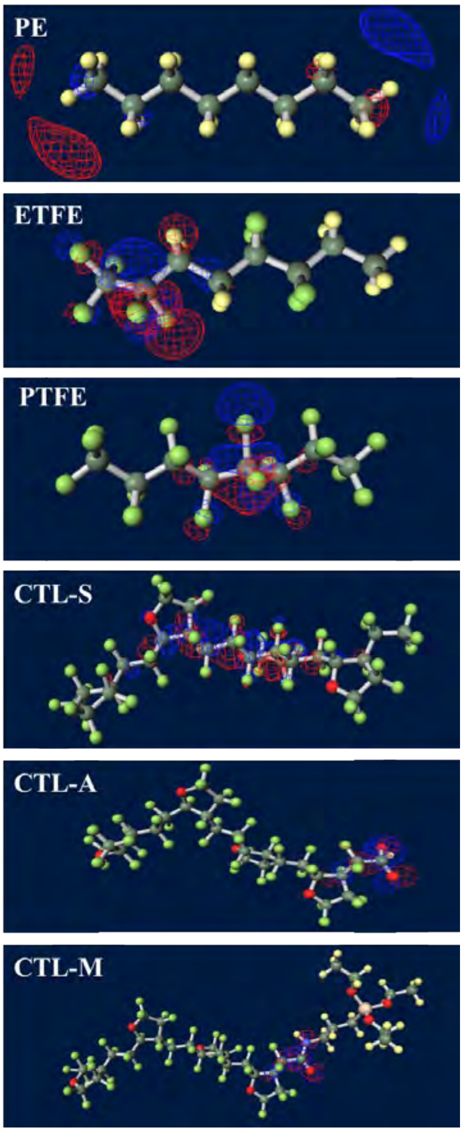

Fig 2. Distribution of trapped electron in electret tetramers (Green: fluorine, Blue: nitrogen, Red: oxygen, Khaki: carbon, Yellow: hydrogen, Pink: silicon)

end group (-COOH of CTL-A and -CONH of CTL-M), implying that the end group attracts the electron even more than perfluorinated back-bone structure itself. The orbital energies of each molecules are calculated. The energy of orbital where the electron is trapped is used to estimate the electron affinity (EA) following Koopmans' theorem. Calculated EAs have order as follows: CTL-M (5.83 eV) > CTL-A (4.7 eV) > CTL-S (4.39 eV) > PTFE (3.56 eV) > ETFE (3.02 eV) > PE (-1.93 eV). Acquired EAs of CYTOP make qualitative agreement with the thermally stimulated discharge (TSD) current peaks [2]. Note that the order of PE, ETFE, PTFE is also in accordance with that of TSD peaks. However, their trap energy cannot be fully described by present simulation because their performance as electret depends on not only by its single molecular EA but also by their morphology. Although our analysis on single molecule cannot perfectly interpret the real system of electret, we expect our method can be used as an indicator to predict performance of amorphous polymer electrets.

The computation is performed with SGI ICE XA ISSP system B F4cpu nodes, using quantum mechanical simulation package NWChem [3]. Every computation was held with 4 nodes (96 CPUs). In case of CYTOP tetramers, the calculation cost was approximately 9200 hours of CPU time for each case. For PE, ETFE and PTFE, 7000 hours of CPU time was necessary in total.

References

[1] Y. Suzuki: IEEJ Trans. Electr. Electron. Eng. 6 101–11

[2] K. Kashiwagi et al.: J. Micromech. Microeng. **21** (2011) 125016.

[3] M. Valiev et al.: Comput. Phys. Commun. **181** (2010) 147.

Singlet-triplet splitting of thermally activated delayed fluorescence molecules

Yoshifumi NOGUCHI

Department of Applied Chemistry and Biochemical Engineering, Graduate School of Engineering, Shizuoka University, Johoku 3-5-1, Hamamatsu, Shizuoka 432-8561, Japan

Thermally activated delayed fluorescence (TADF) in which triplet exciton transits to higher energy singlet exciton via a reverse intersystem crossing (RISC) is a key mechanism to achieve high efficiency in third generation organic light-emitting diodes (OLEDs) [1]. TADF molecules with nearly zero energy difference between the singlet and triplet excitons or singlet-triplet splitting (Δ^{ST}) are required for RISC. A great deal of efforts have been invested in the experimental cycle involving design → synthesizing → measurement to detect *good* TADF molecules. Although certain some simulations within the time-dependent density functional theory (TDDFT) have been applied to TADF molecules for the purpose of reducing the experimental effort, the theoretical attempts have been hampered by the peculiarity of TADF molecules of which the charge transfer excitation occurs in small-middle molecules size. That is, conventional functionals such as the (semi-)local and range-separation type functionals fail to describe the optical properties of TADF molecules. In addition, according to Ref. [2], in case that the hybrid functional is used, the mixing parameters should be optimized individually for each molecule and for singlet and triplet excitations.

In this study, we proposed an efficient computational method capable of simulating accurate Δ^{ST} in TADF molecules within the available computational facilities from first-principles. Our method evaluates Δ^{ST} as an expectation value of bare exchange Coulomb interaction, $< i|2v^{ex}|i >$, where $|i >$ is the exciton wave function ($= \sum_{e,h} A^{i}_{e,h}\psi_e(r_1)\psi^*_h(r_h)$) at the i-th exciton level [3]. We applied it to eighteen TADF molecules composed of 30-110 atoms, and confirmed that our method is sufficiently accurate for Rydberg and charge transfer-type excitons and slightly less accurate for local excitons [4].

References

[1] H. Uoyama, et. al.: Nature **492**, 234 (2012).

[2] S. Huang, et. al.: J. Chem. Theory Compt., **9** 3872 (2013).

[3] D. Hirose, Y. Noguchi, and O. Sugino: J. Chem. Phys. **146** (2017) 044303.

[4] Y. Noguchi and O. Sugino: J. Phys. Chem. C. **121** 20687 (2017).

Reduction of Rare Metals in Fuel Cell Catalysts and Hydrogen Permeable Membrane

Yuji KUNISADA

Center for Advanced Research of Energy and Materials, Faculty of Engineering,
Hokkaido University, Sapporo, Hokkaido 060-8628

We investigated the catalyst atom adsorption and diffusion properties on non-metal element doped graphene and hydrogen adsorption and diffusion properties on the surfaces and in the interfaces of ceramic materials, with the aid of the first principles calculation based on the density functional theory (DFT).

At first, we investigated adsorption and diffusion properties of Pt and Fe atoms on non-metal element doped graphene. We performed the total energy and electronic structure calculations using The Vienna Ab initio simulation package (VASP). We installed parallelized VASP with Intel® MPI Library and Intel® Math Kernel Library. We found that the adsorption energies of both Pt and Fe atoms increase by non-metal element doping into graphene lattice. From the electronic structure analysis, we revealed that Pt atoms form covalent bonds with graphene, while Fe atoms adsorb on graphene with the attractive Coulomb interaction. We also calculated the dopant dependence of diffusion properties of Pt and Fe atoms. From these calculations, we found that the non-metal dopants in graphene can prevent the surface diffusion of Pt and Fe atoms.[1,2]

We also investigated the hydrogen adsorption and diffusion properties on the surfaces and in the interfaces of TiN and HfN. We found that the nanocrystalline TiN and HfN membrane show high hydrogen permeability from experiments. We revealed that hydrogen atoms become hydride ions on surfaces and in interfaces of these materials using DFT calculations. [3,4]

References

[1] S. Hasegawa, Y. Kunisada, N. Sakaguchi: J. Phys. Chem. C 121 (2017) 17787.

[2] S. Hasegawa, Y. Kunisada, N. Sakaguchi: e-J. Surf. Sci. Nanotech. accepted.

[3] C. Kura, Y. Kunisada, E. Tsuji, C. Zhu, Hi. Habazaki, S. Nagata, M. Patrick Müller, R. A. De Souza, Y. Aoki: Nat. Ener. 2 (2017) 786.

[4] C. Kura, S. Fujimoto, Y. Kunisada, D. Kowalski, E. Tsuji, C. Zhu, H. Habazaki, Y. Aoki: J. Mater. Chem. A 6 (2018) 2730.

First-principles calculations of magnetic ultrathin films on surfaces

Yoshihiro GOHDA
Department of Materials Science and Engineering, Tokyo Institute of Technology
J1-3, Nagatsuta-cho 4259, Midori-ku, Yokohama 226-8502, Japan

Low-dimensional ferromagnetic nanostructures are of fundamental interest. However, ferromagnetism in realistic two-dimensional atomic structures is quite rare, because any finite-temperature magnetic order is prohibited for the isotropic two-dimensional Heisenberg model due to the Mermin-Wagner theorem. In addition, the stability of ferromagnetism in two-dimensional ferromagnetic structures is partially due to the surface magnetic anisotropy. Therefore, it is important not only to examine the magnetic order of the groud state, but also to analyze the magnetic anisotropy. Even though MnN monolayer films on Cu(001) have been reported to have an antiferromagnetic order [1], monolayer films of Mn compounds exhibiting the ferromagnetism have not been reported.

In this study, we demonstrate ferromagnetism in new two-dimensional strcutures on nonmagnetic transition-metal (TM) surfaces [2]. First-principles calculations were performed on the basis of density functional theory with the generalized gradient approximation by the OpenMX code [3]. We have found that MnB/TM(001) and MnC/TM(001) are ferromagnetic, whereas MnN/TM(001) is antiferromagnetic, irrespective of the kind of TM we studied. In Fig. 1, we show the calculated partial density of states (PDOS) of the Mn $3d$ states in MnB/Ag(001). The high PDOS of the nonmagnetic state at the Fermi energy ε_F is avoided by the exchange splitting in the ferromagnetic state, which is the characteristic of the itinerant ferromagnetism. With the detailed analysis, we have identified the ferromagnetism in MnB/TM(001) and MnC/TM(001) comes from the double-exchange mechanism, whereas the antiferromagnetism in MnN/TM(001) originates from the superexchange. We also investigated the local magnetic anisotropy energy using second-order perturbation theory [2, 4]. We have clarified the main contributions to the in-plane anisotropy in MnB/Pd(001) as hybridization between Mn and Pd states.

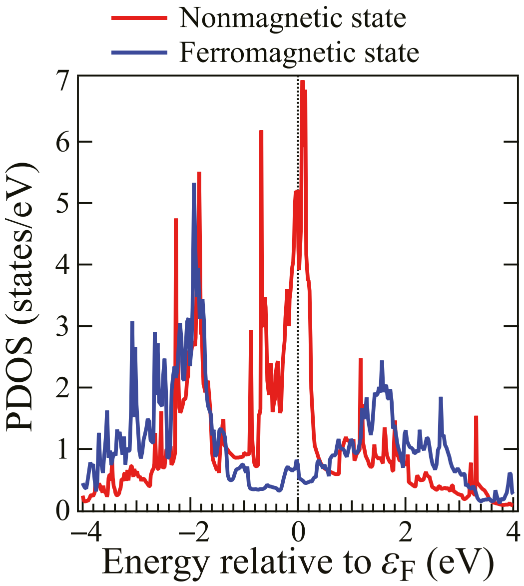

Figure 1: The calculated PDOS of the Mn $3d$ states in MnB/Ag(001) for the nonmagnetic state as well as the ferromagnetic state plotted as the summation of the majority- and minority-spin states.

[1] X. D. Liu, B. Lu, T. Iimori, K. Nakatsuji, and F. Komori, Phys. Rev. Lett. **98**, 066103 (2007); K. Nakatsuji, S. Nakamura, T. Tanaka, Y. Gohda, *et al.*, in preparation.

[2] S. Nakamura and Y. Gohda, Phys. Rev. B **96**, 245416 (2017).

[3] T. Ozaki, Phys. Rev. B. **67**, 155108 (2003).

[4] Z. Torbatian, T. Ozaki, S. Tsuneyuki, and Y. Gohda, Appl. Phys. Lett. **104**, 242403 (2014).

First-Principles DFT Calculations for Transition-Metal Oxides

Kunihiko YAMAUCHI
ISIR-SANKEN, Osaka University, Ibaraki, Osaka 567-0047

Transition-metal oxides show fascinating physical properties such as high temperature superconductivity, magnetism, ferroelectricity and even topological property. As aiming at finding novel multifunctional materials, we have explored spin-crossover phenomenon in $LaCoO_3$-related system. In $LaCoO_3$, Co^{3+} (d^6) ion shows the low-spin state (S=0) at the ground state in the rhombohedral structure. On the other hand, it has been reported that Co ion shows intermediate spin state (S=1) when the uniaxial pressure is applied. In order to understand the relation between Co spin state and the structural distortion, we first analyzed the phonon modes of the distorted crystal structure with respect to the ideal cubic perovskite structure via group theory. Then the electronic structure and the Co spin state were calculated under the several distortion modes via first-principles approach. Finally, we found that intimidate spin state can be invoked by combination between two modes, i.e., R_3^- mode which induces cooperative Jahn-Teller distortion and Γ_3^+ mode which modulates c/a ratio. The resulted distortion stabilizes the orbital ordering of Co e_g electrons as shown in Fig.1.

We also studied the electronic states in iridiates. Among them, Na_4IrO_4 exhibits unusual square planar coordination of IrO_4. In the square planar crystal field, Ir 5d state adopts an intermediate spin state as leading to the strong single-site anisotropy.[1] Here, spin-orbit coupling plays a minor role in shaping the electronic structure, but leads to strong magnetocrystalline anisotropy.

Some of iridates are known to show the "$J_{\rm eff}$=1/2" Mott insulating state. In order to explore the metal-insulator transition, rutile-based IrO_2/TiO_2 superlattices were theoretically designed. The heterostructure exhibit a thickness-controlled metal-to-insulator transition, crucially related to the connectivity among IrO_6 octahedra.

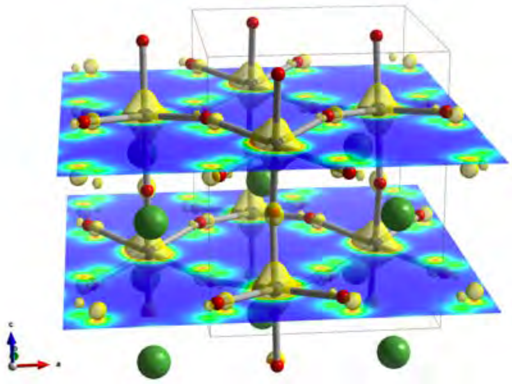

Figure 1: Orbital ordering of Co e_g state with intermediate spin state in monoclinic $LaCoO_3$.

References

[1] Xing Ming, Carmine Autieri, Kunihiko Yamauchi, and Silvia Picozzi, Phys. Rev. B **96**, 205158 (2017).

[2] Xing Ming, Kunihiko Yamauchi, Tamio Oguchi, Silvia Picozzi, arXiv:1702.04408 (2017).

Large scale ab initio calculations on the fundamental processes of solar energy convergence devices and on designing principles for new materials

Koichi YAMASHITA

Department of Chemical System Engineering, School of Engineering,

The University of Tokyo, 7-3-1, Hongo, Bunkyo-ku, Tokyo 113-8656

Water-splitting photocatalyst materials are required to have suitable band positions, band gap, and carrier effective masses. Recently, arrangements of N^{3-} and O^{2-} anions in perovskite-type oxynitride crystals, i.e., anion ordering, have been found to be specific and controllable, but further discussions are required to show guidelines to tune electronic properties by anion ordering. Thus, we aim to clarify the relationship between the anion ordering and perovskite oxynitride band structures by means of first-principles calculations.

We performed density-functional theory (DFT) calculations of electronic properties of $MgTaO_2N$ by Vienna ab-initio simulation package (VASP) to discuss its applicability to water-splitting photocatalyst, in consideration of such structural factors as octahedral tilting, anion ordering, and the interplay between perovskite and ilmenite polymorphs. Most of the configurations of the perovskite-type $MgTaO_2N$ were more suitable for water-splitting than ilmenite-type $MgTaO_2N$ polymorphs due to their favorable band edge position and effective masses (Figure 1). We found the strong correlation between the conduction band structures and octahedral tilting—configurations with more tilted octahedra had larger overlap between Ta-5d and anion-2p bands, resulting in bandgap opening and band dispersion reduction. There-fore, reducing octahedral tilting (e.g. via A-site doping) is highly desirable in the perovskite-type $MgTaO_2N$ material design for photocatalytic applications [1].

We have also studied organic-inorganic hybrid perovskite (OIHP) solar cells, namely lead halide perovskites ($APbX_3$: A and X are a monovalent cation and a halogen, respectively). OIHP solar cells are attracting much interest for their high photoconversion efficiency, but it is not sufficiently understood why OIHP has such remarkable properties.

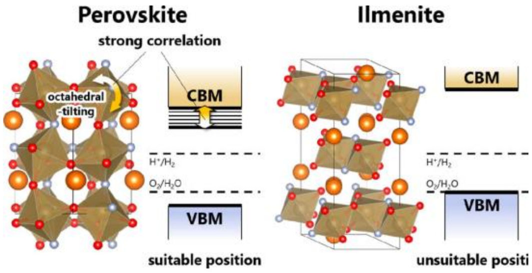

Figure 1: Schematic illustration of structures and band edge positions of perovskite- and ilmenite-type $MgTaO_2N$. Reprinted from [1].

We already investigated charge carrier trapping at defects on surfaces or grain boundaries, and proposed that moderate condition—the balance between Pb-rich and I-rich ones—is the best choice in terms of the defect formation energies [2]. In this year we approached the origin of high charge separation efficiency of OIHPs by DFT calculations and ab initio molecular dynamics simulations implemented in VASP, which revealed that inorganic frame dynamics induced charge separation [3]. We investigated lead iodide perovskites, $APbI_3$ (A is methyl ammonium, formamidinium, guanidinium, or cesium; in descending order of dipole moment), under two conditions: inorganic frames were fixed or all atoms moved (type I and II, respectively). We calculated the overlap integrals of valence band maxima (VBM) and conduction band minima (CBM), which revealed that type II condition tended to have less overlap integrals independently of A-site cations. Then we evaluated electrostatic potentials contributed by holes and electrons at VBM and CBM levels, respectively, which revealed that the overlap integrals and the potentials were highly correlated, and that the total potentials were dominantly governed by inorganic frames.

References

[1] A. Kubo, G. Giorgi, and K. Yamashita: J. Phys. Chem. C **121** (2017) 27813–27821.

[2] H. Uratani and K. Yamashita: J. Phys. Chem. Lett. **8** (2017) 742–746.

[3] H. Uratani and K. Yamashita: J. Phys. Chem. C **121** (2017) 26648–26654.

Theoretical studies on the energy storage materials

Atsuo YAMADA
Department of Chemical System Engineering,
The University of Tokyo, Hongo, Bunkyo-ku, Tokyo 113-8656

Pseudocapacitive energy storage at the electrochemical double layer can provide efficient devices to allow huge power and excellent reversibility. RuO_2 is one of the benchmarking materials that has been widely studied. It utilizes the fast redox reaction of Ru accompanied by the electroadsorption of protons,

$$RuO_a(OH)_b + \delta H^+ + \delta e^- \leftrightarrows RuO_{a-d}(OH)_{b+d}$$

However, detailed analysis of the reactions has not yet been achieved either theoretically or experimentally due to a lack of structural information on electrochemical interface. Recently structures of RuO_2/water interface were first provided using a theoretical scheme that considers the effects of electrode potential and pH [1]. In the present study, based on the provided structures, charge storage mechanism was calculated as a function of electrode potential at fixed pH = 0 to analyze the electron orbitals contributing to the pseudocapacitive reaction.

We demonstrated the extensive and unique contribution of oxygen orbitals at specific surface sites to pseudocapacitive reactions depending on the electrode potential. In potential region between −0.5 V and −0.1 V vs. RHE where averaged formal valence of surface Ru changes from Ru(III) to Ru(IV), Bader charge changes of Ru and O atoms at br sites are +0.52e, +0.26e. Moreover, in the higher potential region between 1.1 V and 1.5 V vs. RHE where averaged formal valence of surface Ru changes from Ru(IV) to Ru(V), Bader charge changes of Ru and O atoms at cus sites are 0.32e and 0.65e. Surprisingly large contributions of O 2p orbitals are observed; more of the electrons are extracted from O rather than Ru [2].

All the calculations were performed using GPAW code together with GGA/RPBE functional and PAW method. The k-points were sampled using a (4 × 4 × 1) mesh and electronic structures were calculated by thefinite difference method with a grid parameter of 0.20 ± 0.01 Å.

References

[1] E. Watanabe et al : *J. Phys. Chem. C.* **120** (2016) 8096.

[2] E. Watanabe, H. Ushiyama, K. Yamashita, Y. Morikawa, D. Asakura, M. Okubo and A. Yamada: *J. Phys. Chem. C.* **121** (2017) 18975

Prediction of properties of organic ferroelectrics and piezoelectrics by first-principles calculation

Shoji ISHIBASHI
Research Center for Computational Design of Advanced Functional Materials (CD-FMat),
National Institute of Advanced Industrial Science and Technology (AIST)
Tsukuba, Ibaraki 305-8565

Organic ferroelectrics and piezoelectrics are promising materials since they contain neither toxic nor rare elements. In addition, they are flexible and printable. Recently, we have experimentally found that organic antiferroelectrics undergo the antiferroelectric-to-ferroelectric transition by applying a electric field for squaric acid (SQA), [H-55dmbp][Hca] (55dmbp = 5,5'-dimethyl-2,2'-bipyridine; H2ca = chloranilic acid) [1], and 2-Trifluoromethylnaphthimidazole (TFMNI) [2]. Usually, an antiferroelectric consists of two sublattices oppositely polarized. We evaluated the total polarization values for ferroelectric SQA and [H-55dmbp][Hca] by calculating polarization of one sublattice and doubling it for each compound. We used the experimentally obtained sublattice structures for the antiferroelectric phases. As for the hydrogen positions, they were computationally optimized. The obtained polarization values are in good agreement with the experimental results [1]. As for TFMNI, the crystal structure of the ferroelectric phase under a electric field has been successfully obtained [2]. We evaluated the spontaneous polarization using the experimental structure of the ferroelectric phase with the hydrogen positions computationally optimized. The obtained value is in good agreement with the experimental result.

The above calculations have been done with the GGA-PBE functional on the experimental structures with only the hydrogen positions computationally optimized. For SQA, we have tried to optimize computationally the whole of the crystal structure. In addition to the standard LDA and GGA-PBE functionals, we applied the vdW-DF-cx and rvv10 functionals, which are recent versions of the van der Waals DFT. Among the four functionals, the rvv10 reproduces the low-temperature structure of SQA best. We, therefore, applied the rvv10 for further calculations. By computationally applying a electric field, we have succeeded in simulating the antiferroelectric-to-ferroelectric transition in SQA [3]. Depending on the electric-field direction, two different ferroelectric phases have been obtained. One of them is thought to correspond to the experimentally-obtained phase [1] while the other is yet to be experimentally confirmed.

We utilized the System B of the Supercomputer Center, the Institute for Solid State Physics, the University of Tokyo for some calculations.

References

[1] S. Horiuchi, R. Kumai, and S. Ishibashi: Chem. Sci. **9** (2018) 425.

[2] K. Kobayashi, S. Horiuchi, S. Ishibashi, Y. Murakami, and R. Kumai: J. Am. Chem. Soc. **140** (2018) 3842.

[3] S. Ishibashi, S. Horiuchi, and R. Kumai: submitted to Phys. Rev. B.

Large-scale computational simulations of non-equilibrium transport phenomena

Yoshihiro Asai, Marius Bürkle, Jun-ichi Ozaki
Research Center for Computational Design of Advanced Functional Materials,
National Institute of Advanced Industrial Science and Technology (AIST),
Central 2, Umezono 1-1-1, Tsukuba, Ibaraki 305-8568

We studied the following subjects in the non-equilibrium transport problem using large-scale computational simulations:

1-1) Thermoelectric transport (Electrons and Phonons) calculation based on the first-principles DFT calculations.
1-2) Comparing first-principles transport results with scanning tunneling microscope break junction measurements of molecular devices.
1-3) The resistive switching mechanism and the topological physics of GeTe–Sb_2Te_3 interfacial phase change memory material are discussed based on the first-principles DFT calculations.
2-1) Time-dependent density matrix renormalization group study of the electric conductance of strongly correlated Hubbard chain.
3-1) Electronic properties of silicon-based nanocrystals in the quantum confinement regime.

In the following we outline these subjects and give the main results:

1-1) Ballistic electron and phonon transport calculations for metallic nano-contacts. We studied the difference of the thermoelectric transport properties for mono and multi-valent metals investigating the validity of the Wiedemann-Franz law in the quantum transport regime. We can show that depending on conformation and type of metal violations of the Wiedemann-Franz law can be up to 20%, even in the Ballistic regime and without significant phonon contribution. 【1】

1-2) Using accurate first-principle (DFT+$\sum$) based calculations we investigate the gate-dependence of the transport properties for different isomers of molecular conductors. This enables us to probe the transmission properties locally in energy space. Our first-principles results are used to elucidate the corresponding results experimental findings which show a clear dependence of the transport properties on the gate voltage. 【2】

1-3) The first-principles calculations of the current voltage characteristic of the possible 'on' and 'off' states of the GeTe–Sb2Te3 interfacial phase change memory (iPCM) material were used to identify the memory mechanism. The spectrum function in the channel area and the transmission probability function were used to discuss the important wave number for the memory as well as the role played by the topological physics.【3】

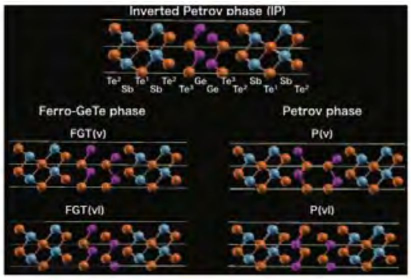

Fig.1 Model structure of the iPCM memory device material.

2-1) The time-dependent density matrix renormalization group【4】was used to discuss the length dependent conductance of the Hubbard chain. The contact effect is included the calculation, otherwise not included previously in the Tomonaga-Luttinger liquid (TLL) based theory. Unlike the TLL based theory predicting the perfect transmission leading to the unit conductance $G_0=2e^2/h$ in the infinite chain limit of the strong correlation regime, our calculation predicts a non-perfect transmission there, which we obtain after the damped oscillation in the finite length region.【5】We presume it being due to the inelastic component of the strong Coulomb repulsion and the renormalization of the single particle energy.

3-1) Nanocrystals in the quantum confinement regime are a promising candidates for third generation solar cells as they allow to tune their band-gap over a wide range. The gap can be tailored by an appropriate combination of size and surface functionalization. Using first-principles calculations and a quasi-band structure approach we mapped the band-gap of silicon nanocrystals as shown in Fig.2. Our theoretical predictions have been confirm by experiment.【6】

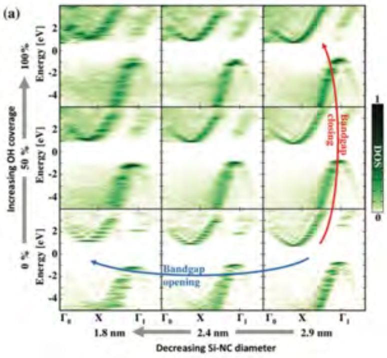

Fig.2 Quasi-band structure obtained from DFT calculations for 0%, 50%, and 100% OH coverage (for brevity 25% and 75% have been omitted), where the energy origin has been set into mid gap. We derived the bandgap as a function of the Si-NC diameter and the OH coverage, which agrees with the experimental results.

References

[1] M. Buerkle and Y. Asai, in preparation

[2] Y. Li, M. Buerkle, G. Li, A. Rostamian, D.R. Bowler, T. Miyazaki, Y. Asai, G Zhou, and N.J. Tao, in preparation

[3] H Nakamura, I. Rungger, S. Sanvito, N. Inoue, J. Tominaga and Y. Asai, *Nanoscale*, **9**, 9386 (2017).

[4] S. R. White and A. E. Feiguin, *Phys. Rev. Lett.* **93**, 076401 (2004).

[5] J. Ozaki and Y. Asai, in preparation

[6] M. Buerkle, M. Lozach, C. McDonald, D. Mariotti, K. Matsubara, Vladimir Svrvcek, *Adv. Funct. Mater.* **27**, 1701898 (2017)

Exploration of hydrogen-1s metallic state and superconductivty in oxyhydride compounds

Ryosuke AKASHI
Department of Physics, University of Tokyo
Hongo, Bunkyo-ku, Tokyo 133-0033

In this project, we pursued metallic states formed by 1s orbitals of hydrogen, especially focusing on the superconductivity. It has actually been long since the possible high-temperature superconductivity has been predicted in compressed elemental hydrogen and hydrogen compounds [1, 2]. Theoretically it is a trivial consequence of the BCS formula [3],

$$T_{\rm c} \simeq \omega {\rm exp}\left[-\frac{1}{\lambda}\right], \qquad (1)$$

with ω and λ being the frequency of the phonon mode that mediates the superconducting pairing and its pairing strength, respectively: Namely, if the mass of the ions is small, ω is large and so is $T_{\rm c}$. What is difficult is to realize the compressed situation required for the metallization. The recent discovery of the 200 K superconductivity in H_2S [4] proved that the predicted high T_c phase can indeed occur, but the required pressure was above 100 GPa, which renders difficult further studies on this phase, as well as its practical applications. We therefore focused on how to metallize the hydrogen electronic states more efficiently, from the computational viewpoint.

Recently, some of our colleagues have predicted transition metal oxyhydride ATiO$_2$H (A =Li, Na, K, Rb, Cs), that could be synthesizable in ambient pressure [5, 6]. According to the electronic structure calculation, the valence-top states involve the hydrogen-1s orbitals. To see the possibility of hole-doping in these states, using System B (Sekirei), we calculated the lattice-dynamical properties of the doped ATiO$_2$H. For the uniformly hole-doped case, we found sensitive dependence of the phonon dispersion on the $\mathbf{q}$ point. Namely, as the $\mathbf{q}$ for the dynamical matrix increases significant softening occurs around the X point in the orthogonal Brillouin Zone (Fig. 1), which seems to reflect the nesting property of the valence band. We also examined if this softening character persists in the chemically doped supercell configuration. This result has been presented in American Physical Society Annual Meeting in 2018, and the paper is in preparation [7].

We also studied of H-S systems under pressure to further understand the pressure induced transformation in the compressed H_2S. Through the first-principles structure search by a genetic algorithm, we found various thermodynamically stable sulfur-rich phases. Among them, we calculated with System B the electron-phonon coupling properties of HS_2 and H_5S_8, which are stabilized under pressure around 100 GPa. The result shows that sulfur phonon modes dominate the superconducting coupling, which yield $T_{\rm c}$ around 10 K [8]. Also, in the course of this work, we found a hidden relation between some previously found thermodynamically stable H_3S phases. Extending that relation, we theoretically formed numerous phases. The first-principles structure optimizations performed in System B have confirmed that these phases energetically competes with the previously known sturctures [9]. These results give us an insight into what happens through the pressure induced transition in hydrogen sulfide, which could be useful for systematic exploration of the superconducting hydrogen compounds.

The first-principles electronic structure calculations were done with the plane-wave basis code package QUANTUM ESPRESSO (5.0.3)(Ref.

[10]). The phonon and electron-phonon properties were calculated with the PHonon program in this package, which is based on the density functional perturbation theory [11]. The Brillouin-Zone integration for the metallic systems were done with the optimized tetrahedron method [12]. The GGA-PBE [13] and PBEsol [14] exchange-correlation potentials were used for the H_xS and $A\mathrm{TiO}_2\mathrm{H}$ systems, respectively. Parallelization was performed with respect to **k** points (-*npool* option) as implemented in *ph.x* code. The calculations were mainly done in System B. Using the electronic and lattice properties calculated with these programs, for HS_2 and H_5S_8, we calculated T_c by the gap equation in the density functional theory for superconductors [15–17].

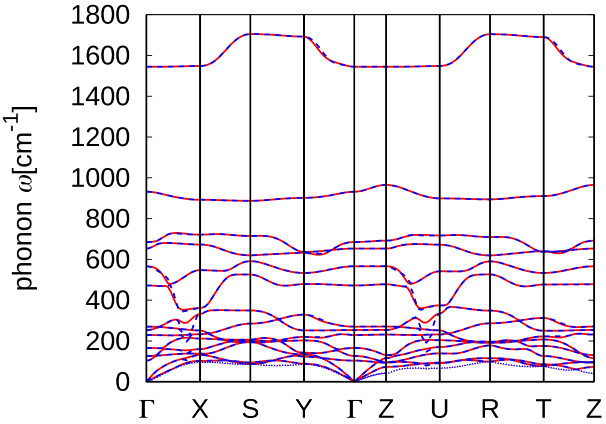

FIG. 1. Phonon dispersions for $\mathrm{RbTiO_2H}$ with 1/4 uniform hole doping, obtained from the dynamical matrices calculated on the (red) 6x6x2 and (blue) 8x8x2 **q** point meshes, respectively. In the latter case, softening around X is observed.

[1] N. W. Ashcroft, Phys. Rev. Lett. **21**, 1748 (1968).

[2] N. W. Ashcroft, Phys. Rev. Lett. **92**, 187002 (2004).

[3] J. Bardeen, L. N. Cooper, and J. R. Schrieffer, Phys. Rev. **108**, 1175 (1957).

[4] A. P. Drozdov, M. I. Eremets, and I. A. Troyan, V. Ksenofontov, and S. I. Shylin, Nature (London) **525**, 73 (2015).

[5] N. Sato and S. Tsuneyuki, Appl. Phys. Lett. **109**, 172903 (2016).

[6] N. Sato, R. Akashi, and S. Tsuneyuki, J. Chem. Phys. **147**, 034507 (2017).

[7] M. Ghim, N. Sato, R. Akashi, S.-H. Jhi, and S. Tsuneyuki, in preparation.

[8] I. Kruglov, R. Akashi, S. Yoshikawa, A. R. Oganov, and M. M. D. Esfahani, Phys. Rev. B **96**, 220101(R) (2017).

[9] S. Yoshikawa, R. Akashi, and S. Tsuneyuki, in preparation.

[10] P. Giannozzi *et al*, J. Phys.: Condens. Matter **21**, 395502 (2009); http://www.quantum-espresso.org/.

[11] S. Baroni, S. de Gironcoli, A. Dal Corso, and P. Giannozzi, Rev. Mod. Phys. **73**, 515 (2001).

[12] M. Kawamura, Y. Gohda, and S. Tsuneyuki, Phys. Rev. B **89**, 094515 (2014).

[13] J. P. Perdew, K. Burke, and M. Ernzerhof, Phys. Rev. Lett. **77**, 3865 (1996).

[14] J. P. Perdew, A. Ruzsinszky, G. I. Csonka, O. A. Vydrov, G. E. Scuseria, L. A. Constantin, X. Zhou, and K. Burke, Phys. Rev. Lett. **100**, 136406 (2008).

[15] M. Lüders, M. A. L. Marques, N. N. Lathiotakis, A. Floris, G. Profeta, L. Fast, A. Continenza, S. Massidda, and E. K. U. Gross, Phys. Rev. B **72**, 024545 (2005).

[16] M. A. L. Marques, M. Lüders, N. N. Lathiotakis, G. Profeta, A. Floris, L. Fast, A. Continenza, E. K. U. Gross, and S. Massidda, Phys. Rev. B **72**, 024546 (2005).

[17] R. Akashi, M. Kawamura, S. Tsuneyuki, Y. Nomura, and R. Arita, Phys. Rev. B **91**, 224513 (2015)

Relativistic *ab initio* calculations for valence fluctuation engineering of $4f$-$3d$ intermetallics

Munehisa MATSUMOTO
Institute for Solid State Physics, University of Tokyo
Kashiwa-no-ha, Kashiwa, Chiba 277-8581

April 30, 2018

We look at the intertwined relation between magnetism and superconductivity with a renewed interest in the effects of spin-orbit interaction and valence fluctuations. In $4f$-$3d$ intermetallics of which $3d$-electron part is carried by Fe-group transition metal (TM) elements, strong hybridization can be triggered between magnetically polarized conduction-electron band (c-electron band) and localized f-electrons. Here a hybridized electronic state with an intermediate nature between well localized $4f$-electron state and delocalized $3d$-electron state that mimicks the nature of $5f$-electron state may be found.

Among f-electron based superconductors the highest-temperature superconductivity so far is found for $\mathrm{PuCoGa_5}$ with $T_\mathrm{c} = 18.5$ K. This is to be contrasted with $T_\mathrm{c} = 2.3$ K found for $\mathrm{CeCoIn_5}$, both of which are most likely magnetically-mediated unconventional superconductors. There is also $\mathrm{CeRu_2}$ with $T_\mathrm{c} = 6.3$ K even though this is presumably a conventional BCS superconductor. Tuning the c-f hybridization strength and bandwidth in the proximity to a magnetic quantum critical point, we seek a candidate material made of rare-earth (RE) and TM elements to have an electronic state common to the electronic state of $\mathrm{PuCoGa_5}$. This may pave a way to a champion material among Ce-based superconductors.

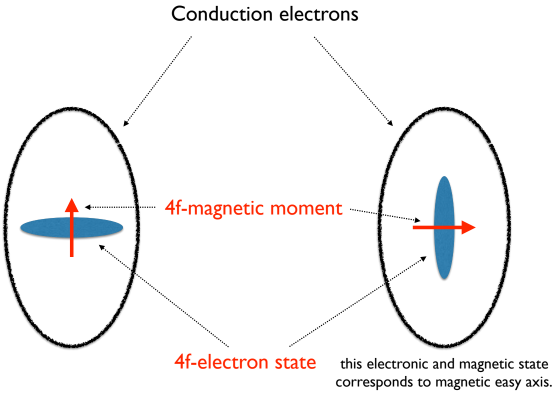

Figure 1: Schematic picture for potential-energy driven magnetic anisotropy realized in RE-TM compounds with localized $4f$-electrons.

Since the spin-orbit interaction that is relatively strong in RE locks the $4f$-electron states with $4f$-magnetic moments, exchange coupling between $4f$-moments and $3d$-electron magnetization leads to bulk magnetic anisotropy when localized $4f$-magnetic moments are put into a particular crystal field. It is pictorically shown in Fig. 1 where the Coulomb interaction between the localized $4f$-electron state and the crystal field environment determines the magnetic easy direction. Interesting flipping of the magnetic easy direction happens when the valence fluctuation comes in as shown in Fig. 2. Kinetic energy gain in $4f$-electrons as an outcome of c-f hybridization brings about orders of magnitude stronger magnetic anisotropy in a direction that is on the opposite side of

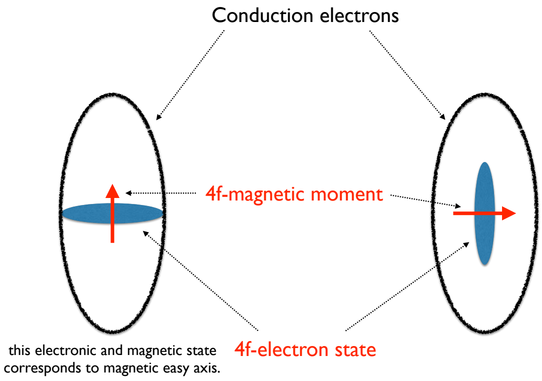

Figure 2: Schematic picture for kinetic-energy driven magnetic anisotropy realized in RE-TM compounds with delocalized $4f$-electrons.

the direction as realized in the conventional magneto-crystalline anisotropy.

Thus magnetic anisotropy and relatively high-temperature superconductivity can potentially be found for the same materials family in a way that is reminiscent of U-based compounds. We investigated effects of valence-fluctuations and spin-orbit interaction for $4f$-$3d$ intermetallics via relativistic *ab initio* calculations and numerical solutions of the associated quantum many-body problems via continuous-time quantum Monte Carlo (CT-QMC) method.

Methods Our *ab initio* calculations were done utilizing OpenMX [1] and LmtART [2]. With OpenMX structure optimization of a complex compound $R_2T_{14}B$ (R=RE element and T=TM element) with 68 atoms in the unit cell has been done utilizing the memory-intensive FAT nodes. Proceeding with OpenMX, fully relativistic calculations with the direction of magnetization being constrained to a specified angle enables us to inspect the magnetic anisotropy. Interfacing with CT-QMC is mostly done with LmtART on the basis of scalar-relativistic calculations. Effects of spin-orbit interaction and crystal fields are described on a model basis. With LmtART k-point parallelization is doable while all of the rest of the calculations scales almost linearly with the number of nodes.

Calculated results are fed back to experimental processes from materials fabrication and macroscopic characterization to microscopic probing of electronic states. Close contacts with experimental groups make an overall joint process to reach a desired material through a few iterations between theoretical calculations and experimental processes.

Effects of kinetic energy gain coming from valence fluctuations in the bulk stability of $4f$-$3d$ intermetallics have been reported elsewhere [3].

So far we have been working on a set of microscopic calculations combining *ab initio* calculations and many-body calculations in a thermal equilibrium state. Bridging the gap between such microscopic data and mesocopic observation slightly off equilibrium [4] makes the next steps toward providing calculated data that can be directly compared to experimental observations, such as the finite-temperature coercivity of RE permanent magnets made of $4f$-$3d$ intermetallics.

Acknowledgments Helpful discussions with Hiroaki Shishido and Tetsuro Ueno are gratefully acknowledged.

References

[1] http://www.openmx-square.org

[2] S. Y. Savrasov, Phys. Rev. B **54**, 16470 (1996).

[3] MM in the 73rd annual JPS meeting (2018).

[4] R. Kubo: J. Phys. Soc. Jpn. **12** (1957) 570.

STM simulations for modifeid β-FeSi$_2$(100) and Fe-adsorbed Si(111) surfaces

Kei Tanimoto and Ken HATTORI
Graduate School of Science and Technology, Nara Institute of Science and Technology
Takayama, Ikoma, Nara 630-0192

Using scanning tunneling microscopy (STM), author's group has been studied the growth of β-FeSi$_2$(100) nano-films on Si(001) [1] and iron-silicides formation on Si(111) [2] prepared in ultra-high vacuum. On β-FeSi$_2$(100) surface, STM showed a dip line on a bending region of the nano-film at a Si substrate step-edge [3]. Transmission electron microscopy results in cross section denied the geometrical dip. Thus in this research, first, we examined the possibility of electronic effects induced by in-plain strains, for the dip property. STM images were created with Simulation Tool for Atom TEchnology (STATE)-Senri under the dipole corrections in the vacuum region [4]. The β-FeSi$_2$(100) surface structure with Si tetramer on top has been established [1]. Here, the model is based on a free-standing single quintuple layers (QL) (Si/Fe/Fe/Si/Fe) with a Si bottom layer.

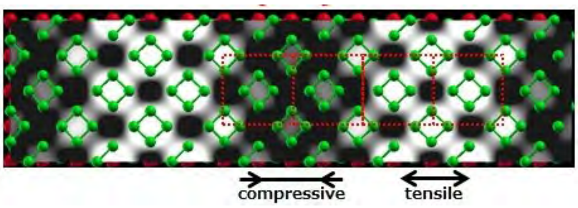

Figure 1: A simulated STM image of β-FeSi$_2$(100) with 10 % of in-plain compressive and tensile strains at sample bias voltage (V_S) of -1.0 V.

Figure 1 displays a topographic image at a filled state with in-plain compressive and tensile strains of $\Delta x/L = 0.1$ in maximum (L is the unit length in the x direction.) Here 4×1 unit cells, consisting of 32 Fe and 96 Si atoms, were used. In the calculation, the bottom-layer Si atoms were fixed to the ideal positions shifted with $[(\Delta x/L)\sin(2\pi x/4L), 0, 0]$, while the other atoms were relaxed $\leq$0.05 eV/Å. Obviously the compressive region indicates a dark (dip) feature while the tensile bright. The images at empty states showed the similar features. These STM simulations suggest that the dip lines at the downer side of the bending region in the experimental images are caused by compressive strain.

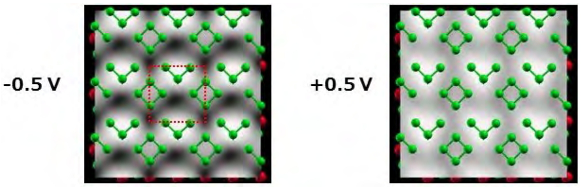

Figure 2: A simulated STM image of β-FeSi$_2$(100) with a mono vacancy in a Si tetramer at V_S = -0.5 and +0.5 V.

The β-FeSi$_2$(100) surfaces showed two types of defects experimentally in STM [3, 5]. One is a depression at a tetramer site [namely, dark (D) site] and another is a pair of high protrusion [bright (B)-site pair] at filled and empty states. In order to survey the defect structures, STM images of vacancy models and molecular-adsorption models were simulated in 1×1 or 2×2 unit-cell frames with the fixed bottom-layer. The simulations indicated that mono, di, tri, and tetra Si-vacancies in the Si tetramer present BB (bright in filled and bright in empty states, Fig. 2), DB, DB, and DD features, respectively.

For the hydrogen adsorption, the stable configuration was a bridge type among atop (8 different cases were simulated), bridge (8), and hollow (2) ones; a bridge H configuration did not induce any distinct change in both STM images (Fig. 3). For the hydroxyl adsorption, the stable configuration was also a bridge type among atop (1 case was simulated), bridge (1), and hollow (1) ones; a bridge OH configuration showed BB feature. For the oxygen adsorption, a bridge O configuration showed DD feature. One of the interpretations for experimentally-observed single DD site is tetra Si-vacancies which would explain an increase of the dark defects by high-temperature annealing, but the BB-site pair is under the discussion though a pair of OH bridge-sites is a candidate.

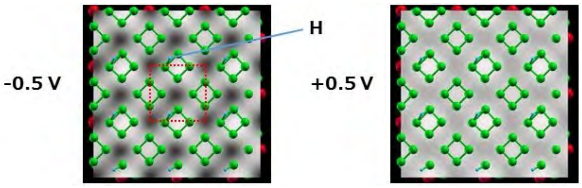

Figure 3: A simulated STM image of β-$FeSi_2$(100) with a hydrogen atom at a brige site of a Si tetramer at V_S = -0.5 and +0.5 V.

For the system of Si(111)7×7 with isolated Fe atoms, we observed 5 different adsorption types in experimental STM images [6]. Here, some configurations for a Fe atom on Si(111)7×7 and 4×4 surfaces based on the dimer–adatom–stacking-fault model [7] were simulated. First, clean Si(111) surfaces consisting of a Si adatom-layer, six Si-layers, and a bottom H-terminated layer were imaged for 7×7 (347 atoms) and 4×4 (118 atoms, a simple model of 7×7 keeping key structures [8]) models under relaxing top six layers.

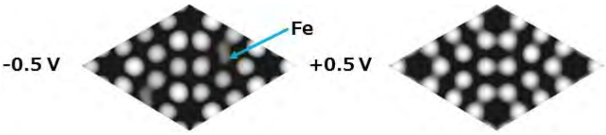

Figure 4: A simulated STM image of Si(111)7×7 with an iron atom at a H_3 site close to a center adatom on an unfaulted half unitcell at V_S = -0.5 and +0.5 V.

On the 4×4 surface, an Fe atom was located above 17 different Si atoms in the adatom, 1st, 2nd (3rd) and 4th (5th) layers, and fully relaxed without spin polarization. The stable configuration was a H_3 type (above 4th-layer Si close to an adatom), showing a dark adatom at V_S = -0.5 V which resembles one of the experimental images. On the 7×7 surface, 13 configurations were converged among 18 configurations, and the stable configuration was a H_3 type showing a dark adatom at -0.5 V (Fig. 4). In order to discuss the other adsorption types, we require the calculations for much more configurations with the spin polarization.

The authors thank Profs. Morikawa, Hamada, and Inagaki in Osaka University, and Prof. Yanagisawa in Ryukyu University for their great support in STATE-Senri calculations.

References

[1] O. Romanyuk, K. Hattori, M. Someta, and H. Daimon, Phys. Rev. B **90** (2014) 155305.

[2] K. Kataoka, K. Hattori, Y. Miyatake, and H. Daimon, Phys. Rev. B **74** (2006) 155406.

[3] M. Someta, M. Thesis, Nara Institute of Science and Technology, Nara (2008) [in Japanese].

[4] Y. Morikawa, Phys. Rev. B **63** (2001) 033405, and references therein.

[5] H. Yang, Dr.. Thesis, Nara Institute of Science and Technology, Nara (2018).

[6] K. Kataoka, Dr.. Thesis, Nara Institute of Science and Technology, Nara (2006).

[7] Guo-Xin Qian and D. J.Chadi, Phys. Rev. B **35** (1987) 1288.

[8] This corresponds to the extension of the 4×2 structure [A. Vittadini and A. Selloni, Phys. Rev. Lett. **75** (1995) 4756.]

Development of crystal structure prediction method and search for magnet and spintronics materials

Tomoki YAMASHITA
Research and Services Division of Materials Data and Integrated System (MaDIS),
National Institute for Materials Science (NIMS)
1-2-1 Sengen, Tsukuba, Ibaraki 305-0047

We developed a crystal structure prediction method based on Bayesian optimization [1]. Crystal structure prediction with Bayesian optimization can efficiently select the most stable structure from a large number of candidate structures with a lower number of searching trials using a machine learning technique. Crystal structure prediction simulations were carried out for $\mathrm{Y_2Co_{17}}$, which is important compositions of Sm-Co magnets, to discuss the efficiency of Bayesian optimization. In these simulations, total energy calculations and structure optimization were done using the density functional theory with the projector-augmented wave method [2], as implemented in the VASP code [3]. These structure optimization calculations were performed using the supercomputer system at the ISSP. The results demonstrate that Bayesian optimization can significantly reduce the number of searching trials required to find the global minimum structure by 30–40% in comparison with pure random search, which leads to much less computational cost.

We collected the data of magnetocrystalline anisotropy (MA) in Co-based 3d transitions-metal thin films to perform machine learning analyses in future. First-principles calculations were done using the supercomputer system at the ISSP. Full-potential linearized augmented plane wave (FLAPW) method [4, 5] with generalized gradient approximation (GGA) was employed. Spin-orbit coupling was treated within the second-variation method and the magnetic anisotropy energy (MAE) was estimated by the force theorem. The MAE of possible atomic-layer alignments of Co-based 3d transition-metal films with $ABAB$ and $ABCABC$ stacking including Mn, Fe, and Ni layers are presented. The results predict that large perpendicular MA (PMA) can be achieved by tuning the atomic-layer alignments in Co-Ni films. We provide useful guidelines for the choice of atomic-layer alignments in Co-Ni thin films for realizing large MAE.

References

[1] T. Yamashita, N. Sato, H. Kino, T. Miyake, K. Tsuda, and T. Oguchi, Phys. Rev. Materials **2**, 013803 (2018).

[2] Blöchl, Phys. Rev. B **50**, 17953 (1994).

[3] G. Kresse and J. Furthmüller, Phys. Rev. B **54**, 11169 (1996).

[4] M. Weinert, J. Math. Phys. **22**, 2433 (1981).

[5] W. Wimmer, H. Krakauer, M. Weinert, and A. J. Freeman, Phys. Rev. B **24**, 864 (1981).

Elucidation of Catalytic Activity of Solid Acid and Base by Protonic Activity Estimation via Hydrated Multilayer

Ryuhei Sato and Shu Yamaguchi
Department of Materials Engineering,
The University of Tokyo, Bunkyo-ku, Hongo, Tokyo 113-0032

Proton activity on oxide surface is paid considerable attention to the application as electrolytes and metal/oxide catalysts. For example, a significant contribution of proton conduction on a CeO_2 surface was reported as a critical factor to an enhanced catalytic efficiency of electrochemical steam reforming of CH_4 on Pd/CeO_2 [1]. According to previous AIMD simulations, this proton migration on hydrated oxide surface is a kind of neutralization reaction of H_2O adsorbates. Therefore, to study the emergence of Brønsted acidity by the adsorption of acid-base molecules like H_2SO_4, HCOOH, CH_3OH, etc. is crucial for the catalytic reaction. Here, we studied the relationship between molecule adsorption and subsequent emergence of Brønsted acidity.

Adsorption reaction of H_2O, HCOOH, and CH_3OH on bare cubic ZrO_2(110) surface is analyzed by ab initio molecular dynamic (AIMD) simulation to study the adsorption mechanism. After adsorption reaction, we also examine the hydration reaction of HCOOH and CH_3OH-terminated surface to understand the interaction between these organic and H_2O molecules on the surface. All the simulations were performed by home-made code written by F. Shimojo et al. [2]. The author employed the GGA/PBE functional and PAW method with L4cpu and L36cpu queues.

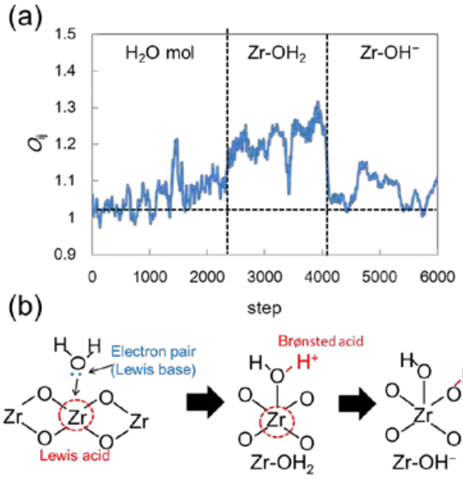

Figure 1. (a) time series of sum of bond overlap population around O atom in an adsorbed H_2O molecule during AIMD simulation of H_2O adsorption on cubic ZrO_2 (110) surface, and (b) schematic image of neutralization of surface strong Lewis acid (Zr ion sites) by molecule adsorption and subsequent deprotonation reaction by an adsorbed molecule.

According to the observation from these AIMD simulations, molecule adsorption is a neutralization reaction of surface ion sites as a strong Lewis acid (metal ion sites) or base (oxide ion sites). After this neutralization reaction, these adsorbed molecules subsequently release protons because of the strong Lewis acid/base interaction between surface sites and molecules. Owing to significant stabilization by the additional covalent bond formation, Brønsted acidity emerges by the increased instability of hydrogen. For example, H_2O molecules first chemisorb on Zr ion sites and then dissociate H^+ to form Zr-OH^- by the help of basic surface oxide ion site (>O) as shown schematically in Fig.1(b). Therefore, the strength of covalent bonding formed between Zr ion sites and molecules, in other words, the strength of the neutralization reaction of Lewis-acidic Zr ion sites by non-dissociative adsorbates, gives primary influence to Brønsted acidity of adsorbates.

Figure 1(a) shows time series of the sum of bond overlap population around O atom in adsorbed H_2O molecules during AIMD simulation of H_2O adsorption on cubic $ZrO_2(110)$ surface in reference to O in H_2O molecule. As shown in Fig. 1(a), the number of bonds around O atom become excessive compared to H_2O molecule, when H_2O molecule adsorbs on a surface Zr ion site to form Zr-OH_2. This excessive bond is relaxed after proton dissociation, which implies that this excessive bond formed by non-dissociative adsorption contributes to the deprotonation reaction. This postulate is further confirmed by comparing bond overlap population between O and H atom in adsorbates and the one between surface Zr ion site and O atom in adsorbates in Fig. 2, showing that the strength of O-H bond decreases with the increase of Zr-O bond strength. Also, the rate of decrease in O-H bond is independent on adsorbate species, as far as these molecules are composed of same elements (here they are composed of C, H, and O atoms.), which implies there is a common mechanism for molecule adsorption and subsequent emergence of Brønsted acidity. Analysis of the bond property of adsorbates based on the energetics is now underway to directly compare the deprotonation behavior of adsorbed molecules, which include different elements and have different electronegativity.

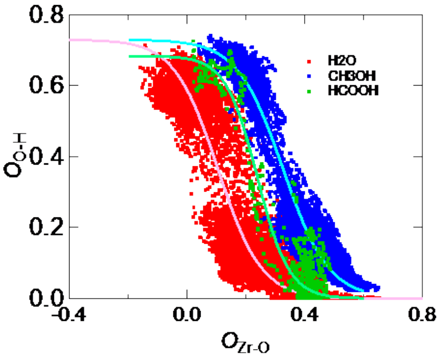

Figure 2. Bond overlap population between O and H atom in adsorbed molecules ($O_{O\text{-}H}$) vs that between O in adsorbed molecules and surface Zr ion sites ($O_{Zr\text{-}O}$) during AIMD simulation of molecule adsorption on ZrO_2 surface. Each dot represents the bonding property of an adsorbate in particular time step. Curves show the fitting result of these data by sigmoid function.

References

[1] R. Manabe, S. Okada, R. Inagaki, K. Oshima, S. Ogo, Y. Sekine, *Sci. Rep.* 6, (2016) 38007.

[2] F. Shimojo, R.K. Kalia, A. Nakano, P. Vashishta, *Comp. Phys. Comm.* **140** (2001) 303.

Functionality of solid-liquid interface

Osamu Sugino
Institute for Solid State Physics,
The University of Tokyo, Kashiwa-no-ha, Kashiwa, Chiba 277-8581

We have studied the H adsorption at the Pt(111)/solution interface using the density functional theory (DFT) within the level of random phase approximation (RPA). This system was studied intensively in the past using the DFT-PBE in the past [1] but reliable view on the adsorption isotherm has not been established. Considering its significance on the understanding of fuel-cell reactions, we have revisited this problem using the time-consuming DFT-RPA; most of the computational time was spent in this problem in this fiscal year.

After very stringently testing the convergence of the DFT-RPA total-energy with respect to the number of plane wave basis, k-points and Pt layers, we have estimated the value for the adsorption energy on the fcc and atop sites. Compared with DFT-PBE, RPA provide strong competition between the adsorption sites, supporting a coexisting feature at the coverage close to the full-monolayer. This result, together with additional calculation on the coverage-dependent adsorption energy, explains why H adsorbed on the atop site, H_{atop}, appears close to the full-monolayer condition and suggests that importance of the Heyrovsky reaction, by which the discharging reaction of a hydronium ion occurs on H_{atop}, was underestimated by PBE.

Major difference between PBE and RPA is found originated from the different value for the equilibrium lattice parameter. The difference can thus be made very smaller by letting the PBE calculation using the experimental (or RPA-optimized) lattice parameter. This provides a practical way to empirically adjusting the PBE calculation.

The difference in the adsorption energy between atop and fcc was found quite small, about twice the value of the thermal energy at room temperature. It is important to note that this small energy difference can be reliably predicted only when using the RPA level.

The different adsorption energy for the different sites is found mainly due to the difference in the zero-point energy, indicating an importance of the isotope mass in determining the most stable adsorption site. The RPA calculation showed that the order of the stability between H and D is the same but relative abundance of the atop adsorbate is significantly different between them. This suggests a possibility of separating D from H using the fuel cell system consistent with the existing experiment.

References

[1] T.T.T.Hanh, Y. Takimoto and O. Sugino, Surf. Sci. 625, 104-111 (2014).

First-Principles Molecular-Dynamics Study of Structural and Electronic Properties of Covalent Glasses under Pressure

Fuyuki SHIMOJO, Akihide KOURA, Masaaki MISAWA, and Shintaro HAYASHI
Department of Physics, Kumamoto University, Kumamoto 860-8555

So far, permanent densification of SiO_2 glass has been widely studied both experimentally and theoretically since its discovery in the 1950s [1]. It has been known that silicate glasses, such as $MgSiO_3$, also show permanent densification when the glasses are decompressed from high pressures. In this study, we investigate the microscopic structure of densified $MgSiO_3$ glass compared with SiO_2.

To clarify the microscopic mechanism of the densification, we have carried out first-principles molecular-dynamics simulations on the decompression process of $MgSiO_3$ glass in its relaxed state from high pressures up to 20 GPa. First, the temperature was increased to 3000 K at high pressures to obtain the liquid state. Second, the densified glass was obtained by decreasing the temperature to 300 K while keeping high pressures. Third, the pressure was decreased to 0 GPa, and permanently densified glass was obtained at ambient conditions.

We confirmed that the density of densified glass at ambient conditions is in good agreement with experiments [2]. Also, the static structure factors obtained by neutron and X-ray experiments were well reproduced by our simulations. In comparison of ordinary glass, some difference of structure factors in the long-wave length region was seen, while the overall profiles are very similar to each other. This result shows that the structure in the intermediate range, such as ring structure, is changed in permanently densified glass, while the local structure is almost the same as the coordination number is unchanged.

In the case of SiO_2 glass, the ring size distribution shows that the network of densified glass is formed from smaller size rings than ordinary glass, which suggests that permanent densification is caused by the reconstruction of the network structure. On the other hand, the network structure in $MgSiO_3$ glass is not clearly defined because many non-bridging, *i.e.* one-fold coordinated, oxygen atoms exist, and the connectivity between Si and O atoms is broken. The investigation of the densification mechanism in $MgSiO_3$ glass is underway.

References

[1] P. W. Bridgman and I. Šimon: J. Appl. Phys. **24**, 405 (1953).

[2] M. C. Wilding *et al.*: Europhys. Lett. **67**, 212 (2004).

First-Principles Calculation on Reversible Hydrogenation Reaction of Toluene using Heterogenous Catalyst

Hiromi NAKAI

Faculty of Science and Engineering,

Waseda University, Okubo, Shinjuku, Tokyo 169-8555

Reversible dehydrogenation reaction of methylcyclohexane into toluene, by using Pt catalyst is a prospective hydrogen storage and transportation technology. One of the issues is the demethylation reaction producing toxic benzene (BZ). Addition of small amount of Sn to the Pt catalyst suppresses the side reaction, whereas the mechanism is unknown.

The present study investigated the mechanisms of Sn addition effects by using density functional theory (DFT) calculations. The kinetics of the present system was detailed via micro-kinetic analyses; the reaction rate equations that are simultaneous ordinary differentiation equations for all elementary steps are solved numerically. All kinetic parameters, i.e., reaction rate constants (activation energies) were calculated by DFT. We have considered 12 elementary reactions occurring on Pt(111), Pt(311), Pt_3Sn(111), and Pt_3Sn(311), taking the reaction site dependences into account. Calculations were performed by using the VASP code, which is available on the System B with a number of computational nodes, installed at the Institute for Solid State Physics, the University of Tokyo.

Figure 1 shows the time-course changes of the ratio of side-reactions: ratio of partial pressure of BZ to hydrogen molecule. In the case of Pt surface, the selectivity rapidly increased and reached to the steady-state. In the case of Pt_3Sn, BZ/H_2 ratio gradually increased. Consequently, in the short time region of $t <$ ca. 400 s, BZ/H_2 ratio was smaller than Pt case. This means that the demethylation reaction is kinetically suppressed with Sn addition. Detailed analyses on surface coverages revealed that suppress of side reaction would be attributed to the smaller coverages of reactant species on Pt_3Sn surface than that on Pt surface, which were due to the smaller absorption energies of hydrocarbons onto the Pt_3Sn surface.

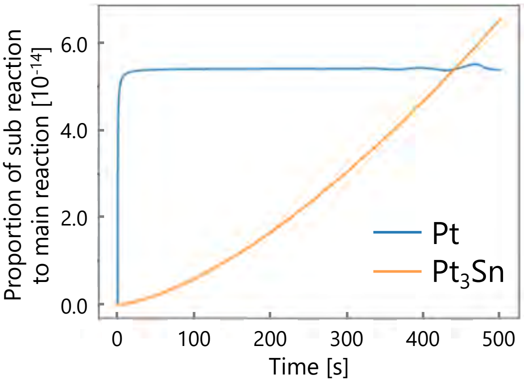

Figure 1. Time-course changes of the ratio of side reaction to main reactions.

Electronic States and Thermodynamic Stability of Two-Dimensional Crystals of Group IV Elements

Masaaki Araidai

Institute of Materials and Systems for Sustainability, Nagoya University
Furo-cho, Chikusa-ku, Nagoya, 464-8603

Two dimensional crystals consisting of group IV element heavier than carbon, such as silicene, germanene, and stanene, are supreme thin-film materials. They have been theoretically predicted to possess high carrier mobility and some intriguing functions such as band-gap control and topological insulator [1,2]. They have been recently synthesized on metallic substrate [3,4,5,6]. However, it has been reported that the electronic state of silicene on a metallic substrate are dramatically modified by the strong interactions with the surface atoms [7,8]. This indicates that one cannot utilize the intriguing electronic states inherent in two-dimensional crystals successfully and perfectly when they are placed on a metallic substrate. Therefore, toward the device fabrication utilizing the electronic states inherent in the two-dimensional crystals, it is prerequisite for understanding their properties on insulating substrates.

In this work, we investigated the optimized structures and the electronic states of germanene and stanene with larger spin-orbit interactions than silicene on α-Al$_2$O$_3$ (0001), using the first-principles calculations based on the density-functional theory. The calculations were performed using the VASP code [9]. We employed the projected-augmented-wave potential and the exchange-correlation functional of PBE-type generalized gradient approximation. All atomic configurations were relaxed until the Hellmann-Feynman force becomes smaller than 5 meV/Å.

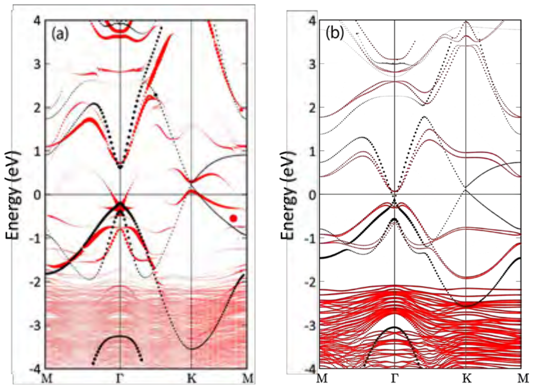

Fig.1 Electronic band structures of (a) 2x2 germanene on α-Al$_2$O$_3$ (0001) $\sqrt{3}$x$\sqrt{3}$ surface and (b) 1x1 stanene on α-Al$_2$O$_3$ (0001) 1x1 surface. The vasp_unfold code [10] was used to draw the unfolded band structure of germanene.

Figure 1 shows the electronic band structures of (a) germanene and (b) stanene on α-Al$_2$O$_3$ (0001) surfaces. The black dotted lines in each panel denote the band structure of the corresponding freestanding one. The bundles of the electronic band below ~1.7 eV in (a) and ~2.0 eV in (b) represent the valence bands of the surfaces. We can observe from Fig. 1 that the band structures are affected owing to the surface adsorptions, especially around K point, at which low-energy quasi-particles of free-standing germanene and stanene are massive Dirac fermions. The degree of the modulation depends on the strength of the interactions. We found from population analyses for chemical bonds that the electronic states are perturbed not by bondings with surface aluminum atoms but surface oxygen atoms.

References

[1] K. Takeda and K. Shiraishi, Phys. Rev. B **50**, 14916 (1994). [2] M. Ezawa, New J. Phys. **14**, 033003 (2013). [3] A. Fleurence, et al., Phys. Rev. Lett. **108**, 245501 (2012). [4] P. Vogt, et al., Phys. Rev. Lett. **108**, 155501 (2012). [5] L. Li, et al., Adv. Mat. **26**, 4820 (2014). [6] J. Yuhara, et al., 2D Mater. **5**, 025002 (2018). [7] Z.-X. Guo, et al., J. Phys. Soc. Jpn. **82**, 063714 (2013). [8] M. X. Chen and M. Weinert, Nano Lett. **14**, 5189 (2014). [9] G. Kresse and D. Joubert, Phys. Rev. B **59**, 1758 (1999). [10] M. Tomić, H. O. Jeschke and R. Valentí, Phys. Rev. B **90**, 195121 (2014).

Exploration of structure motifs characterizing the metal oxides

Kazuto AKAGI

AIMR, Tohoku University, Katahira, Aoba-ku, Sendai, Miyagi 980-8577

Electron trap site in a-HfO_2

Amorphous HfO_2 (a-HfO_2) is a prototype high dielectric constant insulator with wide technological applications. Using classical MD and DFT (PBE, HSE) calculations, we found that excess electrons and holes can be trapped as deep polaron states. They were localized at precursor sites and the polaronic relaxation was amplified by the local disorder of amorphous network [1]. Based on these findings, we tried extraction of structural motifs of the electron trapping site to identify the precursor structures in classical-MD calculations. First, we prepared 35 samples of electron trapping sites by DFT calculations and calculated persistent-homology. The topological information was translated to vectors via persistence diagrams where birth and death of "rings" with increasing radius of virtual spheres at atomic positions are recorded. Using a few common structural motifs obtained by principal component analysis (PCA) of these vectors, potential precursor structures in the classical-MD calculations were searched by evaluating “distance” between these principal component vectors and the vectors representing snapshots from the trajectories. The result was encouraging, but some precursors were failed to detect when structure relaxation by DFT calculation is significantly large.

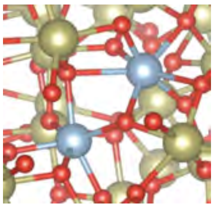

Fig.1 An example of the electron trapping sites well represented by PCA of persistence diagrams.

Shallow trap state in Rh:$SrTiO_3$

Rh^{3+}-doped $SrTiO_3$ is a highly active photocatalyst with visible light response for water splitting. The oxygen vacancy (Vo) formation required for charge compensation in this material leads to a complex defect-related electronic state, especially a shallow unoccupied trap state reducing the lifetime of photocarrier. Based on the systematic DFT (GGA and hybrid-functional) calculations of 4×4×4 $SrTiO_3$ cells containing one or two Rh^{3+} and Vo, we found shallow unoccupied trap state are closely related to Rh^{3+}-Vo complexes. We also found that the charge state of Rh is controlled by both the configuration and the ratio of Rh and Vo. While the valence state of an octahedrally-coordinated Rh can be reduced no further than the 3+ state, Rh in complex cluster configurations with other Rh atoms or Vo can be further reduced to lower valence states.

References

[1] M. Kaviani *et al.*, PRB, **95**, 075117 (2017).

First-principles calculation for surface electron dynamics

Kazuhiro YABANA
Center for Computational Sciences,
University of Tsukuba, Tsukuba 305-8577

We develop a first-principles computational method to investigate electron dynamics induced by ultrashort laser pulses based on time-dependent density functional theory (TDDFT) in real time. We develop the code SALMON (Scalable Ab-initio Light-Matter simulator for Optics and Nanoscience) and make it open to the public at our website, http://salmon-tddft.jp. At present, SALMON is capable of describing electron dynamics in either isolated or periodic boundary conditions. In the present project, we aim to extend the code so that we can describe the electron dynamics in a thin film, periodic in two-dimensions and isolated boundary condition for one-dimension. We expect we can investigate the electron dynamics at a surface calculating sufficiently thick films.

To describe the interaction of pulsed light with thin films, we solve the coupled equations: the Maxwell's equations for the electro-magnetic fields of the pulsed light and the time-dependent Kohn-Sham equation for electrons in the thim film. We can then directly investigate the reflection, transmission, and absorption of the pulsed light. A finite difference scheme with the uniform grids in the three-dimensional Cartesian coordinate is used to solve the equations. A common spatial grid is used for both electron and light-wave dynamics. Since the speed of light is much faster than that of electrons, we use different time steps for two dynamics.

As a test case, we applied the method for a thin silicon film with the surface atoms terminated with hydrogen atoms. We calculate the reflection, transmission, and absorption for several thin films of different thickness, changing the frequency and the intensity of the pulsed light, and compare them with results of ordinary macroscopic electromagnetism in which we utilize the dielectric function obtained from the TDDFT calculation. In our preliminary analysis, it is found that the results by the coupled Maxwell-TDDFT calculations and by the macroscopic electromagnetism agree well even for a rather thin film of a few nano-meters. For the film of thickness less than 1nm, the optical properties changes drastically at certain frequency region. We also find a large change in the reflection for an intense laser pulse due to the nonlinear effects.

Magnetic anisotropy analysis of transition-metal-doped Nd-Fe-B magnets by first-principles calculations

Yasutomi TATETSU

Tokyo Institute of Technology, Nagatsuta, Yokohama, Kanagawa 226-8502

Nd-Fe-B sintered magnets, known as the strongest magnets, are used in various kinds of applications, for example, vehicles, turbines, etc., since they have the largest $(BH)_{\max}$ among permanent magnets. However, the mechanism of the thermal instability in the coercivity of Nd-Fe-B magnets is not clear because there are numerous unknown factors that reduce the coercivity. Controlling the grain boundary phase of these magnets by annealing processes or doping some elements is the most effective way to enhance the coercivity of Nd-Fe-B magnets.

Previously, we performed first-principles calculations for the Cu-doped $Nd_2Fe_{14}B/Nd_4O$ systems using a computational code OpenMX [1] in order to understand the role of Cu in this system [2]. By calculating the formation energies of some model structures, we found that the models with Cu existing at the interstitial space and Fe site at the interface are energetically stable compared to the non-Cu-doped model structure. Especially, in the model with Cu at the Fe site at the interface, the magnetic anisotropy of Nd near Cu at the interface is improved due to Cu, which is in good agreement with experimental results [3].

There is a possibility that other elements, which have not been added into Nd-Fe-B magnets, may enhance the ability of Nd-Fe-B magnets. We study the magnetic properties of the substitution effects in $Nd_2(Fe, X)_{14}B$ (X = Mg, Al, Si, Ca, Sc, Ti, V, Cr, Mn, Fe, Co, Ni, Cu, Zn, Ga, Ge) by first-principles calculations in order to understand which added elements have the ability to improve the coercivity of Nd-Fe-B magnets [4]. We replace one Fe atom at different Wyckoff positions with one X atom in each calculation in order to determine the stability of the systems (see figure). System B was mainly used to optimize the Fe-substituted systems. By calculating the formation energy of

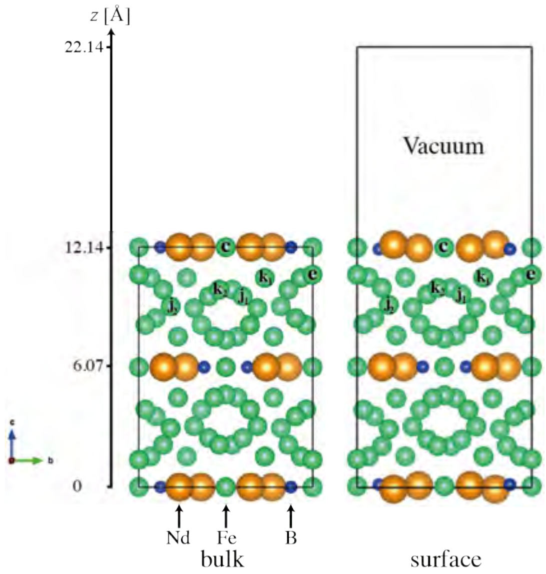

Figure: Fe-substituted model system of $Nd_2(Fe, X)_{14}B$.

the Fe-substituted system with X, only replacing Fe at the c site with Mg, Ca, Sc, Cu, Zn, or Ga in the bulk or surface system shows the improvement of the magnetic anisotropy of Nd near X because of the *p*-*d* interaction between Nd and these added elements. The charge transfer between Nd 5*d* and X *p* occurs in order to reduce the exchange interaction. This charge transfer increase/decreases the number of Nd 5*d* electrons in uniaxial/in-plain orbitals, which triggers the magnetic anisotropy improvement of Nd. Our calculation result suggests that one can consider the possibility of improving the coercivity of Nd-Fe-B magnets by adding these elements.

References

[1] http://www.openmx-square.org

[2] Y. Tatetsu, S. Tsuneyuki, and Y. Gohda, Phys. Rev. Appl. **6**, 064029 (2016).

[3] H. Sepehri-Amin *et al.*, Acta Mater. **60**, 819 (2012).

[4] Y. Tatetsu, S. Tsuneyuki, and Y. Gohda, submitted.

Hybrid *ab initio* QM/MM calculations of functional mechanisms of biological macromolecular systems recognizing supercoiled DNA

Masaru Tateno

Graduate school of Life Science, University of Hyogo, 3-2-1 Kouto, Kamigori-cho, Hyogo 678-1297

We have studied the functional mechanisms of biological macromolecular systems that interact with supercoiled DNA. The targets are the following two systems; i.e., supercoiled DNA recognition (SDR) peptide and DNA topoisomerase IIβ (topoIIβ). Moreover, the electronic structures of iron-sulfur [4Fe-3S] clusters in hydrogenases were also investigated this FY.

SDR peptide

The SDR peptide is a designed small protein that is composed of 27 amino acid residues, $(Lys)_9(Glu)_9(Lys)_9$. The SDR peptide was found to bind to the supercoiled DNA selectively and cooperatively. These significant properties are originated from its characteristic amino acid sequence. In this study, we analyzed the mechanisms of the selective and cooperative binding of the SDR peptide to supercoiled double strand DNA molecules, based on our previous studies [1].

We first focused on the physico-chemical properties of the SDR peptide in the free state. The conformational ensemble of the SDR peptide in solution was generated by an advanced molecular dynamics (MD) method (*i.e.*, temperature replica exchange; REMD). In this calculation, we performed 128-replica MD simulations in parallel, and generated a 24.32 μs (190 ns × 128 replicas) trajectory as the total. The numerous replicas (128 replicas) were derived from the fully-solvated system, which included 166,981 atoms. On average, a 20-ns MD simulation consumed 5 hours with 22 nodes (512 cores) or 10 hours with 2 nodes (total 48 cores) accelerated by 4 × 2880 CUDA cores, of SGI ICE XA (×4 Intel Xeon E5-2680v3 CPU and ×4 NVIDIA Tesla K40).

The REMD revealed that substantial amounts of ordered, helical structures were unexpectedly present in our obtained conformational ensemble, which was found to be consistent with our biophysical experimental analysis employing circular dichroism (CD) spectroscopy. Furthermore, we performed the statistical analysis of the structural ensemble, and identified the hydrophobic nucleus, which was stabilized by closely cohesive residue contacts formed through “hybrid” hydrophobic and electrostatic residue contacts. This is the first report to address the mechanisms of formation of the core packing in the semi-stable conformations of a peptide.

TopoIIβ

DNA topoisomerase IIβ (topoIIβ) is an enzyme to recognize and cleave the supercoiled double stranded (ds) DNA molecules, and thereby is involved in the regulation of the transcription and replication. By employing MD simulations, we built a structural model of the initial state (prior to the enzymatic reaction) of the enzyme-substrate (ES) complex of topoIIβ and dsDNA, toward hybrid *ab initio* QM/MM calculations to analyze the catalytic mechanisms of the dsDNA cleavage reaction.

This FY, we focused on the analysis of the frontier orbitals in the catalytic site. As a consequence, we found that the highest occupied molecular orbital (HOMO) was located on a tyrosine (Tyr) residue, which thus led us to a novel scheme of the catalytic reaction by topoIIβ. This identified mechanism may be closely relevant to the degenerated sequence motifs that are recognized by topoIIβ, and so we also performed a genome wide analysis to identify the motifs by our novel bioinformatics approach [2]. These combined methods would elucidate the reasons and mechanisms of the correlation between the catalysis, and the degeneracy of the recognition sequence motifs.

Hydrogenase

Hydrogenases are a metalloenzyme family, and catalyze both dissociation and production of dihydrogen (H_2); i.e., $H_2 \rightleftharpoons 2H^+ + 2e^-$. The crystallographic and spectroscopic experiments showed that a membrane bound hydrogenase (MBH) included a hydroxyl ion (OH^-) that was bound to an Fe of the super-oxidized $[4Fe\text{-}3S]^{5+}$ cluster that is located in the proximity of the [Ni-Fe] active site. However, the functional role of the hydroxyl ion was still left to be unknown. In this study, we investigated the electronic structure of the super-oxidized $[4Fe\text{-}3S]^{5+}$ proximal cluster in the presence/absence of the OH^-, employing *ab initio* density functional theory (DFT) calculation.

The analysis revealed that the OH^- ion significantly altered the electronic structure, thereby inducing localization of the HOMO and delocalization of the lowest unoccupied molecular orbital (LUMO) toward the [Ni-Fe] active site. The analysis also showed that the LUMO was consistent with the ET pathways found by the independent semi-empirical theoretical analysis. Thus, this is the first report to address the mechanisms for creating an ET pathway in a biological system, based on the electronic structure [3].

References

[1] J. Kang and M. Tateno: J. Phys. Soc. Jpn. **86** (2017) 074802.

[2] A. Sugimoto, T. Sumi, J. Kang and M. Tateno: J. Phys. Soc. Jpn. **86** (2017) 074803.

[3] J. Kim, J. Kang, H. Nishigami, H. Kino and M. Tateno: J. Phys. Soc. Jpn. **87** (2017) 034804.

First-principles study of ionization and diffusion of metal atoms at metal/solid interfaces in electric fields

Takashi NAKAYAMA
Department of Physics, Chiba University
1-33 Yayoi, Inage, Chiba 263-8522

Metal/solid interfaces are essential structures for various electronic/optical devices. However, metal atoms often diffuse from electrodes into solids such as SiO_2 by the thermal annealing processes and applied electric fields. This diffusion causes serious damage to recently developed nanoscale devices. In this view, the microscopic understanding of diffusion is important, especially in an electric field. However, there is little theoretical work on metal-atom diffusion around metal/solid interfaces. In this works, we studied the ionization and diffusion of various metal atoms in an electric field around metal/SiO_2 interfaces using first-principles calculations.

To simulate the interfaces, we adopt a (2×2) metal/SiO_2 (001) repeated-slab model made of 3-4 ML metal atoms and 16 ML α-quartz SiO_2. We consider eleven metals: Ta, Ag, Pt, Au, Al, Ni, W, Nb, V, Ti, and Cu. The adiabatic diffusion potential of a metal atom from the interface into SiO_2 was calculated by the standard first-principles method in the density functional theory. We employ a primitive method to produce an electric field perpendicular to the interface by simply removing electrons from the present slab system. All atom positions are optimized during the diffusion.

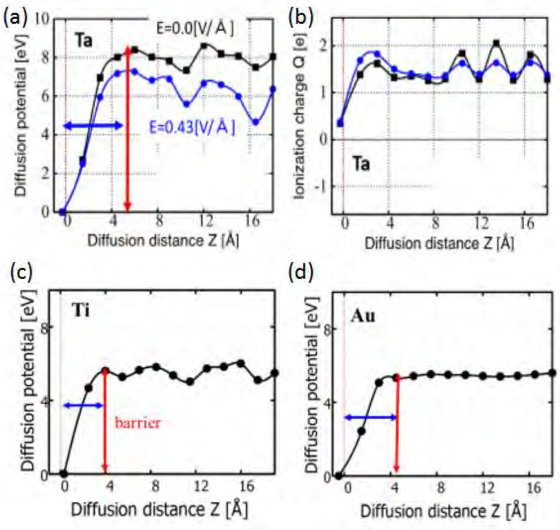

Fig.1. Adiabatic diffusion potentials at metal/SiO_2 interfaces as a function of distance from the interface, for (a) Ta, (c) Ti, and (d) Au atoms. (b) shows the ionization charge of Ta atom during the diffusion. In (a) and (b), the results in an electric field are also shown by blue lines.

Figs. 1(a) and 1(b) show the diffusion potential and ionization charge of the Ta atom, respectively, as a function of the distance z from the Ta/SiO_2 interface, while Figs. 1(c) and 1(d) are the potentials for the Ti and Au atoms. From these figures, we note two features: (1) the diffusion barrier height ϕ_B for penetrating into SiO_2 depends on the kind of atom. Fig. 2(a) shows the relationship between ϕ_B and $-\mu$ (chemical potential of a metal atom in metal). From these analyses, we found that the cohesive energy of metal atom layers is the leading factor for the penetration barrier ϕ_B.

(2) As shown in Figs. 1(a), 1(c), and 1(d), most of the metal atoms show the increase of potential in a similar 0-4 Å region near the interface. This region is closely related to the metal-induced gap states (MIGSs). Fig. 2(b) shows the electron density profile of one MIGS at a clean Ta/SiO_2 interface, and those of the electron-occupied states of a diffusing Ta atom when such a Ta atom is located at z=4.5 and 7.5 Å away from the interface. It is clearly seen that the electronic state of Ta decreases the hybridization with MIGS as the Ta atom leaves the interface. Since the hybridization of the Ta state with MIGS stabilizes the Ta atom, the hybridization with MIGS is the origin of the

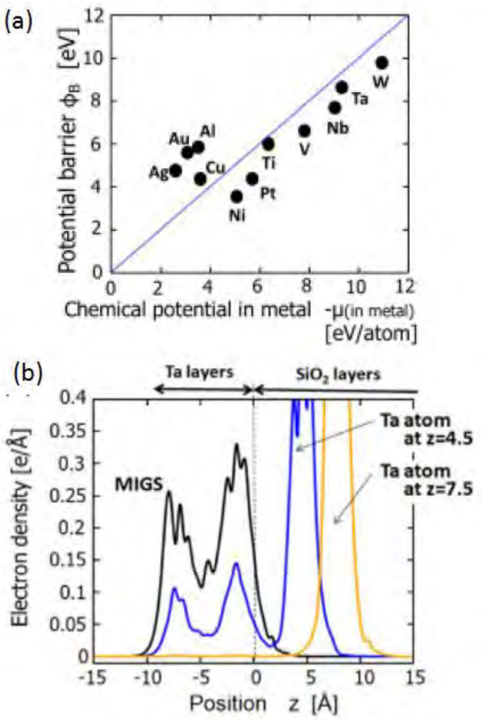

Fig.2. (a) Calculated potential barrier for metal-atom penetration into SiO_2 as a function of metal-atom chemical potential in bulk metal. (b) Electron density profile of original MIGS of Ta metal layers and Ta-atom states around Ta/SiO_2 interface.

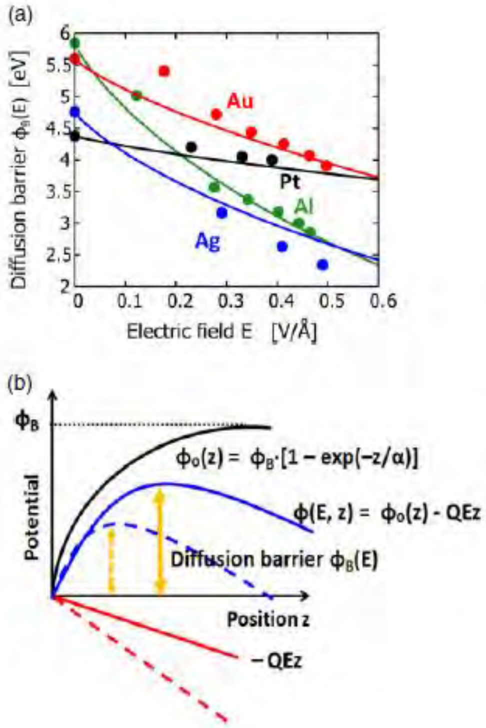

Fig.3. (a) Calculated diffusion barrier for the metal-atom penetration into SiO_2 as a function of electric field. The dots are obtained by first-principles calculations, while the lines are estimated using the model formula. (b) Model potential representing the metal-atom diffusion into insulators in electric fields. $\phi_B(E)$ is the potential barrier, while $\phi_0(z)$ and $-QEz$ are the diffusion potential in the case of no electric field and the electrostatic potential produced by the electric field, respectively. The solid and broken lines represent the cases of small and large electric fields, respectively.

region of potential increase with a similar width.

Next, we consider how the electric field accelerates the metal-atom penetration into SiO_2. Fig. 3(a) shows the diffusion penetration barrier for various atoms as a function of electric field strength. It is seen that the barrier height $\phi_B(E)$ decreases almost linearly with increasing electric field strength. We showed that the diffusion potential and the diffusion barrier in an electric field E are described as $\phi(E, z) = \phi_0(z) - QE$. and $\phi_B(E) = \phi_B - QE\alpha\ [1 - \log(QE\alpha/\phi_B)]$, respectively, as shown in Fig. 3(b). Here, ϕ_B, Q, and α are the potential barrier in the case of no electric field, the ionization charge of metal atom in SiO_2, and the penetration length of MIGS into SiO_2.

In this way, the barrier height $\phi_B(E)$ in an electric field is described by the universal formula, not depending on the kind of substrates and metal atoms. It is interesting to note that the MIGS are known to determine the Schottky barrier height and the defect density at metal/solid interfaces. By the present study, we also demonstrated that the MIGS work to determine the ionization and metal-atom penetration into SiO_2 in electric fields.

All these calculations were performed using the xTAPP, VASP, and pspwf codes. In order to realize the calculations for the present interface systems in electric fields, because the system is made of a large number of atoms (300-1000 atoms), the advanced computing facility having multi-task and higher-speed CPU (more than 64 cores × 2.5GHz), larger-size memory (around 128GB), and larger-size strange (more than 1 TB) is indispensable. These conditions are realized only by the ISSP supercomputing systems.

First-Principles Study on New Group-IV Semiconductor Alloys

Yuki NAGAE[1], Masashi KUROSAWA[1, 2, 3], Masaaki ARAIDAI[1, 2, 4],
Osamu NAKATSUKA[1, 4], Kenji SHIRAISHI[1, 4], and Shigeaki ZAIMA[4]
[1] *Graduate School of Engineering, Nagoya University*
[2] *Institute for Advanced Research, Nagoya University*
[3] *PRESTO, Japan Science and Technology Agency*
[4] *Institute of Materials and Systems for Sustainability, Nagoya University*

Silicon tin ($Si_{1-x}Sn_x$) alloy is a promising material for optical communication of intra- and interchip technology in silicon-based high-performance large-scale integrated circuits due to their preferable energy bandgap (E_g). However, comprehensive understandings of the energy band offset (EBO) with whole composition has not been clarified experimentally due to its low solubility (0.1%) of Sn in Si. In this study, we investigated the EBO of $Si_{1-x}Sn_x$ theoretically and compared it with conventional theoretical and experimental results.

The first-principles calculation was performed using the Vienna ab initio simulation package (VASP) code [1, 2] We used the modified Becke and Johnson (MBJ) exchange potential [3] to avoid the underestimation of E_g in conventional DFT calculation. To consider the electron-ion interaction, we used the PAW potential [4]. The unit cell and k-points were composed of 8 atoms of diamond lattice ($Si_{8-n}Sn_n$, n=0–8) and 2×2×2 mesh, respectively. We considered all of the unique atomic configuration by “Hakoniwa-method” [5], under the structurally relaxed situation in the hydrostatic pressure.

We calculated the charge neutrality level (CNL) of $Si_{1-x}Sn_x$ based on the interface hybridization that induced dipoles to compare the valence band maximum (VBM) for each Sn-content $Si_{1-x}Sn_x$ as the following equation [6],

$$\phi(\mathrm{CNL}) = \mathrm{VBM} + E_g D_{\mathrm{VB}}/(D_{\mathrm{VB}}+D_{\mathrm{CB}}),$$

where D_{VB} and D_{CB} correspond to the density of states (DOS) of valence and conduction bands, respectively. Figure 1 shows EBO of $Si_{1-x}Sn_x$ relative to Si with setting CNL of each $Si_{1-x}Sn_x$ as an equal level. The broken line represents a linear approximation of the referenced conventional conduction band minimum (CBM) and VBM between Si and α-Sn from the previous report [7]. We estimated a bowing parameter of 1.15 ± 0.02eV. The obtained Sn content dependence of VBO showed a similar tendency to the experimental results of $Si_{1-x}Sn_x$ with Sn content ranging between 0 and 40% [8,9], which cannot be ignored for designing band alignment. By estimating the energy band offset using calculations of E–k dispersion and the VBO, we could estimate the dependences of the VBM and CBM in the entire Sn content range not only in the low-Sn-content region.

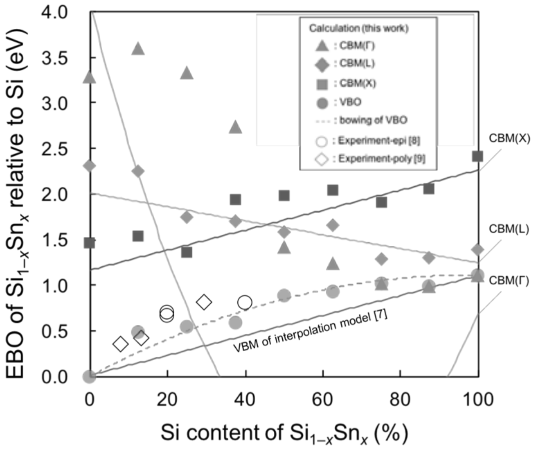

Fig. 1: EBO of $Si_{1-x}Sn_x$ relative to Si as a function of the Sn content. Solid lines show VBO and CBMs from previous report by Sun [7]. For the calculation results, the VBO and the CBMs at the Γ, L, and X valleys are shown as circles, triangles, diamonds, and squares, respectively. Experimental [8,9] and calculation results [10] are shown as opened and closed symbols, respectively. Copyright 2017 The Japan Society of Applied Physics [10].

References

[1] G. Kresse and J. Furthmüller, Phys. Rev. B **54**, 11169 (1996).

[2] B. Adolph, J. Furthmüller, and F. Bechstedt, Phys. Rev. B **63**, 125108 (2001).

[3] A. D. Becke and E. R. Johnson, J. Chem. Phys. **124**, 221101 (2006).

[4] P. E. Bröchl, Phys. Rev. B **50**, 24 (1994).

[5] K. Sueoka, E. Kamiyama, and J. Vanhellemont, J. Appl. Phys. **114**, 153510 (2013).

[6] M. Cardona and N. E. Christensen, Phys. Rev. B **35**, 6182 (1987).

[7] G. Sun, R. A. Soref, and H. H. Cheng, J. Appl. Phys. **108**, 033107 (2010).

[8] M. Kurosawa, M. Kato, K. Takahashi, O. Nakatsuka, and S. Zaima, Appl. Phys. Lett. **111**, 192106 (2017).

[9] M. Kurosawa, M. Kato, T. Yamaha, N. Taoka, O. Nakatsuka, and S. Zaima, Appl. Phys. Lett. **106**, 171908 (2015).

[10] Y. Nagae, M. Kurosawa, M. Araidai, O. Nakatsuka, K. Shiraishi, and S. Zaima, Jpn. J. Appl. Phys. **56**, 04CR10 (2017).

van der Waals density functional theory study of molecular adsorption on solid surfaces

Ikutaro HAMADA

Department of Precision Science and Technology, Graduate School of Engineering,
Osaka University, 2-1 Yamada-Oka, Suita, Osaka 565-0871

Molecular adsorption on the electrode surface is one of the important building blocks in diverse devices relevant to energy harvesting and storage, such as fuel cell, solar cell, and secondary battery, to name only a few. The accurate description of the molecular adsorption is challenging in the conventional density functional theory based on the local density and generalized gradient approximations, because they are static and local, and cannot capture the dynamic and nonlocal nature of the van der Waals interaction, which is crucial in the molecule-surface interaction. In this work, we use rev-vdW-DF2[1], an offspring of the van der Waals density functional (vdW-DF)[2], which has been show to describe the molecular adsorption on solid surfaces accurately.

All the calculations were performed using the STATE code[3], which employs ultrasoft pseudopotentials and plane wave basis set. The surfaces was modeled by a slab. Molecules are put on one side of the slab, and the spurious electrostatic interaction with image slabs was eliminated by using the effective screening medium method[4]. We used an efficient algorithm[5] of the self-consistent vdW-DF.

In this work I put emphasis on a polycyclic aromatic hydrocabon adsorbed on a metal surface, namely, diazuleno[1,2-c:2′,1′-g]phenanthrene (DAPh) and on the Cu(001) surface, and investigate the adsorption state and the on-surface reactions observed in the experiment[6]. As a first step, I investigated the adsorption site for the reactant and product and obtained the most stable adsorption sites in good agreement with the experiment. The investigation of the reaction mechanism is underway.

References

[1] I. Hamada: Phys. Rev. B **89** (2014) 121103(R)

[2] M. Dion et al., Phys. Rev Lett. **92** (2014) 246401.

[3] Y. Morikawa, H. Ishii, and K. Seki: Phys. Rev. B. **64** (2004) 041403.

[4] M. Otani and O. Sugino: Phys. Rev. B **73** (2006) 115407.

[5] J. Wu and F. Gygi: J. Chem. Phys **136** (2012) 224107.

[6] A. Shiotari et al. Nat. Commun. 8 (2017) 16089.

Hydrogen state in a rutile titanium dioxide by first-principles calculation

Kanako YOSHIZAWA
Research Organization for Information Science and Technology,
Kobe, Hyogo 650-0047

Titanium dioxide (TiO_2) has attracted increasing attention in recent years due to its numerous technological applications, such as photocatalysts, photovoltaics, and devices. Impurity hydrogen (H) and oxygen vacancy (V_O) affect electronic properties of TiO_2 and we study the effect of H doping of it. It is known that the electrons can localize at Ti 3d orbitals, forming Ti^{3+} ions [1, 2]. The trapped electrons form small polarons that consist of the electrons coupled to the distortion of the lattice around the Ti^{3+} ions.

We examine the electronic structure of H in rutile TiO_2 by using DFT calculation. We calculated using VASP package [3] on System B in ISSP. The large scale calculation was carried in 216-atom supercell with HSE hybrid functional in DFT. The spin density for a localized electron in Ti site exists and it is verified that the excess electrons are described as localized small polarons by DFT calculation.

We also understand H behavior by calculating the isotropic and anisotropic hyperfine coupling constants. Because muonium in crystals behaves similarly to H, muon spin rotation (μSR) has played an important role in identification of hydrogen-like states in TiO_2. We evaluate the accuracy of DFT calculation for H in TiO_2 by the comparison with hyperfine parameters of μSR [4] in the structure shown as the figure. As shown in the table, the hyperfine parameters of DFT calculation has anisotropy, the DFT calculation and μSR are qualitatively the same.

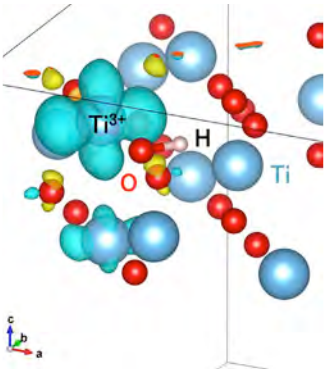

Figure: The position of Ti^{3+} ions (same structure as μSR [4]).

[MHz]	Axx	Ayy	Azz
H	−15.231	−13.761	26.074

Table: Hyperfine parameters of DFT calculation (gyromagnetic ratio $\gamma = 135.53$ MHz T^{-1})

References

[1] A. Janotti, C. Franchini, J. B. Varley, G. Kresse, and C. G. Van de Walle, Phys. Status Solidi RRL **7**, 199 (2013).

[2] F. Filippone, G. Mattioli, P. Alippi, and A. Amore Bonapasta, Phys. Rev. B **80**, 245203 (2009).

[3] http://www.vasp.at.

[4] K. Shimomura, R. Kadono, A. Koda, K. Nishiyama, and M. Mihara, Phys. Rev. B **92**, 075203 (2015).

First-principles theoretical study on ionization energy and electron affinity of organic semiconductors: Role of the electrostatic interaction

Susumu Yanagisawa
Department of Physics and Earth Sciences, Faculty of Science, University of the Ryukyus
1 Senbaru, Nishihara, Okinawa 903-0213

Ionization energy (IE) and electron affinity (EA) of organic semiconductor (OSC) are important quantities dominating charge injection barrier. Experimentally, IE (EA) is determined as the energy difference between the highest occupied (lowest unoccupied) energy level and the vacuum level. It was proposed that the orientation of the constituent organic molecules at the surface crucially affects IE and EA[1]. The electrostatic interaction such as the charge-permanent quadrupole interaction was proposed to be of importance[2].

In this study, using the periodic slab model of the OSC surface with the semi-local density functional theory (DFT) calculation, the surface facet or molecule orientation-dependent IE and EA of the pentacene polymorphs (see Fig. 1) were theoretically determined [3]. For DFT calculations, STATE code was used[4]. For accurate treatment of the induced polarization upon the injected charge in the bulk, the many-body perturbation theory within the *GW* approximation was employed. For the calculation of the bulk with the one-shot *GW*, the *GW* space-time code[5] was used. To gain insights into the polarization energy in terms of the electrostatic and induced polarization contributions, a following strategy was employed:

- The electrostatic term (W^+/W^-) was estimated by the energy difference in highest occupied/lowest unoccupied level between the isolated molecule and the periodic slab.
- The induced polarization terms E_P^+ and E_P^- were assumed to be of the same magnitude, and thus were estimated as half of the difference in transport gap between the isolated molecule and the bulk system.

The polarization energies P^+ and P^- upon the injected hole and electron, respectively, were determined as

$$P^+ = E_\mathrm{P}^+ + W^+, \tag{1}$$

$$P^- = E_\mathrm{P}^- + W^-. \tag{2}$$

The calculation was done for IE and EA of the different polymorphs of pentacene, i.e. thin-film and single crystal phases in which the molecules are standing and lying on the substrate, respectively[6]. The thickness of the slab treated with DFT was three (seven) monolayer for the thin-film (single crystal) phase, and the energy of their highest occupied/lowest unoccupied level was determined as average of the valence band/conduction edge energies over the Brillouin zone. For the fundamental gap or IE and EA of the isolated molecule, the experimental values were used[7].

Table 1 shows the calculated IE and EA for the facets of the pentacene polymorphs. The result is in agreement with the experiments. The IE and EA are found to be similar to those determined by the recent theoretical approach

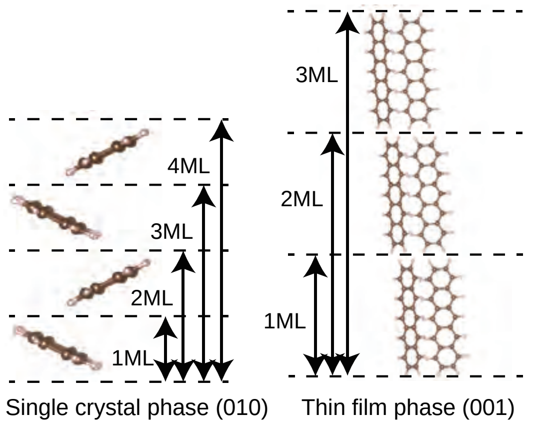

Figure 1: Schematics of the pentacene polymorphs

Table 1: Ionization potential (IP) and electron affnity (EA) of the pentacene polymorphs depending on the facets. Experimental results[8] are in parentheses.

	Pentacene	
	Thin film (001)	Single crystal (010)
IE	4.80 (4.90)	5.25 (5.45)
EA	2.31 (2.35)	2.83 (3.14)

at the same level of theory, in which the electrostatic potentials of the slab and the bulk were aligned[9].

Fig. 2 displays the polarization energies P^+/P^- for the polymorphs in terms of E_P and W. It is found that the different polarization energies for the different facets come from the electrostatic terms W^+/W^-, while the E_P are similar. The different charge-permanent quadrupole interaction for the standing/lying pentacene (see Fig. 1) dominates the different electrostatic contribution[2].

Overall, this work demonstrates the impact of the electrostatic terms affecting the IE and EA of OSC, which seems to come from the molecular orientation at the surface. The same approach has been also applied to elucidation of the measured IE and EA in thin films of a pentacene derivative[10].

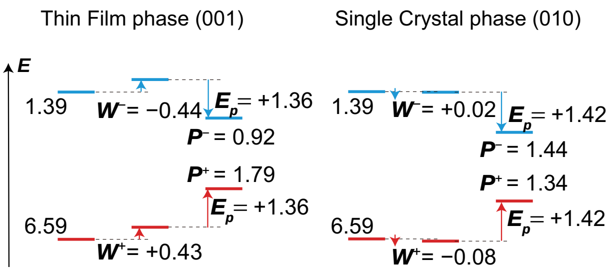

Figure 2: Effects of the electrostatic and the induced polarization terms on the polarization energies

References

[1] G. Heimel et al.: Nat. Chem. **5** (2013) 187.

[2] B. J. Topham and Z. G. Soos: Phys. Rev. B **84** (2011) 165405.

[3] S. Yanagisawa: AIP Conf. Procs. **1906** (2017) 030014.

[4] Y. Morikawa, H. Ishii, and K. Seki: Phys. Rev. B **69** (2004) 041403(R).

[5] M. M. Rieger et al.: Comput. Phys. Commun. **117** (1999) 211.

[6] T. Siegrist et al., Angew. Chem. Int. Ed. Engl. **40** (2001) 1732; H. Yoshida, K. Inaba, and N. Sato, Appl. Phys. Lett. **90** (2007) 181930.

[7] V. Coropceanu et al.: Phys. Rev. Lett. **89** (2002) 275503; L. Crocker, T. B. Wang, and P. Kebarle: J. Am. Chem. Soc. **115** (1993) 7818.

[8] H. Yoshida et al.: Phys. Rev. B **92** (2015) 075145.

[9] Y. Kang, S. H. Jeon, Y. Cho, and S. Han: Phys. Rev. B **93** (2016) 035131.

[10] K. Yamada, S. Yanagisawa, T. Koganezawa, K. Mase, N. Sato, and H. Yoshida, submitted to Phys. Rev. B.

Controlling magnetic properties of the quantum-well induced ferromagnetism in Pd(100) through the lattice distortion

Yusuke BAN[1], Hiroyuki KAGESHIMA[2], and Tetsuya SATO[1]

1Department of Applied Physics and Physico-Informatics, Keio University, 3-14-1 Hiyoshi, Kohoku-ku, Yokohama 223-0061, Japan

2Interdisciplinary Graduate School of Science and Engineering, Shimane University, 1060 Nishikawatsu-cho, Matsue 690-8504, Japan

Recently, we found the appearance of ferromagnetism in the ultrathin film of Pd(100) based on d-electron quantum-well states[1]. Moreover, it was revealed that the saturation magnetization of the Pd (001) ultrathin film changed accompanied by the structural phase transition of the $BaTiO_3$ substrate. In order to clarify the magnetization change accompanied by a phase transition of $BaTiO_3$, we performed the density functional calculation for distorted Pd films using the PHASE/ 0 program [2].

In the calculation, we used the pseudopotential method and LDAPW92 to the exchange and correlation interactions. A slab of vacuum (two monolayers) /Pd (N monolayers) /vacuum (three monolayers), 56 × 56 × 1 k-points, and 36Ry of cut-off energy were used. First, we calculated the out of plane lattice constant of Pd to obtain the lowest energy under the condition that the in-plane lattice constant is consistent with that of $BaTiO_3$ substrate. Changes in the magnetization of Pd (001) induced during the structural phase transitions of $BaTiO_3$ substrate were calculated. The change in magnetization is consistent with the experiment suggesting that the strain caused by the structural phase transition of $BaTiO_3$ modulates the magnetism. In order to investigate the mechanism of magnetization change accompanying strain, DOS was calculated considering strain effect. Near the Fermi energy, steep changes in the DOS were observed. This suggests that a slight change in the electronic structure of Pd(001) can induce a change in magnetization.

Based on this study, the relation between metallic ferromagnetism induced by the quantum well states and strain can be understood from the viewpoint of electronic structure. In addition this indicates the possibility to realize a multiferroic ~~devices~~ for magnetic switching using strain as an external field.

References

[1] S. Sakuragi *et al.*: Phys. Rev. B **90** (2014) 054411.

[2] Y.Ban *et al.*: Appl. Phys. Lett. **112** (2018) 142409.

Ab initio study of viscosity and local structures of basaltic melt under high pressure.

Satoshi OHMURA
Research Center for Condensed Matter Physics / Department of Environmental and Civil Engineering,
Hiroshima Institute of Technology Saeki-ku, Hiroshima, 731-5143

We have studied static and dynamical properties of covalent liquids under high-pressure and high-temperature conditions by *ab initio* molecular dynamics (MD) simulations. This year, we applied *ab initio* MD simulations to basaltic melt and investigated dynamical properties such as viscosity under high pressure conditions. The simulations have been done in System B in ISSP.

High-pressure behavior of basaltic aluminosilicate melt has been intensively studied due to its importance in deep Earth science related to such as early magma ocean and subsequent differentiation processes.

Recently, experimental studies reported that the viscosity of basaltic melt decreases with increasing pressure [1]. They suggested that this anomalous behavior is related to the coordination change of Al. However, so far, there exist no *ab initio* simulations of basaltic melt in the pressure range, where the anomaly in viscosity is observed experimentally.

In this study, we therefore performed *ab initio* MD simulations with gradually changing volume. We calculated the pressure dependence of the viscosity and successfully reproduced a viscosity minimum in the pressure range corresponding to the experiments. We also analyzed the atomic local-structures in the melt under pressure. The obtained pressure dependence of density and radial distribution functions do not show drastic structural changes and the coordination number around Si and Al increase continuously with increasing pressure. However, the coordination number around Al atoms increases more rapidly than that around Si atoms. We also investigated pressure dependence of atomic diffusion. It was clarified that pressure enhances atomic diffusion up to 5 GPa. However, when pressure is over 5 GPa, atomic diffusion becomes suppressed by pressure effects. From the atomic diffusion mechanism observed in the simulations, we clarified a relationship between the anomalous pressure dependence of viscosity and variations in the atomic-scale local structure.

[1] T. Sakamaki *et al.*, Nature Geoscience **6**, 1041 (2013).

First-Principles Study of Electronic Structures of Energy Device Materials

Hiroyoshi MOMIDA, Motoyuki HAMAGUCHI, Hiroshi KATSUMOTO
Institute of Scientific and Industrial Research, Osaka University
8-1 Mihogaoka, Ibaraki, Osaka 567-0047

We have studied electronic and atomistic properties of materials, which are used in energy storage and conversion devices, by the first-principles calculations. As to the energy storage materials, we have investigated electrode properties of the transition-metal (TM) fluoride and oxide materials for Li-ion and Na-ion batteries [1, 2]. Piezoelectric materials can be used for an energy conversion between mechanical and electric ones, and we have studied piezoelectric properties of wurtzite materials [3]. Related to this subject, mechanical properties of 5d-TM carbides have been studied by the first-principles calculations [4]. We have studied topological electronic properties in a layered material consisting of strong- and non-topological insulators using the supercomputer system in the last fiscal year, and the result is published recently in a journal [5].

1. Cathode properties of Li$_2M$TiO$_4$ (M = 3d TMs) for Li-ion batteries [2]

Cathode properties of Li$_2M$TiO$_4$ (M = V, Cr, Mn, Fe, Co, and Ni) for Li-ion batteries have been studied by the first-principles calculations. Structure stabilities and voltage–capacity curves for Li$_{2-x}M$TiO$_4$ ($0 \leq x \leq 2$) models with the rock-salt-based structures are calculated considering several Li concentration ($2-x$). It is found that battery reaction mechanisms associated with redox reactions of M and O dominates mainly in the ranges of lower and higher x, respectively. The O redox reactions can destabilize atomic structures in the higher x region, because the electron removal from O-p states produces high peaks at the Fermi level in the density of states. We actually calculate the structural stability of O using the models with O deficiency, and the result shows that O can be released easier than Li in the higher x region. We estimate the critical Li concentration (x_c) at which the vacancy formation energy of O becomes lower than that of Li, and find that the critical x value decreases with increasing number of 3d electrons as M changes from V to Ni. The O dissociations from the cathodes degrade the battery performance, because the calculated voltages of Li$_2M$TiO$_4$ with O deficiency are lower than those without O deficiency. Our systematic study for the series of M predicts that Li$_2$CrTiO$_4$ can be the best cathode material considering its cathode properties of high voltage and stability against O dissociation.

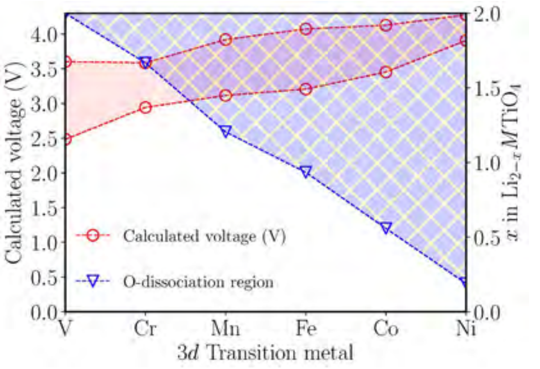

Figure 1: Calculated voltage ranges (circles) and the critical Li concentration x_c (triangles) in Li$_{2-x}M$TiO$_4$ (M = 3d TMs) [2].

2. Piezoelectricity of wurtzite materials: First-principles and statistical-learning calculations [3]

We calculate piezoelectric e constants along the c axis (e_{33}) by the first-principles method for more than a dozen of binary wurtzite materials, which are listed in the Inorganic Crystal Structure Database (ICSD). We investigate a relationship between e_{33} and several materials parameters using the statistical learning methods. It is theoretically shown that wurtzite materials with high e_{33} generally have small lattice constant ratios (c/a) almost independent of constituent elements, and approximately expressed as $e_{33} = -A[c/a - (c/a)_0]$ (in the c/a ranges higher than about 1.3) with the ideal lattice constant ratio $(c/a)_0 \sim 1.633$ and a constant parameter $A > 0$. We also find the better description of $e_{33} = -A'Z_v[c/a - (c/a)_0]$ (in the c/a ranges higher than about 1.3) with nominal ionic valences Z_v. This relation also holds for ternary materials such as $Sc_xAl_{1-x}N$. Based on the above relation, we have conducted a search for highly piezoelectric wurtzite materials by identifying materials with smaller c/a values. It is theoretically proposed that the piezoelectricity of ZnO can be enhanced by substitutions of Zn with Ca.

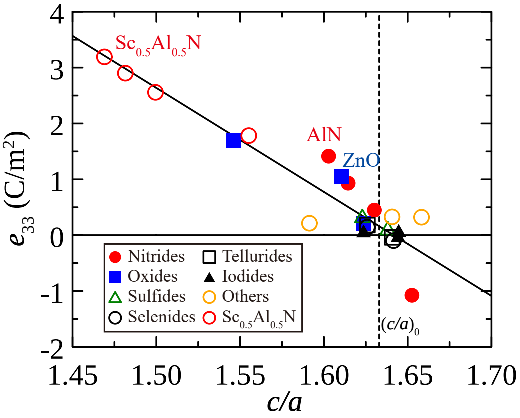

Figure 2: Piezoelectric e constants (e_{33}) versus lattice constant ratios (c/a) calculated for binary wurtzite materials listed in ICSD and $Sc_{0.5}Al_{0.5}N$ models [3].

References

[1] A. Kitajou, Y. Ishado, T. Yamashita, H. Momida, T. Oguchi and S. Okada, Cathode properties of perovskite-type NaMF$_3$ (M = Fe, Mn, and Co) prepared by mechanical ball milling for sodium-ion battery, Electrochimica Acta **245** (2017) 424.

[2] M. Hamaguchi, H. Momida and T. Oguchi, First-principles study on cathode properties of Li_2MTiO_4 (M = V, Cr, Mn, Fe, Co, and Ni) with oxygen deficiency for Li-ion batteries, J. Phys. Soc. Jpn., in press.

[3] H. Momida and T. Oguchi, Effects of lattice parameters on piezoelectric constants in wurtzite materials: A theoretical study using first-principles and statistical-learning methods, Appl. Phys. Express **11** (2018) 041201.

[4] M. Fukuichi, H. Momida, M. Geshi, M. Michiuchi, K. Sogabe and T. Oguchi, First-principles calculations on the origin of mechanical properties and electronic structures of 5d transition metal monocarbides MC (M = Hf, Ta, W, Re, Os, Ir, and Pt), J. Phys. Soc. Jpn. **87** (2018) 044602.

[5] H. Momida, G. Bihlmayer, S. Blügel, K. Segawa, Y. Ando and T. Oguchi, Topological interface states in the natural heterostructure $(PbSe)_5(Bi_2Se_3)_6$ with Bi_{Pb} defects, Phys. Rev. B **97** (2018) 035113.

Ab initio molecular dynamics study of static structure of glasses

Akihide KOURA

Student Affairs Department,

Kumamoto University, Kurokami, Kumamoto, Kumamoto 860-8555

We have studied static structure, electronic and dynamic properties of liquid, crystal, and glassy systems. In this project, we focused on the static structure of network forming glasses under pressure by using *ab initio* molecular dynamics simulations.

In this project, we have studied the static structure of liquid GeTe and liquid GeSe under pressure, and the static structure of the densified $GeSe_2$ glass. The study of the pressure dependence of the static structure on the liquid GeTe was published [1].

On the static structure of the densified glass $GeSe_2$, there is a different point comparing with that of the densified SiO_2 glass. In the densified SiO_2 glass, although the local structure is quite similar to the ordinary glass, the intermediate range order is different. Using ring analysis, the number of small rings increases in the densified glass [2]. On the other hand, in the densified $GeSe_2$ glass, the peak of bond angle distribution shifts from approximately 108° in the ordinary glass to 90° in the densified glass. The fact means the deformed tetrahedral units remains after depressurization. Using the ring analysis, which is more complicated than that in SiO_2 case because of the existence of Ge-Ge and Se-Se homo-polar bonds, it is shown that the tendency of decrease number of large size ring is the same as that in SiO_2. These features are supported by various covalent bond strengths.

We have also studied the pressure dependence of the static structure of liquid GeSe. The pressure and temperature ranges are from 0 to 240 GPa and 1000 to 4500 K, respectively. At ambient pressure, liquid GeSe shows the semiconducting property. With increasing pressure, the semiconductor-metallic (SCM) transition occurs between about 8 and 12 GPa. On the other hand, numbers of three- and five-fold coordinated Ge to Se atoms decrease and increase at about 12 GPa, respectively. The structural change and the SCM transition suggest that the Peierls-type distortion is completely dissolved at this pressure range.

References

[1] A. Koura and F. Shimojo: EPJ Web of Conferences **151,** 01002 (2017).

[2] E. Ryuo, D. Wakabayashi, A. Koura, and F. Shimojo, Phys. Rev. B **96** (2017) 054206.

First-principles meta-dynamics analysis of Catalyst Referred Etching method

– Analysis on dissociative adsorption of water molecule and etching reaction at interface between Pt and material surface –

Kouji Inagaki

Graduate School of Engineering, Osaka University
Yamadaoka 2-1, Suita, Osaka 565-0871

Atomic-level planarization of hard-to-work materials such as wide-band gap semiconductors has attracted much attention for a power electronic devices. Recently, a newly developed wet chemical surface planarization technique named CARE (Catalyst-Referred Etching) [1] realizes step-and-terrace shaped smoothened surfaces, only by wiping work surface with a catalytic metal plate in an etching solution. At present, as the etchant and the catalyst, dangerous and toxic concentrated hydrogen fluorine aqueous solutions and expensive Pt plates are utilized for etchant and catalyst, respectively. It is important to clarify the reaction process in the atomic level in SiC-HF-Pt system to find out alternative, effective and practical etchant and catalyst materials.

In this project, we performed first-principles reaction path calculations on the initial stage of the etching process, as well as developed a new metadynamics method for reaction path analysis with no initial knowledge. All reaction analyses for former theme were performed using a program package ‘STATE’ (Simulation Tool for Atom TEchnology) [2]. Reaction process for SiC-H_2O-Pt[3] and GaN- H_2O-Pt systems are investigated.

In the SiC analysis, the role of Pt as catalyst in the dissociative adsorption of a water molecule as an elemental reaction of the process is discussed from a viewpoint of chemical and mechanical interactions. It was shown from calculations that the distance between SiC work surface and Pt catalyst found to play an important role to the reaction barrier height. The chemical stabilization by forming Pt-O-Si bond and destabilization by mechanical distortion show different tendency for the initial, metastable and final structures against the distance; formation of multiple bonds both at Si-O-Pt and Si-SiC substrate in a metastable state make system rigid and sensitive to the distance while the other cases (initial and final) contains less number of bonds and become flexible. Therefore, the barrier becomes low at a particular distance between Pt and SiC surfaces.

In the development of a new metadynamics method, we proposed a new method for stacking penalty potential in which the potential height and width are simultaneously expanded or shrunk with the kinetic energy corresponding to the freedom which we are interested in, with considering that system has larger kinetic energy at lower potential energy. The test program built with Fortran and Lammps and the efficiency of the method is tested. It was shown that the method basically works well and possibility for higher performance than previous method is clarified.

References

[1] H.Hara, et al., J.Electron.Mater. **35** (2006) L11.
[2] Y. Morikawa, Phys. Rev. B **63** (2001) 033405.
[3] P.V. Bui, D. Toh, A. Isohashi, S. Matsuyama, K. Inagaki, Y. Sano, K. Yamauchi, and Y. Morikawa, Jpn. J. Appl. Phys. 57, 055703 (2018).

Ab initio studies toward functional nanomaterials based on abundant elements

Tetsuya TAKETSUGU
Faculty of Science, Hokkaido University
N10W8, Sapporo, Hokkaido 060-0810

Ab initio studies on various nano materials are crucial to understand and design new functional materials with abundant elements. Heterogeneous catalysts used in automotive gas exhausts control, water gas shifts, and fuel cells rely mostly on the precious metals (PMs) such as Pt, Rh, Pd. Platinum and palladium are also used for hydrogen based energy strategies. Due to their high cost and limited amounts, to reduce or even replace these metals is emergent issues in industry. To that end, we perform density functional theoretical (DFT) computations under the periodic boundary conditions together with projector augmented wave method with VASP using ISSP supercomputers to gain chemical insights.

Concerning the automotive catalysis, NO is reduced while CO and CH (hydrocarbons) are oxidized at the same time under the drastic temperature and oxygen concentration changes. With such extreme conditions, only Pt, Rh, and Pd turned out to be effective. To understand the reason as well as to clarify the possible chemical reaction pathways for TWC, we focus on the NO reduction reaction at the Pd surface and perform DFT calculations at the generalized gradient approximation level. Adsorption of NO, CO, O_2, as well as O to various Pd surfaces such as (111), (100), steps, and edges are studied and then nudged elastic band calculations are performed to study NO reduction reactions. We have also studied CO adsorption onto Pt surfaces by using hybrid functionals of HSE06 for a 4-layer slab of 2 by 2 super cells. As for the abundant elemental nano catalysis, we have studied structural and electronic properties of 3d transition metals (TM^{3d}) supported by an oxide surface. Electronic properties of optimized structures for one TM^{3d} atom doping with pristine and O-defective oxide substrates are studied and some adsorption states of small molecules are obtained. Here, for calculations including transition metals with localized f-electrons, we used DFT+U technique to account for the localized electrons. We have also tried hybrid functionals such as HSE06 but using those functionals for a large TM/Oxide surface turned out to be computationally too demanding to the present purpose.

On the hydrogen storage materials, we study PdAu alloy materials, to complement a hydrogen uptake and release experiment using thin films of Au:Pd alloys. DFT calculations are performed for Au:Pd alloy thinfilms modeled by alternating Au and Pd layers in 2-by-2 manner in the $\langle 001 \rangle$ direction using the unit cell consisting of Au_4Pd_4 and 1-by-2 in the $\langle 111 \rangle$ direction using unit cell consisting of $AuPd_2$. Density of states are obtained using a 21 × 21 × 11 k-point meshes with the curoff energy of 500 eV.

References

[1] Y. Nishijima, S. Shimizu, K. Kurihara, Y. Hashimoto, H. Takahashi, A. Balcytis, G. Seniutinas, S. Okazaki, J. Juodkazyte, T. Iwasa, T. Taketsugu, Y. Tominaga, and S. Juodkazis, Optics Express, 25, 24081 (2017).

Ab-initio Study on Amorphization Dynamics and Ion Diffusion in Biogenous Iron Oxide

Kenji TSURUTA, Keiichi MITANI, Satoshi OHMURA[a], and Atsushi ISHIKAWA

Graduate School of Natural Science and Technology, Okayama University, Okayama 700-8530
[a] *Department of Civil and Environmental Engineering, Hiroshima Institute of Technology, Hiroshima 731-5193*

The chemical versatilities of nanostructured iron oxide (n-FeO) have long been attracting attention in the research of functional materials. Since ordinary synthesis of intrinsic n-FeO involves high-temperature processes and many of experimental observations have proven that n-FeOs possess amorphous structure, rapid and low-temperature generation of stable amorphous iron oxides is important for industrial applications. In the field of the microbiology, on the other hand, it has long been known that iron oxidizing bacteria, called *Leptothrix ochracea*, produces an iron oxide sheath. The recent reports have shown [1] that the sheath produced by the bacteria consists of agglomerated iron oxide nanoparticles of ~3 nm diameter with an amorphous structure involving uniformly distributed non-stoichiometric composition of Fe,O, Si, and P. It also suggests that amorphous iron oxide can be formed under the ambient temperature with the doping condition. Detailed mechanisms how the bacteria can produce the amorphous nanostructure under the conditions are yet elusive.

In the present work, we performed a first-principles molecular dynamics (FPMD) study on the models of a glassed iron oxide (GIO) and a non-stoichiometric iron oxide (NIO); the former is an amorphous derived from molten iron oxide [2], the latter is a hematite codoped with Si and P, which has been inspired by the aforementioned biogenous iron oxide.

In order to evaluate local bond order and orientational correlations, we calculated the local bond-orientational order parameter w_l and bond-angle correlation function, proposed by Steinhardt *et al.* for each atomic species. The parameter w_l can specify the symmetry of a particular cluster. Since the maximum/minimum values of the w_4 and w_6 are rigorously known, one can grasp a cluster shape and its fluctuations visually by plotting their instantaneous values into the (w_4, w_6)-plane, as depicted in Fig. 1. Also, the inter-cluster correlation based on the Landau theory of bond-orientational free energy (BOF), are applied to these models, and we consequently show that the GIO and NIO are unexpectedly the same structure despite their totally different fabrication processes. The BOF analysis revealed that the compositional changes of the hetero-oxide clusters caused the increase of their pair correlation entropy, and in turn triggered their network topology fluctuation such as a transformation of the sharing form. We thus concluded that the incipient formation of hetero-oxide clusters is essential in the rapid amorphization process and has been a hidden route of the amorphization under the ambient condition [3].

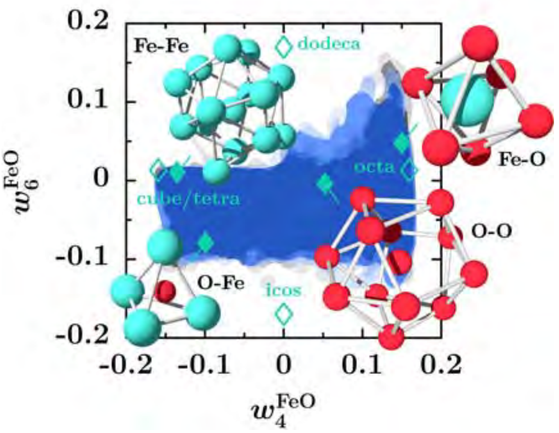

Fig. 1: Local bond-orientational order parameters (w_l) of Fe-O clusters. The gray and blue regions indicate the probability density in the FPMD trajectory for GIO and NIO, respectively.

References

[1] H. Hashimoto *et al.*, ACS Appl. Mater. Interface **6**, 5374-5378 (2014).

[2] M. Misawa, S. Ohmura, and F. Shimojo, J. Phys. Soc. Jpn. **83**, 105002 (2014).

[3] K. Mitani, S. Ohmura, A. Ishikawa, and K. Tsuruta, submitted.

First-principles calculation of solid oxygen using the vdW-DF+U method

Shusuke KASAMATSU
Institute for Solid State Physics, University of Tokyo
Kashiwa-no-ha, Kashiwa, Chiba 277-8581

Solid O_2 is a unique molecular crystal system in that it is comprised of elementary molecules carrying spin $S = 1$. In this system, magnetic and van der Waals (vdW) interactions compete with each other leading to a feature-rich temperature-pressure phase diagram with a variety of structural/magnetic phases. In addition, it It was shown recently that ultra-high magnetic fields can also induce a structural/magnetic phase transition to a previously unknown Θ phase [1]. Support from first-principles density functional theory (DFT) calculations is highly desired for understanding such phase transition behavior. However, it is known that conventional semilocal functional approximations fail rather miserably in describing the experimentally well-known ground state monoclinic α phase of solid O_2. This failure isn't surprising considering the lack of nonlocal correlation in semilocal functionals. However, even recently-developed vdW-DF functionals show only marginal improvement. This has been attributed to the inaccuracy in the description of the magnetic interaction, i.e., overbinding of antiparallel-spin O_2 pairs compared to parallel-spin pairs. Attempts have been made to build in the correct spin-polarization dependence into the vdW-DF functionals, but with limited success [2].

In this work, we took an alternative approach of employing the DFT+U approach to correct for such overpairing of antiparallel spins. The vdW-DF-optB86b functional applied to α-O_2 predicts lattice constants that differ by as much as 30% from experiment. We found that by combining this functional with DFT+U, all monoclinic lattice constants improve continuously with increasing U_{eff} up to $U_{\text{eff}} = 12$ eV. At $U_{\text{eff}} = 12$ eV, the calculated values are all within 2.1% of experiment, which is the best description of α-O_2 thus far achieved in the literature using DFT. The effect of the U_{eff} parameter was examined in detail using chemical bonding analysis. We also calculated the candidate Pa$\bar{3}$ structure for the high-field Θ phase, and the energetics are consistent with the experimentally measured critical field for the phase transition. Details are given in Ref. [3].

References

[1] T. Nomura *et al.*: Phys. Rev. Lett. **112** (2014) 247201.

[2] M. Obata I. Hamada, and T. Oda: Phys. Proc. **75** (2015) 771.

[3] S. Kasamatsu, T. Kato, and O. Sugino: Phys. Rev. B **95** (2017) 235120.

First principles study of Pt clusters adsorbed on graphene edges

Yuji HAMAMOTO

Department of Precision Science and Technology,

Osaka University, Yamada-oka, Suita, Osaka 565-0871

Today, researchers are exploring the possibilities of industrial applications of graphene due to its exceptional electronic and structural properties. One of the most promising candidates is the application of graphene as a support material for metal nanoparticle catalysts. Experimentally, it has been demonstrated that Pt clusters supported on graphene displays higher catalytic activity than those on conventional support materials such as carbon black [1]. A possible scenario for the enhanced catalytic activity of Pt clusters on graphene is that carbon monoxide (CO) tolerance of Pt clusters is improved by strong interactions with the graphene support. So far we have taken lattice vacancies in graphene as an origin of such interactions, where Pt clusters take various adsorption structures depending on the size of vacancies.

Similar strong Pt-graphene interactions can be realized if one consider the adsorption of Pt clusters on the edges of graphene nanoribbons. As a simple examples of such systems, we show Pt atoms adsorbed on zigzag edges of graphene in Figs. 1(a) and (b). As a result of the difference in the coordination numbers, the Pt adsorption energies for structures (a) and (b) are calculated to be -5.04 and -6.28 eV, respectively, indicating that structure (b) is much more preferable than (a). To investigate the CO tolerance of these systems, we also consider CO adsorption on Pt as shown in Figs. 1(c) and (d). The calculated CO adsorption energies for structures (c) and (d) are -2.10 and -1.35 eV, respectively. This suggests that the highly coordinated Pt adsorption structure (b) is more preferable both in terms of stability and CO tolerance.

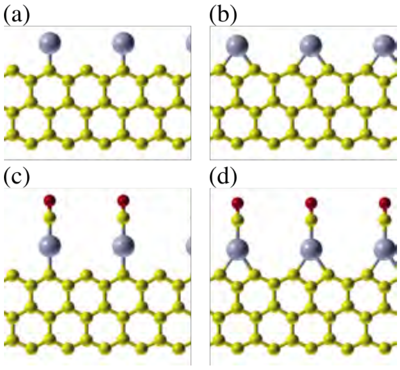

Fig. 1: Pt adsorption on graphene edges (a,b) and CO adsorption on the Pt atoms (c,d).

References

[1] E. Yoo, T. Okata, T. Akita, M. Kohyama, J. Nakamura, and I. Honma, Nano Lett. **9**, 2255 (2009).

[2] Y. Hamamoto et al., for preparation.

Elucidation of high-order harmonic generation from solids by atomistic simulations

Yasushi SHINOHARA

Photon Science Center,

The University of Tokyo, Hongo, Bunkyo-ku, Tokyo 113-8656

High-order harmonic generation (HHG) from crystalline solids has become an active field with intense and ultrashort coherent light sources. HHG in the gas phase is well developed by both theoretical and experimental point of view, leading attosecond resolution via optical science and engineering [1]. In contrast, the solid state HHG is still under intensive discussion, *e.g.* quantitative discussion of intraband current as an extra source of HHG.

We have developed an atomistic simulation framework to describe electronic real-time dynamics of crystalline solids based on time-propagation of one-body density-matrix. We obtain high-order harmonic spectra, taking Fourier transform of the induced current evaluated by the density-matrix. All parameters we need are field-free Hamiltonian and momentum operator because of velocity gauge. Matrix elements for the operator are derived from an *ab-initio* theory, density-functional-theory with local-density-approximation, by using the Elk FP-LAPW code [2].

We perform the simulation for GaSe crystal. Number of active orbital is 103 bands per each Brillouin zone sampling, corresponding to 39 eV energy range. We use 64x64x12 points for the Brillouin zone sampling to see converged results for polarization angle dependence. This simulation reproduces experimental angle dependent HHG spectra for both parallel and perpendicular components [3], at 0.25 eV central frequency, 100 fs pulse duration, and 10 MV/cm field strength imitating experimental condition.

In order to investigate role of intraband current and interband polarization in the HHG, we develop a way to decompose a total current into the two contributions by use of instantaneous eigenfunction of the Hamiltonian based on explicit numerical diagonalization among active bands. This analysis reveals that odd-order harmonics are dominated by the intraband current and even-order harmonics are exclusively contributed by the interband contribution.

References

[1] F. Krausz and M. Ivanov, Rev. Mod. Phys. **81** (2009) 163.

[2] http://elk.sourceforge.net/

[3] K. Kaneshima, Y. Shinohara, K. Takeuchi, N. Ishii, K. Imasaka, T. Kaji, S. Ashihara, K.L. Ishikawa, and J. Itatani, accepted.

First-Principles Molecular Dynamics Study of Biomolecule Synthesis on Primitive Ocean

Kohei Shimamura
Graduate School of System Informatics,
Kobe University, 1-1 Rokkodai, Nada-ku, Kobe 657-8501

We are conducting research on the origin of life using the first-principles molecular dynamics simulation package "QXMD" [1]. The origin of life is thought to have two stages. At the first stage (1), various kinds of reductive molecules were originated on a global scale in the harsh oxidizing environment of the early Earth. Next stage (2), using specific molecules from these various reductive molecules resulted in that primitive life was emerged. The stage (1) is important for preparing a reducing environment where the primitive life appeared easily and the stage (2) is important for providing food groupings for the primitive life. Although there are a lot of hypotheses to mention the stage of (1), we are interested in the possibility of the production of a large amount of organic molecules by the ocean collisions of iron meteorites which the simulation experiments have shown recently. This hypothesis was built on the fact of meteorite collisions at the late heavy bombing period which lasted about 3.8 billion years ago. Since the trace of life of 3.7 billion years ago have already been discovered, the meteorite collision events is considered to be greatly involved in the birth of life. We investigated the reaction processes in which reductive nitrogen and carbon reductive molecules were produced from N_2 and CO_2 as sources by the ocean collision of iron meteorite by means of the first-principles molecular dynamics simulations. Ammonia production was observed as the nitrogen reductive molecule. Interestingly, it was found that a large amount of ammonia produced by meteorite collision as a driving force by three different mechanisms [1]. As carbon reductive molecules, hydrocarbons and carboxylic acids were produced, where bicarbonate produced from CO_2 and H_2O played an important intermediate role in these reaction processes [2].

Such reductive molecules produced were primarily preserved in the early ocean but could not proceed to stage (2) because high concentrations are needed. It was necessary to provide a place where concentration of the reductive molecules could be done. While various kinds of concentrating plants have been considered so far, we are paying attention to the alkaline deep sea hydrothermal vent environment. In this environment some micrometer vesicular iron sulfides can be formed, where reductive organic molecules can be concentrated. Also, since there are abundant reducing agents such as hydrogen, it is a place capable of producing reductive organic molecules using iron sulfides as catalysts. We mimicked this environment and confirmed that carboxylic acid was produced from carbon dioxide on iron sulfide [3]. As a future work, we elucidate the concentration process by making larger simulation system.

References

[1] K. Shimamura, F. Shimojo, A. Nakano, and S. Tanaka: Phys. Chem. Chem. Phys. accepted.

[2] K. Shimamura, F. Shimojo, A. Nakano, and S. Tanaka: submitted.

[3] K. Shimamura, F. Shimojo, A. Nakano, and S. Tanaka: The 55th Annual Meeting of the Biophysical Society of Japan. Poster-number 3Pos163 (2017).

Construction and application of anharmonic potentials for adsorbed molecule on crystal/nanoparticle surface

Wataru Mizukami
Department of Advaced Matrerials Science and Engineering, Fackulty of Engineering Sciences
Kyushu University, 6-1 Kasuga Park, Fukuoka, 816-8580, Japan

Vibrational spectroscopy such as infrared or Raman spectroscopy is a vital tool to probe chemical phenomena at atomic/molecular level. Computational simulations are often used to get a clue to understanding vibrational spectra, where the harmonic approximation is predominantly used owing to its low computational costs. While evaluating vibrational energy levels beyond harmonic approximation is becoming increasingly commonplace for small molecules in gas phase, such methods for a molecule on a surface are not well developed.

This year, we have extended one of our potential-energy-surface (PES) construction methods, which utilizes the LASSO regression technique [1], to consider anharmonic effects on adsorbed molecules. As a test case, we have constructed an analytic PES for H_2O on Pt(111) surface. Thousands of electronic energy data points have been generated randomly for the regression. Those energies have been computed using DFT with the PBE functional. We have employed the VASP program for DFT calculations. An energy extrapolation scheme ONIOM has been used to correct DFT energies. The H_2O monomer has been chosen as a model system for the ONIOM extrapolation. The high-level model system energies (i.e., water-monomer energies) have been evaluated from Partridge–Schwenke potential [2], which is known as the most accurate PES for a single H_2O molecule. The accuracy of PES has been checked by vibrational configuration interactions implemented in the DYNAMOL program [1].

Apart from the PES construction, we have investigated a widely used Pt nanocluster catalyst. Recently, Einaga and his coworkers found that post-processing improves the performance of Pt/TiO_2 catalysis. The experimental analyses suggested that the TiO_2 surface with Pt clusters is prone to be reduced. We have computed the vacancy formation energy on TiO_2-rutile(100) surface with or without an adsorbed Pt cluster in the framework of DFT using the VASP program package. It has been found that interactions between Pt and TiO_2 decrease the vacancy formation energy by 1.4 eV, and the oxygen vacancy shortens the Pt-TiO_2 distance. Our computational result is consistent with the experimental observation using HAADF and STEM-EELS analyses. The stronger interaction between Pt and a reduced TiO_2 surface may explain the change of catalytic activities owing to post-processing.

References

[1] W. Mizukami, S. Habershon, D.P. Tew: J. Chem. Phys. **141** (2014) 144310.

[2] H. Partridge, D.W. Schwenkei: J. Chem. Phys. **106** (1997) 4618.

Calculation of electronic structure of $CH_3NH_3Pb(I,Cl)_3$ mixed crystals

Takayuki Makino

Department of Electric and Electronics Engineering,

University of Fukui, Bunkyo Fukui, Fukui 910-8557

Perovskite type halide compound is known to exhibit several interesting properties. They are , for example, strong excitonic effect and photovoltaic action. Deeper understandings for the corresponding mixed crystals are important from both technological and basic viewpoints [1]. In this research, we intended to calculate electronic structures of $CH_3NH_3Pb(I,Cl)_3$ mixed crystals.

First, we aimed to reproduce the result of previous research [2] conducted on $CH_3NH_3PbI_3$ by obeying the procedure shown in flowchart, corresponding to Fig. 1. We used PWscf package for this kind of calculations. Specifically, we use a set of the optimized norm-conserving Vanderbilt pseudo-potentials generated by Schlipf and Gygi. We confirmed that evaluated band-gap energy can be reproduced in accordance with the values evaluated by Brivio and coworkers [2]. We then moved into study of the electronic structure of $CH_3NH_3PbCl_3$.

Here, we explain about the detailed parameters used for these calculations and show a representative result gotten on a $CH_3NH_3Pb(I,Cl)_3$ mixed crystal. We used SC15 ONCV potential as a Pseudo potential for the structural optimization calculation, starting from the tetragonal symmetry. The used options in PWscf calculation are “vc-relax” and “cell_dofree=xyz”, respectively. We also used a pseudo-potential selected from Pseudo Dojo Potentials for band calculation. Figure 2 shows a band diagram calculated for a mixed crystal including 10% chlorine concentration. In the representation, the energetic origin was shifted so as to the top of the valence band becomes zero. We can notice that an abscissa axis corresponding to the direct optical band-gap is deviated from the Γ point, rather approaching to the R point somehow. We interpret this fact as being due to the change of the crystal structure, approaching to a cubic structure somehow. As one of evidences, relation between the *a*- and *c*-lattice constants becomes closer each other in case of 10% mixed crystal, compared with the purely iodide crystal. We are currently analyzing and summarizing the results because of completion of the calculations for several Cl concentrations.

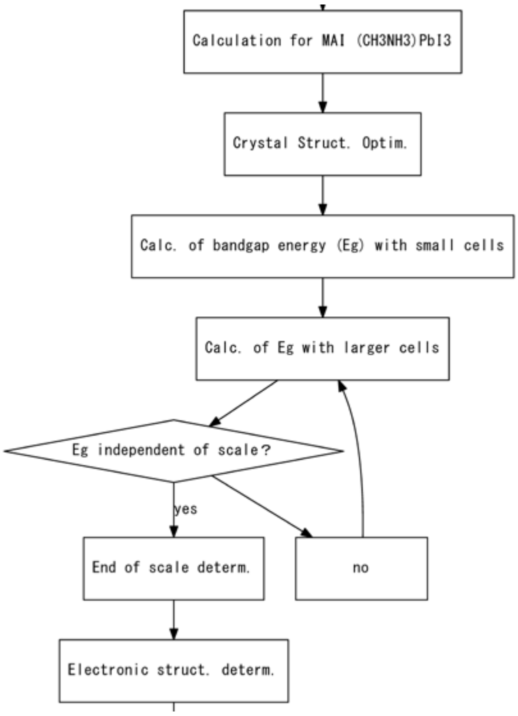

Fig. 1

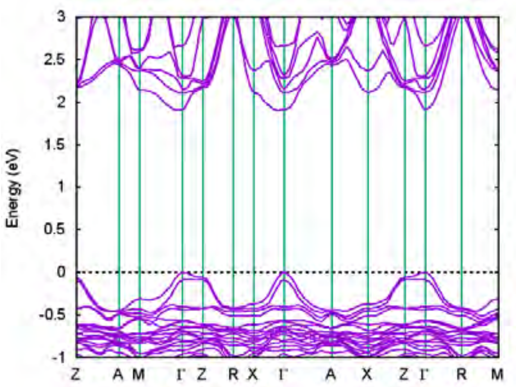

Fig. 2

References

[1] J. H. Heo and S. H. Im: Nanoscale **8** 2554 (2016).

[2] F. Brivio *et al.*, APL Materials **1**, 042111 (2013).

Curious chemical reactions of the entangled singlet state in nanographene VANG

Koichi KUSAKABE
Graduate School of Engineering Science, Osaka University
1-3 Machikaneyama, Toyonaka, Osaka 560-8531

1. The Kondo singlet in nanographene

In a study of tri-hydrogenated atomic vacancies V_{111}, Morishita, *et al.* discovered a series of molecular nanographene structures called VANG.[1] There are degenerated zero modes, *i.e.* the vacancy-centered quasi-localized zero mode and an extended zero mode at the Dirac point. The degeneracy is topologically protected as long as the mirror symmetry of VANG is preserved.[2] Owing to the degeneracy, these alternate hydrocarbon systems possesses the singlet ground state owing to topological nature of π network with $N_A = N_B$. This state is identified as the Kondo singlet.

2. Hydrogen storage application

Hydrogen adsorption on the graphene is affected by detailed conditions of surface morphology.[3] On an atomic vacancy, we have characteristic hydrogenation processes.[4] Among them, the V_{111} structure shows low energy barrier ~ 1.3eV for both adsorption on it and desorption to it. This effect coming from steric hindrance allows us to derive the solution for the hydrogen storage application.[5] On VANG, we have a realistic reaction process composed of migration paths and the $V_{221} \to V_{111}+H_2$ process (Figure 1). This process overcome the difficulty in organic hydrides, making nanographene the unique solution for economically efficient materials for storage.

3. Development of simulation tools

We have established a method to find new classes of edge states at armchair edge,[6] which is applicable for deformed graphene with armchair edges. The electron correlation effects are discussed in several contexts.[7]

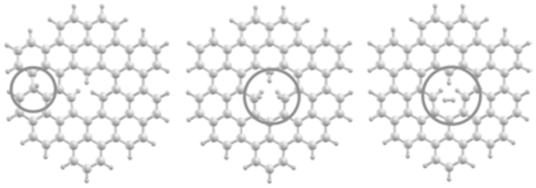

Figure 1: Hydrogen migration paths for a hydrogenated nanographene molecule, VANG, *i.e.* migration from the left panel having stable V_{211} to the middle panel with V_{111} and desorption of H_2 as $V_{221} \to V_{111} + H_2$ (the right).

Acknowledgement

This work was partly supported by KAKENHI (No. 26107526, 26400357, 16H00914).

References

[1] N. Morishita, *et al.* J. Phys. Soc. Jpn., **85**, 084703 (2016). [2] S. Miyao, *et al.* J. Phys. Soc. Jpn. **86**, 034802 (2017). [3] G.K. Sunnardianto, *et al.* J. Comput. Theor. Nanosci. **13**, 4883 (2016). [4] G.K. Sunnardianto, *et al.* Adv. Sci., Eng. Med., **8**, 421 (2016). [5] G.K. Sunnardianto, *et al.* Int. J. Hydro. Energy **42**, 23691 (2017). [6] M. Ziatdinov, *et al.* Phys. Chem. Chem. Phys. **19**, 5145-5154 (2017). [7] K. Nishiguchi, *et al.* J. Phys. Soc. Jpn. **86**, 084707 (2017) .

References

[1] N. Morishita, G.K. Sunnardianto, S. Miyao, K. Kusakabe, J. Phys. Soc. Jpn., **85**, 084703 (2016).

[2] S. Miyao, N. Morishita, G.K. Sunnardianto, K. Kusakabe, J. Phys. Soc. Jpn. **86**, 034802 (2017).

[3] G.K. Sunnardianto, I. Maruyama, K. Kusakabe, J. Comput. Theor. Nanosci. **13**, 4883 (2016).

[4] G.K. Sunnardianto, I. Maruyama, K. Kusakabe, Advanced Science, Engineering and Medicine, **8**, 421 (2016).

[5] G.K. Sunnardianto, I. Maruyama, K. Kusakabe, Int. J. Hydrogen Energy **42**, 23691 (2017).

[6] M. Ziatdinov, H. Lim, S. Fujii, K. Kusakabe, M. Kiguchi, T. Enoki, and Y. Kim, Phys. Chem. Chem. Phys. **19**, 5145-5154 (2017).

[7] K. Nishiguchi, S. Teranishi, K. Kusakabe, J. Phys. Soc. Jpn. **86**, (2017).

Development and application of time-dependent electron-transport simulator based on first-principles method

Yoshiyuki EGAMI
Division of Applied Physics, Faculty of Engineering, Hokkaido University
Kita 13, Nishi 8, Kita-ku, Sapporo, Hokkaido 060-8628

Recently, computational simulations with a high accuracy and efficiency have attracted much attention in both fields of fundamental science and engineering. For example, in the research on and development of electronic devices, numerical approaches play important roles to understand the relationship between atomic and electronic structures of materials and electric, magnetic and optical characteristics of devices. A large number of notable studies using first-principles calculations have been performed so far to elucidate the relationship and characteristics. However, most of the calculations are based on the density functional theory which describes the static characteristics of electrons in the steady state, and there remains to be discussed a time-dependent behavior of electrons.

In order to demonstrate the time-dependent transport properties of electrons through the nanoscale materials, we developed the impulse response (IR) method [1] based on the real-space finite-difference approach [2] within the framework of the time-dependent density functional theory. In this subject, for the IR method, we have worked on the improvement of the efficiency of parallel computing in the spatial dimensions since we cannot parallelize the calculations in the direction with respect to time due to the sequential evolution of scattering wave functions.

On the other hands, we have calculated the electron transport properties of the impurity-embedded carbon nanotube (CNT)[3] and molecular junction consisting of a transition metal complex molecule[4] using the conventional time-independent electron transport simulator[5, 6] in order to compare the characteristics obtained by the IR method. As the results, we found a high transmission probability near unity for electrons transporting the BN-embedded CNT when the geometrical coordinates of impurities coincident with spacial node positions of wave functions of propagating electrons. Moreover, the circular current flow around Mn atom in a Mn(dmit)$_2$ molecular junction is observed, where the *d*-orbitals of Mn atom play a key part. These work have been performed on System B.

References

[1] Y. Egami and K. Hirose: JPS Conf. Proc. **1**, 016012 (2014).

[2] K. Hirose *et al.*: *First-Principles Calculations in Real-Space Formalism*, (Imperial College Press, London, 2005).

[3] Y. Egami and H. Akera: Physica E **88** (2017) 212.

[4] Y. Egami and M. Taniguchi: Jpn. J. App. Phys. **57** (2018) 021601.

[5] Y. Egami, K. Hirose and T. Ono: Phys. Rev. E **82**, 56706 (2010).

[6] Y. Egami, S. Iwase, S. Tsukamoto, T. Ono and K. Hirose: Phys. Rev. E **92**, 033301 (2015).

Development of materials of proton-conducting solid electrolyte fuel cells and analysis of ion conduction

Gen Kojo, Junichiro Otomo

Graduate School of Frontier Sciences,

The University of Tokyo, Kashiwa-no-ha, Kashiwa, Chiba 277-8581

1. Introduction

Solid oxide fuel cells (SOFC) are one of the key electrochemical devices as energy and environmental devices. Recently, proton-conducting solid oxide fuel cells (p-SOFC) have attracted attention due to their energy conversion efficiency. Many kinds of materials have been studied for proton conducting solid electrolyte.

In this study, we discussed two proton conducting materials. The former material was lanthanum tungstate (LWO). It has been developed as an electrolyte materials for p-SOFC, and LWO has intrinsic oxygen vacancies in its crystal structure. For this material, we examined the proton diffusion mechanism in LWO by quantum chemical calculations.

The latter material was $La_2Ce_2O_7$ (LCO). LCO shows proton conductivity at intermediate temperatures (T < 600 °C). The proton conduction in $La_2Ce_2O_7$ depends on the amount of oxygen vacancies, which could be formed according to reaction (1):

$$\mathrm{La_2O_3} \rightarrow 2\mathrm{La}'_{\mathrm{Ce}} + 3\mathrm{O}_{\mathrm{O}}^{\mathrm{X}} + \mathrm{V}_{\mathrm{O}}^{\cdot\cdot} \qquad (1)$$

In this study, we tried to investigate the relationship between the crystal structure and the amount of oxygen vacancies using the density functional theory (DFT).

2. Computational methods

The proton diffusion pass was calculated by the NEB method [1] using the revised SIESTA code developed by Ohto et al [2]. The number of atoms was 89, and the number of images was 10.

DFT calculations were carried out for $La_2Ce_2O_7$ with VASP [3] code. The generalized gradient approximation (GGA) proposed by Perdew, Burke, and Ernzerhof (PBE) [4] represents the exchange-correlation energy functional. The valence configurations of the pseudopotentials were 4p5s26d1 for La, s2d1f1 for Ce, and s2p4 for O. The energy cutoff for the plane-wave basis was set at 500 eV. As for the structural models, $\mathrm{Fm}\bar{3}m$ was used. The structural relaxation of the unit cell was conducted using Monkhorst-Pack k-point sets with 4 × 4 × 4 until the total energy difference converged to less than 0.001 eV.

3. Results and discussion

The crystal structures are shown in Fig. 1a and the proto-conducting paths considered in this study are shown in Fig. 1b. To simplify the calculations, we used the oxygen at the O2 site with average O1-O2 and O2-O2 distances. The result of the NEB calculation are shown in Fig. 2; the barrier of proton diffusion in the O1-O1 jump is lower than those in the O2-O2 and O1-O2 jumps. This indicates that protons are likely to be trapped at O2 sites and once they

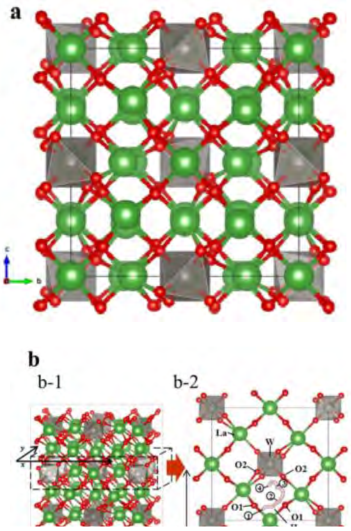

Fig. 1 (a) Optimized crystal structure of LWO and (b) image of proton diffusion paths in LWO calculated using the NEB method.

leave the O2 sites and jump across the high O1-O2 barrier, they diffuse over a long range through cycles of O1-O1 jumps until they are trapped at other O2 sites.

As for the LCO, in order to understanding the results observed in our experiment, the total energies of crystal structures were compared with different positions of oxygen vacancies (see Fig. 2). The calculation result was as follows: (a) -704. 184 eV, (b) -704.190 eV. Under the experimental conditions, i.e. sintering temperature or synthesis method, the samples might have the different position of the oxygen vacancy. Considering the results of this study, the conductivities of the samples synthesized with different methods will have the several conductivities.

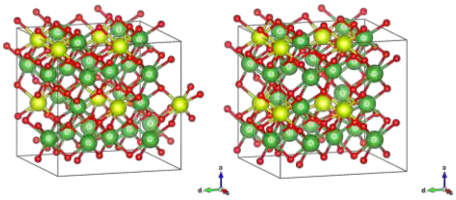

Fig. 2 Schematic images of the structures of $La_2Ce_2O_7$s.

4. Conclusion

The calculation with NEB method showed that proton diffusion in LWO occurred through an O1-O1 route. The DFT calculation results indicated that the conductivity of LCO was independent of the synthesis method.

References

[1] G. Henkelman *et al.*, *J. Chem. Phys.* **113** (2000) 9901.

[2] T. Ohoto *et al.*, *Phys. Rev. B*. **87** (2013) 1.

[3] G. Kresse *et al.*, *Phys. Reb. B: Condens. Matter. Phys.* **54** (1996) 11169.

[4] Perdew, J. P. *et al.*, *Phys. Rev. Lett.* 77 (1996) 3865.

Organic Molecule on Graphene: Electronic Structure at the Interface and Crystal Growth

Kazume NISHIDATE and Masayuki HASEGAWA

Faculty of Science and Engineering, Iwate University Ueda 4-3-5, Morioka, Iwate 020-8551

Intact graphene with this electronic structure is a zero-gap semiconductor and electronically behaves like a semimetal. Electronic properties of this pristine nanostructure are usually not preserved in graphene under internal or external perturbations such as mechanical strains, deformations, adsorption of foreign atoms or molecules, electric field, contact with substrates, and other interactions with the environment. In the last decade a large-scale epitaxial graphene of high quality has been successfully grown by thermal decomposition of silicon carbide (SiC) surfaces and it is, in fact, recognized and theoretically supported that the Dirac band with linear dispersion is lost in the so called “buffer” graphene layer due to the strong bonding to the SiC surface. On the other hand, a modified Dirac band with a substantial gap at the Dirac point has been observed in the so called “first” graphene layer on SiC and interpreted as a band gap opening due to A-B sublattice symmetry breaking as in the case of graphene on hexagonal boron nitride (h-BN). However, this interpretation has not been supported by any explicit analysis and, therefore, is not fully recognized at present. We also note that recently angle resolved photoemission spectroscopy (ARPES) has demonstrated that the “buffer” graphene layer on SiC is also electronically quasi-freestanding with a band gap larger than 0.5 eV for highly ordered interactions with the substrate, exemplifying that understanding electronic structure of graphene on substrates is still far from complete.

In our DFT calculation, we first use a lattice matched model to demonstrate that a substantial band gap is induced in graphene by sufficiently strong A-B sublattice symmetry breaking[1]. This band gap opening occurs even in the absence of hybridization between graphene π states and Au states, and a strong sublattice asymmetry is established for a small separation (d) between the graphene and Au layer, typically, $d < 3.0$ Å. In realistic situations, which are mimicked using lattice mismatched models, graphene π states near the Dirac point easily hybridize with nearby (in energy) Au states even for a van der Waals distance, $d \sim 3.4$ Å, and this hybridization usually dictates a band gap opening in graphene. In that case, the top parts of the intact Dirac cones survive the hybridization and are isolated to form midgap states within the hybridization gap, denying that the band gap is induced by sublattice symmetry breaking. This feature of a band gap opening is similar to that found for the so called “first” graphene layer on silicon carbide (SiC) and the predicted band gap and doping level are in good agreement with the experiments for graphene/Au/Ru(0001).

References

[1] K. Nishidate, S. Tanibayashi, N. Yoshimoto, and M. Hasegawa: Phys. Rev. B **97** (2018) 115437.

First-principles analysis for the iron-based superconductors and the related

Hiroaki IKEDA
Department of Physics, Ritsumeikan University
Kusatsu, Shiga 525-8577

We have investigated unconventional superconductivity in the strongly correlated electron systems. Our aim is to develop the first-principles calculations and reasonably describe the electronic structure of SCES. This year, we studied two topics using a Class B; the application of the quasiparticle GW method (QSGW) to the iron-based superconductors, and a study of gap structure in non-symmorphic superconductors.

First, we performed the QSGW in several typical iron-based superconductors. In the conventional LDA/GGA calculations for the iron-based superconductors, the compensated semi-metallic structure can be roughly described, but the size and curvature of the Fermi surface and the composed orbital characters are significantly deviated from the experimental results. Thus, the electron correlation is important. Here, we applied the QSGW, which improves the band gap of semiconductors. We realized that the obtained band structure (Fig.1) can be improved to explain experimental Fermi surface. This is complementary to the DFT+DMFT studies.

Second, we performed the group-theoretical classification of gap functions in non-symmorphic structure [1], and investigated recently discovered BiS_2-based layered superconductors. The electronic band structure is mainly composed of the Bi 6p orbitals with a relatively large spin-orbit coupling (SOC). The Bi site does not have inversion symmetry. Recent angle-resolved spectroscopies have indicated remarkable gap anisotropy and/or a sign change on a small Fermi pocket around X point. It implies a possibility of unconventional pairing state in this material. Here we have studied the gap structure in an extended Hubbard model with Bi-S inter-site interactions. The band structure was obtained by the first-principles downfolding. We found that the ferroic charge/quadrupole fluctuation driven by the inter-site interaction leads to a fully-gapped $d_{x^2-y^2}$-wave pairing state, in which the gap amplitude has sizable anisotropy on the Fermi surface. This work was published in [2].

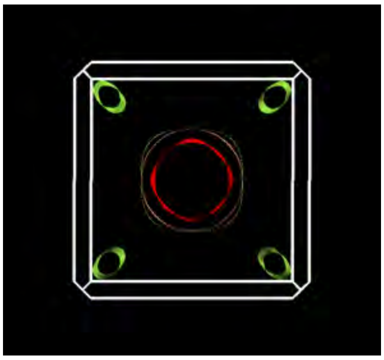

Figure 1: Fermi surface in QSGW for KFe_2As_2.

References

[1] T. Nomoto, and H. Ikeda: J. Phys. Soc. Jpn. **86** (2017) 023703.

[2] K. Suzuki, H. Usui, K. Kuroki, and H. Ikeda: Phys. Rev. B **96** (2017) 024513.

First-principles Study of Defects of Magnesium Alloys

Daisuke Matsunaka

Department of Mechanical Systems Engineering,
Shinshu University, 4-17-1 Wakasato, Nagano 380-8553

Magnesium (Mg) has been of increasingly interest from the engineering viewpoint, because of its low density and relatively high specific strength. Despite intensive research efforts, there remain various problems to be overcome; low ductility and low toughness at room temperature. In order to investigate deformation behavior of Mg at the atomic level, we have carried out molecular dynamics simulations. Particularly, we have focused on effects of normal stress components on the <a> slip systems; basal, prismatic, and first-pyramidal slips. For the basal slip, partial dislocation s were generated and glided on the slip plane, irrespective of the applied normal stress. On the other hand, for the prismatic and first-pyramidal slips, distinct dislocation gliding was not observed and alternatively deformation twins were generated. In the simulations of the prismatic slip under the high normal stress of 300MPa, double twins were formed additionally.

In Mg alloys with rare earth elements, the addition in solid solution causes a significant increase in ductility. It is an important issue to elucidate effects of an alloying element on each deformation mode such as deformation twinnings and non-basal slips. First-principles calculations give us valuable information of alloying elements. Development of interatomic potentials for alloys which can describe the first-principles results is necessary for atomistic simulations of deformation in Mg alloys. In this study, we have investigated two-body potential forms between species in the embedded atom method (EAM) potentials. Although the invariance to a transform in which a term linear in the electron density is added to or subtracted from the embedding function and an appropriate adjustment is made to the two-body potential is not always hold, the transform was set so that the substitution energy got close to the first-principles values. Using the obtained alloy EAM potentials, the generalized stacking fault energy curves of the basal and prismatic slips were calculated and compared with the first-principles results.

References

[1] S. Yoshikawa and D. Matsunaka: to be submitted.

[2] D. Matsunaka and F. Kimura: Conf. Proc. Jpn. Soc. Comp. Eng. Sci. **23** (2018) B-01-07.

Electronic structure of light rare earth permanent magnets

H. Akai
Institute for Solid State Physics, University of Tokyo
Kashiwa-no-ha, Kashiwa, Chiba 277-8581

Despite intensive efforts to develop permanent magnets whose performances exceed that of the $Nd_2Fe_{14}B$ magnet, no essentially novel magnet has been developed so far. In this situation, one might question whether it is possible at all to obtain a permanent magnet material that is superior to the currently available maximum performance.

To answer this, one should have a perspective on the possible maximum performance of permanent magnet materials. One of way to do this is to estimate the upper limits of magnetization J_{S}, Curie temperature T_{C}, and lowest order uniaxial magnetic anisotropy constant K_1, which make a prospect about the performance of magnets. We discuss each of these quantities on the basis of the results obtained through first-principles calculation.

The discussions are based on all-electron electronic structure calculations performed within the local density approximation (LDA/GGA) of density functional theory (DFT). Machikaneyama (AkaiKKR) KKR-CPA package [1] was used, and for the calculation of T_{C}, Liechtenstein's method [2] was employed.

Figure 1 shows the calculated magnetization J_{S} of $3d$ elements as a function of the lattice constant a and atomic number Z. The fractional atomic number of a fictitious atom is used. The number of total electrons per atom is equal to Z. The crystal structure is assumed bcc. A prominent feature is that it has a domelike structure appearing around $a = 2.65$ A and z=26.4, where J_{S} takes the maximum value of 2.66 T. It is pointed out that this is related to the fact that in the bcc structure, the interatomic distance between nearest neighbor pairs becomes small, forming a considerable bonding–antibonding splitting with a pseudo gap in between. Unfortunately, the lattice constant $a = 2.65$ A is 7 % too small compared with the equilibrium lattice constant of bcc Fe. Contrary to the general behavior of the magnetic moment that increases as the volume increases, the magnetic polarization increases with decreasing a up to some point where the magnetic state collapses.

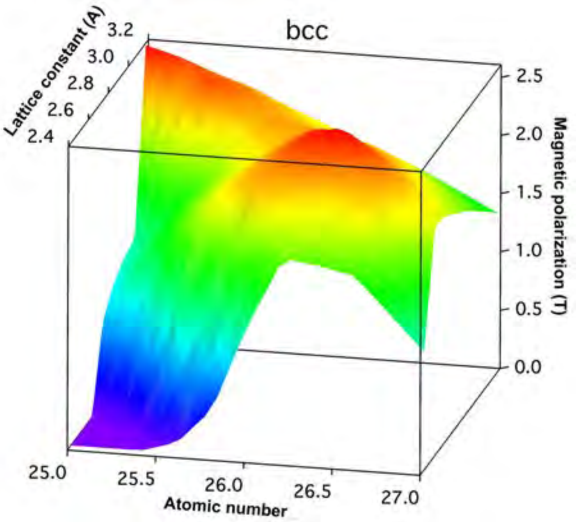

Figure 1: Saturation magnetic polarization J_{S} of the system plotted against the lattice constant and the fictitious atomic number[3].

Magnetic polarization takes on a large value at one of the corner points in the Z-a plane,

$Z = 25$ and $a = 3.2$ A, but this is not real. In this region, the antiferromagnetic state is more stable than the ferromagnetic state. Combining this fact with the information given by Fig. 1, we may conclude that a large J_{S} is expected only in the vicinity of the dome-like structure, and the upper limit of J_{S} would not exceed ~ 2.7 T.

Figure 2 shows the behavior of magnetic transition temperature T_{C} as a function of Z and a. Here, we again see a dome-like structure near $Z = 26.5$ and $a = 2.9$ A. This position approximately coincides with the position of the similar dome-like structure in J_{S}. This indicates that if $Z = 26.5$ and $a = 2.9$ A is forced by crystal structure, chemical composition, pressure, temperature, etc., $J_{\mathrm{S}} \sim 2.7$ T is achieved. T_{C} drops rapidly toward the corner in the Z-a plane, $Z = 25$ and $a = 3.2$ A, where T_{C} becomes negative, meaning that the antiferromagnetic state should be the ground state. Now, we may say that the upper limit of T_{C} is ~ 2000 K (if fcc structure were assumed, the upper limit would be ~ 1500 K).

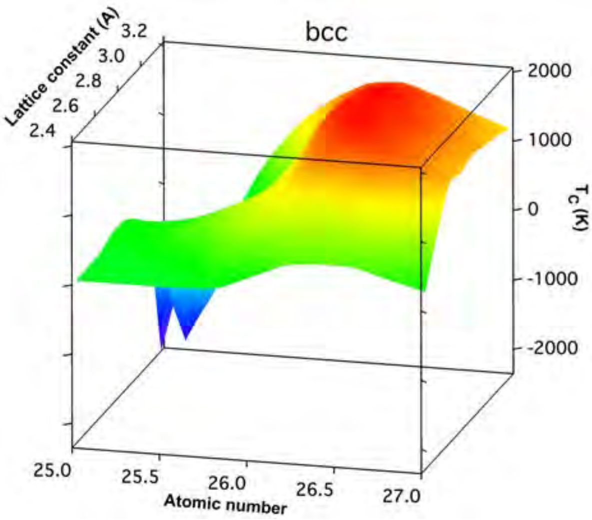

Figure 2: Magnetic transition temperature T_{C} of the system plotted against the lattice constant and the fictitious atomic number[3].

The main origin of magnetocrystalline anisotropy is spin orbit coupling. For Sm (Sm^{3+} in Sm-type Sm element), assuming that the orbitals are firmly bound to the lattice, the upper limit of the magnetic anisotropy constant K_1 estimated from the strength of the spin-orbit coupling , together with the values of $\langle L \rangle$, is as high as ~ 1000 MJm^{-3}. The upper limit of K_1 for other lanthanides, if scaled by the value of L, also would be similar to that of Sm. However, K_1 of rare earth magnetic materials is one to three orders of magnitude smaller than this values. This is because the anisotropy in lattice geometry is not large enough to firmly bind the orbital to the lattice: the $4f$ electron density rotates in line with magnetization to some extent. Therefore, the upper limit of K_1 is bound by the lattice geometry. Also, the magnetic moment carried by $3d$ orbitals of transition metal ions is only weakly coupled to the $4f$ orbitals of rare earth ions (through $3d$–$5d$ indirect and $5d$–$4f$ direct exchange coupling), the latter producing a large magnetic anisotropy. Accordingly, the magnetization is rather loosely bound to the lattice. The effect is in particular prominent at high temperature $T \gtrsim (2/3)T_{\mathrm{C}}$, where the coupling between $3d$ and $4f$ becomes progressively weaker because of the thermal fluctuation.

In conclusion, calculations based on density functional theory conclude that the plausible upper limits of saturation magnetic polarization, magnetic transition temperature, and the magnetocrystalline anisotropy constant of permanent magnet materials could be $\sim$2.7 T, $\sim$2000 K, and $\sim$1000 MJm^{-3}.

References

[1] H. Akai, AkaiKKR, `http://kkr.issp.u-tokyo.ac.jp/` (2002).

[2] A. I. Liechtenstein, M. Katsnelson, V. Antropov, V. Gubanov, J. Magn. Magn. Mater. 67 (1987) 65.

[3] H. Akai: Scripta Materialia (2018), in press.

Ab initio design of an optimal anisotropic ferromagnet

M. Matsumoto (Akai group)
Institute for Solid State Physics, University of Tokyo
Kashiwa-no-ha, Kashiwa, Chiba 277-8581

Introduction Rare-earth permanent magnets (REPM) have been and will be one of the most important materials for industrial applications in these several decades. In REPM a three-dimensional Ising ferromagnet is realized with the magnetization mostly coming from Fe-group elements and uni-axial anisotropy from rare-earth elements. Metastable states in the magnetization curve at finite temperature is exploited as a seemingly permanent magnetization as measured in a human-scale observation time. The theoretical challenge posed by one of the most common utility of REPM is to find a way to optimize the magnetization and the uni-axial magnetic anisotropy energy, in the temperature range between 230K and 450K. The $4f$-electrons are only loosely coupled to the $3d$-electron magnetization via an indirect exchange coupling mediated by $5d$-electrons of which scale is $O(1)$ meV. This weak coupling is on a par with the room-temperature scale as combined with the coordination number between rare-earth and Fe-group atoms. Thus $4f$-electron contribution to the bulk magnetism gets rapidly blurred out as the magnet is heated in the operation temperature range. The intrinsic solution to sustain the ferromagnetism with uni-axial anisotropy is to enhance $4f$-$3d$ coupling [1] possibly via $5d$-electron engineering and enhancing $3d$-electron magnetism which is mostly in charge of the operation-temperature magnetism. Pursuing the latter line of attack, we revisit the Slater-Pauling curve of Fe-Co alloys along which the magnetization M is maximized. Target quantities to be maximized as a function of Fe-Co mixing ratio are extended to Curie temperature T_{Curie}, uni-axial magnetic anisotropy energy K, together with the formation energy to ensure that the desired magnetic properties in the focus temperature range is realized with a bulk-stable material. We take $\mathrm{RCo_5}$ (R=rare earth) as a prototypical materials family and set R=Y.

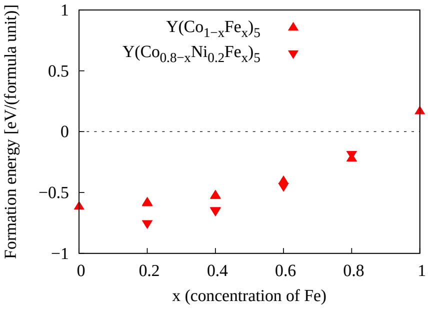

Figure 1: Calculated formation energy of Y(Co,Fe)$_5$ and Y(Ni,Co,Fe)$_5$ as a function of Fe concentration.

We calculate magnetization, magnetic anisotropy energy, and Curie temperature of Y(Co,Fe)$_5$. All of them are summarized as a function of Fe concentration and the optimal chemical composition to extract the best performance in terms of intrinsic magnetism is inspected. On a basis of atom-by-atom substitution the lattice constants are calculated by a structure optimization scheme with OpenMX [3]. These results are given discretely for $\mathrm{YCo}_{5-n}\mathrm{Fe}_n$ with $n = 0, 1, 2, 3, 4,$ and 5. Continuous interpolation on the Fe concentration is done on the basis of coherent potential approximation as implemented in

AkaiKKR [2]. Resultant formation energy of Y(Co,Fe)$_5$ is shown in Fig. 1. These runs set up a working lattice for calculating M, K, and $T_{\rm Curie}$.

Results Having in mind utility as a permanent magnet compound, calculated results for $\mathrm{Y(Co}_{1-x}\mathrm{Fe}_x)_5$ are summarized on a plane spanned by magnetization M and uni-axial magnetic anisotropy energy K. Materials that reside the upper and the right-hand side of M-K plane pop up as the promising candidates. Discrete results obtained with OpenMX at $T = 0$ shown in Fig. 2 combined with continuous results obtained with AkaiKKR for $M(x, T = 0)$ and $T_{\rm Curie}(x)$ shown in Fig. 3 indicate that Co concentration of around 20% would give an optimal performance in the observed trade-off between $K(x)$ and $M(x)$, also between K and $T_{\rm Curie}$.

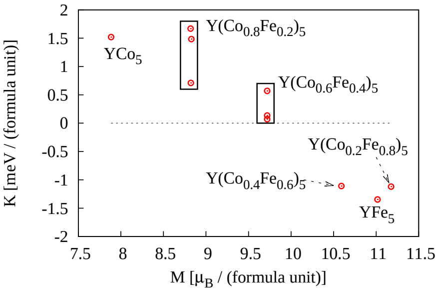

Figure 2: Calculated magnetization and magnetic anisotropy energy of Y(Co,Fe)$_5$ at $T = 0$.

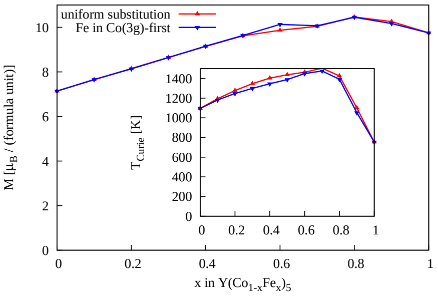

Figure 3: Calculated Curie temperature of Y(Co,Fe)$_5$.

Since Fe-rich side faces the significant instability as seen in Fig. 1 trade-off is going on also between $(M, T_{\rm Curie})$ and formation energy where a peak for the former is found on the Fe-rich side while Fe-rich side is excluded from the loss of utility in the latter. Recently it has been discussed [4] that addition of Ni can stabilize Fe-rich composition for Sm(Ni,Co,Fe)$_5$ compounds. We have collected similar data for Y(Ni,Co,Fe)$_5$ as was plotted in parallel in in Fig. 1. Our Y-based materials with the common crystal structure share the trends in the range of Fe concentration from 20% to 60% with the observed trend that Ni helps the stabilization of 1:5 structure at a fixed concentration. Meanwhile the stability range of Fe concentration might not be quite enhanced for our particular case of Y-based compounds. The overall trends depend on the species of rare earth. A study over the comprehensive trends spanning a wider range of rare earth elements is reported elsewhere.

Conclusions Prerequisites for a good permanent magnet compound, namely, magnetization, uni-axial magnetic anisotropy energy, Curie temperature, and formation energy has been investigated *ab initio* as a function of Fe-Co mixing ratio for Y(Co,Fe)$_5$. The overall trend concerning 3d-electron part has been clarified and an optimal concentration range of a small amount of Fe in the middle of trade-off between the anisotropy and the rest has been identified.

References

[1] MM, H. Akai, Y. Harashima, S. Doi, and T. Miyake, J. Appl. Phys. **119**, 213901 (2016).

[2] http://kkr.issp.u-tokyo.ac.jp/jp/

[3] http://www.openmx-square.org

[4] P. Söderlind, A. Landa *et al.*, Phys. Rev. B **96**, 100404(R) (2017)

Geometric and electronic structures of two-dimensional atomic-layered materials

Noriaki TAKAGI[1], Ryuichi ARAFUNE[2], and Emi MINAMITANI[3]
[1]*Department of Advanced Materials Science, University of Tokyo*
Kashiwa-no-ha, Kashiwa, Chiba 277-8561,
[2]*International Center for Materials Nanoarchitectonics, National Institute for Materials, Science, 1-1 Namiki, Ibaraki 304-0044,*
[3]*Department of Materials Engineering, The University of Tokyo, 7-3-1 Hongo, Bunkyo-ku, Tokyo 113-8656, Japan.*

The discovery of graphene has fueled the competition to explore exotic two-dimensional (2D) materials. One-atom thick honeycomb sheets consisting of heavy atoms such as Si, Ge, Bi, etc., are attracting because these are strong candidates of 2D topological insulator. Semimetallic $MoTe_2$ and WTe_2, members of transition metal dichalcogenides, are theoretically categorized into type-II Weyl semimetal.

Recently, we have investigated the geometric and electronic structures of Bi thin films grown Au(111), $MoTe_2$ and WTe_2 mainly by using scanning tunneling microscopy (STM).

We carried out density functional theory (DFT) calculations to elucidate the structure for Bi monolayer on Au(111) and quasi-particle interference (QPI) occurring at the surfaces of $MoTe_2$ and WTe_2. The DFT calculations were carried out by the plane-wave-based Vienna Ab initio Simulation Package (VASP) [1, 2] with the projected augmented wave method [3].

For the structure of Bi monolayer, a structure model was optimized and the calculated STM image was compared with that observed by STM. Both images were reasonably agreed with each other. The results were presented in [4]

For QPIs of $MoTe_2$ and WTe_2, bulk band structures were calculated and the iso-energy cuts of the band structure were calculated. The several structures appearing in the QPIs were reasonably reproduced. Some of the structures were not explained by the bulk band structure and we assigned these structures to be Fermi arc surface states inherent to Weyl semimetal. The results are nicely agreed with the theoretical calculations presented previously [5]. The results were published in [6,7].

Reference

[1] G. Kresse and J. Furthmüller: Phys. Rev. B **56**, 11169 (1996).
[2] G. Kresse and J. Furthmüller: Comput.

Mater. Sci. **6**, 15 (1996).
[3] P. E. Blöchl: Phys. Rev. B **24**, 17953 (1994) 17953.
[4] N. Kawakami *et al.*:Phys. Rev. B **96**, 205402 (2017).
[5] A. A. Soluyanov *et al.*: Nature **527,** 495 (2015).
[6] C. -L. Lin *et al.*: J. Phys. Condensed Matters 30, 105703 (2018).
[7] C.-L. Lin *et al.*: ACS Nano **11**, 11459 (2017).

Geometric and electronic structures of magnetic molecules at surfaces

Noriaki TAKAGI[1], Ryuichi ARAFUNE[2], and Emi MINAMITANI[3]
[1]*Department of Advanced Materials Science, University of Tokyo*
Kashiwa-no-ha, Kashiwa, Chiba 277-8561,
[2]*International Center for Materials Nanoarchitectonics, National Institute for Materials, Science, 1-1 Namiki, Ibaraki 304-0044,*
[3]*Department of Materials Engineering, The University of Tokyo, 7-3-1 Hongo, Bunkyo-ku, Tokyo 113-8656, Japan.*

Adsorption of metal phthalocyanines (MPcs) on solid surfaces has gathered considerable attention because these molecules exhibit unique properties [1-3]. MnPc, FePc and CoPc are typical members of MPc family and the adsorption of these molecules on solid surfaces has been intensively studied. Recently, we have investigated the magnetism of FePc on noble metal surfaces, especially the relation between the spin state and the molecule-surface (Mol-S) interaction, by using scanning tunneling microscopy (STM) and spectroscopy (STS) and photoelectron spectroscopies. We have elucidated that the S=1 spin state of the bulk FePc is converted when the molecule directly contacts Cu(110) [4]. In contrast, the S=1 state is preserved by inserting atom-thick oxide layer between the molecule and the Cu substrate [4]. On Au(111), two unpaired spins of S=1 FePc exhibit Kondo effect because of the exchange coupling with the substrate electrons [5,6,7]. These examples indicate the spin state is sensitive to the molecule-surface interactions.

Using the plane-wave-based Vienna Ab initio Simulation Package (VASP) [8,9] with the projected augmented wave method [10], we performed the DFT calculations for MnPc molecules on In atomic layers grown on Si(111). The substrate was described as a slab model and the molecular adsorption structures were calculated as functions of molecular configuration and adsorption site. The results were compared with those acquired by STM. We found the DFT results reasonably explain the adsorption structures of MnPc on In layers grown on Si(111).

Reference

[1] R. Bonnett: Chem. Soc. Rev. **24**, 19 (1995).

[2] C. C. Lanznoff and A. B. P. Lever: *Phthalocyanines, Properties and Applications* (Wiley, New York, 1996).

[3] K. Kadish, and R. Guillard: *Applications of Phthalocyanines, The Porphyrin Handbook* (Academic Press, San Diego, 2003).
[4] N. Tsukahara *et al.*: Phys. Rev. Lett. **102**, 167203 (2009).
[5] N. Tsukahara *et al.*: Phys. Rev. Lett. **106,** 187401 (2011).
[6] E. Minamitani *et al.*: Phys. Rev. Lett. **109**, 086602 (2012).
[7] R. Hiraoka et al.: Nat. Commun. **8**, 16012 (2017).
[8] G. Kresse and J. Furthmüller: Phys. Rev. B **56**, 11169 (1996).
[9] G. Kresse and J. Furthmüller: Comput. Mater. Sci. **6**, 15 (1996) 15.
[10] P. E. Blöchl: Phys. Rev. B **24**, 17953 (1994).

Reaction processes of polyalcohols in high temperature water by First Principles Calculations

Chang Yong Lik[1], Takehiko Sasaki[1], Motoyuki Shiga[2]

1 Department of Complexity Science and Engineering, Graduate School of Frontier Sciences,
The University of Tokyo, Kashiwa-no-ha, Kashiwa, Chiba 277-8561
2 Center for Computational Science and E-Systems, Japan Atomic Energy Agency
148-4 Kashiwanoha Campus, 178-4 Wakashiba, Kashiwa, Chiba, 277-0871

1 Introduction

Conventional chemical reactions taking place in organic solvents would cause negative effects on the environment. In recent years, the need to find eco-friendlier means of producing chemical products has driven a surge of interest to carry out chemical reactions in high-temperature water (HTW) as a reaction medium in green chemistry. To fully comprehend the reaction mechanisms behind this, it is necessary to carry out extensive studies in simulations with first-principles calculations. In this study, the dehydration reaction of 1,2,5-pentanetriol (PTO) to tetrahydrofurfuryl alcohol (THFA) and 3-hydroxytetrahydropyran (3-HTHP) is conducted with Metadynamics of first-principles calculations in HTW at 573 K and 20 MPa. The free energy surface (FES) analysis is carried out to study the reaction mechanism behind the dehydration process, and compare it with the previous experimental study [1].

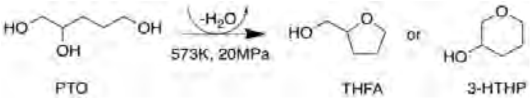

Fig. 1: The dehydration of PTO.

The dehydration reaction pathways of PTO are labeled as 5PTO2, 5PTO5, 6PTO1 and 6PTO5 as shown in Figure 2.

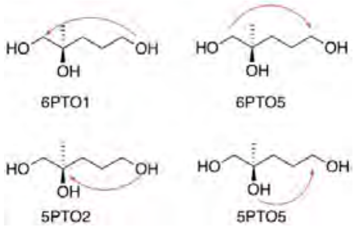

Fig. 2: The dehydration reaction pathways of PTO.

2 Method

By using PIMD[2]/DFTB3[3] (Metadynamics software) developed by Shiga Motoyuki of Japan Atomic Energy Agency, we analyzed the FES by Metadynamics and observed the dehydration reaction by Molecular Dynamics; to obtain the energy barrier of the transition state from the free energy analysis and estimate the number of calculation steps and required time for the reaction to happen. Furthermore, the same calculation is performed with PIMD/VASP [4] to obtain the energy barrier more accurately.

In Metadynamics, the FES of the system is sampled based on the reaction coordinates

(Collective Variables: CV) of the system, then a positive Gaussian function potential is added to the actual FES to bias the reaction. The definition of CV is shown in Figure 3.

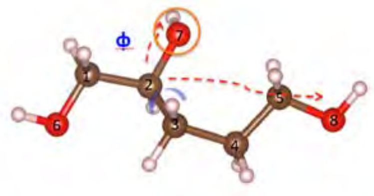

Fig. 3: The definition of CV [5PTO2] : Dihedral angle Φ (C2-07&C3-C4), the difference in bond length r ($d=r_{28}-r_{27}$,) coordination number n_2 (the number of hydrogen attached to O7).

3 RESULTS

The free energy of (R)-PTO was calculated with Metadynamics by adding a Gaussian function potential of height=100 K, width={Φ = 12.0 °, r = 0.20, n = 0.066}. 6PTO1, 6PTO5 via S_N2 yielded 3-HTHP, while 5PTO2, 5PTO5 via S_N2 yielded THFA. The free energy of each reaction pathway is summarized in Table 1.

Table 1: Free Energy of each reaction pathway.

Product	Reaction Pathway	Free Energy[kcal/mol]		
		1	2	Average
THFA	5PTO2	33.86	32.67	33.27
	5PTO5	32.29	27.30	29.80
3-HTHP	6PTO1	33.02	34.76	33.89
	6PTO5	38.71	37.01+	37.86+

In the previous study,[1] the free energy of THFA and 3-HTHP in acidic condition at 573K under 20MPa; were 41.70 kcal/mol and 43.92kcal/mol respectively. In this calculation, it was found that the activation energy for THFA was smaller by 4.09kcal/mol than that for 3-HTHP, in agreement with the experimental results. Furthermore, the S_N2 reaction occurs when the oxygen atom attached to the attacking carbon atom is protonated, indicating that the acidic condition and the presence of protons play an important role in this reaction. However, the calculated free energy is much smaller than the experimental value. The error seems to be caused by the roughness on the FES when the sampling is stochastically performed.

4 CONCLUSION

The free energy of (R)-PTO was calculated with Metadynamics and the qualitative agreement with the experimental results was obtained. To minimize the error and free energy fluctuation, it is necessary to perform this calculation four times, and to sample the FES in the vicinity of the transition state with a smaller CV. In addition, we increase the calculation accuracy of free energy by the Well-Tempered Metadynamics [5].

References

[1]A. Yamaguchi, N. Hiyoshi, O. Sato, K.K. Bando, M. Shirai, Green Chem., 2009, 11, 48-52.

[2]PIMD.https://ccse.jaea.go.jp/ja/download/pimd/index.jp.html.

[3]Density Functional Theory based Tight Binding. https://www.dkb.org.

[4]VASP. https://www.vasp.at/.

[5]A. Barducci, G. Bussi, M. Parrinello, PRL 100, 2008, 020603.

Theoritical analysis of vibronic mode and spin ordering of thin film of transition metallated porphyrin-derivative

Ken-ichi SHUDO
Yokohama Nat'l Univ.
Tokiwadai 79-5, Hodogaya-ku Yokohama 240-8501

Porphyrin-derivatives with transition metal cores are of great interest from view points of the spin theory and the magnetism application. We build a metal-organic framework (MOF) structure of a monolayer molecular films of tetrakis(4-carboxyphenyl)porphyrin (TCPP) with the carboxyl groups bridged by copper ions [1]. This MOF structure has regular arrangement of the electronic spins interacting each other in the planar membrane. So-realized spin lattice is a good prototype among two-dimensional Ising systems.

To investigate the magnetism, we observed experimentally the magnetic circular dichroism (MCD) in optical absorption of Fe-cored MOF of TCPP in near-IR to UV region, which showed strong signal due to the spin–angular-momentum coupling. It has temperature-dependence, as suggests the films has ferromagnetism [?]. At the same time, in this ISSP project, the theoretical calculation of spin-dependent density of state (DOS) of the Fe-cored TCPP-MOF was performed using VASP code [3], suggesting that the MOF exhibits ferromagnetic component near Fermi level. The charge density projected onto the Fe atom resolved the spin polarization (shown in Fig. 1) originating from the Fe core. Several states derived from the Fe orbitals are also found spreading over the molecules at the energy in the molecular HOMO/LUMO gap in the isolated TCPP molecules. Thus, the ferromagnetism newly emerges in the spin lattice in MOF structure.

Author acknowledge Mr. T. Sumiya and Dr. H. Raebiger (YNU), and Dr. A. Muranaka and Prof. M. Uchiyama (Riken) for their contribution.

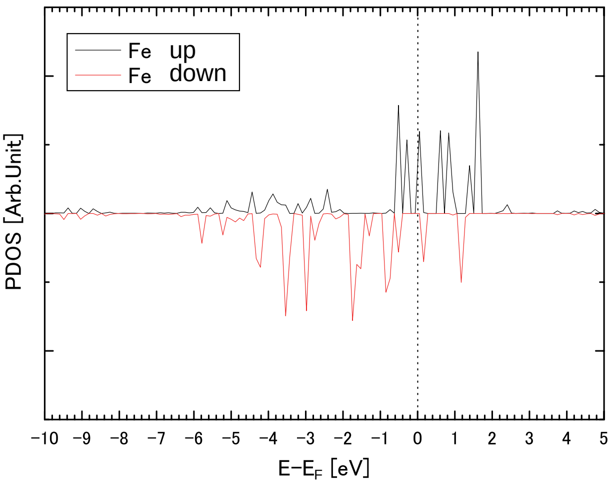

Figure 1: Spin polarization of the partial DOS projected onto the Fe atom in MOF of Fe-cored TCPP.

References

[1] R. Makiura, S. Motoyama, Y. Umemura, H. Yamanaka, O. Sakata and H. Kitagawa: Nature Mat. **9** (2010) 565–571.

[2] M. Gouterman: Optical Spectra and Electronic Structure of Porphyrins and Related Rings, in *The Porphyrins, Vol. III : Physical Chemistry part A* ed. by D. Dolphin, Academic Press (1978, ISBN: 978-0-12-220103-5)

[3] http://www.vasp.at

Study of interaction between radiation damage and interstitial atom

Kazuhito Ohsawa

Institute for Applied Mechanics,

Kyushu University, Kasuga-koen, Kasuga, Fukuoka 816-8580

Hydrogen (H) isotope trapping in tungsten (W) and its alloys are paid attention in the field of fusion reactor because W is one of the important plasma facing materials. Stable configurations of H atoms in mono-vacancy in a bulk W have been reported in the previous work. So, in the present work, we will show stable configurations of H atoms in di-vacancy. Formation energies of di-vacancy and binding energies of H atoms to the di-vacancy are calculated by first-principle calculations based on density functional theory.

Figure 1 shows four H atoms trapped in di-vacancy in a bulk W, as an example. Stable structure of W di-vacancy is two mono-vacancy arranging in <111> direction. There are 12 octahedral interstitial sites (O-sites) in the di-vacancy. Six O-sites are located in the junction of the two mono-vacancies. The H atoms are located close to O-sites and H atoms prefer to O-sites in the junction, as shown in Fig. 1. Binding energies of H atoms to mono- and di- vacancy are shown in Fig.2. Binding energies of H atoms to di-vacancy are much larger than those to mono-vacancy.

According to Fig. 2, H atoms enhances di-vacancy formation. In the fusion reactors, H isotopes are supplied to plasma facing materials. So, the presence of H isotopes is supposed to affect on the growth of vacancy type defects in W of plasma facing materials.

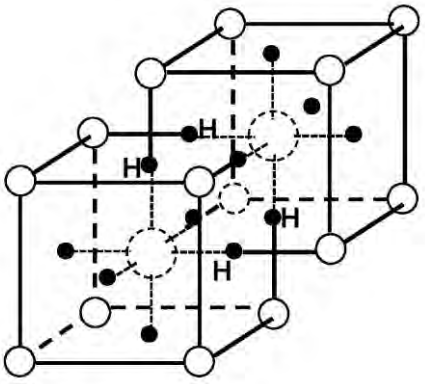

Fig. 1: Stable configuration of four H atoms in W di-vacancy. Black close circles are O-sites.

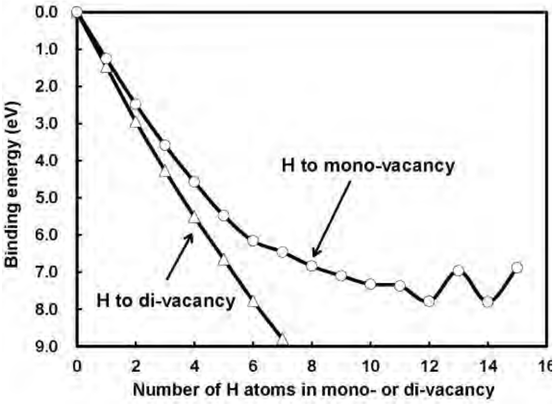

Fig. 2: Binding energy of H to mono- and di-vacancy in W lattice.

Study on physical properties of structural elementary excitations of semiconductor surfaces and interfaces

Hiroyuki KAGESHIMA
Interdisciplinary Graduate School of Science and Engineering, Shimane University
1060 Nishi-Kawatsucho, Matsue, Shimane 690-8504

Our project has been focused on the physical properties of structural elementary excitations of semiconductor surface and interfaces. We have performed two topics in this year. One is the supporting effect on physical properties of vacancies of monlayer $\mathrm{MoS_2}$ [1, 2]. The other is the dynamical properties of $\mathrm{SiO_2}$ at the interface with Si [3, 4]. The calculations were performed based on the first-principles calculation. Program package VASP was employed.

In the first topic, we focus on the properties of vacancies of monolayer $\mathrm{MoS_2}$. Our previous studies revealed that the formation energies of vacancies such as $\mathrm{V_S}$, $\mathrm{V_{S2}}$, and $\mathrm{V_{Mo}}$ are very small in case of negatively charged. We put the monolayer $\mathrm{MoS_2}$ on another monolayer $\mathrm{MoS_2}$, and examine the change of vacancy stabilities. The calculated results indicate that the formation energies increase by more than 0.2 eV. Further, when we put on monolayer $\mathrm{MoSe_2}$, the formation energies increase by more than 0.5 eV. We can understand this stabilization by the vacancy stability on surfaces. Because monolayer $\mathrm{MoS_2}$ is two-dimensional material and has exactly two bare surfaces, vacancies can be easily formed. However, one of the monolayer surface is covered by some other material, it is not a surface any more. Now $\mathrm{MoS_2}$ has only one bare surface. Therefore, the atoms in $\mathrm{MoS_2}$ interact with more atoms before, and vacancies are stabilized.

In the second topic, we focus on the oxygen vacancy effect. During oxidizing Si, we previously found that excess Si is emitted from the interface into the oxide. The excess Si in the oxide causes oxygen vacancies in the oxide. We study the effect of such oxygen vacancy on the diffusivity of Si and O in the oxide based on the first-principles molecular dynamics. We perform the study in the temperature range from 3000 K to 6000 K, and find that the incorporation of oxygen vacancy surely enhances the diffusion of Si and O. We analyze the calculated results, and successfully obtain the equation for the enhanced diffusion. When we compare the obtained equation with the empirical equation experimentally obtained previously, we find good consistencies in their activation energies, prefactors, and enhancement coefficients.

References

[1] S. Urasaki and H. Kageshima, 29th International Conference on Defects of Semiconductors (ICDS2017), Matsue, Japan, ThA1-1.

[2] H. Kageshima and S. Urasaki, International Conference on Solid States Devices and Materials, Sendai (SSDM2017), Japan, PS-13-10.

[3] Y. Yajima and H. Kageshima, International Workshop on Dielectric Thin Films (IWDTF2017), Nara, Japan, P-21.

[4] Y. Yajima, K. Shiraishi, T. Endoh, and H. Kageshima, Jpn. J. Appl. Phys. **57**, 06KD01 (2018).

Search and realization of novel electronic properties of solid surfaces and interfaces and of small particles

Takeshi INAOKA
Department of Physics and Earth Sciences, Faculty of Science,
University of the Ryukyus, 1 Senbaru, Nishihara, Okinawa 903-0213

We describe two of those subjects which we addressed this year.

In view of application to high-speed electronic devices, we examined the subband structure of InSb quantum wires with gates on both sides. We employed those computer programs which we developed ourselves and which incorporate the nonparabolic conduction-band dispersion in the local density approximation. It is quite important to realize how we can control the subband structure effectively by side gates.

Graphene is a very popular single-layer structure of carbon (C) atoms arranged in a hexagonal lattice. This layered material has been examined widely and intensively. It is expected to have extremely high electron mobility. However, we consider that there might be another monolayer structure of C atoms. Using the program package 'Vienna Ab initio Simulation Package' (VASP) [1,2], we explored the possibility of another monolayer structure of C atoms.

(1) Control of the subband structure of InSb quantum wires by side gates [3]

Narrow gap semiconductor InSb has a remarkably nonparabolic conduction-band dispersion, and it is a promising candidate material for high-mobility devices because of its extremely small band-edge effective mass. We can fabricate a quantum wire (QW), namely a two-dimensional (2D) electron system confined in a strip region, by digging trenches in a AlInSb wafer which has a InSb layer as a 2D quantum well. Figure 1 shows the configuration of the QW, side gates and a doping layer which extend infinitely in the z direction. The doping layer above the QW provides electrons to the QW, and the electrons can be controlled by the gates on both sides of the WQ. We assumed the charge neutrality of the QW, the side gates, and the doping layer as a whole. Incorporating the nonparabolic conduction-band dispersion as such in the local-density approximation, we investigated the subband structure to control it effectively by the side gates.

Nonparabalicity of the bulk conduction band reveals itself in subband dispersions as well. When vacuum space extends on both sides of the slab substrate, the electric field produced by the side gates are reduced significantly in the slab substrate, because the electric field is screened conspicuously by polarization of the dielectric substrate with a large static dielectric constant ε_s=17.88. However, when we fill both sides of the slab substrate with dielectric medium, the lateral electric field from the side gates starts to operate effectively on the subbands, especially on the 1st subband, and simultaneously the electron density of the QW, and consequently the number of occupied subbands increases. As for real systems, we should also note that the depth of each trench is finite and that dielectric medium lies below the bottom of the trench.

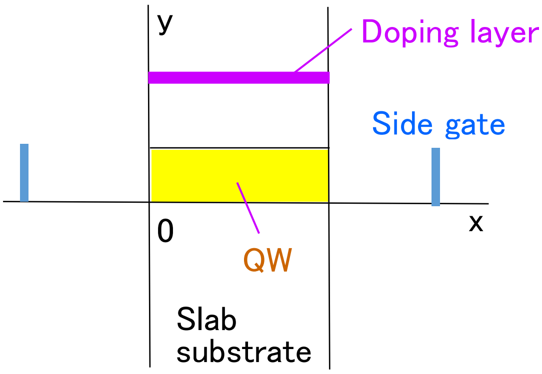

Fig. 1 Configuration of the quantum wire, the side gates, and the doping layer

(2) Proposal of a new single-layer structure of carbon atoms [4]

Graphene has carbon (C) atoms arranged in a hexagonal lattice. Its band structure is characterized by the so-called Dirac cones, and its conduction band and its valence band touches at the Dirac points in the Brillouin zone. Is it the only monolayer structure of C atoms? As another possible structure, we considered the monolayer structure in Fig. 2 which is composed of tetragonal and octagonal patterns. Hückel's rule asserts that cyclobutadiene molecule with its C atoms at four corners of a regular tetragon and cyclooctatetraene molecule with its C atoms at eight corners of a regular octagon are unstable because of generation of an unpaired electron. However, combination of tetragonal and octagonal patterns as in Fig. 2 results in a stable electronic structure. By means of the hybrid density functional method and the generalized gradient approximation in a comparative manner, we optimized the lattice in Fig. 2, and identified the ground state of the electron system. The eighth and ninth bands, each of which is spin-degenerate, cross the Fermi level. It was found that the electron system is a semi-metal which is characterized by the electron pocket around the $\bar{\mathrm{M}}$ point and the hole pocket around the $\bar{\Gamma}$ point. The areal density of the electrons or the holes is more than $2\mathrm{x}10^{14}$ cm^{-2}. The electron system is stable to atom displacement normal to the plane with C atoms on it.

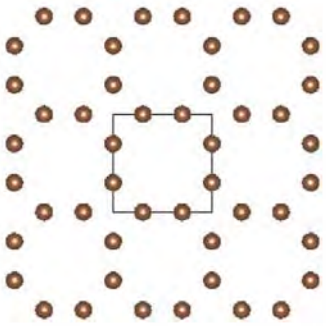

Fig. 2 Proposed monolayer structure of C atoms

References

[1] G. Kresse and J. Hafner: Phys. Rev. B **47** (1993) 558-561.
[2] G. Kresse and J. Furthmüller: Comput. Mat. Sci. **6** (1996) 15-50.
[3] T. Inaoka: to be prepared.
[4] T. Inaoka: in preparation.

First-principles simulation of magnetism and formation of amorphous grain boundary phase of Nd-based permanent magnets

Asako TERASAWA
Department of Materials Science and Engineering, Tokyo Institute of Technology
J1-3, Nagatsuta-cho 4259, Midori-ku, Yokohama 226-8502, Japan

Improvement of Nd-Fe-B magnets without heavy rare earth elements is one of the topics of increasing importance in the applied physics and materials science. The key for high-coercivity Nd-Fe-B magnets lies in the Nd-rich grain boundary (GB) phases [1]. However, the details of structural and magnetic properties of those GB phases are not clarified yet. Some experiments revealed the relationship between the crystallinity of GB phases and the relative angles between the interfaces and the c-plane of neighboring grains [2], which indicates the complexity of the physics in grain boundary phases in Nd-Fe-B magnets. Considering these backgrounds, we targeted the amorphous grain boundary phase for a computational study of magnetism in Nd-based permanent magnets. To simulate the grain boundary phase, we created a model of amorphous Nd-Fe alloy containing 54 atoms computationally on the basis of density functional theory (DFT). For the DFT calculations, we adopte OpenMX [3] code. To create amorphous structures, we performed melt-quench molecular dynamics simulations [4] which contain 0.6 ps of melting, 0.6 ps of quenching, and 0.6 ps of stabilizing procedures at 300K. An example of created amorphous structure is shown in Fig. 1.

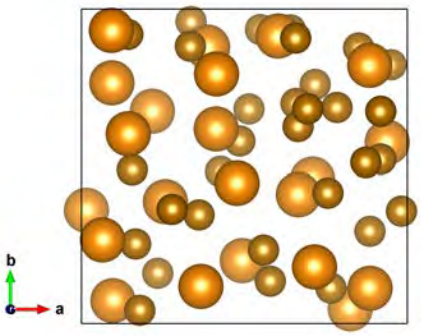

Figure 1: An example of calculated amorphous Nd-Fe alloy, which contains 22 atoms of Nd and 32 atoms of Fe. In the figure, the larger spheres correspond to the Nd atoms and the smaller spheres correspond to the Fe atoms.

Even though we could create amorphous structures from melt-quench MD simulations, we had three problems that makes it difficult to calculate those magnetism. First, the anti-ferromagnetic spin configuration in amorphous structure is not self-evident. This make it difficult to discuss the magnetism of amorphous systems by the energetics. Moreover, spin-dependent density functional calculations tend to become unstable when calculating disordered structures and disordered spin configurations. Finally, complicated structures of amorphous systems makes it difficult interpret the calculated results, even when we attain convergence in some calculations. To solve this problem, we constructed a method to analyze amorphous systems using the Gabriel graph [5], a graph based on the distance between the set of point shown in Figure 2 (a). Using the Gabriel graph, it is possible to define the nearest neighbors in an amorphous systems. It is then possible to draw Gabriel graph of calculated amorphous alloy, as in Fig. 2 (b).

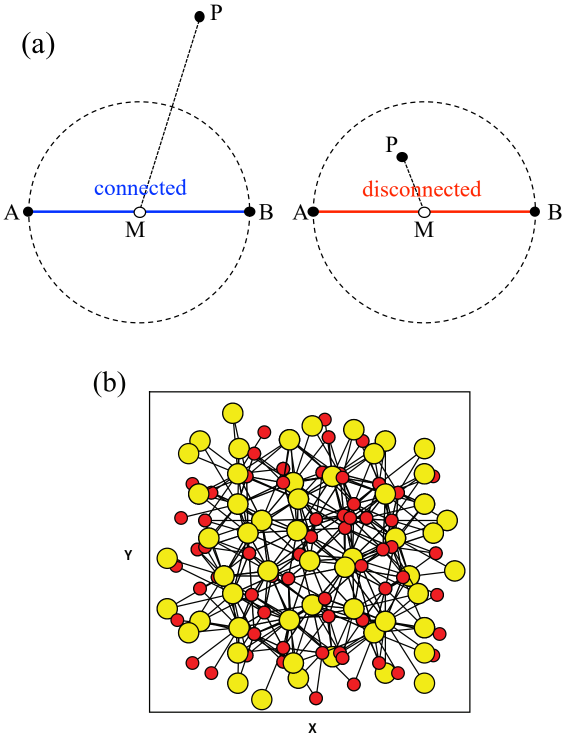

Figure 2: (a) A schematic of Gabriel graph. In the Gabriel graph, the criterion to connect points A and B is judged from the distance from the middle point M between A and B. When there are no nearer points than A or B, A and B are connected. If any other nearer points are found, they are disconnected. (b) A Gabriel graph calculated from the amorphous Nd-Fe alloy, containing about 40 % of Nd. The larger yellow circles and smaller red circles correspond to Nd and Fe atoms, respectively.

Determining the nearest neighbor sets of atoms by Gabriel graph, it is possible to examine the magnetism using a simple Heisenberg model. When assuming exchange coupling between only nearest neighbors which depends on the species of two atoms and independent of distances, it is possible to write the relationships between total energy and the magnetic moment as follows:

$$\begin{aligned} E &\approx E_0 - 2\bar{J}_{\text{Fe-Fe}}\sum_{i\text{-}j\in\text{Fe-Fe}}\mu_i\mu_j \\ &\quad -2\bar{J}_{\text{Fe-Nd}}\sum_{i\text{-}j\in\text{Fe-Nd}}\mu_i\mu_j \\ &\quad -2\bar{J}_{\text{Nd-Nd}}\sum_{i\text{-}j\in\text{Nd-Nd}}\mu_i\mu_j, \end{aligned} \tag{1}$$

where E is the total energy of DFT calculations, μ_i is the magnetic moment of atom i, $\bar{J}_{\text{X-Y}}$ is the exchange coupling between nearest neighbor pairs of atoms of species X and Y. Since E and μ_i can be obtained from DFT calculations, it is possible to determine $\bar{J}_{\text{Fe-Fe}}$, $\bar{J}_{\text{Fe-Nd}}$, $\bar{J}_{\text{Nd-Nd}}$ from several sets of calculations having the same atomic coordinates and different spin configurations. It was possible for us to obtain 8 different spin configurations which gave converged results for the amorphous Nd-Fe alloy shown ing Fig. 1, and the exchange coupling constants were calculated as follows: $\bar{J}_{\text{Fe-Fe}} = 3.637$ [meV/μ_B^2], $\bar{J}_{\text{Fe-Nd}} = 1.614$ [meV/μ_B^2] and $\bar{J}_{\text{Nd-Nd}} = -3.594$ [meV/μ_B^2]. And using these exchange coupling constants, we are able to calculate the paramagnetic curie temperature of the alloy as 871 K.

Calculations and interpretations of magnetism of amorphous materials had been a big challenge for materials science for many decades, and our approach can open up a new perspective to the amorphous magnetism.

References

[1] K. Hono *et al.*, Scripta Mater. **67**, 530 – 535 (2012).

[2] T. T. Sasaki *et al.*, Acta Mater. **115**, 269 (2016).

[3] T. Ozaki, Phys. Rev. B **67**, 155108 (2003).

[4] I. Štich *et al.*, Phys. Rev. B **44**, 11092 (1991).

[5] K. R. Gabriel *et al.*, Society of Systematic Biologists, **18**, 259 – 270 (1969).

Electron-Phonon Interactions in Isotopic Diamond Superlattice

Yuki Bando, Toyoda Masayuki, and Susumu Saito
Department of Physics Tokyo Institute of Technology
2-12-1 Ookayama, Meguro-ku, Tokyo 152-8550 Japan

The isotopic diamond superlattices that are periodic arrays of layers of carbon isotopes, such as ^{12}C and ^{13}C, with diamond structure, have been known to confined carriers to the layers of the lighter isotope (12C) due to the isotope effect on the electron-phonon interaction [1]. This phenomena has a great potential to realize the band-gap engineering in diamonds and to utilize diamonds as electronic devices. In this study, we developed the tight-binding model which enables us to calculate the electron-phonon interactions for various structures of isotope diamond superlattice efficiently. We compared the result of adiabatic Allen-Heine-Cardona theory between tight-binding model and density functional perturbation theory (DFPT) [2]. The DFPT calculations were performed by using ABINIT code [3] on the cpu nodes of system B. The visualized images of the crystal structures were created by using XCrySDen [4].

Figure 1(a) shows the crystal structures of the superlattices. The stacking direction is along [001] and each structure is labeled as $\{m, n\}$ that means it consists of periodic arrays of m atomic layers of ^{12}C and n atomic layers of ^{13}C. The tetragonal unit cells of the superlattices have a lower symmetry than the original $Fd\bar{3}m$ symmetry and thus the electron-phonon interaction would modify the electronic structure in such a way that it breaks the original symmetry. One of such examples is schematically shown in Figure 1(b), where the six identical electron pockets in diamonds are separated into two groups in superlattices: two pockets along Γ-Z line and four along Γ-M line.

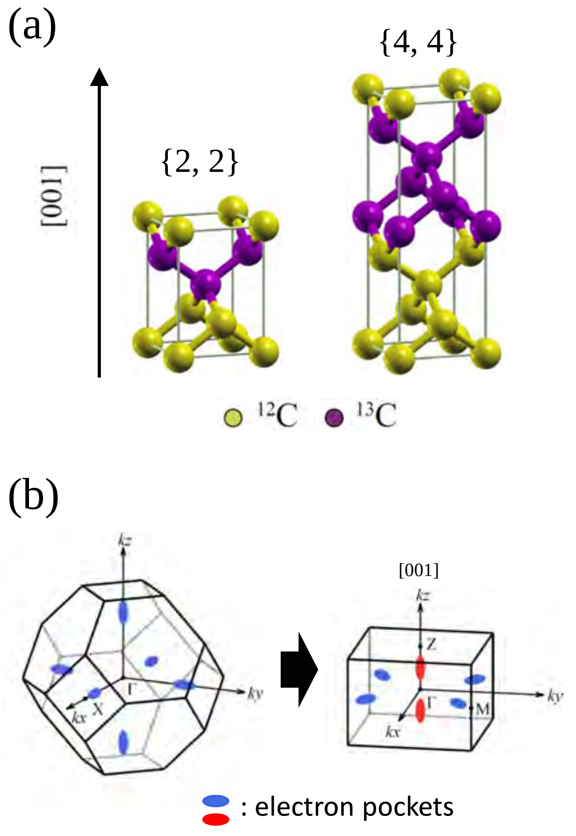

Figure 1: Tetragonal unit cells of $\{2, 2\}$ and $\{4, 4\}$ isotope diamond supperlattices (see text for the defnition of the labels). (b) Schematic image of the electron-pockets in the fcc (simple diamond) and tetragonal (superlattices) Brillouin zones.

We constructed a tight binding model to calculate electron-phonon interactions using localized orbitals. This tight binding model is based on Wannier representation of electron-phonon interactions [5]. The electron-phonon matrix elements are strongly localized with respect to the distance between atomic vibrations and electronic orbitals in the case of diamond. Therefore, we can consider these quantities just as hopping parameters. We used one hopping parameter to describe FAN term Σ_{FAN} of electron-phonon interactions among valence states. This parameter was fitted with the sum of Σ_{FAN} + diadonal Debye-Waller term Σ_{dDW} calculated by DFPT at Γ.

Figure 2 shows zero point renormalization (ZPR) calculated by tight binding model and DFPT in fcc diamond. Even though we used only one parameter and not include Σ_{dDW} term directly, the ZPRs of tight binding model on momentum space are highly similar to those of DFPT.

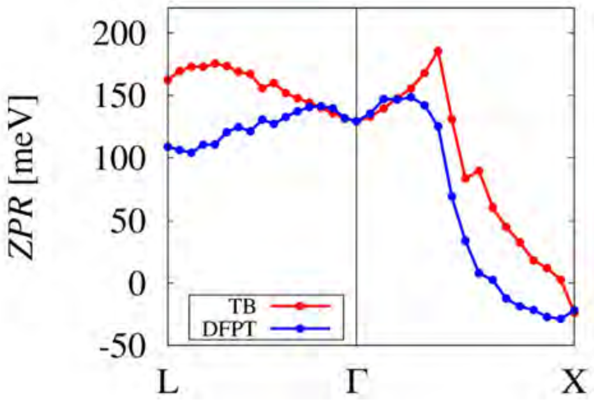

Figure 2: ZPR of the valence band top state calculated by tight binding (TB) model and DFPT

Figure 3 shows the valence band structure in tetragonal diamond along [001] direction. The valence band top state rise up due to ZPR. On the other hand, the valence band bottom state fall down slightly due to ZPR. These behavior are good agreement with those in case of DFPT calculation in fcc diamond.

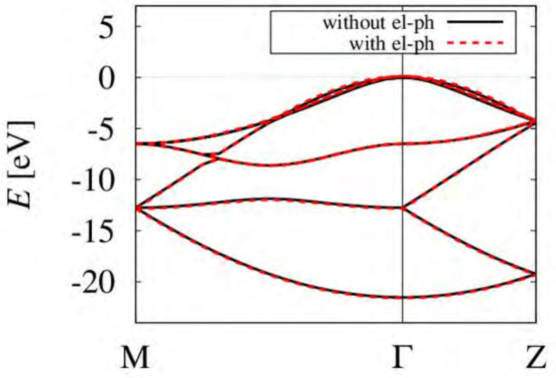

Figure 3: Valence band structure computed by tight binding model in tetragonal diamond

As a conclusion, we found that newly developed tight binding model has the possibility to compute electron-phonon interactions in isotopic diamond superlattice quantitatively. In the future research, we will include Σ_{dDW} and a couple of conduction states into electron phonon interactions, and will carry out more detailed analysis in various structures of isotopic diamond superlattice.

References

[1] H. Watanabe, et al, Science **324** (2009) 1425.

[2] S. Ponce, et al, Phys. Rev. B **90** (2014) 214304.

[3] X. Gonze, et.al, Computer Physics Communications **180** (2009) 2582-2615.

[4] A. Kokalj, Comp. Mater. Sci., **28** (2003) 155.

[5] F. Giustino, et.al, Phys. Rev. B**90** (2007) 165108.

Organic Molecules under High Pressure and Electronic Structures of B-C-N materials

Toshihiro Shimada, Ichiro Yamane, Takahiro Tamura, Takashi Yanase, Taro Nagahama
Division of Applied Chemistry, Faculty of Engineering
Hokkaido University, Sapporo 060-8628

Nitrogen and/or boron containing carbon materials are important because various functions are expected. However, the synthesis of these materials are in primitive stage and it is very difficult to obtain three dimensional solid as designed.

Synthesis under high pressure is a powerful technique to obtain novel materials. We are experimentally studying what happens when high pressure is applied to organic crystals to study possible synthesis of new carbon materials. In order to explain the experimental results and extract knowledge about the chemical reactions, we used ISSP supercomputer.

First, we explain our research on nitrogen containing molecules. Experimentally, single crystals of an organic molecule with nitrogen atoms (quinoxalino[2',3':9,10]phenanthro [4,5-abc]phenazine (TQPP), Fig. 1) are used as precursor. After high pressure treatment at room temperature, precursor molecules underwent oligomerization accompanied by transformation from sp^2-hybridization carbon atoms to sp^3 ones. We used a DFT package VASP [2] to understand the process in computer. We used PBE functional[3] and plane wave. Hydrostatic pressure was simulated by adjusting cell parameters and calculating the total energy change. To analyze oligomerization and structure of product, structural optimization calculation was performed starting from structure of TQPP crystal obtained by single crystal X-ray diffraction. When the structure was compressed with quasi-hydrostatic condition in simulation, TQPP molecules in the crystal polymerized and column-like one dimensional polymer was obtained (Fig. 2).

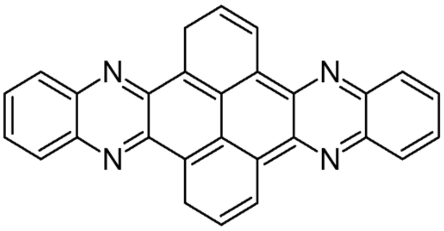

Fig. 1. Molecular structure of TQPP

Second, we computationally studied the electronic structures of graphene-like layered structures consisting of carbon, boron and nitrogen atoms. We replaced boron or nitrogen atoms to carbon atoms starting from hexagonal boron nitride. We previously reported that oddnumbered uneven substitution has given two dimensional metals with very different work functions (3.01 eV and 4.88 eV) [4].

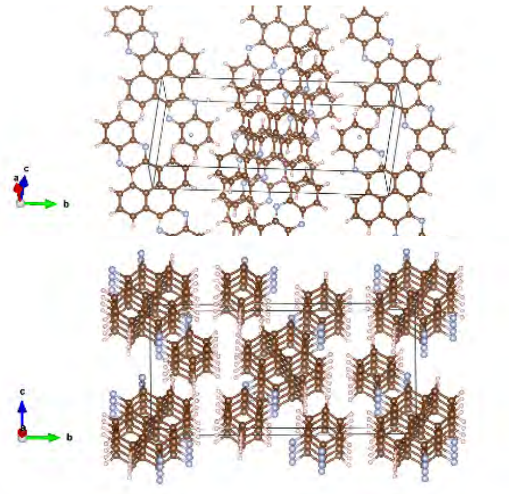

Fig. 2. Crystal structure of TQPP determined experimentally (above) and Structure of tube-like polymerized TQPP obtained by structural optimization under compression (below)

Using ISSP supercomputer, we examined the effect of C doping to hexagonal boron nitride (h-BN) to its electronic structure is examined by first principles calculations using the association from π-electron systems of organic molecules embedded in a two-dimensional insulator. In a monolayered carbon-doped structure, odd-number doping with carbon atoms confers metallic properties with different work functions. Various electronic interactions occur between two layers with odd-number carbon substitution. A direct sp^3 covalent chemical bond is formed when C replaces adjacent B and N in different layers (Fig.3, electron localization function by VASP). A charge transfer complex between layers is found when C replaces B and N in the next-neighboring region, which results in narrower band gaps (e.g. 0.37 eV). Direct bonding between C and B atoms is found when two C atoms in different layers are at a certain distance.

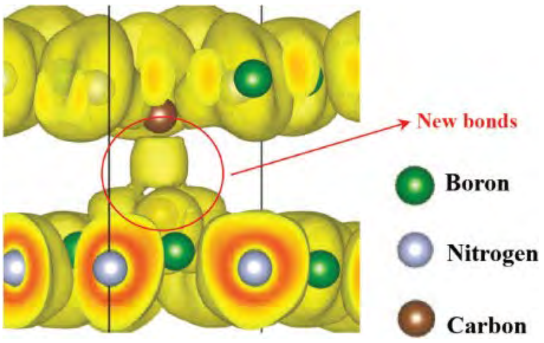

Fig. 3. sp^3 C-C bond formation between layers

References

[1] S. Yamanaka et al., J.Am.Chem.Soc. 130, 4303(2008).

[2] G. Kresse and J. Furthmüller,, Phys. Rev. B 54, 11169 (1996).

[3] J. P. Perdew, K. Burke, M. Ernzerhof, Phys. Rev. Lett. 77, 3865 (1996).

[4] Wei Xie, T. Yanase, T. Nagahama, T. Shimada, C-J.Carbon Res. 2 (2016) 2.

[5] Wei Xie, T. Tamura, T. Yanase, T. Nagahama, T. Shimada, Jpn. J. Appl. Phys. 57 (2018) 04FL11.

Finding the ground state of Prussian blue derivatives

Yoyo HINUMA
Center for Frontier Science
Chiba University, 1-33 Yayoicho, Inage, Chiba, Chiba 263-8522

$Na_xCo[Fe(CN)_6]_{0.09}\bullet 2.9H_2O$ is a Prussian blue analogue material that can be used as a sodium battery cathode (crystal structure without Na and H_2O shown in Fig. 1). There are two transition metal elements that change valence; at $0<x<0.6$, Co is 3+ and Fe valence changes between low spin (LS) +3 and LS +2, while at $0.6<x<1.6$ Fe is LS 2+ and Co is between +3 and +2. [1] The crystal structure of a similar material, $Na_xMn[Fe(CN)_6]_y\bullet zH_2O$, has a similar crystal structure and can be cubic, rhombohedral, and monoclinic depending on x and temperature.

Ground state structure search from a high symmetry crystal by iterating calculation of supercell force constants, finding dynamic instabilities and then deforming along the direction indicated by the instabilities has been demonstrated in Cu using VASP and phonopy codes [3].

Interestingly, no imaginary phonon modes were found in cubic $MnFe(CN)_6$ (space group $Fm\text{-}3m$) based on PBEsol+U and SCAN approximations. This was unexpected because octahedral LS Fe^{3+} should be subject to Jahn-Teller distortion.

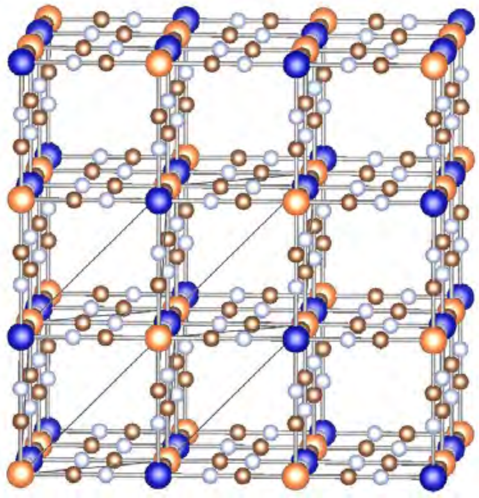

Fig. 1 Jungle gym like crystal structure of cubic $CoFe(CN)_6$. Lines indicate the primitive cell. Large blue, large orange, small brown, and small gray balls are Co, Fe, C, and N respectively. Na can enter cubes with 12 Co-C-N-Fe edges.

References

[1] M. Takachi et al.: Appl. Phys. Express **6** (2013) 025802.

[2] Y. Moritomo et al.: J. Phys. Soc. Jpn. **80** (2011) 103601.

[3] A. Togo and I. Tanaka, Phys. Rev. B. **87** (2013), 184104.

First-principles study of atomic structures, stabilities, and electronic properties of atomic-layered materials

Yoshitaka FUJIMOTO
Depertment of Physics, Tokyo Institute of Technology
Oh-okayama, Meguro, Tokyo 152-8551

Graphene has received much interest from fundamental nanoscience and applicable nanotechnology due to various unique properties, and is a good candidate material for future nanoelectronics devices including gas sensors.

We here report first principles density functional study to examine atomic structures, stabilities, and electronic properties of various gas molecules including environmentally polluting gas molecules adsorbed on the B-doped graphene [1, 2].

We first study the adsorption energies and atomic structures of various gas molecules adsorbed on the B-doped graphene monolayer. It is found that the NO and NO_2 molecules can bind with chemical bonds with large adsorption energies and short distances between gas molecules and the B-doped graphene. The B atom protrudes from the planar graphene sheet due to a chemical bond between the O atom in the NO_2 molecule and the B atom in the B-doped graphene, whereas it still resides in the planar sheet for the NO molecule adsorption.

We next study the energy band structures near the Fermi energy for the B-doped graphenes adsorbed with NO and NO_2 molecules. When the NO molecule is adsorbed, the two unoccupied flat NO-molecule related states appear above the Fermi energy. When the NO_2 molecule is adsorbed, the unoccupied NO_2-related state appears above the Fermi energy.

We also study the electronic properties of the NO and NO_2 molecules adsorbed on the B-doped graphene monolayer. The adsorption of the NO (NO_2) molecule induces the charge transfers between the N (O) atom in the NO (NO_2) molecule and the B atom in the graphene: for the adsorption of the NO molecule, electrons move from the NO molecule to the B-doped graphene, while for the adsorption of NO_2 molecules, electrons move from the B-doped graphene to the NO_2 molecule.

We here study the work functions of B-doped graphenes with and without NO and NO_2 molecules. Our calculated work function of the pristine monolayer graphene is 4.44 eV, and is in agreement with the experimental observations. The work function of the B-doped graphene is larger than that of the pristine graphene. When the NO molecule is attached to the B-doped graphene, the work function decreases. On the other hand, the work function of the B-doped graphene increases when the single NO_2 molecule is adsorbed.

We study the scanning tunneling microscopy (STM) images of the B-doped graphenes with NO and NO_2 molecules. The theoretical STM image of the B-doped graphene without adsorbates has the triangle-shaped corrugation, and agrees with the experimentally observed images. The STM image of the graphene surface with the NO molecule has two ring-like corrugations above the NO molecule when the NO molecule is adsorbed. For the case of the NO_2-molecule adsorption, there exist large and small spherical-shaped protrusions above the NO_2 molecule.

In summary, we have examined the adsorptions of the various molecules including environmentally polluting gases on B-doped graphene monolayers using first-principles density-functional calculations. The NO and NO_2 molecules can bind with chemical bonds on the B-doped graphene monolayer. The adsorptions of the NO molecule and the NO_2 molecule give rise to the charge transfers between the NO (NO_2) molecule and the B-doped graphene.

References

[1] Y. Fujimoto and S. Saito, Chem. Phys. **478**, 55 (2016).

[2] Y. Fujimoto and S. Saito, submitted.

Research on work functions of mixed anion layered compounds LaCuSO

Yoichi KAMIHARA
Department of Applied Physics and Physico-Informatics, Keio University
3-14-1 Hiyoshi, Yokohama, Kanagawa 223-8522

The mixed anion compounds with a ZrCuSiAs-type structure (known as 1111-like systems) has attracted a great interest due to their important properties of potential applications. LaCuSO is one of the typical examples of having the structure. It has alternately stacked layered structures composed of a lanthanum oxide layer with a large band gap and a copper sulfide layer as a conductive layer. It is possible to exhibit functionality by a two-dimensional electronic structure controlled electronic state by making lattice defect at the respective element sites.

In this report, we focus and analyze surfaces of LaCuSO, which are expected as a candidate for new catalytic materials with crystallographically vacant sites at several sites. In first, we analyze work functions of these materials.

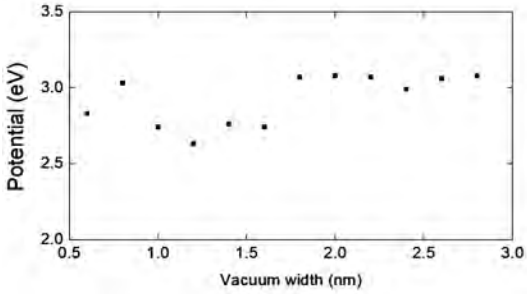

Figure 1: Vacuum energy level as a function of vacuum width for LaCuSO (001) slab model. Positions of atoms are relaxed where the Hellman-Feynman forces were reduced until 0.1 eV nm^{-1}.

Considering the two-dimensional crystal structure, only the surface in the c-axis direction was treated. For description of the surface, we used a slab geometry, which is infinite and periodic in the direction parallel to the surface but finite in the perpendicular direction. The supercell consists of an atomic region where unit cells are expanded to 2×2×1 and a vacuum region with a thickness of 1.8 nm determined by preliminary test calculation (Fig. 1). We consider the LaO-terminated LaCuSO surface and CuS-terminated one (Fig. 2). The surface relaxation was considered a slab thickness of 3 layers from surface and 4-6 layers are fixed. Work function Φ is defined as follows.

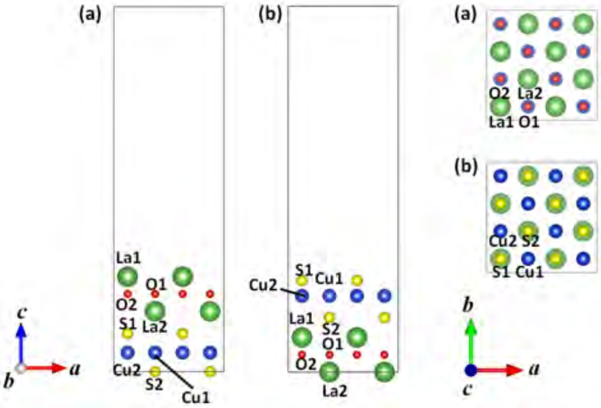

Figure 2: (a) LaO-terminated 2×2×1 LaCuSO (001) slab model. (b) CuS-terminated 2×2×1 LaCuSO (001) slab model. The thickness of vacuum region is 1.8 nm.

$$\Phi = E_{\mathrm{vac}} - E_{\mathrm{F}} \tag{1}$$

where E_{vac} is the energy level of the vacuum and E_F is the Fermi energy. E_F is calculated by the following formula because of the difference in Fermi energy between slab and bulk.

$$E_{\mathrm{F}} = E_{\mathrm{fermi}}^{\mathrm{bulk}} - E_{\mathrm{core}}^{\mathrm{bulk}} + E_{\mathrm{core}}^{\mathrm{slab}} \tag{2}$$

where $E_{\mathrm{fermi}}^{\mathrm{bulk}}$, $E_{\mathrm{core}}^{\mathrm{bulk}}$, $E_{\mathrm{core}}^{\mathrm{slab}}$ are calculated Fermi energy of bulk, energy level of the core-like state of bulk and that of slab, respectively. An example of the result is shown below. Fig. 3 is a diagram of the potential distribution in the surface vertical direction. The potential here includes potential due to ions and Hartree term, not including exchange correlation term.

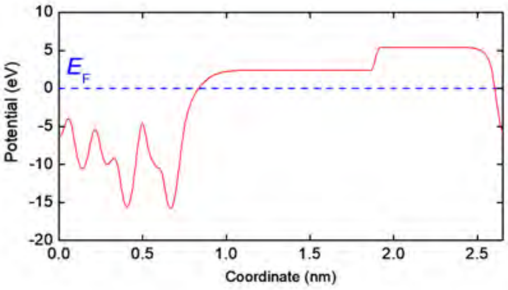

Figure 3: Electronic potential distribution of LaCuSO (001) slab model. The horizontal axis is a coordinate perpendicular to the surface. The constant region in the right corresponds to the vacuum region.

Each calculation has been carried out based on density functional theory (DFT) using Projector Augmented Wave (PAW) method[1] implemented in the Vienna ab-initio Simulation Package (VASP)[2]. Generalized gradient approximation (GGA) of Perdew-Burke-Ernzerhof (PBE) functional[3] was adopted for exchange-correlation energy. Dipole correction based on Neugebauer's method[4] is adopted in order to correct error due to artificial electric field asymmetry caused by periodic boundary condition of model.

Fig. 4 shows that the work function of LaO-terminated LaCuSO surface tends to be lower than that of CuS-terminated surface. Besides, on the LaO-terminated surface, the changes in the work function with respect to the vacancy is more remarkable than the other surface. The plots on Fig. 4 show the average displacement of surface atoms. The difference in displacement between the stoichiometric surface and the defect surface is larger on the CuS-terminated surface than on the LaO-terminated one. Therefore, the stabilization by surface relaxation is more pronounced on the CuS-terminated surface. For this reason, it is considered that the change in work function due to defect is smaller on the CuS surface and larger on the LaO surface.

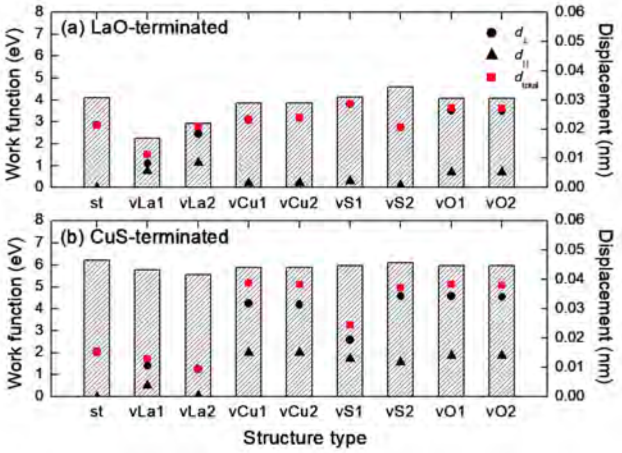

Figure 4: Summary of the surface properties of (a) LaO-terminated and (b) CuS-terminated LaCuSO surface with and without deficiency. Work functions are shown by bar graph with the left axis. The average displacements are plotted with the right axis. Structure "st" means a surface having a stoichiometric composition. Structure vXX means the surface having vacancy defects on XX site of Fig. 2. Each defect surface has the rate of 12.5 % vacancy.

The work function of two different surfaces of LaCuSO are calculated. The work function of the LaO terminating surface tends to be smaller. Moreover, it is suggested that dependence of work function on vacancy is larger on the LaO-terminated surface than on the CuS-terminated surface.

References

[1] P. E. Blöchl: Phys. Rev. B **50** (1994) 17953.

[2] G. Kresse and J. Hafner: Phys. Rev. B **47** (1993) 558.

[3] J. P. Perdew, K. Burke and M. Ernzerhof: Phys. Rev. Lett. **77** (1996) 3865.

[4] Jorg Neugebauer and Matthias Scheffl: Phys. Rev. B **46** (1992) 16067.

Quantitative Calculations of Momentum Distribution Function and Quasiparticle State in Ferromagnetic Transition Metals and Compounds Based on the First-Principles Momentum Dependent Local Ansatz Theory

Yoshiro KAKEHASHI
Department of Physics and Earth Sciences, Faculty of Science, University of the Ryukyus,
1 Senbaru, Nishihara, Okinawa, 903-0213, Japan

Though the density functional theory (DFT) is an excellent method to calculate the ground state properties, it is well-known that the quantitative aspects become worse with increasing Coulomb interaction strength. In order to describe correlated electrons quantitatively and to remove the difficulties in the DFT, we have recently proposed the first-principles momentum dependent local ansatz (MLA) wavefunction method on the basis of the tight-binding LDA+U Hamiltonian [1].

In this project, we have extended the MLA to the ferromagnetic case, and performed the numerical calculations of the ground state for Fe, Co, and Ni to clarify the quantitative aspect of the theory.

In the ferromagnetic state, we have to introduce the momentum dependent variational parameters so that the two-particle excited states are independent each other. In the cubic system, self-consistent 26 parameters appear including correlation energy ϵ_c, chemical potential μ, local charge n_L, as well as the magnetization m_L.

Assuming μ, n_L, and m_L which determine the potential energy, we solve the Hartree-Fock type one electron energy eigen value equations, as shown in Fig. 1. After we obtain the energy bands, we solve the self-consistent equations obtained from the variational principle. Then we know the wavefunction and calculate new chemical potential μ, local charge n_L, and the magnetization m_L. We perform the iteration loop until the self-consistency is achieved.

We obtained the spin magnetizations 2.44 μ_B for Fe, 1.71 μ_B for fcc Co, and 0.54 μ_B for Ni, respectively. These values are compared with 2.15 μ_B (LDA) and 2.46 μ_B (GGA) for Fe, 1.59 μ_B (LDA) and 1.66 μ_B (GGA) for Co, 0.62 μ_B (LDA) and 0.66 (GGA) for Ni, and show better agreement with the experimental values (2.22 μ_B for Fe, 1.72 μ_B Co, and 0.57 μ_B for Ni).

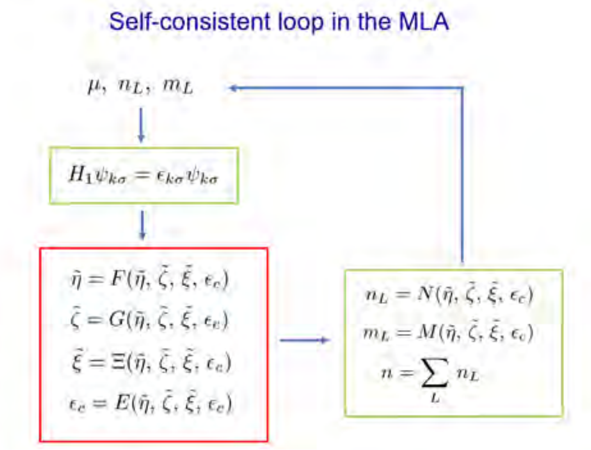

Figure 1: Self-consistent loop in the Momentum-dependent Local Ansatz (MLA) theory.

References

[1] Y. Kakehashi and S. Chandra, J. Phys. Soc. Jpn. **85**, 043707 (2016); **85**, 064714 (2016), 084708 (2016); **86**, 034711 (2017).

Computational Phase and Morphology Design of Electrochromic WO_3

Ahin Roy and Yukio Sato

Department of Materials Science and Engineering,
Kyushu University, 744 Motooka, Nishi-ku, Fukuoka 819-0395

WO3, an electrochromic material, exists in a myriad of phases. Recent experiments show that through use of oxalate capping in a hydrothermal reaction, it is possible to control phase and morphology of WO_3. [1] In order to elucidate the electronic interaction in the capping process, we carried out *ab initio* simulations for oxalate capping on hexagonal (11-20) and orthorhombic (001) surfaces, as shown in Figure 1a and 1b. The calculations with all electron projector augmented wave PBE potentials with generalized gradient approximation were carried out with the Vienna Ab Initio Simulation Package (VASP) code. [2]

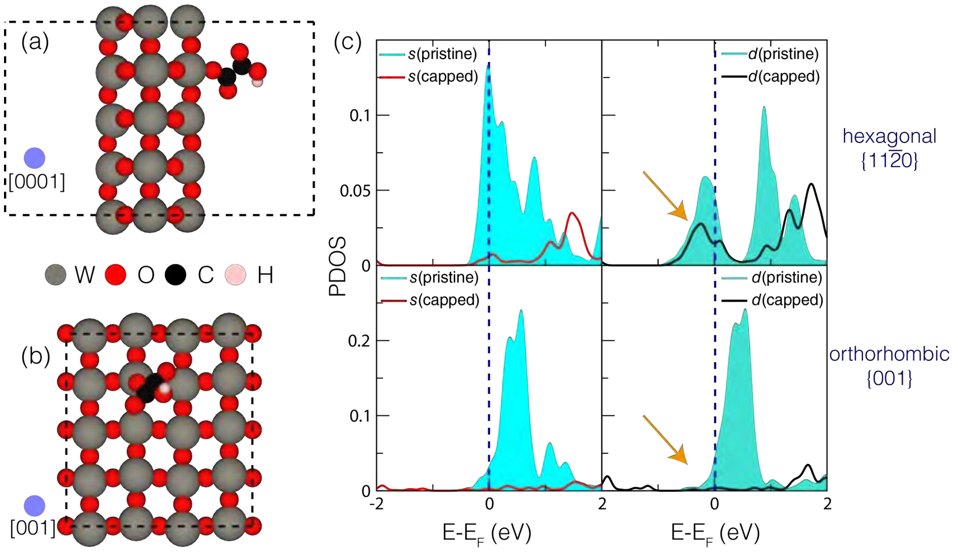

Figure-1: Relaxed geometries of the oxalate capped (a) hexagonal (11-20) and (b) orthorhombic (001) surfaces, the unit cell is marked in black dotted solid line; (c) shows the *l*-decomposed electronic density of states (DOS) projected on the adsorption site. The upper panel shows the adsorption-induced changes in the DOS for hexagonal (11-20) surface, and the lower panel shows the changes for the orthorhombic (001) surface.

In such a scenario, the binding energy of the oxalate on the hexagonal (11-20) surface and orthorhombic (001) surface was found to be -0.61 eV, and -1.26 eV respectively. This clearly shows that the oxalate species binds more strongly on orthorhombic phase, leading to a lower interfacial energy, and hence can act as a phase-directing agent.

To understand the electronic interaction during the capping of different facets of WO_3, we calculated the *l*-decomposed electronic density of states (DOS) projected on the capping site. As can be seen from Figure 1c, there is a large depletion of the both *s*- and *d*-states near Fermi energy, in the case of capping in orthorhombic WO_3 compared to that of hexagonal WO_3. The simulation results clearly show that oxalate interacts with the orthorhombic surface more strongly compared to hexagonal surface. A stronger interaction implies a lower interfacial energy, leading to a phase-selection during nucleation. Moreover, because of the binding of the oxalate on (001) surface, the growth in the [001] direction is prohibited, and forms a 2-D morphology. Whereas, absence of oxalate leads to formation of hexagonal phase, which grows in anisotropic *c*-direction leading to a rod morphology.

The two synthesized phases exhibit very different electrochromic property. Experiments illustrate that under an applied voltage H^+ can intercalate into the phases changing its color from yellow to blue. The H^+ diffusion co-efficient was found to be higher in the case of hexagonal WO_3 compared to that of orthorhombic one. Hence, the color switching was faster for hexagonal phase.

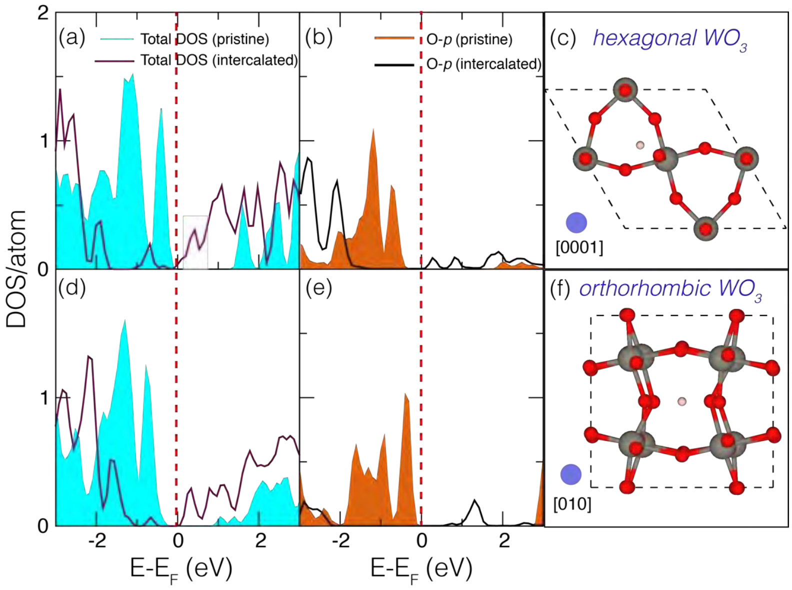

Figure-2: (a) Total DOS and (b) PDOS of the hexagonal phase before and after intercalation of H^+; (c) shows the H^+-intercalated hexagonal WO_3; (d) and (e) are the Total DOS and PDOS of the orthorhombic phase before and after intercalation of H^+; (f) is the structure of H^+-intercalated orthorhombic WO_3.

In order to understand the H^+-intercalation in details, we investigated the intercalation induced electronic structure changes. The intercalation energy E_{int} of the H^+-ion in the hexagonal/orthorhombic phase can be calculated as follows:

$$E_{int} = E_{int-struc} - E_{bulk} - E_{H2O/H^+}$$

where, $E_{int-struc}$ is the total energy of the H^+-intercalated unit cell, E_{bulk} is the energy of the hexagonal/orthorhombic WO_3 phase in bulk state, and E^0_{H2O/H^+} is the ionization potential of H_2O to generate H^+ ion (0.42 eV, considering the process as a one-electron process). The calculated E_{int} for hexagonal phase is 0.18 eV, whereas that for orthorhombic phase is 2.09 eV. This large contrast in the intercalation energy clearly rationalizes that the threshold voltage for H^+-intercalation would be lesser for the hexagonal phase compared to that of the orthorhombic phase. This also indicates that once intercalated, it would be harder for the H^+ ions to de-intercalate from the orthorhombic phase. Thus, the transmission switching is expected to be faster for the hexagonal phase, in agreement with the experiments.

To look at the electronic interaction in detail, the total and partial electronic DOS of the systems were carried out. As can be seen from Figure 2, there is a clear switching of the WO_3 from a semiconductor to metal upon H^+-intercalation. Such transition has been reported before, owing to the reduction of the WO_3. As can be seen from Figure 2b and 2e, the H^+-intercalation leads to a huge depletion of the oxygen *p*-states. This effect is more pronounced in case of the orthorhombic WO_3. The trend of such oxygen *p*-state depletion also follows the trend of E_{int}, reflecting a stronger electronic interaction and slower intercalation kinetics for the orthorhombic phase.

References:

[1] K. Ghosh*, A. Roy*, S. Tripathi, S. Ghule, A. K. Singh, and N. Ravishankar, Journal of Materials Chemistry C, 5, 7307-7316 (2017) (*equal contributions)

[2] G. Kresse and J. Hafner, Phys. Rev. B 47 , 558 (1993); ibid. 49 , 14 251 (1994)

Search for new electronic properties of new nanoscale interfaces

Katsuyoshi KOBAYASHI and Akiho KUBO
Department of Physics, Ochanomizu University
2-1-1 Otsuka, Bunkyo-ku, Tokyo 112-8610

In 2017 we theoretically studied the transition-metal dichalcogenide (TMD) monolayers in asymmetrical structures. TMDs are layered material having three-layer structures consisting of monatomic transition-metal layer sandwiched between two monatomic chalcogen layers. The two chalcogen layers are usually formed of identical elements. New structures with different chalcogen layers were experimentally synthesized in 2017 [1, 2]. We studied the atomic and electronic structures of the asymmetric TMD monolayers by the density-functional method. We used the program package VASP.

The atomic structures of TMD monolayers are 1H or 1T structures. The 1T structure has a modified structure with a double period named 1T′ structure. It is theoretically predicted that the TMDs in the 1T′ structure are quantum spin Hall insulators in the monolayer structure [3] and Weyl semimetals in stacked structures [4]. The total energy difference between the 1T and 1H structures are small, and it was experimentally succeeded to undergo the transition between these two structures by electron doping [5]. We calculated the atomic and electronic structures of MoSTe, MoSeTe, WSTe, and WSeTe as examples of asymmetric TMD monolayers. We studied the effect of electron doping in these systems. Following results were obtained from the calculations.

One is that the 1H structure has lower total energy than the 1T structure for all the four asymmetrical systems above. The 1H structure is the stable structure of the TMD monolayers in the symmetrical structure except for WTe_2 [6]. WSeTe is an intermediate system between WSe_2 and WTe_2 and may be regarded as one near to the former.

Next we studied the effect of electron doping. The total energy difference between the 1H and 1T structures decreases with increasing the amount of electron doping for all four systems. It undergoes the transition of stable structures from 1H to 1T at some amounts of doping in all the systems. This result is the same as the symmetrical structures [5]. It may be possible to materialize the 1T′ structure by electron doping in the case of the asymmetrical structures also.

Finally we calculated the electronic structures. The electronic states in the 1H structure are semiconductors for all four asymmetrical TMD monolayers. MoSeTe and WSeTe are direct gap semiconductors, and MoSTe and WSTe are indirect gap semiconductors. Both the top of valence bands and the bottom of conduction bands are located at the K point in the Brillouin zone in the former case. The top of valence bands is changed to the Γ point in the latter case. Band inversion between the d bands of transition metals and the p bands of chalcogens appear for all four asymmetical TMD monolayers in the 1T′ structure.

References

[1] A.-Y. Lu *et al.*: Nat. Nanotech. **12** (2017) 544.

[2] J. Zhang *et al.*: ACS Nano **11** (2017) 8192.

[3] X. Qian *et al.*: Science **346** (2014) 1344.

[4] A. A. Soluyanov *et al.*: Nature **527** (2015) 495.

[5] Y. Wang *et al.*: Nature **550** (2017) 487.

[6] Y. Li *et al.*: Nat. Commun. **7** (2016) 10671, Supplementary information.

Strain control of carrier localization in polar semiconductor materials

Hannes RAEBIGER
Department of Physics, Yokohama National University
Graduate School of Engineering
Tokiwadai, Hodogaya-ku, Yokohama 240-8501

Carrier localization or delocalization is typically considered a material property, i.e., shallow defects yield mobile, delocalized charge carriers, and deep defects trap charge carriers. We have previously demonstrated that in some particular systems, charge carriers exhibit a duality between trapped and delocalized, and by increasing the defect concentration, we may observe a second order phase transition from trapped to delocalized state [1]. This duality and ensuing physics of excitonic phases [2] is corroborated by numerous experiment (see Refs. in [1]). The key to unveiling such localization-delocalization dualities is the inclusion of a self-interaction correction [3], which have optimized for the use in magnetic semiconductors.

Motivated by our previous results, we investigated the coexistence of localized and delocalized states in Mn and Fe doped p-type GaN. In these systems, we find a variety of differently localized and delocalized states [4]: carrier holes localized on single anion sites are not equivalent, and we find a variety of extended states, including states delocalized along quasi-1D chains or 2D planes. These differently localized states have markedly different structural relaxations, and are very sensitive to lattice strain.

We exploit the strain sensitivity, and demonstrate that the carrier localization can be controlled by applying axial strain, as illustrated in Figure 1. This is explained by the interplay of the piezoelectric effect and the electric polarization of the differently localized charge carriers. This discovery offers the new perspective to switch on and off carrier channels in GaN, and other polar semiconductors.

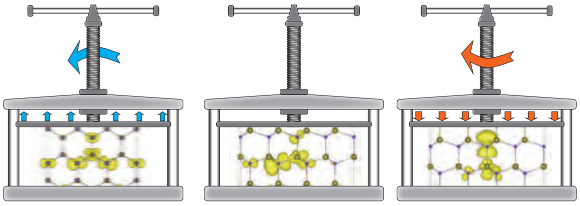

Figure 1: Hole localization around Fe impurities in GaN. Tensile strain (left) delocalizes hole carriers in plane perpendicular to strain axis, and compressive strain (right) localizes them along the strain axis. In unstrained GaN (center) holes around Fe impurities localize in the ab-plane.

References

[1] S. Bae and H. Raebiger: Phys. Rev. B (Rapid Communications) **94** (2016), 241115(R).

[2] W. Kohn: Phys. Rev. Lett. **19** (1949) 416.

[3] S. Lany and A. Zunger: Phys. Rev. B **80** (2009) 085202.

[4] H. Raebiger, S. Bae, C. Echeverria-Arrondo and A. Ayuela: Phys. Rev. Mater. **2** (2018) 024402.

First-principles statistical thermodynamics simulations on the structure and reactivity of heterogeneous catalysts

Fahdzi MUTTAQIEN, Teruo HIRAKAWA, Sasfan Arman WELLA, Yuji HAMAMOTO,
Kouji INAGAKI, Hidetoshi Kizaki, Ikutaro HAMADA, and Yoshitada MORIKAWA
Department of Precision Science and Technology,
Osaka University, Yamada-oka, Suita, Osaka 565-0871

We focus on chemical reactions at surfaces and interfaces including ligand-free Suzuki-Miyaura cross coupling reactions in aqueous solutions [1,2], CO_2 adsorption and hydrogenation on Cu surfaces [3,4], dependence of absorption spectra of Ru-complex on pH [5], oxygen vacancy diffusion in $Sr_3Fe_2O_{7-\delta}$ [6], and etching of SiC by Pt catalyst in water solution [7]. In the present report, we discuss CO_2 adsorption and hydrogenation on Cu(111) [3,4].

One of the most important intermediate steps in the methanol synthesis over Cu-based catalysts is CO_2 hydrogenation into formate (HCOO). Based on a kinetics analysis, it was suggested that formate synthesis takes place through an Eley-Rideal (ER) type mechanism, in which gas phase CO_2 directly reacts with adsorbed H. In the ER type mechanism, there is a possibility to enhance the reaction rate of formate synthesis by controlling the translational, vibrational, and rotational energies of impinging CO_2. The initial impinging CO_2 energies must be related to the energy states of desorbed CO_2 from formate decomposition bacause formate synthesis and decomposition are reversible reactions. Therefore, elucidation of formate decomposition dynamics is important for improving catalytic formate synthesis.

Very recently, the dynamics of desorbed CO_2 produced from the formate decomposition reaction has been studied by measuring the angle-resolved intensity and translational energy distribution of the steady-state reaction of formic acid (HCOOH) and oxygen on a Cu surface [8]. It was reported that the translational energy of desorbed CO_2 is approximately 0.10 eV and independent of the surface temperature. The measured CO_2 translational energy is much smaller than the activation energy of formate synthesis, which is 0.59 ± 0.05 eV, suggesting that internal modes, such as vibrational and rotational modes, should be excited in the desorbed CO_2. In this study, we therefore investigate the energy distribution of desorbed CO_2 as a formate decomposition product by means of *ab initio* calculations. We also show the importance of the van der Waals (vdW) correction in describing the adsorption and desorption processes of CO_2 on Cu surfaces[4]. From knowledge of desorbing product dynamics, we can deduce optimal conditions for the formate synthesis reaction through CO_2 hydrogenation.

The calculations were performed using a plane-wave pseudopotential code named "Simulation tool for Atom TEchnology (STATE)" [9,10]. Since the vdW correction is important to describe the adsorption and chemical reaction of inert molecules, we compare the Perdew-Burke-Ernzerhof (PBE) results and those obtained using vdW density functionals (vdW-DFs), i.e., the original vdW-DF (vdW-DF1), optB86b-vdW, and rev-vdW-DF2 functionals as implemented in the STATE code [11]. We performed *ab initio* molecular dynamics (AIMD) simulations starting from the transition state (TS) structure of the formate decomposition process to gas phase CO_2 and adsorbed H to evaluate the translational and internal (rotational and vibrational) energies of desorbed CO_2.

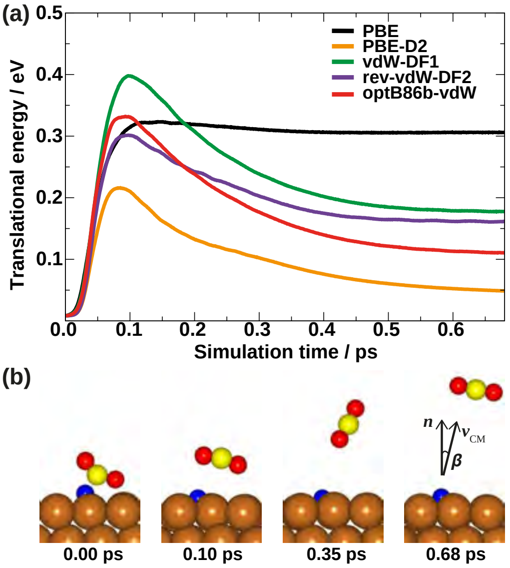

Fig. 1. a) Time evolution of the translational energy of desorbed CO_2 from formate decomposition calculated using PBE, PBE-D2, and vdW-DFs. (b) Representative snapshots from AIMD trajectory of CO_2 desorption.

We have investigated the minimum energy path of CO_2 hydrogenation into formate and the dynamics of formate decomposition into gas phase CO_2 and adsorbed hydrogen using density functional theory calculations. Based on the dynamics analysis of formate decomposition as shown in Fig. 1, the bending energy of desorbed CO_2 is twice larger than the translational energy. Since formate synthesis from CO_2 and H_2, the reverse reaction of the formate decomposition, is experimentally suggested to occur by the ER type mechanism, our results indicate that the reaction rate of formate synthesis can be enhanced if the bending vibrational mode of CO_2 is excited rather than the translational and/or stretching modes.

References

[1]. T. Hirakawa, Y. Uramoto, D. Mimura, A. Takeda, S. Yanagisawa, T. Ikeda, K. Inagaki, and Y. Morikawa, J. Phys. Chem. B, **121**, 164-173 (2017).

[2]. T. Hirakawa, Y. Uramoto, S. Yanagisawa, T. Ikeda, K. Inagaki, and Y. Morikawa, J. Phys. Chem. C, **121**, 19904-19914 (2017).

[3]. F. Muttaqien, H. Oshima, Y. Hamamoto, K. Inagaki, I. Hamada, and Y. Morikawa, Chem. Comm., **53**, 9222-9225 (2017).

[4]. F. Muttaqien, Y. Hamamoto, I. Hamada, K. Inagaki, Y. Shiozawa, K. Mukai, T. Koitaya, S. Yoshimoto, J. Yoshinobu, and Y. Morikawa, J. Chem. Phys., **147**, 094702-1-8 (2017).

[5]. S.-S. Tan, S. Yanagisawa, K. Inagaki, Y. Morikawa and M. B. Kassim, Phys. Chem. Chem. Phys., **19**, 25734-25745 (2017).

[6]. T. Ohta, H. Kizaki, and Y. Morikawa, J. Phys. Chem. C, **122**, 4172-4181 (2018).

[7]. P.-V. Bui, D. Toh, A. Isohashi, S. Matsuyama, K. Inagaki, Y. Sano, K. Yamauchi, and Y. Morikawa, Jpn. J. Appl. Phys., **57**, 055703-1-5 (2018).

[8]. J. Quan, T. Kondo, G. Wang, and J. Nakamura, Angew. Chem. Int. Edit., **56**, 3496-3500 (2017).

[9]. Y. Morikawa, Phys. Rev. B, **51**, 14802 (1995).

[10]. Y. Morikawa, K. Iwata, and K. Terakura, Appl. Surf. Sci. **169-170**, 11-15 (2001).

[11]. Y. Hamamoto, I. Hamada, K. Inagaki, and Y. Morikawa, Phys. Rev. B, **93**, 245440-1-9 (2016).

Study on an automatic derivation technique of first-principles effective model based on the many body electron theory

Hirofumi SAKAKIBARA

Department of Applied Physics and Mathematics,

Tottori University, Koyama-cho Minami, Tottori city, Tottori 680-8552

The automation of the derivation of low-energy models from fist-principles is one of the major purposes in condensed matter physics. The derivation of the Hubbard model, which is a minimal model for magnetisms and superconductivities driven by unconventional paring mechanisms, is very useful because the electron correlation effects can be accurately taken into account in such models. Therefore the automation possibly enables us to find novel magnetic/superconducting materials fully theoretically.

In the previous study, we have constructed a method to estimate Hubbard-type electron interactions denoted by U. We assume the equality between the screened interaction in full-orbital spaces and in model spaces, only consisting of target bands, to determine U. This constraint removes the double counting of screening effects between first-principles calculation and model calculations. We have named this method model-mapped RPA (mRPA) [1].

Here we explain more details of the mRPA. mRPA reconciles the two values; one is the "value" of the screened Coulomb interactions W from first-principles and the other is the screened interaction W_m from model calculation. The recently developed constrained random phase approximation (cRPA) is similar in its concepts, but actually different. Its "constraint" is the equality between the "operator", $W = W_{\mathrm{m}}$. This constraint leads to the equation $U=v/\{1-v(P - P_m)\}$, where v is the bare Coulomb interaction, P is the full-space polarization and P_m is the polarization among the model space [2]. Namely, cRPA actually calculate the expectation value of the operator $v/\{1-v(P - P_m)\}$. Therefore, the U_{mRPA} and U_{cRPA} are not necessarily equal to each other. Our previous report have shown that U_{cRPA}=2.0eV and U_{mRPA}=3.9eV in the single-band model of $\mathrm{HgBa_2CuO_4}$, which is a layered cuprate superconductor [1].

We have extended mRPA to apply to the multi-orbital system, because general systems require the multi-orbital degrees of freedom. Then the U becomes a matrix consists of four orbital legs. Generally, we cannot algebraically solve the equation $W=W_m$ in mRPA because W_m is a q-integral value denoted as $\Sigma U/(1-U\ P_m)$. However, since we can calculate W_m from a parameter set (U, U', J, J'), we can obtain the appropriate parameter set by some updating algorisms approaching the "solution" which satisfy the $W=W_m$. In the actual mRPA code, a simple recursive substitution algorism is implemented.

We have determined the interaction matrix U of two-orbital model in La_2CuO_4 and in $HgBa_2CuO_4$ by the extended mRPA. Because the d_{z^2} orbital is heavily mixes with the $d_{x^2-y^2}$ orbital in La_2CuO_4, the two-orbital model incorporating the d_{z^2} orbital is necessary [3]. In contrast, in $HgBa_2CuO_4$ the orbitals are less mixed implying such system can be describe a conventional single-orbital model [4].

Based on the value of U from mRPA, we have also performed many-body calculations based on the fluctuation exchange approximation (FLEX). FLEX considers the self-energy from the spin and the charge fluctuations, and can estimate the superconducting pairing driven by such fluctuations.

By substituting Green's functions with the self-energy to the linearized Eliashberg's equation, we estimate the theoretical measure λ of the transition temperature (T_c) of superconductivity, where λ reaches unity at $T=T_c$. From the results, it is revealed that the orbital mixture effect from the d_{z^2} orbital controls T_c [3,4] rather than the material dependence of U. This independency of U is caused by the fact that the total pairing strength saturates as the self-energy becomes sufficiently large. This picture is obtained in the parametric region where $U > 2$eV. Note that the hopping integrals between the nearest neighbor copper sites are estimated to be about 0.45eV in general cuprates superconductors. The other cuprates superconductors are expected to be in the region of $U > 2$eV.

References

[1] H. Sakakibara *et al*: J. Phys. Soc. Jpn. **86,** 044714 (2017).

[2] F. Aryasetiawan, M. Imada, A. Georges, G. Kotliar, S. Biermann, and A. I. Lichtenstein, Phys. Rev. B **70**, 195105 (2004).

[3] H. Sakakibara *et al.,* Phys. Rev. Lett. **105** 057003 (2010).

[4] H. Sakakibara *et al*, Phys. Rev. B **89**, 224505 (2014).

3.3 Strongly Correlated Quantum Systems

Numerical analysis for extotic quantum states in strongly correlated electron systems

Akihisa Koga
Department of Physics, Tokyo Institute of Technology, Meguro, Tokyo 152-8551

Strongly correlated electron systems with orbital degrees of freedom have attracted much interest. One of the intriguing examples is the series of the Mott insulators with a honeycomb structure such as $A_2\mathrm{IrO}_3$ ($A = \mathrm{Na, Li}$), and β-$\mathrm{Li_2IrO_3}$. In these compounds, a strong spin-orbit coupling for $5d$ electrons lifts the degeneracy in t_{2g} levels and the Kramers doublet plays an important role at low temperatures. Furthermore, there exists the orbital dependent hoppings due to the lattice structure. These result in the anisotropy in the exchange coupling between isospins, and the system can be regarded as the $s = 1/2$ Kitaev model [1, 2]. This should stimulate the extensive theoretical study for the Kitaev and related models. Recently, the compound α-$\mathrm{RuCl_3}$ with $4d$ electrons has been synthesized and fermionic response characteristic of the Kitaev model has been discussed. In general, in the $4d$ electron system, the spin-orbit coupling is not so large, comparing with the $5d$ electron system. Therefore, a simple question naturally arises how the finite spin-orbit interaction realizes interesting ground-state and low temperature properties. Furthermore, the above compounds show the magnetic order at low temperatures, and it is desired to clarify the stability of the spin liquid state in the correlated electron system with the orbital degeneracy.

Motivated by this, we have studied the spin-orbital models with the Kugel-Khomskii type superexchange interactions on the two-dimensional honeycomb lattice. Since this model is reduced to the Kitaev model in the large spin-orbit coupling limit (Kitaev limit), we can discuss how the disordered state, which is adiabatically connected to the spin liquid state in the Kitaev limit, competes with the magnetically ordered state naively expected. We first use the cluster mean-field theory with the exact diagonalization to determine the ground state phase diagram in the model (see Fig. 1). Furthermore, calculating the specific heat and entropy in terms of the thermal pure quantum state, we have discussed how thermodynamic properties characteristic of the Kitaev model appear in the intermediate spin-orbit coupling region [3].

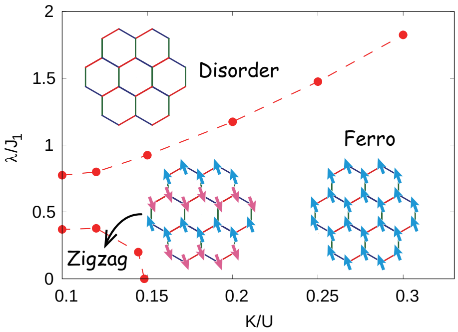

Figure 1: The ground state phase diagram of the spin-orbital model.

[C class 7000 (B); D class; 8000 (B)]

References

[1] A. Kitaev, Ann. Phys. **321**, 2 (2006).

[2] G. Jackeli and G. Khaliullin, Phys. Rev. Lett. **102**, 017205 (2009).

[3] A. Koga, S. Nakauchi, and J. Nasu, Phys. Rev. B **97**, 094427 (2018).

Study of correlated topological materials using many-variable variational Monte Carlo method

Takahiro Misawa
Institute for Solid State Physics, University of Tokyo
Kashiwa-no-ha, Kashiwa, Chiba 277-8581

Topological insulators that show exotic surface metallic states [1] have been attracted much attention because the topologically protected metallic surface states are expected to be useful for new generation devices. Recent theoretical and experimental studies have proven the existence of the topological *semimetals* [2] such as the Weyl semimetals and the topological Dirac semimetal. In these topological semimetals, although the bulk gap is zero and the point nodes such as the Weyl points or the Dirac points exist in the bulk state, the exotic surface states called Fermi arcs appear.

In this project, we study the quantum transport phenomena originating the exotic surface states in the topological semimetals by directly solving the time-dependent Schrödinger equations, which is given by

$$\mathrm{i}\frac{\partial\left|\phi(t)\right\rangle}{\partial t}=H(t)\left|\phi(t)\right\rangle, \tag{1}$$

where $|\phi(t)\rangle$ is a single Slater determinant and $H(t)$ is time-dependent Hamiltonian. To efficiently solve the time-dependent Schrödinger equations, we use the fourth-order Suzuki-Trotter decomposition [3, 4].

We first analyze the charge pumping in the disordered Weyl semimetal. To perform the charge pumping we introduce the time-dependent vector potentials $A_y(t)$ in y direction as follows:

$$T_y(t)=e^{\mathrm{i}A_y(t)}\times T_y, \tag{2}$$

$$A_y(t)=\frac{2\pi t}{L_yT}, \tag{3}$$

where T_y is the hopping matrix in y direction and L_y is the linear dimension in y direction. By introducing $A_y(t)$ in y direction, the charge pumping in x directions occurs if the Hall conductivity is finite. Actually in the clean limit, we confirm that the charge pumping ΔN is quantized [5, 6, 7] as follows:

$$\Delta N=2\Delta k\times\frac{L_z}{2\pi}, \tag{4}$$

where L_z is the linear dimension in z direction and Δk is the distance between Weyl points in the momentum space. We examine the effects of the disorders in the chemical potentials and show that charge pumping is robust against the disorders. Interestingly, the charge pumping is enhanced in the intermediate strength of the disorder, which is consistent with previous studies [8, 9, 10].

By using the same method, we analyze the quantum transport phenomena in the bilayer system of the ferromagnetic insulator and the topological Dirac semimetals. In this system, we show that the oscillating magnetic moment in the ferromagnetic insulator induces the spin and charge current in the topological Dirac semimetals. We also show that the induced charge current is governed by the topological nature and robust against the disorder.

These results show that real-time evolution of the wave functions is useful for analyzing the exotic quantum transport phenomena in the topological materials. The real-time evolution of the correlated quantum many-body system is possible based on the variation Monte Carlo method [11, 12]. By using the many-variable variational Monte Carlo method [13, 14], we are now examining the stability of the topological magnetic insulators (Chern insulator) in the correlated electron systems. We are also examining the quantum transport phenomena in the topological magnetic insulators by using the real-time evolution of the correlated many-body wavefunctions.

References

[1] M. Z. Hasan, C. L. Kane, Rev. Mod. Phys. **82**, 3045 (2010).

[2] A. Burkov, Nat. Mat. **15**, 1145 (2016).

[3] M. Suzuki, Commun. Math. Phys. **163**, 491 (1994).

[4] T. Nakanishi, T. Ohtsuki, T. Kawarabayashi, J. Phys. Soc. Jpn. **66**, 949 (1997).

[5] R. Shindou, N. Nagaosa, Phys. Rev. Lett. **87**, 116801 (2001).

[6] S. Murakami, New Journal of Physics **9**, 356 (2007).

[7] X. Wan, A. M. Turner, A. Vishwanath, S. Y. Savrasov, Phys. Rev. B **83**, 205101 (2011).

[8] C.-Z. Chen, J. Song, H. Jiang, Q.-f. Sun, Z. Wang, X. C. Xie, Phys. Rev. Lett. **115**, 246603 (2015).

[9] H. Shapourian, T. L. Hughes, Phys. Rev. B **93**, 075108 (2016).

[10] Y. Takane, J. Phys. Soc. Jpn. **85**, 124711 (2016).

[11] G. Carleo, F. Becca, M. Schiró, M. Fabrizio, Sci. Rep. **2**, 243 (2012).

[12] K. Ido, T. Ohgoe, M. Imada, Phys. Rev. B **92**, 245106 (2015).

[13] D. Tahara, M. Imada, J. Phys. Soc. Jpn. **77**, 114701 (2008).

[14] T. Misawa, S. Morita, K. Yoshimi, M. Kawamura, Y. Motoyama, K. Ido, T. Ohgoe, M. Imada, T. Kato, arXiv:1711.11418.

Numerical study of correlated electron systems with strong spin-orbit coupling

Yukitoshi MOTOME
Department of Applied Physics,
The University of Tokyo, Bunkyo, Tokyo 113-8656

We have theoretically studied intriguing properties originating from electron correlations and spin-orbit coupling. During this fiscal year (project number: H29-Ca-0060 and H29-Cb-0034), we have been making substantial progress on the following topics. We summarize the main achievements for each topic below.

(i) *Exotic magnetism and electronic states in spin-charge coupled systems*: We constructed a new effective spin model for the Kondo lattice model, on the basis of higher-order perturbation theory in terms of the spin-charge coupling [1]. The model includes the bilinear and biquadratic spin interactions in momentum space: the exchange interactions are characterized by specific wave numbers dictated by the Fermi surfaces. We demonstrated that the model well reproduces variety of peculiar magnetic orders, such as vortex crystals and skyrmion crystals. We also extended the study to the systems with the relativistic spin-orbit coupling and predicted the realization of unconventional skyrmions [2]. Another topic is the chiral soliton lattice in quasi-one-dimensional chiral magnets. To clarify the magnetic and electronic properties, we have studied a model explicitly including itinerant electrons. By Monte Carlo simulations at finite temperature, we revealed nonlinear magnetoresistance proportional to the soliton density [3]. We also found lock-in of the period of chiral soliton lattices at a particular set of values related with the Fermi wave number [4]. In addition, we studied the generation and control of exotic magnetism by supercurrent in heterostructures [5].

(ii) *Off-diagonal and nonreciprocal responses in parity broken systems*: We analyzed a model for e_g electron systems on a diamond structure, bearing AOsO$_4$ (A=K, Rb, and Cs) in mind [6]. We predicted possible band structures and magnetoelectric responses under various electronic orders that break spatial inversion symmetry. The results will be useful for identifying the unknown order parameters in AOsO$_4$. We also summarized the first-principles studies for honeycomb-monolayer transition metal trichalcogenides [7]. In addition, we studied bilayer and bulk cases [8]. Furthermore, we investigated the nonreciprocal spin Seebeck effect in antiferromagnets with asymmetric magnon dispersions [9]. We theoretically predicted spin rectification and directional dependence of the nonreciprocal spin Seebeck effect.

(iii) *Spin fractionalization in the Kitaev models*: We summarized our studies on spin dynamics at finite temperature in the Kitaev models, obtained by the newly-developed numerical techniques on the basis of Majorana fermion representation [10,11]. Comparing our results with those by inelastic neutron scattering for a candidate material α-$RuCl_3$, we found a good agreement in a wide range of energy scale and temperature [12]. We also studied thermal conductivities in the Kitaev model [13] and compared the results with experiments [14]. In addition, we studied a gas-liquid type phase transition on a hyperoctagon lattice [15], and phase transitions to chiral spin liquids on a hypernonagon lattice [16]. We also proposed a new mechanism for the Kitaev type anisotropic interactions in d^7 high-spin systems [17].

References

[1] S. Hayami, R. Ozawa, and Y. Motome, Phys. Rev. B **95** (2017) 224424. [*selected in Kaleidoscope*]

[2] S. Hayami and Y. Motome, preprint (arXiv:1803.01543).

[3] S. Okumura, Y. Kato, and Y. Motome, J. Phys. Soc. Jpn. **86** (2017) 063701.

[4] S. Okumura, Y. Kato, and Y. Motome, J. Phys. Soc. Jpn. **87** (2018) 033708.

[5] R. Takashima, Y. Kato, Y. Yanase, and Y. Motome, Phys. Rev. B **97** (2018) 081107(R).

[6] S. Hayami, H. Kusunose, and Y. Motome, Phys. Rev. B **97** (2018) 024414.

[7] Y. Sugita, T. Miyake, and Y. Motome, Phys. Rev. B **97** (2018) 035125 [*selected in Kaleidoscope*].

[8] Y. Sugita, T. Miyake, and Y. Motome, preprint Physica B: Cond. Matter, in press.

[9] R. Takashima, Y. Shiomi, and Y. Motome, preprint (arXiv:1804.03780).

[10] J. Yoshitake, J. Nasu, Y. Kato, and Y. Motome, Phys. Rev. B **96** (2017) 024438.

[11] J. Yoshitake, J. Nasu, and Y. Motome, Phys. Rev. B **96** (2017) 064433.

[12] S.-H. Do, S.-Y. Park, J. Yoshitake, J. Nasu, Y. Motome, Y. S. Kwon, D. T. Adroja, D. J. Voneshen, K. Kim, T.-H. Jang, J.-H. Park, K.-Y. Choi, and S. Ji, Nature Physics, **13** (2017) 1079.

[13] J. Nasu, J. Yoshitake, and Y. Motome, Phys. Rev. Lett. **119** (2017) 127204.

[14] Y. Kasahara, K. Sugii, T. Ohnishi, M. Shimozawa, M. Yamashita, N. Kurita, H. Tanaka, J. Nasu, Y. Motome, T. Shibauchi, and Y. Matsuda, preprint (arXiv:1709.10286), accepted for the publication in Phys. Rev. Lett.

[15] P. A. Mishchenko, Y. Kato, and Y. Motome, Phys. Rev. B **96** (2017) 125124.

[16] Y. Kato, Y. Kamiya, J. Nasu, and Y. Motome, Phys. Rev. B **96** (2017) 174409.

[17] R. Sano, Y. Kato, and Y. Motome, Phys. Rev. B **97** (2018) 014408.

Topological phase reduction and magnetoelectric effect in strongly-correlated electron systems with spin-orbit interaction

Norio KAWAKAMI
Department of Physics, Kyoto University,
Kitashirakawa, Sakyo-ku, Kyoto 606-8502

Spin-orbit interaction provides the possibility to manipulate the spin polarization of a material by applying electric fields as desired for spintronics, as well as the possibility to create an inverted gap in the band structure necessary for topologically nontrivial phases. Although many new phenomena can be expected, the interplay between spin-orbit interaction and the Coulomb interaction in strongly correlated materials is still not well understood.

Electron correlation can change the topological classification of a system. For example, Fidkowski and Kitaev have found that for a one-dimensional topological superconductor of class BDI, electron correlation changes the topological classification from Z to Z_8.

We have studied the topological classification of superconducting phases in a superlattice system composed of $CeCoIn_5$/$YbCoIn_5$ layers. We have found that in the case of quad-layer of $CeCoIn_5$ the strongly correlated system is topologically trivial, while eight pairs of helical edge modes are predicted at the non-interacting level. Thus, this system can serve as a test bed for the reduction of the topological classification. [1]

Also, we aimed at understanding the effect of the interplay between the spin-orbit interaction and electron correlation on anomalous transport such as the magnetoelectric effect. We have studied a periodic Anderson model including the Rashba spin-orbit interaction, which describes noncentrosymmetric f-electron materials such as $CePt_3Si$, using the combination of dynamical mean field theory and the numerical renormalization group to calculate transport properties with high precision. Our calculations demonstrate that while at low temperatures the magnetoelectric effect is small due to cancellation effects of bands with different spin polarization, at high temperatures, where f-electrons become localized due to strong interactions, the magnetoelectric effect is strongly enhanced. [2]

References

[1] Tsuneya Yoshida, Akito Daido, Youichi Yanase, and Norio Kawakami: Phys. Rev. Lett. **118** (2017), 147001.

[2] Robert Peters and Youichi Yanase, Phys. Rev. B **97** (2018), 115128.

Microscopic analysis of the vortex state in superconductors using the augmented quasiclassical equations with the Lorentz force, Kopnin force and slope in the density of state

Takafumi KITA
Department of Physics, Hokkaido University
Sapporo, Hokkaido 060-0810

We derived augmented Eilenberger equations that incorporate the following missing force terms: (i) the Lorentz force, (ii) the pair-potential gradient (PPG) force (or Kopnin force), and (iii) the pressure difference arising from the slope in the density of states (DOS). Using it, we studied the vortex-core charging due to the three force terms. This study have been performed to calculate the sign change of the flux-flow Hall coefficient microscopically. We required much memory due to the presences of the spatial inhomogeneity in the system.

The *vortex-core charging* in type-II superconductors has been pointed out to be related to the sign change of the flux-flow Hall conductivity [1], and numerous studies on the charging of a superconducting vortex have been carried out. However, the forces responsible for the charging of a superconducting vortex are not fully understood. This is because all the force terms used to describe charging in superconductors are missing from the standard Eilenberger equations (i.e., the quasiclassical equations of superconductivity) used to study superconductors in a magnetic field microscopically.

The existence of the Lorentz force acting on the supercurrent was first pointed out by London [2]. In 2001, the Lorentz force was microscopically recovered in augmented quasiclassical equations of superconductivity in the Keldysh formalism. The PPG force was first discussed by Kopnin [3]. In recent years, Arahata and Kato first included the Lorentz and PPG force terms in their augmented quasiclassical equations as an extension of the standard quasiclassical equations of superconductivity in the Keldysh formalism [6]. The charging mechanism of a superconducting vortex due to the pressure or chemical potential difference between the normal and superconducting states was first proposed by Khomskii and Freimuth [4]. They regarded the core as a normal region and considered its chemical potential difference from the surroundings due to the particle–hole asymmetry in the DOS. For the general case of the DOS, Khomskii and Kusmartsev have also given a formula for the chemical potential difference between the normal and superconducting states due to the slope in the DOS [7]. However, despite this, quasiclassical equations considering this pressure dependence have not yet been derived microscopically. Therefore, quasiclassical equations for superconductors still have room for improvement.

We perform numerical calculations for the isolated vortex systems of clean s-wave superconductors with a spherical Fermi surface based on the augmented Eilenberger equations. We assume the spin-singlet pairing

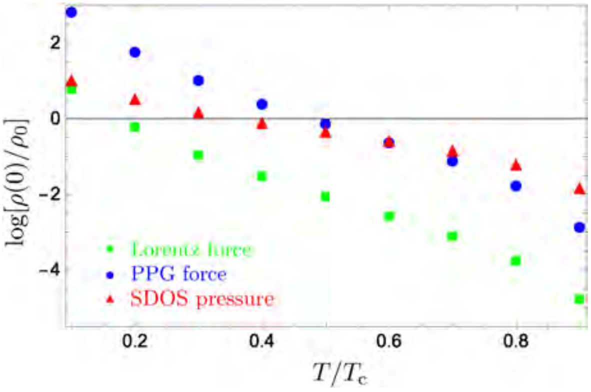

Figure 1: (Color online) Normalized charge density due to the Lorentz force (green square points), PPG force (blue circular points), and SDOS pressure (red triangular points) at the vortex center for $\lambda_0 = 5\xi_0$ as a function of temperature.

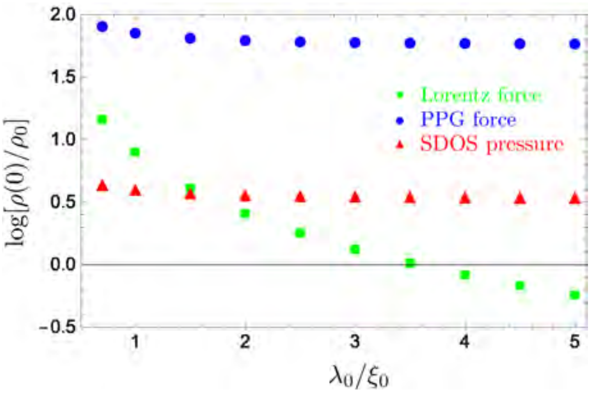

Figure 2: (Color online) Normalized charge density due to the Lorentz force (green square points), PPG force (blue circular points), and SDOS pressure (red triangular points) at the vortex center for $\lambda_0 = 5\xi_0$ as a function of λ_0 calculated for $T = 0.2T_c$.

without spin paramagnetism. The parameters of this system are the coherence length ξ_0, magnetic penetration depth λ_0, Thomas–Fermi screening length $\lambda_{\rm TF}$, quasiclassical parameter δ, and the smearing factor η in the advanced and retarded Green functions. We fixed the parameters to $\lambda_{\rm TF} = 0.01\xi_0$, $\delta = 0.01$, and $\eta = 0.01\Delta_0$. Figures 1 and 2 plot the logarithm of the charge density at the vortex center for $\lambda_0 = 5\xi_0$ as a function of temperature and for $T = 0.2T_c$ as a function of λ_0.

We observe that when the London penetration depth is much larger than the coherence length, the contribution of the Lorentz force to the vortex-core charge is negligibly small compared with that of the other forces, the contribution of the SDOS pressure becomes dominant near the transition temperature, and the contribution of the PPG force is so large that the other forces are negligible near absolute zero temperature. We also find that when the London penetration depth is about the same as the coherence length, the contribution of the Lorentz force to the core charge becomes substantial over the value of that of the SDOS pressure, but smaller than that of the PPG force. Thus, because the force that dominantly contributes to quantities may vary with the parameters of the materials, the temperature, the external field, and the system, we need to consider all three forces to study charging and transport phenomena such as the flux-flow Hall effect in type-II superconductors.

References

[1] S. J. Hagen, C. J. Lobb, R. L. Greene, M. G. Forrester, and J. H. Kang, Phys. Rev. B **41**, 11630 (1990).

[2] F. London, *Superfluids* (Dover, New York, 1961), Vol. 1, p. 56.

[3] N. B. Kopnin, J. Low Temp. Phys. **97**, 157 (1994).

[4] D. I. Khomskii and A. Freimuth, Phys. Rev. Lett. **75**, 1384 (1995).

[5] T. Kita, Phys. Rev. B **64**, 054503 (2001).

[6] E. Arahata and Y. Kato, J. Low. Temp. Phys. **175**, 364 (2014).

[7] D. I. Khomskii and F. V. Kusmartsev, Phys. Rev. B **46**,14245 (1992).

Microscopic analysis of cuprate superconductors in FLEX-S approximation

Takafumi KITA
Department of Physics, Hokkaido University
Sapporo, Hokkaido 060-0810

Fluctuation-exchange (FLEX) approximation [1] is a method that succeeds in describing various normal-state properties of high-T_c superconductors qualitatively [2]. In the FLEX approximation, we include the contributions of spin fluctuations caused by the Coulomb interaction into the self-energy. We can incorporate not only Feynman diagrams called "ring diagrams" which represent particle-hole scattering processes, but also those called "ladder diagrams" which represent particle-particle scattering processes in this framework.

Subsequently, Dahm and Tewordt performed a theoretical study on the superconducting phase of high-T_c's by incorporating only the particle-hole scattering processes [3]. Specifically, they incorporated some anomalous diagrams characteristic of the superconducting state besides the ring diagrams in the normal state. Their results agree with the properties of the cuprate superconductors which are measured in experiments qualitatively.

FLEX-S approximation [4] adopted in our study is an extension of the FLEX approximation. However, in this improved framework, we can consider both the normal-state and anomalous diagrams systematically beyond the ring and/or ladder approximations by introducing a symmetrized vertex. Therefore, we can incorporate more processes from spin fluctuations than the previous framework.

In our study, we calculated one particle Green's function for cuprate superconductors using both frameworks, i.e., Dahm-Tewordt framework and FLEX-S approximation. We compared the density-of-states between the two frameworks that can be obtained from the one particle Green's function. In both frameworks, we have to solve self-consistently the Dyson–Gor'kov equation and equation for the self-energy given in terms of the one-particle Green's function, and it took a lot of computational cost to perform these calculation. For this reason, we use parallel machine to perform these calculations, so we need to use the supercomputer in ISSP. In our calculation, we use two-dimensional Hubbard model, and the band dispersion $\epsilon_{\mathbf{k}}$ is given as follows

$$\begin{aligned}\epsilon_{\mathbf{k}} = -2t_0(\cos k_x + \cos k_y) + 4t_1 \cos k_x \cos k_y \\ +2t_2(\cos 2k_x + \cos 2k_y).\end{aligned}$$

t_0, t_1, and t_2 are the first, second, and third nearest neighbor hopping pareameter, and we choose $t_0 = 1, t_1 = 1/6$, and $t_2 = -1/5$ to represent the band structure of YBCO [5]. Moreover, we choose the on-site interaction parameter as $U = 6.5t_0$.

Figure 1 shows the density-of-states in the superconducting state calculated in both frameworks. In this figure, we present the result for dimensionless temperature $T/t_0 = 0.01$ and filling $n = 0.85$. The peak-to-peak values of both lines that represents the value of superconducting pair potential is 0.1 correspond to 10[meV], and it is consistent with the result from STM experiments [6]. However, we can't find a large difference between two lines in Fig.

1.

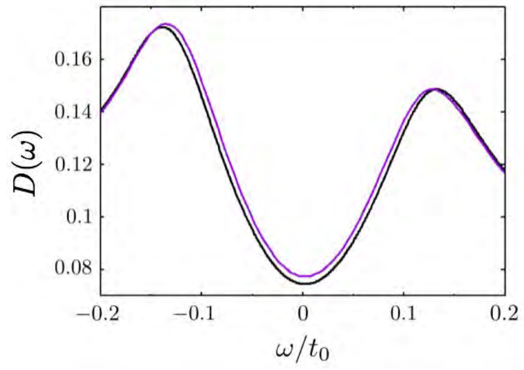

Figure 1: The black line is calculated by the FLEX-S approximation, and purple one is calculated in the framework that incorporates particle-hole scattering processes.

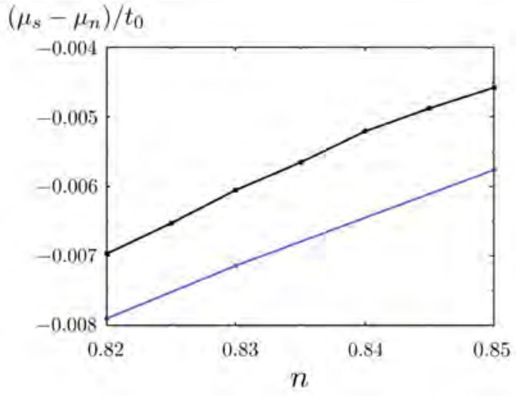

Figure 2: The black line is calculated in the FLEX-S approximation, and purple one is calculated in the framework that incorporates particle-hole scattering processes.

Figure 2 compares the chemical-potential difference between the normal and superconducting states calculated in the two frameworks using the same parameters at $T/t_0 = 0.01$. We can see that the difference between two results is about 10% at most. So we conclude that the ladder diagrams contribute little to the physical property obtained from one particle Green's function in this model.

This framework is important to obtain the precise temperature and filling dependence of various physical properties in the superconducting state concisely. We are planning to investigate the difference between these two frameworks to analyze two particle Green's function or calculate in other models such as the *d*-*p* model. From these, we aim to clarify various parameter dependences such as the temperature and filling ones more precisely, and we aim to find those physical properties which are overlooked in the previous work where the ladder diagrams were neglected.

References

[1] N. E. Bickers and D. J. Scalapino, Ann. Phys. (N.Y.) **193**, 206 (1989).

[2] H. Kontani, K. Kanki, and K. Ueda, Phys. Rev. B **59**, 15723 (1999).

[3] T. Dahm and L. Tewordt, Phys. Rev. Lett. **74**, 793 (1995).

[4] T. Kita, J. Phys. Soc. Jpn. **80**, 124704 (2011).

[5] T. Tanamoto, H. Kohno, and H. Fukuyama, J. Phys. Soc. Jpn. **61**, 1886 (1992).

[6] Ø. Fischer, M. Kugler, I. M. Aprile, C. Berthod, and C. Renner, Rev. Mod. Phys. **79**, 353 (2007).

Effect of Hund's coupling on non-local correlations in two-orbital Hubbard model

Yusuke Nomura

Department of Applied Physics

The University of Tokyo, Hongo 7-3-1, Bunkyo-ku, Tokyo 113-8656

In multi-orbital strongly correlated materials, it has been found that the Hund's coupling plays a crucial role in the electronic correlations [1]. The Hund's coupling has two effects. It influences the energy scale of the Mott gap, extending the metallic region when the filling is away from half-filling. At the same time, it suppresses the coherence temperature to form the fermi liquid. With these effects, there emerge strongly-correlated metals even when the system is away from Mott insulator. Such kind of strongly-correlated metals are called "Hund's metal".

So far, the effect of Hund's coupling in Hund's metal has mainly been studied by the dynamical mean-field theory (DMFT) [2]. However, the DMFT cannot capture the spatial correlations. Therefore, the effect of Hund's coupling on non-local correlations is still not understood well. In this study, we employ a cluster extension of DMFT [3], cellular DMFT, to study the interplay between Hund's coupling and spatial correlations.

For this purpose, we employ an improved continuous-time quantum Monte Carlo solver based on interaction expansion (CT-INT) [4]. The improved CT-INT makes use of efficient update schemes, "submatrix update" and "double-vertex update". With the improvements, applications to multi-orbital cluster DMFT become feasible [5]. We study the two-orbital Hubbard model on the square lattice using the 2x2 cluster. We set the size of Hund's coupling J_{H} to be $J_{\mathrm{H}}/U = 1/4$ with U begin the Hubbard interaction.

We first try the model with Ising-type interaction form, namely we neglect spin-flip and pair-hopping interactions. When the filling n is $n = 1.5$ ($n = 2$: half-filled), around $U/t = 16$ ($J_{\mathrm{H}}/t = 4$), we have found that the non-local correlations become significant. If we set $J_{\mathrm{H}} = 0$, we do not see such significant non-local correlations. Therefore, the significant non-local correlations are induced by Hund's coupling. This result suggests that the Hund's coupling strongly affects not only the onsite correlations but also the spatial correlations. The simulations with $SU(2)$ symmetric interactions are now under way.

References

[1] A. Georges, L. de' Medici, and J. Mravlje,

Annual Review of Condensed Matter Physics, **4**, 137 (2013)
[2] A. Georges, G. Kotliar, W. Krauth, and M. J. Rozenberg, Rev. Mod. Phys. **68**, 13 (1996)
[3] T. Maier, M. Jarrell, T. Pruschke, and M. H. Hettler, Rev. Mod. Phys. **77**, 1027 (2005)
[4] Y. Nomura, S. Sakai, and R. Arita, Phys. Rev. B **89**, 195146 (2014)
[5] Y. Nomura, S. Sakai, and R. Arita, Phys. Rev. B **91**, 235107 (2015)

Exotic phenomena induced by topology and strong correlations

Tsuneya YOSHIDA
Department of Physics, Kyoto University,
Kitashirakawa, Sakyo-ku, Kyoto 606-8502

In these years, topological perspective on condensed matter has increased its importance. One of the significant issues of this field is to understand the correlation effects on topological insulators/superconductors where novel phenomena are expected due to combination of these two effects. In particular, it is found that electrons correlations induce the reduction of topological classifications; only eight topologically distinct phases are allowed under the electron correlations for one-dimensional topological superconductors of symmetry class BDI, while infinite number of topologically distinct phases are allowed in the absence of correlations.

This remarkable phenomenon induced by electron correlations is extensively studied in these several years. In spite of the extensive studies, the reduction has not been well understood. In particular, the following questions remain unsolved: (i) what happens in the bulk when the reduction occurs for edges?; (ii) In which systems can one observe the reduction in experiments? In this project, we have addressed these questions.

Firstly, in order to understand bulk behaviors, we have carried out numerical simulation of the reduction phenomena for a weak-topological insulator in two dimensions. Our analysis based on real-space dynamical mean-field theory combined with continuous-time quantum Monte Carlo have elucidated that all of the gapless edge modes are gapped out without symmetry breaking while the bulk remains a band insulator characterized with the winding number w=4. This result indicates that a gapped Mott insulator emerges only around the boundary.

Secondly, we have addressed theoretical proposal of candidate materials of the reduction. Specifically, we have pointed out that the superlattice systems composed of CeCoIn5/YbCoIn5 can be a promising platform for the reduction of topological classification, ZxZ to ZxZ$_8$; the all of the gapless edge modes are gapped out without symmetry breaking when the number of Ce-layer is multiple of four.

References

[1] Tsuneya Yoshida, Norio Kawakami: Phys. Rev. B **95** (2017), 045127.

[2] Tsuneya Yoshida, Akito Daido, Youichi Yanase, and Norio Kawakami: Phys. Rev. Lett. **118** (2017), 147001.

Numerical Studies on the Superconductivity in Systems with Coexisting Wide and Narrow Bands

KAZUHIKO KUROKI
Department of Physics, Osaka University
1-1 Machikaneyama, Toyonaka, Osaka, 560-0043, Japan

In this report, we present two of the studies, related to superconductivity due to electron correlation, performed in our group in 2017 fiscal year using the supercomputer at ISSP.

HIGH T_c SUPERCONDUCTIVITY ARISING FROM WIDE AND INCIPIENT NARROW BANDS

An ideal situation for realizing high-T_c superconductivity is to have strong pairing interaction and light electron mass simultaneously, but strong pairing interaction usually induces heavy effective mass. In ref.[1], we proposed that high-T_c superconductivity is possible in Hubbard-type systems (with the on-site U) having wide and narrow bands, where light effective mass and strong pairing interaction is realized when the Fermi level sits in the vicinity of, but does not intersect, the narrow band (i.e., the incipient narrow band) (Fig.1). The two-leg Hubbard ladder with diagonal hoppings, a model for the ladder-type cuprates, was studied as a system in which such a situation is realized, where a possible occurrence of extremely high T_c was suggested. More recently, the so-called diamond chain model, which has a flat band and two dispersive bands when a certain condition is satified, was studied using DMRG, and there it was shown that superconductivity is strongly enhanced when the Fermi level sits in the vicinity of, but not within the flat band[2]. Motivated by the study in ref.[2], in 2017 fiscal year, we have extended the study of ref[1], showing that this high-T_c mechanism works in a variety of systems that consist of wide and incipient narrow (or flat) bands, such as the diamond lattice, three-leg ladder, and the crisscross ladder. We have applied the fluctuation exchange approximation to the Hubbard model on these lattices, and have shown that superconductivity is strongly enhanced when the Fermi level sits close to the narrow band[3](Fig.2). This shows the generality of the mechanism of high-Tc superconductivity originating from wide and incipient narrow bands.

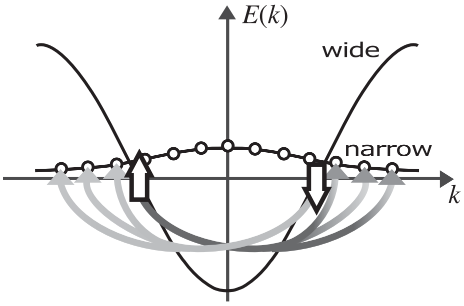

FIG. 1. Schematic image of pair scattering processes in systems with wide and incipient narrow bands

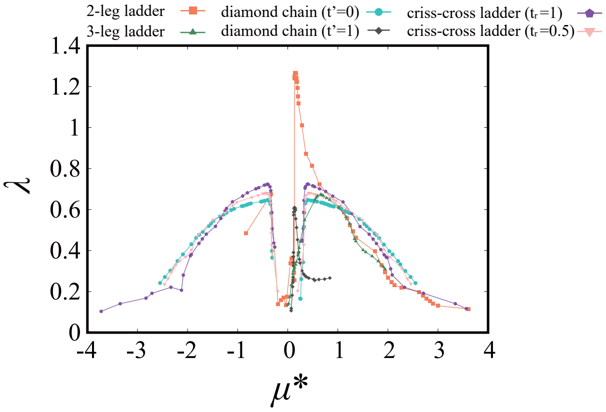

FIG. 2. Eigenvalue of the Eliashberg equation for various systems with wide and flat bands. They are plotted as functions of the chemical potential measured from the flat band energy. The on-site U is taken as $U = 6t$, and the temperature is fixed at $0.05t$, where t is the nearest neighbor hopping.

WIDE AND INCIPIENT NARROW BANDS IN RUDDLESDEN-POPPER BILAYER COMPOUNDS ORIGINATING FROM "HIDDEN LADDERS"

In reality, it is very difficult to control carrier doping in ladder-type cuprates. As a way to realize in actual materials the coexising wide and incipient narrow band systems mentioned in the previous section, we have introduced a concept of " hidden ladder " electronic structure in the bilayer Ruddlesden-Popper compounds, where anisotropic d-orbitals give rise to ladder-like elec-

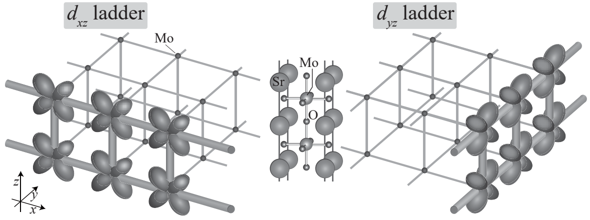

FIG. 3. Schematic image of the hidden ladders in RP327 bilayer systems.

tronic structures[4](Fig.3). Namely, considering the case in which t_{2g} orbitals form the bands crossing (or lie near) the Fermi level, an electron in the $d_{xz/yz}$ orbital selectively hops in the x/y direction as well as in the z direction normal to the bilayer. This means that the $d_{xz/yz}$ orbitals form ladders with x/y and z directions being the leg and rung directions, respectively. Furthermore, considering that the best situation for superconductivity in the ladder-type cuprates occurs for about 30 percent electron doping from half-filling[1], we expect that materials with two electrons per three t_{2g} orbitals (d^2 configuration) should bring about the ideal situation, where the Fermi level sits in the vicinity of the narrow-band edge without large amount of carrier doping. Hence we expect that $Sr_3Mo_2O_7$ and $Sr_3Cr_2O_7$ are good candidates, and this is indeed confirmed from first principles band calculation. We have performed fluctuation exchange study on a 6 orbital model that is derived from the first principles band structure, and proposed the possibility of high-T_c superconductivity in these materials.

[1] K. Kuroki, T. Higashida, and R. Arita, Phys. Rev. B **72**, 212509 (2005).
[2] K. Kobayashi *et al.*, Phys. Rev. B **94**, 214501 (2016).
[3] K. Matsumoto, D. Ogura, and K. Kuroki, Phys. Rev. B **97**, 014516 (2018).
[4] D. Ogura, H. Aoki, and K. Kuroki, Phys. Rev. B **96**, 184513 (2017).

Two-channel Kondo effect and multipole susceptibility

Takashi HOTTA
Department of Physics, Tokyo Metropolitan University
1-1 Minami-Osawa, Hachioji, Tokyo 192-0397

In this research, we have analyzed a seven-orbital impurity Anderson model hybridized with Γ_8 conduction electrons for the case with three local f electrons corresponding to a Nd^{3+} ion by employing a numerical renormalization group technique [1, 2]. The model Hamiltonian is given by

$$\begin{aligned} H &= \sum_{\mathbf{k},\mu,\tau} \varepsilon_{\mathbf{k}} c^{\dagger}_{\mathbf{k}\mu\tau} c_{\mathbf{k}\mu\tau} + \sum_{\mathbf{k},\mu,\tau} V(c^{\dagger}_{\mathbf{k}\mu\tau} f_{a\mu\tau} + \text{h.c.}) \\ &+ H_{\text{loc}}, \end{aligned} \quad (1)$$

where $\varepsilon_{\mathbf{k}}$ is the dispersion of a Γ_8 conduction electron with wave vector $\mathbf{k}$, $c_{\mathbf{k}\mu\tau}$ denotes the annihilation operator of a Γ_8 conduction electron, μ distinguishes the cubic irreducible representation, Γ_8 states are distinguished by $\mu = \alpha$ and β, while Γ_7 and Γ_6 states are labeled by $\mu = \gamma$ and δ, respectively, τ is the pseudospin which distinguishes the degeneracy concerning the time-reversal symmetry, $f_{j\mu\tau}$ indicates the annihilation operator of a localized f electron in the bases of (j, μ, τ), j is the total angular momentum, $j = 5/2$ and $7/2$ are denoted by "a" and "b", respectively, V is the hybridization between conduction and localized electrons, and H_{loc} denotes the local f-electron term. In the present case, we consider the hybridization between Γ_8 conduction electrons and the Γ_8 quartet of $j = 5/2$.

The local term, H_{loc}, is given by

$$\begin{aligned} H_{\text{loc}} &= \sum_{j,\mu,\tau} (\lambda_j + B_{j,\mu} + E_f) f^{\dagger}_{j\mu\tau} f_{j\mu\tau} \\ &+ \sum_{j_1 \sim j_4} \sum_{\mu_1 \sim \mu_4} \sum_{\tau_1 \sim \tau_4} I^{j_1 j_2, j_3 j_4}_{\mu_1 \tau_1 \mu_2 \tau_2, \mu_3 \tau_3 \mu_4 \tau_4} \\ &\times f^{\dagger}_{j_1 \mu_1 \tau_1} f^{\dagger}_{j_2 \mu_2 \tau_2} f_{j_3 \mu_3 \tau_3} f_{j_4 \mu_4 \tau_4}, \end{aligned} \quad (2)$$

where $\lambda_a = -2\lambda$, $\lambda_b = (3/2)\lambda$, λ is the spin-orbit coupling of f electron, $B_{j,\mu}$ denotes the CEF potential energy, E_f indicate the f-electron level, and I denotes the Coulomb interactions between f electrons.

The Coulomb interaction I is expressed with the use of four Slater-Condon parameters, F^0, F^2, F^4, and F^6. Although the Slater-Condon parameters of a material should be determined from experimental results, here we simply set the ratio as $F^0/10 = F^2/5 = F^4/3 = F^6 = U$, where U is the Hund rule interaction among f orbitals. The CEF potentials for f electrons from ligand ions are given in the table of Hutchings for the angular momentum $\ell = 3$. For a cubic structure with O_{h} symmetry, CEF parameters are expressed by two CEF parameters, B_4^0 and B_6^0. Following the traditional notation, we define B_4^0 and B_6^0 as $B_4^0 = Wx/F(4)$ and $B_6^0 = W(1-|x|)/F(6)$, respectively, where x specifies the CEF scheme for the O_{h} point group, while W determines the energy scale for the CEF potential. We choose $F(4) = 15$ and $F(6) = 180$ for $\ell = 3$.

Now, we consider the case of $n = 3$ by appropriately adjusting the value of E_f. As U denotes the magnitude of the Hund rule interaction among f orbitals, it is reasonable to set $U = 1$ eV. The magnitude of λ varies between 0.077 and 0.36 eV depending on the type of lanthanide ions. For a Nd^{3+} ion, λ is $870-885$ cm^{-1}. Thus, we set $\lambda = 0.11$ eV. Finally, the magnitude of W is typically of the order of millielectronvolts, although it depends on the

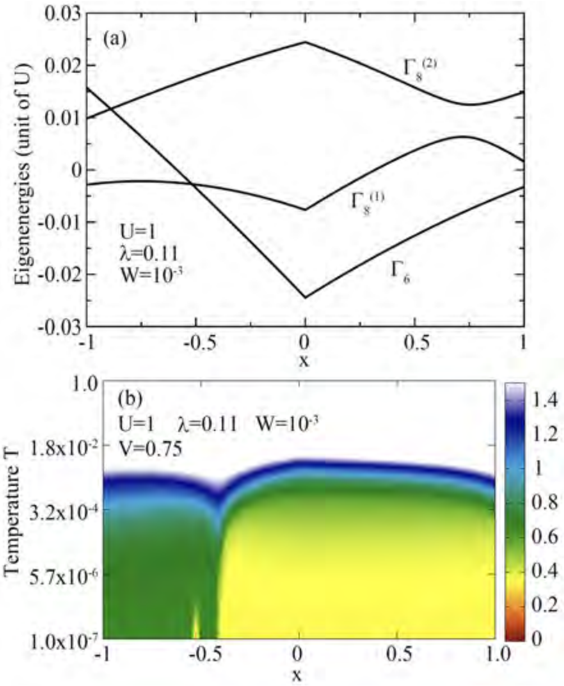

Figure 1: (a) Low-lying eigenenergies of $H_{\rm loc}$ versus x for $n = 3$. (b) Contour color map of the entropy on (x, T) plane for $W = 10^{-3}$.

material. Here, we simply set $|W| = 10^{-3}$ eV.

In Fig. 1(a), we depict curves of ten low-lying eigenenergies of $H_{\rm loc}$ for $n = 3$ since the ground-state multiplet for $W = 0$ is characterized by $J = 9/2$, where J denotes the total angular momentum of multi-f-electron state. We appropriately shift the origin of the energy to show all the curves in the present energy range. We emphasize that the results are almost the same as those of the *LS* coupling scheme. For the case of $W > 0$, we find the $\Gamma_8^{(1)}$ ground state for $x \leq -0.5$, while the Γ_6 ground state is observed for $x \geq -0.5$. However, for $W < 0$, the Γ_6 ground state appears only in the vicinity of $x = -1.0$. For the wide range of $-0.9 < x \leq 1$, we obtain another $\Gamma_8^{(2)}$ ground state.

In this study, we analyze the model by employing a numerical renormalization group (NRG) method. We introduce a cut-off Λ for the logarithmic discretization of the conduction band. Owing to the limitation of computer resources, we keep M low-energy states. Here, we use $\Lambda = 5$ and $M = 4,000$. In the following calculations, the energy unit is D, which is a half of the conduction band width. Namely, we set $D = U = 1$ eV in this calculation. In the NRG calculation, the temperature T is defined as $T = \Lambda^{-(N-1)/2}$ in the present energy unit, where N is the number of renormalization steps.

In Fig. 1(b), we show the contour color map of the entropy for $W = 10^{-3}$ and $V = 0.75$. To visualize precisely the behavior of entropy, we define the color of the entropy between 0 and 1.5, as shown in the right color bar. We immediately notice that an entropy of $\log 2$ (green region) appears at low temperatures for $-1.0 < x < -0.4$, while an entropy of $0.5 \log 2$ (yellow region) is found for $-0.4 < x < 1.0$. The region with an entropy of $0.5 \log 2$ almost corresponds to that of the Γ_6 ground state in comparison with Fig. 1, although we find a small difference between them around $x \sim 0.5$. The residual entropies, $0.5 \log 2$ and $\log 2$, are eventually released at extremely low temperatures in the numerical calculations. Approximately at $x = -0.5$, the release of an entropy of $\log 2$ seems to occur at relatively high temperatures. This is considered to be related with the accidental degeneracy of Γ_6 and $\Gamma_8^{(1)}$ states. In any case, the details on the entropy behavior at low temperatures will be discussed elsewhere in the future.

In summary, we have found the two-channel Kondo effect in the seven-orbital impurity Anderson model hybridized with Γ_8 conduction electrons for the case of $n = 3$ with the local Γ_6 ground state. In near future, we expect that the two-channel Kondo effect will be discovered in Nd 1-2-20 compounds.

References

[1] T. Hotta, J. Phys. Soc. Jpn. **86**, 083704 (2017).

[2] T. Hotta, Physica B **536C**, 203-210 (2018).

Numerical study on interplay between stripes and electron-phonon interactions in the Hubbard model

Takahiro OHGOE

Department of Applied Physics, The University of Tokyo,
7-3-1 Hongo, Bunkyo-ku, Tokyo 113-0033

Since the discovery of high- T_c cuprates, many experiments have been performed to unveil its mechanism and revealed its rich and complex physics. Especially in the underdoped region, exotic phenomena such as pseudogap or stripe order were observed and they are still intensively studied both experimentally and theoretically. Owing to the recent advancements of the scanning tunneling microscope (STM) and X-ray experiments, charge orders have been widely observed in the underdoped region of several families of high-T_c cuprates, establishing their presence as a universal feature [1].

In our recent work [2], we studied the stripe states in the Hubbard model by using the many-variable variational Monte Carlo (mVMC) method. As a result, we found that several stripes with different periodicities are severely competing especially in the underdoped region. Furthermore, we found that the ground states are stripe states instead of homogeneous superconducting state for the doping concentration $0.1 \lesssim \delta \lesssim 0.3$. However, the electron-phonon interactions are neglected and its roles on stripes remains elusive.

In this study, we studied the effect of electron-phonon interactions on the competition between stripe states and homogeneous states. To this purpose, we used the extended VMC method for electron-phonon coupled systems which we proposed [3]. As a result, we found that electron-phonon interactions with realistic phonon frequencies do not change the physical quantities such as spin/charge structure factors so much. On the other hand, it has been turned out that the electron-phonon interactions can change the ground states from stripe states to homogeneous states. In this study, we considered the particular modes of phonons individually. The more realistic analysis based on fully ab-initio electron-phonon interactions will be reported elsewhere.

References

[1] R. Comin and A. Damascelli, Annu. Rev. Condens. Matter Phys. **7**, 369 (2016)

[2] K. Ido, T. Ohgoe and M. Imada, Phys. Rev. B. **97**, 045138 (2018)

[3] T. Ohgoe and M. Imada, Phys. Rev. B **89**, 195139(2014)

Quantum Monte Carlo approach to local electronic correlations in unconventional superconductors

Shintaro HOSHINO
Department of Physics, Saitama University, Saitama 338-8570, Japan

Unconventional superconductivity in strongly correlated electron systems has been one of the central issues in condensed matter physics due to their rich physical properties and presence in a wide range of materials with p, d, f electrons. Fullerene-based superconductors are typical cases which show unconventional superconductivity, where the Mott insulator phase is located near superconducting phase [1]. Since the symmetry of pairing state is identified as s-wave, the local electronic correlations are capable to describe its physical properties which are still different from that of conventional BCS superconductors. For A_3C_{60}, the three electrons are doped per fullerene molecule. The underlying mechanism for superconductivity has been clarified as an effectively sign-reversed Hund's coupling. With this antiferromagnetic Hund coupling, the low-spin state is favored instead of high-spin state for usual Hund's rule coupling. Recent experiments show the presence of the anomalous metalic state [2]. Once electrons are localized in the Mott phase, the electron-phonon coupling leads to the defomation of the fullerene molecule, which has been detected by the IR spectroscopy. On the other hand, the metalic regime show a neary spherical shape. Interestingly, in the metallic regime close to the Mott phase, the fulleren molecule is detected to be deformed, which is called the Jahn-Teller metal [2], as distinct from the above two cases.

As a microscopic origin for the Jahn-Teller metal, we have theoretically proposed the spontaneous orbital-selective Mott transition [6] using the dynamical mena-field theory combined with quantum Monte Carlo method (DMFT+CTQMC) [3, 4]. We have further clarified the characteristics of this phase based on the realistic band structures derived in Ref. [5]. It is found that once the system enters into the Jahn-Teller metal phase, the strongly anisotropic conductivity appears [7]. Recently, using the supercomputer in ISSP, the University of Tokyo, the phase diagram for the doping regime has also been mapped out by means of the DMFT+CTQMC. For a strong coupling regime, the orbital order that breaks original cubic symmetry has been found. The supercondcuting region shrinks by tuning the number of the doped electrons from three toward two per fullerene. At the filling number two, the low-spin Mott insulator is realized. These results would be useful to explore the pressure and carrier number dependences experimentally.

References

[1] Y. Takabayashi et al., Science **323**, 1585 (2009).

[2] R.H. Zadik et al., Sci. Adv. **1**, e1500059 (2015).

[3] P. Werner et al., Phys. Rev. B **74**, 155107 (2006).

[4] E. Gull et al., Rev. Mod. Phys. **83**, 349 (2011).

[5] Y. Nomura, K. Nakamura and R. Arita, Phys. Rev. B **85**, 155452 (2012).

[6] S. Hoshino and P. Werner, Phys. Rev. Lett. **118**, 177002 (2017).

[7] S. Hoshino, R. Arita and P. Werner, talk at JPS March Meeting (2018).

Theoretical study of strong correlations in $Cd_2Os_2O_7$

Hiroshi Shinaoka
Department of Physics, Saitama University, 338-8570, Japan

The pyrochlore oxide $Cd_2Os_2O_7$ is one of the few compounds whose low-T magnetic structure has been experimentally determined among a number of magnetic $5d$ pyrochlore oxides. Os^{5+} ions have a $5d^3$ configuration, where t_{2g} is half-filled. This compound exhibits a magnetic transition at $T \simeq 227$ K accompanied by a change of the temperature dependence of the resistivity from metallic behavior to insulator one [1]. The low-T magnetic structure was identified as the so-called all–in–all–out magnetic oder by resonant X-ray scattering [2]. Then, this was supported by a first-principles study based on local-density-approximation (LDA) + U method [3]. The LDA+U calculations indicate that the metal-insulator transition is a Lifshitz transition driven by the emergence of the magnetic order. However, there has been no finite-T first-principles calculations for the compound. Thus, the origin of the finite-T transition still remain to be solved.

In this project, we performed a finite-T first-principles calculations based on the dynamical mean-field theory (DMFT). We constructed a three-orbital tight-binding model for the t_{2g} manifold projected on the maximally localized Wannier functions. We employed a first-principles code, Quantum ESPRESSO, for constructing the maximally localized Wannier functions in the two-component formalism. In the DMFT calculations, we solved quantum impurity problems by the continuous-time quantum Mote Carlo method using the current state-of-the-art implementation [4].

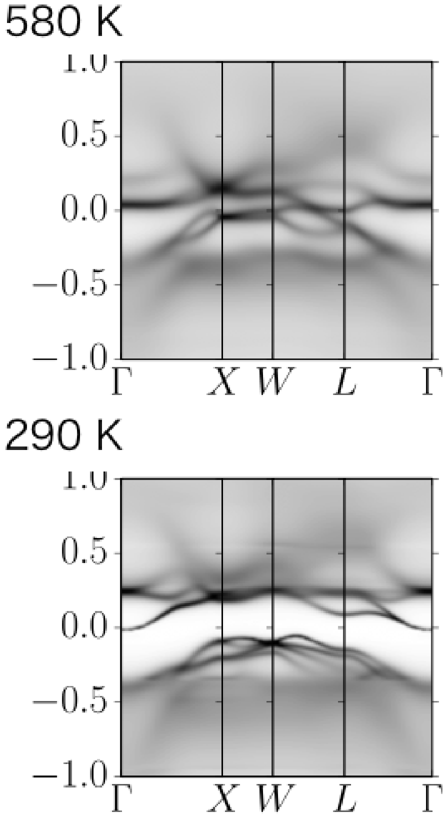

Figure 1: Momentum-resolved spectrum $A(k, \omega)$ computed with $U = 2$ eV.

Figure 1 shows the computed momentum-resolved spectrum function $A(k, \omega)$ at $U = 2$ eV for different temperatures T. The all–in–all–out magnetic order emerges at low T. Below the magnetic transition temperature, the quasi-particle bands are split and the spectrum is gapped out. This is consistent with the scenario of the Lifshitz transition. The quasi-particle bands survive down to the lowest T computed, being in a clear contrast to the Mott nature of the insulating pyrochlore oxides [5].

The above results were obtained in a collaboration with Y. Nomura, T. Kondo and M.

Nakayama.

References

[1] For a review, Z. Hiroi, J. Yamaura, T. Hirose, I. Nagashima, and Y. Okamoto, APL Materials **3**, 041501 (2015).

[2] J. Yamaura *et al.*, Phys. Rev. Lett. **108**, 247205 (2012).

[3] H. Shinaoka, T. Miyake, and S. Ishibashi, Phys. Rev. Lett. **108**, 247204 (2012).

[4] H. Shinaoka, E. Gull, P. Werner, Computer Physics Communications **215**, 128 (2017).

[5] H. Shinaoka, S. Hoshino, M. Troyer, and P. Werner, PRL **115**, 156401 (2015).

Dynamical mean-field calculations of electronic states and multipolar fluctuations in strongly correlated electron systems

Junya OTSUKI
Department of Physics, Tohoku University, Sendai 980-8578

Interesting magnetic properties are often observed in transition-metal and rare-earth compounds. Those includes orbital ordering in $3d$ electron systems and multipolar ordering in $4f$ electron systems. For theoretical descriptions of those peculiar ordered states, strong electronic correlations in the atomic orbitals need to be taken into account. For this reason, the dynamical mean-field theory (DMFT) gives a good starting point in studies of long-range ordering observed in strongly correlated electron materials [1].

Here, we give a brief description of our computation scheme based on the DMFT implemented on top of first-principles calculations. We first perform DFT calculations within LDA/GGA using `WIEN2k` package on a local computer. The Bloch states are projected to Wannier orbitals using `DFTTools` [2] of `TRIQS` library [3]. An effective lattice Hamiltonian is thus defined. Electronic correlations in a specific orbitals ($4f$ orbital in the case with rare-earth materials) are incorporated through a local self-energy $\Sigma(i\omega_n)$ computed in an effective Anderson impurity problem within DMFT. In actual computation, we applied the Hubbard-I approximation in the strong-coupling regime using an exact diagonalization library, `pomerol` [4], and a `triqs`-converter, `pomerol2triqs1.4` [5]. The correlated band structure $A(\boldsymbol{k}, \omega)$ is obtained in the procedure thus above.

To discuss long-range ordering, we compute the static susceptibilities by solving the Bethe-Salpeter (BS) equation. Since the susceptibilities generally have four orbital indices, it is essentially impractical to compute the full orbital dependence in d or f orbitals without special treatment of the vertex part in the BS equation.

We derived a simplified BS equation which is valid in the strong-coupling regime [6]. We analytically demonstrated that the equation gives kinetic exchange interaction in the Hubbard model and the RKKY interaction in the periodic Anderson model. Practically, the equation requires only a partial information of the vertex part, and hence is possible to treat full orbital dependence of susceptibilities in d and f electron systems. This equation provides a practical way to access multipolar ordering in first-principles-based calculations.

References

[1] G. Kotliar *et al.*, Rev. Mod. Phys. **78**, 865 (2006).

[2] M. Aichhorn *et al.*, Comp. Phys. Comm. **204**, 200 (2016).

[3] O. Parcollet *et al.*, Comp. Phys. Comm. **196**, 398 (2015).

[4] A. E. Antipov, I. Krivenko, and S. Iskakov, `http://doi.org/10.5281/zenodo.825870`

[5] `https://github.com/j-otsuki/pomerol2triqs1.4`

[6] J. Otsuki, K. Yoshimi, and H. Shinaoka, in preparation.

Skyrmion crystal phase in itinerant magnets with spin-orbit coupling

Satoru Hayami
Department of Physics, Hokkaido University, Sapporo, 060-0810

Noncoplanar magnetic textures have attracted great interest in condensed matter physics, as they often lead to topologically nontrivial quantum states and related intriguing phenomena. Such noncoplanar magnetic orders have been extensively studied in noncentrosymmetric systems where the spin-orbit coupling plays an essential role. For example, skyrmion crystals with noncoplanar spin textures are stabilized in noncentrosymmetric crystals under an applied magnetic field. These skyrmion crystals are categorized according to their vorticity and helicity: a Bloch-type skyrmion with the helicity $\pm\pi/2$ in chiral magnets with the Dresselhaus-type spin-orbit coupling in Fig. 1(a) and a Néel-type one with the helicity 0 or π in polar magnets with the Rashba-type spin-orbit coupling in Fig. 1(b).

In this project, we investigate how the interplay between the spin-orbit coupling and spin-charge coupling in magnetic conductors affects the formation of noncoplanar magnetic textures [1]. To this end, we begin with a Kondo lattice model with the spin-orbit coupling on a square lattice in polar systems. The Hamiltonian is given by

$$\begin{aligned}\mathcal{H} &= \sum_{\mathbf{k}\sigma}(\varepsilon_{\mathbf{k}}-\mu)c^{\dagger}_{\mathbf{k}\sigma}c_{\mathbf{k}\sigma} + J_{\mathrm{K}}\sum_{\mathbf{kq}}\mathbf{s}_{\mathbf{k}+\mathbf{q}}\cdot\mathbf{S}_{\mathbf{q}} \\ &+ \sum_{\mathbf{k}}\mathbf{g}_{\mathbf{k}}\cdot c^{\dagger}_{\mathbf{k}\sigma}\boldsymbol{\sigma}_{\sigma\sigma'}c_{\mathbf{k}\sigma'}, \qquad (1)\end{aligned}$$

where $c^{\dagger}_{\mathbf{k}\sigma}$ ($c_{\mathbf{k}\sigma}$) is a creation (annihilation) operator of an itinerant electron at wave number $\mathbf{k}$ and spin σ. The first term in Eq. (1) represents the kinetic energy of itinerant electrons where $\varepsilon_{\mathbf{k}}$ is the energy dispersion and μ is the chemical potential. The second term represents the spin-charge coupling between itinerant electron spins and localized spins where $\boldsymbol{s}_{\boldsymbol{k}+\boldsymbol{q}} = \sum_{\sigma\sigma'}c^{\dagger}_{\mathbf{k}\sigma}\boldsymbol{\sigma}_{\sigma\sigma'}c_{\mathbf{k}+\mathbf{q}\sigma'}$, $\boldsymbol{\sigma} = (\sigma^x, \sigma^y, \sigma^z)$ is the vector of Pauli matrices, $\mathbf{S}_{\mathbf{q}}$ is the Fourier transform of a localized spin $\mathbf{S}_i$ at site i with the fixed length $|\mathbf{S}_i| = 1$, and J_{K} is the exchange coupling constant (the sign of J_{K} is irrelevant owing to the classical spins). The third term in Eq. (1) represents the antisymmetric spin-orbit coupling, which originates from the atomic spin-orbit coupling in noncentrosymmetric systems. In the present model, this term represents the Rashba-type spin-orbit coupling: $\mathbf{g}_{\mathbf{k}} = (g^x_{\mathbf{k}}, g^y_{\mathbf{k}}) \propto (\sin k_y, -\sin k_x)$, which is induced by the mirror symmetry breaking with respect to the square-lattice plane.

Instead of directly examining the ground state of the model in Eq. (1), we here extract important magnetic contributions by deriving an effective spin model, whose Hamiltonian is summarized as

$$\begin{aligned}\mathcal{H} &= -2\sum_{\eta}\sum_{\alpha\beta}J^{\alpha\beta}_{\eta}S^{\alpha}_{\mathbf{Q}_\eta}S^{\beta}_{-\mathbf{Q}_\eta} \\ &- 2i\sum_{\eta}\mathbf{D}_{\eta}\cdot(\mathbf{S}_{\mathbf{Q}_\eta}\times\mathbf{S}_{-\mathbf{Q}_\eta}) - H\sum_i S^z_i, \qquad (2)\end{aligned}$$

where the sum of η is taken for the set of $\mathbf{Q}_\eta$ giving the multiple maxima in the bare susceptibility of itinerant electrons. $J^{\alpha\beta}_{\eta}$ and $\mathbf{D}_\eta$ are the coupling constants for symmetric and antisymmetric exchange interactions in momentum space ($\alpha, \beta = x, y, z$), which are long-ranged in real space. These exchange cou-

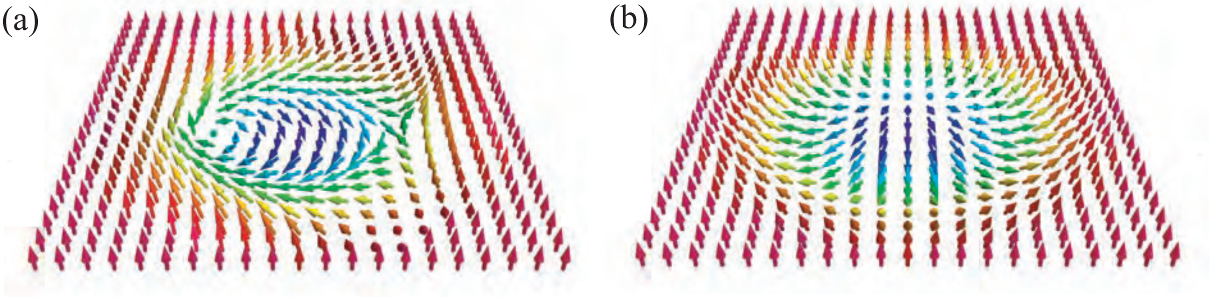

Figure 1: Schematic pictures of (a) Bloch-type and (b) Néel-type spin textures.

plings are related to the second-order perturbative Hamiltonian with respect to J_{K}. In Eq. (2), we add the Zeeman coupling to an external magnetic field in the out-of-plane direction. The model in Eq. (2) will give a good approximation under two conditions: (1) J_{K} is small enough compared to the bandwidth of itinerant electrons and (2) the bare susceptibility shows conspicuous peaks at $\mathbf{Q}_\eta$ in the Brillouin zone.

We investigate the magnetic phase diagram of the effective spin model in Eq. (2) by performing simulated annealing from high temperature. Our simulations are carried out with the standard Metropolis local updates under periodic boundary conditions in both directions. In the simulation, we first perform simulated annealing to find the low-energy configuration by gradually reducing the temperature with the rate $T_{n+1} = \alpha T_n$, where T_n is the temperature in the nth step. We set the initial temperature $T_0 = 10^{-1}$-10^0 and take the coefficient $\alpha = 0.9995$-0.9999. The final temperature, which is typically taken at $T = 10^{-4}$, is reached after 10^5-10^6 Monte Carlo sweeps in total.

As a result, we discover a vortex crystal of Néel type even in the absence of a magnetic field. Furthermore, we demonstrate that a Bloch-type vortex crystal, which is usually associated with the Dresselhaus-type spin-orbit coupling, can also be stabilized in the Rashba-based model. We also show that a magnetic field turns the vortex crystals into Néel- and Bloch-type skyrmion-like crystals with a finite scalar chirality. Our results indicate that a variety of noncoplanar spin textures including vortices and skrymions can be realized and controlled by the interplay between the spin-orbit coupling and the spin-charge coupling in itinerant magnets.

References

[1] S. Hayami and Y. Motome, preprint (arXiv: 1803.01543).

Theoretical studies of strongly correlated electron systems by variational cluster approximation

Atsushi Yamada
Department of Physics, Chiba University
Chiba 263-8522, Japana, Chiba 277-8581

When kinetic and Coulomb repulsion energies are competing, low dimensional materials with geometric frustration exhibit rich phenomena like superconductivity with various pairing symmetries and purely paramagnetic insulator (spin liquid). The organic charge-transfer salts κ-(BEDT-TTF)$_2$X [1, 2, 3, 4] are good examples of such materials, where a transition from paramagnetic metal to spin liquid (Mott transition) has been detected with X=Cu$_2$(CN)$_3$[3, 4].

We have studied the magnetic and metal-to-insulator transitions of some systems[5, 6, 7] using variational cluster approximation(VCA)[8, 9, 10]. For example, spin liquid state in κ-(BEDT-TTF)$_2$X is analyzed in Ref **??**.

VCA is an extension of the cluster perturbation theory[8] based on the self-energy-functional approach.[10] This approach uses the rigorous variational principle $\delta\Omega_{\mathbf{t}}[\Sigma]/\delta\Sigma = 0$ for the thermodynamic grand-potential $\Omega_{\mathbf{t}}$ written as a functional of the self-energy Σ

$$\Omega_{\mathbf{t}}[\Sigma] = F[\Sigma] + \mathrm{Tr}\ln(-(G_0^{-1} - \Sigma)^{-1}). \quad (1)$$

In the above expression, $F[\Sigma]$ is the Legendre transform of the Luttinger-Ward functional[11] and the index $\mathbf{t}$ denotes the explicit dependence of $\Omega_{\mathbf{t}}$ on all the one-body operators in the Hamiltonian. The stationary condition for $\Omega_{\mathbf{t}}[\Sigma]$ leads to the Dyson's equation. All Hamiltonians with the same interaction part share the same functional form of $F[\Sigma]$, and using that property $F[\Sigma]$ can be evaluated from the exact solution of a simpler Hamiltonian H', though the space of the self-energies where $F[\Sigma]$ is evaluated is now restricted to that of H'. In VCA, one uses for H' a Hamiltonian formed of clusters that are disconnected by removing hopping terms between identical clusters that tile the infinite lattice. Rewriting $F[\Sigma]$ in Eq. 1 in terms of the grand-potential $\Omega' \equiv \Omega'_{\mathbf{t}}[\Sigma]$ and Green function $G'^{-1} \equiv {G'_0}^{-1} - \Sigma$ of the cluster Hamiltonian H', the grand-potential is expressed as

$$\Omega_{\mathbf{t}}(\mathbf{t}') = \Omega' - \int_C \frac{d\omega}{2\pi} \mathrm{e}^{\delta\omega} \sum_{\mathbf{K}} \ln\det\left(1 + (G_0^{-1} - {G'_0}^{-1})G'\right) \quad (2)$$

and is now a function of $\mathbf{t}'$, which denotes all the one-body operators in H'. The functional trace has become an integral over the diagonal variables (frequency and super-lattice wave vectors) of the logarithm of a determinant over intra-cluster indices. The frequency integral is carried along the imaginary axis and $\delta \to +0$. The stationary solution of $\Omega_{\mathbf{t}}(\mathbf{t}')$ and the exact self-energy of H' at the stationary point, denoted as Σ^*, are the approximate grand-potential and self-energy of H in VCA.

In our analyses we have exactly diaogonalized H' numerically using Lanczos methods. Parts of numerical calculations were done using the computer facilities of the ISSP. We now try to improve our exact diagonalization program using the computer facilities of the ISSP.

References

[1] S. Lefebvre , P. Wzietek, S. Brown, C. Bourbonnais, D. Jérome, C. Mézière, M. Fourmigué, and P. Batail, Phys. Rev. Lett. **85**, 5420 (2000).

[2] Y. Shimizu, K. Miyagawa, K. Kanoda, M. Maesato, and G. Saito, Phys. Rev. Lett. **91**, 107001 (2003).

[3] F. Kagawa, T. Itou, K. Miyagawa, and K. Kanoda, Phys. Rev. B **69**, 064511 (2004).

[4] R.S. Manna, M. de Souza, A. Brühl, J.A. Schlueter, and M. Lang, Phys. Rev. Lett. **104**, 016403 (2010).

[5] A. Yamada, K. Seki, R. Eder, and Y. Ohta, Phys. Rev. B **83**, 195127 (2011); Phys. Rev. B **88**, 075114 (2013).

[6] A. Yamada, Phys. Rev. B **89**, 195108 (2014).

[7] A. Yamada, Phys. Rev. B **90**, 235138 (2014); Phys. Rev. B **90**, 245139 (2014); Int. J. Mod. Phys. B **30**, 1650158 (2016).

[8] D. Sénéchal, D. Perez, and M. Pioro-Ladriére, Phys. Rev. Lett. **84**, 522 (2000); D. Sénéchal, D. Perez, and D. Plouffe, Phys. Rev. B **66**, 075129 (2002).

[9] M. Potthoff, M. Aichhorn, and C. Dahnken, Phys. Rev. Lett. **91** 206402 (2003); C. Dahnken, M. Aichhorn, W. Hanke, E. Arrigoni, and M. Potthoff, Phys. Rev. B **70**, 2451100 (2004).

[10] M. Potthoff, Eur. Phys. J. B **32**, 429 (2003).

[11] L. M. Luttinger and J. C. Ward, Phys. Rev. **118**, 1417 (1960).

Transient dynamics in many electronic systems

Sumio ISHIHARA
Department of Physics, Tohoku University
Aramaki, Aoba, Sendai 980-8578

It is widely recognized that the nonequilibrium steady and transient dynamics in correlated electron systems are one of the central issues in recent modern solid state physics. This research trend is owing to the great development of the experimental techniques as well ans the theoretical calculation methods, for example, the nonequilibrium Green function methods, the numerical real-time dynamics and so on. We report our recent research results obtained by the numerical calculations.

(1) *Non equilibrium light induced dynamics in the double exchange system.* We analyze the light induced dynamics in the double exchange (DE) model [1]. The intense pulse/CW light are applied to the ferromagnetic metallic phase which is widely realized in the DE model. We show by solving numerically the Schrödinger equation and Landau-Lifshitz-Gilbert equation that the DE interaction in highly photoexcited states is antiferromagnetic, an almost perfect Néel state (see Fig. 1). A time characterizing the ferromagnet-to-antiferromagnet conversion is scaled by light amplitude and frequency. This observation is highly in contrast to the conventional DE interaction in the thermal equilibrium state in which the carrier motion promotes the ferromagnetic state. This hidden antiferromagnetic interaction is attributable to the electron-spin coupling under nonequilibrium electron distribution.

(2) *Dynamical localization in Hubbard model.* Suppression of electron motion under an alternating current electric field, termed the dynamical localization effect, is examined in a one-dimensional Hubbard model [2]. It is found by using the iTEBD method that magnitudes of the kinetic-energy suppressions are influenced sensitively by the Coulomb interaction as well as the electron density. The results are interpreted as a combined effect of the Coulomb interaction and the AC field, and provide a guiding principle for the photocontrol of correlated electron motion.

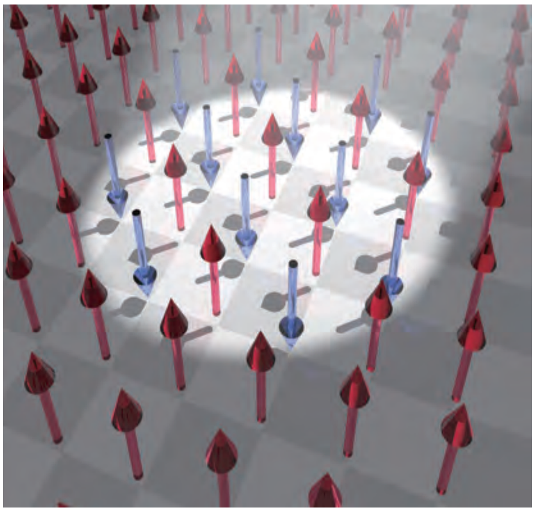

Figure 1: A schematic view of the light induced spin conversion.

References

[1] A. Ono and S. Ishihara: Phys. Rev. Lett. **119** (2017) 207202.

[2] A. Ono, H. Hashimoto, and S. Ishihara: Phys. Rev. B **95** (2017) 085123.

Quantum Monte Carlo simulation and electronic state calculations in correlated electron systems

Takashi YANAGISAWA
Electronics and Photonics Research Institute
National Institute of Advanced Industrial Science and Technology (AIST)
AIST Central 2, 1-1-1 Umezono, Tsukuba 305-8568

We investigated the ground-state properties of strongly correlated electron systems by using an optimization variational Monte Carlo method for two-dimensional Hubbard model. We improved wave functions by taking into account intersite correlations to go beyond the Gutzwiller ansatz. The wave function is an $\exp(-\lambda K)-P_G$-type wave function, which can be improved systematically by multiplying by P_G and $e^{-\lambda K}$ where K is the kinetic-energy operator.

The on-site Coulomb interaction U induces strong antiferromagnetic (AF) correlation. The AF correlation increases as U increases in weakly correlated region. The AF correlation has a peak at U_c, in the intermediate region of U, and decreases as U increases further. U_c is of the order of the bandwidth. This is a crossover from weakly correlated region to strongly correlated region induced by U. We expect that there is a large fluctuation when AF correlation is suppressed. Our idea is that this large fluctuation induces high-temperature superconductivity.

The single-band Hubbard model is given by

$$H=\sum_{ij\sigma}t_{ij}c_{i\sigma}^{\dagger}c_{j\sigma}+U\sum_{i}n_{i\uparrow}n_{i\downarrow}, \qquad (1)$$

where t_{ij} are transfer integrals and U is the on-site Coulomb energy. The transfer integral t_{ij} is non-zero $t_{ij}=-t$ for nearest-neighbor pair $\langle ij\rangle$ and $t_{ij}=-t'$ for next-nearest neighbor $\langle\langle ij\rangle\rangle$. Otherwise t_{ij} vanishes. We denote the number of sites as N and the number of electrons as N_e. The energy unit is given by t.

The well-known Gutzwiller wave function is given by $\psi_G = P_G\psi_0$ where P_G is the Gutzwiller operator defined by $P_G = \prod_j(1-(1-g)n_{j\uparrow}n_{j\downarrow})$ with the variational parameter g in the range of $0\le g\le 1$. The one way to improve the wave function is to take account of nearest-neighbor doublon-holon correlation: $\psi_{d-h}=P_{d-h}P_G\psi_0$. We can take into account inter-site correlations by multiplying by P_J such as $P_JP_{d-h}P_G\psi_0$.

In our study, we take account of inter-site correlation by multiplying the Gutzwiller function by the kinetic operator. A typical wave function of this type is written as[1]

$$\psi_\lambda\equiv\psi^{(2)}=e^{-\lambda K}P_G\psi_0, \qquad (2)$$

where K is the kinetic term in the Hamiltonian: $K=\sum_{ij\sigma}t_{ij}c_{i\sigma}^{\dagger}c_{j\sigma}$ and λ is a variational parameter to be optimized to lower the energy. This wave function is further improved by multiplying $\psi^{(2)}$ by the Gutzwiller operator again: $\psi^{(3)}\equiv P_G\psi_\lambda = P_Ge^{-\lambda K}P_G\psi_0$. The expectation values are evaluated by using the variational Monte Carlo method.

The trial wave function $P_{d-h}P_G\psi_0$ was used to develop the physics of Mott transition following the suggestion that the Mott transition occurs due to doublon-holon binding. We examined the Mott transition with the wave function $e^{-\lambda K}P_G\psi_0$[4] because the variational energy by this wave function is much lower than that of the doublon-holon wave function.

The correlation function $S(\mathbf{q})$ has a maximum at $\mathbf{q}=(\pi,\pi)$. $S(\pi,\pi)$ has a peak near $U\simeq 10t$. The spin correlation is suppressed when U is extremely large being larger than the bandwidth. There is a crossover from weakly to strongly correlated regions as U increases. The antiferromagnetic correlation induced by U is reduced for hole doping when U is large. being greater than the bandwidth.

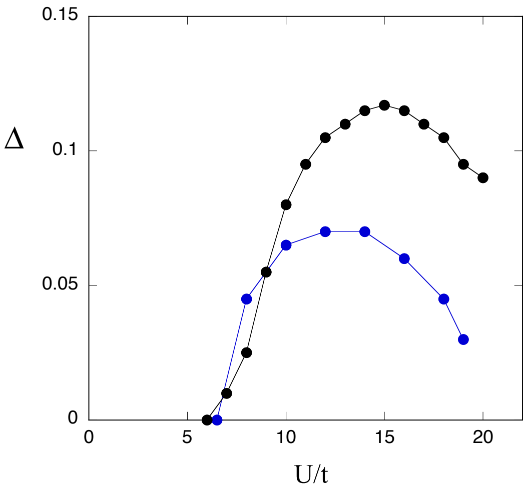

Figure 1: Superconducting order parameter as a function of U in units of t on 10×10 lattice. The number of electrons is $N_e = 88$ and we set $t' = 0.0$. The upper curve is for the BCS-Gutzwiller function and the lower one is for the optimized wave function.

The optimized superconducting order parameter Δ increases as U increases, and also has a maximum at some U (Fig.1). We show Δ and the antiferromagnetic (AF) order parameter as functions of U in Fig.2. The superconducting correlation is developed in the region where the AF correlation is suppressed. The reduction of the antiferromagnetic correlation the strongly correlated region suggests the existence of a large antiferromagnetic spin fluctuation. The development of a superconducting correlation is understood to be induced by spin and charge fluctuations that are induced by the process to gain the kinetic energy. The charge fluctuation induced by the kinetic operator is appreciable and helps electrons to form pairs. The spin fluctuation in the strongly correlated region should be distinguished from that in a weakly correlated region. The latter is the conventional spin fluctuation.

The ground-state energy is lowered greatly compared to that of the Gutzwiller wave function. In the strongly correlated region where U is greater than the bandwidth, the AF correlation is reduced, indicating that we have large spin and charge fluctuations. This kind of fluctuations would induce electron pairing and lead to high-temperature superconductivity.

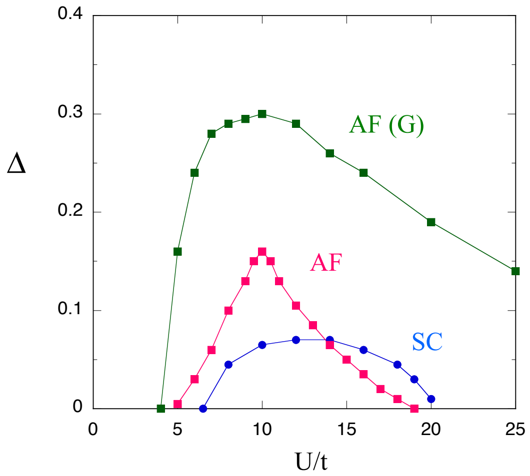

Figure 2: Superconducting and antiferromagnetic order parameters as functions of U in the range of $0 \leq U \leq 25t$ on 10×10 lattice. The number of electrons is $N_e = 88$ and $t' = 0.0$. The solid circles show the SC gap for the improved wave function. The squares represent the antiferromagnetic order parameter, where the upper curve is for the Gutzwiller wave function and the lower curve is for the improved wave function. The boundary condition is periodic in one direction and anti-periodic in the other direction.

References

[1] T. Yanagisawa et al., J. Phys. Soc. Jpn. 67, 3867 (1998).

[2] T. Yanagisawa, Phys. Rev. B75, 224503 (2007) (arXiv: 0707.1929).

[3] T. Yanagisawa, New J. Phys. 15, 033012 (2013).

[4] T. Yanagisawa and M. Miyazaki, EPL 107, 27004 (2014).

[5] T. Yanagisawa, J. Phys. Soc. Jpn. 85, 114707 (2016).

[6] T. Yanagisawa, M. Miyazaki and K. Yamaji, Int. J. Mod. Phys. B32, 1840023 (2018).

Electron-hole doping asymmetry in κ-type molecular conductor

Hiroshi WATANABE
Waseda Institute for Advanced Study, Waseda University
1-6-1 Nishi Waseda, Shinjuku-ku, Tokyo 169-8050

The family of quasi two-dimensional molecular conductors κ-(BEDT-TTF)$_2$X has been extensively studied as a typical example of strongly correlated electron system. Depending on the monovalent anion X, they show various quantum phases such as antiferromagnetic and spin-liquid dimer-Mott insulators, and superconductivity (SC) [1]. Owing to the similarities in the experimental phase diagrams, κ-(BEDT-TTF)$_2$X system is often compared with high-T_c cuprates, which exhibit Mott metal-insulator transition and SC [2]. Recently, carrier doping in κ-(BEDT-TTF)$_2$X has been realized using electric-double-layer transistor [3], and the direct comparison with cuprates becomes possible. The experimental result shows the electron-hole doping asymmetry, reminiscent of the high-T_c cuprates.

Here, we theoretically study the electron-hole asymmetry in κ-(BEDT-TTF)$_2$X by taking account the intradimer charge degree of freedom. We consider a four-band extended Hubbard model including onsite (U) and intersite Coulomb interactions (V_{ij}) with κ-type geometry with the largest hopping integral t_{b_1} as an energy unit. The ground state properties are studied with the variational Monte Carlo (VMC) method. The Gutzwiller-Jastrow type wave function is used for the VMC trial wave function. The system sizes for calculation are from 288 (4×12×6) to 1152 (4×24×12).

Figure 1 shows the ground-state phase diagram for κ-(BEDT-TTF)$_2$X in a n-U/t_{b_1} space. The largest intersite Coulomb interaction is fixed at V_{b_1}/U=0.5. There appear various competing phases and significant electron-hole asymmetry is observed. The SC phase appears only for electron-doped side and its symmetry is the extended-s+$d_{x^2-y^2}$-wave type [4, 5, 6], which is a different type with cuprates .

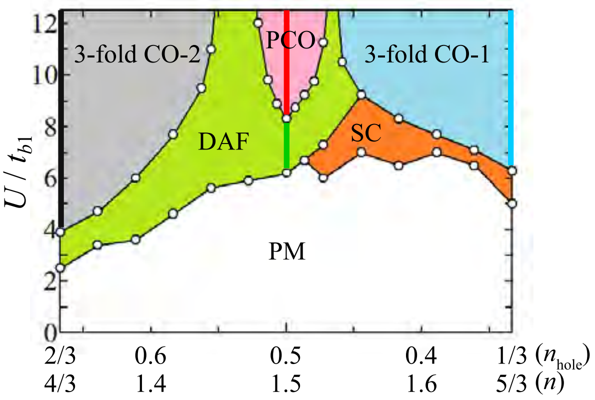

Figure 1: Ground-state phase diagram of the extended Hubbard model for κ-(BEDT-TTF)$_2$X. PM, DAF, PCO, 3-fold CO-1 (2), and SC denote paramagnetic metal, dimer-type antiferromagnetic phase, polar charge-ordered phase, 3-fold charge-ordered phase 1 (2), and superconductivity, respectively.

References

[1] K. Kanoda: J. Phys. Soc. Jpn. **75** (2006) 051007.

[2] R. H. McKenzie: Science **278** (1997) 820.

[3] Y. Kawasugi et al., Nat. Commun. **7** (2016) 12356.

[4] K. Kuroki, T. Kimura, R. Arita, Y. Tanaka, and Y. Matsuda: Phys. Rev. B **65** (2002) 100516(R).

[5] D. Guterding, M. Altmeyer, H. O. Jeschke, and R. Valentí, Phys. Rev. B **94** (2016) 024515.

[6] H. Watanabe, H. Seo, and S. Yunoki: J. Phys. Soc. Jpn. **86** (2017) 033703.

3.4 Cooperative Phenomena in Complex Macroscopic Systems

Nonequilibrium superconductivity emerging from synergistic effects of light and phonons in strongly correlated systems

Kota IDO, Takahiro OHGOE and Masatoshi IMADA
Department of Applied Physics, The University of Tokyo,
Hongo 7-3-1, Bunkyo-ku, Tokyo 113-8656

Recently, laser-controlled superconductivity (SC) has been studied extensively to go beyond the limit of superconducting critical temperature T_{C} in equilibrium. One of the approaches is selective excitations of phonon modes of correlated electron materials by strong laser irradiation. Surprisingly, in the case of a bi-layered cuprate, indication of superconductivity above T_{c} has been reported [1,2]. This fascinating experiment has motivated theoretical studies for understanding its mechanism.

On the other hand, proposals for an alternative strategy ascribed to a more generic mechanism are also desirable. This is because the strategy based on coherent phonon excitations does not seem to be general in correlated electron materials at present due to strong restriction on the details of phonon modes in materials. Recently, we have proposed an alternative way to enhance SC in a correlated electron system without lattice degrees of freedoms [3]. In this study, we have shown that strong and non-resonant laser irradiation to a charge uniform state dynamically enhances SC without deteriorating into inhomogeneities that suppress SC in equilibrium. However, this approach can be applied only to uniform states in cuprates. Since inhomogeneous states were observed in a number of cuprates below optimal doping [4], it is important to verify whether strong and non-resonant laser irradiation dynamically melts static inhomogeneity and enhances SC.

Our purpose in this project is to clarify microscopic origin of the light-enhanced SC observed in the experiments. In addition, we also aim to clarify what happens when strong lasers are irradiated to equilibrium systems with inhomogeneity. Here, we summarize our main achievements for each topic.

(i) *Development of time-dependent variational Monte Carlo method for electron-phonon coupled systems:* In order to analyze an effective model for cuprates with light-driven phonon excitations, we need to treat not only strong electron correlations but also many phonons excited by laser irradiation. For this purpose, we extended a many-variable variational Monte Carlo (mVMC) method to nonequilibrium electron-phonon coupled systems. As a trial state, we adopt a tensor product state of an electron wave function and a phonon wave function with an electron-phonon correlation factor [5]. By introducing a large number of variational parameters to the phonon part, we can treat multi-phonon excitations by light.

As benchmarks of the mVMC method, we calculated relaxation dynamics after an electron-phonon interaction quench protocol of the one-dimensional Holstein model. We found that our trial wave function well reproduces the exact results for the time evolution of double occupancy and charge correlations. This result shows that the mVMC method offers an efficient and accurate way to study challenging problems of nonequilibrium electron-phonon coupled systems. The analysis of an effective model for the cuprates with phonons under laser irradiation will be reported elsewhere.

(ii) *Laser-enhanced superconductivity caused by dynamically melting charge inhomogeneity:* By using the mVMC method [6,7], we numerically study dynamics of *d*-wave SC and charge inhomogeneity when laser pulses are irradiated to an inhomogeneous ground state in a two-dimensional correlated electron system. We found that strong and non-resonant laser irradiation can melt charge inhomogeneity, and enhance *d*-wave SC. We observed that the lifetime of such enhanced SC is prolonged by keeping the laser intensity constant in the middle of the laser irradiation. Our findings will shed light on a new way to realize SC that is not attainable in equilibrium in strongly correlated electron systems.

References

[1] W. Hu *et al.*: Nat. Mater. **13** (2014) 705.

[2] S. Kaiser *et al.*: Phys. Rev. B **89** (2014) 184516.

[3] K. Ido, T. Ohgoe, and M. Imada: Sci. Adv. **3** (2017) e1700718.

[4] R. Comin and A. Damascelli: Annu. Rev. Condens. Matter Phys. **7**, 369 (2016).

[5] T. Ohgoe, and M. Imada, Phys. Rev. B. **89** 195139 (2014).

[6] D. Tahara and M. Imada: J. Phys. Soc. Jpn. **77** (2008) 114701.

[7] K. Ido, T. Ohgoe, and M. Imada: Phys. Rev. B **92** (2015) 245106.

Determination of Scattering Length of Bose-Hubbard Model by Quantum Monte Carlo Simulations[1]

Naoki KAWASHIMA
Institute for Solid State Physics, University of Tokyo
Kashiwa-no-ha, Kashiwa, Chiba 277-8581

The Bose-Hubbard model is the simplest non-trivial model for interacting boson system. It is widely believed that, in the dilute limit, the model is equivalent to the continuous model characterized by a single parameter, i.e., the s-wave scattering length. However, there has been no quantitative estimation of the scattering length in the unit of lattice constant. In the ISSP supercomputer project of SY2017, we aim at establishing the quantitative correspondence between the lattice model and the continuous-space model.

Here, the Bose-Hubbard model defined as

$$H = -t \sum_{(ij)} (b_i^\dagger b_j + \mathrm{h.c.}) - \mu \sum_i b_i^\dagger b_i,$$

which is compared in our project to

$$H = \int d\mathbf{x} \phi^\dagger(\mathbf{x}) \left(-\frac{\hbar^2}{2m} \nabla^2 \right) \phi(\mathbf{x}) + \int d\mathbf{x} d\mathbf{x}' \phi^\dagger(\mathbf{x}') \phi^\dagger(\mathbf{x}) V(\mathbf{x}' - \mathbf{x}) \phi(\mathbf{x}) \phi(\mathbf{x}')$$

with

$$V(\mathbf{x}) \equiv \begin{cases} \infty & (|\mathbf{x}| \le a_s) \\ 0 & (|\mathbf{x}| > a_s) \end{cases}$$

We carried out Monte Carlo simulation on the Bose-Hubbard model in dilute region, $10^{-3} < na^3 < 10^{-1}$. We used our original package DSQSS[2], which can be downloaded from the GITHUB and can be used under GPL license. We varied the system size L and the inverse temperature β to confirm that the result does not depend on these parameter beyond the statistical error, i.e., our result can be identified with those at zero temperature in the thermodynamic limit.

Figure 1 is our result compared with the analytical predictions made by Lee, Huang and Yang [3]. From this comparison we estimated the s-wave scattering length in the unit of the lattice constant as $a_s/a = 0.315$.

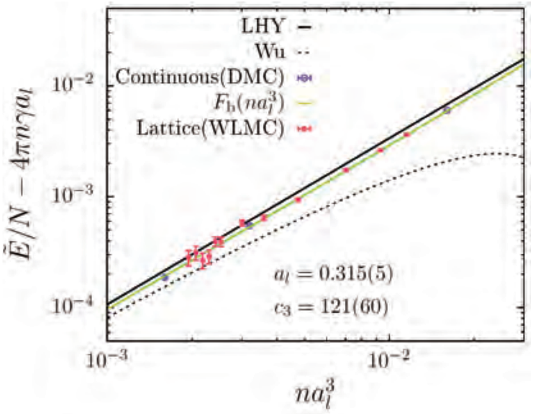

Figure 1: The correction in the normalized energy. The three curves labeled as "LHY", "Wu", and "F_b" represent the analytical prediction up to the first correction, up to the second correction and the third (logarithmic) correction, respectively. The open symbols labeled as "Continuous" are the results of the diffusion Monte Carlo for the continuous-space model whereas the closed symbols are for the present calculation of the lattice system.

[1] This report is based on A. Masaki-Kato, Y. Motoyama and N. Kawashima (unpublished).

[2] https://github.com/qmc/dsqss/wiki
[3] T. D. Lee, K. Huang and C. N. Y. Yang Phys. Rev. 106, 1135 (1957).

Study on Complex Systems by Generalized-Ensemble Algorithms

Takuya HAYASHI, Yuhei TACHI, and Yuko OKAMOTO
Department of Physics, Graduate School of Science, Nagoya University
Furo-Cho, Chikusa-ku, Nagoya, Aichi 464-8602

Despite the experimental discovery of the residual entropy of ice Ih in the 1930's [1], highly accurate measurements have yet to be made in experiments. The calculation started from Pauling in the 1930's [2]. As a recent calculation, there are results [3,4] by multicanonical simulations [5]. In this work, we aim to drastically improve the accuracy in large scale and complex systems.

The entropy is proportional to a logarithm of the density of states. In Refs. [3,4] multicanonical weight factor was obtained by the Wang-Landau method [6], and a multicanonical production run was performed to obtain an accurate estimate of the density of states.

In order to obtain the multicanonical weight factor for a larger system, we propose to combine the multicanonical replica-exchange method [7] and replica-exchange Wang-Landau method [8]. In order to confirm the effectiveness of this new method, test simulations were performed with the 2-dimensional Ising model (with the number of spins up to 128 × 128), and we found that this combination gives the most effective method for the determination of the density of states (a manuscript is in preparation). We are now ready to perform simulations to improve the value of the residual entropy of ice.

We have also studied an artificial glycan cluster in which 24 GM1 glycans were transplanted to a metal-ligand complex using cluster B. The complex with GM1 glycans was developed to investigate the interaction between amyloidgenic proteins and GM1 glycan clusters [9]. GM1 glycan is glycan moiety in glycolipid called GM1 ganglioside. The structural information of the GM1 glycan clusters is important for understanding the mechanism of glycan cluster recognition of amyloidgenic proteins. Therefore, we focused on the structural properties of GM1 glycans on the metal-ligand complex.

In this study, molecular dynamics (MD) simulations of the artificial glycan cluster and a monomeric GM1 glycan were performed to compare the structural distribution of the GM1 glycan on the complex and that of the monomeric GM1 glycan.

In this simulation, we found that about 65% GM1 glycans on the complex forms clusters by hydrogen bonding. It was also found that GM1 glycans interacts with the ligands on the complex by tilting. Furthermore, we revealed that some local minimum structures of GM1 glycans on the complex are stabilized as the monomeric GM1 glycan (a manuscript is in preparation).

The above results give important information for investigating the mechanism of the glycan cluster recognition of amyloidgenic proteins. In the future work, we plan to perform the binding MD simulations of amyloidgenic proteins to the artificial glycan cluster.

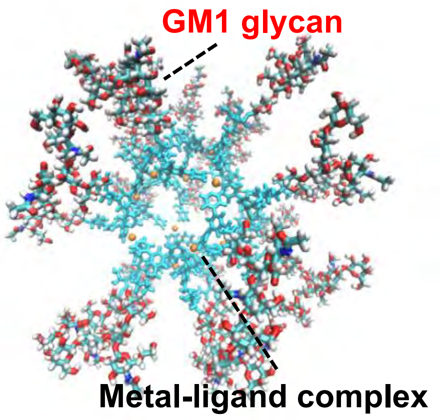

Fig. 1: Metal-ligand complex with GM1 glycans.

References

[1] J. D. Bernal and R. H. Fowler: J. Chem. Phys. **1** (1933) 515.

[2] L. Pauling, J. Am. Chem. Soc. **57** (1935) 2680.

[3] B. A. Berg, C. Muguruma, and Y. Okamoto, Phys. Rev. B **75** (2007) 092202.

[4] B. A. Berg, C. Muguruma, and Y. Okamoto, Mol. Sim. **38** (2012) 856.

[5] B. A. Berg and T. Neuhaus, Phys. Rev. Lett. **68** (1992) 9.

[6] F. Wang and D. P. Landau, Phys. Rev. Lett. **86** (2001) 2050.

[7] Y. Sugita and Y. Okamoto, Chem. Phys. Lett. **329** (2000) 261.

[8] T. Vogel, Y. W. Li, T. Wüst and D. P. Landau, Phys. Rev. Lett. **110** (2013) 210603.

[9] S. Sato, Y. Yoshimasa, D. Fujita, M. Yagi-Utsumi, T. Yamaguchi, K. Kato, and M. Fujita, Angew. Chem. Int. Ed. **54** (2015) 8435.

Coarse grained MD simulation for fracture and reinforcement of polymer materials

Katsumi HAGITA

Department of Applied Physics, National Defense Academy, Yokosuka, Kanagawa 239-8655

We investigated fracture behaviors of polymers such as morphology changes and chain breaking by uniaxial elongations. Understanding of fracture mechanisms with molecular level is considered to be important on reinforcement of polymer materials. We performed coarse grained (CG) molecular dynamics (MD) simulations of polymer materials. Here, we considered Kremer-Grest (KG) model, united atom (UA) model and reactive force field (ReaxFF) MD. KG is bead spring model. UA and ReaxFF can be regarded as CG of all atomistic MD simulations and DFT simulations, respectively. These simulation methods can be performed by LAMMPS (Large-scale Atomic/Molecular Massively Parallel Simulator), which was used in the present studies. We also studied Dissipative particle dynamics (DPD) which is a stochastic simulation method that can handle larger time scales than the KG model. This year, we focused on ABA tri-block copolymers (BPCs) and crystallized polyethylene (PE).

For ABA tri-BCPs, we studied morphology changes via two-dimensional scattering patterns (2DSPs) for correspondences between simulations and experiments. Recently, we proposed Thinning Approximation (TA) to calculate 2DSPs under shear flows for KG model [1]. We performed CGMD simulations of KG model of ABA tri-BCPs for various fractions. Systematic changes of 2DSPs under uniaxial elongations were observed by using TA [2]. Also, we performed CGMD simulations of KG model to examine filler-filled systems such NC-clay nanocomposites [3], and nano-particle (NP) filled rubbers [4]. On the study of NC-clay nanocomposites, we could reproduce the stress-strain curve and the change of 2DSPs during elongation at the same time. For the NP-filled rubbers, we found that effect of polymer-NP interactions and nanostructures on glass transition temperature.

In order to investigate the fracture behaviors from the equilibrium structure of phase separated ABA tri-BPCs by elongations, we considered an improvement of segmental repulsive potential (SRP) of DPD simulations. To reduce bond crossing probabilities and keep the equilibrium structure before and after introducing of SRP, we proposed multipoint SRP [5].

As studies behaviors of 2DSPs of NP-filled rubbers, we proposed filler network model of filled rubber materials in order to study system size dependence of 2DSPs and obtain a rough model to reproduce structure-property relationship for machine learning studies [6].

To study fracture of realistic materials, we considered crystallization of PE chains. As produces in our usual life, branched PE chains such as high- and low-density PE (HDPE and LDPE) are used. We found that branched junctions are mainly localized in amorphous layer. To study formations of amorphous layers, we compared ring and linear PE polymers. Here, amorphous layers have important role on fractures of PE materials. We found that crystallization of ring PE polymers is faster than that of linear PE polymers [7]. In addition, we also investigated the topological effect of a knot of a ring on crystallization of ring PE polymers [8]. To reproduce chain breaking, we used ReaxFF MD simulations. In our study, UAMD was used to prepare crystallized PE and ReaxFF MD was used to study chain breaking under stretching.

To enhance material researches including developments of real materials, we examined AI based information analysis methods. As the first example, we studied image classification of images of NPs in rubbers [9]. As the second example, we considered super resolution for asymmetric resolution of FIB-SEM (focused ion beam scanning electron microscopy) 3D imaging of NPs in rubbers [10].

References

[1] K. Hagita, T. Murashima, H. Takano, and T. Kawakatsu: J. Phys. Soc. Jpn. **86** (2017) 124803.

[2] K. Hagita, K. Akutagawa, T. Tominaga, and H. Jinnai: in preparation.

[3] K. Hagita, Y. Shudo, and M. Shibayama: Submitted to Polymer.

[4] K. Hagita and H. Morita: Submitted to Macromolecules.

[5] N. Iwoaka, K. Hagita, and H. Takano: in preparation.

[6] K. Hagita, T. Tominaga, T. Hatazoe, T. Sone, and H. Takano: J. Phys. Soc. Jpn. **87** (2018) 014802.

[7] K. Hagita, S. Fujiwara, and N. Iwaoka: in preparation.

[8] K. Hagita, E. Uehara and T. Deguchi: in preparation.

[9] K. Hagita, T. Tominaga, T. Sone, I. Takahashi, C. Lee, and M. Ogino: Nippon Gomu Kyokaishi **91** (2018) 3-8 in Japanese.

[10] K. Hagita, T. Higuchi and H. Jinnai: Scientific reports **8** (2018) 5877.

Numerical Studies on Finite Temperature Excitation Spectra of Quantum Spin Liquids

Youhei Yamaji
Deparment of Applied Physics, The University of Tokyo
Hongo 7-3-1, Bunkyo-ku, Tokyo 113-8656

A growing demand for finite-temperature simulation of excitation spectra has originated from experimental researches on many-body quantum systems. Raman scattering and inelastic neutron scattering measurements on a class of quantum magnets, *Kitaev materials* [1], have brought attention to the temperature dependence of the excitation spectra. Shortly after the finding of the quantum spin liquid in the Kitaev model [2], it has been proposed that the Kitaev model captures low-energy spin degrees of freedom in honeycomb networks of heavy transition metal ions, which are typified by an iridium oxide α-$\mathrm{Na_2IrO_3}$ [3]. So far, the Kitaev materials including α-$A_2\mathrm{IrO_3}$ (A=Na, Li), α-$\mathrm{RuCl_3}$, β-$\mathrm{Li_2IrO_3}$, and γ-$\mathrm{Li_2IrO_3}$ exhibit spontaneous time-reversal symmetry breakings. However, these materials expected in proximity to the Kitaev's spin liquid stimulate the experimental research on the excitation spectra at finite temperatures, which requires theoretical counterparts. In addition to the theoretical studies on Raman spectra and dynamical spin structure factors of the simple Kitaev model at zero temperature [4] and finite temperatures [5], theoretical and numerical studies on the Kitaev-like Hamiltonian on variety of tricoordinate networks are highly desirable.

This year, we have developed an $\mathcal{O}(N_{\mathrm{F}})$ algorithm for simulating exact finite-temperature excitation spectra in frequency domain [6], where N_{F} is the dimension of the Fock space of the target system, by combining the typical pure state approach [7] and the shifted Krylov subspace method [8]. We applied the present algorithm to the simplest effective Hamiltonian of the two-dimensional Kitaev-like systems on honeycomb lattices, namely, the Kitaev-Heisenberg model on a honeycomb lattice [9] that consists of S=1/2 spins. The nearest-neighbor bonds on the honeycomb lattice have three different directions. When the three bonds are labeled as x, y, and z, the Kitaev-Heisenberg Hamiltonian,

$$\hat{H} = \sum_{\gamma=x,y,z} \sum_{\langle i,j\rangle\in\gamma} \hat{H}_{ij}^{(\gamma)}, \tag{1}$$

is defined by the exchange coupling for the γ ($= x, y, z$) bond,

$$\hat{H}_{ij}^{(\gamma)} = J\vec{\hat{S}}_i \cdot \vec{\hat{S}}_j + K\hat{S}_i^{\gamma}\hat{S}_j^{\gamma}, \tag{2}$$

where $K = J_0 \sin\varphi$ is the Kitaev coupling constant and $J = (J_0/2)\cos\varphi$ is the Heisenberg exchange coupling constant. Below, we set the energy unit as $J_0 = 1$.

We have focused on the proximity of the phase boundary between the spin liquid phase and a zigzag ordered phase around $\varphi \simeq 92.2^\circ$, and examined temperature dependence of dynamical spin structure factors $S(\vec{Q},\omega)$. We found that the crossover from a spin-excitation continuum, which is a characteristics of the quantum spin liquid, to a damped high-energy magnon mode occurs at temperatures higher than the energy scale of the Heisenberg exchange couplings or the spin gap that is a signature of the quantum spin liquid at zero temperature. The crossover and the closeness to the quantum spin liquid are quantitatively measured by a dimensionless ratio of the width of the excitation continuum or the damped magnon spectrum and the energy at which the spectral weight becomes maximum. As shown in Fig. 1, we calculated $S(\vec{Q},\omega)$ at $\vec{Q} = \Gamma$ $(= \vec{0})$. To extract the peak width, we fit the high energy peak by an asymmetric Lorentzian function,

$$s(\omega) = \frac{\gamma_{\rm f}}{\gamma_{\rm f}^2 + (\hbar\omega - \epsilon_{\rm f})^2}\left\{a + \frac{b}{1 + e^{c(\hbar\omega - \epsilon_{\rm f})}}\right\}, \quad (3)$$

where a, b, c, $\gamma_{\rm f}$, and $\epsilon_{\rm f}$ are fitting parameters. The dimensionless ratio of $\epsilon_{\rm f}$ and $\gamma_{\rm f}$ is an estimate of the peak width and characterizes the finite-temperature crossover from the continuum excitations to damped magnon as summarized in Fig. 2. The present results shed new light on analysis of neutron scattering and other spectroscopy measurements on the spin-liquid candidates.

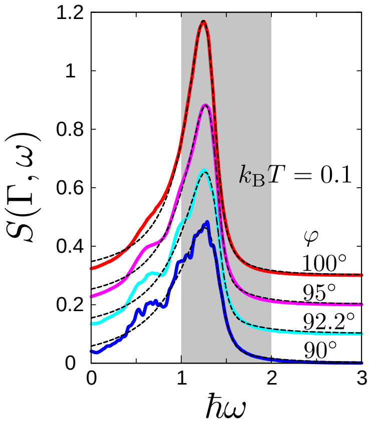

Figure 1: $S(\Gamma,\omega)$ of a 24 site cluster at $k_{\rm B}T = 0.1$ for $\varphi = 90°$, 92.2°, 95°, and 100°. The broken curves represent the asymmetric Lorentzian function $s(\omega)$ defined in Eq.(3) fitted to $S(\Gamma,\omega)$ in $1 \le \hbar\omega \le 2$. These curves are horizontally shifted for visibility.

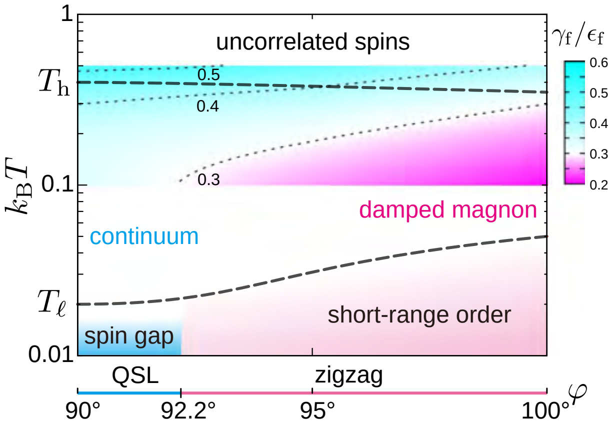

Figure 2: Summary of temperature dependence of $\gamma_{\rm f}/\epsilon_{\rm f}$ and temperature scales of the Kitaev-Heisenberg model for $90° \le \varphi \le 100°$. The two temperature scales $T_{\rm h}$ and T_ℓ for the 24 site cluster at which temperature dependence of heat capacity shows peaks.

References

[1] As reviews, S. Trebst: arXiv:1701.07056.

[2] A. Kitaev: Ann. Phys. **321** (2006) 2.

[3] G. Jackeli and G. Khaliullin: Phys. Rev. Lett. **102** (2009) 017205.

[4] J. Knolle, D. L. Kovrizhin, J. T. Chalker, and R. Moessner: Phys. Rev. Lett. **112** (2014) 207203; J. Knolle, G.-W. Chern, D. L. Kovrizhin, R. Moessner, and N. B. Perkins: Phys. Rev. Lett. **113** (2014) 187201.

[5] J. Nasu, J. Knolle, D. L. Kovrizhin, Y. Motome, and R. Moessner: Nat. Phys. **12** (2016) 912; J. Yoshitake, J. Nasu, and Y. Motome: Phys. Rev. Lett. **117** (2016) 157203.

[6] Y. Yamaji, T. Suzuki, and M. Kawamura: arXiv:1802.02854.

[7] S. Lloyd Ph.D. Thesis, Rockefeller University, 1988; A. Hams and H. De Raedt: Phys. Rev. E **62** (2000) 4365.

[8] A. Frommer: Computing **70** (2003) 87.

[9] J. Chaloupka, G. Jackeli and G. Khaliullin: Phys. Rev. Lett. **105** (2010) 027204.

Randomness-induced quantum spin liquid behavior in the s=1/2 random $J1$-$J2$ Heisenberg antiferromagnets on the honeycomb and square lattices

Kazuki Uematsu and Hikaru Kawamura
Graduate School of Science, Osaka University, Toyonaka 560-0043

The quantum spin liquid (QSL) state without any spontaneously broken Hamiltonian symmetry, which accompanies no magnetic long-range order down to low temperatures, has long received much attention. For the realization of such QSL state, geometrical frustration is considered to be essential, and frustrated magnets have been the main target of the quest for QSL materials. In particular, the s=1/2 organic triangular-lattice salts and s=1/2 inorganic kagome-lattice compound herbertsmithite are well-studied examples, which were reported in common to exhibit the QSL-like behaviors down to very low temperatures with gapless (or nearly gapless) behaviors.

Despite such recent experimental progress, the true origin of the experimentally observed QSL-like behaviors still remains not fully understood and is under hot debate. In many theoretical studies, it has been assumed that the system is sufficiently clean so that the possible effect of randomness or inhomogeneity is negligible and unimportant. Meanwhile, one of the present authors (H.K.) and collaborators have claimed that the QSL-like behaviors recently observed in triangular-lattice organic salts and kagome-lattice herbertsmithite might be the randomness-induced one, the random-singlet state [1-3]. The advocated random-singlet state is a gapless QSL-like state where spin singlets of varying strengths are formed in a hierarchical manner on the background of randomly distributed exchange interactions Jij. The state may also be regarded as a sort of ``Anderson-localized resonating valence bond (RVB) state". Indeed, it was demonstrated that the random-singlet state exhibited the T-linear specific heat and the gapless susceptibility with an intrinsic Curie tail, accompanied by the gapless and broad features of the dynamical spin structure factor.

In this year’s project, in order to examine the genericity of the proposed randomness-induced QSL state (random-singlet state) , we have extended our previous calculations in search the random-singlet state in the geometrically frustrated lattices like triangular and kagome lattices to unfrustrated, *i.e.*, bipartite lattices like honeycomb and square lattices. Frustration is introduced not by the underlying lattice geometry, but by the competition between the nearest-neighbor and the next- nearest-neighbor intereactions J_1 and J_2. We compute both the ground-state and finite-temperature properties of both the honeycomb and square models by means of the the exact diagonalization and the Hams-de Raedt methods. The ground-state phase diagram of the models is then constructed in the randomness versus the frustration (J_2/J_1) plane, with the aim of clarifying the effects of randomness and frustration in stabilizing a variety of distinct phases. The results on the honeycomb-lattice model was published in [4].

We have found that the random-singlet state similar in its nature to the one previously found in the geometrically frustrated triangular and kagome lattices are stabilized in a rather wide range of the parameter space even for the J_1-J_2 model on the honeycomb- and square-lattice models so long as the extent of frustration exceeds a critical value. We then conclude that the randomness-induced QSL state, the random-singlet state, is a generic state expected to be realized in quantum magnets in the presence of strong frustration and randomness.

References

[1] K. Watanabe, H. Kawamura, H. Nakano, and T. Sakai, J. Phys. Soc. Jpn. **83**, 034714 (2014).

[2] H. Kawamura, K. Watanabe, and T. Shimokawa, J. Phys. Soc. Jpn. **83**, 103704 (2014).

[3] T. Shimokawa, K. Watanabe, and H. Kawamura, Phys. Rev. B **92**, 134407 (2015).

[4] K. Uematsu and H. Kawamura, J. Phys. Soc. Jpn. **86**, 0447704 (2017).

Slow-Slip Phenomena Represented by the One- and Two-Dimensional Burridge-Knopoff Models of Earthquakes

Hikaru Kawamura and Jun Akutagawa

Graduate School of Science, Osaka University, Toyonaka, Osaka 560-0043

An earthquake is a stick-slip dynamic instability of a pre-existing fault driven by the motion of a tectonic plate. Numerical simulations of earthquakes based on a simplified statistical model, the so-called Burridge--Knopoff (BK) model, are popular in statistical physics, and they provide considerable information about the statistical properties of earthquakes[1]. Although the BK model has been successful in describing earthquakes, almost all studies so far have been limited to the high-speed rupture of earthquakes or to main shocks.

Meanwhile, recent development in modern GPS technology and in high-density GPS and seismograph networks has revealed a rich variety of slow-slip phenomena, including afterslips, silent earthquakes, deep tremors, *etc.*, where the fault sliding velocity is several orders of magnitudes slower than that of the standard high-speed rupture. Thus, the concept of seismicity has been broadened dramatically. Then, to gain a complete understanding of earthquake phenomena, one needs to incorporate these slow-slip phenomena.

It is a challenge to understand such a wide variety of seismicity from a general physical viewpoint, including slow slips. Therefore, questions such as what are the characteristics of slow-slip phenomena, how it differs from the standard high-speed rupture of a main shock, what conditions cause them to occur, *etc*, need to be answered.

In this year's project, we have addressed this issue from the statistical-physics viewpoint by employing the 1D and 2D BK models obeying the rate-and-state dependent friction (RSF) law. We successfully reproduce a variety of seismic phenomena, including high-speed rupture of main shocks, its precursory nucleation processes, afterslips, and silent earthquakes, by varying only a few fundamental parameters of the model. The results on the 1D model was published in [2]. Regarding the occurrence of slow-slip phenomena, the relative magnitude of the frictional parameters a and b characterizing the RSF law turns out to be crucial.

References

[1] For review, see, H. Kawamura, T. Hatano, N. Kato, S. Biswas and B.K. Chakrabarti, Rev. Mod. Phys. 84, 839-884 (2012).

[2] H. Kawamura, M. Yamamoto and Y. Ueda, J. Phys. Soc. Jpn. 87, 053001-(1-4) (2018).

Molecular Dynamics Simulation of Complex Fluids

Yuta ASANO, Hiroshi WATANABE, and Hiroshi NOGUCHI
Institute for Solid State Physics, University of Tokyo
Kashiwa-no-ha, Kashiwa, Chiba 277-8581

The addition of an extremely small amount of long-chain polymer into a Newtonian fluid causes a dramatic change in the fluid behavior. Turbulent drag reduction [1] and the change in vortex structure in Kármán vortex street [2] are the major examples of these phenomena. Because almost all industrial flows are accompanied by the turbulence and vortices, polymer effects on fluids have been intensively studied for energy saving, environmental protection, and so forth. Despite the dramatic change of the flow behavior by adding polymers is an important issue in engineering fields, the detailed mechanism remains unclear due to the difficulty of the polymer rheology in flow. So far, it is considered that the relation between the polymer and the vortical motion plays a key role in the change in fluid behavior. Therefore, in order to elucidate the mechanism of the phenomena, it is necessary to investigate polymer behavior in the vortex as directly as possible.

In the present study, we investigated the polymer effects on the Kármán vortex behind a circular cylinder by a molecular dynamics (MD) simulation using ISSP supercomputer [3]. Here, two-dimensional MD simulations were carried out to elucidate the polymer effects on the Kármán vortex street. A solvent particle and polymer molecule are modeled by Weeks–Chandler–Andersen (WCA) particle [4] and Kremer–Grest model [5], respectively. The circular cylinder is modeled by a set of WCA particles whose positions are fixed. The simulations were performed for the reference liquid (no polymer) and the polymer solutions. As for the polymer solutions, short- and long-polymer chains are considered. The number of the segment of the short- and long-polymer are $N_\mathrm{s} = 10$ and 100, respectively. The polymer concentrations are $\phi = 0.024$, 0.043, 0.085, and 0.107 in each type of polymer. These concentrations are less than the overlap concentration.

The characteristics of the vortex shedding are distinctly different for short and long polymer solutions (see Fig. 1). The characteristics of the short-polymer solution and the reference liquid are almost identical. On the other hand, the long-polymer solution exhibits two different behaviors from the reference liquid. One is a reduction in the vortex shedding frequency, and the other is a broadening of the lift coefficient spectrum. These facts are consistent with the experiments [6]. Because the gyration radius and the orientational order of the long-polymer are highly inhomogeneous in wake region, we conclude that the extensional property of the polymer plays an important role in suppression of the vortex shedding.

References

[1] G. E. Gadd: Nature **206** (1965) 463.

[2] G. E. Gadd: Nature **211** (1966) 169.

[3] Y. Asano, H. Watanabe, and H. Noguchi: J. Chem. Phys. **148** (2018) 144901.

[4] J. D. Weeks, D. Chandler, and H. C. Andersen: J. Chem. Phys. **54** (1971) 5237.

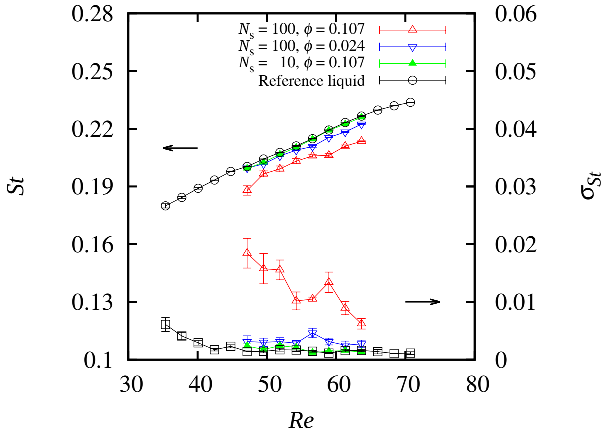

Figure 1: The Strouhal number St and the spectral width σ_{St} as a function of the Reynolds number Re.

[5] K. Kremer and G. S. Grest: J. Chem. Phys. **92** (1990) 5057.

[6] J. R. Cressman, Q. Bailey, and W. I. Goldburg: Phys. Fluids **13** (2001) 867.

Bilayer sheet protrusions and vesicle budding induced by chemical reactions

Koh M. NAKAGAWA and Hiroshi NOGUCHI
Institute for Solid State Physics, University of Tokyo, Kashiwa, Chiba 277-8581

In living cells, membrane composition continually changes by lipid metabolism. However, the effects of non-constant membrane composition on shape transformations of cells are not understood so well. We have studied membrane shape transformations under hydrolysis and condensation reactions using dissipative particle dynamics simulation [1]. The hydrolysis and condensation reactions result in the formation and dissociation of amphiphilic molecules, respectively as shown in Fig. 1. Because the dissociated hydrophilic and hydrophobic molecules are typically dissolved in surrounding fluids and embedded in the bilayer, we refer to them as the hydrophilic solute (HS) and embedded oil (EO), respectively.

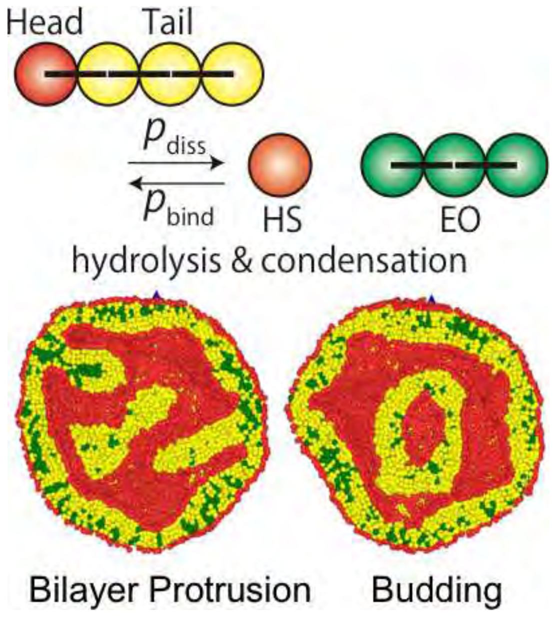

Figure 1: Top: Schematic picture of hydrolysis and condensation reactions. Bottom: Snapshots of bilayer sheet protrusions (BP) and budding of vesicles at a low reduced volume.

Asymmetric reactions between the inner and outer leaflets of a vesicle can transport amphiphilic molecules between the leaflets via EO diffusion. We consider high HS density in the inner fluid of the vesicle and investigate how the transport into the inner leaflet changes the membrane shapes. We found that the resulting area difference between the two leaflets induces bilayer sheet protrusion (BP) and budding at low reduced volumes of the vesicles (see the snapshots in Fig. 1), whereas BP only occurs at high reduced volumes.

The probabilities of these two types of transformations depend on the shear viscosity of the surrounding fluids compared to the membrane as well as the reaction rates. For a high surrounding fluid viscosity, BP formation occurs at high reaction rates. but for a low viscosity, budding always occurs before BP formation. A higher surrounding fluid viscosity leads to more BP formation. Thus, the viscosity of the surrounding fluids affects budding more than it does BP formation, while the viscosity in the membrane affects BP formation more. The inhomogeneous spatial distribution of the hydrophobic reaction products forms the nuclei of BP formation, and faster diffusion of the products enhances BP formation. Our results revealed that adjustment of the viscosity is important to control membrane shape transformations.

References

[1] K. M. Nakagawa and H. Noguchi: Soft Matter **14**, 1397 (2018).

Dynamical properties of effective models for α-RuCl$_3$

Takafumi SUZUKI
Graduate school of Engineering, University of Hyogo
Shosha, Himeji, Hyogo, 671-2280

In this project, we have studied dynamical properties of effective models for α-RuCl$_3$ [1, 2]. A honeycomb lattice magnet α-RuCl$_3$ is considered to be a candidate material for the Kitaev spin liquid because the strong Kitaev-type anisotropic interaction works between Ru^{3+} ions thanks to the edge-shared RuCl$_6$ octahedra. Many effective models for this compound have been proposed so far. However, the discussions for the proper model for this compound have not been converged yet.

In this study, we have focused on four effective models [3, 4, 5, 6]. Three of them have been proposed by the ab-initio calculations[3, 4, 5] and the other has been obtained by the ab-initio-guided method [6]. For these four models, we have calculated dynamical spin structure factors and thermal properties by using the numerical exact diagonalization method. From the results obtained from these four effective models, we have found that the four models fail to explain heat-capacity measurements whereas two of the four models succeed in explaining inelastic-neutron-scattering experiments. In the four models, the heat capacity shows a prominent peak at a high temperature when the temperature decreases. However, the peak temperature in the heat capacity is too low in comparison with that observed in the experiments.

In order to explain both the inelastic-neutron-scattering and heat-capacity experiments, we have proposed an effective model that includes the strong ferromagnetic Kitaev coupling. From the numerical calculations, we have confirmed that our model quantitatively reproduces both inelastic-neutron-scattering experiments and heat-capacity experiments. To further examine the adequacy of our model, we have calculated the field dependence of the polarized terahertz spectra. The obtained results have succeeded in explaining the experimental results: the spin-gapped excitation survives up to the critical field where the zigzag magnetic order disappears and the spin gap increases almost linearly above the critical field.

Based on these numerical results, we argue that, rather than the strong Kitaev interactions, the interactions such as off-diagonal interactions and weak Heisenberg interactions between nearest-neighbor pairs are important to explain the low-energy magnetic excitation in α-RuCl$_3$.

References

[1] T. Suzuki and S. Suga, Phys. Rev. B in press.

[2] T. Suzuki and S. Suga, J. Phys.: Conf. Sers, **969**, 012123 (2017).

[3] H.-S. Kim and H.-Y. Kee, Phys. Rev. B **93**, 155143 (2016).

[4] S. M. Winter, Y. Li, H. O. Jeschke, and R. Valenti, Phys. Rev. B **93**, 214431 (2016).

[5] R. Yadav, N. A. Bogdanov, V. M. Katukuri, S. Nishimoto, J. van den Brink, and L. Hozoi, Sci. Rep. **6**, 37925 (2016).

[6] S. M. Winter, K. Riedl, A. Honecker, and R. Valenti, Nature Comm. **8**, 1152 (2017).

Novel phases in classical and quantum frustrated spin systems

Tsuyoshi OKUBO
Department of Physics, The University of Tokyo
7-3-1 Hongo, Bunkyo-ku, Tokyo 133-0033

Anisotropic interactions due to the strong spin-orbit interaction have attracted recent interest. In Na_2IrO_3 and α-$RuCl_3$, effective spins $J_{\rm eff} = 1/2$ form the two-dimensional honeycomb lattice and they interact through the Kitaev interaction. The Kitaev interaction is an anisotropic interaction $S_i^\gamma S_j^\gamma$ with easy axis γ depending on the direction of the interacting bonds. In the case of $S = 1/2$ quantum spins with the Kitaev interaction only (Kitaev model), its ground state is proved to be a quantum spin liquid state [1]. In real compounds other interactions such as the isotropic Heisenberg interaction, the further neighbor interactions, and the off-diagonal interactions exist in addition to the Kitaev interaction [2–4]. These interaction might stabilize magnetically ordered states.

In order to clarify the effect of additional interactions, we have investigated two kinds of systems, *ab initio* Hamiltonian of Na_2IrO_3 [4,5] and Kitaev-Gamma model [6,7], by means of an infinite Tensor Product State (iTPS) method. In this iTPS method, we represent the ground state wave-function of the infinite system as a two-dimensional network of tensors. By optimizing each tensor so as to minimize the energy, we obtain wave-functions close to the ground state.

Based on iTPS calculations, we showed that the ground state of Na_2IrO_3 calculated from the *ab initio* Hamiltonian was the zigzag state [5]. The zigzag state is consistent with experimental observations, which could not be explained from the simple Kitaev-Heisenberg model. We also showed that in the parameter space away from the *ab initio* value of Na_2IrO_3, variety of magnetically ordered state were stabilized. It suggests that rich magnetic structures may appear in A_2IrO_3.

As an effective model for α-$RuCl_3$, we also investigated the ground state phase diagram of Kitaev-Gamma model where an off-diagonal interaction, the gamma term, exists in addition to the Kitaev interaction [6, 7]. The Hamiltonian of the model is given by

$$\mathcal{H} = \sum_{\gamma \in x,y,z} \mathcal{H}_\gamma, \tag{1}$$

and on z-bond,

$$\mathcal{H}_z = \sum_{\langle i,j \rangle_z} [K S_i^z S_j^z + \Gamma(S_i^x S_j^y + S_i^y S_j^x)]. \tag{2}$$

Similar to the Kitaev model, the classical ground state of the pure gamma model, where only the gamma term exists, is macroscopically degenerated and thus, one can expect possible quantum spin liquid state induced by quantum fluctuations. Actually, based on the exact diagonalization (ED) and the infinite density matrix renormalization group (iDMRG), previous studies indicated that the Kitaev spin liquid survives wide regions when the gamma term was included and it was adiabatically connected to the ground state of the pure gamma model [6, 7]. In the iTPS calculations, however, we found that magnetically ordered states had lowest energies than the Kitaev spin liquid state in wide regions, and the Kitaev spin liquid was stabilized at only the vicinity of the pure Kitaev model. The discrepancy from the previous studies might be explained by the effect of anisotropy, which was included in the previous calculations explicitly (ED) or implicitly due to the cylindrical geometry (iDMRG).

References

[1] A. Kitaev: Ann. Phys. **321** (2006) 2.

[2] G. Jackeli, and G. Khaliullin: Phys. Rev. Lett. **102** (2009) 017205.

[3] J. Chaloupka, G. Jackeli, and G. Khaliullin: Phys. Rev. Lett. **105** (2010) 027204.

[4] Y. Yamaji, Y. Nomura, M. Kurita, R. Arita, and M. Imada: Phys. Rev. Lett. **113** (2014) 107201.

[5] T. Okubo, K. Shinjo, Y. Yamaji, N. Kawashima, S. Sota, T. Tohyama, and M. Imada: Phys. Rev. B **96** (2017) 054434.

[6] A. Catuneanu, Y. Yamaji, G. Wachtel, H.-Y. Kee, and Y. B. Kim: arXiv:1701.07837.

[7] M. Gohlke, G. Wachtel, Y. Yamaji, F. Pollmann, and Y. B. Kim: Phys. Rev. B **97** (2018) 075126.

Randomness Effects on Quantum Spin Systems Coupled to Lattice Degrees of Freedom

Chitoshi YASUDA and Shouta MIYARA
Department of Physics and Earth Sciences, Faculty of Science,
University of the Ryukyus, Nishihara, Okinawa 903-0213, Japan

Since the inorganic compound $\mathrm{CuGeO_3}$ was synthesized, randomness effects of the spin-Peierls (SP) system have attracted considerable attention. When nonmagnetic impurities are doped in the SP compound, an antiferromagnetic long-range order (AFLRO) is induced. The mechanism is understood by a cluster of magnetic moments induced near an impurity, which is called an 'effective spin'. By substituting nonmagnetic atoms for magnetic atoms, effective spins are induced near the nonmagnetic atoms. Since the effective spins interact through a sea of spin-singlet pairs, the AFLRO is induced [1]. However, Cu nuclear quadrupole resonance (NQR) data contradictory to this interpretation was reported for $\mathrm{CuGe}_{1-x}\mathrm{Si}_x\mathrm{O}_3$: the effective spins are not induced near diluted sites [2]. We need to take the lattice degrees of freedom into account in order to investigate positions of the effective spins.

In this project, we investigated the appearance of the AFLRO induced by site dilution in an $S = 1/2$ two-dimensional antiferromagnetic Heisenberg model composed by the intrachain interaction J coupled to the lattice distortion and the interchain interaction J'. The method is the quantum Monte Carlo (QMC) simulation with the continuous-imaginary-time loop algorithm [3]. Since this QMC simulation is suitable to parallel computing, we mainly performed parallel computing with the Message Passing Interface.

The staggered magnetizations M_s at zero temperature were evaluated by assuming that the effective spins arise away from diluted sites for $J'/J = 0.3$ and 0.2. This assumption is necessary to recreate the NQR result for $\mathrm{CuGe}_{1-x}\mathrm{Si}_x\mathrm{O}_3$. The value of M_s for system size $N = 64 \times 64$ converges a constant value at the temperature $T/J = 0.0001$. Since the dilution-induced AFLRO for J' calculated is a physical phenomenon that occurs at a very small energy scale, we have needed the large scale numerical simulations.

We found that the AFLRO is induced by site dilution even when effective spins arise away from diluted sites. The values of M_s, however, become smaller than those in bond-alternated systems with the same parameters, where effective spins are induced near diluted sites. The decrease in M_s indicates that the AFLRO is difficult to induce in the system with the lattice degrees of freedom. By calculating the distribution of the correlation function, the dimerization order parameter, and the local-field susceptibility, we concluded that the disturbance of the singlet-pair sea and the weakening of the effective spin are the origins of the decrease in M_s. On the other hand, the width of the effective spin in the system with the lattice degrees of freedom is the similar to that in the bond-alternated system. It is expected that the locality of the effective spin is important for the appearance of the AFLRO by dilution.

References

[1] C. Yasuda, *et al.*: Phys. Rev. B **64**, 092405 (2001); J. Phys. Soc. Jpn. **75**, 124704 (2006).

[2] J. Kikuchi, *et al.*: Phys. Rev. Lett. **88**, 037603 (2002).

[3] S. Todo and K. Kato, Phys. Rev. Lett. **87**, 047203 (2001).

Excitation dynamics of two-dimensional quantum spin systems

Akiko MASAKI-KATO

RIKEN Center for Computational Science,
Wako, Saitama 351-0198

The ground state property of two-dimensional quantum lattice models such as two-dimensional quantum Heisenberg spin systems has been theoretically understood rapidly in recent years. On the other hand, excitation dynamics are not well understood even in simple models such as S=1/2 square lattice antiferromagnetic Heisenberg models (SLAHM). For example, although the staggered order in which the adjacent spins are antiparallel each other is realized, the staggered magnetic moment is 40% smaller than that expected in the classical Néel order due to the quantum fluctuation. How this giant quantum effect is reflected in the ground state and how it appears in the excitation dynamics have been discussed as an essential problem of quantum spin systems since it was discovered in high-T_c cuprates [1]. As consensus of the experiment results until recent years, it can be mentioned that the magnon excitation spectrum of the wave number **k** = (π, 0) becomes much broader than that of **k** = (π/2, π/2), and the peak position also shifts to the lower energy side [2,3]. These features are observed not only with high-T_c cuprates but also with other materials. That is, experimental results suggest that this is the universal nature of S=1/2 SLAHM without being attributed to specific properties of each material. According to the linear spin-wave theory, the magnon excitation energy at these two wavenumbers is the same and it is expected to behave similarly. Furthermore, the incoherent excitation observed at these wave numbers can not be explained by the linear spin wave theory. Recent neutron scattering experiments with metal-organic compound Cu(DCOO)2・4D2O (CFTD) have argued that the source of incoherent excitation at wave number **k** = (π, 0) is spinon excitation. However, no effective theoretical interpretation has been obtained so far.

One of the reasons why the excitation dynamics of low-dimensional quantum lattice system is poorly understood is that it is not easy to calculate the dynamic physical quantity even when the numerical calculation method has dramatically advanced recently.

The worldline QMC method[4] based on Feynman's path integral representation is one of the most powerful tool that can be obtained an exact solution within the range of the statistical error with respect to the equilibrium state of the quantum lattice system free from the negative sign problem at the finite temperature. With this method it is possible to treat huge lattice systems of thousands to millions sites. However conventional spectrum estimation methods such as the maximum entropy method are not sufficiently accurate and it is difficult to quantitatively discuss line shapes of unexplained excitation spectra because bias such as prior knowledge and artificial tuning parameters work strongly. Recently, a new numerical analytic continuation method which is the hybrid of the stochastic optimization method and consistent constraints (SOCC) method proposed by Mishchenko *et al*, who is a co-worker of us, have been succeeded [5]. SOCC method is unbiased method for estimating the spectrum function with statistical error-bars. With this method, it was possible to evaluate delta function like peaks and widths of peaks for which MEM is not good.

We calculated on the excitation spectra of S=1/2 SLAHM which is an effective model of CFTD at two distinctive wavenumbers **k** using QMC+SOCC method. To obtain imaginary time correlations with ultra-high precision by QMC calculation, we executed huge-scale parallel computations using supercomputer in *ISSP*. I have obtained results that quantitatively and precisely coincide with the neutron scattering experiment result for CFTD. A remarkable feature is that the sharp peak at **k** = (π/2, π/2) suggests the existence of symmetric well-defined magnon excitation, while the peak at **k** = (π, 0) is broad and asymmetric. As a result of investigating the temperature dependence, the delta function like peak grow at **k** = (π/2, π/2), whereas at **k** = (π, 0), no change was observed when the temperature was sufficiently low. It indicates that the excitation of this model has the incoherent property [6].

References

[1] N. B. Christensen, et al., Proc. Nati. Acad. Sci. USA (2007) and so on.

[2] B. Dalla Piazza *et al.*, Nat. Phys. **11**, 62 (2015)

[3] N. S. Headings *et al.*, Phys. Rev. Lett. 105, 247001 (2010) and so on.

[4] A. Masaki-Kato *et al.*, Phys. Rev. Lett. 112, 140603 (2014); dsqss [https://github.com/qmc/dsqss]; and so on.

[5] O. Goulko *et al.*, Phys. Rev. B 95, 014102 (2017).

[6] Akiko Masaki-Kato *et al.*, submitted (2018).

Finite-Sized effects and hysteresis in chiral helimagnets

Yusuke Kato
Department of Basic Science, The University of Tokyo
Komaba 3-8-1, Meguro-ku, Tokyo 153-8902

We have studied two subjects of mono-axial chiral helimagnets using class C.
(i)We examined the properties of isolated chiral soliton as constituent of chiral soliton lattice in mono-axial chiral helimagnets at finite temperatures with use of three-dimensional lattice model[1]. In the plane of magnetic field and temperature, we numerically found the instability line of isolated chiral soliton, the region where the interaction between two solitons is repulsive/attractive and the region where the isolated chiral soliton can not exist. We found that the three regions correspond to the continuous phase transition of nucleation-type (repulsive soliton region), the discontinuous phase transition (attractive soliton region) and the continous phase transition of instability-type (no soliton region). This coincidence between the properties of soliton and the type of phase transition implies crucial role of chiral soliton in the mechanism for the phase transition. In this study, we used the supercomputers to examine the properties of isolated soliton and the types of phase transition in the mean-field theory.
(ii) We argue that the surface barrier is an underlying mechanism for large hysteresis observed in magneto-resistance (MR) measurement for micrometer-sized samples of mono-axial chiral magnet CrNbS[2]. The hysteresis of MR in those specimens consists of conspicuous jump at the field H_b in decreasing field process and relatively gradual change in field increasing process. We attribute the large jump in the decreasing field process to the disappearance of the surface barrier. This interpretation is justified through agreement between the experimental results at 10K (which is much lower than the transition temperature $T_\mathrm{c} \sim 130\mathrm{K}$ in zero field) and theoretical result of a universal ratio $H_\mathrm{b}/H_\mathrm{c} = 4/\pi^2 \sim 0.4$ (with thermodynamic critical field H_c) at zero temperature in the configuration of the least demagnetization effect. We discuss that surface barrier is regarded as a common property shared among various systems (superconductors, chiral magnets and chiral liquid crystals) with nucleation type of continuous phase transition. In early state of this study, we used the supercomputers to examine the metastable properties of chiral magnet in the mean-field type relaxation method. We also used it to discuss the experimental results on hysteretic properties in magnetization-curve in this material in [3]
A doctor degree has been given on the basis of the two studies[4].

References

[1] M. Shinozaki, S. Hoshino, Y. Masaki, A. O. Leonov, J. Kishine and Y. Kato: submitted to JPSJ.

[2] M. Shinozaki, Y. Masaki, R. Aoki, Y. Togawa and Y. Kato: submitted to PRB.

[3] M. Mito, et al, PRB **97**, 024408 (2018).

[4] M. Shinozaki, Doctor Thesis (2017) The University of Tokyo.

Nonequilibrium relaxation analysis for critical properties of the antiferromagnetic triangular Heisenberg model

Y. Ozeki and R. Tobise
Graduate School of Informatics and Engineering, The University of Electro-Communications

We investigate the phase transition and critical properties for the antiferromagnetic (AF) triangular Heisenberg model by means of the nonequilibrium relaxation (NER) method [1]. While it has been well-known that there is no long-range order with continuous symmetry-breaking in 2D continuous spin systems, a topological phase transition has been explored in this model and discussed for a long time [2]. Previously, we analyzed the relaxation of the z-component for the chiral order parameter, $\kappa(t)$, from a 120° structure in the XY-plane, and estimated the precise transition temperature as $T_{\mathrm{KT}} = 0.2767$ using the NER method with recently improved dynamical scaling analysis [3], where we assumed the transition type as the Kosterlitz-Thouless (KT) one.

In the present study, we estimate the static and dynamical critical exponents z and η, where just these two critical exponents exist independently in the KT transition. Together with the relaxation of order parameter, the NER of fluctuation $f_{\kappa\kappa}(t) \equiv N\left[\langle\kappa(t)^2\rangle/\langle\kappa(t)\rangle^2 - 1\right]$. is used for the analysis. The asymptotic forms for these dynamical functions are expected as $\kappa \sim t^{-\eta/2z}$ and $f_{\kappa\kappa} \sim t^{2/z}$, which provide the estimations for z and η. Calculations are carried out for 1001×1002 triangular lattice with a skew boundary condition at the transition temperature obtained above up to an observation time of 2000 Monte Carlo steps (MCSs). About 3×10^6 samples are taken for statistical averaging. Making numerical derivatives for $f_{\kappa\kappa}(t)$ and $\kappa(t)$, we evaluate the functions $z(t)$ and $\eta(t)$, which converge to $z = 1.90$ and $\eta = 0.370$ asymptotically, as shown in Figs. 1-2. The present estimations suggest that the static exponent η is much deviated from those for the FM-XY model $\eta = 0.25$ and for the triangular AF-XY model $\eta \sim 0.31$, while the dynamical one z are almost the same with those model $z \sim 2$. This indicates that the universality class of the triangular AF Heisenberg model would be distinct with that of the triangular AF XY model. Farther investigations are necessary to settle these problems.

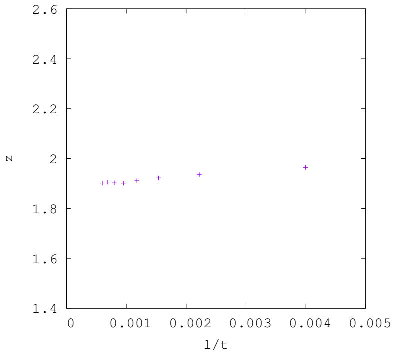

Figure 1: Local exponent $z(t)$.

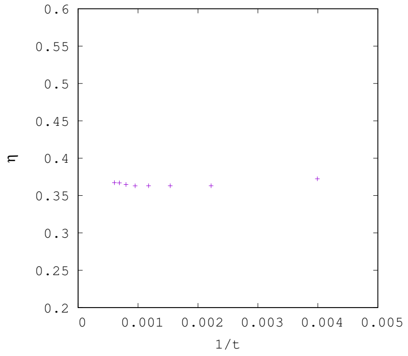

Figure 2: Local exponent $\eta(t)$

References

[1] Y. Ozeki and N. Ito, Phys. Rev. B**68** 054414 (2003); Y. Ozeki and N. Ito, J. Phys.: Math. Theor. **40** R149 (2007).

[2] H. Kawamura and S. Miyashita, J. Phys. Soc. Jpn. **53** 4138 (1984); H. Kawamura, et. al., J. Phys. Soc. Jpn. **79** 023701 (2010).

[3] Y. Echinaka and Y. Ozeki, Phys. Rev. E**94** 043312 (2016).

Molecular dynamics simulations to reveal aggregation mechanism of amyloid-β peptides

Satoru G. Itoh and Hisashi Okumura
Research Center for Computational Science,
Institute for Molecular Science, Okazaki, Aichi 444-8585

Protein aggregates such as oligomers and amyloid fibril, which is a fibrous aggregate of proteins, are known to be associated with more than 40 human neurodegenerative diseases (Fig. 1). For example, Alzheimer's disease is related to amyloid-β (Aβ) peptides, and Parkinson's disease is caused by α-synuclein. To overcome these diseases, it is essential to understand the formation mechanism of protein oligomers and amyloid fibrils. For this purpose, we have been performed several molecular dynamics (MD) simulations of oligomers and amyloid fibrils: We have revealed (a) the aggregation mechanism of Aβ fragments [1,2], (b) structural difference between two ends of the Aβ amyloid fibril [3], and (c) disruption process of Aβ amyloid fibril by supersonic wave [4]. As for the aggregation of Aβ, we have dealt with relatively simple systems such as Aβ fragments (not full length) in pure solvent so far, but we tried more realistic systems including the full length Aβ peptides in this fiscal year.

Aβ has two types, Aβ 40 (40 residues) and Aβ 42 (42 residues), which differ in the number of amino acids in the C-terminal region. It is known that the oligomerization and amyloid formation speed of Aβ42 are faster than those of Aβ40, but it is not clear why such a difference occurs. Initial formation of amyloid fibrils in the brains of Alzheimer's disease patients is thought to be caused by aggregation of Aβ42 rather than Aβ40. Understanding the difference in aggregation mechanism of Aβ40 and Aβ42 is also essential for the development of Alzheimer's disease treatment. We performed a Hamiltonian replica-permutation MD simulation, the method of which was developed by our group, on each of the Aβ 40 dimer and Aβ 42 dimer systems and examined the effect of the C-terminal region on oligomer formation. As a result, we found that Aβ42 forms intermolecular β-sheet more than Aβ40. We also found that this difference is caused by the fact that Aβ42 tends to form a β-hairpin more easily and a stable intermolecular β-sheet is formed between this β-hairpin and another Aβ42.

We plan to increase the statistic by performing the simulations further and investigate the details of the dimerization mechanism of Aβ40 and Aβ42 and its differences.

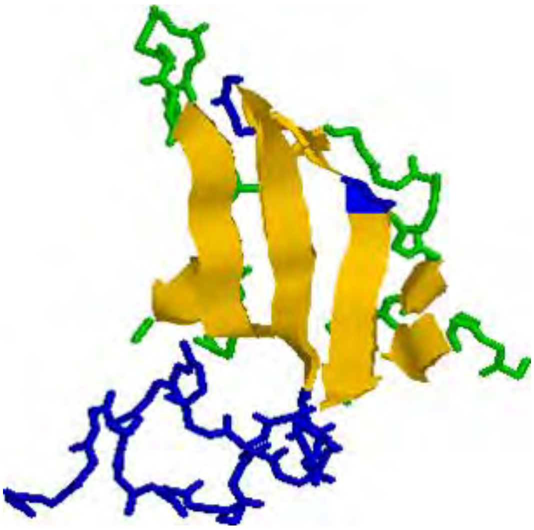

Fig. 1: Aggregated Aβ peptides of Aβ peptides.

References

[1] S. G. Itoh and H. Okumura: J. Phys. Chem. B **118** (2014) 11428.

[2] S. G. Itoh and H. Okumura: J. Comput. Chem. **120** (2016) 6555.

[3] H. Okumura and S. G. Itoh: Sci. Rep. **6** (2016) 28422.

[4] H. Okumura and S. G. Itoh: J. Am. Chem. Soc. **136** (2014) 10549.

Elucidation of softness hidden in glass-forming liquids

Kang KIM[1] and Hayato SHIBA[2]
[1]*Division of Chemical Engineering, Graduate School of Engineering Science,*
Osaka University, Toyonaka, Osaka 560-8531
[2]*Institute for Materials Research, Tohoku University*
2-1-1, Katahira, Aoba-ku, Sendai 980-8577

We are investigating the universal feature for emergence of softness in glass-forming liquids. One of our recent findings is long-wavelength fluctuation in two-dimensional (2D) glassy liquids forming originating in the same mechanism as Mermin-Wagner theorem. In this year, we have performed several extended analyses of 2D fluctuations. One is the normal mode analysis of 2D and 3D supercooled liquid for Lennard-Jones binary mixtures with Kob-Andersen parameters, so that we can establish the Debye asymptote, in a more quantitative manner than the estimation using the velocity autocorrelation function performed in our previous publication [1]. We have especially working on solution of sparse Hessian matrix, with more than 10^{13} matrix elements, to elucidate its low-frequency vibration behaviors. In addition, we began to investigate the response of 2D liquids to the external field, owing to the mechanical softness that is inherent to the 2D glassy systems. The details are under preparation for our forthcoming publication [2].

In addition, we have developed to new methodologies to clarify the unified mechanism for emergence of fragility in various types of glassy liquids. We are developing classical molecular models with tunable fragilities, in order to investigate its correlation with the viscous relaxation, diffusion, and energy transport. Up to now, we clarified that the diffusion is associated with breakage of hydrogens and stress relaxation, and emergence of rigidity is decoupled from these, by investigating the breakdown mechanism of Stokes-Einstein relaxation in water systems [3]. Its relation to anomalous properties of glasses, including Boson peak and hidden structural ordering, is now under investigation.

References

[1] H. Shiba, Y. Yamada, T. Kawasaki, and K. Kim: Phys. Rev. Lett. **117**, 245701 (2016).

[2] H. Shiba, T. Kawasaki, and K. Kim: in preparation.

[3] T. Kawasaki and K. Kim: Sci. Adv **3**, e1700399 (2017).

The effect of bond-randomness on the quantum magnetisms in low dimension

TOKURO SHIMOKAWA[1] and HIKARU KAWAMURA[2]
[1]*Okinawa Institute of Science and Technology Graduate University,*
Onna, Okinawa, 904-0495, Japan
[2]*Department of Earth and Space Science, Graduate School of Science, Osaka University,*
Toyonaka, Osaka 560-0043, Japan

S=1/2 antiferromagnetic Heisenberg model on the kagome lattice with nearest-neighbor interaction is well known as a candidate of the possible realization of a quantum spin liquid (QSL) state. In spite of the tremendous efforts, the true natures still remain unclear.

We investigate the effect of the bond-randomness to the thermal properties of the S=1/2 kagome antiferromagnet by means of Hams-de Raedt (thermal pure quantum state) method [1, 2, 3]. This method enables us to compute exact finite-temperature physical quantities for larger system sizes than those treated by the conventional exact diagonalization method and the negative sign problem does not occur. We treat here up to 36-site kagome cluster which has full symmetry of the infinite kagome lattice under periodic boundary condition.

In the 36-site cluster, we identified before the additional 3rd and 4th peaks in the low-temperature specific heat and found that the 3rd peak is associated with a crossover phenomenon occurring between the QSL states with distinct magnetic short-ranged orders (SROs). We investigate here the effect of the bond-randomness to the crossover phenomenon observed in the regular kagome-lattice antiferromagnet. We find that the low-temperature specific heat shows T-linear behavior in the strong randomness case even in the 36-site cluster as reported in smaller system sizes by means of the exact diagonalization method [4]. Almost no size dependence of the T-linear specific heat is also confirmed from 12 to 36-site clusters in the strong randomness case.

Our results were obtained by using CPU node of system B. Our MC code is executed in parallel by using OpenMP technique.

References

[1] M. Imada and M. Takahashi,J. Phys. Soc. Jpn. **55**, 3354 (1986).

[2] A. Hams and H. De Raedt, Phys. Rev. E **62**, 4365 (2000).

[3] S. Sugiura and A. Shimizu, Phys. Rev. Lett. **111**, 010401 (2013).

[4] H. Kawamura, K. Watanabe, and T. Shimokawa, J. Phys. Soc. Jpn. **83**, 103704 (2014)

Multiple-Q states of the frustrated Heisenberg model on the honeycomb lattice

TOKURO SHIMOKAWA[1] and HIKARU KAWAMURA[2]
[1] *Okinawa Institute of Science and Technology Graduate University, Onna, Okinawa, 904-0495, Japan*
[2] *Department of Earth and Space Science, Graduate School of Science, Osaka University, Toyonaka, Osaka 560-0043, Japan*

Motivated by recent theoretical study by Okubo *et al* [1] of the possible realization of the triple-q skyrmion-lattice state in the J_1-J_2 or J_1-J_3 triangular-lattice Heisenberg model, we here investigate the ordering properties in the J_1-J_2 classical honeycomb-lattice Heisenberg model under magnetic field.

The Hamiltonian of the honeycomb-lattice Heisenberg model is given by,

$$\begin{aligned}\mathcal{H} = & - J_1 \sum_{\langle i,j \rangle} \mathbf{S}_i \cdot \mathbf{S}_j - J_2 \sum_{\langle\langle i,j \rangle\rangle} \mathbf{S}_i \cdot \mathbf{S}_j \\ & - H \sum_i S_i^z, \end{aligned} \tag{1}$$

where $\mathbf{S}_i = (S_i^x, S_i^y, S_i^z)$ is the classical Heisenberg spin with the fixed length of $|\mathbf{S}_i| = 1$ located at the i-th site on the honeycomb lattice, $J_1 < 0$ and $J_2 < 0$ represent the antiferromagnetic NN and NNN interactions, while the $\sum_{\langle i,j \rangle}$ and $\sum_{\langle\langle i,j \rangle\rangle}$ are taken over the NN and NNN pairs J_1 and J_2, respectively.

This model has been known that the ground state of the model in zero field exhibits, for $J_2/J_1 > 1/6$, a single-q helical order with an incommensurate wavevector with an infinite ring-like degeneracy in the q-space, while, for $J_2/J_1 \leq 1/6$, the standard two-sublattice antiferromagnetic order [2]. Finite-temperature ordering properties in zero field have also been investigated by Okumura *et al* [3], and then only a single-q helical ordered state has been found as an quasi-long ranged ordered state. The in-field ordering process of the present honeycomb-lattice model is a remaining big issue since the interplay between macroscopic degeneracy in the ground state and fluctuations might lead to a intriguing behavior.

We focus here to the region $1/6 < J_2/J_1 < 0.2$ in which the incommensurability is very strong. We succeed to find an exotic multiple-q state by means of extensive monte carlo (MC) method. The corresponding real-space spin texture seems to be like a “water ripple”, therefore, we call the new multiple-q state as “ripple state”. We also find appearance of the vector chiral domain in the new state and the relationship to the spin-liquid compound, $\mathrm{Bi_3Mn_4O_{12}(NO_3)}$ is discussed. [4]

Our results were obtained by using CPU node of system B. Our MC code is executed in parallel by using both OpenMP and MPI techniques.

References

[1] T. Okubo, S. Chung, and H. Kawamura, Phys. Rev. Lett. **108**, 017206 (2012).

[2] S. Katsura, T. Ide, and T. Morita: J. Stat. Phys. **42**, 381 (1986).

[3] S. Okumura, H. Kawamura, T. Okubo, and Y. Motome, J. Phys. Soc. Jpn. **79**, 114705 (2010).

[4] T. Shimokawa, and H. Kawamura, to be submitted.

Numerical Diagonalization Study on the Spin Gap of Frustrated Systems

T. SAKAI[1,2,3], H. NAKANO[1,2], Y. Hasegawa[1,2], T. SHIMOKAWA[4], and A. Shimada[5]
[1]*Graduate School of Material Science, University of Hyogo,*
Kouto, Kamigori, Hyogo 678-1297, Japan
[2]*Research Center for New Functional Materials, University of Hyogo,*
Kouto, Kamigori, Hyogo 678-1297, Japan
[3]*Synchrotron Radiation Research Center, Kansai Photon Science Institute,*
Quantum Beam Science Research Directorate,
National Institute for Quantum and Radiological Science and Technology (QST)
SPring-8, Kouto, Sayo, Hyogo 679-5148, Japan
[4]*Okinawa Institute of Science and Technology Graduate University, Okinawa, Japan*
[5]*Graduate School of Science, Kyoto University, Kyoto 606-8502, Japan*

The S=1/2 kagome-lattice antiferromagnet is one of interesting frustrated quantum spin systems. The systems exhibit the quantum spin fluid behavior, which was proposed as an origin of the high-Tc superconductivity. The spin gap is an important physical quantity to characterize the spin fluid behavior. Whether the S=1/2 kagome-lattice antiferromagnet is gapless or has a finite spin gap, is still unsolved issue. Because any recently developped numerical calculation methods are not enough to determine it in the thermodynamic limit. Our large-scale numerical diazonalization up to 42-spin clusters and a finite-size scaling analysis indicated that the S=1/2 kagome-lattice antiferromagnet is gapless in the thremodynamic limit[1, 2, 3]. It is consistent with the U(1) Dirac spin liquid theory of the kagome-lattice antiferromagnet[4, 5]. On the other hand, the density matrix renormalization group calculations supported the gapped Z2 topological spin liquid theory[yan,hotta]. We propose one of better methods to determine whether the spin excitation is gapless or gapped, based on the finite-size scaling analysis of the spin susceptibility calculated by the numerical diagonalization. The present work indicates that the kagome-lattice antiferromagnet is gapless, as well as the triangular-lattice one[8, 9, 10].

References

[1] H. Nakano and T. Sakai: J. Phys. Soc. Jpn. 80 (2011) 053704.

[2] H. Nakano and T. Sakai, J. Phys. Soc. Jpn. 84 (2015) 063705.

[3] T. Sakai and H. Nakano, Phys. Rev. B 83 (2011) 100405(R).

[4] Y. Ran, M. Hermele, P. A. Lee and X. -G. Wen: Phys. Rev. Lett. 98 (2007) 117205.

[5] Y. Iqbal, F. Becca, S. Sorella and D. Poilblanc: Phys. Rev. B 87 (2013) 060405(R).

[6] S. Yan, D. A. Huse and S. R. White: Science, 332 (2011) 1173.

[7] S. Nishimoto, N. Shibata and C. Hotta: Nature Commun. 4 (2013) 2287.

[8] T. Sakai and H. Nakano: POLYHEDRON 126 (2017) 42.

[9] H. Nakano and T. Sakai: J. Phys.: Conf. Ser. 868 (2017) 012006.

[10] T. Sakai and H. Nakano: to appear in Physica B.

Numerical Study on Spin Flop Phenomena in Low-Dimensional Quantum Spin Systems

T. SAKAI[1,2,3], H. NAKANO[1,2], Y. Hasegawa[1,2], T. SHIMOKAWA[4], and A. Shimada[5]
[1]*Graduate School of Material Science, University of Hyogo,*
Kouto, Kamigori, Hyogo 678-1297, Japan
[2]*Research Center for New Functional Materials, University of Hyogo,*
Kouto, Kamigori, Hyogo 678-1297, Japan
[3]*Synchrotron Radiation Research Center, Kansai Photon Science Institute,*
Quantum Beam Science Research Directorate,
National Institute for Quantum and Radiological Science and Technology (QST)
SPring-8, Kouto, Sayo, Hyogo 679-5148, Japan
[4]*Okinawa Institute of Science and Technology Graduate University, Okinawa, Japan*
[5]*Graduate School of Science, Kyoto University, Kyoto 606-8502, Japan*

The spin flop is one of interesting magnetic phenomea. It was initially proposed as a first-order phase transition accompanied by the change of the direction of the Néel order. It has been supposed to occur only in antiferromagnets with the easy-axis anisotropy. However, our previous large-scale numerical diagonalization study indicated that a spin-flop-like magnetization jump in someantiferromagnets without any spin anisotropy[1, 2, 3]. The systems which exhibit such a magnetization jump are the $S = 1/2$ square-kagome- and Cairo-pentagon-lattice antiferromagnets. The magnetization jump is supposed to induced by the strong spin frustration. However, the detailed mechanism is still an open problem. Thus we study on the spin flop phenomena of these frustrated systems using the exact small cluster analysis. As a result, it is found that the magnetization jump is induced by an entangled state[4].

References

[1] H. Nakano and T. Sakai: J. Phys. Soc. Jpn. 82 (2013) 083709.

[2] H. Nakano, M. Isoda and T. Sakai: J. Phys. Soc. Jpn. 83 (2014) 053702.

[3] H. Nakano, T. Sakai and Y. Hasegawa: J. Phys. Soc. Jpn. 83 (2014) 084709.

[4] Y. Hasegawa, H. Nakano and T. Sakai: submitted to Phys. Rev. B.

Efficient Sampling Simulation of the Soft Modes Significantly Contribute to Protein Properties

Kazuhiro TAKEMURA, Duy TRAN, Hisham DOKAINISH, Jacob SWADLING,
Hiroaki HATA, Kenichiro TAKABA, Ai SHINOBU, and Akio KITAO
School of Life Science and Technology, Tokyo Institute of Technology
Ookayama, Meguro, Tokyo 152-8550

Proteins carry their function by interacting with other proteins or ligands. Thus, accurate prediction of protein-protein/ligand complex structures is a key to understanding their function. We proposed the Concentrated ligand Docking (ColDock) method, an efficient but accurate method to generate protein-ligand complex structures using molecular dynamics (MD) simulations at relatively high ligand concentrations. The procedure of ColDock for a given protein-ligand pair is as follows. (i) Multiple ligands are distributed randomly around the protein at relatively high concentration (~100 mM). (ii) Multiple short (100 ns) independent MD simulations are conducted. To prevent ligand aggregations which might be caused by high concentration, extra repulsive forces are applied between ligands (Fig.1). (iii) Ligands in contact with the protein are selected. (iv) The selected ligands are clustered according to root-mean-square-deviation (RMSD). Ligand poses are predicted as the representatives poses of each of the dominant clusters.

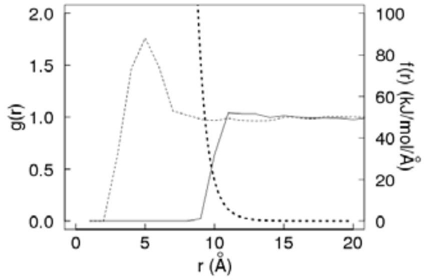

Fig.1 Pair distribution functions, g(r)s, of ligand with (solid line) and without (broken line) repulsive force, f(r) (dotted line)

We applied ColDock to four systems; FK506 binding protein in complex with 1) dimethylsulfoxide (DMS) and 2) methyl sulfinyl-methyl sulfoxide (DSS), 3) a complex of human plasminogen kringle 4 with ε-aminocaproic acid (ACA), and 4) the X-linked inhibitor of apoptosis protein in complex with 4-(4-bromo-1H-pyrazol-1-yl) piperidinium (BPP). We used the protein structure in holo form (taken from the crystal complex structure for DMS, ACA, and BPP as an initial test. To examine the performance of ColDock we later used the protein structures in apo form for all four systems.

Since ligands bound to the correct

position are stably held at that position, the population of ligands at the correct binding site is expected to be high. The assumption was verified by analyzing probabilities of ligand contact per residue (Fig.2). As expected, residues with high contact probability (dark region in Fig.2) are located around the correct binding site. Ligands in contact with the protein from all MD snapshot were gathered, then RMSD-based clustering was conducted. To reduce the computational cost for clustering, only ligands in contact with 6 or more residues were selected.

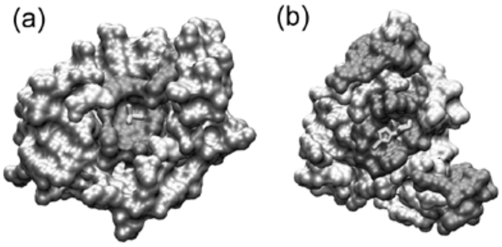

Fig.2 Probabilities of ligand contact per residue in DMS (a) and BPP (b). Darker regions represent residues with high contact probability. Ligands in the crystal structure of the complex are shown for reference.

Despite the simplicity of the procedure, ColDock successfully predicted the structure of the three complexes starting from the holo structure. Ligand RMSDs (RMSD of ligand from the crystal structure after superposing protein structures) for DMS, ACA, and BPP were 0.3, 1.3, and 0.4 Å, respectively. All the native contacts were successfully reproduced. When protein structures in the apo forms were used, ColDock successfully predicted three out of four cases (Fig.3). For BPP, the ligand binding site of the protein in the apo form is closed (Fig.4) and was unable to open within 100 ns. The combination with a pocket expansion technique is required for such targets and is currently under investigation. Since ColDock uses standard MD simulations with an extra repulsive force, it can be easily combined with any method.

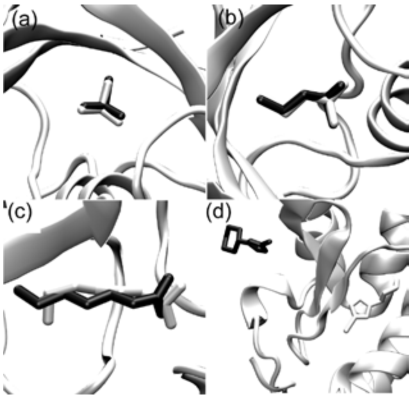

Fig.3 Predicted (black) and crystal (white) structures of ligands in (a) DMS, (b) DSS, (c) ACA, and (d) BPP.

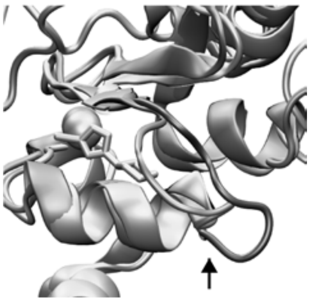

Fig.4 Structures of the X-linked inhibitor of apoptosis protein in the crystal holo (dark) and apo (light) forms. The arrow indicates the loop which closes the binding pocket in the apo form.

Elucidation of binding and unbinding processes of a ligand to a protein using a hybrid of the manifold theory and the Markov state model

Takashi YOSHIDOME

Department of Applied Physics,

Tohoku University, 6-6-05, Aoba, Aramaki, Aoba-ku, Sendai 980-8579

To construct an in-silico drug-design protocol, an accurate computation of the dissociation rate for protein-ligand systems is required. However, the computation is impossible with the molecular dynamics (MD) simulations because the time scale of the dissociation is second and is too long to perform the conventional MD for dissociation. A solution is to employ the Markov-state model (MSM). The model is constructed through the following steps: (i) Classify conformations into major states; (ii) Calculate the transition probabilities between the states, and; (iii) Compute physical quantities. We have recently proposed that an accurate computation of a physical quantity is possible when a manifold-learning technique employed for the classification [1].

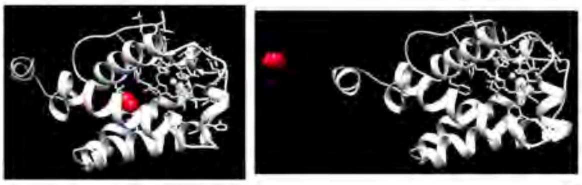

Fig. 1: The snapshots of the initial (left) and final (right) MD steps. Spheres are the O_2.

Here, we performed MD simulations of hemoglobin-O_2 system to demonstrate that the dissociation rate can accurately compute using MSM. The program AMBER16 [3] was used for the MDs. The calculations were primarily performed using L4cpu and L2fat. To investigate whether accurate computation of the dissociation rate is possible, its correct answer is required. To obtain the answer, dissociation should occur within the time scale (t_{MD}) that MD can be performed. As shown in Fig. 1, The dissociation of O_2 was successfully reproduced within t_{MD}.

References

[1] R. Ito and T. Yoshidome, Chem. Phys. Lett., **691**, 22 (2018).

[2] D.A. Case, *et al.*, AMBER 2016, University of California, San Francisco (2016).

Accurate computation of the free-energy change of apoplastocyanin using the end-points method

Takashi YOSHIDOME
Department of Applied Physics,
Tohoku University, 6-6-05, Aoba, Aramaki, Aoba-ku, Sendai 980-8579

To elucidate the mechanism for a variety of biophysical processes such as protein folding and aggregation and binding of drug molecules, accurate and efficient computation of the free energy of proteins is inevitable. The standard methods enable us to exactly compute the free energy of proteins within a force field used. However, molecular dynamics (MD) simulations of many intermediate states connecting the initial (reference system containing only water molecules) and final (solution system consisting of water and solute) states are required. On the other hand, we have recently proposed accurate computation methods for the hydration-free energy [1] and for the configurational entropy [2]. These methods enable us to compute those quantities using the MD simulation data for the initial and final states. Thus, our computational method, referred to as "end-point method", is more efficient than the standard method.

To demonstrate the usefulness of the end-point method through an accurate computation of the free-energy change of protein folding, we applied the method to the protein folding of apoplastocyanin. We first performed a replica-exchange MD (REMD) simulation to sample the conformations including the native and unfolded states. The program AMBER16 [3] was used for the REMD, and generalized Born model was employed for the implicit solvent model. We then calculated the entropy change upon folding of apoplastocyanin using the end-point method and the morphometric approach [4]. The calculations were primarily performed using the L36cpu. The result was 1.7 kcal/mol, and experimental value was ~ 0 kcal/mol. A reason of discrepancy would be the force field for proteins.

References

[1] T. Yoshidome, T. Ekimoto, N. Matubayasi, Y. Harano, M. Kinoshita, and M. Ikeguchi, J. Chem. Phys., **142**, 175101 (2015).

[2] S. Hikiri, T. Yoshidome, and M. Ikeguchi, J. Chem. Theory Compt., **12**, 5990 (2016).

[3] D.A. Case, *et al.*, AMBER 2016, University of California, San Francisco (2016).

[4] R. Roth, Y. Harano, and M. Kinoshita, Phys. Rev. Lett., **97**, 078101 (2006).

Physical Property Analysis of Macromolecular Self-Assembly using Quantitative Coarse-Grained Molecular Model

Wataru Shinoda
Department of Materials Chemistry, Nagoya University
Furo-cho, Chikusa-ku, Nagoya 464-8653

Coarse grained (CG) model has been widely used in macromolecular and biological simulations. To investigate molecular processes at the meso- and macroscopic scales, "phenomenological" CG models have mostly been used. However, chemical details often significantly affect the physical properties of molecular assembly, suggesting the need of a quantitative CG model that can reflect the difference of molecular species at an appropriate resolution. Our CG model is one of these trials to conduct a quantitative simulation particularly focusing on the interfacial problems in soft materials. Thus, we have been developing a CG model that can capture the interfacial thermodynamic properties of molecular assembly correctly.[1] The CG model is often called the SDK (Shinoda-Devane-Klein) model.[2] Based on the SDK approach, we are developing a new CG model for polymers and biological macromolecules. In this report, we write specifically a polymer CG model for perfluoro sulfornic acid (PFSA) membranes.[4]

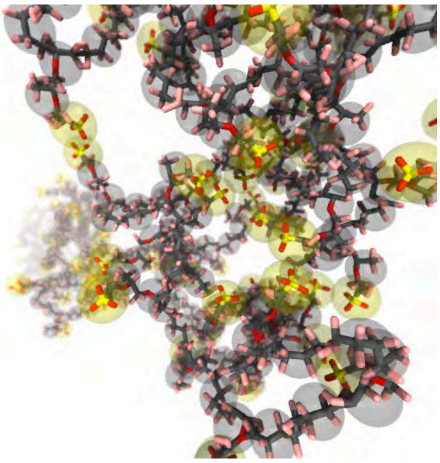

Figure 1: The CG mapping of PSFA ionomer. All-atom representation is given in stick and CG representation is given in transparent particle.

In our CG approach, we use experimental and computational data as references for the parameter optimization of the CG model. As shown in Fig. 1, we define a single CG site to represent a group of about 10 atoms. The computational data is usually obtained by a series of all-atom molecular dynamics (AA-MD) simulations of relatively small systems. Using the supercomputer at ISSP, we can conduct a large-scale simulation of PFSA membrane even with the all-atomic force field. 100ns-long AA-MDs of PSFA system containing 200,000 atoms have been routinely conducted, which produces well converged results for structural properties for relatively short chained polymers (connected 10 monomer units). This produces a reliable reference data for structural properties of PSFA membranes. However, polymers that are experimentally used for the electrolyte purpose have much higher molecular weight typically, so we need to handle the longer polymer chains including more than a hundred of monomer units to simulate the experimentally relevant system. This is prohibitively difficult for AA-MD, so we need a quantitative CG model at least to reproduce the morphology made by PFSA including some amount of water. Thus, we extended the SDK model to simulate the PSFA membranes. One finding is that, in order to reproduce the interfacial properties as well as rather fine structure, a hybridization of the SDK and IBI (Iterative Boltzmann Inversion) models could be useful.[4] The hybrid SDK/IBI CG model was confirmed to successfully reproduce the structural properties from AA-MD. This also enables us to simulate reasonable target membrane systems including long polymer chains with the realistic length. We have run a large scale CG-MD of PFSA membrane containing 0.3 million CG particles, which represents about three million atom system. We successfully equilibrated the CG system after a series of annealing simulations, and then, generated the corresponding all-atom configuration using a reverse-mapping technique. In this way, we generated a reasonable all-atom configuration for the glass polymer membrane, and a relatively short equilibration MD simulation was just required to prepare a large-scale polymer membrane system, thanks to the pre-equilibrated structure produced by the quantitative CG-MD simulation. Here we used the LAMMPS and GROMACS softwares for CG and AA-MD simulations, respectively. Both of these simulation were significantly accelerated by GPU. The obtained well-equilibrated all-atom structure (Fig. 2) should be useful for the mechanical and ion conductivity examination of the polyelectrolyte membrane.

References

[1] W. Shinoda, R. DeVane, and M. L. Klein: Mol. Simul. **33** (2007) 27.

[2] W. Shinoda, R. DeVane, and M. L. Klein: Curr. Opin. Struct. Biol. **22** (2012) 175.

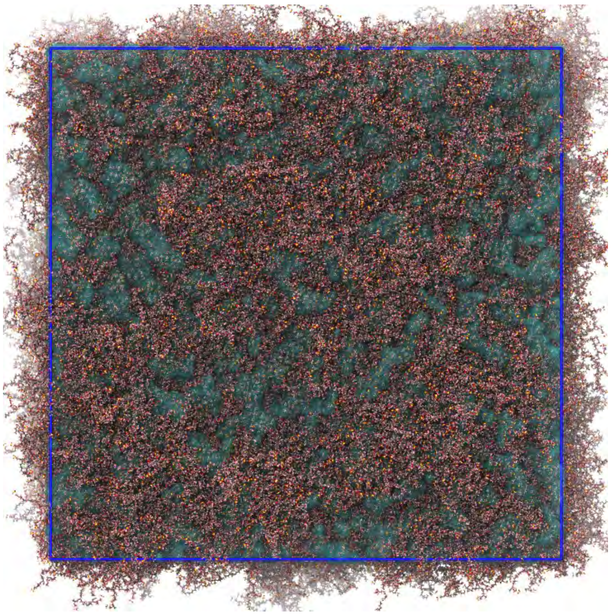

Figure 2: A snapshot from a large-scale all-atom MD simulation of the PFSA membrane system including three million atoms. This system was first generated and equilibrated by a CG-MD, and then was converted to atomic representation by the reverse mapping, then finally, again equilibrated by a short (30 ns) all-atom MD simulation. PFSA ionomers are represented by lines and water are drawn by cyan continuum volume.

[3] A. Kuo, A. Tanaka, J. Irisawa, W. Shinoda, and S. Okazaki: J. Phys. Chem. C **121** (2017) 21374.

[4] A. Kuo, S. Okazaki, and W. Shinoda: J. Chem. Phys. **147** (2017) 094904.

Numerical study on low-energy states of quantum spin systems

Hiroki NAKANO
Graduate School of Material Science, University of Hyogo
3-2-1 Kouto, Kamigori-cho, Ako-gun, Hyogo 678-1297, Japan

In condensed matter physics, generally, it is very difficult to estimate physical quantities precisely in systems of many-body problems. For such systems, therefore, numerical approaches have widely been used as effective ones. From this motivation, many researchers have carried out a lot of computational studies, which contribute much to our deeper understanding of quantum spin systems. Even for the situation, numerical studies are particularly difficult when spatial dimensions of target systems with frustrations are larger than one. This difficulty occurs under the situation that applicable numerical methods are limited. It is well known that such systems cannot be treated by the quantum Monte Carlo simulations and the density matrix renormalization group calculations. Only the numerical diagonalization method based on the Lanczos algorithm is generally applicable when a target system includes frustrations and when the spatial dimension of the system is larger than one. At the same time, this method also has a serious weak point. Only very small system sizes can be treated by this method. We then succeeded in developing a hybrid-type parallelized code of Lanczos diagonalization[1] to overcome this disadvantage. Using this Lanczos-diagonalization code that we developed, we examine various quantum spin systems as a primary approach.

The primary study of this year in the present project examines the $S = 1/2$ Heisenberg antiferromagnet on the triangular lattice with next-nearest-neighbor interactions under the magnetic field[2]. The amplitude of the nearest-neighbor interactions and the next-nearest-neighbor interactions are denoted by J_1 and J_2, respectively. It is widely known that the system shows the magnetiztaion plateau at one-third height of the saturation in the magnetization curve when $J_2 = 0$. On the other hand, when J_2 is infinitely larger than J_1, the system is reduced to three isolated systems, each of which is the triangular-lattice antiferromagnet with only the nearest-neighbor interaction with its amplitude J_2. Therefore, the one-third-height plateau exists for $J_2 \gg J_1$. The primary question of our study is what happens in the case of intermediate J_2. We examine whether or not the plateau of this height disappears. We carry out Lanczos diagonalizations and obtain the magnetization curves for 27 and 36-site clusters. Our calculations clarify that the plateau at this height closes ar around $J_2/J_1 = 0.2$, that the plateau disappears at least until $J_2/J_1 = 0.7$, and that the plateau opens again for even larger J_2. The clarified behavior becomes a fundamental information concerning the triangular-lattice antiferromagnet.

Since 2016, our project also treats the case when the triangular-lattice antiferromagnet includes the distortion of the $\sqrt{3} \times \sqrt{3}$ type. Note here that this distortion links the two cases of the triangular and dice lattices. Our calculations clarified that there exists an intermediate region where the ground state shows continuously increasing spontaneous magnetization[3]. In 2017, the thermodynamic properties such as the specific heat and the susceptibility are also studied around the phase boundaries of the intermediate phase[4, 5].

Our studies contribute to our understandings of the triangular-lattice antiferromagnet and the nontrivial effect of frustration in magnetic materials.

References

[1] H. Nakano and A. Terai: J. Phys. Soc. Jpn. **78** (2009) 014003.

[2] H. Nakano and T. Sakai: J. Phys. Soc. Jpn. **86** (2017) 114705.

[3] H. Nakano and T. Sakai: J. Phys. Soc. Jpn. **86** (2017) 063702.

[4] A. Shimada, H. Nakano, T. Sakai, and K. Yoshimura: J. Phys. Soc. Jpn. **87** (2018) 034706.

[5] A. Shimada, H. Nakano, T. Sakai, and K. Yoshimura: J. Jpn. Soc. Powder Powder Metallurgy **65** (2018) 3.

Numerical study of non-equilibrium systems

Kenji HARADA
Graduate School of Informatics, Kyoto University, Kyoto 606-8501, Japan

Many systems in Nature are open systems coupled to external reservoirs. Sometimes the systems in the microscopic level break a detailed balance condition between microstates. This type of systems shows non-equilibrium behavior. In particular, the interesting phenomena in a non-equilibrium system is a phase transition. In the last decades, our understanding for a phase transition of non-equilibrium systems makes the remarkable progress. A highlight is a universality in a continuous phase transition of directed percolation (DP) problem[1]. If we regard an allowed direction of percolation in a DP problem as a time, a $(d+1)$-dimensional DP problem describes a d-dimensional time evolutional system as a reaction-diffusion model, or a d-dimensional quantum system defined by a non-Hermitian Hamiltonian. If there is no active element in a system at a time, the time evolution of the system freezes. Since a system cannot escape from the state, it is called an absorbing state. Increasing a local percolation probability, a phase transition occurs at which a convergence into the absorbing state disappear. For various DP problems, the density of active sites continuously appears at the phase transition point which is called an absorbing phase transition. Interestingly, it shows a criticality as like a conventional continuous phase transition of equilibrium systems. Many previous studies confirmed the universality of continuous absorbing phase transiton. The idea of universality in equilibrium systems was generalized into non-equilibrium systems.

To study this problem, we tried to use a tensor network scheme. There are two approaches in a tensor network for this problem. Because the temporal evolution of a system is described a master equation of a state probability distribution, the first method is a time-evolution of a state probability distribution in which the state probability distribution is defined as a tensor network. The second method is a renormalization of a time-evolutional operator in a master equation.

We applied the first method to the one-dimensional DP problem. A promised tensor network of a state probability distribution, in this case, is a matrix product state. In particular, we find a better performance of a specialized matrix product form to keep a precision in a time-evolution of a state probability distribution. It is a canonical form. Because a time evolutional operator of DP problem is a tensor network of local time evolutional operators, the standard SVD approximation for multiplication of a local time evolutional tensor in a part of a canonical form satisfies a global optimization condition. The precision of a canonical form calculation can be compared with that of a standard Monte Carlo simulation.

For the second method, we consider a key feature of many tensor network renormalization techniques. Then, we introduce an entanglement branching operator to split a composite entanglement flow in a tensor network[2]. The entanglement branching is a new useful operation to manipulate a tensor network. For example, finding a particular entanglement structure by an entanglement branching operator, we can improve a conventional tensor renormalization method to catch a proper renormalization flow in a tensor network space.

[1] M. Henkel, H. Hinrichsen, and S. Lübeck, "Non-Equilibrium Phase Transitions. Volume 1: Absorbing Phase Transitions" (Springer, 2008).

[2] K. Harada, "Entanglement branching operator", Phys Rev B **97** (2018) 045124.

Designing Thermal Functional Materials via Materials Informatics

Junichiro SHIOMI

Department of Mechanical Engineering, The University of Tokyo

7-3-1 Hongo, Bunkyo, 113-8656

Materials informatics (MI), which has been considered as the fourth paradigm of science in addition to theory, simulation, and experiment, is now gaining a great attention in the field of heat transfer as a powerful and efficient tool to accelerate the discovery and design of materials with desired thermal property. This year, we focused on designing nanostructures for thermal functional materials via MI.

The first main part of last year work is about multifunctional structural design of graphene thermoelectrics by Bayesian optimization (BO). We have applied BO to design nanostructures with optimal thermal transport before [1]. This year, we extend the BO to consider multi-evaluation (phonon and electron) during the designing [2]. We consider two different models as shown in Fig. 1: periodically nanostructured GNR (Model A) and antidot GNR (Model B).

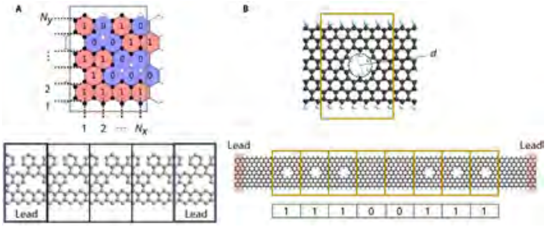

Figure 1: Nanostructured thermoelectric graphene nanoribbons (GNRs). (A) Periodically nanostructured GNR (Model A) and (B) antidot GNR (Model B).

Figure 2A shows average, maximum and minimum ZT of Model A with different numbers of vacancies. The Bayesian search accelerates the exploration of high *ZT* structures in all cases as shown in Fig. 2B. In most cases, top-0.5% of the structures can be found by the Bayesian search with half the calculations for the random search.

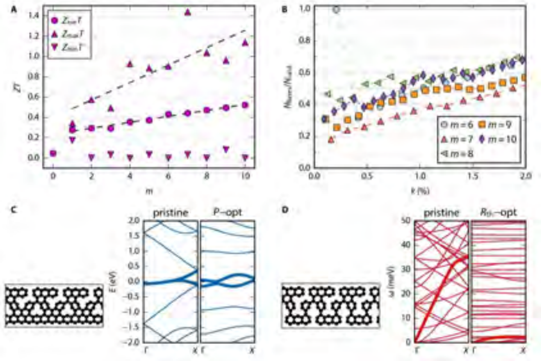

Figure 2: (A) The maximum, minimum, and average *ZT* of all candidates. Dashed lines show the linear fitting. (B) Efficiency of Bayesian optimization. (C)/(D) show the optimal structure and electron/phonon band structure.

Figures 2C and 2D show GNR structures that have the largest power factor and thermal resistance. As for the structure with optimized power factor, vacancies are introduced over the entire area of GNR except for the hexagonal lattices along an edge. The structural optimization leads to strong flattening of electronic bands around energy levels of the edge state and eventually band gaps are generated. Nanostructuring in middle areas of zigzag GNRs leads to phonon scattering without a significant change of the edge state and enhances the thermoelectric performance.

Figure 3A compares thermoelectric properties of the pristine structure, the periodic antidot structure, and the optimal structure, the last two of which are shown in Fig. 3B. The optimal structure has an aperiodic array of antidots, which increases *ZT* by 11 times. It is interesting to note that simply arranging the antidot periodically increases *ZT* by 5.0 times compared with the pristine structure, yet the remaining 2.1 times does require the optimization. This indicates that the optimization of the arrangement of antidots can effectively improve thermal and electronic properties, simultaneously.

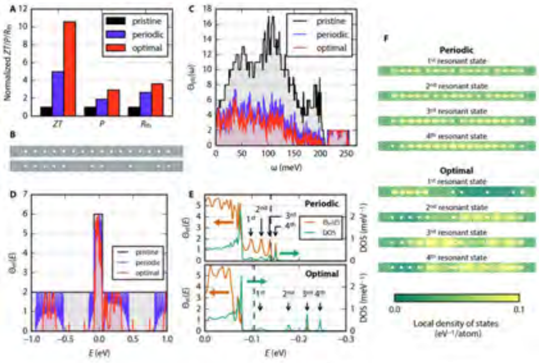

Figure 3: Optimization of antidot GNR structure. (A) Thermoelectric properties of representative structures. (B) Periodic and optimal aperiodic structures. (C)/(D) Phonon/Electron transmission functions. (E) Electron transmission functions and density of states periodic/optimal structures. (F) Local DOS distribution of resonant states of periodic/optimal structures.

Figure 3C shows the phonon transmission functions of the pristine, periodic, and optimal aperiodic structures. The phonon transmission decreases significantly by introducing the periodic antidots and hence thermal resistance increases. Electron transmission functions of representative structures are compared in Fig. 3D. Unlike pristine GNRs that have low Seebeck coefficient due to the absence of the band gap, periodic antidot GNRs have higher Seebeck coefficient because of the presence of transport gaps, corresponding to energy gaps of an infinite periodic antidot GNR. The introduction of periodic antidots, therefore, can enhance the thermoelectric performance. The optimal antidot arrangement can suppress resonant peaks. In Fig. 3E, the electron transmission functions and density of states (DOS) show that although resonant states exist near the edge state in both the periodic and optimal structures, their electron transmission functions are strongly suppressed in the optimal structure. The local density of states (LDOS) at the resonant energy mapped onto each atom are shown in Fig. 3F. LDOS in the finite periodic structure spreads over the whole nanostructured region while the optimal aperiodic structure clearly leads to the localization of states in limited areas. It is intuitively comprehensible that the widely-spreading states, which can be regarded as Bloch states, contribute to electron transport while the strong localization generates the region with extremely low DOS and suppresses the electron transport as shown in Fig. 3E.

The second main part of last year work is about the development of Monte Carlo tree search method. The Bayesian optimization is very effective and accurate when the total number of candidate is around several hundred thousand. However, when dealing with cases with huge or even unlimited number of candidates, it becomes very difficult. Here, we introduce our developed another effective method named Monte Carlo Tree Search (MCTS) [3], which combines the generality of random simulation with precision tree search. Tree search is a popular method for making optimal decisions in artificial intelligence (AI) problems, such as Go games.

The MCTS algorithm is based on a search tree built node by node according to the evaluation of each simulated case, as shown in Fig. 4. Each node contains two important information: an estimated value based on simulation results and the number of times it has been visited. The process of MCTS is composed of four steps: selection, expansion, simulation, and backpropagation. (i) Selection: Starting at root node R, recursively select optimal child nodes according to larger or small upper confidence bound (UCB) score until a leaf node L is reached. (ii) Expansion: If the leaf node L is a not a terminal node then creates one or more child nodes and select one C. (iii) Simulation: Randomly select one playout from C and do the conductance calculation. (iv) Backpropagation: Use the calculated thermal conductance value to update the node information on the path back from C to R. It has to be mentioned that MCTS does not guarantee finding global optimal structure, and instead it offers structure close to the global optimal one with high efficiency.

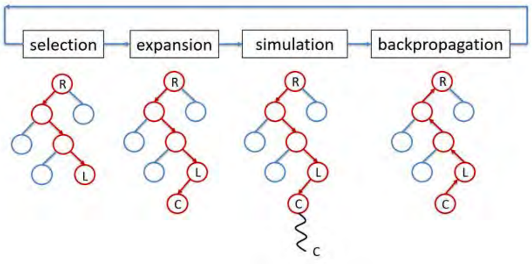

Figure 4: Schematics of Monte Carlo tree search method.

To test the performance Monte Carlo tree search, we applied MCTS to design the Si/Ge alloy interfacial structure to tune heat conduction across the Si-Si and Si-Ge interfaces. The convergence of MCTS shown in Fig. 5 is slower compared with BO [1]. Not all the 10 rounds of optimization can target the global optimal structures with the same number of calculated candidate structures as BO, however they are approaching the global optimal conductance. The advantage of MCTS is that it can deal with optimization cases with unlimited or huge number of candidates that BO cannot deal with. With the increase of number of candidates, the consumed time for selection of next candidate in BO will increase quickly, which make the BO optimization rather time consuming, while the MCTS is able to obtain the quasi-optimal structures with high efficiency.

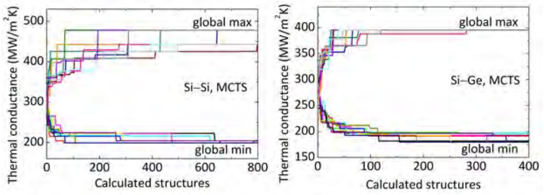

Figure 5: Performance test of Monte Carlo tree search for Si-Si and Si-Ge alloy interface.

In summary: (1) By taking graphene nanoribbons (GNRs) as a representative thermoelectric material, we carried out structural optimization by alternating multifunctional (phonon and electron) transport calculations and the Bayesian optimization to overcome the trade-off. We achieved multifunctional structural optimization with efficiency more than five times that of the random search. The obtained GNRs with optimized antidots significantly enhance the thermoelectric figure of merit (ZT) up to 11 times that of the pristine GNR. The knowledge of the optimal structure further provides new physical insights that independent tuning of electron and phonon transport properties can be realized by making uses of the zigzag edge states and aperiodic nanostructuring. (2) We have designed Monte Carlo tree search method which can provide approaching global optimal structures with high efficiency and it can be applied to optimal/design cases with unlimited number of candidates that Bayesian optimization cannot deal with.

References

[1] S. Ju, T. Shiga, L. Feng, Z. Hou, K. Tsuda, J. Shiomi: Physical Review X **7** (2017) 021024.

[2] M. Yamawaki, M. Ohnishi, S. Ju, J. Shiomi: Science Advances (under revision).

[3] T. M. Dieb, S. Ju, K. Yoshizoe, Z. Hou, J. Shiomi, K. Tsuda: Science and Technology of Advanced Materials 18 (2017) 498.

Control of Phonon and Electron Transport Properties Using Mechanical Strain

Masato OHNISHI and Junichiro SHIOMI

Department of Mechanical Engineering,

The University of Tokyo, Hongo, Bunkyo-ku, Tokyo 113-8656

A recent advance of nanotechnology allows us to design materials in nanoscale. When the length scale of nanostructures in materials reaches in the order of phonon wavelength, wave nature is expected to dominate their thermal transport properties. Despite many attempts to observe such coherent wave nature of phonons in experiments, coherent phonons had been observed only except for at low temperature (< 10 K) [1] or low frequency (< 1 THz) [2] because phonons easily lose their phase information during scattering processes. Recently, Kodama *et al.* [3] have revealed that thermal conductivity of carbon nanotubes (CNTs) decreases by ≈ 60% at room temperature and peak temperature of temperature dependent thermal conductivity decreases by ≈ 50 K due to encapsulation of fullerenes. These results indicate that the encapsulated fullerenes do not act as simple phonon scatters like impurities but modulate phonon dispersion of outer single-walled CNTs (SWNTs).

Observation of carbon nanopeapods with transmission electron microscope has shown that the fullerene encapsulation induces radial expansion in outer SWNTs [3]. We, therefore, have attempted to reveal effects of fullerene encapsulation. We analyzed phonon dispersion of SWNTs and peapods based on spectral energy density (SED) analysis.

We found that the radial expansion leads to softening and hardening of axial and radial modes, respectively, which should be caused by variation of force constants due to the induced strain. Moreover, the periodic strain leads to zone-folding effect of phonon modes in outer SWNT and encapsulated fullerenes. Zone-folding effect leads to reduction of group velocity. Figure 1 shows that magnitude of reduction of thermal conductivity along radial direction due to relaxation time and group velocity. This figure clearly shows that thermal conductivity decreases due to the decrease in phonon group velocity.

Our simulations reveal that the encapsulation-induced periodic strain makes an artificial superlattice of CNTs, which provides a new concept of tuning of microscopic thermal transport and strain-thermal engineering. We believe that experimantal study based on our simulations can realize use of coherece wave nature for advanced thermal devices such as thermal rectification and thermal cloaking.

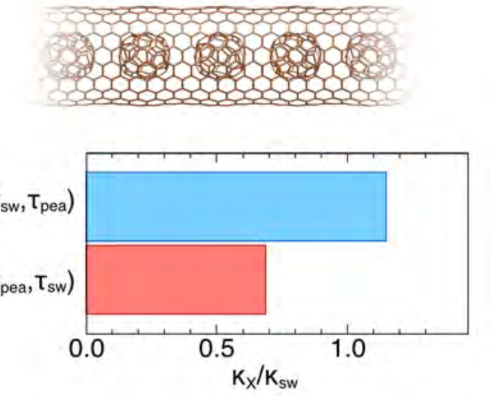

Fig. 1. Suppression of thermal conductivity along radial direction. Decrease in group velocity dominates the suppression of thermal conductivity.

References

[1] J. Maire, *et al.*, Science Advances 3, e1700027 (2017).

[2] M. R. Wagner, *et al.*, Nano Letters 16, 5661 (2016).

[3] T. Kodama, *et al.*, Nat. Mater. 295, 828 (2017)

Magnetic excitation and spin transport in frustrated quantum spin chain

Hiroaki ONISHI
Advanced Science Research Center, Japan Atomic Energy Agency,
Tokai, Ibaraki 319-1195

In ordinary magnetic insulators, elementary excitation is described by magnon and the flow of magnons causes spin current and thermal current. In contrast, frustrated magnets often show nontrivial ground states and elementary excitations. Thus we expect that novel types of carriers would contribute to spin and thermal transport phenomena. Here we focus on a spin nematic state in a spin-1/2 J_1-J_2 chain with ferromagnetic J_1 and antiferromagnetic J_2 in a magnetic field. As for magnetic excitations, we have found gapless quadrupole excitations [1] as well as gapless longitudinal and gapped transverse spin excitations [2]. These indicate that bound magnons can be created without energy cost and contribute to transport.

In the present work, to gain an insight into bound-magnon-mediated transport, we study temperature and field dependencies of spin and thermal Drude weights. For this purpose, we perform exact diagonalization calculations to obtain all eigenvalues and eigenvectors of the Hamiltonian, using ScaLAPACK designed for distributed memory parallel computers, and evaluate thermal expectation values. Utilizing the total magnetization and the momentum as conserved quantities, the maximum dimension is 9252 for 20 sites, which can be handled with workstations. It grows to 112720 for 24 sites, accessible due to MPI parallel simulations on the system B of the ISSP supercomputer.

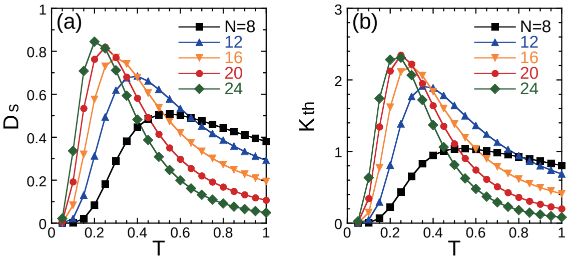

Figure 1: Temperature dependence of (a) spin and (b) thermal Drude weights at zero field for $J_1 = -1$ and $J_2 = 1$.

Figure 1 shows the temperature dependence of the Drude weights at zero field. Note that the system size dependence is large even with 24 sites, and results with up to 24 sites are not enough to obtain a conclusive statement about the behavior in the thermodynamic limit. We find a peak structure, since the Drude weights drop to zero as the temperature goes to zero due to the finite-size effect. As the system size increases, the Drude weights become large at low temperature, while they become small at high temperature. For the spin Drude weight, the peak seems to approach zero temperature, indicating that the spin Drude weight is zero at finite temperature, i.e., the spin transport is diffusive. Analyses on the magneto-thermal effect in the magnetic field are in progress.

References

[1] H. Onishi, Physica B (in press).

[2] H. Onishi, J. Phys. Soc. Jpn. **84**, 083702 (2015); J. Phys.: Conf. Ser. **592**, 012109 (2015).

Phase diagrams of random topological matters

TOMI OHTSUKI[1]
TOHRU KAWARABAYASHI[2]
KEITH SLEVIN[3]
KOJI KOBAYASHI[4]
1) Dept. Phys., Sophia University, Chiyoda-ku, Tokyo 102-8554, Japan
2) Dept. Phys., Toho University, Miyama 2-2-1, Funabashi 274-8510, Japan
3) Dept. Phys., Osaka University, Toyonaka, Osaka 560-0043, Japan
4) IMR, Tohoku University, Sendai 980-8577, Japan

Recent discoveries of two-dimensional quantum spin Hall states and three-dimensional (3D) topological insulators (TIs) have inspired extensive research of these novel topological materials. Here we have studied disordered topological insulators as well as Weyl semimetals (WSM), which are constructed by stacking 2D Chern insulator (CI) layers.

Based on the renormalization group analysis, we have proposed the scaling theory near the multicritical point of WSM-CI-Metal, and have verified the scaling behavior numerically [1]. We have shown that the Anderson localized phase appears between CI-Metal, while the transition is direct for WSM-Metal and CI-WSM. We have also discussed novel scaling behavior of CI-WSM transition [2].

We have demonstrated that the image recognition based on multilayer convolutional neural network (so called deep learning) works well for drawing the phase diagram of disordered topological insulators and Weyl semimetals [3,4]. In addition, we have applied 3D image recognition to analyze entire 3D wave functions. We have shown that a full phase diagram of the disorder-energy plane is obtained once the 3D convolutional neural network has been trained at the band center (Fig. 1). We have further demonstrated that the full phase diagram for 3D quantum bond and site percolations (which are topologically disordered systems) can be drawn by training the 3D Anderson model at the band center [5].

References

1. X. Luo, B. Xu, T. Ohtsuki, R. Shindou: Physical Reivew B **97**, 045129 (2018).
2. X. Luo, T. Ohtsuki, R. Shindou: arXiv:1803.09051.
3. T. Ohtsuki, T. Ohtsuki: Journal of the Physical Society of Japan **85**, 123706 (2016).
4. T. Ohtsuki, T. Ohtsuki: Journal of the Physical Society of Japan **86**, 044708 (2017).
5. T. Mano, T. Ohtsuki: Journal of the Physical Society of Japan **86**, 113704 (2017).

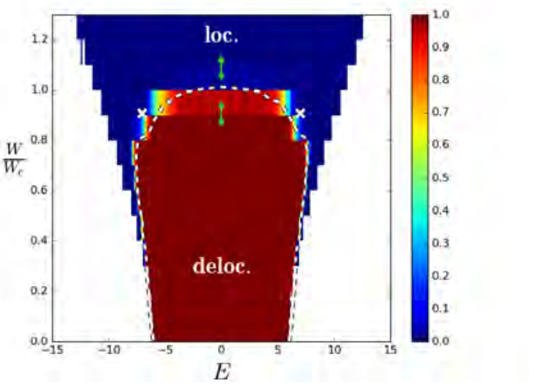

Figure 1: Color map of the intensity P_{deloc} (probability that the system is a metal) for all the energy spectrum of 3D Anderson model. An average over 5 samples was performed. The two green arrows indicate the region where the neural network is trained. Dashed line and the cross are the phase boundaries derived by other methods. Taken from [5].

Liquid–gas spinodal of the modified Lennard-Jones fluid: A preliminary study

Kazuhiro Fuchizaki and Kei Watanabe
Department of Physics, Ehime University, Matsuyama 790-8577
Hiroshi Noguchi
The Institute for Solid State Physics, The University of Tokyo, Kashiwa 277-8581

Spinodal line shows a boundary beyond which a thermodynamic phase no longer stably exists. The name reminds us of the mean-field (classical) spinodal derived from ϕ^4 theory. When fluctuations of a system are taken into consideration, the location of the lines would change. As for the location of the spinodal lines, the research was already performed for a 3D Ising system. The spinodal line was shown to approach the magnetization curve when $L \gg \xi$ [1], where L and ξ denote the linear dimension of a cell, obtained by dividing the system, and the correlation length, respectively. Because a fluid system is believed to belong to the same universality class as that of the Ising system, a similar behavior is expected regarding the spinodal and binodal lines. However, this expectation has never been proved yet. The present research is to try to demonstrate that the liquid–gas spinodal line is gradually proximity to the binodal line for $L \gg \xi$. As a fluid system, the modified Lennard-Jones (mLJ) system was employed because its thermodynamic behavior is precisely known [2]. We also make comments on the validity of the equation of state (EOS), recently proposed for dense fluids [3] based on a new cluster expansion.

Here and after, all quantities are expressed in units of σ and ϵ, which are the length and energy scales of the mLJ potential function, respectively. A cubic system with a side of $N = 35.22$ was employed. Periodic boundary conditions were imposed on the system, in which 16384 particles were contained. The number density was $\rho = 0.375$, which is slightly larger than the critical density, $\rho_c = 0.331(3)$ [4]. The isothermal molecular dynamics simulation was conducted. After sufficient equilibration at a temperature T below the critical temperature $T_c = 1.0762(2)$ [4], the system was divided into cubic cells with a side L, and the probability, $P_L^{(2)}(\rho_1, \rho_2)$, of finding simultaneously the densities, ρ_1 and ρ_2, in the adjacent cell was evaluated during subsequent production runs. We expect that $-\ln P_L^{(2)}(\rho_1, \rho_2)\Big|_{\rho_1=\rho_2=\rho} = -\ln P(\rho)$ behaves as the coarse-grained free energy, which cannot be calculated directly. In this preliminary study, we focused on low-temperature behaviors at $T/T_c = 0.7, 0.8$, and 0.9. Three lengths, 5.87, 7.044, and 8.805, were chosen for the side L. To assess the location of the binodal lines, the EOS [3] was used as a guide.

Figure 1 shows snapshots of the system after equilibration, i.e., after separation into liquid and gas phases, at those temperatures. A flat interface resulted in at the lowest temperature examined. Because the temperatures were well below T_c, the correlation length ξ was not assessed from the critical parameters [4], but were directly evaluated by fitting the density profile in x-direction around the interface to a function, $\sim \tanh[(x - x_0)/\xi]$, where x_0 denotes the interface position.

The binodal and spinodal densities are de-

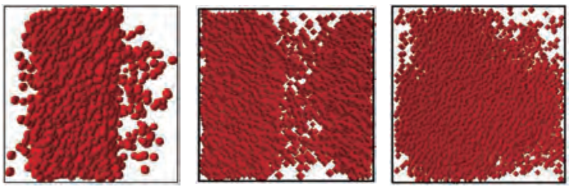

Figure 1: Snapshots showing liquid–gas coexistence at $T/T_\mathrm{c} = 0.7, 0.8$, and 0.9 (from left to right).

noted by ρ_b and ρ_s, respectively (and their gas branches are denoted by $\rho_\mathrm{b}^\mathrm{g}$ and $\rho_\mathrm{s}^\mathrm{g}$ upon necessary). Those densities correspond to the minima and the inflection points of the coarse-grained free energy, respectively. The resulting $P(\rho)$ had indeed two peaks centered around the binodal densities.

To discuss the universal behavior, from which the dependence of the relationship between ρ_b and ρ_s on L/ξ is to be extracted, we invoke the Ising–fluild correspondence regarding criticality. That is, the order parameter, the magnetization, and the spinodal magnetization of the Ising system are regarded as ρ, $|\rho_\mathrm{b} - \rho_\mathrm{c}|$, and $|\rho_\mathrm{s} - \rho_\mathrm{c}|$, respectively. The interface free energy per cell volume, $\Delta f \sim (R/\xi)^{d-1}/L^d$, is expressible in terms of the change in density upon condensation $\Delta\rho \sim (R/L)^d \rho \sim (R/L)^d(\rho_\mathrm{c} - \rho_\mathrm{b}^\mathrm{g})$, as

$$\Delta f \sim \left(\frac{\Delta\rho}{\rho_\mathrm{c} - \rho_\mathrm{b}^\mathrm{g}}\right)^{1-\frac{1}{d}} \frac{\xi}{L} \xi^{-d}.$$

The interface free energy is also evaluated as the free-energy barrier between the two minima:

$$\Delta f \sim \frac{k_\mathrm{B}T}{L^d} \sim (\Delta\rho)^2 \chi^{-1}.$$

Equating these two relations, we obtain

$$\frac{\Delta\rho}{\rho_\mathrm{c} - \rho_\mathrm{b}^\mathrm{g}} \sim 1 - \frac{\rho_\mathrm{c} - \rho_\mathrm{s}^\mathrm{g}}{\rho_\mathrm{c} - \rho_\mathrm{b}^\mathrm{g}} \sim \left(\frac{\xi}{L}\right)^{\frac{1}{1+d^{-1}}}.$$

The left-hand side, $1 - \frac{\rho_\mathrm{c} - \rho_\mathrm{s}^\mathrm{g}}{\rho_\mathrm{c} - \rho_\mathrm{b}^\mathrm{g}}$, evaluated at the temperatures are plotted against $(L/\xi)^{-3/4}$ in Fig. 2. (The points recently obtained at $T = 0.7T_\mathrm{c}$ are also included.) The points seem to fall into a single curve delineated by an orange line, showing a universal behavior. Moreover, the points seem to approach asymptotically the origin in the limit $L/\xi \to \infty$. Indeed, when the points are naively fitted to a quadratic function of $(L/\xi)^{-3/4}$, the function intercepts the ordinate at -0.0097, which is regarded virtually as zero under the statistics of the present data.

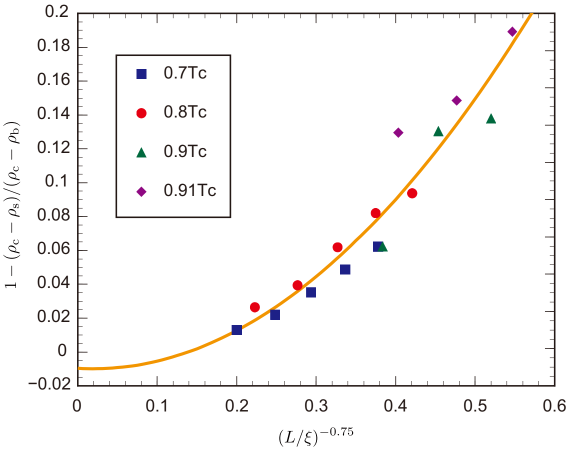

Figure 2: $\Delta\rho/(\rho_\mathrm{c} - \rho_\mathrm{b}^\mathrm{g})$ at four temperatures indicated are plotted against $(L/\xi)^{-3/4}$.

As consistent with the consequences obtained from the Ising model [1], the location of effective spinodal curve changes with the coarse-graining size. Furthermore, it asymptotically approaches the binodal curve in the thermodynamic limit. Finally, it should be recorded that Ushcats' EOS [3] overestimates the pressure of the mLJ fluid for the temperature range investigated.

References

[1] K. Kaski, K. Binder, and J. D. Gunton, Phys. Rev. B **29**, 3996 (1984).

[2] Y. Asano and K. Fuchizaki, J. Chem. Phys. **137**, 174502 (2012).

[3] M. V. Ushcats, J. Chem. Phys. **141**, 101103 (2014).

[4] K. Okamoto and K. Fuchizaki, J. Phys. Soc. Jpn. **86**, 034006 (2017).

SIMD Vectorization of Force Calculation with AVX-512 instructions

Hiroshi Watanabe
Institute for Solid State Physics, University of Tokyo
Kashiwa-no-ha, Kashiwa, Chiba 277–8581

The recent increase in computational power is mainly due to an increase in the number of CPU-cores and the width of registres. Therefore, the SIMD vectorization is unavoidable to make full use of the computational power. The CPU architecture of System C at ISSP is Intel Skylake, which supports AVX-512 instructions. In this report, we describe the effect of optimizations with AVX-512 instructions for calculating the force of Lennard-Jones potential. The AVX-512 instruction set uses registers with 512-bit width. Each register can treat eight 64-bit double-precision floating point numbers simultaneously. The AVX-512 instruction sets include gather, scatter, and mask operations which are useful for the vectorization of loop involving indirect accesses. While the auto-vectorized codes by Intel compiler work efficiently, there is still room for optimization. We have tried the following optimization techniques. Collision Detection Elimination (CDE); The compiler produces the code which checks the conflicts between the indices of j-atoms. Since there are no conflicts, the check code can be eliminated. Remainder Loop Elimination (RLE); Since the number of loop count is not so large, the computational time to process the remainder loop can be significant. Therefore, we eliminate the remainder loop by using mask operations. Software Pipelining (SWP); We adopt the software pipelining technique for the vectorized kernel. SWP is one of the loop optimization techniques to increase the number of instructions which can be executed simultaneously. In order to evaluate the effects of optimizations, we performed benchmark simulations. We observe the time to perform force calculation of Lennard Jones potential 100 times. The number of atoms is 119164. The cutoff length is 3.0 σ. The results are shown in Fig. 1. A sample code is available online [1]. The vectorized codes with AVX-512 was 78% faster than the codes automatically vectorized by the compiler. However, we find that the code vectorized with AVX2 is slightly faster than the code vectorized with AVX-512.

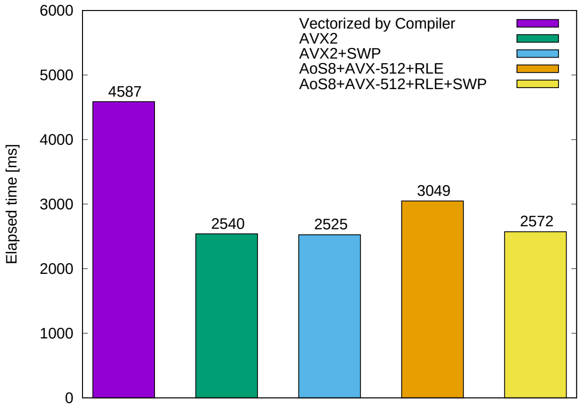

Figure 1: Improvements by optimization techniques.g

References

[1] `https://github.com/kaityo256/lj_simdstep`

Magnetization plateaus in the spin-1/2 Heisenberg model with kagome structures

Takami TOHYAMA
Department of Applied Physics, Tokyo University of Science, Tokyo 125-8585

Frustrated quantum spin systems containing kagome-type structures give rise to novel quantum states. Magnetization plateaus provide a good playground for such novel quantum states. It is, therefore, interesting to investigate magnetization plateaus in spin-1/2 frustrated Heisenberg models with kagome-type structures .

In this project, we have examined magnetization plateaus of two kagome-based lattices, i.e., a kagome-strip chain [1] and a square-kagome lattice [2], as shown in Fig. 1. Both lattices have with three nonequivalent antiferromagnetic exchange interactions whose Hamiltonian in the magnetic field is defined as $H = \sum_{\langle i,j \rangle} J_{i,j} \mathbf{S}_i \cdot \mathbf{S}_j - h \sum_i S_i^z$, where $\mathbf{S}_i$ is the spin-$\frac{1}{2}$ operator at site i, $\langle i,j \rangle$ runs over the nearest-neighbor spin pairs, $J_{i,j}$ corresponds to one of J_1, J_2, and J_3 shown in Fig. 1, and h is the magnitude of the magnetic field in the z-direction.

We use the density-matrix renormalization-group (DMRG) for the kagome-strip chain up to system size $N = 5 \times 65$ in the open boundary condition [1]. The number of states kept in DMRG is $m = 400$ and truncation error is less than 5×10^{-7}. We accurately determine the magnetic structures in a certain parameter range, and we find various types of plateaus. In total, we identify twelve kinds of magnetization plateaus, nine of which have magnetic structures that break translational and/or reflection symmetry spontaneously. The structures are classified by an array of five-site unit cells with specific bond-spin correlations.

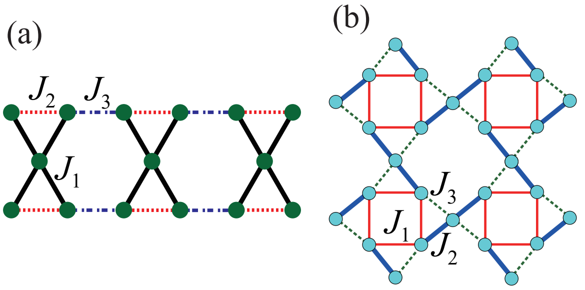

Figure 1: (a) Kagome-strip chain and (b) square-kagome lattice with three nonequivalent exchange interactions.

Among the plateaus, we find a nontrivial 3/10 plateau, whose magnetic structure consists of a period of four unit cells. Such long-period magnetic structure has not been reported before in one-dimensional quantum spin systems.

We perform the Lanczos-type exact diagonalization calculations for the square-kagome lattice with $N = 18$, 24, 30, and 36 under the periodic boundary conditions [2]. We obtain magnetic phase diagrams at $h = 0$ and finite h inducing 1/3 and 2/3 plateaus. We find a new 2/3 plateau that breaks four-fold rotational symmetry spontaneously. The origin of the plateau is attributed to the presence of the three nonequivalent exchange interactions.

References

[1] K. Morita *et al.*: Phys. Rev. B **97** (2018) 014412.

[2] K. Morita and T. Tohyama: J. Phys. Soc. Jpn. **87** (2018) 043704.

Speeding up of the effective physical model estimation by machine learning

Ryo TAMURA
International Center for Materials Nanoarchitectonics,
National Institute for Materials Science
1-1 Namiki, Tsukuba, Ibaraki, 305-0044

The importance of data-driven techniques using machine learning is recognized in materials science[1, 2]. Using machine learning, we are currently developing a generic effective physical model estimation method from experimentally measured data[3]. In the estimation method, plausible model parameters that explain the given measured data are determined by maximizing the posterior distribution. Thus, in each effective physical model estimation, we should search the maximizer of the posterior distribution, which is the computationally extensive probability distribution.

To accelerate an estimation of effective physical model, an efficient method for finding a better maximizer of computationally extensive probability distributions is proposed on the basis of a Bayesian optimization technique. Bayesian optimization has recently attracted much attention as a method to search the maximizer/minimizer of a black-box function in informatics and materials science[4]. In this method, the black-box function is interpolated by Gaussian processes, and the interpolated function is used to predict the maximizer/minimizer of the black-box function. A key idea of the proposed method is to use extreme values of acquisition functions by Gaussian processes for the next training phase, which should be located near a local maximum or a global maximum of the probability distribution.

Our Bayesian optimization technique is applied to the posterior distribution in the effective physical model estimation[5]. Here, instead of searching the maximizer of posterior distribution (P), the minimizer of energy function defined by $E = -\log P$ is searched. Even when the number of sampling points on the posterior distributions is fixed to be small, the Bayesian optimization provides a better minimizer of the energy function in comparison to those by the random search method, the steepest descent method, or the Monte Carlo method(Figure 1). In this demonstration, the quantum Heisenberg model is used as the target Hamiltonian and the temperature dependence of specific heat is inputted. Furthermore, the Bayesian optimization improves the results efficiently by combining the steepest descent method and thus it is a powerful tool to search for a better maximizer of computationally extensive probability distributions. Because the maximizer of a probability distribution is searched in many scientific fields, our method will play an important role in the promotion of science.

References

[1] T. Suzuki, R. Tamura, and T. Miyazaki, Int. J. Quantum Chem. **117**, 33 (2017).

[2] K. Shiba, R. Tamura, G. Imamura, and G. Yoshikawa, Sci. Rep. **7**, 3661 (2017).

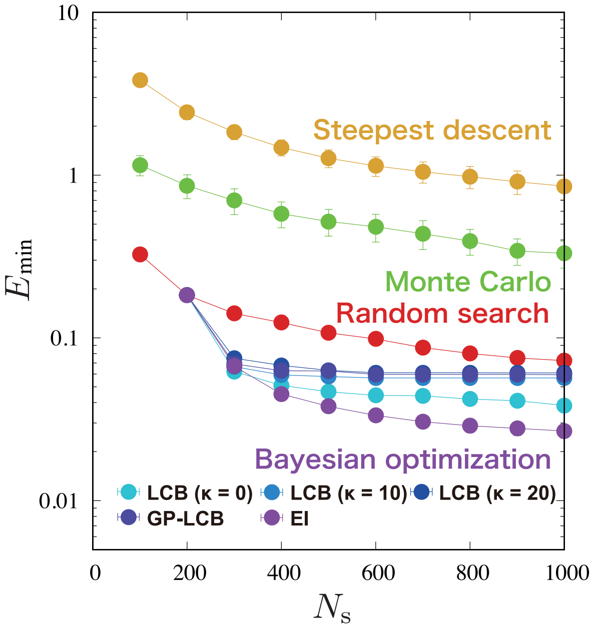

Figure 1: Obtained minimum value of the energy function ($E_{\rm min}$) depending on the number of sampling points ($N_{\rm s}$) by some methods.

[3] R. Tamura and K. Hukushima, Phys. Rev. B **95** 064407 (2017).

[4] T. Ueno, T. D. Rhone, Z. Hou, T. Mizoguchi, and K. Tsuda, Materials Discovery **4**, 18 (2016).

[5] R. Tamura and K. Hukushima, PLoS ONE **13**, e0193785 (2018).

Direct numerical method for quantum response and quantum dynamics

Seiji MIYASHITA
Department of Physics, University of Tokyo
Hongo, Bunkyo-ku, Tokyo 113-0033

We studied the following topics related to our subject.

1. Optical bistability (OB) in the strong coupled quantum region

We studies the microscopic mechanism of the optical bistability by making use of an extended parallel algorithm. In particular, we pointed out OB takes place in the so-called quantum region where the number of atoms is larger than that of photons. We found the distribution of photon number in a cavity and the futures of bistability from the view point of dynamical first order phase transition and the transmission spectrum for the detuning frequency. We also study the properties of metastability including the hysteresis behavior, in particular, the size dependence of the relaxation time[1]

2. Population dynamics of the quantum Storner-Wohlfarh model

Dynamics under external sweeping field is also studied. The size(S)- and sweeping velocity-dependences of scattered population distribution of the quantum Stoner-Wohlfarth model was studied and it is found that a sharp change of the distribution occur after the SW point with a delay which persist in the large S. Dissipation effects on the quantum beating was also clarified by making use of a quantum master equation[2].

3. Shortcuts to Adiabaticity

If we sweep the external field very slowly, the system exhibits the adiabatic motion. In order to realize the adiabatic state in a finite time, the so-called counter adiabatic method has been proposed. But it is generally has a complicated form. We proposed an approximated counter adiabatic method and demonstrated that it practically works well to create the cat state in a Bose-Einstain condensate[3].

4. Quantum responses with the spin-orbit coupling (SOC)

We studied how the synergetic effect of spin-orbit coupling (SOC) and Zeeman splitting (ZS) affects the optical conductivity in the one-dimensional Hubbard model using the Kubo formula[4]: the dependences of resonance (EDSR) in the metallic regime and the optical conductivity in the Mott-insulating phase on the relative angle between the SOC vector and the magnetic field direction. The effect of U was also studied. We studied a mechanism of a sub-gap optical conductivity through virtual hopping of the electron. Motivated by recent terahertz absorption measurements in α-RuCl3, we developed a theory for the electromagnetic absorption of materials described by the Kitaev model on the honeycomb lattice using the formulation in terms of Majorana fermions[5].

5. Structure of an impurity-induced effective spin

We also studied properties of induced effective spin due to inhomogeneous structures in one dimensional spin chaines. e.g. the AKLT model and the alternate-bond antiferromagnetic Heisenberg model. We found that with an appropriate magnetic field the induced effective spins can be operated independently, and also found there are two scales of length, i.e., that of magnetization profile and that of structure of the matrix product wavefunction for the state.[6]

6. New types of phase diagram in the spin-crossover material

We also found a specific phase diagram with a horn structure in spin-crossover systems exhibiting an internal temperature phase. We also studied the dynamis of transition in 3D. Moreover we study dynamics of transitions after photo-irradiation and analyzed the so-called elastic expansion before the thermal one[7].

Study on permanent magnets

We have studied microscopic mechanisms of the coercive force of permanent magnets at finite temperatures[8]. We have studied magnetic properties of $Nd_2Fe_{14}B$ in a realistic atomic scale at finite temperatures. For the purpose, we developed numerical methods such as Monte Carlo (MC) methods for the free energy landscape by making use of the Wang-Landau method, with which temperature dependence of the coercive force was obtained.

In parmanent magnets, the dipole-dipole interaction plays important roles. To perform MC simulation, we developed a new algorithm extending the idea of the stochastic cutoff method and the Fukui-Todo $O(N)$ method, and found that the anisotropy of the Fe atom which has been considered to be weak has an important role to maintain coercivity at relaviely high temperatures.[9]. We also studied peculiar properties of the ferromagnetic resonance of the $Nd_2Fe_{14}B$ magnet which has a tilted magnetization from the c axis at low temperatures by making use of the LLG method.

References

[1] Tatsuhiko Shirai, Synge Todo, Hans de Raedt, and Seiji Miyashita, in preparation.

[2] Takuya Hatomura, Bernard Barbara, and Seiji Miyashita, Phys. Rev. B **96**, 134309 (2017).

[3] T. Hatomura, J. Phys. Soc. Jpn. 86, 094002 (2017). T. Hatomura, New J. Phys. 20, 015010 (2018); Invited paper for the special issue “ Focus on Shortcuts to Adiabaticity ” .

[4] Adrien Bolens, Hosho Katsura, Masao Ogata, and Seiji Miyashita, Phys. Rev. B **95**, 235115 (2017).

[5] Adrien Bolens, Hosho Katsura, Masao Ogata, and Seiji Miyashita, Phys. Rev. B **97**, 161108 (2018).

[6] Hayate Nakano and Seiji Miyashita, in preparation.

[7] Masamichi Nishino, Seiji Miyashita, and Per Arne Rikvold, Phys. Rev. B **96**, 144425 (2017). Cristian Enachescu, et al. Laurentiu Stoleriu, Masamichi Nishino, Seiji Miyashita, Alexandru Stancu, Maciej Lorenc, Roman Bertoni, Herve Cailleau, and Eric Collet, Phys. Rev. B **95**, 224107 (2017).

[8] Satoshi Hirosawa, Masamichi Nishino and Seiji Miyashita, Adv. Nat. Sci.: Nanosci. Nanotechnol.**8**, 013002, (2017).

[9] Taichi Hinokihara, Masamichi Nishino, Yuta Toga, and Seiji Miyashita, Phys. Rev. B 97, 104427 (2018).

Pressure dependence of electronic structure and superconductivity in intercalated FeSe

Harald O. Jeschke
Research Institute for Interdisciplinary Science, Okayama University
Kita-ku, Okayama, Okayama 700-8530

Iron based superconductors are among the most intensively studied class of materials of the past decade. Significant insight into unconventional superconductivity was precipitated by the discovery of the first large family of high temperature superconductors since the discovery of the cuprates. At present, FeSe which belongs to the iron chalcogenide class of materials is at the forefront of theoretical and experimental efforts. In particular, the exceptionally large nematic region, the peculiar magnetism and the strong sensitivity to pressure are hot topics in this field. Among iron chalcogenide superconductors, FeS can be viewed as a simple, highly compressed relative of FeSe without nematic phase and with smaller electronic correlations. However, under pressure, the superconductivity of stoichiometric FeS disappears and reappears, forming two domes [1].

We perform electronic structure and spin fluctuation theory calculations for tetragonal FeS in order to analyze the nature of the superconducting order parameter. In random phase approximation we find a gap function with d wave symmetry at ambient pressure, in agreement with several reports of a nodal superconducting order parameter in FeS.

Our calculations show that as function of pressure, the superconducting pairing strength decreases until at 4.6 GPa, a Lifshitz transition happens in the electronic structure. Due to an additional hole like Fermi surface sheet, the pairing symmetry changes to sign changing s wave, and the pairing strength increases to a new maximum at 5.5 GPa as shown in Fig 1. Thus, the occurrence of two domes in the superconducting transition temperature can be linked to the occurrence of a Lifshitz transition in pressurized FeS [2].

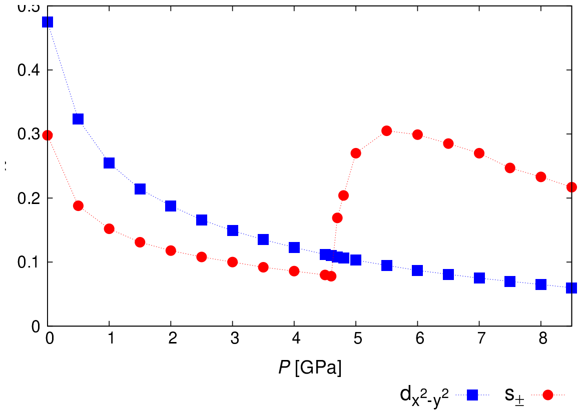

Figure 1: Pressure dependence of pairing eigenvalues λ in tetragonal FeS

References

[1] J. Zhang, F. L. Liu, T. P. Ying, N. N. Li, Y. Xu, L. P. He, X. C. Hong, Y. J. Yu, M. X. Wang, J. Shen, W. G. Yang, and S. Y. Li, npj Quantum Materials **2**, (2017) 49.

[2] M. Shimizu, N. Takemori, D. Guterding, and H. O. Jeschke: in preparation.

Emergent particles at deconfined quantum criticality

Hidemaro Suwa
Department of Physics, University of Tokyo
7-3-1 Hongo Bunkyo, Tokyo 113-0033

Many phase transitions are well described in the picture of the Landau-Ginzburg-Wilson (LGW) paradigm, where an effective action is expanded in powers of an order parameter and its derivatives. This paradigm is very powerful for understanding a generic phase transition and experimental results. Deconfined quantum criticality (DQC) is a non-trivial phenomenon beyond the LGW paradigm: an effective action in the low-energy limit is described by internal degrees of freedom or fractional excitations rather than the original degrees of freedom in a Hamiltonian. It is expected to appear at the quantum phase transition point between the Néel and the valence-bond-solid (VBS) phases. In terms of quantum spins, fractional excitations are spinons; while confined in the VBS phase, they are deconfined at the quantum critical point. Several numerical studies have reported evidence of a continuous phase transition and validity of DQC scenario at the phase transition points of the quantum spin systems, the classical loop model, the fermionic system coupled to Z_2 gauge fields, and so on. Moreover, the DQC can emerge on the surface of symmetry protected topological phases, which may be experimentally observed in the near future.

We numerically studied the criticality in the two-dimensional quantum spin system, namely the SU(2) J-Q model, in the use of the system B as a class C project (ID: H29-Ca-0097). Dynamical quantities were calculated using the worldline quantum Monte Carlo method with the generalized moment method and the analytic continuation. Independent worldline quantum Monte Carlo simulations with the single loop update were efficiently run by MPI parallelization.

If spinons are deconfined, the lowest singlet and triplet excited energies cost by two spinons should be identical in the thermodynamic limit. We tested this necessary condition estimating the singlet and triplet energy gaps at several wavevectors. Our simulations clarified that the singlet and triplet dispersions indeed converge to the same form and spinons are linearly dispersing around $k = (0,0)$, $(\pi,0)$, $(0,\pi)$, and (π,π) for the square lattice. Moreover, we showed that the velocity around these gapless points is unique, which is another strong evidence of spinon deconfinement.

In the meantime, the DQC theory predicts another emergent particle, a Higgs boson, around the transition point in a similar way to the Standard Model. It is intriguing to identify such an emergent particle in a material as well as the universe, which would show a universal mechanism working for both particle physics and condensed matter physics. To capture a hidden excitation, we studied the dynamical spin structure factor using the numerical analytic continuation. We found a nontrivial quasi particle excitation appearing both in the singlet and triplet sectors. Nevertheless, the identification has not been conclusive because of relatively large statistical noise. We will continue to run simulations for longer time and larger system sizes aiming at clear identification.

Rotational dynamics in [$C_n$mim][PF_6] ionic liquids

Hailong PENG and Hayato SHIBA
Institute for Materials Research, Tohoku University
2-1-1, Katahira, Sendai 980-8577

We performed classical molecular dynamics simulation on 1-alkyl-3-methylimidazolium hexafluorophosphate ionic liquids (ILs). The bonded parameters of potential are based on OPLS-AA force field, and nonbonded parameters utilize Lennard-Jones formula with the Lorentz-Berthelot combining rules for different atomic pairs. All the force field parameters are taken from Zhong *et al.*,[1] where the hydrogens on the alkyl chain are incorporated within the carbon but the ones on the imidazolium ring are sustained. All the computer simulations are conducted by open source code package LAMMPS [2]. The simulated systems include 1000 ionic pairs, which are contained in a cubic box.

Important relaxation modes in these ILs include the transitional dynamics of the center of mass, rotational dynamics of the immidiazolum ring, and orientational dynamics of the alkyl chain. In our simulation study, we found the orientational dynamics of the alkyl chain is the slowest relaxation mode in the ILs with long alkyl chain, and accounts for the slow structural relaxation in the liquid. In order to highlight the role played by the rotational dynamics of the alkyl chain, we change the alkyl-chain length, i.e., in [$C_n$mim][PF_6] (n =2, 4, 6, 8, 10, 12) ILs.

Upon cooling down the [$C_n$mim][PF_6] ILs, structural relaxation time drastically increases with temperature decreasing. At the same temperature, the structural relaxation time also increases with alkyl-chain length. Transport coefficients, including self diffusion coefficient and shear viscosity, are calculated at different temperatures with the variation of alkyl chain. Stokes-Einstein relation, which connects diffusivity and viscosity in liquids, found to be broken down at low temperatures. The critical temperature points for the onset of the breakdown is found to decrease with the increment of alkyl chain length.

In order to reveal the coupling and decoupling behavior between the translational and rotational dynamics in these ILs. We measured the characteristic time for the translational dynamics via self-intermediate scattering function, and the time scale for rotational dynamics via self-correlation function of rotational vectors in terms of second Legendre polynomial.

At hight temperatures, the translational and rotational dynamics couple with each other. But they decouple with each other at low temperatures. The critical temperatures for the decoupling behavior is found to decrease with the alkyl-chain length. This decoupling behavior can possibly be connected with the breakdown of Stokes-Einstein relation. Further analysis is required to reveal the underlying mechanism.

References

[1] X. J. Zhong, Z. P. Liu, and D. P. Cao: J. Phys. Chem. B **115** (2011) 10027.

[2] S. Plimpton: J. Comput. Phys. **117** (1995) 1.

Majorana stripe order

Yoshitomo. Kamiya
RIKEN
Hirosawa, Wako, Saitama 351-0198

We studied a system of interacting Majorana fermions on a square lattice that may be realized on the surface of a three-dimensional topological insulator subject to a superconducting proximity effect and an external magnetic field. Specifically, we looked into the strong coupling limit of this problem (corresponding to the so-called neutrality condition [1]), which can be faithfully mapped to a quantum spin model with only local interactions. This spin model comprises four-spin interactions and two-spin interactions, some of which do not commute with each other. Most importantly, from a methodological viewpoint, this spin model can be studied with a quantum Monte Carlo simulation free from a negative sign problem. We employed the directed-loop algorithm and simulated the clusters of different system sizes with $L \times L$ up to $L = 60$ by using the resource of the Supercomputer Center, the Institute for Solid State Physics, the University of Tokyo. Such a cluster corresponds to $L \times (2L - 1)$ Majorana fermion modes, and the one for $L = 60$ is significantly larger than the system size in the the previous exact diagonalization study with only 60 Majorana fermion modes [1]. We found that the interacting Majorana fermions on the square lattice spontaneously breaks translational and rotational symmetries of the lattice, ordering into a novel state that we call a Majorana stripe state [2]. This corresponds to a fourfold degenerate ground state (modulo some one-dimensional gauge-like symmetries, which are not broken), inducing a finite-temperature phase transition. Our conclusion based on the much larger-scale quantum Monte Carlo simulations was in fact able to modify the one in the previous work [1], where a peculiar quantum critical behavior was conjectured based on the exact diagonalization study on a small cluster.

References

[1] C.-K. Chiu, D. I. Pikulin, and M. Franz: Phys. Rev. B **91** (2015) 165402.

[2] Y. Kamiya, A. Furusaki, J. C. Y. Teo, and G.-W. Chern: arXiv:1711.03632 (under review).

Numerical studies of bulk-edge correspondence in topological phases

Y. Hatsugai
Department of Physics, University of Tsukuba
1-1-1 Tennodai, Tsukuba 305-8571, Ibaraki, Japan

Bulk-edge correspondence[1] is a basic feature of topological phases, which has been intensively studied recently. Apart from the symmetry breaking, phases of matter can be distinguished based on the topology. Although topology is an abstract concept of mathematics, it is useful to classify phases of matter. It gives a new way of understanding of the phases and the novel class of the phase transition. Typical examples are the quantum Hall effects and Haldane phases of the 1D quantum spin chains of spin integers. "Topology" gives a new classification scheme of the phases, at least, theoretically. However in most cases, the topology is hidden, in a sense, they can not be observed directly. Also the system is (mostly) gapped and there is no low energy excitation. This feature is for the bulk. On the other hand, if the system is with boundaries or some geometrical perturbation as impurities, there exists low energy excitation which characterizes the topological phases. This is the bulk-edge correspondence. The bulk is characterized by the edge states and the localized states near the boundaries are governed by the non trivial bulk. Hidden topological feature of the bulk is directly observed through the edge states. Boundary (edge) currents of the quantum Hall states and the fractionalized (1/2) spins near the boundaries of the Haldane (integer) spin chain (Kennedy triplets) are the edge states governed by the principle. Also surface states of topological insulators observed by the ARPES is another recent typical example.

Although the bulk-edge correspondence has been mainly discussed for quantum systems, it is valid also for classical systems such as photonic crystals governed by the Maxwell equation and even mechanical systems obeying the Newton's law.

To establish the universal feature of the bulk-edge correspondence, we have performed several numerical studies. For the formation of the energy gap as a topological non-trivial vacuum, periodic structure due to lattice is useful. Then to investigate many body physics for the topological phases, we have constructed pseudo-potentials on various lattices[2] (See Fig.1)) and demonstrated its validity by showing topological quantum phase transition on a honeycomb lattice[3]. Also novel topological numbers associated with the entanglement hamiltonian is discussed in three dimension[4], which can be useful with interaction in principle. A classical analogue of diamond as the mechanical diamond is considered in relation to the chiral symmetry breaking and the Weyl points and the classical analogue of the Fermi arcs are discussed[5] (See Fig.2)).

References

[1] Y. Hatsugai, "Chern Number and Edge States in the Integer Quantum Hall effect", Phys. Rev. Lett. 71, 3697 (1993). DOI:10.1103/PhysRevLett.71.3697

[2] K. Kudo and Yasuhiro Hatsugai, "Many-Body Chern Numbers of $\nu = \frac{1}{3}$ and $\frac{1}{2}$ States on Various Lattices", J. Phys. Soc. Jpn. 86, 103701 (2017). DOI: 10.7566/JPSJ.86.103701

[3] K. Kudo and Y. Hatsugai, "Fractional Quantum Hall Effect in n = 0 Landau Band of Graphene with Chern Number Matrix", J. Phys. Soc. Jpn. to appear, arXiv:1803.09978.

[4] H. Araki, T. Fukui, and Y. Hatsugai, "Entanglement Chern number for three-dimensional topological insulators: Characterization by Weyl points of entanglement HamiltoniansMechanics", Phys. Rev. B 96, 165139 (1-8) (2017). DOI: 10.1103/PhysRevB.96.165139

[5] Y. Takahashi, T. Kariyado and Y. Hatsugai, "Weyl points of mechanical diamond", arXiv:1801.06784.

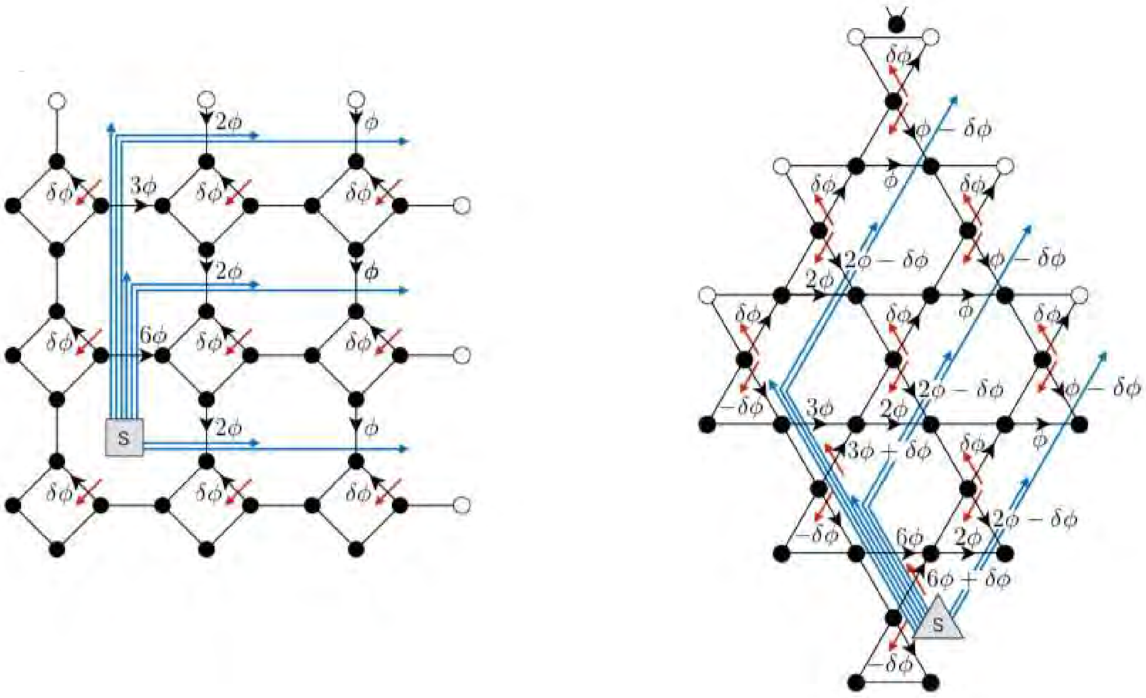

Figure 1: String gauges for square-octagon (left) and kagome (right) lattices [2].

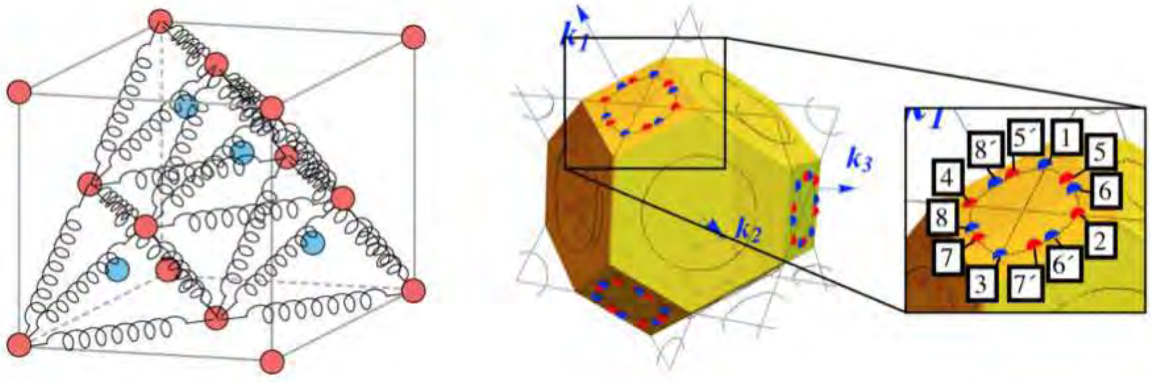

Figure 2: Mechanical diamond with next neighbor interaction (left) and its Weyl points(right) [5].

Molecular Dynamics Simulation Study of Crystal Nucleation Mechanism of Hydroxyapatite via Formation of Pre-Nucleation Clusters

Hiroki NADA

National Institute of Advanced Industrial Science and Technology (AIST),
16-1 Onogawa, Tsukuba, Ibaraki 305-8569

The crystal nucleation mechanism of hydroxyapatite (HAP) is an important research subject in connection with the development of biomaterials and water treatment materials. The nucleation of HAP crystals occurs via the formation of amorphous calcium phosphate (ACP), and the formation of ACP occurs via the formation of pre-nucleation clusters. Thus, it is important for understanding the mechanism of HAP crystal nucleation to elucidate a transition process from the structure of the clusters to that of ACP, in addition to a transition process from the structure of ACP to that of HAP.

However, the structure of the clusters is still poorly understood. This is because it is difficult to observe the clusters by experimental means. Therefore, molecular dynamics (MD) simulation was used for elucidating the structure of the clusters in this study.

The simulation was performed for three different clusters, $Ca_3\ (PO_4)_2\ 10H_2O$, $Ca_9\ (PO_4)_6\ 20H_2O$, and $Ca_9\ (PO_4)_6\ 30H_2O$ (hereafter, clusters A, B, and C, respectively). Simulation results suggested that the structures of clusters B (Figure 1) and C are more stable than the structure of cluster A. This result is consistent with a recent X-ray diffraction study, which suggested that cluster C may be a structural unit of ACP [2].

In addition, a large-scale MD simulation of bulk ACC was also performed. Simulation results indicated the existence of crystal-like short-range order in the atomic arrangement of the ACC [1]. However, more detailed studies are needed to elucidate whether the ordered atomic arrangement in the ACC is the same as that of cluster C (or cluster B).

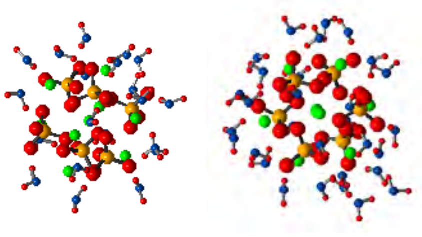

Fig. 1: The structures of clusters B (left-hand panel) and C (right-hand panel).

References

[1] L.-W. Du et al.: Cryst. Growth. Des. **13** (2013) 3103.

Analysis of magnetization reversal process based on atomistic models

Taichi HINOKIHARA

Graduate School of Science, The University of Tokyo, 7-3-1 Hongo, Bunyo-ku, Tokyo 113-8656, Japan

Analyzing the origin of the coercivity is important for developing high-performance permanent magnets. Recently, it has been reported that the physical properties, such as magnetization and anisotropy, have been successfully reproduced using an atomistic spin model derived from the first-principle calculations [1]. However, it is known that the coercivity strongly depends on the grain size due to the dipole-dipole interactions (DDI). Since it is difficult to evaluate such the effect by using the atomistic spin model, efficient method to calculate the DDI and an efficient coarse-graining method to reduce the number of spins are required. This year, we have proposed a new efficient method to calculate the long-range interacting system without any approximations [2]. The new method is based on the stochastic cut-off (SCO) method. Although the SCO method becomes efficient when systems have a simple lattice structure, our method enables us to calculate efficiently even in amorphous systems. We have applied this method to the atomistic model for $Nd_2Fe_{14}B$ magnets, and have confirmed that present method is approximately three times faster than the SCO method above the room temperatures.

We have also developed the coarse-graining method with variable spin momentum length. We first derive the momentum distribution for coarse-grained spins by means of the Wang-Landau method at given temperatures. Then, the exchange couplings between the coarse-grained spins are evaluated by adjusting physical quantities, such as the spin-spin correlations in both the atomistic and coarse-grained systems. We have confirmed that the magnetization, anisotropy, and domain wall width calculated by the coarse-grained model correspond reasonably well with those calculated by the atomistic model.

References

[1] Y. Toga, M. Matsumoto, S. Miyashita, H. Akai, S. Doi, T. Miyake, and A. Sakuma : Phys. Rev. B **94**, 174433 (2016).

[3] T. Hinokihara, M. Nishino, Y. Toga, and S. Miyashita: Phys. Rev. B **97,** 104427 (2018)

Deformation and fracture dynamics of crystalline polymers by large-scale coarse-grained molecular dynamics simulation

Yuji Higuchi
Institute for Solid State Physics, University of Tokyo
Kashiwa-no-ha, Kashiwa, Chiba 277-8581

We have studied fracture processes of polymers such as polyethylene [1, 2] and double-network gels [3] using coarse-grained molecular dynamics simulations. This year, we focused on fracture dynamics of the lamellar structure consisting of amorphous and crystalline layers in polyethylene. Tie chains and entanglements in amorphous layers connect solid crystalline layers, called as stress transmitters; however, their functions and differences are still unclear. Thus, their effects against the stretching is studied by large-scale coarse-grained molecular dynamics simulations on System B.

The stretching simulation of the lamellar structure consisting of 4×10^6 monomers (Fig. 1) is performed. Compression and voids are observed in amorphous layers, while crystalline layers are solid and not broken. To estimate local stress of stress transmitters, all forces are divided into two-body interaction and the stress is evenly divided into the monomers. Polymer chains in the amorphous layers are sorted into tie chains, entanglement, and so on. Then, the local stress for each types is estimated. The important results are as follows. (i) The local stress for tie chains and entanglements are almost equal against the stretching, whereas the stress for entanglements relaxes rapidly and is finally less than that for tie chains when the strain is fixed. (ii) The local stress for tie chains in each amorphous layer is equal although it was experimentally suggested that they are active and inactive [4]. (iii) The local stress for tie chains in the amorphous layers with defects becomes little larger than those without defects after voids are generated. This may correspond to the active and inactive states as suggested by the experiment. However, the difference appears only after the fracture, indicating the difficulty of the prediction of the broken layer.

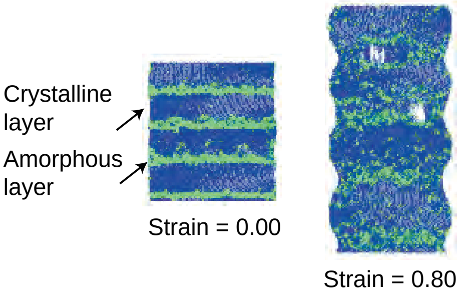

Figure 1: Deformation and fracture processes of lamellar structure in crystalline polymers.

References

[1] Y. Higuchi and M. Kubo: Macromolecules **50** (2017) 3690.

[2] Y. Higuchi: Polym. J. in press.

[3] Y. Higuchi, K. Saito, T. Sakai, J. P. Gong, and M. Kubo: Macromolecules in press.

[4] K. Nitta and M. Takayanagi: J. Macromol. Sci. B **42** (2003) 107.

Molecular Dynamics Simulation of Ferroelectrics Using a Shell Model III

T. Hashimoto
Research Center for Computational Design of Advanced Functional Materials (CD-FMat),
National Institute of Advanced Industrial Science and Technology (AIST),
Tsukuba Central 2, 1-1-1 Umezono, Tsukuba, Ibaraki 305-8568, Japan

(Ba,Sr)TiO_3 is a potential candidate for Pb free piezoelectric materials. $BaTiO_3$ undergoes phase transitions among, listing from high temperature to low temperature, cubic (C), tetragonal (T), orthorhombic (O), and rhombohedral (R) phases. (Ba,Sr)TiO_3 also undergoes phase transitions among the same phases, but the transition temperatures are shifted to the lower temperatures.

In this study, we performed molecular dynamics (MD) simulations using the shell model[1, 2]. We used an MD program developed by us. We used the smooth particle mesh Ewald method for computing the Coulomb interactions. We used MD cells made up with 12×12×12 unit cells. The cutoff length for the nonbonded interactions were 10.0 Å. We used the adiabatic method in which the shells are given a small mass. One MD step (Δt) was 0.1 fs. The Nosé-Hoover chain method and the Parrinello-Rahman method were used for generating constant temperature and constant pressure (NPT) ensembles. The externally applied pressure was set to 0 Pa.

The piezoelectric constants were calculated by[3] $d_{kij} = \frac{1}{k_B T} \langle \Delta M_k \Delta \eta_{ij} \rangle$. Here, $\eta_{ij} = \frac{1}{2} \left(H_0^{t-1} G H_0^{-1} - 1 \right)$ is the strain tensor, where $G = H^t H$ with $H = \{\mathbf{a}, \mathbf{b}, \mathbf{c}\}$ representing the MD cell, and H_0 is the reference state of H. $\mathbf{M}$ is the total dipole moment of the MD cell. ΔX represents $X - \langle X \rangle$, where X is M_k or η_{ij}. The dielectric susceptibilities were calculated by $\chi_{\alpha\beta} \simeq \frac{1}{\varepsilon_0 <\Omega> k_B T} < \Delta M_\alpha \Delta M_\beta >$, where ε_0 and $< \Omega >$ are the permittivity of vacuum and the average of the volume of the MD cell, respectively.

First, we considered the x=0.25 system of $Ba_{1-x}Sr_xTiO_3$. The transition temperatures were shifted to the lower temperatures as shown by Tinte *et al.*[4], but the dielectric susceptibilities and the piezoelectric coefficients were not dramatically changed from the x=0 system for the x= 0.25 system. The detailed results will be published elsewhere.

References

[1] M. Sepliarsky, S. R. Phillpot, D. Wolf, M. G. Stachiotti, and R. L. Migoni, Appl. Phys. Lett. **76** (2000) 3986.

[2] T. Hashimoto and H. Moriwake, Mol. Simul. **41** (2015) 1074.

[3] A. García and D. Vanderbilt, Appl. Phys. Lett. **72** (1998) 2981.

[4] S. Tinte *et al.*, J. Phys.: Condens. Matter **16** (2004) 3495.

Quantum Annealing for Machine Learning

Shu TANAKA
Waseda Institute for Advanced Study, Waseda University
Nishi-waseda, Shinjuku, Tokyo, 169-8050

We have considered the performance of quantum annealing for machine learning. Quantum annealing is an algorithm to obtain better solutions of combinatorial optimization problem [1, 2]. This year, we focused on the following two topics.

(A) Simulated quantum annealing for clustering [3]

We proposed a scheme of simulated quantum annealing for machine learning previously [4, 5, 6]. In these studies, we considered the performance of hybrid quantum annealing for machine learning in which the temperature and quantum fluctuation decrease simultaneously by real-world data. In this project, to consider the performance of quantum annealing systematically, we compared the performance of simulated quantum annealing and that of simulated annealing for clustering by using artificially generated data. In addition, in order to determine the number of clusters, we used the concept of gap statistics. As a result, our calculation succeeded to obtain an appropriate clustering result which is consistent with the generated data.

This work was done in collaboration with Ryo Tamura (NIMS/The University of Tokyo).

(B) Dynamical properties of quantum annealing for singular value decomposition [7]

Hashizume et al. studied the framework of quantum annealing for singular value decomposition (SVD) previously [8]. In [8], they considered properties of quantum annealing for SVD in the adiabatic limit. In this project, we examined dynamic behavior of quantum annealing for SVD by solving the Schrödinger equation directly. As a result, we found that the setting of the initial gap is significant for the performance of quantum annealing for SVD.

This work was done in collaboration with Yoichiro Hashizume (Tokyo University of Science) and Ryo Tamura (NIMS/The University of Tokyo).

References

[1] T. Kadowaki and H. Nishimori: Phys. Rev. E **58** (1998) 5355.

[2] S. Tanaka, R. Tamura, and B. K. Chakrabarti: “Quantum Spin Glasses, Annealing and Computation” (Cambridge University Press, 2017).

[3] S. Tanaka and R. Tamura: in preparation.

[4] K. Kurihara, S. Tanaka, and S. Miyashita: Proceedings of the 25th Conference on Uncertainty in Artificial Intelligence (UAI2009).

[5] I. Sato, K. Kurihara, S. Tanaka, H. Nakagawa, and S. Miyashita: Proceedings of the 25th Conference on Uncertainty in Artificial Intelligence (UAI2009).

[6] I. Sato, S. Tanaka, K. Kurihara, S. Nakagawa, and H. Nakagawa: Neurocomputing, **121** (2013) 523.

[7] Y. Hashizume, R. Tamura, and S. Tanaka: in preparation.

[8] Y. Hashizume, T. Koizumi, K. Akitaya, T. Nakajima, S. Okamura, and M. Suzuki: Phys. Rev. E **92** (2015) 023302.

Investigation of Cell Elongation Effect on Collective Motion

Katsuyoshi Matsushita
Osaka University
Graduate School of Science, Toyonaka, Osaka 563-0043

The collective motion of cells is indispensable in the various biological processes. In this motion, cells align their polarities of movement (or their directions of cytoskeleton) in the same direction and directionally move with mechanically contacting with each other. The collective motion occurs on the based of the cell-cell communication through the cell-cell interaction. One of the important cell-cell interactions is the so-called contact inhibition of locomotion [1] and have intensively investigated in the researchers in the field of physics. This effect is regarded as an excluding volume effect associating with cell-cell adhesive contact between cells. This effect regulates cell polarities of movements and thereby drives the collective behavior of cells in their movement.

Excluding volume effect depends on the shape of cells and is possible to induce various collective behavior in the movement of cells. In particular, the elongated shape of cells has been investigad for suspended rigid bacteria in fluid and is known to crucially affect the order of movement [2]. In contrast, whereas a similar elongation has been well known in collective motions of cultured cells [3], the elongation effect on the order is not unclear today. Since the cultured cells can deform, the result in the rigid bacteria cannot be simply applied to them. Furthermore, the collective motion of cells in 2D culture medium largely differs from the bacteria swimming in fluid in their flocking mechanism because the cultured cells utilize the contact inhibition of locomotion in regulating the cell polarity of movement. These imply that the effect of excluding volume of elongated shape differs in the cases of bacterial and cultured cells. To clarify the effect on the cultured cells, the theoretical investigation based on thought experiment, which gives guidance information of the effect, is effective to design the experiment clarifying its effect because the corresponding experiment regulating the elongation is not so easy.

To investigate the effect of elongation in the case of cultured cells in medium, we consider in the cellular Potts model [4] with cell polarity of movements with feedback [5]. To do this, we assumed that the change in the elongation direction results in the elongation driven by the actin polymeraization. To the express the polymerization velocity $\dot{\rho}$ on the cellular Potts model, we introduce equivalent peripheral tension of cells, γ, as follows:

$$\gamma = \chi R \dot{\rho}, \tag{1}$$

where R is the reference radius of cell and χ is a certain constant representing response coefficient [6]. By considering the multipolar expansion along the polar angle of cell periphery [7, 8], we can derive both the propulsion force and the elongation force of cells, which are correlated with the cell polarity of movement. Furthermore, this formulation can express the softness of cell shape, in contrast to the previous investigation of rigid cell [9], because the elongation driven only by the tension in the present work differs from that driven by

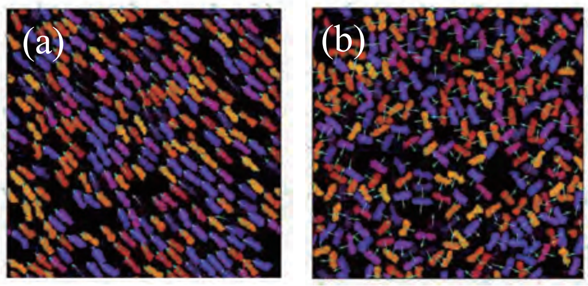

Figure 1: (a) unordering motion in cells elongated in the perpendicular direction of the cell polarity of movement and (b) ordering motion in cells elongated in the parallel direction of the cell polarity of movement.

rigidity energy from reference shape in the previous work.

By using this model, we examine the elongation direction dependence of the collective motion of cells. As a typical elongation, we consider the elongation in the perpendicular and parallel directions of the cell polarity of movement. The former and latter elongations are observed in wildtype and mutant of Dictyostelium Discoideum [10], respectively. As a result for same parameter sets excepting elongation directions, we observed the difference between their order of movement [11]: as shown in Fig. 1(a), we observed the order of movement and hence the collective motion for the cells perpendicularly elongated. Contrary to this, as shown in Fig 1(b), we did not observe the order of movement and individual diffusive motions. This result indicates that the elongation affects the formation of collective motion.

References

[1] R. Mayor and C. Carmona-Fontaine: Trends Cell Biol. . **12** (2010) 319.

[2] H. H. Wensink *et al.*: Proc. Natl. Acad. Sci. USA. **109** (2012) 14308.

[3] J. T. Bonner, *The Social Amoebae: The Biology of Cellular Slime Molds*, (Princeton University Press, 2008)

[4] J. A. Glazier and F. Graner Phys Rev, E **47** (1993) 2128; T. Hirashima *et al.*, Develop. Growth Differ. **59** (2017) 329.

[5] A Szabó *et al.*, Phys. Biol. **7** (2010) 046007.

[6] K. Matsushita, Proc. Sympo. Simul. Traffic Flow **22**, (2016) 5.

[7] K. Matsushita, Phys. Rev. E **95**, (2017) 032415.

[8] K. Matsushita, Phys. Rev. E **97**, (2018) 042413.

[9] R. M. H. Merks, *et al.*, Dev Biol. **289**, (2006) 44.

[10] Y. Asano *et al.*, Cytoskeleton **59**, (2004) 17.

[11] K. Matsushita, The abstract of the 55th Annual Meeting of the BSJ, (2017) 1Pos095.

Analysis on Structuring and Dynamics of Electrolyte Solutions Forming Electric Double Layer at Electrode Interfaces

Ken-ichi FUKUI

Department of Materials Engineering Science, Graduate School of Engineering Science, Osaka University, Machikaneyama, Toyonaka, Osaka 560-8531

Ionic liquids (ILs) are promising electrolytes for electrochemical devices such as secondary battery, capacitor, electric double layer (EDL)-FET, etc., due to their high chemical stability with negligible vaporization. Structuring and dynamics of the interfacial IL faced to a neutral graphite electrode or a negatively charged mica surface were analyzed by molecular dynamics (MD) calculations [1].

The MD simulations were performed with AMBER 11. The mica and graphite substrates consisted of unit cells of linear dimensions 73.9×68.3×20.0 Å^3 and 83.0×72.1 ×30.2 Å^3, respectively. For both systems, 800 BMIM-TFSI ion pairs (46000 atoms) were sandwiched between the substrates and a vacuum layer (> 4 nm). The systems were equilibrated at a constant volume for 100 ps, followed by a constant volume simulation for 5 ns with fixing all of the substrate atoms. The MD simulations were performed at 300, 350, 400, and 450 K.

As shown by the MD snapshot in Fig. 1, the density profile for both systems is modulated up to ~3 nm, but the analyses did not show apparent difference of the orientations and structures against the bulk liquid except for the first layer ($z < 6$ Å). The first layer was apparently more structured for the mica interface because of the larger interaction to the substrates. The two-dimensional arrangement of the first-layer ions are also specific to the substrates: two-dimensional ionic crystals for the mica substrate, and liquid or liquid crystals for the graphite substrate. Such structuring directly affects the mobility of ions at the interface These characteristic properties of the first layer are found to be consistent with the experimental results. Analyses of electrified (charged) interface for the graphite electrode are in progress.

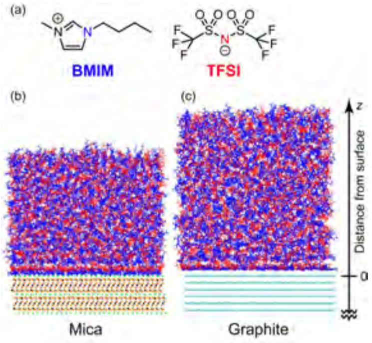

Fig. 1: (a) Ionic liquid (BMIM-TFSI) and (b)(c) MD snapshot for (b) mica and (c) graphite interfaces. BMIM cations and TFSI anions are represented by blue and red colors, respectively.

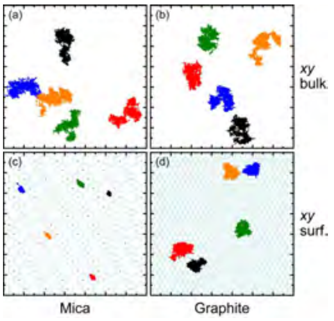

Fig. 2: XY contour maps (7×7 nm^2) for five BMIM cations during a 5 ns simulation (a)(b) at the bulk region and (c)(d) at the first layer ($z < 6$ Å); (a)(c) mica and (b)(d) graphite interfaces.

References

[1] Y. Yokota, H. Miyamoto, A. Imanishi, K. Inagaki, Y. Morikawa, K. Fukui, *Phys. Chem. Chem. Phys.* **20**, 6668-6676 (2018).

Design of organic structure-directing agents for the synthesis of zeolites with controlled active sites

Tatsuya Okubo
Department of Chemical System Engineering, The University of Tokyo
7-3-1 Hongo, Bunkyo-ku, Tokyo 113-8656

Syntheses of materials need to involve trial-and-error in time-consuming wet experiments. We have been working on the syntheses of zeolites with the aid of computational techniques to accelerate the speed of the material design. Zeolite is a class of crystalline microporous materials composed of tetrahedral atoms and oxygen atoms. Especially we focus on the crystal structures, chemical compositions, and atomic locations that are critical factors in the syntheses and applications of zeolites.

The site of Al in zeolite frameworks can influence the physicochemical properties of zeolites. It is of great interest to develop synthetic methods that allow for the siting Al into the specific tetrahedral sites (T-sites) within zeolite frameworks. The synthesis of zeolites with desired sites of Al, however, is very challenging mainly because of the unclarified formation mechanisms of zeolites and the limitation of analytical techniques. Thus far, some successes in controlling over the Al distribution in zeolite frameworks have been reported, but they have mainly relied on a trial-and-error approach by alteration of synthesis parameters such as types of organic structure-directing agents (OSDAs) and sources of Si and Al. Recently, computational calculations suggested that the placement of Al into the specific T-sites is not restricted as there exist thermodynamically favorable sites for Al in some zeolite frameworks[1, 2].

We synthesized IFR-type zeolite with controlled Al locations. The effects of OSDAs on the Al distribution were clarified by combining computational and experimental techniques. The molecular dynamics simulations on GULP suggested that the OSDAs are likely to be tightly fitted inside the zeolite cavities and can alter the relative stability of Al sites. IFR-type zeolites synthesized under an identical condition but with three different OSDAs were characterized by ^{27}Al solid-state NMR with the aid of DFT calculations using Quantum ESPRESSO. The results showed that the Al distribution of IFR-type zeolites can be tuned in accordance with energies derived from the zeolite–OSDA complexes. This combined computational and experimental approach provide a paramount step forward the rational synthesis of zeolites with controlled Al locations[3].

References

[1] K. Muraoka, W. Chaikittisilp, T. Okubo, Journal of the American Chemical Society, 2016, 51, 10718.

[2] M. D. Oleksiak, K. Muraoka, M.-F. Hsieh, M. T. Conato, A. Shimojima, T. Okubo, W. Chaikittisilp, J. D. Rimer, Angewandte Chemie International Edition, 2017, 56, 13366.

[3] K. Muraoka, W. Chaikittisilp, Y. Yanaba, T. Yoshikawa, T. Okubo, Angewandte Chemie International Edition, 2018, 57, 3742.

Dynamics of isolated quantum many-body spin systems

Takashi Mori
Department of Physics, University of Tokyo
Bunkyo-ku, Tokyo 113-0033, Japan

The adiabatic theorem in quantum mechanics tells us that if we change the parameter of the Hamiltonian infinitely slowly, the quantum system evolves without showing any excitation. However, an infinitely slow modulation of the Hamiltonian requires an infinitely long operation time. Since the coherence of a quantum system is destroyed due to the coupling to an external dissipative environment, a fast adiabatic control of the quantum system is desired.

Recently, theory of shortcuts to adiabaticity has been developed as a strategy to achieve adiabatic dynamics within a finite time [1, 2]. In this theory, non-adiabatic excitations are canceled out by applying the counter-diabatic driving field to the system [3]. A major difficulty of this method is that the Hamiltonian representing the counter-diabatic driving field is usually nonlocal and many-body operator, and therefore it is practically very difficult to implement such a driving field in experiment.

We have studied shortcuts to adiabaticity in many-body systems, and have found that shortcuts to adiabaticity tracking the instantaneous stationary states is possible by applying rather simple counter-diabatic fields, which is expressed by local magnetic fields, in *classical* spin systems [4]. In order to test this theory, I have performed numerical calculations of many-body dynamics in classical spin systems under the counter-diabatic driving. Since the theory requires a randomness in the counter-diabatic driving field, the ensemble average is calculated by performing parallel computations. As a result, it has been shown that the theory works very well, and we can realize the adiabatic tracking of the instantaneous stationary states within a finite time.

Our original motivation was to control adiabatic dynamics in many-body *quantum* systems. Although our proposal to achieve a shortcut to adiabaticity by a simple driving field is only applicable to classical spin systems, it is expected that we can obtain an approximate counter-diabatic driving field in quantum systems by considering the quantization of the classical counter-diabatic driving field [5]. It is a future problem to construct a good approximation of shortcuts to adiabaticity in quantum systems.

References

[1] M. Demirplak and S. A. Rice, J. Phys. Chem. A **107** (2003) 9937.

[2] M. V. Berry, J. Phys. A: Math. Theor. **42** (2009) 365303.

[3] A. del Campo, Phys. Rev. Lett. **111** (2013) 100502.

[4] T. Hatomura and T. Mori, in preparation.

[5] C. Jarzynski, Phys. Rev. E **95** (2017) 032122.

Effects of Z_3 anisotropy in antiferromagnetic XY model in a simple cubic lattice

Kazumasa HATTORI
Dept. of Physics, Tokyo Metropolitan University
Minami-Oosawa, Hachioji, Tokyo 192-0397

Antiferro 3-state Potts model in three-dimensional bipartite lattice is known to exhibit one (or two) phase transition(s) at finite temperature, while, at zero temperature, macroscopic degeneracy still remains due to the strong frustration[1, 2]. The nature of the partial-ordered state at finite temperature depends on the details of the lattice structure. For example, in a cubic or bcc lattices, the broken sublattice symmetry state is realized and for a diamond structure, permutationally symmetric sublattices state is favored.[3]

Recently, we have studied antiferro-quadrupole systems in a diamond structure on the basis of classical Monte Carlo simulations[4, 5], where we have analyzed an XY model with Z_3 single-ion anisotropy, which is a simple generalization of the 3-state Potts model. The macroscopic degeneracy in the 3-state Potts model at zero temperature is lifted in this model and the antiferro orders posses only 3 domains. Thus, it is interesting to examine how 3-state Potts model and the XY model with Z_3 anisotropy are related as a function of the anisotropy parameter.

In this study we have studied an antiferromagnetic XY model with Z_3 anisotropy $\sim \gamma \int d^3x \cos 3\theta(x)$ in a simple cubic lattice by using classical Monte Carlo simulations. We have mainly used the System-B F144 job for (up to) 888 parallelizations in order to obtain the data accuracy for low-temperature calculations. We find that there are two transitions for finite γ. One is the known 3d-XY type second-order transition and the other is the first-order at low temperature T^*. The existence of the second transition at T^* is clearly different from the case for the diamond structure model, where there is no such transition.[5] It turns out that T^* decreases as γ increases from the data for the system size up to 32^3. At the present status of the research, it is still insufficient to conclude the fate of T^* for $\gamma \to \infty$, and we need further efforts to analyze this system with larger system size and larger γ.

References

[1] J. R. Banavar, G. S. Grest, and D. Jasnow, Phys. Rev. Lett. **45**, 1424 (1980).

[2] A. Rosengren and S. Lapinskas, Phys. Rev. Lett. **71**, 165 (1993).

[3] S. Lapinskas and A. Rosengren: Phys. Rev. Lett. **81**, 1302 (1998).

[4] K. Hattori and H. Tsunetsugu: J. Phys. Soc. Jpn. **83**, 034709 (2014).

[5] K. Hattori and H. Tsunetsugu: J. Phys. Soc. Jpn. **85**, 094001 (2016).

Analysis of Glassy State of Bead-Spring Chains

Takahiro MURASHIMA
Shogo ASO
Department of Physics, Tohoku University,
Aramaki-Aza-Aoba, Aoba-Ward, Sendai, Miyagi 980-8578

We have studied a glassy polymer melt at high density using coarse-grained molecular dynamics simulation. The Kremer-Grest model [1] was used to represent a melt state of polymer chains. We used OCTA-COGNAC [2] to perform the molecular dynamics simulation. We have investigated the auto-correlation function of the stress and the radial distribution function in equilibrium state. The results are summarized in SA's thesis [3].

References

[1] K. Kremer, G. S. Grest: J. Chem. Phys. **92** (1990) 5057.
[2] http://octa.jp
[3] S. Aso: Master's Thesis (2018).

Structure and dynamics of tetrahedral liquids

Rui Shi and Hajime Tanaka
Department of Fundamental Engineering, Institute of Industrial Science, University of Tokyo
4-6-1 Komaba, Meguro-ku, Tokyo 153-8505

As the most abundant materials in our planet, water and silica play crucial roles in many biological, geological and industrial processes. Preferring local tetrahedral symmetry, they are both tetrahedral liquids. Water and silica have many similar but unique properties. For example, they both exhibit anomalous density maximum as a function of temperature in the liquid state [1]. Recently, we studied the density anomaly in water and silica by molecular dynamics simulations and found that the density anomaly commonly originates from the locally translational structural ordering in water and silica [2].

Besides density anomaly, water and silica also show unusual dynamics, known as “ fragile-to-strong ” transition [3, 4]. Their dynamic slowing down upon cooling shows a crossover from super-Arrhenius law at high temperature to Arrhenius law at low temperature. The origin of this dynamic anomaly is a hot topic and remains elusive until today.

Accessing to the microscopic information, molecular dynamics simulation provides a powerful tool to investigate the dynamic anomaly in water and silica. However, due to the extremely slow dynamics, the lack of simulation data at low temperatures largely obstructs the study of these important materials.

In this study, by utilizing the supercomputer at SCC-ISSP, the University of Tokyo, we are able to reach 2800 and 3000 K in our simulation of silica system, which is very low for this liquid.

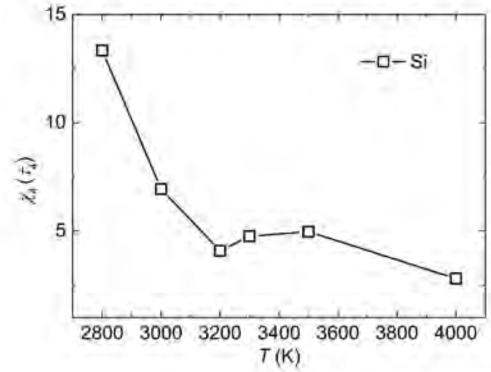

Figure 1: Dynamic susceptibility χ_4 of silicon in silica as a function of temperature. Based on this finding, we are now analyzing the local structure and dynamics of silica at these low temperatures.

For normal glass-forming liquids, dynamic heterogeneity, measured by dynamic susceptibility χ_4, monotonically increases with decreasing temperature. By analyzing the new data at low temperatures, however, we observed a maximum of dynamic susceptibility χ_4 at around 3500K for the first time, as shown in Fig.1. This is a crucial finding, since it suggests a two-state scenario, instead of popular glass transition scenario for the “ fragile-to-strong ” transition in silica.

Based on this finding, we are now analyzing the local structure and dynamics of silica at these low temperatures. We believe that the low temperature data of silica will provides new insight into the dynamic anomaly of the extremely important material, SiO2.

References

[1] CA. Angell, and H. Kanno: Science. 193 (1976) 1121.

[2] R. Shi, and H. Tanaka: Proc. Natl. Acad. Sci. U.S.A. 115 (2018) 1980.

[3] K. Ito, CT. Moynihan, and CA. Angell: Nature 398 (1999) 492.

[4] I. Saika-Voivod, PH. Poole, and F.Sciortino: Nature. 412 (2001) 514.

Study of finite-size effects on colloidal gelation originating from momentum conservation

Michio Tateno and Hajime Tanaka
Department of Fundamental Engineering, Institute of Industrial Science, University of Tokyo
4-6-1 Komaba, Meguro-ku, Tokyo 153-8505

The goal of this project is to reveal the physical mechanism of colloidal gel formation by focusing on the role of momentum conservation law imposed by a liquid component, i.e., hydrodynamic interactions (HI) between colloids. We previously showed that HI has crucial effects on the process of network structure formation in a colloidal suspension: hydrodynamic interactions tend to assist formation of elongated clusters rather than compact one due to “squeezing effects” originating from the imcompressibility of a liquid component, which is absent if HI is neglected [1, 2]. This further leads to the shift of the percolation threshold volume fraction toward a lower value compared to that of the corresponding Brownian dynamics simulation [2]. However, considering the nonlocal nature of HI, it is expected that these results may be affected by the system size. Moreover, colloidal gel intrinsically has a multiscale structure. Thus it is interesting to examine the influence of finite-size effects on the formation process of such structures in colloidal suspensions. To answer these questions, we numerically study the aggregation kinetics of colloidal particle with HI for different system sizes by using Fluid Particle Dynamics (FPD) method, which can properly incorporate many-body HI between colloids [3, 4].

In FPD method, we numerically solve the Navier-Stokes equation by approximating solid colloids as undeformable fluid particles. For simlations, however, there are two key time scales, the momentum diffusion time over the lattice unit and the colloid diffusion time over the size of a particle. Since there is a large gap between these two times scales, the study of slow dynamics of colloidal suspensions inevitably require an extremely high computational cost, which severely limits the size of simulations if we employ conventional codes (Open MP and/or MPI implementation). To overcome this problem, we implement GPU on our FPD codes utilizing a service provided by ISSP.

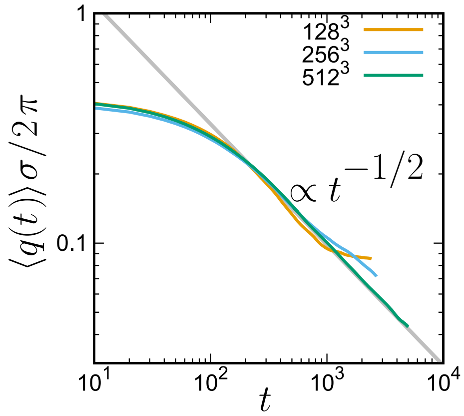

Figure 1: Time evolution of the characteristic wave number $\langle q(t)\rangle$ for various system sizes, $L^3 = 128^3, 256^3, 512^3$. Here we nomarilze $\langle q(t)\rangle$ with the diameter of colloids σ.

Figure 1 shows the temporal change of the characteristic wave number, $\langle q(t)\rangle$, defined as the first moment of the structure factor for different system sizes: $L^3 = 128^3, 256^3, 512^3$ in the lattice unit. (see Fig. 2) This characteristic wavenumber is inversely proportional to

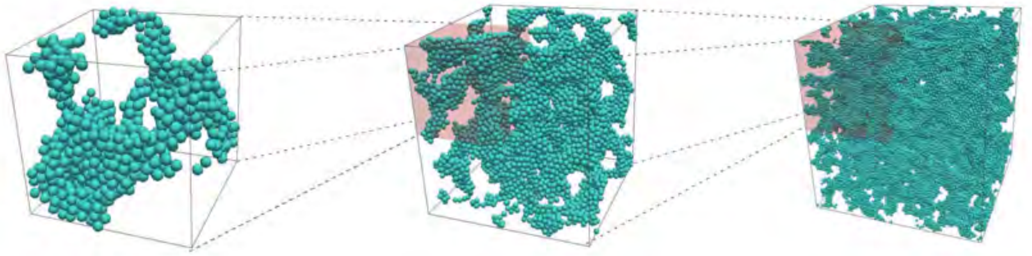

Figure 2: 3D structures of colloidal gels at time $t = 1000$ for different system size: $L = 128^3$(left), 256^3(middle), 512^3(right).

the typical size of the aggregates. Here we can see that all the samples show almost identical coarsening behaivour, decaying with power law whose the exponent is 1/2 in the late stage. However, the results for $L^3 = 128^3, 256^3$ deviate from the power law decay at certain times. In contrast, the one for $L^3 = 512^3$ maintains the power law decay in the entire time range of the simulation. This tells us that the deviation from the power law decay should be a consequence of the finite size effects. We note that the similar exponent has been already reported in the network-forming process in colloidal systems [2, 5], but the range of the power law decay observed there was too narrow to justify its power law nature in a convincing manner. In the largest system, we can see, for the first time, that the power law regime can extend over one order of magnitude. Furthermore, we also analyze the data based on the dynamic scaling law and find that the distribution functions characterizing the phase-separation structures (more specifically, the structure factor and the chord distribution function) can be collapsed on single master curves after scaling with the growth exponent 1/2. These results imply the self-similar nature of the coarsening of this phenomena and the presence of a unique physical mechanism behind this coarsening process.

In summary, we performed numerical simulations of colloid phase separation by the FPD method, which can deal with many-body hydrodynamic interaction between colloids, and systematically examined the system-size dependence of network-forming phase separation. We found that the power law growth of the exponent 1/2 continues over one decade for a system of the largest size and the coarsening process has self-similarity. The physical mechanism responsible for such a power law growth is now under investigation. Our simulation method also allows us to access the detailed information during the process of coarsening, particularly, spatio-temporal organization of the flow field of a liquid component, which is induced by self-assembly of colloids and stress generated during aggregation. We are planning to address these interesting fundamental open questions.

References

[1] K. Kamata, T. Araki and H. Tanaka: Phys. Rev. Lett. **102**, (2010) 108303.

[2] A. Furukawa and H. Tanaka: Phys. Rev. Lett. **104**, (2010) 245702.

[3] H. Tanaka and T. Araki: Phys. Rev. Lett. **85**, (1999) 1338

[4] A. Furukawa, M. Tateno and H. Tanaka: accepted to Soft Matter.

[5] H. Tanaka, Y. Nishikawa and T. Koyama: J. Phys.: Condens. Matter **17** (2005) L143.

Calculation of ordered structures and their optical properties of soft materials

Jun-ichi FUKUDA

Department of Physics, Kyushu University, Motooka 744, Nishi-ku, Fukuoka 819-0395

In this project, we studied particularly the optical properties of exotic structures exhibited by a chiral liquid crystal confined between two parallel substrates. In previous numerical studies [1], I showed that a highly chiral liquid crystal under such circumstances exhibits various exotic structures containing topological defects, depending on the spacing between the confining substrates and temperature. These structures include a hexagonal lattice of half-Skyrmions whose typical spacing is a few hundred nanometers.

My experimental collaborators were motivated by my previous theoretical studies to carry out experiments, and observed a hexagonal array of dark spots in a thin film of a chiral liquid crystal under a conventional optical microscope with high numerical aperture. One of the main goals of this project was to confirm whether they really observed a lattice of half-Skyrmions. As mentioned above, the typical periodicity of the structures is a few hundred nanometers, and therefore theoretical interpretation of the microscope images is highly challenging because geometrical optics commonly used to explain the principles of optical microscopy is totally useless.

I solved the full Maxwell equations for the electromagnetic wave to investigate the response of the liquid crystal to monochromatic incident light. My calculation was based on plane-wave expansion along the in-plane directions, and finite-difference discretization along the direction normal to the confining substrates. The matrix for the resulting large set of linear equations was of tridiagonal form thanks to the above-mentioned finite-difference discretization, which reduced substantially the amount of numerical resources necessary for solving the equations. The profile of the dielectric tensor in the Maxwell equations was assumed to be linearly dependent of the orientational order parameter of second-rank tensor, which was determined by separate calculations minimizing the free energy functional of the liquid crystal in terms of the order parameter.

In Fig. 1, we show a typical profile of the liquid crystal exhibiting a hexagonal lattice of half-Skyrmions, and a calculated optical image. The calculated image contains a hexagonal array of dark spots as experimental ones do. We also did calculations for different structures of the liquid crystal, and compared the resulting optical images with experimental ones. From all the calculation results, we concluded that the experimental microscope image with a hexagonal array of dark spots is indeed that of a hexagonal array of half-Skyrmions [2].

I also carried out calculations to elucidate the Kossel diagrams visualizing the directions of strong Bragg reflections from a sample with crystalline order. Some results on the exotic structures of a chiral liquid crystal known as cholesteric blue phases are presented in Ref. [3]. I am also investigating what Kossel diagrams for a thin system of a liquid crystal as mentioned above should be like, and I hope the results will be able to be presented next time.

References

[1] J. Fukuda and S. Žumer, Nature Commun. **2**, 246 (2011); Phys. Rev. Lett. **106**, 097801 (2011); Phys. Rev. Lett. **104**, 017801 (2010).

[2] A. Nych, J. Fukuda, U. Ognysta, S. Žumer and I Muševič, Nature Phys. **13**, 1215 (2017).

[3] J. Fukuda, Y. Okumura and H. Kikuchi, Proc. SPIE **10555**, 105550A (2018).

Fig. 1. Structure of a chiral liquid cell (top) and its calculated optical image (bottom). In the former, orientational order at the midplane (short rods) and topological defect lines (red surfaces) are shown. The optical image of the former corresponds to that in the rectangle in the latter.

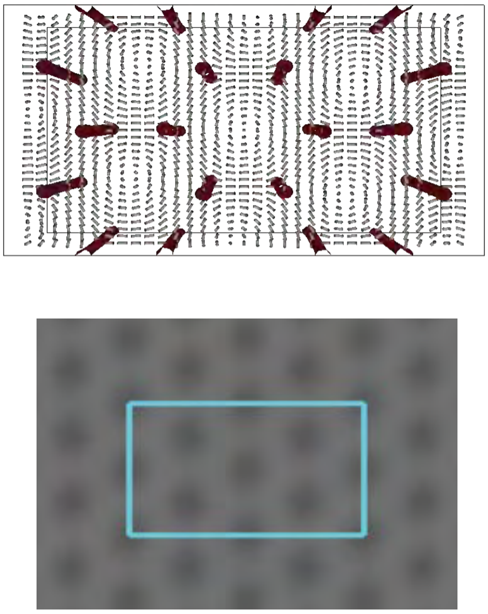

Ground State of an Anisotropic $S=1/2$ Two-Leg Ladder with Different Leg Interactions

Takashi Tonegawa

Professor Emeritus, Kobe Univ. and Visiting Professor, Osaka Prefecture Univ.

This report aims at exploring the ground-state phase diagram of an anisotropic $S=1/2$ two-leg ladder with different leg interactions by using mainly numerical methods. We express the Hamiltonian which describes this system as

$$\begin{aligned}\mathcal{H} = {}& J_{\rm leg,a}\sum\nolimits_{j=1}^{L}[\vec{S}_{j,a},\,\vec{S}_{j+1,a}]_{\rm leg} \\ &+J_{\rm leg,b}\sum\nolimits_{j=1}^{L}[\vec{S}_{j,b},\,\vec{S}_{j+1,b}]_{\rm leg} \qquad (1) \\ &+J_{\rm rung}\sum\nolimits_{j=1}^{L}[\vec{S}_{j,a},\,\vec{S}_{j,b}]_{\rm rung}\end{aligned}$$

with

$$\begin{aligned}&[\vec{S}_{j,\ell},\,\vec{S}_{j+1,\ell}]_{\rm leg} \\ &\quad\equiv S^x_{j,\ell}S^x_{j+1,\ell}+S^y_{j,\ell}S^y_{j+1,\ell}+\Delta_{\rm leg}S^z_{j,\ell}S^z_{j+1,\ell}\,, \quad (2) \\ &[\vec{S}_{j,a},\,\vec{S}_{j,b}]_{\rm rung} \\ &\quad\equiv \Gamma_{\rm rung}\big\{S^x_{j,a}S^x_{j,b}+S^y_{j,a}S^y_{j,b}\big\}+S^z_{j,a}S^z_{j,b}\,. \quad (3)\end{aligned}$$

Here, $\vec{S}_{j,\ell}=\big(S^x_{j,\ell},\,S^y_{j,\ell},\,S^z_{j,\ell}\big)$ is the $S=1/2$ operator acting on the jth rung of the $\ell(=a$ or $b)$ leg; $J_{{\rm leg},a}$ and $J_{{\rm leg},b}$ denote, respectively, the magnitudes of the a and b leg interactions; $J_{\rm rung}$ denotes that of the rung interaction, $\Delta_{\rm leg}$ and $\Gamma_{\rm rung}$ are, respectively, the parameters representing the XXZ-type anisotropies of the former and latter interactions; L is the total number of rungs, which is assumed to be even. It should be noted that this system has a frustration when $J_{{\rm leg},a}J_{{\rm leg},b}<0$ irrespective of the sign of $J_{\rm rung}$.

There exist five interaction parameters in our Hamiltonian $\mathcal{H}$. Throughout the following discussions, we focus our attention upon the case where $J_{{\rm leg},a}=0.2$, $-2.0\le J_{{\rm leg},b}\le 3.0$, $J_{\rm rung}=-1.0$, $\Gamma_{\rm rung}=0.5$, and $0\le\Delta_{\rm leg}\le 1$. Here, we choose $|J_{\rm rung}|$ as the unit of energy. It is noted that the anisotropies of the leg and rung interactions are, respectively, of the XY and Ising types. The motivation of treating this case is as follows. When the ferromagnetic rung interactions with Ising-type anisotropy are much stronger than both of two kinds of the leg interactions ($|J_{{\rm leg},b}|\ll 1.0$), a pair of $S=1/2$ spins at each rung forms a bound state with $S^z_{j,a}+S^z_{j,b}=\pm 1$. This may lead to the spin-nematic Tomonaga-Luttinger liquid (TLL) state, which accompanies two-magnon bound states, as the ground state at least in the frustrated region. Furthermore, the XY-type anisotropy of the leg interactions is expected to stabilize the nematic TLL state.

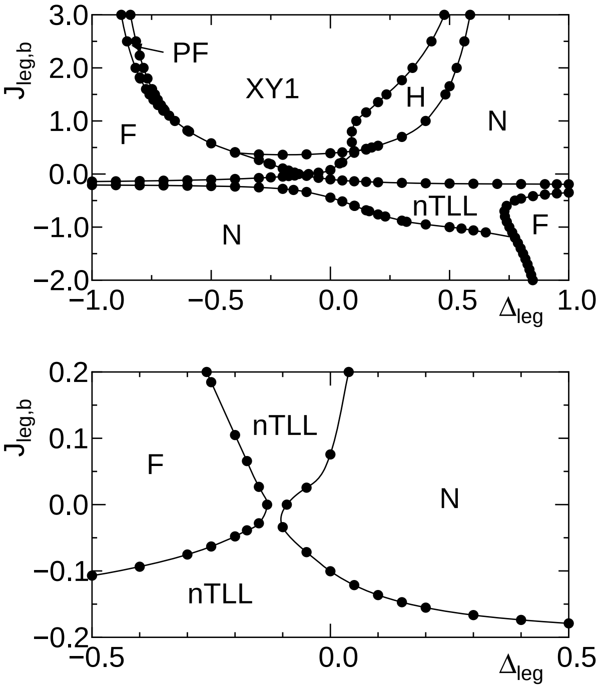

Figure 1: The whole view (top) and an enlarged view around the origin (bottom) of the ground-state phase diagram on the $\Delta_{\rm leg}$ versus $J_{{\rm leg},b}$ plane in the case where $J_{{\rm leg},a}=0.2$, $J_{\rm rung}=-1.0$, and $\Gamma_{\rm rung}=0.5$, obtained in the present work.

Figure 1 shows our final result for the ground-state phase diagram on the $\Delta_{\rm leg}$ versus $J_{\rm leg,b}$ plane, which has been determined by using a variety of numerical methods based on the exact diagonalization (ED) calculation. This phase diagram consists of the six kinds of phases; these are the ferromagnetic (F), partial ferrimagnetic (PF), $XY1$, Haldane (H), Néel (N), and nematic TLL (nTLL) phases. It is noted that the nTLL phase appears as the ground state in the strong-rung frustrated region ($-1.0<J_{{\rm leg},b}<0.0$), as is expected, and survives even in the strong-rung unfrustrated region

$(0.0 \leq J_{\mathrm{leg},b} \lesssim 0.4)$.

At this junction, we denote, respectively, by $E_0^{\mathrm{P}}(L,M)$ and $E_1^{\mathrm{P}}(L,M)$, the lowest and second-lowest energy eigenvalues of the Hamiltonian $\mathcal{H}$ under the periodic boundary condition within the subspace characterized by L and M, where M is the total magnetization which is a good quantum number with the eigenvalues of $M=0$, ± 1, $\cdots$, $\pm L$. We also denote by $E_0^{\mathrm{T}}(L,M)$ the lowest energy eigenvalue of $\mathcal{H}$ under the twisted boundary condition within the subspace determined by L and M. We have numerically calculated these energies for finite-size systems with up to $2L=28$ spins by means of the ED method. The ground-state energy $E_{\mathrm{g}}(L)$ is given by the minimum value among $E_0^{\mathrm{P}}(L,0)$, $E_0^{\mathrm{P}}(L,\pm 1)$, $\cdots$, $E_0^{\mathrm{P}}(L,\pm L)$, and the ground-sate magnetization $M_{\mathrm{g}}(L)$ is the value of M giving $E_{\mathrm{g}}(L)$. It is noted that $M_{\mathrm{g}}(L)=0$ in the $XY1$, H, N, and nTLL states, $0 < M_{\mathrm{g}}(L) < L$ in the PF state, and $M_{\mathrm{g}}(L) = L$ in the F state. Furthermore, we introduce the following three excitation energies:

$$\Delta E_0^{\mathrm{P}}(L,M) = E_0^{\mathrm{P}}(L,M) - E_0^{\mathrm{P}}(L,0)\,, \quad (4)$$

$$\Delta E_1^{\mathrm{P}}(L,0) = E_1^{\mathrm{P}}(L,0) - E_0^{\mathrm{P}}(L,0)\,, \quad (5)$$

$$\Delta E_0^{\mathrm{T}}(L,0) = E_0^{\mathrm{T}}(L,0) - E_0^{\mathrm{P}}(L,0)\,. \quad (6)$$

Let us now discuss how to numerically determine the phase boundary lines shown in Fig. 1. In the following way, we estimate the finite-size critical values of $J_{\mathrm{leg,b}}$ (or Δ_{leg}) for various values of Δ_{leg} (or $J_{\mathrm{leg,b}}$) for each phase transition. Then, the phase boundary line for the transition is obtained by connecting the results for the $L \to \infty$ extrapolation of the finite-size critical values.

Firstly, the phase transition between the N and nTLL phases is of the Berezinskii-Kosterlitz-Thouless (BKT) type [1] with accompanying the spontaneous translational-symmetry breaking [STSB], and therefore, as is well known, the phase boundary line can be accurately estimated by the level spectroscopy (LS) method developed by Okamoto and Nomura [2]. That is to say, we numerically solve the equation,

$$\Delta E_1^{\mathrm{P}}(L,0) = \Delta E_0^{\mathrm{P}}(L,2)/2 \quad (7)$$

to calculate the finite-size critical values.

Secondly, according to the above LS method [2], the finite-size critical values for the phase transition between the $XY1$ and nTLL phases are estimated from the equation,

$$\Delta E_0^{\mathrm{P}}(L,1) = \Delta E_0^{\mathrm{P}}(L,2)/2\,. \quad (8)$$

Thirdly, the phase transition between the $XY1$ and H phases is the BKT transition [1] without the STSB. It is also well known that, in this case, Nomura and Kitazawa's LS method [3] is very powerful to determine the phase boundary line. The finite-size critical values for this transition are calculated by using the equation,

$$\Delta E_0^{\mathrm{P}}(L,2) = \Delta E_0^{\mathrm{T}}(L,0)\,. \quad (9)$$

Fourthly, since the phase transition between the H and N phases is the 2D Ising-type transition, the phase boundary line between these two phases can be estimated by the the phenomenological renormalization group (PRG) method [4]. Then, the finite-size critical values for this transition are calculated by solving the PRG equation,

$$L\,\Delta E_1^{\mathrm{P}}(L,0) = (L+2)\,\Delta E_1^{\mathrm{P}}(L+2,0)\,. \quad (10)$$

Lastly, the results of our calculations show that the phase transition between the F and PF phases is of the second-order, and therefore the finite-size critical values for this transition are estimated from the equation,

$$\Delta E_0^{\mathrm{P}}(L,L) = \Delta E_0^{\mathrm{P}}(L,L-1)\,. \quad (11)$$

These results also show that the phase transition between the PF and $XY1$ phase is of the second-order or the first-order depending on whether $J_{\mathrm{leg},b} \gtrsim 1.55$ or $1.55 \gtrsim J_{\mathrm{leg},b} \gtrsim 1.2$. This means that the finite-size critical values for this transition in the former region of $J_{\mathrm{leg},b}$ are calculated from

$$\Delta E_0^{\mathrm{P}}(L,1) = 0\,, \quad (12)$$

while these in the latter region of $J_{\mathrm{leg},b}$ are from

$$\Delta E_0^{\mathrm{P}}(L,M_{\mathrm{g}}(L)) = 0\,, \quad (13)$$

where $1 < M_{\mathrm{g}}(L) < L$. Furthermore, it is apparent that the finite-size critical values for the phase transitions between the F and one of the $XY1$, N, and nTLL phases, being of course the first-order ones, are estimated by using the equation,

$$\Delta E_0^{\mathrm{P}}(L,L) = 0\,. \quad (14)$$

This work has been done in collaboration with T. Hikihara, K. Okamoto, S. C. Furuya, and T. Sakai.

[1] Z. L. Berezinskii, Sov. Phys. JETP **34**, 610 (1971); J. M. Kosterlitz and D. J. Thouless, J. Phys. C **6**, 1181 (1973).
[2] K. Okamoto and K. Nomura, Phys. Lett. A **169**, 433 (1992); K. Nomura and K. Okamoto, J. Phys. Soc. Jpn. **62**, 1123 (1993); K. Nomura and K. Okamoto, J. Phys. A **27**, 5773 (1994).
[3] K. Nomura A. and Kitazawa, J. Phys. A **31**, 7341 (1998).
[4] M. P. Nightingale: Physica A **83** (1976) 561.

Effect of interface on the structure and properties of water confined in nanopore

Tomoko MIZUGUCHI[1], Katsumi HAGITA[2], and Susumu FUJIWARA[1]

[1]*Faculty of Materials Science and Engineering, Kyoto Institute of Technology,*
Matsugasaki, Sakyo-ku, Kyoto 606-8585
[2]*Department of Applied Physics, National Defense Academy, 1-10-20, Hashirimizu,*
Yokosuka, Kanagawa 239-8686

It is important to understand the properties of supercooled water in many fields such as life sciences, but the research of supercooled water is generally difficult since bulk water crystallizes at deeply supercooled conditions. S.-H. Chen and his co-workers investigated the dynamics of deeply supercooled water confined in nanopores where crystallization of water is prevented, and observed the crossover phenomenon that the temperature dependence of relaxation time changes at a certain temperature [1, 2]. However, it is premature to conclude that this phenomenon occurs in bulk water as well. Indeed, it was reported that confined water can be divided into bound water and free water by their diffusion coefficients [3]. The relationship between these two types of water dynamics and the dynamic crossover phenomenon is not necessarily clear. It is very important to accurately estimate the influence of the interface. To this end, we performed molecular dynamics (MD) simulations of water confined in a nanopore of amorphous silica using the reactive force filed (ReaxFF).

The pore system was created as follows. First, bulk amorphous silica was prepared at 3000 K and 1 atm in the NP_zT ensemble using Morse potential [4], where z direction is parallel to the axis of a cylindrical pore which was created later. Next, switching to ReaxFF MD simulation, the system was relaxed for 200 ps at 3000 K and 1 atm in the NP_zT ensemble, then quenched to 300 K at a cooling rate of 15 K/ps in the NVT ensemble. After 300 ps relaxation at 300 K and 1 atm in the NPT ensemble, a cylindrical pore with a diameter of 2.7 nm was created by removing atoms, and furthermore, some oxygen atoms at the pore surface were removed so that the ratio of the numbers of Si and O became 1:2. We then put water in the pore, and performed MD calculation for 20 ps only for water using TIP3P model with silica immobilized. Finally, ReaxFF MD simulation including silica was started at 300 K and 1 atm in the NPT ensemble. The ReaxFF parameters used in this study were developed in 2015 by Yeon and van Duin to simulate the water/silica interface [5]. All the simulations were conducted with LAMMPS [6], and the ReaxFF MD simulations were performed with the USER-REAXC package of LAMMPS.

Once the ReaxFF MD simulation was started in the system including silica and water, chemical reactions occured between silica surface and water, and silanol groups (-SiOH) were produced. Figure 1 shows the time evolution of the number of silanol groups. We determined the formation of a silanol group only by interatomic distances, and the number of silanol groups is set to 0 at the starting time of MD calculation. It is found that silanol groups are formed in a short time.

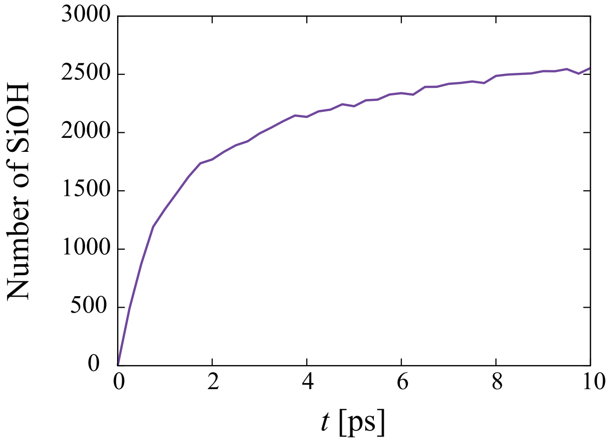

Figure 1: Time evolution of the number of silanol groups.

References

[1] A. Faraone, L. Liu, C.-Y. Mou, C.-W. Yen, and S.-H. Chen: J. Chem. Phys. **121** (2004) 10843.

[2] X.-Q. Chu, A. I. Kolesnikov, A. P. Moravsky, V. Garcia-Sakai, and S.-H. Chen: Phys. Rev. E **76** (2007) 021505.

[3] T. Yamada, R. Yonamine, T. Yamada, H. Kitagawa, M. Tyagi, M. Nagao, and O. Yamamuro: J. Phys. Chem. B **115** (2011) 13563.

[4] S. Leroch and M. Wendland: J. Phys. Chem. C **116** (2012) 26247.

[5] J. Yeon and A. C. T. van Duin: J. Phys. Chem. C **120** (2016) 305.

[6] S. Plimpton: J. Comput. Phys. **117** (1995) 1.

Transport phenomena and optical tomography

Manabu Machida
Institute for Medical Photonics Research
Hamamatsu University School of Medicine, Hamamatsu 431-3192

Let us begin with the time-independent radiative transport equation given by

$$\left\{\begin{array}{l}(\theta\cdot\nabla+\mu_a+\mu_s)\,I(x,\theta)=\mu_s\\ \times\int_{S^2}p(\theta,\theta')I(x,\theta')\,d\theta',\quad (x,\theta)\in R^3_+\times S^2,\\ I(x,\theta)=g(x,\theta),\quad (x,\theta)\in\Gamma_-,\end{array}\right.$$

where $I(x,\theta)$ ($x\in R^3$, $\theta\in S^2$) is the specific intensity of light propagating in random media such as turbid liquids or biological tissue, $p(\theta,\theta')$ is the scattering phase function, and R^3_+ and $\Gamma_\pm$ are defined as $R^3_+=\{x\in R^3;\,x_3>0\}$, $\Gamma_\pm=\{(x,\theta)\in\partial\Omega\times S^2;\,\mp\hat{z}\cdot\theta>0\}$, with $\hat{z}={}^t(0,0,1)$.

We assume that $\mu_s>0$ is a constant but μ_a spatially varies as

$$\mu_a(x)=\bar{\mu}_a+\delta\mu_a(x),$$

with a constant $\bar{\mu}_a$. We assume that $\mu_s,\bar{\mu}_a$ are known but $\delta\mu_a(x)$ is unknown. We also assume a spatially-varying boundary source given by

$$g(x,\theta)=e^{iq_0\cdot\rho}\delta(\theta-\theta_0),$$

where $\rho={}^t(x_1,x_2)$, $q_0\in R^2$, and $\theta_0\in S^2$. We suppose that the exitance or hemispheric flux J_+ is measured on the boundary at $x_3=0$. The exitance is defined as

$$J_+(\rho)=\int_{S^2_+}(\theta\cdot\hat{z})I(\rho,0,-\theta)\,d\theta.$$

Let $J_+^{(0)}(\rho)$ be the exitance in the absence of $\delta\mu_a$. We obtain within the first Born approximation

$$J_+^{(0)}(\rho)-J_+(\rho)=(\theta_0\cdot\hat{z})\int_{S^2}\int_{R^3_+}\times\left[\int_{S^2_+}(\theta\cdot\hat{z})G(x',-\theta';\rho,0,\theta)\,d\theta\right]\delta\mu_a(x')\times\left[\int_{R^2}G(x',\theta';\rho'',0,\theta_0)e^{iq_0\cdot\rho''}\,d\rho''\right]dx'd\theta'.$$

The absorption inhomogeneity $\delta\mu_a$ is thus reconstructed from the above inverse problem, which we can solve by singular value decomposition with a suitable regularization. We will use the three-dimensional F_N method [1] to compute the Green's function $G(x,\theta;\rho_0,0,\theta_0)$.

When the Green's function is calculated with the three-dimensional F_N method, the following functions $\mathcal{J}_{lm}^{(-)jm'}$ have to be computed.

$$\begin{aligned}\mathcal{J}_{lm}^{(-)jm'}&=\frac{\mu_s\xi_j}{2}(-1)^{l+1}\sqrt{\frac{2l+1}{4\pi}\frac{(l-m)!}{(l+m)!}}\\ &\times[\mathrm{sgn}(m')]^{m'}\frac{\sqrt{(2|m'|)!}}{(2|m'|-1)!!}\sum_{m''=-|m'|}^{|m'|}(-1)^{m''}\\ &\times\sqrt{\frac{(|m'|-m'')!}{(|m'|+m'')!}}d^{|m'|}_{m'',-m'}[i\tau(\xi_j|q|)]\\ &\times\int_{S^2_+}\frac{g^{m'}\left(-\xi_j,\hat{k}_z\mu+i\xi_j|q|\sqrt{1-\mu^2}\cos\varphi\right)}{\xi_j+\hat{k}_z\mu+i\xi_j|q|\sqrt{1-\mu^2}\cos\varphi}\\ &\times\mu P^{m''}_{|m'|}(\mu)P^m_l(\mu)e^{i(m+m'')\varphi}\,d\theta,\end{aligned}$$

where $\mu=\cos\vartheta$, $\hat{k}_z=\sqrt{1+(\xi_j|q|)^2}$, $g^{m'}\in C$ are some functions, $\xi_j\in R$ are eigenvalues of a matrix. Here, ϑ,φ are the polar and azimuthal angles of θ. This unavoidable heavy computation is helped by the use of the supercomputer.

References

[1] M. Machida: J. Phys. A: Math. Theor. **48** (2015) 325001.

The radiative transport equation with FDM and FEM

Manabu Machida
Institute for Medical Photonics Research
Hamamatsu University School of Medicine, Hamamatsu 431-3192

The specific intensity of light propagating in random media is governed by the radiative transport equation, which is a linear Boltzmann equation. A typical example of such light is near-infrared light in biological tissue. The equation is a first-order differential equation involving an integral term and has six variables, i.e., time t, positions x_1, x_2, x_3, and angular variables ϑ, φ. We consider light propagation in a domain $\Omega \subset R^3$. Let $I(x, \theta, t)$ ($x \in R^3$, $\theta \in S^2$, $t \in R$) be the specific intensity of light. Let c be the speed of light in the medium and $\mu_a(x), \mu_s(x)$ be the absorption and scattering coefficients, respectively. The radiative transport equation is given by

$$\begin{cases} \left(\frac{1}{c}\partial_t + \theta\cdot\nabla + \mu_a + \mu_s\right) I(x,\theta,t) \\ \qquad = \mu_s \int_{S^2} p(\theta,\theta') I(x,\theta',t)\,d\theta', \\ \qquad x \in \Omega, \quad \theta \in S^2, \quad t \in (0,T), \\ I(x,\theta,t) = g(x,\theta,t), \\ \qquad (x,\theta) \in \Gamma_-, \quad t \in (0,T), \\ I(x,\theta,0) = a(x,\theta), \quad x \in \Omega, \quad s \in S^2, \end{cases}$$

where $p(\theta, \theta')$ is the scattering phase function and $\Gamma_\pm$ is defined as

$$\Gamma_\pm = \left\{(x,\theta) \in \partial\Omega \times S^2;\, \pm\nu\cdot\theta > 0\right\},$$

with ν the outer unit vector normal to $\partial\Omega$.

If $I(x, \theta, t)$ is almost isotropic as a function of θ, we can write

$$I(x,\theta,t) = \frac{1}{4\pi}u(x,t) + \frac{3}{4\pi}J(x,t)\cdot\theta.$$

Then the fluence rate $u \in R$ and current $J \in R^3$ are given by $u(x,t) = \int_{S^2} I(x,\theta,t)\,d\theta$ and $J(x,t) = \int_{S^2} \theta I(x,\theta,t)\,d\theta$. From the radiative transport equation we see that J obeys the Fick law, $J(x,t) = -D\nabla u(x,t)$, where $D = [3(1-g)\mu_s]^{-1}$, $g = \int_{S^2}(\theta\cdot\theta')p(\theta,\theta')\,d\theta$, and u obeys the diffusion equation,

$$\left(\frac{1}{c}\partial_t - \nabla\cdot D\nabla + \mu_a\right)u(x,t) = 0.$$

Using this diffusion approximation, we have started with the numerical calculation of the above diffusion equation.

In finite element method (FEM) we divide the domain Ω into a mesh of nonoverlapping elements and define a basis $v_i(x)$ of limited support. Then the function $u(x,t)$ is approximated in this basis by the piecewise polynomial interpolation, $u^h(x,t) = \sum_i u_i(t)v_i(x)$, where u_i are basis coefficients. The superscript h denotes the finite element mesh basis expansion. The coefficients $D(x)$ and $\mu_a(x)$ are expanded in the same manner into $D^h(x)$ and $\mu_a^h(x)$. Thus we obtain

$$\left[K(D^h) + C(\mu_a^h) + \alpha A\right]U(t) + B\partial_t U(t) = 0,$$

where $U(t) = {}^t(u_1, u_2, \ldots)$,

$$\begin{aligned} K_{ij} &= \int_\Omega D^h(x)\nabla v_i(x)\cdot\nabla v_j(x)\,dx, \\ C_{ij} &= \int_\Omega \mu_a^h(x)v_i(x)v_j(x)\,dx, \\ B_{ij} &= \frac{1}{c}\int_\Omega v_i(x)v_j(x)\,dx, \\ A_{ij} &= \int_{\partial\Omega} v_i(x)v_j(x)\,d\sigma. \end{aligned}$$

Here, α is a parameter appearing in the boundary condition.

Molecular simulation of colloidal crystals

Takamichi TERAO
Department of Electrical, Electronic and Computer Engineering, Gifu university
Yanagido 1-1, Gifu 501-1193

Polymer-nanoparticle composites, also known as spherical polymer brushes, are a typical example of a soft colloidal system. Polymer brushes play an important role in regulating the stability of colloidal suspensions and also in tuning the effective interactions between fine particles due to the polymer-induced repulsive potential. Self-assembly of these particles is a fundamental topic in material science; arrays of these composites have industrial applications such as the production of photonic crystals with bandgaps that forbid the propagation of light from a certain frequency range. The property of effective potential between particles is important to determine the phase diagram of the system. For example, a Gaussian-core model shows re-entrant melting. These studies have implied that the self-assembly of soft colloidal systems exhibits characteristic features which are different from charge-stabilized colloidal systems.

Spherical polymer brushes contain a core particle inside where different core particles cannot overlap. The study of physical properties of these systems, such as structural formation and phase diagrams, has been gaining increasing attention. Recently, spherical dendritic brushes, where many dendrons are grafted onto the spherical surface of a core particle, have been investigated. Dendrimers are highly branched, tree-like macromolecules with numerous free ends and excess polymer densities at the periphery of the brushes. Dendritic polymer brushes comprise dendritic polymers anchored to a surface at one end. Recent theoretical studies have clarified the structural formation of dendritic polymer brushes on flat surfaces by means of self-consistent field theory and scaling analysis. Moreover, molecular simulations have been performed to study the structural formation of dendritic polymer brushes.

In this study, the nature of the effective interaction between a pair of dendritic spherical polymer brushes (Figure 1) was numerically investigated using Monte Carlo simulation. Since much stronger entropic repulsion between particles is expected compared with that of linear polymer brushes, the structural formation of these spherical dendritic brushes was studied. The transferability of the obtained coarse-grained potential at various temperatures was also confirmed.

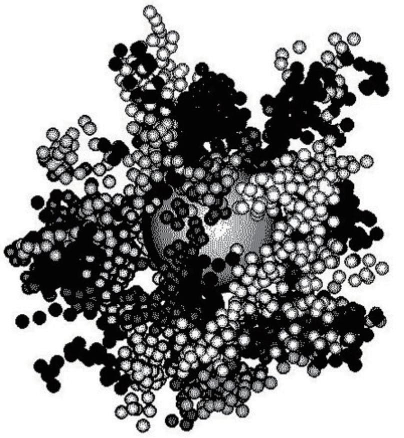

Figure 1: Spherical dendritic polymer brushes

Nonadiabatic Dynamics of Cooperative Domain Growth Triggered by THz-pulse Irradiation

Kunio ISHIDA
Department of Electrical and Electronic Engineering, School of Engineering,
Utsunomiya University, Yoto, Utsunomiaya, Tochigi 321-8585

Photoinduced nucleation by THz pulses is studied by a model of localized electron couple with an optical phonon mode.

Based on the analogy to the photoinduced phase transitions observed in various materials, we consider that cooperative interactions between electrons and coherent phonons will lead to the multiplication of excited electrons and/or growth of a transient phase, which is understood by bifurcation of quantum-mechanical wavepackets on adiabatic potential energy surfaces. Taking a model of localized electrons coupled with a quantized optical phonon mode, we discuss the dynamics of the cooperative phenomena by THz-pulse irradiation and, in particular, the role of the number and/or the initial distribution of phonons in the initial creation process of transient phases.

We employ a model of localized electrons coupled with an optical phonon mode which describes the general properties of the photoinduced structural change. In the present study we consider an array of molecules (unit cells) on a square lattice with two electronic levels and a single phonon mode interacting with each other, which is described by the following Hamiltonian:

$$\begin{aligned} H = \sum_{\vec{r}} \left[\frac{p_{\vec{r}}^2}{2} + \frac{\omega^2 u_{\vec{r}}^2}{2} + (\sqrt{2\hbar\omega^3} s u_{\vec{r}} + \varepsilon\hbar\omega + s^2\hbar\omega)\tilde{n}_{\vec{r}} + \lambda\sigma_{\vec{r}}^x \right] \\ - \sum_{<r,r'>} \left[\alpha\omega^2 (u_{\vec{r}} - \beta\tilde{n}_{\vec{r}})(u_{\vec{r}'} - \beta\tilde{n}_{\vec{r}'}) + \{V - W(u_{\vec{r}} + u_{\vec{r}'})\}\tilde{n}_{\vec{r}}\tilde{n}_{\vec{r}'} \right] \end{aligned}$$

We calculated the dynamics of coupled electron-phonon system excited by THz optical pulses. Since the lattice vibration frequency is of the order of THz, we consider that the applied THz pulses act as an external electric field that directly induces deformation of the lattice. Thus, the initial condition of the simulations is set to be deformed lattice with electrons occupying the ground state.

As a lot of computational resources are required to calculated the dynamics of the system, we used the System B with MPI parallelization[1] and 4 nodes were used in each simulation run.

We found that the electronic transition between the ground state and an excited state is induced by the propagation of phonons, and the region of excited molecules extends over the whole system, although initial deformation of the lattice is limited to the molecules in the vicinity of the surface of samples. As a result, the population of excited electrons increases, which shows that the multiplication of excited electrons is possible by the injection of phonons. Although these features are similar to the photoinduced cooperative phenomena, we also found that the nonadiabatic interaction λ is enhances the nucleation as shown in Fig.1. The present results show that the irradiation of intense THz-pulses is effective to induce the multiplication of excited electrons in various systems, and that it will be another method to discuss the dynamical behavior and/or the hidden phase[1] which is able to access via photoexcited states.

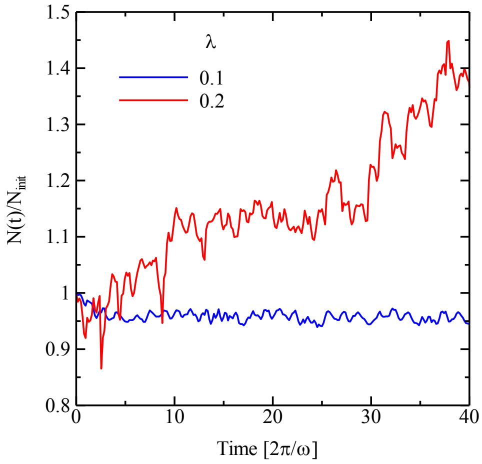

Fig.1 Excited state population as a function of time for λ = 0.1 and 0.2.

References

[1] K. Ishida and K. Nasu, Comp. Phys. Commun. **180**, 1489 (2009).

[2]“Photoinduced phase transitions” ed. K. Nasu (World Scientific, Singapore).

Nonadiabatic Wavepacket Dynamics of Electron-phonon-photon Systems

Kunio ISHIDA

Department of Electrical and Electronic Engineering, School of Engineering,

Utsunomiya University, Yoto, Utsunomiya, Tochigi 321-8585

Since the adaptive control method in coherent regime[1] was proposed to control the reaction rate with certain chemical species, ultrafast coherent control of electron-phonon systems has been studied by many authors. When the quantum-mechanical nature of the electromagnetic field is taken into account, the nonadiabaticity of the electronic transition is relevant to the absorption/emission of photons in femto/picosecond regime. Though this effect is neglected particularly for intense incident light, we still require to understand the interplay of phonons and photons in the case of strongly coupled electron-phonon systems.

We study the wavepacket dynamics of electron-phonon-photon systems in order to clarify the role of nonadiabaticity of electronic transitions. We stress that Raman process which involves creation/annihilation of both phonons and photons is important.

Employing a simple model of an electronic system coupled with both phonons and photons, we numerically solved the time-dependent Schrödinger equation for systems with a single phonon mode and three photon modes. We chose the Fock states as a basis for the vibration mode and the photon modes, and the equation of motion is expressed by the diabatic picture. Since a lot of computational resources are required even for three photon modes, numerical simulations were performed on the System B with hybrid parallelization using up to 18 nodes. We found that induced Raman process enhances the electronic transition and that the trajectories of wavepackets deviate from those under semiclassical approximation as shown in the figure.

As discussed in previous studies[2,3], the conical intersection(CI) in the “adiabatic potential energy surfaces” for phonons and photons is important to reveal the dynamics of the system in this case. The wavepackets always pass the crossing region of the (one-dimensional) PESs in the semiclassical approximation, while they move around the CI in the case of quantized light. Hence, the bifurcation of the wavepackets caused by the nonadiabatic matrix elements of the Hamiltonian takes place in a different manner between quantum-mechanical calculations and semiclassical calculations, which implies that the dressed-state picture is important to discuss the transient dynamics of photoirradiated systems in coherent regime.

References

[1] R. S. Judson and H. Rabitz, Phys. Rev. Lett. **68**, 1500 (1992).

[2] M. Kowalewski, K. Bennett, and S. Mukamel, J. Chem. Phys. **144**, 05439 (2016).

[3] F. Bouakline, Chem. Phys. **442**, 31(2014).

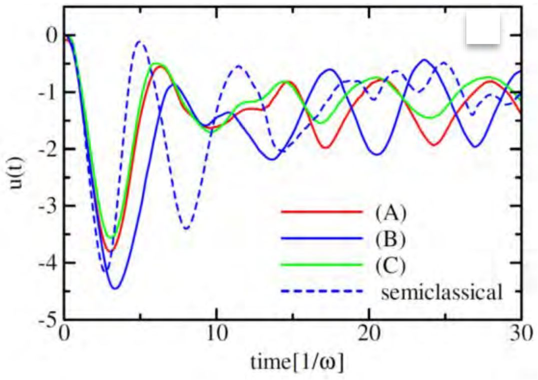

Fig.1 Dynamics of lattice deformation u(t) taking into account: (A) single photon mode, (B) two photon modes with induced Raman process, and (C) two photon modes with spontaneous Raman process. ωdenotes the frequency of the phonon.

Conformational dynamics of proteins studied by molecular dynamics simulations

Yuma SUEMATSU and Munehito ARAI
Department of Life Sciences, Graduate School of Arts and Sciences,
The University of Tokyo, Komaba, Meguro, Tokyo 153-8902

Proteins exert their functions through dynamic motions in general, and thus, elucidation of conformational dynamics of a protein is necessary to understand the mechanism of its action and to improve its biological activity. Cyanobacteria are known to synthesize alkanes/alkenes corresponding to diesel oils using the proteins inside the organism. Because these hydrocarbons are produced from carbon dioxide by photosynthesis, such sustainable “bio-energies” are expected to be substitutes for petroleum-based hydrocarbons [1,2]. In 2010, Schirmer *et al.* revealed that cyanobacteria use an aldehyde-deformylating oxygenase (ADO) to convert aldehydes into alkanes/alkenes [3]. However, the catalytic mechanism of ADO has been poorly understood.

To elucidate the conformational dynamics of ADO, here we performed molecular dynamics (MD) simulations of the ADO protein from a cyanobacterium *Nostoc punctiforme* PCC 73102, which has been reported to have the highest activity among ADOs from various cyanobacterial strains [3]. Because ADO is known to bind two metal ions, we performed MD simulations both in the presence and absence of zinc ions. In addition, we did simulations in the presence and absence of a heptadecane (C17) molecule, resulting in four types of MD simulations (-Zn/-C17; -Zn/+C17; +Zn/-C17; +Zn/+C17). Preliminary simulations have been performed last year, and thus longer simulations up to 400 ns were performed here for each types of simulations.

All MD simulations were performed using the AMBER12 software. The ADO protein was immersed in TIP3P water molecules with periodic boundary conditions. The force fields of ff98SB were used for the protein, while those for C17 were calculated using the ANTECHAMBER program. After energy minimization, the temperature of the system was raised up to 298 K with restraints on protein structure. Finally, the MD simulations were performed for ~400 ns at 298 K without structural restraints.

Our simulations showed that the metal-free forms of ADO exhibited large structural fluctuations around the metal-binding sites, consistent with crystal structures of metal-free ADOs. Interestingly, we could observe conformational changes of the C17 molecule inside the ADO protein. Moreover, the open/close dynamics was observed at the product-exit site of ADOs, and the dynamics was dependent on the presence/absence of the metals and product in the ADO molecule.

These results suggest that the conformational dynamics of ADO is controlled by the binding/release of the metals and product during the catalytic cycle. Further studies by longer simulations will elucidate the time scale of the open/close dynamics of the substrate-entry/product-exit site of ADO. The open/close dynamics may be directly related to the catalytic efficiency of ADO, and manipulation of the conformational dynamics may enable us to improve the alkane-producing activity of ADO.

References

[1] Y. Hayashi, Yasugi, F. and M. Arai: PLoS ONE, **10** (2015) e0122217.

[2] H. Kudo, R. Nawa, Y. Hayashi, and M. Arai: Biotechnology for Biofuels, **9** (2016) 234.

[3] A. Schirmer, M.A. Rude X. Li, E. Popova, and S.B. del Cardayre: Science, **329** (2010) 559-562.

Spin-lattice-coupling effects in pyrochlore antiferromagnets

Kazushi AOYAMA
Department of Earth and Space Science, Graduate School of Science, Osaka University
Machikaneyama-cho, Toyonaka-shi, Osaka 560-0043

In frustrated magnets, it often happens that spins are coupled to the lattice degrees of freedom and the underlying lattice is distorted spontaneously to resolve the magnetic frustration, leading to a long-range magnetic order. The spinel chromium oxides $\mathrm{ACr_2O_4}$ provide a typical example of such a spin-lattice-coupled (SLC) ordering, where the magnetic ion Cr^{3+} forms the pyrochlore lattice, a three-dimensional network of corner-sharing tetrahedra. Of recent particular interest is antiferromagnets on a breathing pyrochlore lattice realized in the chromium oxides $\mathrm{AA'Cr_4O_8}$. In the breathing case, the lattice nonuniformity of the breathing structure, the alternating array of small and large tetrahedra, should be reflected in the system parameters such as the ratio of the nearest neighbor interaction for large tetrahedra to that for small ones J'/J. In this work, we investigate effects of the breathingness measured by J'/J on the SLC ordering.

Our model Hamiltonian is given by $\mathcal{H}_{\rm eff} = \mathcal{H}_0 + \mathcal{H}_{\rm SL}$,

$$\begin{aligned}
\mathcal{H}_0 &= J\sum_{\langle i,j\rangle_s} \mathbf{S}_i\cdot\mathbf{S}_j + J'\sum_{\langle i,j\rangle_l} \mathbf{S}_i\cdot\mathbf{S}_j, \\
\mathcal{H}_{\rm SL} &= -Jb\sum_{\langle i,j\rangle_s} (\mathbf{S}_i\cdot\mathbf{S}_j)^2 - J'b\sum_{\langle i,j\rangle_l} (\mathbf{S}_i\cdot\mathbf{S}_j)^2 \\
&- \Big\{Jb\sum_{\langle i,j,k\rangle_s} + J'b\sum_{\langle i,j,k\rangle_l}\Big\}(\mathbf{S}_i\cdot\mathbf{S}_j)(\mathbf{S}_i\cdot\mathbf{S}_k) \\
&- b\sqrt{JJ'}\sum_i\sum_{j\in N_s(i)}\sum_{k\in N_l(i)} \mathbf{e}_{ij}\cdot\mathbf{e}_{ik} \\
&\qquad\qquad \times(\mathbf{S}_i\cdot\mathbf{S}_j)(\mathbf{S}_i\cdot\mathbf{S}_k), \qquad (1)
\end{aligned}$$

where $\mathbf{S}_i$ is a classical Heisenberg spin, the dimensionless parameter b measures the strength of the SLC, and $\mathbf{e}_{ij}$ is a unit vector connecting sites i and j

To investigate ordering properties of the model (1), we perform Monte Carlo simulations by using the facilities of the Supercomputer Center, ISSP, the University of Tokyo. In the simulation, we basically perform 10^6 Metropolis sweeps under periodic boundary conditions, where the first half is discarded for thermalization. Our single spin flip at each site consists of the conventional local update and a successive over-relaxation process in which we try to rotate a spin by the angle π around the local mean field.

By measuring various physical quantities such as the spin collinearity and the spin structure factor, we determined the low temperature phases. It is found that the system exhibits the first order transition into collinear spin states characterized by $(1,1,0)$ or $(\frac{1}{2},\frac{1}{2},\frac{1}{2})$-type magnetic Bragg peaks. The $(1,1,0)$ state is realized in the weaker SLC regime, while the $(\frac{1}{2},\frac{1}{2},\frac{1}{2})$ states, which have three ordering patterns (type I, II, and III) depending on the ratio J'/J and the strength of the SLC, are favored in the relatively stronger SLC regime. In contrast to the $(1,1,0)$ and the type I $(\frac{1}{2},\frac{1}{2},\frac{1}{2})$ states appearing in the uniform case, the type II and III phases are peculiar to the breathing pyrochlores. It is also found that the difference in the ordering patterns of three $(\frac{1}{2},\frac{1}{2},\frac{1}{2})$ phases is reflected in the residual entropy, which could be observed as signatures of the type II, III orders.

Computer-simulated *n*-beam X-ray pinhole topographs based on the Ewald-Laue dynamical diffraction theory and FFT

Kouhei OKITSU

Institute of Engineering Innovation, School of Engineering,
The University of Tokyo, 2-11-16 Yayoi Bunkyo-ku Tokyo 113-8656

The difficulty of phase determination in X-ray crystal structure analysis has been overcome by the direct method invented by Hauptman and Karle for small molecular-weight crystals. However, it is almost not effective for protein crystals whose molecular sizes are significantly large. Then, non-native protein crystals in which heavy atoms or selenium atoms are introduced, are usually used for phase determination.

The idea of '*n*-beam method' to solve the phase problem was reported by Lipscomb in 1949 for the first time. However, this method has not been successfully used to extract phase information of protein crystals up to today. The ultimate purpose of the present study is to give the final solution of the phase problem for native protein crystals by using the *n*-beam method.

Incidentally, the present author has two hypothesizes about too large *R*-factor (up to 20-30%) for protein crystals. The former is that *R*-factor can be decreased by using '*n*-beam approximation' in place of usually used two-beam approximation when estimating the *R*-factor. The above hypotheses is based on an assumption that intensity perturbation is caused by interference effect among simultaneously reflected X-rays. A large number of reflection spots are taken simultaneously on two-dimensional detector for protein crystals since their reciprocal lattice node density is extremely high compared with small molecular-weight crystal.

The latter hypothesis is that the phase information can be extracted only by taking into account the crystal orientation that is not usually used but has information about reflection indices giving simultaneous Bragg reflections.

The purpose of the present report is describing a method to calculate X-ray intensity from a crystal whose orientation is known and shape is complex.

A numerical method to solve the Ewald-Laue (E-L) dynamical diffraction theory for an *n*-beam case was reported by Colella in 1974 for the first time. However, it was effective only for a parallel plate crystal. The present author extended the Takagi-Taupin (T-T) equation to *n*-beam condition and gave a numerical method to solve it [1-3]. Further, it has been clarified that the *n*-beam T-T equation can be numerically solved for an arbitrary-shaped crystal from a comparison between experimentally obtained and computer-simulated six-beam pinhole topographs for a channel-cut silicon crystal [4,5].

He has also reported three-, four-, five-, six-, eight- and twelve-beam pinhole topographs experimentally obtained and computer-simulated

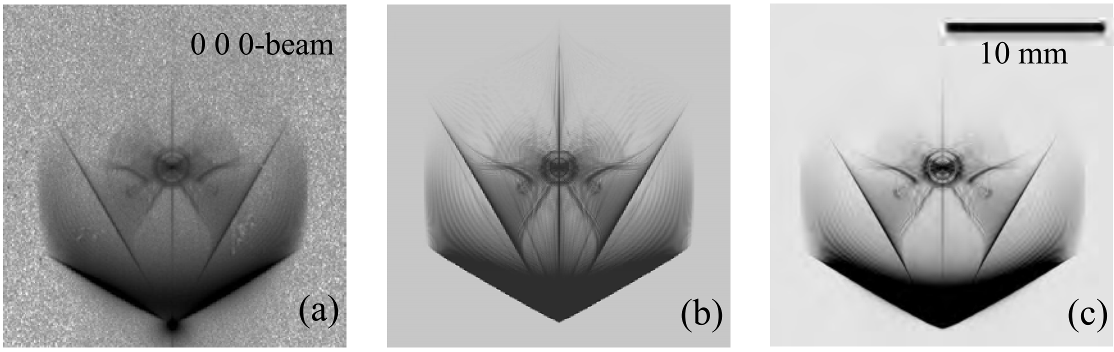

Fig.1 Six beam pinhole topographs (a) Experimentally obtained at SPring-8 and computer-simulated based on (b) the T-T equation and (c) E-L theory and FFT. The photon energy was 18.245 keV. The thickness of the silicon crystal was 9.6 mm. (a) and (b) have been published in reference [3].

based on the T-T equation and has verified the equivalence between the *n*-beam E-L and T-T theories, for the first time [6]. The applicable number of waves comes from a restriction that the *n* reciprocal lattice nodes should be on a circle in the reciprocal space. (circular case).

However, he has not found a method to solve the T-T equation for non-circular n-beam case, unfortunately, in spite that *n*-beam condition in a protein crystal is always non-circular. On the other hand, the *n*-beam E-L theory can be solved even for a non-circular case.

Recently in 2016-2017, a numerical method to solve the E-L theory and then Fourier-transform the solution to obtain a six-beam pinhole topograph has been reported by Kohn. The present author has got an inspiration to solve the eigen value problem of the E-L theory and apply a fast Fourier transform (FFT) to the solution to obtain a non-circular case *n*-beam pinhole topgraph.

Figure 1 shows forward-diffracted images of six-beam pinhole topographs (a) experimentally obtained, computer-simulated based on (b) the T-T equation and (c) the E-L theory and FFT. This method can be applied to calculation of pinhole topographs even for a protein crystal whose shape is complex in general since it has been found that pinhole topographs for a complex-shaped crystal can be simulated by piecing together several parts of topographs for parallel plate crystals simulated by using the E-L theory and FFT. Then, the present author has prepared to calculate reflected X-ray intensity for a non-native protein crystal to verify the first hypothesis [7].

References

[1] K. Okitsu: Acta Cryst. **A59** (2003) 235-244.

[2] K. Okitsu et al.: Acta Cryst. **A59** (2003) 311-316.

[3] K. Okitsu et al.: Acta Cryst. **A62** (2006) 237-247.

[4] K. Okitsu et al.: Acta Cryst. **A67** (2011) 550-556.

[5] K. Okitsu: Acta Cryst. **A67** (2011) 559-560.

[6] K. Okitsu, Y. Imai and Y. Yoda: InTech *Resent Advances in Crystallography* (2012) 67-86 [Invited].

[7] K. Okitsu: Submitted to Acta Cryst. **A77** (2018).

Transport properties of one-dimensional interacting electron systems by a quantum Monte Carlo method

Takeo KATO
Institute for Solid State Physics, University of Tokyo
Kashiwa-no-ha, Kashiwa, Chiba 277-8581

Conductance quantization in electron transport through a quantum contact is one of highlights in mesoscopic physics because it clearly demonstrates importance of quantum mechanics. However, appearance of another non-quantized conductance plateau, which is called "0.7 anomaly", has been a mystery for long time from the first discovery of the conductance quantization. This phenomenon is thought to be a many-body effect due to Coulomb interaction between electrons near the point contact. For example, numerical calculation for zero-temperature transport based on functional renormalization group indicates suppression of conductance due to singularity induced by exchange interaction [1]. The entire feature of the 0.7 anomaly has, however, not been understood yet.

To tackle this problem, we have tried to construct a procedure to obtain information of conductance from numerical data for a finite one-dimensional lattice model with Coulomb interaction and one-body potential energy by scatterers (point contacts) with a finite width. We employed the stochastic series expansion (SSE) method [2], which is one of quantum Monte Carlo methods, and calculated current-current correlation functions as a function of the imaginary time. Because only finite systems can be treated in the SSE method, the procedure to obtain linear conductance is nontrivial. We first showed that zero-frequency current-current correlation function obtained by a naive analytic continuation loses the information of electronic transport. We found that by introducing an additional broadening factor, we can recover information of phase shift of electrons across a scatter, and succeeded in reproducing a known result, i.e., the Landauer formula if the Coulomb interaction is switched off. We also demonstrated that conductance of a point-like scatterer in the Luttinger liquid obtained from this procedure is consistent with renormalization group analysis [3]. Our method is naturally connected to the formula for the Drude weight in the thermodynamic limit [4].

The present study provides a foundation for calculation of conductance in interacting electron systems. We are now trying to extend our idea toward general one-dimensional interacting electron systems, by reformulating it in terms of the field theory for electronic transport [5].

References

[1] J. Heyder et al., Nature **501** (2013) 73.

[2] A. W. Sandvik, Phys. Rev. B **59** (1999) R14157; A. W. Sandvik, J. Phys. A: Math. Gen. **25** (1992) 3667.

[3] C. L. Kane and M. P. A. Fisher, Phys. Rev. Lett. **68** (1992) 1220.

[4] D. J. Scalapino, et al., Phys. Rev. Lett. **68** (1992) 2830.

[5] N. Shimada and T. Kato, in preparation.

Numerical Large Deviation Analysis of Eigenstate Thermalization Hypothesis

Eiki Iyoda
Department of Applied Physics,Institute for Solid State Physics, the University of Tokyo
Hongo, Bunkyo-ku, Tokyo 113-8656

Recently, thermalization in isolated quantum systems attracts attention, and a plausible mechanism of thermalization is based on the strong version of the eigenstate thermalization hypothesis (ETH) [1]. The ETH states that all the energy eigenstates in the microcanonical (MC) energy shell have thermal properties. Here, the word *thermal* means the expectation value of an observable $\hat{O}$ equals the MC average:

$$O_i := \langle E_i|\hat{O}|E_i\rangle \simeq \langle\hat{O}\rangle_{\mathrm{MC}} \tag{1}$$

We have numerically investigated the ETH by focusing the large deviation property, in other words, we focused on *athermal* eigenstates. We refer to an energy eigenstate $|\rangle E_i$ as athermal eigenstate if $|O_i - \langle\hat{O}\rangle_{\mathrm{MC}}| > \varepsilon$ is satisfied, where ε is a threshold. We define the number of the athermal eigenstates D_{out} as

$$D_{\mathrm{out}} \equiv \sum_{|E_i\rangle\in\mathcal{M}(E,\Delta E)} \theta\left(|O_i - \langle\hat{O}\rangle_{\mathrm{MC}}| - \varepsilon\right), \tag{2}$$

where $\mathcal{M}(E,\Delta E)$ is the microcanonical energy shell with $[E-\Delta E, E]$. We also refer to D as the dimension of the energy shell.

The strong ETH implies that D_{out} is zero if the system size L is sufficiently large. There is a mathematical theorem which gives an upper bound of the ratio D_{out}/D:

$$D_{\mathrm{out}}/D \leq e^{-\gamma L}, \tag{3}$$

where $\gamma > 0$. If the ratio D_{out}/D decays faster than exponentially, D_{out} will become zero with large but finite L.

We have calculated D_{out} by using numerically exact diagonalization and Sakurai-Sugiura method [2]. We used one-dimensional quantum spin chain (XXX model) with next nearest interaction. The XXX model can be represented with hard core bosons, and we used the filling of hard core bosons at 1/3 in this model. The system sizes are taken as $L = 12, 15, 18, 21, 24$. The dimension of the Hilbert space is 735471 for $L = 24$. By using the translation invariance, we divide the whole space into L sectors. We should diagonalize matrices with ~ 30465 dimension. For $L = 24$, we use the Sakurai-Sugiura method to investigate the parameter dependence.

As a result [3], we have obtained D_{out}/D for some observables by changing the integrability breaking parameter. When the system is non-integrable, we have showed D_{out}/D are fitted well with a function $f(L) = a - b\exp(cL)$ with positive constants a, b and c. This implies the strong ETH. This double exponential behavior is seen even in the near integrable system.

References

[1] M. Rigol, V. Dunjko, and M. Olshanii, Nature **452**, 854 (2008).

[2] T. Sakurai and H. Sugiura, J. Comput. Appl. Math. **159**, 119 (2003).

[3] T. Yoshizawa, E. Iyoda, and T. Sagawa, arXiv:1712.07289.

Tensor Renormalization Group with Randomized Algorithm for Singular Value Decomposition

Satoshi MORITA

Institute for Solid State Physics,

The University of Tokyo, Kashiwa-no-ha, Kashiwa, Chiba 277-8581

Tensor network method is a powerful tool for quantum and classical many-body systems. The tensor renormalization group (TRG) method is an efficient method for contracting tensor networks [1]. Its main operations, "decomposition" and "contraction" have the computational complexity proportional to the sixth power of the bond dimension.

We proposed an efficient algorithm of the tensor renormalization group based on a randomized algorithm for singular value decomposition [2]. Avoiding explicit creation of a four-leg tensor reduces the computational complexity to the fifth power of the bond dimension. The oversampling parameter tunes accuracy of the randomized algorithm. We showed that the oversampling parameter larger than the bond dimension is sufficient to reproduce the same result of the full singular value decomposition [3].

References

[1] M. Levin and C. P. Nave, Phys. Rev. Lett. **99** 120601 (2007)

[2] N. Halko, P. G. Martinsonn, J. A. Tropp, SIAM Review **53**, 217 (2011).

[3] SM, R. Igarashi, H.-H. Zhao, and N. Kawashima: Phys. Rev. E **97**, 033310 (2018)

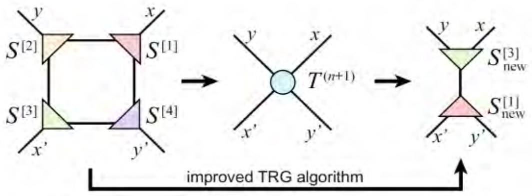

Fig. 1: The chain of deformation in the TRG algorithm [3].

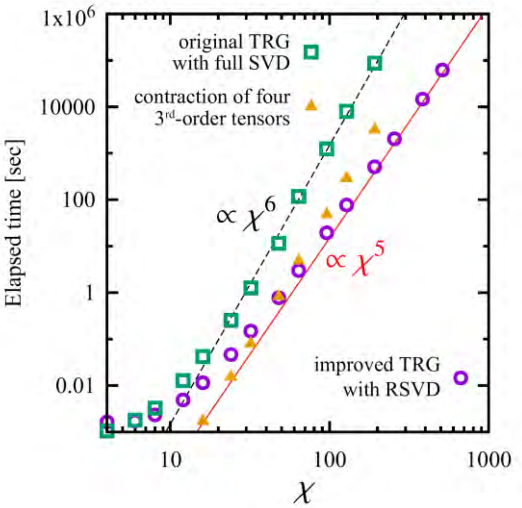

Fig. 2: Elapsed time per TRG step as a function of the bond dimension [3].

Coarse-Grained Molecular Dynamics Simulations of Slide-Ring Gel Networks

Koichi Mayumi[1], Yusuke Yasuda[1], Masatoshi Toda[2], Hideaki Yokoyama[1], Hiroshi Morita[2], and Kohzo Ito[1]

[1] *Dept. of Advanced Materials Science, Graduate School of Frontier Sciences, the Univ. of Tokyo.*

[2]*National Institute of Advanced Industrial Science and Technology*

We have studied the relationship between mechanical properties and the orientation of molecules in slide-ring gels [1] using parallel computer simulations. This year, we focused on orientation of molecules in networks.

Generally conventional fixed-crosslink gels have chemical bond between axle chains, while slide-ring gels fabricated by Ito et. al., do not have direct crosslinks, but have figure-of-eight crosslinks. Slide-ring gels show high extensibility and toughness because figure-of-eight crosslinks act like pulleys and prevent stress concentration on short axle chains, which is called “pulley effect” (Fig. 1). This time we tried to visualize pulley effect, using coarse-grained molecular dynamics simulation.

We have constructed a coarse-grained model of slide-ring gels with beads-spring model established by Kremer and Grest [3]. 20,000 up to 35,000 beads system was used for simulation, and equilibration simulation was performed using OCTA/COGNAC engine for $1.0 \times 10^{7}\ \tau$ time steps, where simulation step was $\Delta t = 1.0 \times 10^{-2}\tau$. We carried out elongation simulation in the range of extension ratio λ = 1-10 at a strain speed $1.0 \times 10^{-5}\ \lambda / \tau$ for slide-ring gels with 4 different crosslinking densities.

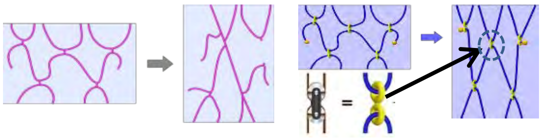

Fig. 1: Stress concentration in conventional gel (left) and pulley effect in slide-ring gel (right)

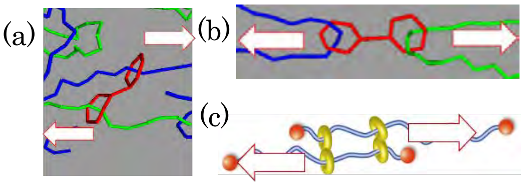

Fig. 2: (a) Orientation of figure-of-eight crosslinks parallel to stretching (b) Orientation of figure-of-eight crosslinks perpendicular to stretching, which leads to the pulley effect (c) Stress relaxation mechanism caused by the orientation of cross-links shown in (a).

We observed the orientation of axial chain and figure-of-eight crosslinks in slide-ring gels under uniaxial deformation. Like pulleys shown in Fig. 1, some figure-of-eight cross-links are oriented parallel to stretch (Fig. 2 (b)). On the other hand, some other cross-linking points are aligned in the direction perpendicular to stretching (Fig. 2 (a)), which suggests a novel stress-relaxation mechanism (Fig. 2(c)).

References

[1] K. Ito et. al., Adv. Mater. **13**(2001) 485.

[2] K. Ito, Polym. J. 39, 489 (2007).

[3] K. Kremer & G. S. Grest, J. Chem. Phys., 92, 5057 (1990).

Manipulation of Topological States by Real-Space Structure

Toshikaze Kariyado
International Center for Materials Nanoarchitectonics, National Institute for Materials Science
Namiki, Tsukuba, Ibaraki 305-0044

This year, we have mainly focused on the analysis of the electronic structure of i) antiperovskite family A_3EO (A=Ca,Sr,Ba, and E=Sn,Pb) [1], and ii) graphene nanomesh (graphene with antidot lattice) [2]. The main part of the analysis was relying on the density functional theory, and was performed using the parallelized version of Quantum Espresso package [3]. As we will see in the following, the systems to be considered in our work contain superstructures or many orbitals, and therefore, the parallelized computational programs play an essential role in our study. The parallelized version of the Quantum Espresso package works fine on the ISSP supercomputing facility.

For the antiperovskite family, we attempted to obtain electronic band structure for $Ca_{3(1-x)}Sr_{3x}SnO$, in relation to the pseudo gauge field, which might be generated by appropriate band structure engineering [1]. For this purpose, we take two approaches. In the first approach, effective models for two end materials ($x = 0$ and $x = 1$) are constructed, and then, effective models for intermediate values of x are obtained by interpolating parameters in the effective models for the two end materials. In the second approach, we consider superstructures like those in Fig. 1. In the two shown structures, the ratios between the number of Sr and Ca atoms are 4/9 and 5/9, respectively. The electronic band structures obtained in this way are reported in ref. 1.

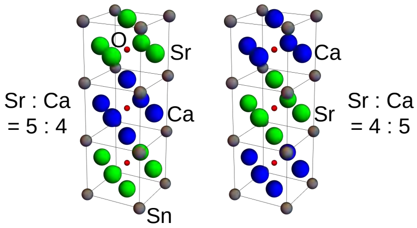

Figure 1: Crystal structures corresponding to $x = 4/9$ and $5/9$.

For graphene nanomesh, the computing facility is used to analyze lattice distortion effects, which are inevitable at the perimeter of antidot (nano-sized hole). For this purpose, we derive Wannier orbitals for relevant bands, and estimate effective transfer integrals. Because of the symmetry breaking at the perimeter of nanoholes (inside vs outside), the centers of Wannier orbitals can be off from the atomic positions. Consequently, transfer integrals are not determined by the distance between atoms alone, rather we have to take the Wannier centers into consideration. However, overall the lattice distortion effects are small and the most of the properties of graphene nanomesh can be addressed by a simple tight-binding model with uniform transfer integrals [2].

References

[1] T. Kariyado: arXiv:1707.08601.

[2] T. Kariyado, Y.-C. Jiang, H. Yang, and X. Hu: arXiv:1801.03115.

[3] P. Giannozzi *et al.*: J. Phys.: Condens. Matter **21** (2009) 395502.

Large-scale Molecular-dynamics Simulation with ANN Potentials: nm-scale Domain Structure in Densified Silica Glass

Daisuke WAKABAYASHI[1] and Fuyuki SHIMOJO[2]

[1]Institute of Materials Structure Science, High Energy Accelerator Research Organization (KEK), Tsukuba 305-0801

[2]Department of Physics, Kumamoto University, Kumamoto 860-8555

Silica glass is well known as an archetypal oxide glass and its compression behavior has attracted considerable attention in various fields of physical sciences. Recent small-angle X-ray scattering measurements have revealed the appearance of subnanometer-scale domains for low-pressure and high-pressure phases in silica glass during the pressure-induced structural transformations [1].

To reveal the detailed structure of subnanometer-scale domains, we conducted some calculations for large-scale molecular-dynamics (MD) simulations with a system of ~10,000 atoms. We have confirmed that ab-initio methods can simulate the compression behavior of silica glass accurately [2]. On the basis of the results of ab-initio calculations, we fitted the potential with a machine-learning technique (ANN potential) and applied it for the calculations with an extended system.

To obtain the data for fitting ANN potentials, we conducted ab-initio calculations. The configurations of six-coordinated and densified four-coordinated glasses (corresponding to high- and low-pressure phases) were prepared by gradually cooling silica melt from 4,000 K at 40 and 15 GPa, respectively, and then the decompression and recompression processes were calculated. There is remarkable agreement between the densities on decompression and recompression and therefore six-coordinated and densified four-coordinated glasses behave in an elastic manner as a single phase. In addition, six-coordinated glass was retrieved, in contrast to the case for experiments, implying that a six-coordinated structure remains at ambient conditions after decompression on a picosecond timescale.

We tested the MD simulations with a system of about 30,000 atoms using the ANN potential determined from the data at 40 GPa. However, the calculations at high temperatures cannot be made due to the numerical divergence, which implies that more machine-learning training is needed to refine the ANN potential.

References

[1] T. Sato, N. Funamori, D. Wakabayashi, K. Nishida, and T. Kikegawa: submitted.

[2] E. Ryuo, D. Wakabayashi, A. Koura, and F. Shimojo: Phys. Rev. B **96** (2017) 05420.

Giant and cross response with ferroelectric-antiferroelectric phase transitions

Kyohei Takae and Hajime Tanaka
Institute of Industrial Science, University of Tokyo
4-6-1 Komaba, Meguro-ku, Tokyo 153-8505, Japan

The dielectric properties and related cross coupling effects such as electromechanical and electrocaloric effects are strongly influenced by structural phase transitions. Here we focus on ferroelectric–antiferroelectric phase transitions, where basic physical picture controlling phase transitions with spontaneous arrangement of crystalline structure still remains elusive. To obtain physical insight into such phase controllability, we construct a molecular model exhibiting ferroelectric–antiferroelectric phase transitions with structural rearrangement. The pair interaction consists of dipolar interaction and Lennard-Jones interaction but slightly modified to realise anisotropic molecular interaction between spheroids. The key point of this model is interplay between the anisotropy of dipolar interaction (changing its sign depending on the direction of the relative position between adjacent particles) and steric (Lennard-Jones) interaction. By varying temperature and the aspect ratio of the spheroids, we realise ferroelectric–antiferroelectric phase transition with spontaneous rearrangement of crystalline structure, where the ferroelectric (antiferroelectric) phase is stable for small (large) aspect ratio. In this year we study electrical, mechanical and thermal control of this phase transitions [1] by molecular dynamics simulations.

Firstly, we examine mechanical switching from antiferroelectric to ferroelectric state under Parrinello-Rahman barostat. The Parrinello-Rahman barostat is necessary since phase transitions involves structural rearrangement. We apply anisotropic uniaxial stress on antiferroelectric states to study mechanical switching. Depending on temperature and the direction of stretching/compression, phase transitions from antiferroelectric state to another antiferroelectric state, ferroelectric state, and paraelectric state are observed, where both the dielectric and mechanical properties are greatly changed. Thus we realise selective mechanical switching of dielectric and electromechanical properties.

Secondly, we examine electrocaloric effects. The electrocaloric effect stands for temperature change induced by applying/removing external electric field. In particular, antiferroelectric phase has lower entropy in our system and hence temperature decreases (increases) by applying (removing) external electric field to induce phase transitions. This effect is called inverse electrocaloric effect, since the sign of temperature change is inverted compared with usual electrocaloric effect. By calculating the dynamical structure factors concerning rotational motions, we reveal that the suppression of rotational vibrations is the origin of small entropy in antiferroelectric state, resulting in the inverse electrocaloric effect.

References

[1] K. Takae and H. Tanaka, submitted.

Nonequilibirum phase transition and shock wave phenomena in the dense hard sphere systems

Masaharu ISOBE
Nagoya Institute of Technology
Gokiso-cho, Showa-ku, Nagoya, 466-8555

As one of the simplest model, the hard disk/sphere systems have been investigated in the field of both equilibrium and non-equilibrium statistical physics. In this project, we investigated non-equilibrium phenomena in the hard disk/sphere model system with modern algorithms, especially for Event-Chain Monte Carlo(ECMC) [1] and Event-Driven Molecular Dynamics(EDMD) [2], where we propose the "Hybrid Scheme", namely, ECMC for equilibration and EDMD for calculation of dynamical properties [3, 4].

Clustering impact regime with shocks in freely evolving granular gas:

Clustering of the granular gas is one of the fascinating phenomena. An evolving process of cooling granular gas systems without gravitational force is usually starting from the initial homogeneous state to the inhomogeneous clustering state, in which the energy decay deviates from the classical Haff's law. Previously [5, 6, 7, 8], we investigated the macroscopic behaviors on the evolving quasi-elastic Inelastic Hard Sphere (IHS) model by performing a microscopic event-driven molecular dynamics with mainly 512^2 [5], 4096^2 [7] in two-dimensional system (2D) and 128^3 [8] in three dimensional system (3D). These large-scale numerical simulations have revealed similarity with fluid Navier-Stokes turbulence, such as enstrophy cascade (Kraichnan-Leith-Bachelor theory), Kolmogorov scaling and Bose-Einstein condensation, which are well-known n the fluid turbulence. The rough estimate of Reynolds number with Taylor's microscale reveals that the IHS system at the onset of clustering regime grow up to $R_\lambda \sim 327$ (2D) and ~ 1470 (3D) [7, 8] respectively.

In this study [9], we focus on the inhomogeneous clustering regimes of evolving granular gas via event-based molecular dynamics simulation [2, 3] with up to 16.7 million disks to clarify the validity of asymptotic behaviors of energy predicted by a couple of theories. Although we confirmed that the theories are consistent in relatively dilute and small system, we found the novel regime regarding on collisions between "clusters" spontaneously appearing after the clustering regime in dense case, which can only be identified more than a few million particles systems. The two-step energy relaxation can be considered as follows: At first, several string-like clusters are organized as an aggregation of inelastic hard spheres, which are sparsely distributed. Those string-like clusters moved actively and are gradually aggregating. Next, a certain amount of cluster begins to collide each other. This giant impact between clusters preceded collectively and made round shape density wave propagation on the cluster. This shock propagation results in the rapid growth of dissipation. The volumetric dilatation pattern of semicircular shape originated from shock density propagation in the clusters after cluster impact can be detected. Our analyses clarify the cause of giant impact between cluster, which is an entirely novel physical mechanism in the field of cooling granular gas.

References

[1] E. P. Bernard, W. Krauth, and D. B. Wilson: Phys. Rev. E **80** (2009) 056704.

[2] M. Isobe: Int. J. Mod. Phys. C **10** (1999) 1281.

[3] M. Isobe: Mol. Sim. **42** (2016) 1317.

[4] M. Isobe: "Advances in the Comutational Sciences — Proceedings of the Symposium in Honor of Dr Berni Alder's 90th Birthday", edited by Eric Shwegler, Brenda M. Rubenstein, and Stephen B. Libby, World Scientific, **Chapter 6** (2017) 83.

[5] M. Isobe: Phys. Rev. E **68** (2003) 040301.

[6] M. Isobe: Proceedings in Powders and Grains 2005, Garcia-Rojo, Herrmann and McNamara(eds), (2005) 1123.

[7] M. Isobe: Int. J. Mod. Phys. C **23** (2012) 1250032.

[8] M. Isobe: J. Phys: Conf. Ser. **402** (2012) 012041.

[9] M. Isobe: EPJ Web Conf., **140** (2017) 04006.

Theoretical study for hydration effects on emitter of bioluminescence

Miyabi HIYAMA

Graduate School of Science and Technology, Gunma University, Tenjin-cho, Kiryu,
Gunma 376-8515

In this year, we calculated the instantaneous absorption spectra of phenolate-keto, phenolate-enol, and enolate aqueous oxyluciferin anions, shown in Figure 1, at room temperature from QM/MM calculations using an explicit solvent. The absorption energies are computed as the ensemble average of 1000 different structures of hydrated clusters of oxyluciferin anions for each isomeric form. All calculations were performed using the GAUSSIAN09 [1] program on system B of Super Computer Center in ISSP.

It was demonstrated that the calculations reproduce experimental results concerning spectral shifts and broadening, for which traditional methods based on quantum chemistry and the Franck-Condon approximation fail because of the molecular vibrations of oxyluciferin anions and dynamical fluctuations of their hydration structures [2].

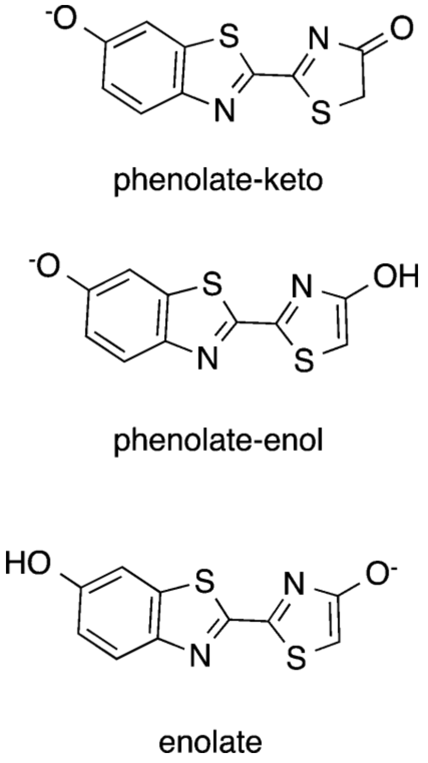

Figure 1: Molecular structures for oxyluciferin anions [2]

References

[1] Gaussian 09, Revision D.01, M. J. Frisch et al.
[2] M. Hiyama et al. Phys. Chem. Chem. Phys. 19 (2017) 10028.

Colloidal suspensions in binary liquid mixtures

Takeaki Araki and Armand Barbot
Department of Physics, Kyoto University
Kitashirakawa-oiwake-cho, Sakyo-ku, Kyoto 606-8505

We numerically study behaviors of colloidal suspensions in one-phase mixed solvents under shear flows (Fig. 1). Far from the phase separation point of the binary solvent, the colloid particles are dispersed well and the suspension shows a Newtonian viscosity (Fig. 2b). When the mixture is brought near the coexistence curve, the colloidal particles are aggregated by attractive interactions due to the concentration heterogeneity caused by the surface wetting. This aggregating interaction is enhanced when the component favored by the colloidal surface is poor. We found its viscosity is increased with approaching to the phase separation point. Near the coexistence curve the suspension shows a shear thinning behavior (Fig. 2b), since the aggregated structure is rearranged into small clusters under the shear flow (Fig. 2a). Our simulations also suggest that the shear flow does not change the concentration profiles around the particles so importantly at the onset of the rearrangement of the aggregates. Thus, we can consider that the effective interaction is almost free from the shear flow and remains isotropic.[1]

References

[1] A. Barbot and T. Araki: Soft Matter **13** (2017), 5911.

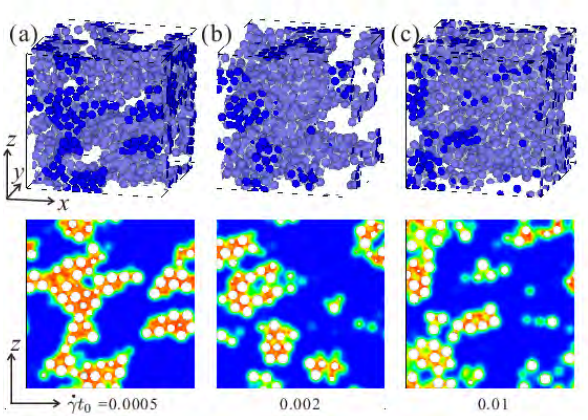

Figure 1: Snapshots of the particle distribution under shear flow (upper panels). The concentration fields are shown in the lower panels. The mixing fraction of the binary solvent is $\bar{\phi} = 0.35$ and the particle fraction is $\psi = 0.128$. The mixtures are at the coexistence curve.

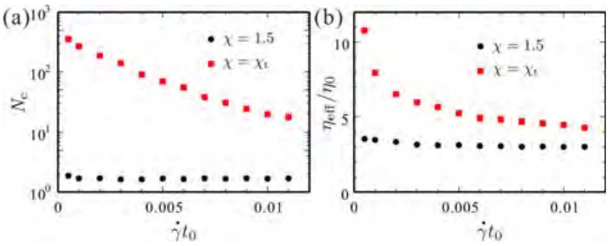

Figure 2: (a) The shear rate dependence of the cluster size. The mixture is in the one phase mixed state far from the coexistence curve (black circle, $\chi = 1.5$) and at the coexistence curve (red squares, $\chi = \chi_t$). (b) The shear rate dependence of the effective viscosity.

Microscopic theory of magnon physics in a three-dimensional chiral magnets

Naoya ARAKAWA

Department of Physics, Toho University, Funabashi, Chiba 274-8510

Magnons can describe low-energy physics of magnets. In contrast to the understanding for nonchiral magnets (e.g., ferromagnets and antiferromagnets), magnons for chiral magnets, magnets with finite spin scalar chirality, remains poor understood. In particular, the differences between magnons of nonchiral and chiral magnets and the differences between magnons of different chiral magnets are unclear.

To improve this situation, we studied the magnon dispersion curve and specific heat of chiral magnets on the pyrochlore lattice [1] by using the linearized-spin-wave approximation. We used an effective spin model consists of the Heisenberg interactions and the Dzyaloshinsky-Moriya interactions, and considered the all-in/all-out (AIAO) type and the three-in-one-out (3I1O) type chiral magnets.

We obtained two main results. The first one is that in all the chiral magnets considered, the magnon dispersion has no gapless excitation. Since nonchiral magnets usually have a Goldstone type gapless excitation, the first main result shows that the absence of the gapless excitations is a characteristic property of the chiral magnets. The second is that the magnon dispersion of the 3I1O type chiral magnets has not only the quasiacoustic branches, but also the optical branch, while those of the AIAO type chiral magnets are all quasiacoustic branches. We have defined a quasiacoustic and an optical branch of the magnon dispersion as follows: a quasiacoustic branch increases with the displacement from $\boldsymbol{q}=\boldsymbol{Q}$, the ordering vector; an optical branch decreases with the displacement. The above difference between the AIAO type and the 3I1O type chiral magnets is a characteristic, experimentally distinguishable difference between these chiral magnets.

We acknowledge support from the Super Computer Center in this study.

References

[1] N. Arakawa: Magnon Dispersion and Specific Heat of Chiral Magnets on the Pyrochlore Lattice, Journal of Physical Society of Japan, 86 (2017) 094705.

A series expansion study on the magnon spectrum of a kagome antiferromagnet in $Cs_2Cu_3SnF_{12}$

Yoshiyuki Fukumoto
Department of Physics, Faculty of Science and Technology, Tokyo University of Science
2641 Yamazaki, Noda, Chiba 278-8510

A spin-1/2 kagome-lattice antiferomagnet $Cs_2Cu_3SnF_{12}$ has a magnetic order with the $q = 0$ structure. Ono *et al.* observed the magnon dispersion curve via inelastic neutron scattering and pointed out that Dzyaloshinskii-Moriya (DM) interactions stabilizes the $q = 0$ structure [1]. It was also reported that the spin-wave analysis with the lowest order of quantum corrections result in exchange parameter as large as about 40% of that determined by a susceptibility measurement. In order to resolve this discrepancy, we intended to make a series expansion study from a Ising limit [2]. However, our obtained series coefficients are up to the second order at this stage, and the development of source codes for higher-order calculations is now in progress. The delay is due to the complexity in generating clusters that contribute to the series.

We used the supercomputer to make exact-diagonalization studies on a similar system, spin-1/2 spherical kagome cluster realized in $\{W_{72}V_{30}\}$ [3], which consists of 30 vertices and 20 corner-sharing triangles. We consider model Hamiltonians with terms which break the conservation of total S^z, as suggested by experiments on magnetization process. Then, the dimension of the Hilbert space is $2^{30} \simeq 1.07\times10^9$, and the memory usage of three complex vectors in this space amounts to 48 GB. We performed our numerical calculations on the SGI Altix ICE 8400EX at the Supercomputer Center, Institute for Solid State Physics, using OpenMP parallelization with up to 24 cores.

For cluster magnets, in general, stepwise structures are expected in zero-temperature magnetization curves. However, for a 30-site cluster $\{W_{72}V_{30}\}$, it was reported that there is no such structure up to 50 T in a magnetization measurement at 0.5 K[4]. In order to understand this behavior, we study the effects of Dzyaloshinsky-Moriya (DM) interactions and tilts of the g tensors, both of which lead to the breaking of the total-S^z conservation [5]. It is found that the D vector component parallel to the radiation direction of the polyhedron cancels out the staircase in a low magnetic field region efficiently. The tilts of the g tensors are inherent to systems defined on the polyhedrons and lead to induced magnetic fields varying site by site. This induced magnetic field affects the magnetization only at high magnetic fields. We also discuss two existing experimental results on the basis of our calculated results.

Next, we turn to the study of temperature dependence of the magnetic susceptibility for the spherical kagome cluster with DM interactions to compare with an existing experimental result [6]. Needless to say, the DM interaction breaks the conservation of total spin and get the evaluation of magnetic susceptibility to be more difficult. As for kagome-lattice antiferromagnets with DM interactions, Rigol and Singh calculated susceptibility up to a 15-site cluster to understand the experimental susceptibility of Herbertsmithite [7]. They calculated all eigenvalues under magnetic fields H, and evaluate magnetic susceptibility from the second-order coefficient in H of the free energy. Instead, we use the method of microcanonical thermal pure quantum (mTPQ) states to carry out calculations for the 30-site spherical kagome cluster.

The mTPQ state is configured to reproduce the equilibrium value in the smooth microcanonical ensemble with a density operator $(l-h)^k$, where h is the Hamiltonian density and l is an arbitrarily real number not less than the maximum eigenvalue of h [8]. We first show that the mTPQ states with sufficiently large l reproduce the equilibrium value in the canonical ensemble. In our susceptibility calculations, we apply magnetic fields, whose strength is chosen to be 10% of the exchange parameter, and calculate the induced magnetizations by using the mTPQ states. The susceptibility is obtained by dividing the magnetizations by the field strength. Although mTPQ expectation values contain statistical errors and the division process by a small field strength enhances the error, we find the present calculation procedure results in meaningful results. It is also found that the DM interaction moves the theoretical susceptibility closer to the experimental one [4].

References

[1] T. Ono, K. Matan, Y. Nambu, T. J. Sato, K. Katayama, S. Hirata, and H. Tanaka, J. Phys. Soc. Jpn. 83, 043701, 2014.

[2] W. Zheng, J. O. Fjaerestad, R. R. P. Singh, R. H. McKenzie, and R. Coldea, Phys. Rev. B 74, 224420, 2006.

[3] A. M. Todae, A. Merca, H. Bögge, T. Glaser, L. Engelhardt, R. Prozorov, M. Luban, and A. Müller, Chem. Commun., 3351, 2009.

[4] J. Schnack, A. M. Todea, A. Müller, H. Nojiri, S. Yeninas, Y. Furukawa, R. Prozorov, and M. Luban, arXiv:cond-mat/1304.2603v1.

[5] Y. Fukumoto, Y. Yokoyama, and H. Nakano: submitted to J. Phys. Soc. Jpn. (arXiv:1803.06485).

[6] Y. Maeda, Tokyo University of Science, 2018, master thesis.

[7] M. Rigol and R. R. P. Singh, Phys. Rev B 76, 184403, 2007.

[8] S. Sugiura and A. Shimizu, Phys. Rev. Lett. 108, 240401, 2012.

Theory of the multiple spin density waves and the magnetic skyrmions in the triangular-lattice Hubbard model

Takashi UCHIDA
Hokkaido University of Science
4-1, 7-15, Maeda, Teine-ku, Sapporo 006-8585

Magnetic skyrmions are topological stable vortex-like magnetic structures with the spin directions distributing in all directions. It has been found that the skyrmions emerge as 3Q multiple helical spin density waves in B20 transition metal compounds and their alloys. Because of the lack of inversion symmetry, the formation of magnetic skyrmions in these materials are well explained by a competition between the ferromagnetic exchange interactions and the Dzyaloshinskii-Moriya (DM) interaction under magnetic field. Recently, frustrated classical systems without the DM interaction have been found to reveal magnetic skyrmions at finite temperatures [1]. The purpose of the present research is to explore theoretically the multiple spin density waves in the frustrated itinerant systems, where the 3Q structures including skyrmions might be expected near the half-filled region. For this purpose, we have investigated the magnetic structure of the single-band Hubbard model on the triangular lattice on the basis of the molecular spin dynamics (MSD) method [2].

The MSD method is based on the functional integral method for the spin fluctuation theories and the isothermal molecular dynamics method. The method allows us to find automatically the magnetic structure of a large system with thousands of atoms in a unit cell at finite temperatures. Starting from the Hamiltonian expressed in terms of the locally rotated coordinates and by adopting the static approximation to the functional integral technique, the MSD method reduces to the generalized Hartree-Fock approximation at the ground state. In the numerical calculations the most time-consuming process is the magnetic force calculation at each time step, where the local electronic structures are calculated in the real space by means of the recursion method. In order to perform the recursion calculation efficiently, we have adopted the automatic parallel calculation scheme.

The magnetic structure is calculated on the supercell with 40×40 triangular lattice, which is embedded in a large cluster consisting of 3×3 supercells, each of which are connected by the periodic boundary condition. For the Coulomb interaction strength $U/t = 8$ and the temperature $T/t = 0.001$, the MSD yields modulated 120° structures for $n = 0.8$ and 0.9, 3Q structures for $n = 0.95$, 1.00 and 1.05, 2Q structure for $n = 1.10$, collinear antiferromagnetism for $n = 1.20$, and ferromagnetism for $n = 1.40$. The 3Q states are found to be skyrmion-like structures with the magnetic moment directions distributing in all directions, where the three Q vectors are directed along the axes of the triangular lattice.

References

[1] T. Okubo, S. Chung, and H. Kawamura, Phys. Rev. Lett. **108** (2012) 017206

[2] Y. Kakehashi, S. Akbar, and N. Kimura, Phys. Rev. B**57** (1998) 8354.

Microscopic description of optical bistability

Tatsuhiko SHIRAI
Institute for Solid State Physics, University of Tokyo
Kashiwa-no-ha, Kashiwa, Chiba 277-8581

We developed an efficient numerical algorithm to treat the quantum master equation (QME) for hybridized systems of many photons and a large number of two-level atoms. The scheme of numerical calculation consists of the parallelization in photon space by making use of the fact that the time-evolution operator of the QME, L, is a sparse matrix. For the Hilbert space representing the atom, we use the permutation symmetry of L, by which we can reduce the number of dimensions drastically from 2^{2N} to $O(N^3)$. The photon number n should be infinite in principle, but we found that the system is well described if we set the upper limit of the photon number, $n_{\max}$, to be larger than a few times of N. With this method, we performed numerical simulations for the system with up to $N = 25$ and $n_{\max} = 57$.

We also study the efficiency of the parallelization in terms of the photon space. The core labeled by the pair of integers (n_1, n_2) stores elements of $\langle n_1|\rho|n_2\rangle$ where ρ is a density matrix, and $\{|n\rangle\}$ are photon number states and the integer n runs from 0 to the cutoff $n_{\max}$. Thus, the total number of cores is $n_{\rm core} = (n_{\max} + 1)^2$. The main part of the numerical calculation is the Bi-CG method, consisting of the multiplication of L and $L^\dagger$ on ρ. The calculation of (n_1, n_2)-elements of L and $L^\dagger$ requires only six elements of ρ as depicted in Fig. 1. Due to the local nature of the calculation independent of $n_{\max}$, good efficiency should be achieved.

By using the above numerical methods, we give size dependences of both static and dynamic properties of the optical bistability, and moreover discuss the weak scaling to evaluate the efficiency of the parallelization [1].

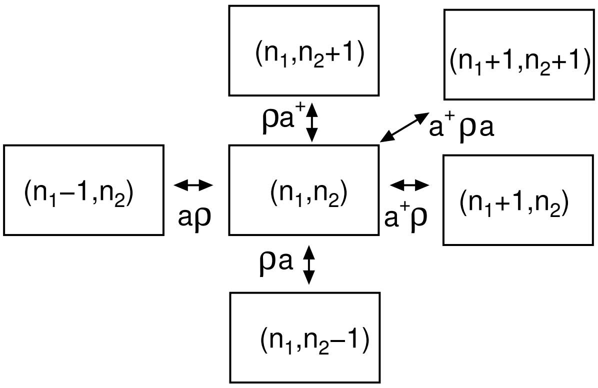

Figure 1: Data exchange among neighboring cores necessary for the multiplication of L on ρ in the parallelization method.

References

[1] T. Shirai, S. Todo, H. De Raedt, and S. Miyashita: submitted to Phys. Rev. A.

Numerical Study of One Dimensional Frustrated Quantum Spin Systems

Kazuo HIDA
Division of Material Science, Graduate School of Science and Engineering
Saitama, Saitama 338-8570

1 Introduction

In this project, we investigate the ground state phase diagram of spin-1 distorted diamond chains with two types of distortion called types A and B. They are described by the following Hamiltonians

type A :

$$\mathcal{H}_{\rm A} = \sum_{l=1}^{N}\Big[(1+\delta_{\rm A})\boldsymbol{S}_l\boldsymbol{\tau}_l^{(1)} + (1-\delta_{\rm A})\boldsymbol{\tau}_l^{(1)}\boldsymbol{S}_{l+1} + (1-\delta_{\rm A})\boldsymbol{S}_l\boldsymbol{\tau}_l^{(2)} + (1+\delta_{\rm A})\boldsymbol{\tau}_l^{(2)}\boldsymbol{S}_{l+1} + \lambda\boldsymbol{\tau}_l^{(1)}\boldsymbol{\tau}_l^{(2)}\Big], \quad (1)$$

type B :

$$\mathcal{H}_{\rm B} = \sum_{l=1}^{N}\Big[(1+\delta_{\rm B})\boldsymbol{S}_l\boldsymbol{\tau}_l^{(1)} + (1+\delta_{\rm B})\boldsymbol{\tau}_l^{(1)}\boldsymbol{S}_{l+1} + (1-\delta_{\rm B})\boldsymbol{S}_l\boldsymbol{\tau}_l^{(2)} + (1-\delta_{\rm B})\boldsymbol{\tau}_l^{(2)}\boldsymbol{S}_{l+1} + \lambda\boldsymbol{\tau}_l^{(1)}\boldsymbol{\tau}_l^{(2)}\Big], \quad (2)$$

where $\boldsymbol{S}_l$, $\boldsymbol{\tau}_l^{(1)}$, $\boldsymbol{\tau}_l^{(2)}$ are spin-1 operators.

2 Undistorted case

For $\delta_{\rm A} = \delta_{\rm B} = 0$, $\boldsymbol{T}_l^2 = T_l(T_l+1)(\boldsymbol{T}_l \equiv \boldsymbol{\tau}_l^{(1)} + \boldsymbol{\tau}_l^{(2)})$ are conserved for each l as $T_l = 0, 1,$ and 2. A pair of spins $\boldsymbol{\tau}_l^{(1)}$ and $\boldsymbol{\tau}_l^{(2)}$ with $T_l = 0$ is called a dimer. The interaction between the spins on both sides of a dimer is decoupled. The ground state of the whole system can be written as a direct product of dimers and the ground states of clusters (called cluster-n) consisting of n nonvanishing $\boldsymbol{T}_l$'s and $n+1$ $\boldsymbol{S}_l$'s between two dimers. The ground state phase consisting of an infinite array of dimers and cluster-n's is called DCn phase. In the absence of distortion, the ground-state phase diagram of the whole system consists of DCn phases with $n = 0, 1, 2,$ and 3, a uniform spin-1 Haldane (UH) phase, a ferrimagnetic phase with spontaneous translational symmetry breakdown (STSB) with $m(\equiv M/M_{\rm s}) = 1/6$ ($\mathrm{F}_{1/6}$ phase), and a ferrimagnetic phase without STSB with $m = 1/3$ ($\mathrm{F}_{1/3}$ phase) as shown in Fig. 1, where M is the spontaneous magnetization and $M_{\rm s}(= 3N)$ is the saturated magnetization. [1, 2]

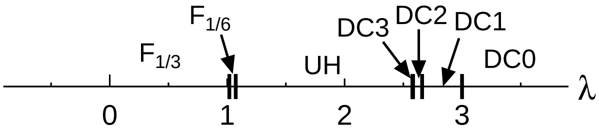

Figure 1: Ground-state phase diagram of undistorted diamond chains with $S = 1$.

3 Distorted Cases

3.1 Type A distortion

The ground-state phase diagram obtained by the DMRG and exact numerical diagonalization for $3N = 18$ is shown in Fig. 2. The $\mathrm{F}_{1/3}$ phase survives distortion, although it shifts to smaller λ regime. The $\mathrm{F}_{1/6}$ phase narrows rapidly with the increase of $\delta_{\rm A}$, and becomes numerically undetectable for large $\delta_{\rm A}$. The DCn phases turn into the Haldane phases

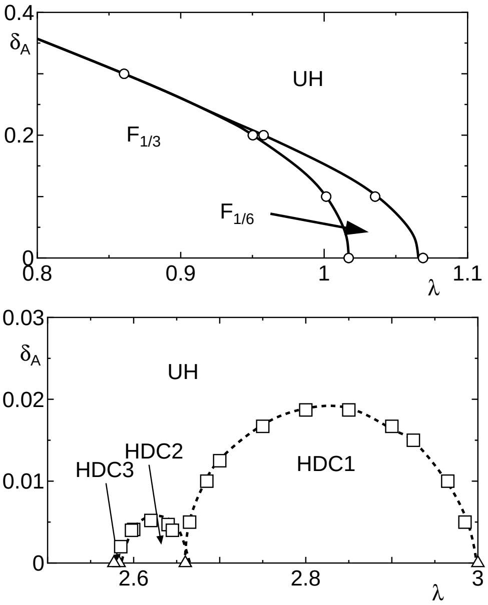

Figure 2: Ground-state phase diagram for type A distortion. Upper panel shows the region with small λ and lower panel, large λ.

with spontaneous $(n + 1)$-fold STSB (HDCn phases) as in the mixed diamond chain with $(S, \tau) = (1, 1/2)$[3]. For large enough $\delta_{\rm A}$, they undergo phase transitions to a UH phase. This phase is continuously connected to the UH phase at $\delta_{\rm A} = 0$ for $1.0726 \le \lambda \le 2.577$.

3.2 Type B distortion

The ground-state phase diagram obtained by the exact numerical diagonalization for $3N = 18$ is shown in Fig. 3. The DCn phases turn into ferrimagnetic phases with $(n + 1)$-fold STSB (FDCn phases) as in the mixed diamond chain with $(S, \tau) = (1, 1/2)$[3]. In these phases, the spontaneous magnetization is given by $m = 1/(3(n + 1))$. Hence, they can be regarded as F$_m$ phases. The F$_{1/3}$ phase for $\delta_{\rm B} = 0$ survives the distortion and shifts to smaller λ regime. The F$_{1/6}$ phase narrows rapidly with the increase of $\delta_{\rm B}$, and becomes numerically undetectable for $\delta_{\rm B} \sim 1$. The width of the UH phase remains finite unless $\delta_{\rm B} = 1$. It has been confirmed by the DMRG calculation with $3N = 72$ that narrow partial ferrimagnetic (PF) phases with continuously varying m are present between these ferrimagnetic phases and UH phase.

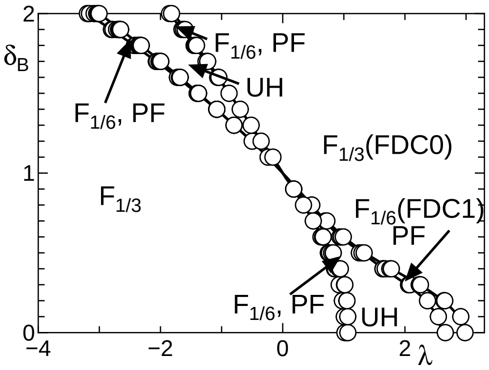

Figure 3: Ground-state phase diagram for type B distortion.

This work is supported by JSPS KAKENHI Grant Number JP25400389.

(collaborator Ken'ichi Takano)

References

[1] K. Takano, K. Kubo, and H. Sakamoto: J. Phys.: Condens. Matter **8** 6405 (1996).

[2] K. Hida and K. Takano: J. Phys. Soc. Jpn. **86**, 033707 (2017).

[3] K. Hida, K. Takano and H. Suzuki : J. Phys. Soc. Jpn. **79** 114703 (2010).

Heat Transfer Characteristics of Condensate Film Flow along Vertical Plates with Microscopic Grooves

Takahiro ADACHI
Department of Mechanical Engineering, Akita University
Tegata-Gakuen 1-1, Akita, Akita 010-8502

The characteristics of thin, falling liquid films due to condensation along a vertical plate have been of interest to engineers, for example, in plate-type absorber, plate-type condenser and so on. In order to enhance the heat transfer, fluted parts along the streamwise direction have been established on the plate. This is because the liquid film spreads as thinly as possible over the plate surface since strong surface tension aids in the removal of film from the top to bottom of the fluted parts, thereby producing a very thin liquid film. This is called a drainage effect[1].

However, it is difficult to clarify the detailed mechanism of the heat transfer enhancement, because the film flow has thin, three-dimensional and unsteady behaviour. Actually, it has been shown that the film flow on the flat plate behaved like a wave and thickness of the film flow became thinner locally in the wavy flow regime, which leads to the enhance of the heat transfer enhancement. In case of the fluted plate, the situation must be more complicated. So, it is greatly depends on numerical calculations to clarify the flow and temperature characteristics.

In this study, we numerically investigate the thin liquid film flow on the vertical rectangular fluted plates in laminar flow resume. Our objective is to clarify effects of grooved geometries and surface tension on both the flow patterns and the heat transfer by setting the fluted parts on the vertical flat plate. Then, we treat our study under the well-known Graetz-Nusselt's problem. This means that the film flow is three-dimensional and fully developed in the stream-wise direction, while the temperature is developing in the thermally inlet region. We will try to show the relation among the heat transfer, fluted geometries and the surface tension effect.

We consider a liquid film flow along a plate with a rectangular groove setting along the stream-wise direction on its surface. Figure 1 shows a geometry of the problem and the coordinate system. The x-axis is taken to be parallel to the vertical direction and the y-axis to be perpendicular to it. Nondimensional parameters to characterize the plate configuration, height h of the groove, width of the groove w_b, inlet length w_i and outlet length w_o are, using δ_0^* at the inlet as a characteristic length, defined as

$$h = \frac{h^*}{\delta_0^*}, \quad w_b = \frac{w_b^*}{\delta_0^*}, \quad w_i = \frac{w_i}{\delta_0^*}, \quad w_o = \frac{w_o}{\delta_0^*} \quad (1)$$

where we represent physical quantities with their dimensions by attaching a superscript $*$ to them, and the total plate length is $L = w_i + w_b + w_o$.

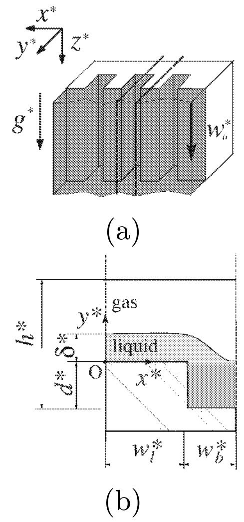

(a)

(b)

Fig.1 Geometry and coordinates.

The governing equations for the velocity and pressure are written in non-dimensional forms as

$$\frac{\partial u}{\partial x}+\frac{\partial v}{\partial y}=0, \tag{2}$$

$$\rho\left(\frac{\partial u}{\partial t}+u\frac{\partial u}{\partial x}+v\frac{\partial u}{\partial y}\right)=\frac{1}{Re}\{\frac{\partial}{\partial x}\left(2\mu\frac{\partial u}{\partial x}\right)$$

$$+\frac{\partial}{\partial y}\left(\mu\frac{\partial v}{\partial x}+\mu\frac{\partial u}{\partial y}\right)\}-\frac{\partial p}{\partial x}, \tag{3}$$

$$\rho\left(\frac{\partial v}{\partial t}+u\frac{\partial v}{\partial x}+v\frac{\partial v}{\partial y}\right)=\frac{1}{Re}\{\frac{\partial}{\partial x}\left(\mu\frac{\partial v}{\partial x}+\mu\frac{\partial u}{\partial y}\right)$$

$$+\frac{\partial}{\partial y}\left(2\mu\frac{\partial v}{\partial y}\right)\}-\frac{\partial p}{\partial y}, \tag{4}$$

$$\rho\left(u\frac{\partial w}{\partial x}+v\frac{\partial w}{\partial y}\right)=\frac{1}{Re}\{\frac{\partial}{\partial x}\left(\mu\frac{\partial w}{\partial x}\right)$$

$$+\frac{\partial}{\partial y}\left(\mu\frac{\partial w}{\partial y}\right)\}+\rho Fr-\frac{\partial p}{\partial z}, \tag{5}$$

where velocity gradient in z direction is ignored such as $\partial u/\partial z=\partial v/\partial z=\partial w/\partial z=0$ in the equations (2), (3), (4) and (5) because of assumption as velocity u is unchanged in z direction.

We show the temporal evolution of the film flow at $t=0$, 30, 100 and 250 in Fig.?? for $d=3$ and $Bo=10$. At the initial state shown in Fig.2 (a), the liquid film is distributed so as to be the same quantity as Nusselt's distribution on the flat plate, which means that the cross sectional area for the liquid phase is $1\times w_l\times w_b=5$. The film flow is developing temporally along the fluted plate surface from the initial distribution as shown in Fig. 2 (a). Thickness of the film flow is decreased at groove edge due to an effect of surface tension seen in Fig. 2 (b)-(d). It is evident that the averaged thickness of liquid film decreases for the fluted plate compared with thickness for the flat plate because the heat transfer area increases in the fluted plate more than one in the flat plate by setting the fluted part. Therefore, it is expected that the heat transfer increases for the fluted plate greater than that for the flat plate.

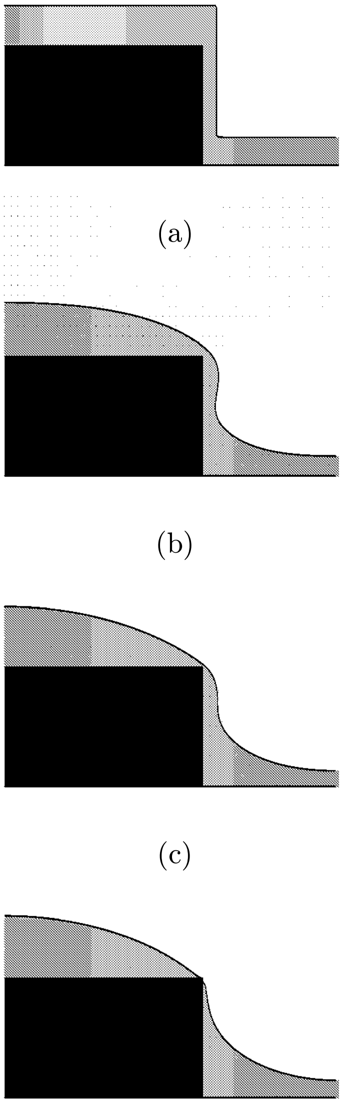
(a)
(b)
(c)
(d)

Fig. 2 Time evolution of the film flow.

Film flow falling along vertical rectangular fluted plates is investigated in this study. We have calculated the temporal evolution of the film flow by using the Combined Level Set and Volume of Fluid(CLSVOF) and Ghost Fluid(GF) methods, and obtained the steady state film and velocity distributions. It is found that the film flow goes inside the fluted part due to the effect of the surface tension for the fluted plate and the thickness near the fluted edge is thinner.

References

[1] R. Gregorig, Z. Angew. Math. Phys., Vol. 5, (1954) 36.

Designing novel quantum materials based on space group symmetries, from filling-enforced quantum band insulators to novel quantum spin liquids

Masahiko G. YAMADA, Masaki OSHIKAWA
Institute for Solid State Physics, University of Tokyo
Kashiwa-no-ha, Kashiwa, Chiba 277-8581

First, we have searched for realistic cadidates for filling-enforced quantum band insulators (feQBI) [1]. The feQBI is a novel quantum phase protected by the space group symmetry of the material. They are distinct from a trivial atomic insulator in the sense that it cannot be adiabatically connected to any atomic insulators unless the energy gap closes or the space group symmetry is broken. In this sense, we can regard the feQBI as an intrinsic band insulator where the band gap is opening purely because of the quantum interference of the Bloch wave functions. In addition, it is known that this band gap can open only by including the spin-oribit coupling (SOC).

It was suggested that the hyperkagome system with SOC can host such phases [1], so we explored some metal-organic frameworks (MOFs) as the first candidate for feQBI. There already exists a material with a space group No. 220 in MOFs [2], which is one of few space groups hosting feQBI, so it is natural to seek first in MOFs. However, after many attempts for the first-principles band calculations for those materials, the gap for the feQBI filling never opens in such MOF-type materials. While this was a negative result on our initial objective, later it was found to be physically reasonable. In fact, a microscopic investigation based on the perturbation theory has revealed that the SOC in the *d*-orbital transition metal systems cannot open the gap for feQBI.

Therefore, we have changed our objective from the search for feQBI to the search for a new candidate for quantum spin liquids with a kagome or hyperkagome lattice structure. This is a natural extension of the feQBI because these lattices are known to host flat-band ferromagnetism or quantum spin liquid with another filling condition. After materials search using first-principles calculations, we discovered [3] some new kagome spin liquid candidates, which can be compared to herbertsmithite. In addition, by increasing the strength of SOC a new type of Dzyaloshinskii-Moriya interactions apper in those materials coming from the SOC hopping similar to the model for feQBI [1].

References

[1] H. C. Po, H. Watanabe, M. P. Zaletel, and A. Vishwanath, Sci. Adv. **2**, e1501782 (2016).

[2] L. E. Darago, *et al.*, J. Am. Chem. Soc. **137**, 15703 (2015).

[3] M. G. Yamada and M. Oshikawa, in preparation

3.5 SCCMS projects

Developments of Machine Learning Solvers

Yusuke Nomura, Andrew S. Darmawan, Youhei Yamaji, Masatoshi Imada
Department of Applied Physics
The University of Tokyo, Hongo 7-3-1, Bunkyo-ku, Tokyo 113-8656

Developing accurate solvers to analyze strongly-correlated systems is a great challenge in condensed-matter physics. Recently, a new form of variational wave function written in terms of restricted Boltzmann machines (RBM) has been proposed [1]. In the RBM wave function, on top of physical spin degrees of freedom (visible spins in the visible layer), we introduce additional degrees of freedom (neurons in the hidden layer). The variational parameters are magnetic fields (bias terms) on visible and hidden spins and the coupling between visible and hidden layers. Then, the quantum correlations among physical variables are taken into account through the couplings to hidden neurons. The RBM wave functions have been shown to give better accuracy for transverse-field Ising and Heisenberg models than those of the tensor-network wave functions [1].

In this project, we have improved the accuracy and extend the range of application of the RBM-based machine learning solver. We have developed i) RBM solver combined with many-variable Monte Carlo (mVMC) method [2] and ii) an exact scheme to construct deep Boltzmann machines to represent ground states of many-body Hamiltonians [3].

In i), we have written down the variational wave function by combining concepts from machine leaning (RBM) and physics (pair-product (PP) wave function), which we call RBM+PP wave function. The RBM allows for flexible and unbiased representations of quantum states. The PP (geminal) wave function is used in the mVMC method [4] and describes nonlocal entanglement properly. The combined RBM+PP wave function can be applied not only to bosonic models but also to fermionic models. The RBM+PP substantially improves the accuracy beyond that ever achieved by RBM and mVMC method separately, thus proving its power as an accurate solver.

In ii) we have shown a deterministic approach to generate deep-Boltzmann-machine (DBM) network to represent ground states of many-body lattice Hamiltonians, using much more flexible representability of the DBM compared to the RBM [5]. The approach reproduces the exact imaginary-time Hamiltonian evolution by dynamically modifying the DBM parameters. The number of neurons grows linearly with the system size and imaginary time, respectively. The physical quantities can be measured by the Monte Carlo sampling of both the visible and hidden variables for the constructed network. The present construction of classical DBM network provides a novel framework of quantum-to-classical mappings (in special cases, it becomes equivalent to the path integral formalism).

A part of this work has been done in collaboration with Giuseppe Carleo.

References

[1] G. Carleo and M. Troyer, Science **355**, 602 (2017).

[2] Y. Nomura, A. S. Darmawan, Y. Yamaji, and M. Imada Phys. Rev. B **96**, 205152 (2017).

[3] G. Carleo, Y. Nomura, and M. Imada, arXiv:1802.09558.

[4] D. Tahara and M. Imada, J. Phys. Soc. Jpn. 77, 114701 (2008).

[5] X. Gao and L.-M. Duan, Nature Communications **8**, 662 (2017).

First-Principles Phase Field Mapping

Kaoru Ohno

Department of Physics, Faculty of Engineering Science,

Yokohama National University, Tokiwadai, Hodogaya-ku, Yokohama 240-8501

Theoretical understanding of microstructure is very important in predicting the durability and performance of alloys. For this purpose, phase field models have been widely used to simulate the time evolution of microstructures and various properties. However, the results strongly depend on the input parameters, which are mostly empirical. Therefore, we propose a new and simple method to determine the input parameters purely from first principles. We calculate the free energy (Fig. 1) using cluster expansion method including atomic vacancies in combination with potential renormalization theory [1]. Then, the chemical potential is obtained as the free energy difference. The validity of the present method is tested for Ni-Al alloy systems. Our results clearly distinguish the local composition of alloys in accord with the experimental phase diagram (Fig 2). We have also succeeded in predicting the time evolution of microstructures of Ni-Al alloys at different compositions at 1300K (Fig. 3) [2].

References

[1] Y. Misumi, S. Masatsuji, R. Sahara, S. Ishii, and K. Ohno, J. Chem. Phys. **128**, 234702 (2008).

[2] S. Bhattacharyya, R. Sahara and K. Ohno, to be submitted.

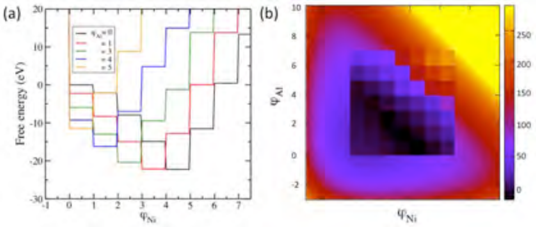

Fig. 1 Resulting free energy (a) 1D, (b) 2D.

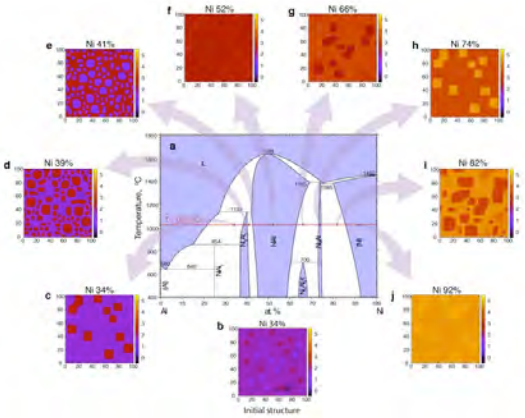

Fig. 2 Comparison with experimental PD.

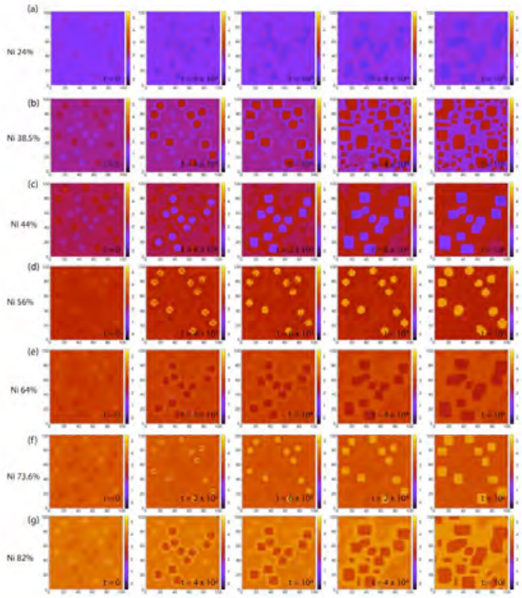

Fig. 3 Time evolution of the pattern.

Oxide electrocatalyst

Osamu Sugino

Institute for Solid State Physics,

The University of Tokyo, Kashiwa-no-ha, Kashiwa, Chiba 277-8581

The purpose of this study is to predict the mechanism for oxygen reduction reaction (ORR) occurring on titania surfaces and to show a way to improve the ORR activity. For this purpose, we have done a first-principles simulation based on the density functional theory (DFT) within a generalized gradient approximation (GGA), which has been used as a standard method to simulate the titania surfaces. To model the surface, we are based on the experimental finding that doped Nb atom and the oxygen vacancy are the key to enhance the ORR activity. We have thus analyzed the surface of $Ti_xNb_yO_z$. In fact, we have simulated for rutile (110) and anatase (101),(100),(001),(001)-(1x4) surfaces with and without the surface Nb impurity and surface oxygen vacancy. Using those surfaces, we followed the ORR pathways by calculating the free-energy of O_2, OOH, OH, and O and obtained the free-energy profile. In the calculation, we have used the computational electrode scheme assuming zero for pH and 1.23 V vs SHE for the bias potential. Here we neglected the solvation effect. With the modeling, we have investigated whether ORR is likely to occur on those surfaces or not. We can expect that ORR is likely occur when the free-energy profile along the ORR pathways is flat within the energy scale of about 1.0 eV; this is the criterion that has been used for Pt surfaces. This criterion is expected to be valid also for titania.

After checking that the pristine titania surface does not provide the free-energy profile flat within 2.0 eV, we investigated the defective surfaces. We first investigated the surface doped with a Nb impurity atom. The calculated result indicates that the free-energy profile is uphill by 1.3 eV when OH* is reduced to form H_2O. That is, this surface is poisoned by OH and activity is not expected. We next investigated the surface with oxygen vacancy. In this case we also included Nb impurity in the surface model because the surface energy becomes too high because of the lack of charge neutrality. When Nb is located close to the vacancy site, the surface energy is high but the energy is lowered when Nb is located apart; the precise position does not affect the result in this case. From the calculation we found that O* is strongly adsorbed with the adsorption energy larger than 2.0 eV for all the surfaces we have investigated. This is due to the existence of Ti^{3+} which donates an electron toward O* to stabilize this reaction intermediate. These results apparently suggest that all the defective surfaces do not remain as a candidate for the reactive surface.

However, this is not the case in fact because of the following reason. We have neglected that the surface oxygen vacancy accepts electrons from OH* stabilizing this species. With this consideration, we have included this adsorbate molecule in the modeling. When this is considered, the surface O* was found to be moderately adsorbed on the surface satisfying the above criterion for the active surface. The oxygen molecule, however, is not adsorbed on rutile (110) nor on anatase (101) and (100). O_2 is too strongly adsorbed on anatase (001)-(1x4). Therefore, only anatase (001) remains as the candidate for the reactive surface. By calculating the free-energy profile, we confirmed that this surface satisfied the criterion. Therefore, we have concluded that only anatase (001) can be expected as the active surface. The rate-determining step is suggested to be the OH* reduction and the activation energy will be larger than 0.85 eV.

From these theoretical studies, we have suggested it is important to design a material to weaken the OH* adsorption.

Mesoscale simulation approach for slow dynamics study of complex and glassy liquids

Hayato SHIBA and Hailong PENG
Institute for Materials Research, Tohoku University
2-1-1 Katahira, Aoba-ku, Sendai 980-8577

For this year, we have numerically studied the slow dynamics of ionic liquid materials and underlying fundamental properties of glassy systems.

1. Study of mesophase transition upon annealing of imidazolium-based ionic liquid with long-alkyl chain

We have performed molecular dynamics simulations of a 1-dodecyl-3-methylimidazolium hexafluorophosphate ([C12mim][PF6]) ionic liquid using a united-atom model. It turned out that the ionic liquid exhibits a second step relaxation at temperatures below a crossover point, where the diffusion coefficient shows Arrhenius to non-Arrhenius transition. Annealing below this crossover temperature makes isotropic-to-mesophase transition, where the smectic A phase or crystal-like smectic B phase forms. From hundreds of nanoseconds to microseconds are required for completing these transitions. A normal diffusion process is found for anions along the layer-normal and -lateral directions in the SmA phase, but only in the lateral directions in the SmB phase. Our results suggests that studying such long-time dynamics opens the way to further understanding of ionic liquids, both on the basic properties of its phase behavior and glasss tarnsitions and on the potential applications utilizing their its nanostructure [1].

2. Cage-relative variables for 2D glassy dynamics

The Principal Investigator for this project and his coworkers have recently revealed that long-wavelength fluctuation exists in two-dimensional (2D) glassy systems, having the same origin as that given by the Mermin-Wagner theorem for 2D crystalline solids. For this year, we have discussed the slow glassy liquids under confinement, for better characterization of long-wavelength Mermin Wagner fluctuation by means of a molecular dynamics simulation of a lightly supercooled liquid. We employ the cage-relative mean-square displacement (MSD), defined on relative displacement to its cage, to quantitatively separate the long-wavelength fluctuation from the original MSD. For increasing system size the amplitude of acoustic long wavelength fluctuations not only increases but shifts to later times causing a crossover with structural relaxation of caging particles. The dynamic correlation grows as the structural relaxation becomes slower with decreasing temperature, uncovering an overestimation by the four-point correlation function due to the long-wavelength fluctuation. These findings motivate the usage of cage-relative MSD as a starting point for analysis of 2D glassy dynamics [2].

References

[1] H. Shiba, M. Kubo, and H.-L. Peng: Phys. Chem. Chem. Phys., in press (2018).

[2] H. Shiba, P. Keim, and T. Kawasaki: J. Phys: Cond. Matter **30** (2018) 094004.

Tensor Network Calculation of Frustrated Quantum Spin Systems[1]

Naoki KAWASHIMA
Institute for Solid State Physics, University of Tokyo
Kashiwa-no-ha, Kashiwa, Chiba 277-8581

The greatest obstacle in studying frustrated quantum system is the notorious negative sign problem. Due to this difficulty, researchers do not have much choice other than numerical diagonalization of small clusters and variational calculations. The numerical diagonalization cannot deal with phenomena involving many degrees of freedom while the variational calculation is hard to control its accuracy.

We have been trying to develop general framework for overcoming this difficulty based on tensor network states. In SY2017, we studied $S = 1$ bilinear-biquadratic model on the star lattice, which is the kagome lattice with each lattice point replaced by a bond. The Hamiltonian is defined as

$$H = \sum_{(ij)} \left[\cos\phi \, (S_i \cdot S_j) + \sin\phi \, (S_i \cdot S_j)^2 \right]$$

Similar to the kagome lattice, antiferromagnets on this lattice have a strong quantum fluctuations that may lead to spin liquid states.

We carried out the iPEPS calculation using the original code based on mptensor [2]. Since the final state depends on the initial condition and the restriction we impose, we tried various sets of the initial conditions and the ansatz for each value of ϕ and chose the state with the lowest energy. We discovered four phases: (1) the ferromagnetic phase ($0.5\pi < \phi < 1.25\pi$), (2) the ferroquadrupolar phase ($1.25\pi < \phi < 1.75\pi$), (3) the antiferromagnetic phase ($1.75\pi < \phi < 0.02\pi$), and (4) the spin liquid phase ($0.02\pi < \phi < 0.5\pi$) In particular, for the spin liquid phase, we found that the method of symmetric simple update, which enforces the symmetry, yielded the best results among all the trials. While this itself is a strong evidence for the liquid nature of this phase, we confirmed the result by computing the correlation length (Fig.1 (c)). The estimation of the correlation length was performed through the computation of the eigenvalues of the transfer matrix constructed from the edge tensor. (ϵ_i ($i = 0, 1, 2, 3$) in Fig.1(b)) It is clear that the correlation length saturates with finite value as the bond dimension increases.

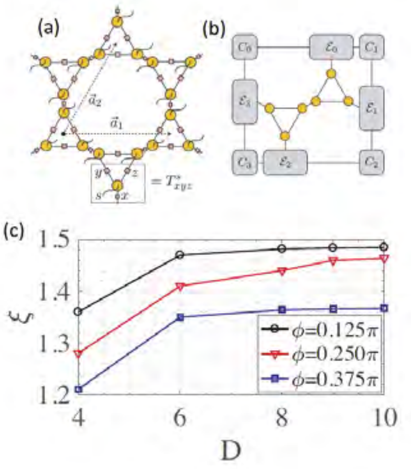

Figure 1: (a) The star lattice. (b) The corner transfer matrix configuration. (c) The correlation length as a function of the bond dimension.

[1] This report is based on Hyun-Yong Lee and Naoki Kawashima arXiv:1802.10281.

[2] https://github.com/smorita/mptensor

Simulation of organic-inorganic interfaces

Shuji OGATA
Nagoya Institute of Technology
Gokiso-cho, Showa-ku, Nagoya 466-8555, Japan

In the fiscal year of 2017, we have addressed three subjects using our order-N DFT code (DC-RGFT) and hybrid quantum-classical (QM-CL) simulation code.

Subject 1: Chemical Reactions Involved in Moisture-Induced Weakening of Adhesion Between Aluminum and Epoxy Resin. The adhesive bonding of metals using epoxy resin is an important technology in manufacturing industries. It is well known that adhesion strength becomes significantly reduced in a moist environment. To understand the mechanisms at the electronic structure level, we perform hybrid QM-CL simulations on various Al and epoxy resin interface systems with water molecules inserted in the contact region. In accordance with experimental conditions, the Al layer is surface oxidized to a depth of 10 Å while the bisphenol-A type epoxy molecule has both OH and ether groups. Shear deformations are simulated using the hybrid quantum-classical method in which about 1,500 atoms at the contact region are treated with density functional theory. For the first time, calculated adhesion strengths compare well with the experimental values. Three types of chemical reactions that affect the adhesion strength occur depending on the terminal functional groups of the Al oxide surface and the water layer formation. Separate calculations confirm small barrier energies for all the reaction processes.

Subject 2: Efficient Calculation Scheme for the Work of Adhesion between a Liquid and Polymer-Grafted Substrates [1]. Complex solid surfaces, such as polymer-grafted surfaces, are used in industrial applications; however, nearly all existing methods are applied to a flat solid surface. We therefore use molecular simulation to develop a novel method for the calculation of the work of adhesion between a liquid and a solid surface. Herein, we separate liquid molecules from the solid surface based on their shape by placing spherically symmetric potentials around atoms selected from the substrate and graft polymers onto them. To avoid the deterioration of accuracy numerical integrations, we update parameters that appear in the potential to suppress sharp variations in the gradient of free energy. This method is applied to the interface between water and gold substrate modified by poly(ethylene oxide) (PEO), revealing that the work of adhesion is greater at intermediate PEO densities.

Subject 3: Large-Scale DFT Simulation of Li-atom Insertion and Extraction in Quinons@SWCNT Rechargeable Battery Cathodes [2]. The system of quinone molecules encapsulated in the single-wall carbon nanotube (SWCNT) has been proposed as a next-generation cathode electrode material for rechargeable battery. We investigate the complex interaction among the SWCNT, phenanthrene-quinone (PhQ), and Li atoms in the encapsulated system by using DC-RGDFT. We thereby find that the shape of the SWCNT changes significantly in the relaxed state depending on the extent of Li atoms inserted. In a typical run using 63 CPU’s, it takes about 9 minutes to evolve the atomic dynamics by a timestep; here, the settings of the parallel computation are the -spatial decomposition of 5x5x5, the electronic level parallelization of 2, and the OpenMP parallelization of 4.

References

[1] M. Urangase and S. Ogata, MRS Adv. **3** (2018) 519-524.
[2] M. Tsuzuki, S. Ogata, and M. Uranagase, MRS Adv. (2018) 1-6, in press.

Analyses of momentum-dependent excitations in hole-doped cuprates observed by inelastic x-ray scattering at the oxygen K edge

Takami TOHYAMA
Department of Applied Physics, Tokyo University of Science, Tokyo 125-8585

Resonant inelastic x-ray scattering (RIXS) is a powerful tool to identify spin and charge excitations in strongly correlated electron systems. RIXS at oxygen K edge in hole-doped cuprates can detect both charge and two-magnon excitations. Recent O K-edge RIXS for $\mathrm{La}_{2-x}(\mathrm{Br,Sr})_x\mathrm{CuO}_4$ has observed clear momentum $\mathbf{q}$ dependence below 1 eV [1]. The broad spectral weight exhibits positive dispersion and shifts to higher energy with increasing x. In order to clarify the origin of the dispersion, it is necessary to compare the experimental data with theoretical calculations.

In this project, we calculated the dynamical charge structure factor on oxygen orbitals in a three-band Hubbard model by the dynamical density-matrix renormalization group (mainly using the K-computer) and found that the calculated result is consistent with the experiments [1]. Therefore, the $\mathbf{q}$ dependent spectral weight can be ascribed tocharge excitations. However, before concluding this, we have to deny a possibility of two-magnon excitations.

We calculate the $\mathbf{q}$ dependent two-magnon excitations for the t-t'-t''-J model with three-site terms, which is one of a realistic models for cuprates, and compare them with charge excitations as shown in Fig. 1. We find that the $\mathbf{q}$ dependence mainly appears for the low-energy region less than energy $\omega = t \sim 0.35$ eV. This energy region is smaller than the region where the RIXS data shows a dispersive mode. In contrast, the $\mathbf{q}$ dependent charge excitations appears even for the high-energy region up to $\omega = 6t \sim 2$ eV. This suggests that two-magnon excitations are not the origin of the observed $\mathbf{q}$ dependent excitations.

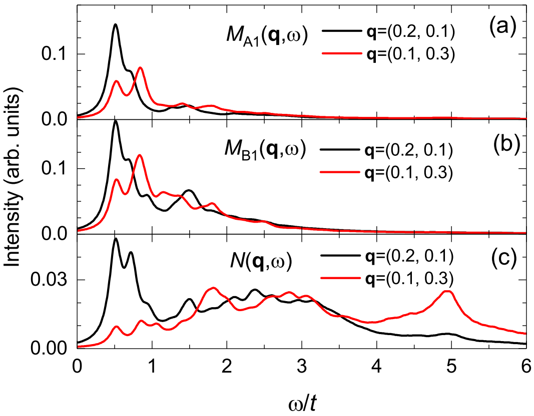

Figure 1: Dynamical two-magnon correlation function for (a) A_1 mode, (b) B_1 mode, and (c) dynamical charge structure factor at $\mathbf{q}/\pi = (0.4, 0.1)$ (black line) and (0.1,0.3) (red line) for a 2-hole $\sqrt{20} \times \sqrt{20}$ periodic lattice of the t-t'-t''-J model with three-site terms: $t = 1$, $t' = -0.25$, $t'' = 0.12$, and $J = 0.4$.

We therefore conclude that the $\mathbf{q}$ dependent spectral weight observed by O K-edge RIXS is ascribed to intraband charge excitations that exhibit damped and incoherent characters inherent in doped Mott insulators.

References

[1] K. Ishii, T. Tohyama *et al.*: Phys. Rev. B **96** (2017) 115148.

Conversion and storage of energy−fuel cells and secondary batteries: Research and development of fundamental technologies of battery simulators.

Susumu OKAZAKI
Department of Materials Chmistry, Nagoya University
Furo-cho, Chikusa-ku, Nagoya 464-8603

The goal of our project is to develop the basic technology of the whole battery simulator. One of the key techniques is molecular-level design of polymer membranes controlling transportation of protons and ions across the membrane with proper stiffness resistant to mechanical deformation under external stress. Such membranes are widely applicable to the fuel cells used in the industrial products.

On the system B, we performed fully atomistic molecular dynamics (MD) calculations of hydrated perfluorosulfonic acid (PFSA) ionomers composed of a hydrophobic polytetrafluoroethylene backbone with hydrophilic side chains terminated by sulfonic acid[1], as a model of proton exchange polymer electrolyte membrane of fuel cells (Figs. 1 and 2). On the basis of these atomistic MD calculations, we constructed a predictive coarse-grained (CG) model for the structure and morphology of PFSA membranes[2]. The CG model reproduced reasonably both the thermodynamic and structural properties of the PFSA membrane for all examined water contents, and has considerable potential for application to realistic long-chained PFSA membranes. Furthermore, in order to realize a tensile test of polymer materials by a large scale MD calculation, we derived microscopic expression of the pressure tensor using the fast multipole method (FMM) with periodic boundary conditions[3]. These results will contribute to the development of higher performance fuel−cells and secondary batteries and to the realization of the entire battery simulator in the near future.

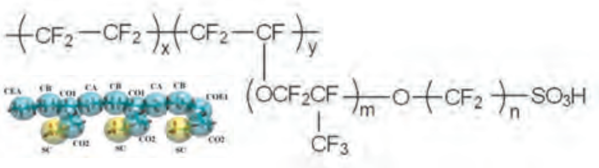

Figure 1: Molecular structure of perfluorosulfonic acid (PFSA) ionomers. Inserted figure is the CG model of PFSA ionomers[2].

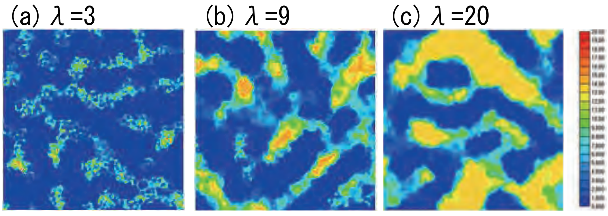
(a) λ=3 (b) λ=9 (c) λ=20

Figure 2: Number density map of sulfonic acid groups, water, and hydronium ions at one cut plane. λ is a mole fraction of water molecule and hydronium ion to sulfonic acid groups.

References

[1] A. T. Kuo, W. Shinoda, S. Okazaki : J. Phys. Chem. C **120** (2016) 25832.
[2] A. T. Kuo, S. Okazaki, W. Shinoda : J. Chem. Phys. **147** (2017) 094904.
[3] N. Yoshii, Y. Andoh, S. Okazaki, J. Comput. Chem., in press.

Excited-state calculations for molecular aggregates based on Green′s function and fragmentation methods

Takatoshi Fujita
Institute for Molecular Science
Myodaiji, Okazaki, Aichi 444-8585

Predicting the energies of charged and neutral excitations is essential for understanding charge transport and optical properties of organic materials. However, quantitative calculations of the electronic states are still difficult due to the interplay of electronic polarization and charge delocalization effects. It is established by photoelectron spectroscopy studies that the ionization potential (IP) and electron affinity (EA) of isolated molecule are significantly different from those of solid phase. One factor contributing the difference is the polarization effects, which originates from the screening of the charge by the electronic polarization of the surrounding molecules. Another factor is the band dispersion; the orbital interactions between highest-occupied molecular orbitals (HOMOs) and lowest-unoccupied molecular orbitals (LUMOs) result in the valence- and conduction-band dispersion, respectively. Therefore, describing the charge delocalization and electronic polarization effects is of critical importance for accurate predictions of the energy levels of quasiparticles.

We have been developing the fragment-based method for calculating charge transport mobilities [1] and electronically excited states. [2] Our method relies on the fragmentation approach; the total system is first divided into a lot of small parts called fragments, and the diabatic statics are defined by the electronic structure calculations of fragment monomers embedded in the electrostatic potential from other fragments. The delocalization effects can be restored by calculating Hamiltonian matrix elements among diabatic states. We have recently shown that the fragment-based approach can provide reasonable and efficient description of electronically excited states of molecular aggregates. [2] The ground-state electronic polarization can be accurately treated by the self-consistent determination of charge density. However, our scheme is incapable to treat induced polarizations after electronic excitations. In this study, we incorporate many-body Green's function theory into the FMO method so that both charge delocalization and electronic polarization can be treated on the same footing.

Here, we employ GW theory [3] to describe electronic polarization effects. Within the GW, the dielectric function is computed for screened Coulomb interactions, and the self-energy is expanded with respect to the screened Coulomb interaction. Following the standard notation, the self-energy and screened Coulomb interaction are calculated according to

$$\Sigma(r, r', \omega) = \frac{i}{2\pi} \int d\omega' G(r, r', \omega + \omega') W(r, r', \omega) e^{i\omega\eta}, \tag{1}$$

$$G(r, r', \omega) = \sum_p \left[\frac{\psi_p(r)\psi_p^*(r')}{\omega - \epsilon_p + i\eta sgn(\epsilon_p - E_F)} \right], \tag{2}$$

$$W(r,r',\omega) = v(r,r) + \int dr_1 dr_1 v(r,r_1)\chi_0(r_1,r_2,\omega)W(r_2,r',\omega). \tag{3}$$

We have developed the fragment-based scheme to calculate the quantities above. The one-body Green's function is approximated as a sum of Green's functions of fragment monomers and dimer corrections. On the other hand, we approximated the independent-electron susceptibility from those of fragment monomers, $\chi^0 = \sum_I \chi_I^0$, and defined the screened-Coulomb potential of the total system. Our GW implementation relies on the real-space auxiliary functions. [4] The auxiliary functions are defined by the direct products of two atomic orbitals and are constructed by the Cholesky decomposition. The fragment-based GW method was incorporated into the developer version of ABINIT-MP program. [5]

As a numerical example, the crystal structure of pentacene thin film phase [6] is considered We calculate self-energy within the static Coulomb-hole plus screened exchange (COHSEX) approximation. One-shot GW calculation was performed with 6-31G* basis set and B3LYP reference. Quasiparticle energies of a pentacene monomer are -6.97 (HOMO) and -1.29 eV (LUMO). The FMO-GW calculation was performed for the thin film structure containing 39 pentacene molecules (Fig.1). The quasiparticle energies were calculated in the range from -6.77 to -6.15 eV for HOMOs and from -1.92 to -1.29 eV for LUMOs. Diagonalization of the HOMOs and LUMOs with transfer integral yields the band gap as 4.03 eV. This significant reduction of the band gap dominantly arises from the electronic polarization effects.

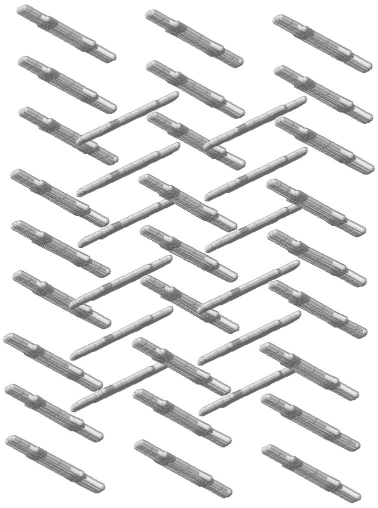

Figure 1: Crystal structure of pentacene thin film.

References

[1] T. Fujita, Y. Haketa, H. Maeda, Y. Mochizuki, Org. Electron. **49** (2017) 53.

[2] T. Fujita, Y. Mochizuki, J. Phys. Chem. A **11** (2018) 3886.

[3] L. Hedin, Phys. Rev. **139** (1965) A796.

[4] X. Ren, P. Rinke, V. Blum, J. Wieferink, A. Tkatchenko, A. Sanfilippo, K. Reuter, M. Scheffler, New. J. Phys. **14** (2012) 053020.

[5] S. Tanaka. Y. Mochizuki, Y. Komeiji, Y. Okiyama, K. Fukuzawa, Phys. Chem. Chem. Phys. **16** (2014) 10310.

[6] S. Schefer, M. Huth, A. Dobrinevski, B. Nickel, J. Am. Chem. Soc. **129** (2007) 10316.

Materials design for energy-saving and energy-creation materials

Tetsuya FUKUSHIMA
Institute for NanoScience Design, Osaka University, Osaka 560-8531, Japan
Institute for Datability Science, Osaka University, Osaka 565-0871, Japan

A "scale-bridging" simulation technique, combining the Korringa-Kohn-Rostoker (KKR) Green's function method and model approaches, was developed this year. On the basis of the "scale-bridging" simulation technique and massively parallel computing, we designed new energy-saving and energy-creation materials, such as high entropy alloys [1], thermo electric materials [2], and dilute magnetic semiconductors (DMSs) [3]. Here, we introduce the materials design of Ge type DMS systems.

Recently, the IV-type semiconductor Ge has attracted much attention as the host material of ferromagnetic DMSs for the following two reasons: (i) Ge possesses higher mobility than that of Si; therefore, it has the possibility of the realization of high-speed and low-power consumption LSI systems; (ii) Ge has a good compatibility with the Si-CMOS technology. We performed the density functional theory calculations or transition-metal (TM) impurities doped Ge by using the KKR Green's function method with the coherent potential approximation (CPA), to theoretically shed light on the ferromagnetic mechanisms of the Ge-based DMS systems.

Our calculations indicated that the ferromagnetic interactions by the double exchange mechanism are dominant for the Fe- and Co-doped Ge systems. However, these ferromagnetic interactions are quite short ranged compared to the (Ga,Mn)As, and are also weak compared to (Ga,Mn)N, so that we cannot expect high ferromagnetic Curie temperature (T_C) in terms of the magnetic percolation effect if the TM impurities are homogeneously distributed in the hosts. Antiferromagnetic states are stable for the V-, Cr-, and Mn-doped Ge, and the Ni-doped system becomes a nonmagnetic. The inhomogeneity of the TM impurities drastically changes the magnetic states and has a crucial role in the experimentally observed high-T_C ferromagnetism in the IV-type DMSs. The cluster expansion method revealed that the Mn-doped Ge systems tend to generate ordered compounds, such as $\mathrm{Ge_3Mn_5}$ and $\mathrm{Ge_8Mn_{11}}$, at Mn-rich regions. These precipitated ordered compounds are the causes of the ferromagnetism in (Ge,Mn); in particular T_C of $\mathrm{Ge_3Mn_5}$ is consistent with the experimentally observed T_C of (Ge,Mn).

The electronic structure of (Ge,Fe) calculated by the variational pseudo-self-interaction-corrected method reproduces the spectra of the Fe-3d states in the SX-ARPES experiment. It was proven by the multi-scale (scale-bridging) simulations that the Fe atoms are not randomly distributed in the Ge host but gathered with keeping the diamond structure by the attractive pair interactions i.e., the spinodal nanodecomposition. T_C of (Ge,Fe) is enhanced by the annealing process, because the number of the first-nearest-neighbor Fe-Fe pairs with the strong ferromagnetic interaction increases by proceeding the spinodal nanodecomposition. Our simulations reproduce the experimental magnetic situation very well, and the T_{C} values estimated by the random phase approximation method are in good agreement with the observed values.

We emphasize that the manipulation of structural, configurational, and spin disorders in DMS systems are very important to obtain colossal magnetic responses. In particular, there is the possibility that a drastic magnetic transition between ferromagnetism and antiferromagnetism can be realized in the Ge-doped DMSs by controlling the nanostructure and dimensionality, and applying the gate voltage. Additionally, compared to the typical III-V and II-VI DMSs, the Ge-based DMSs are rather compatible with the present CMOS technology. Utilizing the Ge-based DMSs is a good way to realize next-generation devices based on semiconductor spintronics.

References

[1] T. Fukushima, H. Katayama-Yoshida, K. Sato, M. Ogura, R. Zeller, and P. H. Dederichs: J. Phys. Soc. Jpn. **86** (2017) 114704.

[2] H. Shinya, A. Masago, T. Fukushima, and H. Katayama-Yoshida: Jpn. J. Appl. Phys. **56** (2017) 081201.

[3] H. Shinya, T. Fukushima, A. Masago, K. Sato, and H. Katayama-Yoshida: Phys. Rev. B **96** (2017) 104415.

Exploration of novel oxide and nitride semiconductors using first-principles calculations

Fumiyasu OBA[1,2] and Yu KUMAGAI[2]

[1]*Laboratory for Materials and Structures, Institute of Innovative Research,*
Tokyo Institute of Technology,
4259 Nagatsuta, Midori-ku, Yokohama 226-8503, Japan
[2]*Materials Research Center for Element Strategy,*
Tokyo Institute of Technology,
4259 Nagatsuta, Midori-ku, Yokohama 226-8503, Japan

The search for novel semiconductors is increasingly important as the applications of semiconductors become more prevalent. Among the compound semiconductors, nitrides and oxides are especially attractive because of the abundant nitrogen and oxygen constituents. Currently commercialized nitride semiconductors are, however, mostly limited to GaN and its based alloys. Several kinds of oxide semiconductors are used in commercial applications such as transparent electrodes and thin-film transistors, but those with improved or different functionalities are required to expand the applications. This situation stimulates not only experimental but also computational exploration of novel nitride and oxide semiconductors.

It is our objective to explore novel nitride and oxide semiconductors with a wide variety of chemical compositions, crystal structures, and properties via high-throughput screening using first-principles calculations. We have been developing methods for predicting fundamental bulk and defect properties systematically [1, 2, 3, 4, 5] and applying them to the search for novel semiconductors such as ternary zinc nitrides [6]. The screening needs to be extended so that a larger number of candidate materials can be evaluated efficiently within feasible computational time whereas sufficient accuracy is kept. In this respect, an appropriate choice of the exchange-correlation functional in density functional theory is important. Therefore, the performance of several types of generalized gradient approximation (GGA) and meta-GGA functionals was systematically assessed using the allocated CPU time. We took elementary substances and binary oxides as test sets because experimental values for fundamental properties and structural parameters are available.

As examples of the results, Fig. 1 shows relative stability of polymorphs of binary divalent cation oxides obtained using the projector augmented-wave method [7] and the PBEsol functional [8] as implemented in the VASP code [9, 10]. Experimentally well-known phases are predicted to be stable among the polymorphs of each oxide. Although explicit comparison of relative formation energies between theory and experiment is difficult because of the lack of experimental values in many cases, systematic assessment on the cohesive energies of elementary substances and the formation energies of binary oxides, as well as their crystal structures, indicated improved accuracy by the PBEsol over the standard PBE functional [11].

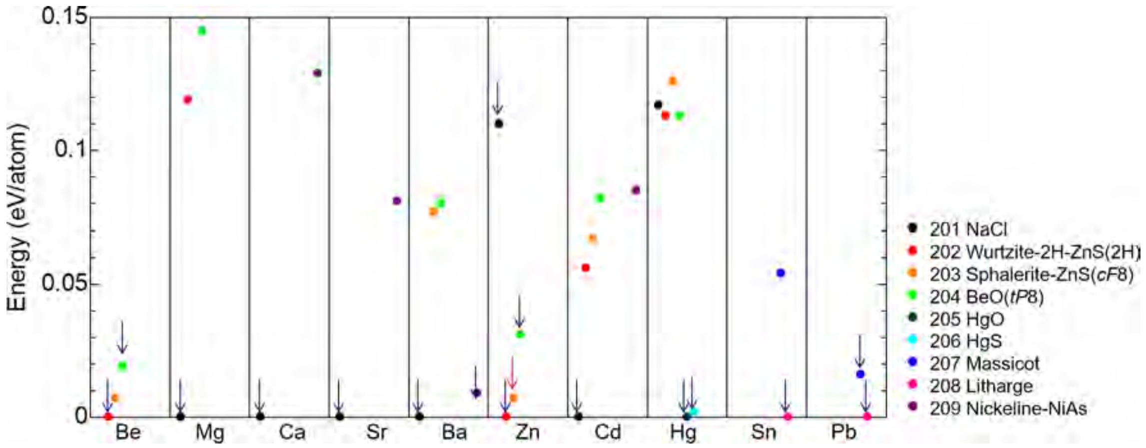

Figure 1: Relative stability of polymorphs of binary divalent cation oxides obtained using the PBEsol functional [11]. Energies are shown with respect to that of the lowest energy phase for each oxide. Experimentally reported phases are arrowed.

References

[1] Y. Kumagai and F. Oba: Phys. Rev. B **89** (2014) 195205.

[2] A. Grüneis, G. Kresse, Y. Hinuma, and F. Oba: Phys. Rev. Lett. **112** (2014) 096401.

[3] Y. Hinuma, A. Grüneis, G. Kresse, and F. Oba: Phys. Rev. B **90** (2014) 155405.

[4] Y. Hinuma, G. Pizzi, Y. Kumagai, F. Oba, and I. Tanaka: Comput. Mater. Sci. **128** (2017) 140.

[5] Y. Hinuma, Y. Kumagai, I. Tanaka, and F. Oba: Phys. Rev. B **95** (2017) 075302.

[6] Y. Hinuma, T. Hatakeyama, Y. Kumagai, L. A. Burton, H. Sato, Y. Muraba, S. Iimura, H. Hiramatsu, I. Tanaka, H. Hosono, and F. Oba: Nat. Commun. **7** (2016) 11962.

[7] P. E. Blöchl: Phys. Rev. B **50** (1994) 17953.

[8] J. P. Perdew, A. Ruzsinszky, G. I. Csonka, O. A. Vydrov, G. E. Scuseria, L. A. Constantin, X. Zhou, and K. Burke: Phys. Rev. Lett. **100** (2008) 136406.

[9] G. Kresse and J. Furthmüller: Phys. Rev. B **54** (1996) 11169.

[10] G. Kresse and D. Joubert: Phys. Rev. B **59** (1999) 1758.

[11] Y. Hinuma, H. Hayashi, Y. Kumagai, I. Tanaka, and F. Oba: Phys. Rev. B **96** (2017) 094102.

Development of Permanent Magnet Materials

Takashi MIYAKE
CD-FMat, AIST
Umezono, Tsukuba, Ibaraki 305-8568

Finite-temperature magnetism of rare-earth magnet compounds is an issue in developing high-performance permanent magnets. It is known that the intersite magnetic exchange coupling between the rare-earh and transition-metal sites, $J_{\rm RT}$, plays an important role in the magnetocrystalline anisotropy at finite temperatures. We have computed $J_{\rm RT}$ in $\rm NdFe_{12}$ and $\rm NdFe_{12}X$ (X=B, C, N, O, F) based on density functional theory and Liechtenstein's method using Akai-KKR. We found that $J_{\rm RT}$ is sensitive to X. Especially, the Nd-Fe($8j$) coupling is significantly reduced for X=N. This suggests that the magnetocrystalline anisotropy decays quickly with increasing temperature in the X=N system, although N enhances the Curie temperature. The Nd-Fe($8j$) coupling has strong correlation with the local magnetic moment at Nd site, which is

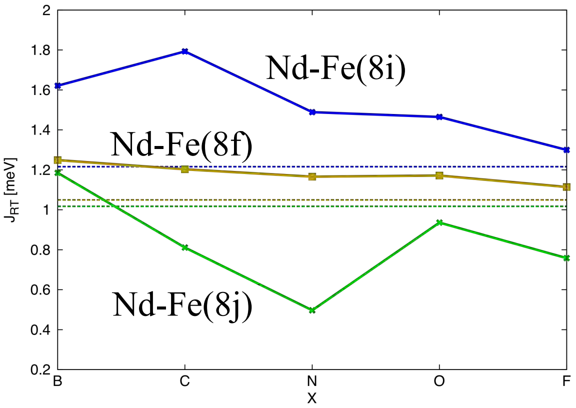

Figure 1: Magnetic exchange coupling between the Nd and Fe sites in $\rm NdFe_{12}X$.

Partial substitution of Fe sites also affects finite-temperature magnetism. We have studied the Curie temperature of $\rm NdFe_{12-\it x}Cr_{\it x}$ in the mean-field approximation. We found that the Curie temperature has strong dependence on the Cr concentration x. It increases with increasing x at low concentration, then turns to decrease above $x \sim 0.75$. We found that both of the following two effects are important for the increase in the small x region. The first effect is that Fe-Fe couplings are partially replaced with stronger Fe-Cr couplings by Cr substitution, which raises the Curie temperature. The other is that introduction of Cr makes surrounding Fe atoms Co-like, which enhances the Fe-Fe coupling [2].

Another important issue is crystal structure prediction of magnetic compounds. We have developed a crystal structure prediction technique in which stable structures are efficiently selected from candidate structures by Bayesian optimization. Applications to $\rm Y_2Fe_{17}$ and NaCl show that the number of searching trials required to find the minimum structure is reduced by 30-40% compared to random search [3].

References

[1] T. Fukazawa et al.: J. Appl. Phys. **122** (2017) 053901.

[2] T. Fukazawa et al.: J. Phys. Soc. Jpn. **87** (2018) 044706.

[3] T. Yamashita et al.: Phys. Rev. Materials **2** (2018) 013803.

Materials design using B, C, and N for next-generation device

Susumu SAITO
Department of Physics, Tokyo Institute of Technology
2-12-1 Oh-okayama, Meguro-ku, Tokyo 152-8551

The hexagonal BN (h-BN) atomic-layer materials are known to possess atomically flat geometries and can serve as the highest-quality substrate for other conducting and semiconducting atomic-layer materials including graphene and transition-metal dichalcogenide atomic-layer materials. We have studied the electronic properties of pristine h-BN atomic layers and their doped phases with substitutional C impurities in the framework of the density-functional theory to investigate the possibilities of utilizing h-BN materials themselves as next-generation semiconductor device materials. In this study we have used the quantum ESPRESSO package.

In our previous work [1] we have clarified that the h-BN bilayers can possess different electronic properties depending on the stacking sequence of two h-BN layers since the h-BN sheet can have two different orientations unlike graphene. We have extended this orientation dependent electronic-structure study for trilayer h-BN systems [2]. Interestingly, it is found that trilayer h-BN can have much more variations than bilayer h-BN, and that the C-doped layer and the conductive layer can become different from each other. This spatial separation of carriers and dopants are of importance in utilizing the h-BN systems as device materials. These interesting and important properties clearly show that h-BN atomic layers are actually the potential nanoelectronics device materials in the future.

We have also studied the electronic properties of the hetero-atomic-layer systes of graphene and h-BN layer [3]. The scanning-tunneling Microscope (STM) images of these hetero atomic layers with the substitutional C impurity at the B or N site in the h-BN layer are simulated. It is found that in the case of the C dopant at the N site of the h-BN layer, its presence can be clearly detected by the STM even from the images taken atop the graphene surface layer. On the other hand, the C dopant at the B site can be detected only by the STM images taken from the h-BN surface.

In addition to the above atomic-layer materials, we have also studied the electronic properties of sp^3 carbon network materials, *i.e.* diamond, with possible polytypes. It is well-known that in the case of SiC there are various polytypes called 3C, 4H, 6H and so on. In the case of diamond, 2H has been already found in addition to the ordinary 3C diamond.

Previously we showed from the constant-temperature molecular-dynamics study that the carbon nanotube solid can transform into various *sp*^{3} carbon phases including 2H and 4H diamond phases under moderate pressure (10 GPa to 20 GPa). From the electronic-structure study using the GW approximation and the Bethe-Salpeter analysis, we have newly clarified the polytype dependent electronic properties of diamond [4].

References

[1] Y. Fujimoto and S. Saito, Phys. Rev. B **94**, 245427 (2016).

[2] Y. Matsuura, Y. Fujimoto, and S. Saito, to be published.

[3] T. Haga, Y. Fujimoto, and S. Saito, to be published.

[4] M. Sakurai, J. R. Chelikowsky, S. G. Louie, and S. Saito, Phys. Rev. Materials **1**, 054603 (2017).

Structures and local magnetic properties of magnetic-material interfaces

Yoshihiro GOHDA
Department of Materials Science and Engineering, Tokyo Institute of Technology
J1-3, Nagatsuta-cho 4259, Midori-ku, Yokohama 226-8502, Japan

Multiferroic materials are of significant interest, because their magnetization can be controlled by the electric field, not by the electric current, which suppresses energy dissipation by the Joule heating [1]. In particular, multiferroic interfaces are good candidates for practical applications: The magnetoelectric coupling in known single-phase multiferroic materials is too weak. Even though interface multiferroicity has been studied intensively for ferromagnetic/ferroelectric interfaces [1, 2], ferromagnetic/multiferroic interfaces should be better, because the interface multiferroicity can be enhanced by the single-phase multiferroicity. First-principles calculations of ferromagnetic/multiferroic interfaces are extremely demanding due to non-collinear configurations of the magnetic moments. For example, $BiFeO_3$ (BFO) has canted magnetization by two nearly-antiparallel Fe magnetic moments due to the Dzyaloshinskii–Moriya interaction.

In this study, we demonstrate the magnetoelectric coupling for a ferromagnetic/multiferroic interface, bcc-Fe/$BiFeO_3$(001) [3]. First-principles calculations were performed on the basis of density functional theory with the generalized gradient approximation by the OpenMX code [4]. For the Fe $3d$ orbitals within BFO, the DFT+U method was used. Considering non-collinear magnetism with the spin-orbit coupling, we successfully reproduced the canted magnetization of BFO due to the Dzyaloshinskii–Moriya interaction. We examined various interfaces by changing the termination and the stacking positions at the interface. We have found that the most suitable interface for evaluating magnetoelectric coupling is the BiO-terminated interface with the bcc-Fe atoms stacked on the bridge sites of BFO(001). With the reversal of the electric polarization of BFO, a drastic change in the directions of exchange-coupled magnetization of bcc Fe and BFO has been obtained as the interface magnetoelectric effect [3]. In addition, the enhancement of the magnetic moment of interface Fe atoms in bcc Fe was found as shown in Fig. 1.

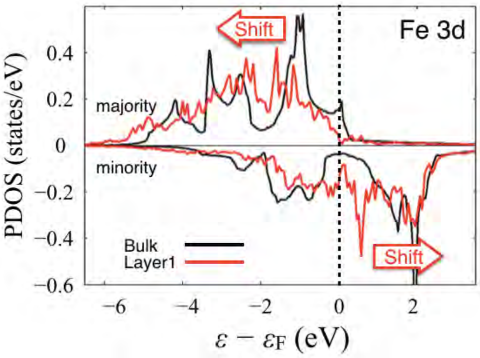

Figure 1: The calculated partial density of states of the Fe $3d$ states in bcc-Fe/BFO(001). The energy origin is set at the Fermi energy ε_F.

[1] T. Taniyama, J. Phys.: Condens. Matter **27**, 504001 (2015).

[2] C.-G. Duan, S. S. Jaswal, and E. Y. Tsymbal, Phys. Rev. Lett. **97**, 047201 (2006).

[3] K. Fujita and Y. Gohda, in preparation.

[4] T. Ozaki, Phys. Rev. B. **67**, 155108 (2003).

Magnetization Process of Permanent Magnets Revealed by Large-scale Simulation

Hiroshi Tsukahara, and Kanta Ono
High Energy Accelerator Research Organization (KEK)
1-1 Oho, Tsukuba, Ibaraki 305-0801 Japan

High-performance permanent magnets are receiving increased attention owing to shifting toward electric vehicles globally. It is indispensable to improve electric motors for power saving electric vehicles, and the permanent magnet is one of the most important parts of the electric motor. The performance of the permanent magnet is governed by coercivity and remanent magnetization. When applied magnetic field approaches the coercivity, nucleation cores are created, and domain walls move inside the permanent magnet. Because magnetization reversal regions are expanded by the motion of the domain wall, it is important for improvement of the permanent magnet to clarify details of the domain wall motion.

Micromagnetic simulations have revealed the magnetization dynamics within magnetic materials including the permanent magnet. The micromagnetic simulation enables us to observe the motion of the domain wall numerically. However, average diameters of grains which consist of the permanent magnet exceed 1.0 μm, and a length of the domain wall is approximately 5 nm. Hence, massively parallel computing is essential to investigate the magnetization dynamics inside the permanent magnet. [1]

We implemented 3 dimensional fast Fourier transform (FFT) subroutine based on MPI parallelization using GPGPU computing and calculated magnetic dipolar fields which occupy over 80 % of a calculation time of our CPU based simulation code. We performed fast Fourier transform using GPGPU according to the following procedure as shown Fig. 1 First, we set magnetization data which is divided into MPI processes. After copying data to GPU, we performed 2 dimensional FFT using cuFFTExecZ2Z and copied data to host. Next, we exchanged data among the MIP processes to performed FFT, and we copied data to GPU. After performing 1 dimensional FFT in the Z direction, we get the 3 dimensional Fourier transform of the magnetization.

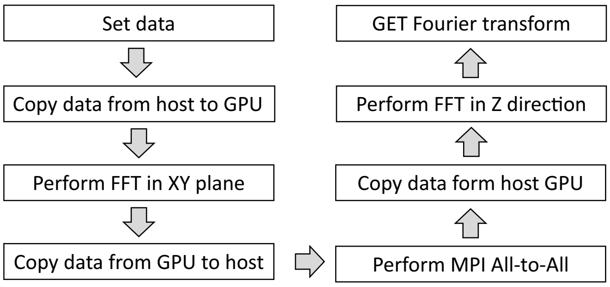

Figure 1: Algorithm of 3 dimensional FFT using GPGPU based on MPI parallelization.

In the case of large-scale micromagnetic simulation, a required memory capacity exceeds a memory of GPU. Hence, this study is the first step for massively parallel computing with many GPUs.

References

[1] H. Tsukahara, K. Iwano, C. Mitsumata, T. Ishikawa, and K. Ono, Comp. Phys. C **207** (2016) 217.

Molecular simulation of ion transport and desolvation at electrode interface

Akihiro MORITA

Department of Chemistry, Graduate School of Science

Tohoku University, Aoba-ku, Sendai, Miyagi 980-8578

The present group has been studying liquid interfaces in close collaboration with interface sensitive nonlinear spectroscopy, such as sum frequency generation (SFG). In particular, this project investigates liquid-solid interfaces in relation to electrochemistry. In applying SFG to such solid-liquid interfaces, however, the spectra could involve significant $\chi^{(3)}$ effect, which influences on the interpretation of the spectra. The excess charge at solid surface may generate a static electric field which penetrates into the liquid and induce additional source of SFG signal. Consequently, the observed SFG signal contains substantial contribution from the region affected by the static field ($\chi^{(3)}$ contribution). In recent applications to solid-liquid interfaces, reliable estimate of c(3) contribution has been an critical concern.

It is not straightforward to separate the intrinsic surface signal of $\chi^{(2)}$ and the $\chi^{(3)}$ contribution experimentally, whereas MD calculation allows for calculating the c(3) signal in a direct manner and well separating the two contributions. Therefore, we performed the computation of the $\chi^{(3)}$ signal of water for the first time, and revealed its spectral lineshape and amplitude. We also demonstrated it possible to evaluate the $\chi^{(3)}$ contribution in the observed SFG signal and to calibrate its contribution to extract the intrinsic signal from the interface.

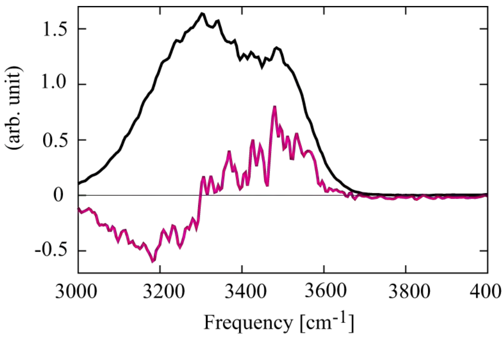

Fig. 1: Calculated Im[χ] spectrum of water-silica interface. Black line stands for the observed SFG signal, while the purple is the intrinsic $\chi^{(2)}$ signal by removing the $\chi^{(3)}$ contribution.

References

[1] T. Joutsuka, T. Hirano, M. Sprik, and A. Morita, Phys. Chem. Chem. Phys., **20** (2018), 3040-3053.

3.6 Software Advancement Projects, GPGPU Implementation, and Workshop Support

Development of an integrated dynamical mean-field theory package for correlated electrons

Hiroshi Shinaoka[1], Junya Otsuki[2], Kazuyoshi Yoshimi[3], Mitsuaki Kawamura[3], Takeo Kato[3]
[1]*Department of Physics, Saitama University, Saitama 338-8570*
[2]*Department of Physics, Tohoku University, Sendai 980-8578*
[3]*Institute for Solid State Physics, University of Tokyo, Kashiwa, 277-8581*

In condensed matter physics, dynamical mean-field theory (DMFT) [1] is a widely used tool for the study of strongly correlated electron systems. In a DMFT calculation, a correlated lattice model is mapped to an impurity problem whose bath degrees of freedom are self-consistently determined. DMFT can be combined with density functional theory based *ab-initio* calculations as the DFT+DMFT method, to describe strongly correlated materials such as transition metal oxides [2]. The DFT+DMFT method is useful particularly for investigating one-particle excitation of the systems. The DFT+DMFT allows us to compute one-particle spectral functions, which can be compared directly with angle-resolved photoemission spectroscopy (ARPES). Although there are several open-source computational libraries for DMFT calculations, the use of these libraries requires some expertise. This prevents wider use of the DFT+DMFT method in studies of condensed matter physics.

To make this method available to non-experts(including students) in the community in condensed matter physics, we have developed an open-source software `DCore` ver.1 [3] in Project for advancement of software usability in materials science [3] at the fiscal year of 2017. `DCore` is an abbreviation of “integrated DMFT software for CORrelated Electrons”. `DCore` is built on the top of elaborate softwares `TRIQS` [5] and `ALPSCore` libraries [6] and related softwares. `DCore` performs calculations based on DMFT with the help of these libraries. As an impurity solver, one can select continuous-time quantum Monte Carlo method or the Hubbard-I approximation. Because `DCore` provides a well-organized text-file-based interface, users can perform the DFT+DMFT calculation with less effort. In a typical DFT+DMFT calculation, the non-interacting Hamiltonian $\mathcal{H}(k)$ is extracted from the results of DFT calculations by projecting the band structure to maximally localized Wannier functions. In `DCore`, we can import $\mathcal{H}(k)$ from outputs of the DFT codes which support `Wannier90` such as `VASP`, `Wien2k`, `Quantum ESPRESSO`, and `OpenMX`.

`DCore` consists of multiple programs, each of which performs a different step of DMFT calculations. To be more specific, `DCore` consists of three layers: interface layer, DMFT loop, and post-processing. Those are performed by the executables `dcore_pre`, `dcore`, `dcore_post`, respectively. Input parameters are provided by a single text file, which is read by all the three programs.

For the interface layer, there are two types of interfaces: standard interface for tight-binding models and `Wannier90` interface for materials. For the standard interface, one can choose one of predefined tight-binding models. On the other hand, for the `Wannier90` interface, one is able to import a tight-binding model constructed by DFT calculations. The data describing the system generated by `dcore_pre` is

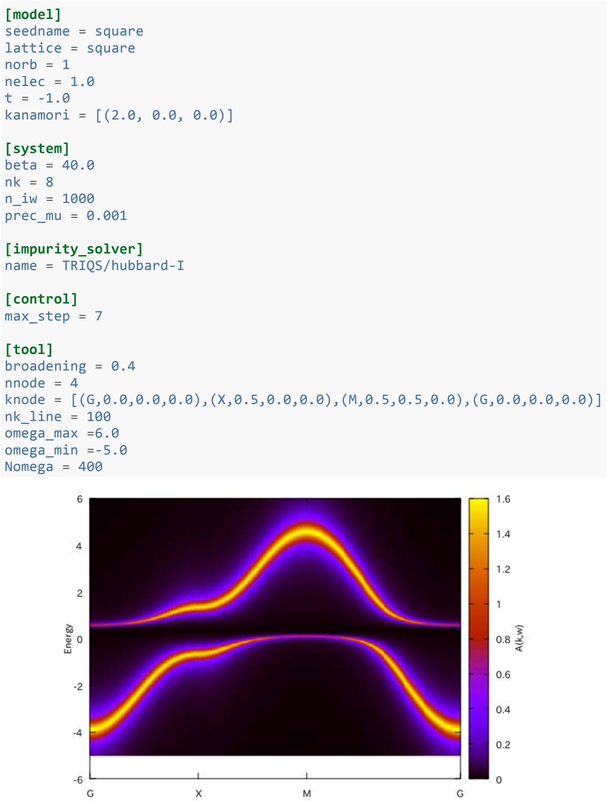

```
[model]
seedname = square
lattice = square
norb = 1
nelec = 1.0
t = -1.0
kanamori = [(2.0, 0.0, 0.0)]

[system]
beta = 40.0
nk = 8
n_iw = 1000
prec_mu = 0.001

[impurity_solver]
name = TRIQS/hubbard-I

[control]
max_step = 7

[tool]
broadening = 0.4
nnode = 4
knode = [(G,0.0,0.0,0.0),(X,0.5,0.0,0.0),(M,0.5,0.5,0.0),(G,0.0,0.0,0.0)]
nk_line = 100
omega_max =6.0
omega_min =-5.0
Nomega = 400
```

Figure 1: The upper panel shows an example of input file for single-orbital Hubbard model on a square lattice. The lower panel shows the computed momentum-resolved spectrum $A(k, \omega)$.

stored in a file in the HDF5 format, which is read in the later processes. Self-consistent calculations are performed by `dcore` and the results are stored in a separated HDF5 file. One can analyze the result and plot the data by using `dcore_post`.

We show an example for a single-orbital Hubbard model on a square lattice in Fig. 1 using the standard interface. In the input file, one can choose the lattice model, the type of local interactions, and their strengths. Here, the impurity solver is the Hubbard-I approximation using an implementation in `TRIQS`. The computed results are processed by `dcore_post` and are converted into human-readable formats. One can plot the data by using standard tools such as gnuplot (see Fig. 1.) With the `Wannier90` interface, one can perform DFT+DMFT calculations by using a single similar text input file for `DCore`. We refer the interested reader to the website [3] for more examples for real materials.

Finally, we introduce some of available features in `DCore` ver 1 and a future development plan of `DCore`. The feature of `DCore` is to treat many kinds of interactions such as multi-orbital models with non-density-density interactions and spin-orbit coupling. Thus, we can perform collinear magnetic calculations. A future version will support the computation of (free) energy, two-particle quantities such as local magnetic susceptibilities, and the calculations of non-collinear magnetic structures. The software will be preinstalled on the supercomputer (Sekirei) at ISSP in 2018. We hope that DCore promotes wide use of the DFT-DMFT calculations, which is one of excellent methods for understanding strongly-correlated electron systems.

References

[1] A. Georges, G. Kotliar, W. Krauth, M.J. Rozenberg, Rev. Mod. Phys. **68**, 13 (1996).

[2] G. Kotliar, S. Savrasov, K. Haule, V. Oudovenko, O. Parcollet, C. Marianetti, Rev. Mod. Phys. **78**, 865 (2006).

[3] `https://github.com/issp-center-dev/DCore`

[4] `http://www.issp.u-tokyo.ac.jp/supercom/softwaredev`

[5] O. Parcollet *et al.*, Comput. Phys. Comm. **196**, 398 (2015).

[6] A. Gaenko *et al.*, Comput. Phys. Comm. **213**, 235 (2017).

GPGPU implementation of Fluid Particle Dynamics (FPD) method

Michio Tateno, Kyohei Takae and Hajime Tanaka
Department of Fundamental Engineering, Institute of Industrial Science, University of Tokyo
4-6-1 Komaba, Meguro-ku, Tokyo 153-8505

Structural ordering in colloidal suspensions is significantly influenced by many-body hydrodynamic interactions among colloids, because the liquid flow field is intrinsically coupled with colloid motion. When numerically studying such a process, we inevitably encounter a complicated moving boundary problem, because the non-slip solid-fluid boundary condition has to be satisfied at the surface of the colloidal particles. However, solving such a boundary problem is numerically costly, because we need to generate a complex adaptive mesh depending on the positions of colloids at every time step [1, 2]. This difficulty can be overcome by treating a solid colloidal particle as an undeformable fluid particle with high viscosity. We call this method Fluid Particle Dynamics (FPD) method [3, 4].

When examining self-assembly kinetics of colloidal suspensions numerically, we need to choose the length/time scale of our simulations large/long enough for problems we study. As an example, we consider phase separation of a dilute colloidal suspension, which is often accompanied by network formation of colloidal particles. To study this problem numerically, we need to use a large simulation box whose size is far beyond the typical length of aggregates such as the typical pore size of the resulting colloidal gel. Considering the long-range nature of hydrodynamic interactions, there is also a possibility that a gelation process may severely be influenced by finite size effects. Therefore, we need a large-size simulation. Furthermore, when we are interested in kinetics of structure formations in dense suspensions, The time scale of simulation becomes important. This is because the diffusive motions of colloids should largely slow down due to steric hindrance by the surrounding colloids in such a dense system. Consequently, the time scale of the structural ordering such as crystallization is usually much slower than that expected from the Brownian time of a free colloid. Thus, in order to numerically follow such a slow dynamics, a long time simulation is required.

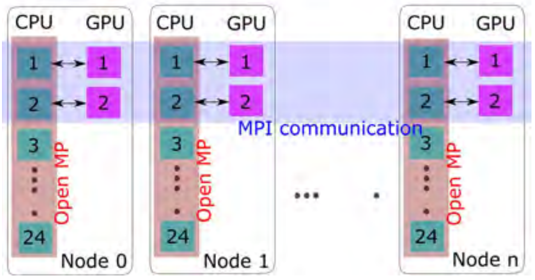

Figure 1: Schematic figure for the way of utilizing computational resources in a large-scale simulation (case(a)). All the computations except for Fast Fourier Transformation (FFT) are performed with a hybrid GPGPU+MPI program. For FFT we transferred the data from devices to hosts and executed it on hosts with a hybrid MPI+OpenMP program.

For the above reasons, we need to overcome the problems of the numerical costs associated with simulation size and time. To this end, we perform GPGPU implementation for (a) colloidal gelation and (b) crystallization, utilizing a service provided by ISSP. In this report we explain the outcome of this project.

In ISSP's Supercomputer Center we used queue of F18acc (class B) where 24 CPUs and 2 GPUs (TeslaK40c) are implemented per Node. Each GPU has approximately 12 GB of memory. For case (b), the system size was set as $(L/\sigma)^3 = 17.3^3$ where L and σ are the side length of the simulation box and the diameter of colloids (the corresponding size of the box in the lattice unit is 128^3). In the above setting, we can perform simulations while storing all the data on device since the amount of data (0.45 GB) is less than that of GPU's memory. For case (a) this system size is not large enough to capture a hierarchical structure of a colloidal gel [5] as explained in the previous paragraph. Therefore we performed larger system size simulations, $(L/\sigma)^3 = 69.2^3$. In this case, the required memory is $\sim$ 30GB, which is beyond the capacity of single GPU. We transfer the large amount of data between hosts and devices, developing a simulation code by hybrid GPGPU+MPI parallelization. By dividing all the data with MPI parallelization and distributing them onto multiple GPUs, we can perform most of computations while keeping the data stored on GPUs. In the FPD method we also use Fast Fourier Transformation(FFT) where only part of FFT is performed on host with hybrid MPI+OpenMP parallelization(see Fig.1), because in CUDA and OpenACC no library that can deal with FFT beyond nodes is provided at this moment.

With the above setting, we examine the performance of simulations by the GPGPU adopted codes. For case (b) where we utilize single GPU, the speed measured is 3.7 times faster than that of our previous non-GPGPU simulations, which are performed by MPI parallelization with 16 threads. By this speeding up, we succeeded in simulating the whole process of crystallization in a colloidal suspension from a metastable liquid state to a crystal state. For case (a), we use 32 GPUs (16 Nodes) and realize 10.4 times speeding up compared with our previous non-GPGPU simulations with 16-threads MPI parallelization. With this codes, we successfully perform simulations with 8 times larger system size (in volume) than the simulations without GPGPU implementation and observe power-law growth behavior over one order of magnitude in time. This power-law behavior, which has never been confirmed with the non-GPGPU simulations because of its slow computational speed, implies a characteristic coarsening process of colloidal gelation [5].

In summary, we have made GPGPU implementation of the FPD method to study colloidal gelation and crystallization. We have succeeded in 10.4 and 3.7 time speeding up compared with the performance of our previous simulations without GPU parallelization. We thank ISSP Supercomputer Center for providing computational resources and a service for GPGPU implementation.

References

[1] H. H. Hu, N. A. Patankar, and M. Y. Zhu: J. Comput. Phys., **169**, (2001) 427.

[2] A. S. Khair and J. F. Brady: Proc. R. Soc. A, **463**, (2007) 223.

[3] H. Tanaka and T. Araki: Phys. Rev. Lett., **85**, (2000) 1338.

[4] A. Furukawa, M. Tateno and H. Tanaka: Soft Matter, doi:10.1039/C8SM00189H.

[5] See an activity report "Study of finite-size effects on colloidal gelation originating from momentum conservation".

Implementation of GPGPU computing in full diagonalization for $\mathcal{H}\Phi$

Takahiro Misawa and Kazuyoshi Yoshimi
Institute for Solid State Physics, University of Tokyo
Kashiwa-no-ha, Kashiwa, Chiba 277-8581

From the 2015 fiscal year, we have been developed the open-source software for exact diagonalization $\mathcal{H}\Phi$ [1, 2] under the support of "Project for advancement of software usability in materials science" by Institute for Solid State Physics (ISSP), University of Tokyo. At the initial stage of the development ($\mathcal{H}\Phi$ ver. 1.0 released at the 2015 fiscal year), we implemented the full diagonalization using the LAPACK routine [3], the exact diagonalization using the Lanczos method [4], and the finite-temperature calculations using the thermal pure quantum states [5] for the general Hamiltonians in the quantum lattice models. Then, in the 2016 fiscal year, we implemented the functions for calculating the dynamical correlation functions using the Lanczos method [4] and the shifted Krylov method [6]. We also implemented the LOBCG method [7] that enables us to obtain many low-energy excited states in one calculations. In the 2017 fiscal year, the real-time evolution is implemented and the developers' manual has been written.

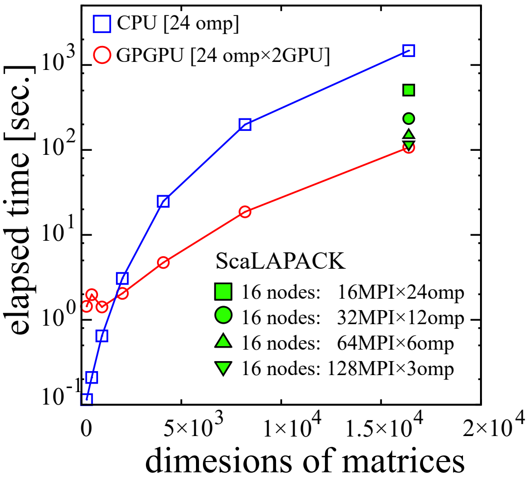

Figure 1: Comparison of elapsed time of full diagonalization for the one-dimensional Heisenberg chain by the LAPACK routine **zheev** with 24 openmp threads and the MAGMA routine **magma_zheevd** with 2 GPGPUs. The calculations are done using single node in F18acc at the supercomputer system B (sekirei). We perform the calculation up to $L = 14$ (matrix dimension is $2^{14} = 16384$) from $L = 8$ (matrix dimension is $2^8 = 256$). Full diagonalization by the GPGPU becomes faster for $L \gtrsim 2500$. We also show the results by the ScaLAPACK performed by 16 nodes in i18cpu for $L = 14$. In the ScaLAPACK, by increasing the number of MPI process, the elapsed time becomes shorter. The full diagonalization by the GPGPU by 1 node is, however, still faster than the ScaLAPACK by 16 nodes.

Several useful methods without full diagonalization such as the Lanczos method and the thermal pure quantum states have been implemented in $\mathcal{H}\Phi$ so far. Although the full diagonalization is widely used in the condensed matter physics and is also useful for examining the accuracy of other methods, it is still done by the LAPACK routine for single CPU processor in $\mathcal{H}\Phi$. To get rid of this weak point in $\mathcal{H}\Phi$, under the support of supercomputing center at ISSP, we have implemented the GPGPU (General Purpose Graphics Processing Unit) computing for the full diagonalization in this project. We also implemented the full diagonalization by the ScaLAPACK [8] for multi processors in another project and compare the results with the GPGPU. In this activity report, we explain how the GPGPU computing accelerates the full diagonalization in $\mathcal{H}\Phi$.

We replace the **zheev** function in LAPACK with the **magma_zheevd** in the MAGMA library for GPGPU computing [9]. We note that the MAGMA library only supports the diagonalization in single process and multi GPGPUs. Thus, we perform the benchmark in single process. In Fig.1, we show elapsed time of the full diagonalization for the one-dimensional Heisenberg chain as a function of the dimension of the matrix. In this calculation, we do not specify z component of the spin (S_z), the dimension of the matrix is given by 2^L, where L is the system size. We find that the GPGPU computing becomes faster than the LAPACK library around $L \sim 2500$. For larger system sizes ($L \geq 5000$), the full diagonalization by GPGPU is about 10 times faster than the LAPACK routine. In addition, surprisingly, we find that the GPGPU computing with 1 node is still faster than the ScaLAPACK with 16 nodes. This result indicates that the GPGPU computing is efficient in performing the full diagonalization for intermediate size of matrices (size of matrices is about 10^4), which can be treated in single node.

For the standard models in the condensed matter physics such as the Heisenberg or the Hubbard model, users can easily perform the full diagonalization using the standard mode in $\mathcal{H}\Phi$ [1, 2] by preparing only one input file as follows:

```
L        = 12
model    = "SpinGC"
lattice = "chain"
method   = "FullDiagh"
J        = 1.0
NGPU     = 2
```

By using the expert mode, users also treat the general Hamiltonian with the arbitrary one-body potentials and the arbitrary two-body interactions. Furthermore, in $\mathcal{H}\Phi$, it is possible to input the arbitrary Hermite Hamiltonians in the Matrix Market format [10] and perform the full diagonalization. Thus, the implemented efficient full diagonalization method by the GPGPU computing in $\mathcal{H}\Phi$ is useful for a wide range of the scientists in the fields of condensed matter physics and the mathematical science, who want to diagonalize and analyze the large-scale matrices.

Acknowledgment: This work was supported by support service of program portability to General Purpose Graphics Processing Unit.

References

[1] M. Kawamura, K. Yoshimi, T. Misawa, Y. Yamaji, S. Todo, N. Kawashima, Comp. Phys. Commun. **217**, 180 (2017).

[2] http://issp-center-dev.github.io/HPhi /index.html.

[3] E. Anderson, Z. Bai, C. Bischof, L. Blackford, J. Demmel, J. Dongarra, J. Du Croz, A. Greenbaum, S. Hammarling, A. McKenney, D. Sorensen, LAPACK Users' Guide, 3rd Edition, Society for Industrial and Applied Mathematics, 1999.

[4] E. Dagotto, Rev. Mod. Phys. **66**, 763 (1994).

[5] S. Sugiura, A. Shimizu, Phys. Rev. Lett. **108**, 240401 (2012).

[6] A. Frommer, Computing **70**, 87 (2003).

[7] A. V. Knyazev, SIAM journal on scientific computing **23**, 517 (2001).

[8] L. S. Blackford, J. Choi, A. Cleary, E. D'Azevedo, J. Demmel, I. Dhillon, J. Dongarra, S. Hammarling, G. Henry,

A. Petitet, K. Stanley, D. Walker, R. C. Whaley, ScaLAPACK Users' Guide, Society for Industrial and Applied Mathematics, Philadelphia, PA, 1997.

[9] http://icl.cs.utk.edu/magma/software.

[10] https://math.nist.gov/MatrixMarket/.

Supercomputer course of Computational Materials Design (CMD®) workshop

Masaaki GESHI[1], Yoshitada MORIKAWA[2], Tomoya ONO[3]
[1]*Institute for NanoScience Design,*
Osaka University, Machikaneyama, Toyonaka, Osaka 560-8531
[2]*Department of Precision Science and Technology,*
Osaka University, Yamada-oka, Suita, Osaka 565-0871
[3]*Center for Computational Science,*
University of Tsukuba, Tenno-dai, Tsukuba, Ibaraki 305-8577

The 31th Computational Materials Design (CMD®) workshop (CMD31) has been held from September 11 to September 15 and the 32th CMD® workshop (CMD32) has been done from February 26 to March 2 at Graduate School of Engineering Science, Osaka University. In this workshop we have the supercomputer course to train up human resources to advance researches by using system B supercomputer of ISSP, the University of Tokyo.

In CMD31 six participants took the supercomputer course and got a tutorial on STATE-Senri developed by Y. Morikawa. After explaining how to use the supercomputer of ISSP and explaining how to use STATE-Senri, calculation models on each research subject of the participants were built and their calculations were carried out. Concrete themes were adsorption states, vibration modes and quantum effect of CH_4 molecule on the Pt surface, formic acid adsorption structure on Cu surface and its vibration modes and decomposition reaction process, and structure and reactivity of Pt atoms supported on graphene and so on. The participants performed the calculations and examined the results.

In CMD32 one participant took the supercomputer course and got a tutorial on RSPACE developed by T. Ono. After describing the calculation method of electronic states and electron conduction property using RSPACE, exercises published in the manual were carried out. Then, electronic state calculations were carried out on a plurality of molecular systems, and the electronic density distribution was visualized. Finally, the atomic structure optimization of the system in which molecules are sandwiched between metal electrodes was carried out, and the calculation of electron conduction properties of molecules was analyzed.

4 PUBLICATION LIST

Example:

LASTNAME, Firstname [project class; # points (B)] (Page #)
Project title
1. First paper
   Names of Authors, etc.
2. Second paper
   ...

□ ISSP Joint Research Projects

ADACHI, Takahiro [C class; 500 (B)] (319)
— *Heat Transfer Characteristics of Condensate/Evaporate Film Flow along Vertical Plates with Microscopic Grooves*

AKAGI, Kazuto [C class; 4500 (B)] (99)
— *Exploration of structure motifs characterizing the metal oxides*
1. Interactions of hydrogen with amorphous hafnium oxide
   M. Kaviani et al.: Phys. Rev. B **95** (2017) 075117.
1. First-principles investigation of local structure deformation induced by x-ray irradiation in κ-(BEDT-TTF)$_2$Cu[N(CN)$_2$]Br
   LJ. Kang et al.: Phys. Rev. B **95** (2017) 214106.
1. Dopant Clustering in Oxygen-Deficient Rh^{3+}:SrTiO$_{3-\delta}$ Visible-Light Photocatalyst
   M. Lippmaa et al.: J. Am. Cham. Soc., submitted.

AKAI, Hisazumi [B class; 1400 (B)] (137,139)
— *Electronic structure of light rare earth permanent magnets*
1. Atomistic-model study of temperature-dependent domain walls in the neodymium permanent magnet Nd$_2$Fe$_{14}$B
   Masamichi Nishino, Yuta Toga, Seiji Miyashita, Hisazumi Akai, Akimasa Sakuma, and Satoshi Hirosawa: Phys. Rev. B **95**, 094429/17 (2017).
2. L-edge resonant magneto-optical Kerr effect of a buried Fe nanofilm
   Y. Kubota, M. Taguchi, H. Akai, Sh. Yamamoto, T. Someya, Y. Hirata, K. Takubo, M. Araki, M. Fujisawa, K. Yamamoto, Y. Yokoyama, S. Yamamoto, M. Tsunoda, H. Wadati, S. Shin, and I. Matsuda: Phys. Rev. B **96**, 134432/16 (2017).
3. Determination of the element-specific complex permittivity using a soft x-ray phase modulator
   Y. Kubota, Y. Hirata,J. Miyawaki, S. Yamamoto, H. Akai, R. Hobara, Sh. Yamamoto, K. Yamamoto, T. Someya, K. Takubo, Y. Yokoyama, M. Araki, M. Taguchi, Y. Harada, H. Wadati, M. Tsunoda, R. Kinjo, A. Kagamihata, T. Seike, M. Takeuchi, T. Tanaka, S. Shin, and I. Matsuda: Phys. Rev. B **96**, 214417/16 (2017).
4. Quantum Theory of Rare-Earth Magnets
   T. Miyake and H. Akai: J. Phys. Soc. Jpn **87**, 041009-110 (2018).
5. First-principles study of intersite magnetic couplings and Curie temperature in RFe$_{12-x}$Cr$_x$ (R = Y, Nd, Sm)
   T. Fukazawa, H. Akai, Y. Harashima, and T. Miyake: J. Phys. Soc. Jpn **87**, 044706/15 (2018).
6. Maximum performance of permanent magnet materials
   H. Akai: Scripta Materialia (2018) in press.
7. First-principles calculation of transition-metal Seebeck coefficients

S. Kou and H. Akai: Solid State Commun. **296**, 15 (2018).

AKASHI, Ryosuke [C class; 5500 (B)] (85)
— *Exploration of hydrogen-1s metallic state and superconductivty in oxyhydride compounds*

1. Weak Phonon-mediated pairing in $\mathrm{BiS_2}$ superconductor from first principles
   C. Morice, R. Akashi, T. Koretsune, S. S. Saxena, and R. Arita: Phys. Rev. B 95, (2017) 180505(R).
2. Refined phase diagram of the H-S system with high-Tc superconductivity
   I. Kruglov, R. Akashi, S. Yoshikawa, A. R. Oganov, and M. M. D. Esfahani: Phys. Rev. B 96, (2017) 220101(R).

AMAMOTO, Yoshifumi [B class; 600 (B)] ()
— *Polymer Fatigue Revealed by Molecular Dynamic Simulation*

AOYAMA, Kazushi [B class; 1200 (B)] (298)
— *Spin-lattice-coupling effects in pyrochlore antiferromagnets*
— *Theoretical study of dynamical spin correlations in frustrated magnets*

ARAI, Munehito [B class; 1300 (B)] (296)
— *Computational rational design of novel binding proteins*
— *Folding mechanisms of the bioactive proteins essential for regenerative medicine*

ARAIDAI, Masaaki [C class; 4500 (B)] (98)
— *Electronic States and Thermodynamic Stability of Two-Dimensional Crystals of Group IV Elements*

1. First-principles study on adsorption structure and electronic state of stanene on α-alumina surface
   M. Araidai, M. Kurosawa, A. Ohta, K. Shiraishi: Jpn. J. Appl. Phys. **56** (2017) 095701.

ARAKAWA, Naoya [B class; 700 (B)] (312)
— *Microscopic theory of magnon physics in a three-dimensional chiral magnet*

1. Magnon Dispersion and Specific Heat of Chiral Magnets on the Pyrochlore Lattice
   N. Arakawa: Journal of Physical Society of Japan, **86** (2017) 094705.
2. Weak localization of magnons in a disordered two-dimensional antiferromagnet
   N. Arakawa and J. Ohe: Phys. Rev. B **97** (2018) 020407(R).
3. Negative magnetothermal resistance in a disordered two-dimensional antiferromagnet
   N. Arakawa and J. Ohe: Phys. Rev. B **96** (2017) 214404.
4. Tunneling between chiral magnets: Spin current generation without external fields
   N. Arakawa: Phys. Rev. B **95** (2018) 235438.

ARAKI, Takeaki [B class; 700 (B)] (311)
— *Conformational changes of polyelectrolyte chains in solvent mixtures*

1. Colloidal suspensions in one-phase mixed solvents under shear flow
   A. Barbot and T. Araki: Soft Matter **13** (2017), 5911.

ASAI, Yoshihiro [C class; 5500 (B)] (83)
— *Theoretical and first principle studies of non-equilibrium transport properties of strongly correlated materials*

1. Resistive switching mechanism of $\mathrm{GeTeSb_2Te_3}$ interfacial phase change memory and topological properties of embedded two-dimensional states
   Hisao Nakamura, Ivan Rungger, Stefano Sanvito, Nobuki Inoue, Junji Tominaga and Yoshihiro Asai: Nanoscale **9** (2017) 9836.
2. Bandgap Engineering in OH- Functionalized Silicon Nanocrystals: Interplay between Surface Functionalization and Quantum Confinement
   Marius Bürkle Mickaël Lozaćh Calum McDonald Davide Mariotti Koji Matsubara Vladimir Švrček: Adv. Funct. Mater. **27** (2017) 1701898.

EGAMI, Yoshiyuki [C class; 2000 (B)] (131)
— *Development and application of time-dependent electron-transport simulator based on first-principles method*

1. First-principles study on electron transport through BN-dimer embedded zigzag carbon nanotubes
   Y. Egami and H. Akera: Physica E **88** (2017) 212.
2. Controlling Rashba spin-orbit interaction in quantum wells by adding symmetric potential
   Y. Egami and H. Akera: Appl. Phys. Express **10** (2017) 063007.
3. ニッケルおよび無電解ニッケルの超精密切削加工におけるダイヤモンド工具の損耗機構
   宇田 豊, 名越 将大, 宇治宮 俊樹, 本田 索郎, 江上 喜幸, 田中 宏明, 古城 直道, 島田 尚一: 精密工学会誌 **83** (2017) 762.a
4. First-principles study on electron transport through Mn(dmit)2 molecular junction depending on relative angle between ligands
   Y. Egami and M. Taniguchi: Jpn. J. App. Phys. **57** (2018) 021601.

FUCHIZAKI, Kazuhiro [C class; 5500 (B)] (252)
— *Melting phenomena and polyamorphism*

1. Pressure-induced structural change in liquid GeI_4
   K. Fuchizaki, H. Nishimura, T. Hase, and H. Saitoh: J. Phys.: Condens. Matter **30** (2018) 045401.
2. An effective way to determine the melting curve
   K. Okamoto and K. Fuchizaki: Molecular Simulation **44** (2018) 384.

FUJIKWA, Sachie [C class; 1000 (B)] ()
— *Study of band structure for InSbN based dilute nitride semiconductor by using first-principle simulation*

FUJIMOTO, Yoshitaka [C class; 500 (B)] (159)
— *First-principles study of atomic structures, stabilities, and electronic properties of atomic-layered materials*

1. Formation and physical properties of h-BN atomic layers: A first-principles density-functional study
   Y. Fujimoto: Nanomaterials and Nanotechnology **2017**, 2676432 (2017).
2. First-principles theoretical investigation of graphene layers for sensor applications: A review
   Y. Fujimoto: Nanomaterials and Nanotechnology **7**, 1 (2017).
3. First-Principles Computational Analysis of Nanocomposite for Detecting Environmental Polluting Gas
   Y. Fujimoto: New Polymer Nanocomposites for Environmental Remediation (Elsevier 2018) Chapter 9, p.207.
4. Gas adsorption effects on the stabilities, electronic structures and scanning tunneling microscopy of graphene monolayers doped with B or N
   Y. Fujimoto and S. Saito: submitted.

FUKUDA, Jun-Ichi [B class; 1900 (B)] (283)
— *Calculation of ordered structures and their optical properties of soft materials*

1. Spontaneous formation and dynamics of half-Skyrmions in a chiral liquid-crystal film
   A. Nych*, J. Fukuda*, U. Ognysta, S. Žumer and I. Muševič: Nature Phys. **13** (2017) 1215
2. Reflection spectra and near-field images of a liquid crystalline half-Skyrmion lattice
   J. Fukuda and S. Žumer: Opt. Exp. **26** (2018) 1174.
3. Numerical calculation of Kossel diagrams of cholesteric blue phases
   J. Fukuda, Y. Okumura and H. Kikuchi: Proc. SPIE **10555** (2018) 105550A

FUKUI, Ken-Ichi [C class; 3000 (B)] (274)
— *Analysis on Structuring and Dynamics of Electrolyte Solutions Forming Electric Double Layer at Electrode Interfaces*

1. Computational investigations of electronic structure modifications of ferrocene-terminated self-assembled monolayers: Effects of electron donating/withdrawing functional groups attached on ferrocene moiety

Y. Yokota, S. Akiyama, Y. Kaneda, A. Imanishi, K. Inagaki, Y. Morikawa and K. Fukui:Phys. Chem. Chem. Phys., 19, 32751-32722 (2017).

2. Structural and dynamic properties of 1-butyl-3-methyl-imidazolium bis(trifluoromethanesulfonyl)imide / mica and graphite interfaces revealed by molecular dynamics simulation
   Y. Yokota, H. Miyamoto, A. Imanishi, K. Inagaki, Y. Morikawa, K. Fukui:Phys. Chem. Chem. Phys., 20, 6668-6676 (2017).

FUKUMOTO, Yoshiyuki [B class; 600 (B)] (313)
— *A series expansion study on the magnon spectrum of a kagome antiferromagnet in* $Cs_2Cu_3SnF_{12}$

1. Impact of Dzyaloshinsky-Moriya Interactions and Tilts of the g Tensors on the Magnetization Process of a Spherical Kagomé Cluster in $\{W_{72}V_{30}\}$
   Y. Fukumoto, Y. Yokoyama, and H. Nakano: submitted to J. Phys. Soc. Jpn. (arXiv:1803.06485).

GOHDA, Yoshihiro [C class; 6000 (B)] (77)
— *First-principles calculations of magnetic ultrathin films on surfaces*

1. Prediction of ferromagnetism in MnB and MnC on nonmagnetic transition-metal surfaces studied by first-principles calculations
   S. Nakamura and Y. Gohda: Phys. Rev. B **96**, 245416 (2017).
2. Electron Theory on Grain-Boundary Structures and Local Magnetic Properties of Neodymium Magnets
   Y. Gohda, Y. Tatetsu, and S. Tsuneyuki: Mater. Trans. **59**, 332 (2018).
3. ネオジム磁石の粒界構造と局所磁性の電子論
   合田 義弘、立津 慶幸、常行 真司: 日本金属学会誌 **81**, 26 (2017).

HAGITA, Katsumi [E class; 18000 (B)] (210)
— *Coarse grained MD simulation for fracture and reinforcement of polymer materials*

1. Thinning approximation for two-dimensional scattering patterns from coarse-grained polymer melts under shear flow
   K. Hagita, T. Murashima, H. Takano, and T. Kawakatsu, J. Phys. Soc. Jpn. 86 (2017) 124803.
2. 分子動力学シミュレーションによるフェノール樹脂の架橋構造モデリングと構造の解析
   首藤靖幸, 和泉篤士, 萩田克美, 中尾俊夫, 柴山充弘, ネットワークポリマー 38 (2017) 136-143.
3. 粗視化分子動力学シミュレーョンによるフェノル樹脂架橋ネットワーク構造のモデリングと応力歪解析
   和泉篤士, 首藤靖幸, 萩田克美, 柴山充弘, ネットワークポリマー 38 (2017) 226-231.
4. Filler network model of filled rubber materials to estimate system size dependence of two-dimensional small-angle scattering patterns
   K. Hagita, T. Tominaga, T. Hatazoe, T. Sone, and H. Takano, J. Phys. Soc. Jpn. 87 (2018) 014802.
5. Large-scale reverse Monte Carlo analysis for the morphologies of silica nanoparticles in end-modified rubbers based on ultra-small-angle X-ray scattering data
   K. Hagita, T. Tominaga, and T. Sone, Polymer 135 (2018) 219-229.
6. ディープラーニングを用いたゴム中フィラー凝集構造の画像判別の特性評価
   萩田克美, 冨永哲雄, 曽根卓男, 高橋一郎, Lee Chonho, 荻野正雄, 日本ゴム協会誌 91 (2018.1) 3-8.
7. Molecular dynamics simulations of cross-linked phenolic resins using a united-atom model
   A. Izumi, Y. Shudo, K. Hagita, and M. Shibayama, Macromolecular Theory and Simulations (2018) in press. Super resolution for asymmetric resolution of FIB-SEM 3D imaging of silica nanoparticles in SBR K. Hagita, T. Higuchi, H. Jinnai, Scientific reports, 8 (2018) 5877.

HAMADA, Ikutaro [C class; 4000 (B)] (109)
— *van der Waals density functional theory study of molecular adsorption on solid surfaces*

HAMAMOTO, Yuji [C class; 2500 (B)] (122)
— *First principles study of Pt clusters adsorbed on graphene edges*

HARADA, Kenji [C class; 6000 (B)] (244)
— *Numerical study of non-equilibrium systems*

1. Entanglement branching operator
   K. Harada: Phys Rev B 97, 045124 (2018).

HASHIMOTO, Tamotsu [C class; 4000 (B)] (269)
— *Molecular dynamics simulation of ferroelectrics using a shell model III*

HASHMI, Arqum [C class; 1000 (B)] ()
— *Discovery of new 2D semiconductors*

HATSUGAI, Yasuhiro [C class; 4500 (B)] (264)
— *Numerical studies of bulk-edge correspondence in topological phases*

1. Many-Body Chern Numbers of $\nu = \frac{1}{3}$ and $\frac{1}{2}$ States on Various Lattices
   Hiromu Araki, Toshikaze Kariyado, Takahiro Fukui, Yasuhiro Hatsugai: Journal of the Physical Society of Japan, 86, 103701 (2017).
2. Entanglement Chern number for three-dimensional topological insulators: Characterization by Weyl points of entanglement HamiltoniansMechanics
   Hiromu Araki, Takahiro Fukui, and Yasuhiro Hatsugai: Phys. Rev. B 96, 165139/1-8 (2017).
3. Fractional Quantum Hall Effect in $n = 0$ Landau Band of Graphene with Chern Number Matrix
   Journal of the Physical Society of Japan, to appear

HATTORI, Kazumasa [C class; 2500 (B)] (277)
— *XY model on a diamond lattice: effects of frustration*

HATTORI, Ken [B,C class; 4600 (B)] (89)
— *Model calculations in Si surfaces with adsorbates*

HAYAMI, Satoru [C class; 2500 (B)] (195)
— *Skyrmion crystal phase in itinerant magnets with spin-orbit coupling*

1. Effective bilinear-biquadratic model for noncoplanar ordering in itinerant magnets
   S. Hayami, R. Ozawa, and Y. Motome: Phys. Rev. B **95** (2017) 224424.
2. Shape of magnetic domain walls formed by coupling to mobile charges
   R. Ozawa, S. Hayami, K. Barros, and Y. Motome: Phys. Rev. B **96** (2017) 094417.
3. Manipulating magnetoelectric effect – Essence learned from $\mathrm{Co_4Nb_2O_9}$
   Y. Yanagi, S. Hayami, and H. Kusunose: Phys. Rev. B **97** (2018) 020404.
4. Emergent odd-parity multipoles and magnetoelectric effects on a diamond structure: implication to $5d$ transition metal oxides $A\mathrm{OsO_4}$ (A =K, Rb, and Cs)
   S. Hayami, H. Kusunose, and Y. Motome: Phys. Rev. B **97** (2018) 024414.
5. Microscopic Description of Electric and Magnetic Toroidal Multipoles in Hybrid Orbitals
   S. Hayami and H. Kusunose: J. Phys. Soc. Jpn. **87** (2018) 033709.
6. Néel- and Bloch-Type Magnetic Vortices in Rashba Metals
   S. Hayami and Y. Motome: submitted to Phys. Rev. Lett.

HIDA, Kazuo [B class; 500 (B)] (317)
— *Numerical Study of One Dimensional Frustrated Quantum Spin Systems*

1. Partial Ferrimagnetism in S=1/2 Heisenberg Ladders with a Ferromagnetic Leg, an Antiferromagnetic Leg, and Antiferromagnetic Rungs
   K. Sekiguchi and K. Hida: J. Phys. Soc. Jpn. **86**, 084706 (2017)

HIGUCHI, Yuji [C class; 4000 (B)] (268)
— *Deformation and fracture dynamics of crystalline polymers by large-scale coarse-grained molecular dynamics simulation*

HINOKIHARA, Taichi [C class; 4000 (B)] (267)
— *Analysis of magnetization reversal process based on atomistic models*

1. Exploaration of the effects of dipole-dipole interactions in $Nd_2Fe_{14}B$ thin films based on a stochastic cutoff method with a novel efficient algorithm
   T. Hinokihara, M. Nishino, Y. Toga, and S. Miyashita: Phys. Rev. B **97** (2018) 104427.

HINUMA, Yoyo [B class; 600 (B)] (158)
— *Finding the ground state of prussian blue derivatives*

HIRATSUKA, Masaki [B class; 600 (B)] ()
— *ab initio calculations to determine the phase equilibrium conditions of semiclathrate hydrates*

HIYAMA, Miyabi [B class; 700 (B)] (310)
— *Theoretical study for excited states of bioluminescence related molecules*

1. Theoretical insights into the effect of pH values on oxidation processes in the emission of firefly luciferin in aqueous solution
   M. Hiyama, H. Akiyama and N. Koga: Luminescence: The Journal of Biological and Chemical Luminescence, **32** (2017) 1100.
2. Effect of dynamical fluctuations of hydration structures on the absorption spectra of oxyluciferin anions in aqueous solution
   M. Hiyama, M. Shiga, N. Koga, O. Sugino, H. Akiyama and Y. Noguchi: Phys. Chem. Chem. Phys. **19** (2017) 10028.

HOSHI, Takeo [C,E class; 15500 (B)] (45)
— *Large-scale device-material research by massively parallel electronic structure calculation and data science*

1. Efficient methods for computing integrals in electronic structure calculations
   Hisashi Kohashi, Kosuke Sugita, Masaaki Sugihara and Takeo Hoshi: JSIAM Letters 9, 81-84 (2017).
2. Solution of the k-th eigenvalue problem in large-scale electronic structure calculations
   Dongjin Lee, Takeo Hoshi, Tomohiro Sogabe, Yuto Miyatake, Shao-Liang Zhang, submitted; Preprint (http://arxiv.org/abs/1710.05134)

HOSHINO, Shintaro [C class; 4000 (B)] (191)
— *Quantum Monte Carlo approach to local electronic correlations in unconventional superconductors*

1. Spontaneous Orbital-Selective Mott Transitions and the Jahn-Teller Metal of A3C60
   S. Hoshino and P. Werner: Phys. Rev. Lett. 118, 177002 (2017)a
2. Fan-type spin structure in uni-axial chiral magnets
   Misako Shinozaki, Shintaro Hoshino, Yusuke Masaki, A N Bogdanov, A O Leonov, Junichiro Kishine, Yusuke Kato: arXiv:1705.07778 (2017)
3. Ultrafast switching of composite order in A3C60
   P. Werner, H.U.R. Strand, S. Hoshino, M. Eckstein: Phys. Rev. B 95, 195405 (2017)
4. Field-Induced Transitions in Anisotropic Kondo Lattice - Application to CeT2Al10 -
   T. Kikuchi, S. Hoshino, N. Shibata, Y. Kuramoto: J. Phys. Soc. Jpn. 86, 094602 (2017)a
5. Theory of the magnetic skyrmion glass
   S. Hoshino and N. Nagaosa: Phys. Rev. B 97, 024413 (2018)
6. Enhanced pairing susceptibility in a photodoped two-orbital Hubbard model
   P. Werner, H.U.R. Strand, S. Hoshino, Y. Murakami, M. Eckstein: Phys. Rev. B 97, 165119 (2018)

HOTTA, Takashi [C class; 4500 (B)] (188)
— *Two-channel Kondo effect and multipole susceptibility*

1. Two-Channel Kondo Effect Emerging from Nd Ions
   Takashi Hotta: J. Phys. Soc. Jpn. **86** (2017) 083704/1-4.a
2. Local Nodal Cooper Pairs in Multiorbital Systems

Kazumasa Hattori, Takuya Nomoto, Takashi Hotta, and Hiroaki Ikeda: J. Phys. Soc. Jpn. **86** (2017) 113702/1-5.

3. Mean-field theory for multipole ordering in f-electron systems on the basis of a j-j coupling scheme
   Ryosuke Yamamura and Takashi Hotta: Physica B **536C** (2018) 6-11.
4. Kondo effect in the seven-orbital Anderson model hybridized with Γ_8 conduction electrons
   Takashi Hotta: Physica B **536C** (2018) 203-210.a
5. Multipole interactions of Γ_3 non-Kramers doublet systems on cubic lattices
   Katsunori Kubo and Takashi Hotta: To appear in J. Phys.: Conf. Ser.

HUKUSHIMA, Koji [C class; 3500 (B)] ()
— *Statistical-mechanical study of phase transition and cooperative phenomena*

1. Real-space analysis of scanning tunneling microscopy topography datasets using sparse modeling approach
   MJ Miyama and K Hukushima: J. Phys. Soc. Jpn. **87** (2018) 044801/1-8.
2. Bayesian optimization for computationally extensive probability distributions
   R Tamura and K Hukushima: PloS one **13** (2018) e0193785.a
3. Typical approximation performance for maximum coverage problem
   S Takabe, T Maehara and K Hukushima: Phys. Rev. E **97** (2018) 022138/1-9.
4. An Exact Algorithm Exhibiting RSRSB/EasyHard Correspondence for the Maximum Independent Set Problem
   J Takahashi, S Takabe and K Hukushima: J. Phys. Soc. Jpn. **86** (2017) 073001/1-4.
5. Method for estimating spin-spin interactions from magnetization curves
   R Tamura and K Hukushima: Phys. Rev. B **95** (2017) 064407/1-8.

IGARASHI, Ryo [C class; 1500 (B)] ()
— *Monte Carlo simulation using low-rank approximation to long-range interaction matrices*

IKEDA, Hiroaki [B class; 1500 (B)] (135)
— *Analysis of superconductivity based on a first-principles approach*
— *search for high-temperature superconductors based on a first-principles approach*

IKUHARA, Yuichi [C class; 7000 (B)] (71)
— *Random atomic structure and selective segregation behavior around defects in functional ceramic materials*
— *Study of atomic structure and properties in functional materials*

1. Direct Determination of Atomic Structure and Magnetic Coupling of Magnetite Twin Boundaries
   C. Chen, H. Li, T. Seki, D. Yin, G. Sanchez-Santolino, K. Inoue, N. Shibata, and Y. Ikuhara: ACS Nano, **12** (2018) 2662-2668.
2. Atomic-Scale Origin of the Quasi-One-Dimensional Metallic Conductivity in Strontium Niobates with Perovskite-Related Layered Structures
   C. Chen, D. Yin, K. Inoue, F. Lichtenberg, X. Ma, Y. Ikuhara, J. G. Bednorz: ACS Nano, **11** (2007) 12519-12525.

IMADA, Masatoshi [D,E class; 50500 (B)] (205)
— *Development of neural network method with deep learning as a solver for many-body quantum systems*
— *Nonequilibrium superconductivity emerging from synergistic effects of light and phonons in strongly correlated systems*
— *Numerical Studies on Magnetic Anisotropy and Quantum Anomalous Hall Effect in Perovskite Transition Metal Oxide SrRuO3*

1. Quantum spin liquid signatures in Kitaev-like frustrated magnets
   Matthias Gohlke, Gideon Wachtel, Youhei Yamaji, Frank Pollmann, and Yong Baek Kim: Phys. Rev. B.**97** (2018) 075126
2. Finite-Temperature Signatures of Spin Liquids in Frustrated Hubbard Model
   Takahiro Misawa and Youhei Yamaji: J. Phys. Soc. Jpn. **87** (2018) 023707.

3. Competition among various charge-inhomogeneous states and d-wave superconducting state in Hubbard models on square lattices
   Kota Ido, Takahiro Ohgoe, and Masatoshi Imada: Phys. Rev. B. **97** (2017) 045138.
4. Competition among Superconducting, Antiferromagnetic, and Charge Orders with Intervention by Phase Separation in the 2D Holstein-Hubbard Model
   Takahiro Ohgoe and Masatoshi Imada: Phys. Rev. Lett. **119** (2017) 197001.
5. Restricted Boltzmann machine learning for solving strongly correlated quantum systems
   Yusuke Nomura, Andrew S. Darmawan, Youhei Yamaji, and Masatoshi Imada: Phys. Rev. B. **96** (2017) 205152.
6. Quantum lattice model solver H Phi
   Mitsuaki Kawamura, Kazuyoshi Yoshimi, Takahiro Misawa, Youhei Yamaji,Synge Todo, and Naoki Kawashima: Compt. Phys. Commun. **217**, (2017) 180.
7. Correlation-induced superconductivity dynamically stabilized and enhanced by laser irradiation
   Kota Ido, Takahiro Ohgoe, and Masatoshi Imada: Sci. Adv. **3** (2017) e1700718 .
8. Variational Monte Carlo method for fermionic models combined with tensor networks and applications to the hole-doped two-dimensional Hubbard model
   Hui-Hai Zhao, Kota Ido, Satoshi Morita, Masatoshi Imada: Phys. Rev. B. **96** (2017) 085103.
9. Low-energy effective Hamiltonians for correlated electron systems beyond density functional theory
   Motoaki Hirayama, Takashi Miyake, Masatoshi Imada, and Silke Biermann: Phys. Rev. B. **96** (2017) 075102.
10. Ground state properties of Na_2IrO_3 determined from ab initio Hamiltonian and its extensions containing Kitaev and extended Heisenberg interactions
    Tsuyoshi Okubo, Kazuya Shinjo, Youhei Yamaji, Naoki Kawashima, Shigetoshi Sota, Takami Tohyama, and Masatoshi Imada: Phys. Rev. B. **96** (2017) 054434.

INAGAKI, Kouji [C class; 3500 (B)] (118)
— *First-principles meta-dynamics analysis of Catalyst Referred Etching method (analysis on dissociative adsorption of water molecule and etching reaction at interface between Pt and material surface)*

1. Platinum-catalyzed hydrolysis etching of SiC in water: A density functional theory study
   Pho Van Bui, Daisetsu Toh, Ai Isohashi, Satoshi Matsuyama, Kouji Inagaki, Yasuhisa Sano, Kazuto Yamauchi, and Yoshitada Morikawa: Japanese Journal of Applied Physics 57, 055703 (2018)a

INAOKA, Takeshi [C class; 1000 (B)] (150)
— *Search and realization of novel electronic properties of solid surfaces and interfaces and of small particles*

1. Classical electricity analysis of the coupling mechanisms between admolecule vibrations and localized surface plasmons in STM for vibration detectability
   T. Inaoka and Y. Uehara: J. Appl. Phys.**122** (2017) 085306/1-11.

ISHIBASHI, Shoji [C class; 5500 (B)] (82)
— *Prediction of properties of organic ferroelectrics and piezoelectrics by first-principles calculation*

1. Strong polarization switching with low-Energy loss in hydrogen-bonded organic antiferroelectrics
   S. Horiuchi, R. Kumai, and S. Ishibashi: Chem. Sci. **9** (2018) 425.
2. Field-induced antipolar-polar structural transformation and giant electrostriction in organic crystal
   K. Kobayashi, S. Horiuchi, S. Ishibashi, Y. Murakami, and R. Kumai: J. Am. Chem. Soc. **140** (2018) 3842.
3. Computational findings of metastable ferroelectric phases of squaric acid
   S. Ishibashi, S. Horiuchi, and R. Kumai: submitted to Phys. Rev. B.

ISHIDA, Kunio [B class; 1300 (B)] (292,294)
— *Study of the initial process of THz-light induced structural change*
— *Ultrafast nonadiabatic dynamics of electron-phonon-photon systems*

ISHIHARA, Sumio [B class; 1300 (B)] (199)
— *Electronic state and transient dynamics in complex electronic systems*
— *Transient Quantum Dynamics in Complex Many Electron Systems*

1. Quantum-disordered state of magnetic and electric dipoles in an organic Mott system
   M. Shimozawa, K. Hashimoto, A. Ueda, Y. Suzuki, K. Sugii, S. Yamada, Y. Imai, R. Kobayashi, K. Itoh, S. Iguchi, M. Naka, S. Ishihara, H. Mori, T. Sasaki and M. Yamashita: Nature Communications **8** (2018) 1821.
2. Double-Exchange Interaction in Optically Induced Nonequilibrium State: A Conversion from Ferromagnetic to Antiferromagnetic Structure
   A. Ono and S. Ishihara: Phys. Rev. Lett. **119** (2017) 207202.
3. Coulomb Correlations Intertwined with Spin and Orbital Excitations in $LaCoO_3$
   K. Tomiyasu, J. Okamoto, H. Y. Huang, Z. Y. Chen, E. P. Sinaga, W. B. Wu, Y. Y. Chu, A. Singh, R.-P. Wang, F. M. F. de Groot, A. Chainani, S. Ishihara, C. T. Chen, and D. J. Huang: Phys. Rev. Lett. **119** (2017) 196402.
4. Spin and charge fluctuations near metal-insulator transition in dimer-type molecular solid
   N. Sato, T. Watanabe, M. Naka, S. Ishihara: J. Phys. Soc. Jpn. **86** (2017) 053701/1-5.
5. Optical suppression of electron motion in low-dimensional correlated electron system
   A. Ono, H. Hashimoto, and S. Ishihara: Phys. Rev. B **95**(2017) 085123.
6. ”Photoinduced charge-order melting dynamics in a one-dimensional interacting Holstein model
   H. Hashimoto and S. Ishihara: Phys. Rev. B **96** (2017) 035154.

ISHII, Fumiyuki [B,C class; 9500 (B)] (53,55)
— *First-principles calculation of Rashba effect at oxides/noble-metal interfaces*
— *First-principles calculations of spin textures at the surfaces and interfaces*
— *First-principles study of magnetic stability and transport properties in oxides thin-films and interfaces*

1. Strain-induced large spin splitting and persistent spin helix at LaAlO3/SrTiO3 interface
   N. Yamaguchi and F. Ishii: Applied Physics Express **10**, (2017) 123003.
2. First-principles study of electric-field-induced topological phase transition in one-bilayer Bi(111)
   H. Sawahata, N. Yamaguchi, H. Kotaka, and F. Ishii: Jpn. J. App. Phys., **57**, (2018) 030309 .
3. Large Anomalous Nernst Coefficient in an oxide Skyrmion Crystal Chern Insulator
   Y.P. Mizuta, H. Sawahata, and F. Ishii: arXiv:1803.08148.
4. First-principles study on thermoelectric properties of half-Heusler compounds CoMSb(M=Sc, Ti, V, Cr, and Mn)
   S. Minami, F. Ishii, Y.P. Mizuta, and M. Saito: arXiv:1804.00297.

ISOBE, Masaharu [B class; 700 (B)] (308)
— *Nonequilibirum phase transition and shock wave phenomena in the dense hard sphere systems*

1. Clustering Impact Regime with Shocks in Freely Evolving Granular Gas
   M. Isobe: EPJ Web Conf., **140** (2017) 04006.
2. 剛体球系の結晶化—高速アルゴリズムによる相転移の神秘の解明—
   礒部雅晴：日本結晶成長学会誌, **44** (2017) 44-3-05.

IYODA, Eiki [C class; 1000 (B)] (302)
— *Numerical study of thermalization in isolated quantum systems*

1. Numerical Large Deviation Analysis of Eigenstate Thermalization Hypothesis
   T. Yoshizawa, E. Iyoda, and T. Sagawa: arXiv:1712.07289.

JESCHKE, Harald [C class; 5000 (B)] (260)
— *Pressure dependence of electronic structure and superconductivity in intercalated FeSe*

KAGESHIMA, Hiroyuki [C class; 1000 (B)] (149)
— *Study on physical properties of structural elementary excitations of semiconductor surfaces and interfaces*

1. Oxygen concentration dependence of silicon oxide dynamical properties

Yuji Yajima, Kenji Shiraishi, Tetsuo Endoh, and Hiroyuki Kageshima: Jpn. J. Appl. Phys. **57** (2018) 06KD01.

KAKEHASHI, Yoshiro [B class; 400 (B)] (163)
— *Quantitative Calculations of Momentum Distribution Function and Quasiparticle State in Ferromagnetic Transition Metals and Compounds Based on the First-Principles Momentum Dependent Local Ansatz Theory*

KAMIHARA, Yoichi [B class; 400 (B)] (161)
— *Research on work functions of mixed anion layered compounds*

KAMIYA, Yoshitomo [C class; 4500 (B)] (263)
— *Quantum Monte Carlo study of Majorana Qubits at the surface of topological insulators*

1. Majorana Stripe Order on the Surface of a Three-Dimensional Topological Insulator
   Y. Kamiya, A. Furusaki, J. C. Y. Teo, and G.-W. Chern: arxiv:1711.03632 (under review).

KARIYADO, Toshikaze [B class; 800 (B)] (305)
— *Manipulation of Topological States by Real-Space Structure*

1. Many-Body Chern Numbers of $\nu = 1/3$ and $1/2$ States on Various Lattices
   K. Kudo, T. Kariyado, Y. Hatsugai: J. Phys. Soc. Jpn. **86** (2017) 103701.
2. Evolution of band topology by competing band overlap and spin-orbit coupling: Twin Dirac cones in Ba_3SnO as a prototype
   T. Kariyado and M. Ogata: Phys. Rev. Materials **1** (2017) 061201.
3. Topological States Characterized by Mirror Winding Numbers in Graphene with Bond Modulation
   T. Kariyado and X. Hu: Sci. Rep. **7** (2017) 16515.

KASAMATSU, Shusuke [C class; 2500 (B)] (121)
— *First-principles calculation of solid oxygen using the vdW-DF+U method*

1. First-principles description of van der Waals bonded spin-polarized systems using the vdW-DF+U method: Application to solid oxygen at low pressure
   S. Kasamatsu, T. Kato, and O. Sugino: Phys. Rev. B **95** (2017) 235120.

KATO, Takeo [D class; 1000 (B)] (301)
— *Transport properties of one-dimensional interacting electron systems by a quantum Monte Carlo method*

KATO, Yusuke [C class; 7500 (B)] (226)
— *Finite-size effect and hysteresis in chiral helimagnets*
— *Physical properties of the chiral helimagnet with next-nearest-neighbor interaction*

KAWAKAMI, Norio [C class; 10500 (B)] (178)
— *Pursuit of topologically nontrivial materials and topological phase transition in strongly correlated quantum systems*
— *Topological transport and nonequilibrium phenomena in strongly correlated quantum systems*

1. Fate of Majorana Modes in CeCoIn5/YbCoIn5 Superlattices: A Test Bed for the Reduction of Topological Classification
   Tsuneya Yoshida, Akito Daido, Youichi Yanase, and Norio Kawakami: Phys. Rev. Lett. 118, 147001 (2017).
2. Strong enhancement of the Edelstein effect in f-electron systems
   Robert Peters and Youichi Yanase: Phys. Rev. B 97, 115128 (2018).

KAWAMURA, Hikaru [B,C class; 11400 (B)] (214,216)
— *Novel order in frustrated magnets*
— *Numerical simulations on statistical models of earthquakes*

1. Randomness-Induced Quantum Spin Liquid Behavior in the s = 1/2 Random J1-J2 Heisenberg

Antiferromagnet on the Honeycomb Lattice
K. Uematsu and H. Kawamura: J. Phys. Soc. Jpn. 86, 044704/1-12 (2017).

2. Statistical properties of the one-dimensional Burridge-Knopoff model obeying the date and state dependent friction law
H. Kawamura, Yushi Ueda, Shingo Kakui, Syouji Morimoto and Takumi Yamamoto: J. Phys. Soc. Jpn. 85, Phys. Rev. E 95, 042122/1-14 (2017).

KAWASHIMA, Naoki [E class; 40500 (B)] (207)
— *Effective Model Through Continuous and Descrete Space Quantum Monte Carlo Simulations*

1. Quantum lattice model solver HPhi
Mitsuaki Kawamura, Kazuyoshi Yoshimi, Takahiro Misawa, Youhei Yamaji, Synge Todo, and Naoki Kawashima: Computer Physics Communications. **217**, 180-192.
2. Variational Monte Carlo method for fermionic models combined with tensor networks and applications to the hole-doped two-dimensional Hubbard model
Hui-Hai Zhao, Kota Ido, Satoshi Morita, and Masatoshi Imada: Phys. Rev. B. **96**, 085103/1-16.
3. Ground state properties of Na2IrO3 determined from ab initio Hamiltonian and its extensions containing Kitaev and extended Heisenberg interactions
Tsuyoshi Okubo, Kazuya Shinjo, Youhei Yamaji, Naoki Kawashima, Shigetoshi Sota, Takami Tohyama, and Masatoshi Imada: Phys. Rev. B. **96**, 054434/1-12.
4. Proposal of a spin-one chain model with competing dimer and trimer interactions
Yun-Tak Oh, Hosho Katsura, Hyun-Yong Lee, and Jung Hoon Han: Phys. Rev. B. **96**, 165126/1-8.
5. Disordered quantum spin chains with long-range antiferromagnetic interactions
N. Moure, Hyun-Yong Lee, S. Haas, R. N. Bhatt, and S. Kettemann: Phys. Rev. B. **97**, 014206/1-6.
6. Tensor renormalization group with randomized singular value decomposition
Satoshi Morita, Ryo Igarashi, Hui-Hai Zhao, and Naoki Kawashima: Phys. Rev. E. **97**, 033310/1-6.

KIM, Kang [C class; 7000 (B)] (230)
— *Elucidation of heterogeneous dynamics hidden in glass-forming liquids*

1. Identifying time scales for violation/preservation of Stokes-Einstein relation in supercooled water
T. Kawasaki and K. Kim: Sci. Adv. **3**, e1700399 (2017).
2. Connecting thermodynamic and dynamical anomalies of water-like liquid-liquid phase transition in the FermiJagla model
S. Higuchi, D. Kato, D. Awaji, and K. Kim: J. Chem. Phys. **148**, 094507 (2018).
3. How do hydrogen bonds break in supercooled water?: Detecting pathways not going through the saddle point of two-dimensional potential of mean force
T. Kikutsuji, K. Kim, and N. Matsubayashi: submitted to J. Chem. Phys. (2018).

KITA, Takafumi [C class; 8000 (B)] (179,181)
— *Microscopic analysis of cuprate superconductors in FLEX-S approximation*
— *Microscopic analysis of the vortex state in superconductors using the augmented quasiclassical equations with the Lorentz force, Kopnin force and slope in the density of state*

1. Charging in a Superconducting Vortex Due to the Three Force Terms in Augmented Eilenberger Equations
H. Ueki, M. Ohuchi, and T. Kita, J. Phys. Soc. Jpn. **87**, 044704 (2018).

KITAO, Akio [C class; 6500 (B)] (236)
— *Efficient sampling simulation of the soft modes significantly contribute to protein properties*

1. Binding free energy analysis of protein-protein docking model structures by evERdock.
K. Takemura, N. Matubayasi, and A. Kitao: J. Chem. Phys., **148** (2018) 105101.
2. Origins of biological function in DNA and RNA hairpin loop motifs from replica exchange molecular dynamics simulation.
J.B. Swadling, K. Ishii, T. Tahei, and A. Kitao: Phys. Chem. Chem. Phys. **20** (2018) 2990.

3. Protein–Ligand Dissociation Simulated by Parallel Cascade Selection Molecular Dynamics
   D.P. Tran, K. Takemura, and A. Kitao: J. Chem. Theory Comput. **14** (2017) 404.
4. Salt bridge formation between the I-BAR domain and lipids increases lipid density and membrane curvature
   K. Takemura, S. Suetsugu, and A. Kitao: Sci. Rep. **7** (2017) 6808.

KOBAYASHI, Katsuyoshi [B class; 300 (B)] (166)

— *Search for electronic properties of new nanoscale interfaces*

1. Calculation of spin states of photoelectrons emitted from spin-polarized surface states of Bi(111) surfaces with a mirror symmetry
   K. Kobayashi et al.: Phys. Rev. B **95** (2017) 205436.

KOBAYASHI, Nobuhiko [C class; 8000 (B)] (61)

— *First-principles study of quantum transport in nanostructures*

1. Thermoelectric properties of a magnetic semiconductor CuFeS2
   H.Takaki, K.Kobayashi, M.Shimono, N.Kobayashi, K.Hirose, N.Tsujii, T.Mori: Materials Today Physics 3 85e92 (2017).
2. Enhancement of thermoelectric properties in surface nanostructures
   H.Takaki, K.Kobayashi, M.Shimono, N.Kobayashi, K.Hirose: J. Electron. Mater. 46 5593 (2017).
3. Electronic band structure of TiN/MgO nanostructures
   K.Kobayashi, H.Takaki, M.Shimono, N.Kobayashi, K.Hirose: Jpn. J. Appl. Phys. 56 04CK06 (2017).
4. First-principles calculations of Seebeck coefficients in a magnetic semiconductor CuFeS2,
   H.Takaki, K.Kobayashi, M.Shimono, N.Kobayashi, K.Hirose, N.Tsujii, T.Mori: Appl. Phys. Lett. 110, 072107 (2017).
5. Charge transport calculations by a wave-packet dynamical approach using maximally localized Wannier functions based on density functional theory: Application to high-mobility organic semiconductors
   H.Ishii, N.Kobayashi, K.Hirose: Phys. Rev. B 95, 035433 (2017).

KOGA, Akihisa [C,D class; 17000 (B)] (173)

— *Effect of the spin-orbit coupling in the multiorbital model on the honeycomb lattice*

— *Effect of thermal fluctuation for exotic quantum phases in strongly correlated multiorbital systems*

— *Numerical analysis for extotic quantum states in strongly correlated electron systems*

1. Antiferromagnetic order in the Hubbard model on the Penrose lattice
   A. Koga and H. Tsunetsugu: Phys. Rev. B 96, 214402 (2017).
2. Charge Kondo effect and superconductivity in the Falikov-Kimball model with pair hopping
   R. Shinzaki, J. Nasu, and A. Koga: Phys. Rev. B 97, 125130 (2018).
3. Interlayer coupling effect on a bilayer Kitaev model
   H. Tomishige, J. Nasu, and A. Koga: Phys. Rev. B 97, 094403 (2018).
4. Role of spin-orbit coupling in the Kugel-Khomskii model on the honeycomb lattice
   A. Koga, S. Nakauchi, and N. Joji: Phys. Rev. B 97, 094427 (2018).
5. Majorana fermions in the Kitaev quantum spin system α-RuCl3
   S.-H. Do, S.-Y. Park, J. Yoshitake, J. Nasu, Y. Motome, Y. S. Kwon, D. T. Adroja, D. J. Voneshen, K. Kim, T.-H. Jang, J.-H. Park, K.-Y. Choi and S. Ji: Nat. Phys. 13, 1079 (2017).
6. Thermal Transport in the Kitaev Model
   N. Joji, J. Yoshitake, and Y. Motome:Phys. Rev. Lett. 119, 127204 (2017).
7. Chiral spin liquids at finite temperature in a three-dimensional Kitaev model
   Y. Kato, Y. Kamiya, J. Nasu, and Y. Motome: Phys. Rev. B 96, 174409 (2017).

KOTAKA, Hiroki [C class; 1500 (B)] ()

— *Structural search of negative electrode candidate for sodium ion battery*

KOURA, Akihide [C class; 3500 (B)] (117)

— *Ab initio molecular dynamics study of static structure of glasses*

1. Pressure dependence of the static structure of liquid GeTe based on *ab initio* molecular dynamics simulations
   A. Koura and F. Shimojo: EPJ Web of Conferences **151** (2017) 01002.
2. Static structure of glass $Ag_x(GeSe_3)_{1-x}$ based on *ab initio* molecular dynamics study
   A. Koura and F. Shimojo: Physics Reports of Kumamoto University, **14**(2) (2017) 81-88.
3. *Ab initio* simulation of permanent densification in silica glass
   E. Ryuo, D. Wakabayashi, A. Koura, and F. Shimojo: Phys. Rev. B **96** (2017) 054206.
4. Phonon excitations in a single crystal $Mg_{85}Zn_6Y_9$ with a synchronized long-period stacking ordered phase
   S. Hosokawa, K. Kimura, J. R. Stellhorn, K. Yoshida, K. Hagihara, H. Izuno, M. Yamasaki, Y. Kawamura, Y. Mine, K. Takashima, H. Uchiyama, S. Tsutsui, A. Koura, F. Shimojo: Acta Materialia **146** (2018) 273-279.

KUNISADA, Yuji [C class; 6500 (B)] (76)
— *Reduction of Rare Metals in Fuel Cell Catalysts and Hydrogen Permeable Membrane*

1. 計算科学的手法による水表面上での水素分子の吸着特性の解明
   國貞雄治: J. Vac. Soc. Jpn. **60** (2017) 249.
2. Estimating the Spatial Distribution of Ca Dopants in α-SiAlON by Statistical Analysis of HAADF-STEM Image
   N. Sakaguchi, F. Yamaki, G. Saito, Y. Kunisada: Mater. Trans. **58** (2017) 1341.
3. Diffusion of a Single Platinum Atom on Light-Element Doped Graphene
   S. Hasegawa, Y. Kunisada, N. Sakaguchi: J. Phys. Chem. C **121** (2017) 17787.
4. Hydrogen separation by nanocrystalline titanium nitride membranes with high hydride ion conductivity
   C. Kura, Y. Kunisada, E. Tsuji, C. Zhu, Hi. Habazaki, S. Nagata, M. Patrick Muller, R. A. De Souza, Y. Aoki: Nat. Ener. **2** (2017) 786.
5. 窒化チタン微結晶膜におけるヒドリドイオン伝導の発現とそれによる常温水素膜分離
   青木芳尚，倉千晴，國貞雄治，朱春宇，幅崎浩樹: 真空技術協会誌 **132** (2017) 32.
6. Inelastic Electron Tunneling Mediated by Molecular Quantum Rotator
   T. Sugimoto, Y. Kunisada, K. Fukutani: Phys. Rev. B **96** (2017) 241409(R).
7. Enhanced hydrogen permeability of hafnium nitride nanocrystalline membranes by interfacial hydridic conduction
   C. Kura, S. Fujimoto, Y. Kunisada, D. Kowalski, E. Tsuji, C. Zhu, H. Habazaki, Y. AOKI : J. Mater. Chem. A **6** (2018) 2730.

KUROKI, Kazuhiko [C class; 5000 (B)] (186)
— *Study on correlation and superconductivity in multiorbital/multi-site systems based on realistic electronic structures*

1. Finite-energy spin fluctutations as a pairing glue in systems with coexisiting electron and hole bands
   M. Nakata, D. Ogura, H. Usui, K. Kuroki: Phys. Rev. B. **95** (2017) 214509.
2. DMFT Study on the electron-hole asymmetry of the electron correlation strength in the high T_c cuprates
   R. Mizuno, M. Ochi, K. Kuroki: J. Phys. Soc. Jpn. **86** (2017) 114706.
3. Possible high-T_c superconductivity due to incipient narrow bands originating from hidden ladders in Ruddlesden-Popper compounds
   D. Ogura, H. Aoki, K. Kuroki: Phys. Rev. B **96** (2017) 184513.
4. Wide applicability of high T_c pairing originating from coexisting wide and incipient narrow bands in quasi-one-dimensional systems
   K. Matsumoto, D. Ogura, K. Kuroki: Phys. Rev. B **97** (2018) 014516.

KUROSAWA, Masashi [C class; 4000 (B)] (107)
— *First-Principles Study on New Group-IV Semiconductor Alloys*

KUSAKABE, Koichi [C class; 2000 (B)] (129)
— *Curious chemical reactions of the entangled singlet state in nanographene VANG*

MACHIDA, Manabu [B class; 1500 (B)] (289,290)
— *The radiative transport equation with FDM and FEM*
— *Transport phenomena and optical tomography*

MAKINO, Takayuki [C class; 2000 (B)] (127)
— *Study on electronic structures and density of states in perovskite-type lead-halide mixed crystals*

MASAKI-KATO, Akiko [C class; 8000 (B)] (224)
— *Excitation dynamics of two-dimensional quantum spin systems*
— *The development of the parallelizable Quantum Monte Carlo method and the application to two-dimensional quantum lattice systems*

MATSUKAWA, Hiroshi [E class; 11500 (B)] ()
— *Science of Friction*

MATSUMOTO, Munehisa [C class; 5000 (B)] (87)
— *Relativistic electronic structure calculations for f-d intermetallics*

MATSUNAKA, Daisuke [C class; 1500 (B)] (136)
— *First-principles Study of Defects of Magnesium Alloys*

1. EAM ポテンシャルにおける異種原子間相互作用の検討
   松中大介, 木村文彦: 計算工学講演論文集, **23** (2018) B-01-07.
2. Atomistic study of effets of normal stress on fundametal deformation modes in magnesium
   S. Yoshikawa and D. Matsunaka: to be submitted.

MATSUSHITA, Katsuyoshi [C class; 3000 (B)] (272)
— *Investigation of Cell Elongation Effect on Collective Motion*
— *Numerical study of cell-elongation inducing dynamical transition*

1. Mechanical Morphogenesis in Differential Pattern Growth
   Katsuyoshi Matsushita, Kazuya Horibe, Naoya Kamamoto, Ken-Ichi Hironaka and Koichi Fujimoto: submitted to Proc. ALIFE2018
2. Emergence of collective propulsion through cell-cell adhesion
   Katsuyoshi Matsushita: Phys. Rev. E in print
3. Elementary Movement Step of adhesion-interaction driving
   Katsuyoshi Matsushita: Proceedings of symposium on simulations of traffic flow 23, 37 (2017)

MAYUMI, Koichi [B class; 800 (B)] (304)
— *Coarse-Grained Molecular Dynamics Simulation of Slide-Ring Gel Networks*

MISAWA, Takahiro [E class; 13500 (B)] (174,350)
— *Study of correlated topological materials using many-variable variational Monte Carlo method*

1. Quantum lattice model solver $H\Phi$
   M. Kawamura, K. Yoshimi, T. Misawa, *et al.*, Comp. Phys. Commun. **217**, 180-192 (2017).
2. 量子格子模型の汎用数値対角化パッケージ H Φ—スピン液体近傍の熱・スピン励起への適用—
   山地洋平・三澤貴宏・吉見一慶・河村光晶・藤堂眞治・川島直輝, 固体物理, Vol.52, No10 (2017).
3. ＜コラム＞ mVMC 多変数変分モンテカルロ法のオープンソースソフトウェア
   三澤貴宏・今田正俊, 固体物理, Vol.52, No11 (2017).
4. Superconductivity Emerging from Excitonic Mott insulator - Theory of Alkaline Doped Fullerene
   T. Misawa and M. Imada, arXiv:1711.10205
5. mVMC - Open-source software for many-variable variational Monte Carlo method
   T. Misawa *et al.*, arXiv:1711.11418
6. Asymmetric melting of one-third plateau in kagome quantum antiferromagnets

T. Misawa, Y. Motoyama and Y. Yamaji, arXiv:1801.07128.

7. Finite-Temperature Signatures of Spin Liquids in Frustrated Hubbard Model
   T. Misawa and Y. Yamaji, J. Phys. Soc. Jpn **87**, 023707 (2018).

MIYASHITA, Seiji [C class; 5000 (B)] (258)
— *Direct numerical method for quantum response and quantum dynamics*

1. Nontrivial phase diagram for an elastic interaction model of spin crossover materials with antiferromagnetic-like short-range interactions.1
   M. Nishino, S. Miyashita and P. A. Rikvold : Phys. Rev. B. **96** (2017) 144425.
2. Cluster evolution in molecular three-dimensional spin-crossover systems. 2
   L. Stoleriu, M. Nishino, S. Miyashita, A. Stancu, A. Hauser and C. Enachescu : Phys. Rev. B. **96**(2017) 064115.
3. Theoretical approach for elastically driven cooperative switching of spin-crossover compounds impacted by an ultrashort laser pulse.1
   C. Enachescu, L. Stoleriu, M. Nishino, S. Miyashita, A. Stancu, M. Lorenc, R.Bertoni, H. Cailleau and E. Collet: Phys. Rev. B.**95** (2017) 224107.
4. Synergetic effect of spin-orbit coupling and Zeeman splitting on the optical conductivity in the one-dimensional Hubbard model.3
   A. Bolens, H. Katsura, M. Ogata and S. Miyashita: Phys. Rev. B.**95** (2017) 235115.
5. Perspectives for high-performance permanent magnets: applications, coercivity, and new materials. 2
   S. Hirosawa, M. Nishino and S. Miyashita: Adv. Nat. Sci. **8** (2017) 013002.
6. Perspectives of stochastic micromagnetism of Nd2Fe14B and computation of thermally activated reversal process.
   S. Miyashita, M. Nishino, Y. Toga, T. Hinokihara, T. Miyake, S. Hirosawa and A. Sakuma: Scripta Materialia. (2017) in press.
7. Exploration of the effects of dipole-dipole interactions in Nd2Fe14B thin films based onf a stochastic cutoff method with a novel efficient algorithm.
   T. Hinokihara, M. Nishino, Y. Toga and S. Miyashita: Phys. Rev. B. in press.
8. Systematic Construction of Counterexamples to the Eigenstate Thermalization Hypothesis.
   N. Shiraishi and T. Mori: Phys. Rev. Lett.**119** (2017) 030601.
9. Thermalization without eigenstate thermalization hypothesis after a quantum quench.
   T. Mori and N. Shiraishi: Phys. Rev. E. **96** (2017) 022153.
10. Classical ergodicity and quantum eigenstate thermalization: Analysis in fully connected Ising ferromagnets.
    T. Mori: Phys. Rev. E. **96** (2017) 012134.
11. Distribution of eigenstate populations and dissipative beating dynamics in uniaxial single-spin magnets.
    T. Hatomura, B. Barbara and S. Miyashita: Phys. Rev. B. **96**(2017) 134309.
12. Shortcuts to Adiabaticity in the Infinite-Range Ising Model by Mean-Field Counter-Diabatic Driving.
    T. Hatomura: J. Phys. Soc. Jpn. **86** (2017) 094002.
13. Shortcuts to adiabatic cat-state generation in bosonic Josephson junctions.
    T. Hatomira: New J. Phys. **20** (2018) 015010.
14. Entanglement prethermalization in the Tomonaga-Luttinger model.
    E. Kaminishi, T. Mori, T. N. Ikeda and M. Ueda: Phys. Rev. A **97** (2018) 013622.
15. Diffusive real-time dynamics of a particle with Berry curvature.
    K. Misaki, S. Miyashita and N. Nagaosa: Phys. Rev. B **97** (2018) 075122.

MIZUGUCHI, Tomoko [C class; 1500 (B)] (287)
— *Effect of interface on the structure and properties of water confined in nanopore*

MIZUKAMI, Wataru [C class; 2000 (B)] (126)
— *Construction and application of anharmonic potentials for adsorbed molecule on crystal/nanoparticle surface*

MOMIDA, Hiroyoshi [C class; 3500 (B)] (115)
— *First-principles study of electronic structures of energy device materials*

1. Cathode Properties of Perovskite-Type NaMF$_3$ (M = Fe, Mn, and Co) Prepared by Mechanical Ball Milling for Sodium-Ion Battery
   A. Kitajou, Y. Ishado, T. Yamashita, H. Momida, T. Oguchi and S. Okada: Electrochimica Acta **245** (2017) 424.
2. Topological Interface States in the Natural Heterostructure (PbSe)$_5$(Bi$_2$Se$_3$)$_6$ with Bi$_{\mathrm{Pb}}$ Defects
   H. Momida, G. Bihlmayer, S. Blügel, K. Segawa, Y. Ando and T. Oguchi: Phys. Rev. B **97** (2018) 035113.
3. Effects of Lattice Parameters on Piezoelectric Constants in Wurtzite Materials: A Theoretical Study using First-Principles and Statistical-Learning Methods
   H. Momida and T. Oguchi: Appl. Phys. Express **11** (2018) 041201.
4. First-Principles Calculations on the Origin of Mechanical Properties and Electronic Structures of 5d Transition Metal Monocarbides MC (M = Hf, Ta, W, Re, Os, Ir, and Pt)
   M. Fukuichi, H. Momida, M. Geshi, M. Michiuchi, K. Sogabe and T. Oguchi: J. Phys. Soc. Jpn. **87** (2018) 044602.
5. First-Principles Study on Cathode Properties of Li$_2M$TiO$_4$ (M = V, Cr, Mn, Fe, Co, and Ni) with Oxygen Deficiency for Li-Ion Batteries
   M. Hamaguchi, H. Momida and T. Oguchi: J. Phys. Soc. Jpn., in press.

MORI, Takashi [C class; 2500 (B)] (276)
— *Dynamics of isolated quantum many-body spin systems*

MORIKAWA, Yoshitada [C class; 4500 (B)] (168)
— *First-principles Thermodynamics and Statistical Mechanics Simulations of Catalytic Reactions at Solid Surfaces*

1. Image potential states from the van der Waals density functional
   I. Hamada, Y. Hamamoto, and Y. Morikawa: J. Chem. Phys., **147**, (2017) 044708/1-6.
2. Desorption Dynamics of CO$_2$ from Formate Decomposition on Cu(111)
   F. Muttaqien, H. Oshima, Y. Hamamoto, K. Inagaki, I. Hamada, and Y. Morikawa: Chem. Comm., **53**, (2017) 9222-9225.
3. CO$_2$ Adsorption on the Copper Surfaces: van der Waals Density Functional and TPD Studies
   F. Muttaqien, Y. Hamamoto, I. Hamada, K. Inagaki, Y. Shiozawa, K. Mukai, T. Koitaya, S. Yoshimoto, J. Yoshinobu, and Y. Morikawa:J. Chem. Phys., **147**, (2017) 094702/1-8.
4. First-Principles Molecular Dynamics Analysis of Ligand-Free SuzukiMiyaura Cross-Coupling in Water: Transmetalation and Reductive Elimination
   Teruo Hirakawa, Yuta Uramoto, Susumu Yanagisawa, Takashi Ikeda, Kouji Inagaki, and Yoshitada Morikawa: J. Phys. Chem. C,**121**, (2017) 19904-19914.
5. Augmented pH-sensitivity Absorbance of Ruthenium(II) Bis(bipyridine) Complex with Elongation of the Conjugated Ligands : An Experimental and Theoretical Investigations
   Siew San Tan, Susumu Yanagisawa Kouji Inagaki Yoshitada Morikawa and Mohammad B. Kassim: Phys. Chem. Chem. Phys., **19**, (2017) 25734-25745.
6. Hybrid Image Potential States in Molecular Overlayers on Graphene
   S. A. Wella, H. Sawada, N. Kawaguchi, F. Muttaqien, K. Inagaki, I. Hamada, Y. Morikawa, and Y. Hamamoto: Phys. Rev. Materials, **1**, (2017) 061001/1-5.
7. Individual Atomic Imaging of Multiple Dopant Sites in As-Doped Si Using Spectro-Photoelectron Holography
   Kazuo Tsutsui, Tomohiro Matsushita, Kotaro Natori, Takayuki Muro, Yoshitada Morikawa, Takuya Hoshii, Kuniyuki Kakushima, Hitoshi Wakabayashi, Kouichi Hayashi, Fumihiko Matsui, and Toyohiko Kinoshita,: Nano. Lett., **17**, (2017) 7533-7538.
8. First-principles Study of ZnSnAs$_2$-Based Dilute Magnetic Semiconductors
   Hidetoshi Kizaki, and Yoshitada Morikawa: Jpn. J. App. Phys., **57**, (2018) 020306/1-4.
9. Mechanistic Analysis of Oxygen Vacancy Formation and Ionic Transport in Sr$_3$Fe$_2$O$_{7-\delta}$
   Tadashi Ohta, Hidetoshi Kizaki, and Yoshitada Morikawa: J. Phys. Chem. C, **122**, (2018)

4172-4181.

10. Platinum-catalyzed hydrolysis etching of SiC in water: A density functional theory study
    Pho Van Bui, Daisetsu Toh, Ai Isohashi, Satoshi Matsuyama, Kouji Inagaki, Yasuhisa Sano, Kazuto Yamauchi, and Yoshitada Morikawa Jpn. J. Appl. Phys., **57**, (2018) 055703/1-5.

MORIMOTO, Kenichi [C class; 500 (B)] ()
— *Shape-Optimization Simulation in Turbulent Heat Transfer Problem*

MORITA, Satoshi [B class; 900 (B)] (303)
— *Development of parallel computing library for tensor network methods with symmetries*

1. Variational Monte Carlo method for fermionic models combined with tensor networks and applications to the hole-doped 2D Hubbard model
   H.-H. Zhao, K. Ido, S. Morita and M. Imada: Phys. Rev. B **96** 085103 (2017).
2. Tensor Renormalization Group with Randomized Singular Value Decomposition
   S. Morita, R. Igarashi, H.-H. Zhao, and N. Kawashima: Phys. Rev. E **97** 033310 (2018).

MOTOME, Yukitoshi [C class; 12500 (B)] (176)
— *Numerical study of correlated electron systems with strong spin-orbit coupling*

1. Zero-Field Skyrmions with a High Topological Number in Itinerant Magnets
   R. Ozawa, S. Hayami, and Y. Motome: Phys. Rev. Lett. **118** (2017) 147205.
2. Monte Carlo Study of Magnetoresistance in a Chiral Soliton Lattice
   S. Okumura, Y. Kato, and Y. Motome: J. Phys. Soc. Jpn. **86** (2017) 063701.
3. Effective bilinear-biquadratic model for noncoplanar ordering in itinerant magnets
   S. Hayami, R. Ozawa, and Y. Motome: Phys. Rev. B **95** (2017) 224424.
4. Majorana dynamical mean-field study of spin dynamics at finite temperatures in the honeycomb Kitaev model
   J. Yoshitake, J. Nasu, Y. Kato, and Y. Motome: Phys. Rev. B **96** (2017) 024438.
5. Temperature evolution of spin dynamics in two- and three-dimensional Kitaev models: Influence of fluctuating Z2 flux
   J. Yoshitake, J. Nasu, and Y. Motome: Phys. Rev. B **96** (2017) 064433.
6. Shape of magnetic domain walls formed by coupling to mobile charges
   R. Ozawa, S. Hayami, K. Barros, and Y. Motome: Phys. Rev. B **96** (2017) 094417.
7. Finite-temperature phase transition to a Kitaev spin liquid phase on a hyperoctagon lattice: A large-scale quantum Monte Carlo study
   P. A. Mishchenko, Y. Kato, and Y. Motome: Phys. Rev. B **96** (2017) 125124.
8. Majorana fermions in the Kitaev quantum spin system α-RuCl$_3$
   S.-H. Do, S.-Y. Park, J. Yoshitake, J. Nasu, Y. Motome, Y. S. Kwon, D. T. Adroja, D. J. Voneshen, K. Kim, T.-H. Jang, J.-H. Park, K.-Y. Choi, and S. Ji: Nat. Phys. **13** (2017) 1079.
9. Thermal Transport in the Kitaev Model
   J. Nasu, J. Yoshitake, and Y. Motome: Phys. Rev. Lett. **119** (2017) 127204.
10. Chiral spin liquids at finite temperature in a three-dimensional Kitaev model
    Y. Kato, Y. Kamiya, J. Nasu, and Y. Motome: Phys. Rev. B **96** (2017) 174409.
11. Kitaev-Heisenberg Hamiltonian for high-spin d7 Mott insulators
    R. Sano, Y. Kato, and Y. Motome: Phys. Rev. B **97** (2018) 014408.
12. Multiple Dirac cones and topological magnetism in honeycomb-monolayer transition metal trichalcogenides
    Y. Sugita, T. Miyake, and Y. Motome: Phys. Rev. B **97** (2018) 035125.
13. Emergent odd-parity multipoles and magnetoelectric effects on a diamond structure: Implication for the 5d transition metal oxides AOsO4 (A=K, Rb, and Cs)
    S. Hayami, H. Kusunose, and Y. Motome: Phys. Rev. B **97** (2018) 024414.
14. Generation and control of noncollinear magnetism by supercurrent
    R. Takashima, Y. Kato, Y. Yanase, and Y. Motome: Phys. Rev. B **97** (2018) 081107(R).
15. Lock-in of a Chiral Soliton Lattice by Itinerant Electrons
    S. Okumura, Y. Kato, and Y. Motome: J. Phys. Soc. Jpn. **87** (2018) 033708.

MURASHIMA, Takahiro [C class; 2000 (B)] (278)
— *Analysis of Glassy State of Bead-Spring Chains*

1. Elongational viscosity of weakly entangled polymer melt via coarse-grained molecular dynamics simulation
   T. Murashima et al: submitted to Nihon Reoroji Gakkaishi
2. Inter node parallelization of multiscale fluid particle simulation towards large-scale polymeric fluid simulation
   T. Murashima: Microsystem Technologies, 24, 765-769 (2018).

NADA, Hiroki [C class; 4000 (B)] (266)
— *Molecular Dynamics Simulation Study of Crystal Nucleation Mechanism of Hydroxyapatite via Formation of Pre-Nucleation Clusters*

1. Development of Nanostructured Water Treatment Membranes Based on Thermotropic Liquid Crystals: Molecular Design of Sub-Nanoporous Materials
   T. Sakamoto, T. Ogawa, H. Nada, K. Nakatsuji, M. Mitani, B. Soberats, K. Kawata, M. Yoshio, H. Tomioka, T. Sasaki, M. Kimura, M. Henmi and T. Kato: Adv. Sci., **5** (2018) 1700405.
2. A New Methodology for Evaluating the Structural Similarity between Different Phases Using a Dimensionality Reduction Technique
   H. Nada: submitted to ACS Omega.

NAKAHARA, Akio [B class; 700 (B)] ()
— *Numerical simulation for memory of flow in paste*

NAKAI, Hiromi [C class; 4500 (B)] (97)
— *First-principles calculation on reversible hydrogenation reaction of toluene using heterogeneous catalyst*

NAKAMURA, Kazuma [C class; 8000 (B)] (59)
— *Ab initio phonon calculations for Sr2IrO4 and Ca5Ir3O12*
— *Development of ab initio many-body perturbation calculation software RESPACK*

1. Uniaxial strain effects on superconducting transition in Re-doped Hg-1223 cuprate superconductors
   M. Mito, K. Ogata, H. Goto, K. Tsuruta, K. Nakamura, H. Deguchi, T. Horide, K. Matsumoto, T. Tajiri, H. Hara, T. Ozaki, H. Takeya, and Y. Takano: Phys. Rev. B **95**, (2017) 064503.
2. Nonlinear Conductivity of Geometrically Frustrated Iridate Ca5Ir3O12
   K. Matsuhira, K. Nakamura, Y. Yasukuni, Y. Yoshimoto, D. Hirai, Z. Hiroi: J. Phys. Soc. Jpn. **87**, (2018) 013703.

NAKANO, Hiroki [C class; 6000 (B)] (242)
— *Numerical study on low-energy states of quantum spin systems*

1. Ferrimagnetism in the Spin-1/2 Heisenberg Antiferromagnet on a Distorted Triangular-Lattice
   H. Nakano and T. Sakai: J. Phys. Soc. Jpn. **86** (2017) 063702(1-5)
2. Quantum Spin Liquid in the Kagome-Lattice Antiferromagnet and Related Systems
   H. Nakano and T. Sakai: Journal of Physics: Conference Series **868** (2017) 012006.
3. Magnetization Process of the Spin-1/2 Triangular-Lattice Heisenberg Antiferromagnet with Next-Nearest-Neighbor Interactions — Plateau or Nonplateau —
   H. Nakano and T. Sakai: J. Phys. Soc. Jpn. **86** (2017) 114705(1-6)
4. $\sqrt{3} \times \sqrt{3}$ 型の歪みを持つ三角格子上の S=1/2 ハイゼンベルク反強磁性体 — 磁化過程と磁化率 —
   嶋田ありさ, 中野博生, 坂井徹, 吉村一良: 粉体および粉末冶金 **65** (2018) 3-9
5. Spin-1/2 Triangular-Lattice Heisenberg Antiferromagnet with $\sqrt{3} \times \sqrt{3}$-Type Distortion — Behavior around the Boundaries of the Intermediate Phase
   A. Shimada, H. Nakano, T. Sakai, and K. Yoshimura: J. Phys. Soc. Jpn. **87** (2018) 034706(1-7).

NAKAYAMA, Takashi [C class; 4000 (B)] (105)
— *First-principles study of ionization and diffusion of metal atoms at metal/solid interfaces in electric*

fields

1. Acceleration of metal-atom diffusion under electric field at metal/insulator interfaces: First principles study
   R. Nagasawa, Y. Asayama, T. Nakayama: Jpn. J. Appl. Phys. **57** (2018) 04FB05.
2. Metal-atom Ionization and Diffusion under Electric Field around Metal/insulator Interfaces; First-principles View
   T. Nakayama, Y. Asayama, R. Nagasawa: ECS Transactions **80** (2017) 285.
3. First-principles study of giant thermoelectric power in incommensurate TlInSe2
   M. Ishikawa, T. Nakayama, K. Wakita, Y. G. Shim, N. Mamedov: J. Appl. Phys. **123** (2018) 161575.
4. Material engineering for silicon tunnel field-effect transistors: isoelectronic trap technology
   T. Mori, S. Iizuka, T. Nakayama: MRS communications **7** (2017) 541.

NISHIDATE, Kazume [C class; 1500 (B)] (134)
— *Organic Molecule on Graphene: Electronic Structure at the Interface and Crystal Growth*

1. First-principles study of electronic structure modulations in graphene on Ru(0001) by Au intercalation
   K. Nishidate, S. Tanibayashi, N. Yoshimoto, and M. Hasegawa: Phys. Rev. B **97** (2018) 115437.

NOBUSADA, Katsuyuki [E class; 25000 (B)] ()
— *Computational studies of electronic and photonic functional nano-interfaces*

NOGUCHI, Hiroshi [C class; 11000 (B)] (217,219)
— *Flow analysis of dilute polymer solution by molecular dynamics simulation*
— *Structure formation of biomembranes*

1. Structure formation induced by two types of banana-shaped proteins adsorbed on lipid membranes
   H. Noguchi and J.-B. Fournier: Soft Matter **13**, 4099 (2017).
2. Acceleration and suppression of banana-shaped-protein-induced tubulation by addition of small membrane inclusions of isotropic spontaneous curvatures
   H. Noguchi: Soft Matter **13**, 7771 (2017).
3. Docosahexaenoic acid preserves visual function by maintaining correct disc morphology in retinal photoreceptor cells
   H. Shindou, H. Koso, J. Sasaki, H. Nakanishi, H. Sagara, K. M. Nakagawa, Y. Takahashi, D. Hishikawa, Y. Iizuka-Hishikawa, F. Tokumasu, H. Noguchi, S. Watanabe, T. Sasaki, and T. Shimizu: J. Bio. Chem. **292**, 12054 (2017).
4. Bilayer sheet protrusions and budding from bilayer membranes induced by hydrolysis and condensation reactions
   K. M. Nakagawa and H. Noguchi: Soft Matter **14**, 1397 (2018).
5. Polymer effects on Karman Vortex: Molecular Dynamics Study
   Y. Asano, H. Watanabe, and H. Noguchi: J. Chem. Phys. **148**, 144901(2018).
6. 短距離古典分子動力学シミュレーションコードの GPGPU 化（１）
   中川恒: 分子シミュレーション研究会会誌“アンサンブル”**19**, 267 (2017).
7. 短距離古典分子動力学シミュレーションコードの GPGPU 化（２）
   中川恒: 分子シミュレーション研究会会誌“アンサンブル”**20**, 40 (2018).

NOGUCHI, Yoshifumi [C class; 6500 (B)] (75)
— *First-principles calculation of singlet-triplet splitting*

1. Quantitative characterization of exciton from GW+Bethe-Salpeter calculation
   D. Hirose, Y. Noguchi, and O. Sugino: J. Chem. Phys. **146** (2017) 044303.
2. Molecular Size Insensitivity of Optical Gap of [n]Cycloparaphenylenes (n = 3-16)
   Y. Noguchi and O. Sugino: J. Chem. Phys. **146** (2017) 144304
3. Effect of dynamical fluctuation of hydration structures on absorption spectra of oxylucifein in aqueous solutions
   M. Hiyama, M. Shiga, N. Koga, O. Sugino, H. Akiyama, and Y. Noguchi: PhysChemChemPhys. **19** (2017) 10028.

4. High-Lying Triplet Excitons of Thermally Activated Delayed Fluorescence Molecules
   Y. Noguchi and O. Sugino: J. Phys. Chem. C. **121** (2017) 20687.

NOMURA, Yusuke [C class; 6000 (B)] (183)
— *Non-local correlations induced by Hund's coupling in multi-orbital strongly-correlated materials*

1. Restricted Boltzmann machine learning for solving strongly correlated quantum systems
   Y. Nomura, A. S. Darmawan, Y. Yamaji, and M. Imada: Phys. Rev. B **96** (2017) 205152.

OBATA, Shuji [C class; 500 (B)] ()
— *Nano-materials Magnetization based on magnetic dipole moment interactions*

ODA, Tatsuki [E class; 23000 (B)] (42,43)
— *Analyses on atomic structure, magnetism, and electronic structure in spintronics materials and molecular magnets*
— *Analyses on atomic, magnetic, and electronic structures in high-performance spintronics materials and molecular magnets*

1. Phase Stability and Superconductivity of Compressed Argon-Hydrogen Compounds from First-Principles
   Takahiro Ishikawa, Akitaka Nakanishi, Katsuya Shimizu, and Tatsuki Oda: J. Phys. Soc. Jpn. 86, 124711(2017).

OHGOE, Takahiro [C class; 4000 (B)] (190)
— *Numerical study on interplay of stripes and electron-phonon interactions in the Hubbard model*

1. Correlation-induced superconductivity dynamically stabilized and enhanced by laser irradiation
   K. Ido, T. Ohgoe and M. Imada: Sci. Adv. 3, e1700718 (2017)
2. Competition among Superconducting, Antiferromagnetic, and Charge Orders with Intervention by Phase Separation in the 2D Holstein-Hubbard Model
   T. Ohgoe and M. Imada: Phys. Rev. Lett. 119, 197001 (2017)
3. Competition among various charge-inhomogeneous states and d-wave superconducting state in Hubbard models on square lattices
   K. Ido, T. Ohgoe and M. Imada: Phys. Rev. B 97, 045138 (2018)
4. mVMC - Open-source software for many-variable variational Monte Carlo method
   T. Misawa, S. Morita, K. Yoshimi, M. Kawamura, Y. Motoyama, K. Ido, T. Ohgoe, M. Imada, and T. Kato: submitted

OHMURA, Satoshi [C class; 3500 (B)] (114)
— *Ab initio study of viscosity and local structures of basaltic melt under high pressure*

1. Structures of liquid iron-light-element mixtures under high pressure
   S. Ohmura, T. Tsuchiya, H, IChikawa: Phys. Status Solidi B, under review

OHSAWA, Kazuhito [C class; 1000 (B)] (148)
— *Study of interaction between radiation damage and interstitial atom*

OHTO, Tatsuhiko [C class; 9000 (B)] (57,58)
— *Ab initio molecular dynamics simulation of doped-graphene/water interfaces*
— *Ab initio molecular dynamics simulation of graphene/ionic liquids interfaces*

1. π^+–π^+ stacking of imidazolium cations enhances molecular layering of room temperature ionic liquid at their interfaces
   Fujie Tang, Tatsuhiko Ohto, Taisuke Hasegawa, Mischa Bonn, and Yuki Nagata: Phys. Chem. Chem. Phys. 2017, 19, 2850
2. Trimethylamin-N-oxide: Hydration structure, surface activity, and biological function viewed by vibrational spectroscopy
   Tatsuhiko Ohto, Johannes Hunger, Ellen H. G. Backus, Wataru Mizukami, Mischa Bonn, and Yuki Nagata: Phys. Chem. Chem. Phys. 2017, 19, 6909

3. Chemisorbed and Physisorbed Water at the TiO2/Water Interface
   Saman Hosseinpour, Tang Fujie, Fenglong Wang, Ruth Livingstone, Simon Schlegel, Tatsuhiko Ohto, Mischa Bonn, Yuki Nagata, and Ellen H. G. Backus: J. Phys. Chem. Lett. 8, 2195 (2017)
4. Electrochemical TERS Elucidates Potential-Induced Molecular Reorientation of Adenine/Au(111)
   Natalia Martin Sabanes, Tatsuhiko Ohto, Denis Andrienko, Yuki Nagata, and Katrin F. Domke: Angew. Chem. Ind. Ed. 56, 9796 (2017)
5. Multi-functional Octamethyltetrasila[2.2]cyclophanes: Conformational Variations, Circularly Polarized Luminescence, and Organic Electroluminescence
   Masaki Shimada, Yoshinori Yamanoi, Tatsuhiko Ohto, Song-Toan Pham, Ryo Yamada, Hirokazu Tada, Kenichiro Omoto, Shohei Tashiro, Mitsuhiko Shionoya, Mineyuki Hattori, Keiko Jimura, Shigenobu Hayashi, Hikaru Koike, Munekata Iwamura, Koichi Nozaki, Hiroshi Nishihara: J. Am. Chem. Soc. 139, 11214 (2017)
6. Highly Luminescent 2D-type Slab Crystals Based on a Molecular Charge-Transfer Complex as Promising Organic Light-Emitting Transistor Materials
   Sang Kyu Park, Jin Hong Kim, Tatsuhiko Ohto, Ryo Yamada, Andrew Jones, Dong Ryeol Whang, Illhun Cho, Sangyoon Oh, Jeffrey Hong, Ji Eon Kwon, Jong H. Kim, Yoann Olivier, Roland Fischer, Roland Resel, Johannes Gierschner, Hirokazu Tada, Soo Young Park: Adv. Mater. 29, 1701346 (2017)
7. Analysis of Single Molecule Conductance of Heterogeneous Porphyrin Arrays by Partial Transmission Probabilities
   Takashi Tamaki, Tatsuhiko Ohto, Ryo Yamada, Hirokazu Tada, and Takuji Ogawa: Chem. Select. 2, 7484 (2017)
8. Magnetic Field Effect on Pentacene-Doped Sexithiophene Diodes
   Song-Toan Pham, Marine Fayolle, Tatsuhiko Ohto, Hirokazu Tada: Appl. Phys. Lett. 111, 203303 (2017)
9. Definition of Free O-H Groups of Water at the Air-Water Interface
   Tang Fujie, Tatsuhiko Ohto, Taisuke Hasegawa, Wen Jun Xie, Limei Xu, Mischa Bonn, Yuki Nagata: J. Chem. Theor. Comput. 14, 357 (2018)
10. Aggregation-Induced Emission Enhancement from Disilane-Bridged Donor–Acceptor–Donor Luminogens Based on the Triarylamine Functionality
    Tsukasa Usuki, Masaki Shimada, Yoshinori Yamanoi, Tatsuhiko Ohto, Hirokazu Tada, Hidetaka Kasai, Eiji Nishibori, Hiroshi Nishihara: ACS Appl. Mater. Interfaces, in press.
11. Cooperation between holey graphene and NiMo alloy for hydrogen evolution in an acidic electrolyte
    Yoshikazu Ito, Tatsuhiko Ohto, Daisuke Hojo, Mitsuru Wakisaka, Yuki Nagata, Linghan Chen, Kailong Hu, Masahiko Izumi, Jun-ichi Fujita, and Tadafumi Adschiri ACS Catal. in press.

OHTSUKI, Tomi [C class; 5500 (B)] (251)
— *Phase diagrams of random topological matters*

1. Phase Diagrams of Three-Dimensional Anderson and Quantum Percolation Models Using Deep Three-Dimensional Convolutional Neural Network
   Tomohiro Mano, Tomi Ohtsuki: Journal of the Physical Society of Japan **86**, 113704 (2017)
2. Quantum multicriticality in disordered Weyl semimetals
   X. Luo, B. Xu, T. Ohtsuki, R. Shindou: Physical Review B **97**, 045129 (2018)
3. Unconventional Scaling Theory in Disorder-Driven Quantum Phase Transition
   X. Luo, T. Ohtsuki, R. Shindou: arXiv:1803.09051 (2018)

OKAMOTO, Yuko [E class; 20000 (B)] (208)
— *Study on complex systems by generalized-ensemble algorithms*

OKITSU, Kouhei [C class; 1000 (B)] (299)
— *Basic research for significant cost reduction of molecular target drug discovery*
— *Development of algorithm to solve the n-beam Takagi equation with least square method*

1. Experimentally obtained and computer-simulated non-coplanar eighteen-beam X-ray pinhole topographs
   K. Okitsu: Submitted to Acta Cryst. A **74** (2018).

2. Hypothesis about too large R-factor in X-ray structure analysis for protein crystals
   K. Okitsu: In preparation for publication in Acta Cryst. A **74** (2018).
3. A numerical method to obtain an n-beam X-ray wave field for a complex-shaped crystal
   K. Okitsu: In preparation for publication in Acta Cryst. A **74** (2018).

OKUBO, Tatsuya [C class; 2500 (B)] (279)
— *Design of organic structure-directing agents for the synthesis of zeolites with controlled active sites*

1. 理論計算に基づくゼオライト結晶構造中 Al 原子位置の予測と制御
   村岡恒輝, W. Chaikittisilp, 大久保達也: 化学工学会第 49 回秋季大会, 2017.
2. Highly Siliceous FAU-Type Zeolite with Spatially-Biased Q4(nAl) Si Speciation Synthesized by an Organic-Free Route
   W. Chaikittisilp, K. Muraoka, M. D. Oleksiak, M.-F. Hsieh, M. T. Conato, A. Shimojima, Tatsuya Okubo, J. D. Rimer: 第 33 回ゼオライト研究発表会, 2017.
3. 分離材料スクリーニングのためのメトロポリス法を用いた in silico ゼオライト原子配列生成法の開発
   W. Chaikittisilp, 村岡恒輝, 大久保達也: 化学工学会東京大会 2017, 2017.
4. Understanding structural distortions in borosilicate, aluminosilicate, and gallosilicate zeolites using in silico structural analysis
   K. Muraoka, W. Chaikittisilp, T. Okubo: Gordon Research Conference / Gordon Research Seminar, 2017.
5. In silico Structural Analyses of Borosilicate, Aluminosilicate, and Gallosilicate Zeolites Using Effective Tetrahedral Descriptors
   K. Muraoka, W. Chaikittisilp, T. Okubo: The 2017 AIChE annual meeting, 2017.
6. Zeolite on Demand: Design and Synthesis of Zeolites with Controlled Crystal Morphology and Location of Substituting Tetrahedral Atoms with the Aid of Theoretical Calculations
   W. Chaikittisilp, K. Muraoka, T. Okubo: The 2017 AIChE annual meeting, 2017.
7. Organic-Free Synthesis of a Highly Siliceous Faujasite Zeolite with Spatially-Biased Q4(nAl) Si Speciation
   M. D. Oleksiak, K. Muraoka, M.-F. Hsieh, M. T. Conato, A. Shimojima, T. Okubo, W. Chaikittisilp, and J. D. Rimer: Angew. Chem. Int. Ed. **56** (2017) 13366.
8. Directing Aluminum Atoms into Energetically Favorable Tetrahedral Sites in Zeolite Framework by Organic Structure-Directing Agents
   K. Muraoka, W. Chaikittisilp, Y. Yanaba, T. Yoshikawa, abd T. Okubo: Angew. Chem. Int. Ed. **57** (2018) 3742.
9. Resolving the Framework Position of Organic Structure-Directing Agents in Hierarchical Zeolites via Polarized Stimulated Raman Scattering
   G. Fleury, J. Steele, I. Gerber, F. Jolibois, P. Puech, K. Muraoka, S. H. Keoh, W. Chaikittisilp, T. Okubo, and M. Roeffaers: J. Phys. Chem. Lett. **9**, (2018) 1778.

OKUBO, Tsuyoshi [C class; 8500 (B)] (217)
— *Novel phases in classical and quantum frustrated spin systems*

1. Weak ferromagnetic order breaking the threefold rotational symmetry of the underlying kagome lattice in $CdCu_3(OH)_6(NO_3)_2{\cdot}H_2O$
   R. Okuma, T. Yajima, D. Nishio-Hamane, T. Okubo, and Z. Hiroi: Phys. Rev. B **95** (2017) 094427.
2. Quantum phase transitions driven by rhombic-type single-ion anisotropy in the $S = 1$ Haldane chain
   Y.-C. Tzeng, H. Onishi, T. Okubo, and Y.-J. Kao:Phys. Rev. B **96** (2017) 060404.
3. Ground-state properties of Na_2IrO_3 determined from an *ab initio* Hamiltonian and its extensions containing Kitaev and extended Heisenberg interactions
   T. Okubo, K. Shinjo, Y. Yamaji, N. Kawashima, S. Sota, T. Tohyama, and M. Imada: Phys. Rev. B **96** (2017) 054434.

OKUMURA, Hisashi [C class; 7000 (B)] (228)
— *Molecular dynamics simulations to reveal aggregation mechanism of amyloid-beta peptides at a hy-*

drophilic/hydrophobic interface

1. Development of isothermal-isobaric replica-permutation method for molecular dynamics and Monte Carlo simulations and its application to reveal temperature and pressure dependence of folded, misfolded, and unfolded states of chignolin
   M. Yamauchi and H. Okumura: J. Chem. Phys. **147** (2017) 184107.
2. Classical molecular dynamics simulation to understand role of a zinc ion for aggregation of amyloid-β peptides
   H. Nishizawa and H. Okumura: J. Comput. Chem. Jpn. **147** (2018) 76.
3. Antigen-dependent fluorescence response of anti-c-Myc Quenchbody studied by molecular dynamics simulations
   Y. Mori, H. Okumura, T. Watanabe, and T. Hohsaka: Chem. Phys. Lett. **698** (2018) 223.

ONISHI, Hiroaki [C class; 5500 (B)] (250)
— *Magnetic excitation and spin transport in frustrated quantum spin chain*
— *Magneto-thermal effect in spin nematic state of frustrated ferromagnetic chain*

1. Magnetic structure and dispersion relation of the $S = 1/2$ quasi-one-dimensional Ising-like antiferromagnet $\mathrm{BaCo_2V_2O_8}$ in a transverse magnetic field
   M. Matsuda, H. Onishi, A. Okutani, J. Ma, H. Agrawal, T. Hong, D. M. Pajerowski, J. R. D. Copley, K. Okunishi, M. Mori, S. Kimura, and M. Hagiwara, Phys. Rev. B 96, 024439 (2017).
2. Quantum phase transitions driven by rhombic-type single-ion anisotropy in the $S = 1$ Haldane chain
   Y.-C. Tzeng, H. Onishi, T. Okubo, and Y.-J. Kao, Phys. Rev. B 96, 060404(R) (2017).
3. Dynamical quadrupole structure factor of ferromagnetic frustrated chain
   H. Onishi, Physica B, 10.1016/j.physb.2017.10.056 (2017).
4. Neutron scattering study of yttrium iron garnet
   S. Shamoto, T. U. Ito, H. Onishi, H. Yamauchi, Y. Inamura, M. Matsuura, M. Akatsu, K. Kodama, A. Nakao, T. Moyoshi, K. Munakata, T. Ohhara, M. Nakamura, S. Ohira-Kawamura, Y. Nemoto, and K. Shibata, Phys. Rev. B 97, 054429 (2018).

ONO, Tomoya [C class; 11500 (B)] (47)
— *Development of first-principles electronic-structure and transport calculation method based on real-space finite-difference approach*

1. First-principles study on leakage current caused by oxygen vacancies at $\mathrm{HfO_2/SiO_2/Si}$ interface
   K. Takagi and T. Ono: Jpn. J. Appl. Phys., accepted.
2. Improvement of accuracy in the wave-function-matching method for transport calculations
   S. Tsukamoto, T. Ono, and S. Blügel: Phys. Rev. B **97** (2018) 115450.
3. Theoretical and experimental investigation of the atomic and electronic structures at the 4H-SiC(0001)/$\mathrm{SiO_2}$ interface
   T. Ono, C.J. Kirkham, S. Saito, and Y. Oshima: Phys. Rev. B **96** (2017) 115311.
4. Efficient and Scalable Calculation of Complex Band Structure using Sakurai-Sugiura Method
   S. Iwase, Y. Futamura, A. Imakura, T. Sakurai, and T. Ono: SC '17 Proceedings of the International Conference for High Performance Computing, Networking, Storage and Analysis (2017) 40.

ORITA, Nozomi [B class; 500 (B)] ()
— *Ab initio calculations for superlattices composed of silicon clusters containing more than 300 atoms*

OSHIKAWA, Masaki [C class; 2000 (B)] (321)
— *Designing novel quantum materials based on space group symmetries, including filling-enforced quantum band insulators*

1. Designing Kitaev Spin Liquids in Metal-Organic Frameworks
   M. G. Yamada, H. Fujita, and M. Oshikawa: Phys. Rev. Lett. **119** (2017) 057202.
2. Construction of Hamiltonians by supervised learning of energy and entanglement spectra
   H. Fujita, Y. Nakagawa, S. Sugiura, and M. Oshikawa: Phys. Rev. B **97** (2018) 075114.

OSHIYAMA, Atsushi [E class; 38500 (B)] (40)
— *Atomic Structures and Electronic Properties of Hard- and Soft-Nano Materials*

1. First-principles study of lateral atom manipulation assisted by structural relaxation of a scanning tip apex
   B. Enkhtaivan, Y. Sugimoto and A. Oshiyama: Phys. Rev. B **96** (2017) 155417
2. A novel intrinsic interface state controlled by atomic stacking sequence at interface of SiC/SiO_2
   Y.-i. Matsushita and A. Oshiyama: Nano Letters **17** (2017) 6458
3. Mining single-electron spectra of the interface states from a supercell band structure of silicene on an Ag(111) substrate with band-unfolding methodology
   J.-I. Iwata, Y.-i. Matsushita, H. Nishi, Z.-X. Guo and A. Oshiyama: Phys. Rev. B **96** (2017) 235442
4. Unfolding energy spectra of double-periodicity two dimensional systems: twisted bilayer graphene and MoS_2 on graphene
   Y.-i. Matsushita, H. Nishi, J.-i. Iwata, T. Kosugi and A. Oshiyama: Phys. Rev. Materials **2** (2018) 010801(R)

OTOMO, Junichiro [D class; 1500 (B)] (132)
— *Developemnt of materials of proton-conducitng solid electrolyte fuel cells and analysis of ion conduction*

OTSUKI, Junya [C class; 3000 (B)] (194)
— *Dynamical mean-field calculations of electronic states and multipolar fluctuations in strongly correlated electron systems*

1. Sparse modeling approach to analytical continuation of imaginary-time quantum Monte Carlo data
   J. Otsuki, M. Ohzeki, H. Shinaoka, K. Yoshimi: Phys. Rev. E **95** (2017) 061302(R).
2. Compressing Green's function using intermediate representation between imaginary-time and real-frequency domains
   H. Shinaoka, J. Otsuki, M. Ohzeki, K. Yoshimi: Phys. Rev. B **96** (2017) 035147.
3. Conservation in two-particle self-consistent extensions of dynamical mean-field theory
   F. Krien, E. G. C. P. van Loon, H. Hafermann, J. Otsuki, M. I. Katsnelson, A. I. Lichtenstein: Phys. Rev. B **96** (2017) 075155.
4. Overcomplete compact representation of two-particle Green's functions
   H. Shinaoka, J. Otsuki, K. Haule, M. Wallerberger, E. Gull, K. Yoshimi, M. Ohzeki: submitted to Phys. Rev. B.
5. Performance analysis of physically constructed orthogonal representation of imaginary-time Green's function
   N, Chikano, J. Otsuki, H. Shinaoka: submitted to Phys. Rev. B.

OZEKI, Yukiyasu [C class; 7000 (B)] (227)
— *Improvement for dynamical scaling analysis and its applications to topoligical phase transitions*
— *Improvement for dynamical scaling analysis and its applications to topological phase transitions II*

PENG, Hailong [C class; 4500 (B)] (262)
— *Exploring nano-structured phases in imidazolium-based ionic liquid and water mixtures*

1. Molecular dynamics study of mesophase transition upon annealing of imidazolium-based ionic liquid with long-alkyl chain
   H. Peng, M. Kubo, and H. Shiba: Phys. Chem. Chem. Phys. doi:10.1039/C8CP00698A (2018).

RAEBIGER, Hannes [B class; 800 (B)] (167)
— *Theory of self-organized nano-interfaces for electronic devices*

SAITO, Mineo [C class; 7500 (B)] (66)
— *First-Principles Calculation for Positron and Muon Experiments as Measurements of Crystals*

1. Group theoretical analysis of two-dimensional hexagonal materials

S. Minami, I. Sugita, R. Tomita, H. Oshima, and M. Saito: Jpn. J. Appl. Phys. **56** (2017) 105102.

2. Polarity tuning of spin-orbit-induced spin splitting in two-dimensional transition metal dichalcogenides
   M. A. U. Absor, I. Santoso, Harsojo, K. Abraha, H. Kotaka, F. Ishii, and Mineo Saito: Jpn. J. Appl. Phys. **122** (2017) 153905.

SAKAI, Toru [C class; 6500 (B)] (233,235)
— *Numerical Diagonalization Study on the Spin Gap of Frustrated Systems*
— *Numerical Study on Spin Flop Phenomena in Low-Dimensional Quantum Spin Systems*

1. Dzyaloshinsky-Moriya Interaction and the Ground State in $S = 3/2$ Perfect Kagome Lattice Antiferromagnet $KCr_3(OH)_6(SO_4)_2$ (Cr-Jarosite) Studied by X-Band and High-Frequency ESR
   S. Okubo, R. Nakata, S. Idehara, N. Takahashi, T. Sakurai, W. Zhang, H. Ohta, T. Shimokawa, T. Sakai, K. Okuta, S. Hara, and H. Sato: J. Phys. Soc. Jpn. 86 (2017) 024703.
2. Gapless Quantum Spin Liquid of the Kagome-Lattice Antiferromagnet
   T. Sakai and H. Nakano: POLYHEDRON 126 (2017) 42.
3. Exact ground states of frustrated quantum spin systems consisting of spin-dimer units
   T. Hikihara, T. Tonegawa, K. Okamoto and T. Sakai: J. Phys. Soc. Jpn. 86 (2017) 054709.
4. Frustrated S=1/2 Two-Leg Ladder with Different Leg Interactions
   T. Tonegawa, K. Okamoto, T. Hikihara and T. Sakai: J. Phys.: Conf. Ser. 828 (2017) 012003.
5. Ferrimagnetism in the Spin-1/2 Heisenberg Antiferromagnet on a Distorted Triangular Lattice
   H. Nakano and T. Sakai: J. Phys. Soc. Jpn. 86 (2017) 063702.
6. Quantum Spin Liquid in the Kagome-Lattice Antiferromagnet and Related Systems
   H. Nakano and T. Sakai: J. Phys.: Conf. Ser. 868 (2017) 012006.
7. Magnetization Process of the Spin-1/2 Triangular-Lattice Heisenberg Antiferromagnet with Next-Nearest-Neighbor Interactions -Plateau or Nonplateau-
   H. Nakano and T. Sakai: J. Phys. Soc. Jpn. 86 (2017) 114705.
8. Spin-1/2 Triangular-Lattice Heisenberg Antiferromagnet with $\sqrt{3}\times\sqrt{3}$-Type Distortion -Behavior around the Boundaries of the Intermediate Phse-
   A. Shimada, H. Nakano, T. Saka and K. Yoshimurai: J. Phys. Soc. Jpn. 87 (2018) 034706.
9. The Spin-1/2 Heisenberg Antiferromagnet on a Triangular-Lattice with $\sqrt{3}\times\sqrt{3}$-Type Distortion -Magnetization Process and Magnetic Susceptibility-
   A. Shimada, H. Nakano, T. Saka and K. Yoshimurai: J. Jpn. Soc. Powder Powder Metallurgy 65 (2018) 3.
10. Quantum Spin Fluid Behaviors of the Kagome- and Triangular-Lattice Antiferromagnets
    T. Sakai and H. Nakano: to appear in J. Phys.: Conf. Ser.
11. Spontaneous Magnetization of the Spin-1/2 Heisenberg Antiferromagnet on the Triangular Lattice with a Distortion
    A. Shimada, T. Sakai, H. Nakano and K. Yoshimurai: to appear in J. Phys.: Conf. Ser.
12. Gapless Spin Excitations in the $S = 1/2$ Kagome- and Triangular-Lattice Heisenberg Antiferromagnets
    T. Sakai and H. Nakano: to appear in Physica B

SAKAKIBARA, Hirofumi [B class; 700 (B)] (170)
— *Study on a automatic derivation technique of first-principles effective model based on the many body electron theory*

SASAKI, Takehiko [B class; 1300 (B)] (145)
— *Dehydration process of polyalcohol in hot pressurized water studied by First Principles Calculations*
— *Materials informatics approach for catalysts' activities and properties of metal oxides obtained by First Principles Calculations*

SATO, Tetsuya [C class; 3500 (B)] (113)
— *Controlling magnetic properties of quantum-well induced ferromagnetism in Pd(100) through the lattice distortion*

1. Change in magnetization of ferromagnetic Pd(001) ultrathin films induced by the strain effect of $BaTiO_3$
   Yusuke Ban, Katsuyoshi Komatsu, Shunsuke Sakuragi, Tomoyasu Taniyama, Hiroyuki Kageshima, and Tetsuya Sato: Appl. Phys. Lett. **112**, 142409 (2018)

SATO, Yukio [B class; 300 (B)] (164)
— *Computational Design of Electrochromic Materials through ab initio DFT Simulation*

1. Insights into nucleation, growth and phase selection of WO3: morphology control and electrochromic properties
   K. Ghosh, A. Roy, S. Tripathi, S. Ghule, A. K. Singh, and N. Ravishankar: J. Mater. Chem. C **5** (2017) 7316.

SHIGETA, Yasuteru [C class; 7500 (B)] (31,64)
— *Structural transition analyses on cytochrome c complexes using dissimilarity*
— *Structural transition analyses on nano- and bio-systems using dissimilarity*

1. Programmed Dynamical Ordering in Self-organization Processes of Nano-cube: A Molecular Dynamics Study
   R. Harada, T. Mashiko, M. Tachikawa, S. Hiraoka and Y. Shigeta: Phys. Chem. Chem. Phys. in press.
2. The binding structure and affinity of photodamaged duplex DNA with members of the photolyase/cryptochrome family: A computational study
   R. Sato, R. Harada and Y. Shigeta: Biophys. Physicobiol. 15, 18-27 (2018).
3. On-the-Fly Specifications of Reaction Coordinates in Parallel Cascade Selection Molecular Dynamics Accelerate Conformational Transitions of Proteins
   R. Harada, Y. Shigeta: submitted to J. Chem. Theor. Comput.

SHIMADA, Toshihiro [B class; 600 (B)] (156)
— *Carbonization reaction of organic molecules and electronic structures of the products*

1. Rich interfacial chemistry and properties of carbon-doped hexagonal boron nitride nanosheets revealed by electronic structure calculations
   Wei Xie, Takahiro Tamura, Takashi Yanase, Taro Nagahama, and Toshihiro Shimada: Japanese Journal of Applied Physics 57, 04FL11 (2018)

SHIMAMURA, Kohei [C class; 2000 (B)] (124)
— *Generation Mechanism of Organic/Biological Molecules on Early Earth: Ab Initio Molecular Dynamics Simulation II*

SHIMOJO, Fuyuki [C class; 4500 (B)] (96,302)
— *First-Principles Molecular-Dynamics Study of Structural and Electronic Properties of Covalent Liquids and Glass under Pressure*

1. Picosecond amorphization of SiO_2 stishovite under tension
   M. Misawa, E. Ryuo, K. Yoshida R. K. Kalia, A. Nakano, N. Nishiyama, F. Shimojo, P. Vashishta, and F. Wakai: Sci. Adv. **3**, e1602339 (2017).
2. Meteorite Impacts on Ancient Ocean Opened Up Multiple NH_3 Production Pathways
   K. Shimamura, F. Shimojo, A. Nakano, and S. Tanaka: Phys. Chem. Chem. Phys. **19**, 11655 (2017).
3. Effect of CO_2 Adsorption on Proton Migration on Hydrated ZrO_2 Surface: *Ab initio* Molecular Dynamics Study
   R. Sato, Y. Shibuta, F. Shimojo, and S. Yamaguchi: Phys. Chem. Chem. Phys. **19**, 20198 (2017).
4. *Ab initio* simulation of permanent densification in silica glass
   E. Ryuo, D. Wakabayashi, A. Koura, and F. Shimojo: Phys. Rev. B **96**, 054206 (2017).
5. Reactivity of Sulfur Molecules on MoO_3 (010) Surface
   M. Misawa, S. Tiwari, S. Hong, A. Krishnamoorthy, F. Shimojo, R. K. Kalia, A. Nakano, and P. Vashishta: J. Phys. Chem. Lett. **8**, 6206 (2017).

SHIMOKAWA, Tokuro [C class; 6500 (B)] (231,232)
— *Multiple-Q states of the frustrated Heisenberg model on the honeycomb lattice*
— *The effect of bond-randomness on the quantum magnetisms in low dimension*

SHINAOKA, Hiroshi [D class; 3000 (B)] (192,346)
— *Theoretical study of strong correlations in* $Cd_2Os_2O_7$

SHINODA, Wataru [C class; 6000 (B)] (240)
— *Physical Property Analysis of Macromolecular Self-Assembly using Quantitative Coarse-Grained Molecular Model*

1. Molecular Dynamics Study on the Mechanical Deformation of Hydrated Perfluorosulfonic Acid Polymer Membranes
   A. Kuo, A. Tanaka, J. Irisawa, W. Shinoda, and S. Okazaki: J. Phys. Chem. C **121** (2017) 21374.
2. Transferable coarse-grained model for perfluorosulfonic acid polymer membranes
   A. Kuo, S. Okazaki, and W. Shinoda: J. Chem. Phys. **147** (2017) 094904.
3. Molecular dynamics study of thermodynamic stability and dynamics of [Li(glyme)]+ complex in lithium-glyme solvate ionic liquids
   W. Shinoda, Y. Hatanaka, M. Hirakawa, S. Okazaki, S. Tsuzuki, K. Ueno, and M. Watanabe: J. Chem. Phys. **148** (2018) 193809.
4. Exploring the Effect of Pendent Side Chain Length on the Structural and Mechanical Properties of Hydrated Perfluorosulfonic Acid Polymer Membranes by Molecular Dynamics Simulation
   A. Kuo, K. Takeuchi, A. Tanaka, S. Urata, S. Okazaki, and W. Shinoda: submitted to Polymer.

SHINOHARA, Yasushi [C class; 2000 (B)] (123)
— *First principles simulation for attosecond electron dynamics in crystalline solids*

1. Polarization-Resolved Study of High Harmonics from Bulk Semiconductors
   K. Kaneshim, Y. Shinohara, K. Takeuchi, N. Ishii, K. Imasaka, T. Kaji, S. Ashihara, K. L. Ishikawa, and J. Itatani, submitted

SHIOMI, Junichiro [B,C class; 5800 (B)] (245,249)
— *Control of phonon and electron transport properties using mechanical strain*
— *Screening for Thermal Functional Materials using Materials Informatics*

1. Phonon-interference resonance effects by nanoparticles embedded in a matrix
   Lei Feng, Takuma Shiga, Haoxue Han, Shenghong Ju, Yuriy A. Kosevich, Junichiro Shiomi: Physical Review B, 96, 220301(R) (2017).
2. MDTS: Automatic complex materials design using Monte Carlo tree search
   Thaer M. Dieb, Shenghong Ju, Kasuki Yoshizoe, Zhufeng Hou, Junichiro Shiomi, Koji Tsuda: Science and Technology of Advanced Materials, 18, 49850 (2017).

SHIRAI, Tatsuhiko [B class; 500 (B)] (316)
— *Analysis of optical bistability in a quantum cavity system with Lanczos method*

1. Optical Bistability in a Low Photon-Density Regime
   Tatsuhiko Shirai, Synge Todo, Hans de Raedt, Seiji Miyashita: submitted to Physical Review A

SHIRAISHI, Kenji [C class; 6000 (B)] ()
— *Design of New Phase Change Memories Based on First Principles Calculations*

SHUDO, Ken-Ichi [C class; 1000 (B)] (147)
— *Theoritical analysis of vibronic mode and spin ordering of thin film of transition metallated porphyrin-derivative*

SUGINO, Osamu [C class; 4500 (B)] (94)
— *Functional property of solid-liquid interfaces*

1. Experimental realization of two-dimensional Dirac nodal line fermions in monolayer Cu2Si

G. J. Feng, B. T. Fu, S. Kasamatsu, et al.: Nat. Comm. **8** (2017) 1007.

2. Dirac Fermions in Borophene
   B. J. Feng, O. Sugino, et al., Phys. Rev. Lett. **118** (2017) 096401.

SUWA, Hidemaro [C class; 4500 (B)] (261)
— *Emergent Particles at Deconfined Quantum Criticality*

SUZUKI, Takafumi [C class; 9500 (B)] (220)
— *Ground state phase diagram of SU(N) Heisenberg model on a honeycomb lattice*
— *Ground state phase diagrams of 2D generalized Heisenberg models for SU(N) spins*

1. Magnetic excitations of Kitaev-Heisenberg models on honeycomb lattices
   Takuto Yamada, Takafumi Suzuki, and Sei-ichiro Suga: Physica B, 525C, 91-93 (2017).
2. Dynamical spin structure factors of α-RuCl$_3$
   T. Suzuki and S. Suga: J. Phys.: Conf. Sers, 969, 012123 (2018).
3. Thermal properties of spin-S Kitaev-Heisenberg model on a honeycomb lattice
   Takafumi Suzuki and Youhei Yamaji: Physica B in press

SUZUKI, Tatsuo [C class; 2000 (B)] ()
— *Theoretical search for high-efficient monolayer water-splitting photocatalysts*

SUZUKI, Yuji [C class; 6500 (B)] (73)
— *Development of High-performance Perfluoropolymer Electret*
— *Study on the charge trap mechanism of electret*

1. Quantum Chemical Study of Charge Trap in Amorphous Perfluoro Polymer Electret
   S. Kim and Y. Suzuki: IEEE 16th Int. Symp. Electrets (ISE16), Leuven, p47, (2017).

TAKAE, Kyohei [B class; 700 (B)] (307,348)
— *Giant and cross response with ferroelectric–antiferroelectric phase transitions*

1. Emergence of antiferroelectricity as a consequence of interplay between steric and dipolar interactions
   K. Takae and H. Tanaka: submitted to Nature Commun.
2. Hydrodynamic simulations of charge-regulation effects in colloidal suspensions
   K. Takae and H. Tanaka: submitted to Soft Matter

TAKAGI, Noriaki [B class; 1300 (B)] (141,143)
— *Geometric and electronic structures of magnetic molecules at surfaces*
— *Geometric and electronic structures of two-dimensional atomic-layered materials*

1. Single Molecule Quantum Dot as a Kondo Simulator
   R. Hiraoka, E. Minamitani, R. Arafune, N. Tsukahara, S. Watanabe, M. Kawai, N. Takagi: Nat. Commun. **8** (2017) 16012.
2. Visualizing Type-II Weyl Points in Tungsten Ditelluride by Quasiparticle Interference
   C.-L. Lin, R. Arafune, R.-Y. Liu, M. Yoshimura, B. Feng, K. Kawahara, Z. Ni, E. Minamit ani, S. Watanabe, Y. Shi, M. Kawai, T.-C. Chiang, I. Matsuda, N. Takagi: Acs Nano **11** (2017) 11459.
3. Structural Evolution of Bi Thin Films on Au(111) Revealed by Scanning Tunneling Microscop y
   N. Kawakami, C.-L. Lin, K. Kawahara, M. Kawai1, R. Arafune, N. Takagi: Phys. Rev. B _f 96 (2017) 205402.
4. Quasiparticle Scattering in Type-II Weyl semimetal MoTe2
   C. L. Lin, R. Arafune, E. Minamitani, M. Kawai, N. Takagi: J. Phys. Condensed Matter s **30** (2018) 105703.

TAKETSUGU, Tetsuya [C class; 3000 (B)] (119)
— *Theoretical design on catalysts with abundant elements*

1. Optical readout of hydrogen storage in films of Au and Pd
   Y. Nishijima, S. Shimizu, K. Kurihara, Y. Hashimoto, H. Takahashi, A. Balcytis, G. Seniutinas, S. Okazakis, J. Juodkazyte, T. Iwasa, T. Taketsugu, Y. Tominaga, and S. Juodkazis: Opt. Express,

25 (2017) 24081.

2. Time-Dependent Density Functional Theory Study on Higher Low-Lying Excited States of $Au_{25}(SR)_{18}^-$
   M. Ebina, T. Iwasa, Y. Harabuchi, and T. Taketsugu: J. Phys. Chem. C, **122** (2018) 4097.

TAMURA, Ryo [C class; 5000 (B)] (256)
— *Acceleration of the effective model estimation by techniques in informa- tion science*
— *Development of a method to express the knowledge in materials science as prior distribution*

1. Data-driven nanomechanical sensing: Specific information extraction from a complex system
   K. Shiba, R. Tamura, G. Imamura, and G. Yoshikawa: Sci. Rep. **7** (2017) 3661.
2. 室温磁気冷凍における最適冷凍サイクル探索
   新井 亮祐, 田村 亮, 馬場 浩司, 福田 英史, 中込 秀樹, 沼澤 健則: 日本冷凍空調学会論文集 **34** (2017) 147.
3. Bayesian optimization for computationally extensive probability distributions
   R. Tamura and K. Hukushima: PLoS ONE **13** (2018) e0193785.
4. 量子アニーリングの基礎と応用事例
   田中 宗: 知能と情報、**30** (2018) 42.
5. 量子アニーリング — 計算アルゴリズムの観点から —
   田中 宗: 電子情報通信学会論文誌 C、**J101-C** (2018) 166.
6. 20K スピン CMOS アニーリングマシンを対象とした完全結合イジングモデルマッピング手法と評価
   寺田 晃太朗 , 田中 宗 , 林 真人 , 山岡 雅直 , 柳澤 政生 , 戸川 望 : DA シンポジウム 2017 論文集、(2017) 163.
7. An Ising model mapping to solve rectangle packing problem
   Kotaro Terada, Daisuke Oku, Sho Kanamaru, Shu Tanaka, Masato Hayashi, Masanao Yamaoka, Masao Yanagisawa and Nozomu Togawa: Proc. of 2018 International Symposium on VLSI Design, Automation and Test (VLSI-DAT) in press.

TANAKA, Hajime [B class; 1900 (B)] (279,281)
— *Structure and dynamics of tetrahedral liquids*
— *Study of finite-size effects on colloidal gelation originating from momentum conservation*

1. Impact of local symmetry breaking on the physical properties of tetrahedral liquids
   R. Shi and H. Tanaka: Proc. Natl. Acad. Sci. U. S. A. **115** (2018) 1980.
2. Microscopic structural descriptor of liquid water
   R. Shi and H. Tanaka: J. Chem. Phys. **148**, (2018) 124503.
3. Physical foundation of the fluid particle dynamics method for colloid dynamics simulation.
   A. Furukawa, M. Tateno, and H. Tanaka: accepted to Soft Matter.

TANAKA, Shu [C class; 3000 (B)] (270)
— *Machine Learning by Using Quantum Annealing*
— *Matrix Factorization by Using Quantum Annealing*

1. 量子アニーリングの基礎と応用事例
   田中 宗: 知能と情報、**30** (2018) 42.
2. 量子アニーリング — 計算アルゴリズムの観点から —
   田中 宗: 電子情報通信学会論文誌 C、**J101-C** (2018) 166.
3. 20K スピン CMOS アニーリングマシンを対象とした完全結合イジングモデルマッピング手法と評価
   寺田 晃太朗 , 田中 宗 , 林 真人 , 山岡 雅直 , 柳澤 政生 , 戸川 望 : DA シンポジウム 2017 論文集、(2017) 163.
4. An Ising model mapping to solve rectangle packing problem
   Kotaro Terada, Daisuke Oku, Sho Kanamaru, Shu Tanaka, Masato Hayashi, Masanao Yamaoka, Masao Yanagisawa and Nozomu Togawa: Proc. of 2018 International Symposium on VLSI Design, Automation and Test (VLSI-DAT) in press.
5. Data-driven nanomechanical sensing: Specific information extraction from a complex system
   K. Shiba, R. Tamura, G. Imamura, and G. Yoshikawa: Sci. Rep. **7** (2017) 3661.
6. 室温磁気冷凍における最適冷凍サイクル探索
   新井 亮祐, 田村 亮, 馬場 浩司, 福田 英史, 中込 秀樹, 沼澤 健則: 日本冷凍空調学会論文集 **34** (2017) 147.

7. Bayesian optimization for computationally extensive probability distributions
   R. Tamura and K. Hukushima: PLoS ONE **13** (2018) e0193785.

TANUMA, Yasunari [B class; 600 (B)] ()
— *Study of numerical methods for quantum phenonema of anisotoropic superconductors*

TATENO, Masaru [C class; 4000 (B)] (103)
— *Hybrid ab initio QM/MM calculations of functional mechanisms of biological macromolecular systems recognizing supercoiled DNA*

1. Effects of a Positive Feedback Loop upon the Stability of Bi-Connected Elementary Biochemical Reaction Cycles
   J. Kang : J. Phys. Soc. Jpn. **86** (2017) 074802.
2. Novel Strategy for Discrimination of Transcription Factor Binding Motifs Employing Mathematical Neural Network
   A. Sugimoto : J. Phys. Soc. Jpn. **86** (2017) 074803.
3. Ab Initio Electronic Structure Calculation of [4Fe-3S] Cluster of Hydrogenase as Dihydrogen Dissociation/Production Catalyst
   J. Kim : J. Phys. Soc. Jpn. **87** (2018) 034804.

TATETSU, Yasutomi [C class; 4000 (B)] (101)
— *Magnetic anisotropy analysis of transition-metal-doped Nd-Fe-B magnets by first-principles calculations*

1. First-principles study on substitution effects in $Nd_2(Fe, X)_{14}B$
   Y. Tatetsu, S. Tsuneyuki, and Y. Gohda: submitted to Phys. Rev. B.

TATEYAMA, Yoshitaka [C class; 7000 (B)] (69)
— *DFT sampling studies on interfacial properties of batteries and catalysts*

1. Oxygen redox in hexagonal layered NaxTMO3 (TM =4d elements) for high capacity Na ion batteries
   M. H. N. Assadi, Masashi Okubo, Atsuo Yamada, Yoshitaka Tateyama: J. Mater. Chem. A 6, 3747-3753 (2018).
2. Fire-extinguishing organic electrolytes for safe batteries
   Wang Jianhui, Yuki Yamada, Keitaro Sodeyama, Eriko Watanabe, Koji Takada, Yoshitaka Tateyama, Atsuo Yamada: Nat. Energy 3, 22-29 (2018).
3. First-Principles Study of Electron Injection and Defects at the TiO2/ CH3NH3PbI3 Interface of Perovskite Solar Cells
   Jun Haruyama, Keitato Sodeyama, Ikutaro Hamada, Liyuan Han, Yoshitaka Tateyama: J. Phys. Chem. Lett. 8, 5840-5847 (2017).
4. Surface Hydrogenation of Boron-Doped Diamond Electrodes by Cathodic Reduction
   Seiji Kasahara, Keisuke Natsui, Takeshi Watanabe, Yasuyuki Yokota, Yousoo Kim, Shota Iizuka, Yoshitaka Tateyama, Yasuaki Einaga: Anal. Chem. 89, 11341-11347 (2017).
5. Unusual Passivation Ability of Superconcentrated Electrolytes toward Hard Carbon Negative Electrodes in Sodium-Ion Batteries
   Koji Takada, Yuki Yamada, Eriko Watanabe, Wang Jianhui, Keitaro Sodeyama, Yoshitaka Tateyama, Kazuhisa Hirata, Takeo Kawase, Atsuo Yamada: ACS Appl. Mater. Interfaces 9, 33802-33809 (2017).
6. lobal search for low-lying crystal structures using the artificial force induced reaction method: A case study on carbon
   Makito Takagi, Tetsuya Taketsugu, Hiori Kino, Yoshitaka Tateyama, Kiyoyuki Terakura, Satoshi Maeda: Phys. Rev. B 95, 184110 (2017).

TERAO, Takamichi [B class; 1400 (B)] (291)
— *Molecular simulation of colloidal crystals*

1. Manipulating sonic band gaps at will: vibrational density of states in three-dimensional acoustic metamaterial composites

T. Terao: Wave. Random Complex **28** (2018) 253.

TERASAWA, Asako [B class; 700 (B)] (152)
— *First-principles simulation of magnetism and formation of amorphous grain boundary phase of Nd-based permanent magnets*

TODO, Synge [C class; 5500 (B)] (23)
— *Model Estimation and Critical Phenomena Analysis by Statistical Machine Learning*

1. Quantum Lattice Model Solver H Φ
   M. Kawamura, K. Yoshimi, T. Misawa, Y. Yamaji, S. Todo, and N. Kawashima: Comp. Phys. Comm 217, 180-192 (2017).

TOHYAMA, Takami [C class; 5000 (B)] (255)
— *DMRG study of frustrated quantum spin systems*

1. Static and Dynamic Magnetic Properties of Spin-1/2 Inequilateral Diamond-Chain Compounds $A_3Cu_3AlO_2(SO_4)_4$ (A=K, Rb, and Cs)
   K. Morita, M. Fujihala, H. Koorikawa, T. Sugimoto, S. Sota, S. Mitsuda, and T. Tohyama: Phys. Rev. B **95**, (2017) 184412.
2. Magnetization Plateaus in the Spin-1/2 Antiferromagnetic Heisenberg Model on a Kagome-Strip Chain
   K. Morita, T. Sugimoto, S. Sota, and T. Tohyama: Phys. Rev. B **97**, (2017) 014412.
3. Cluster-Based Haldane State in an Edge-Shared Tetrahedral Spin-Cluster Chain: Fedotovite $K_2Cu_3O(SO_4)_3$
   M. Fujihala, T. Sugimoto, T. Tohyama, S. Mitsuda, R. A. Mole, D. H. Yu, S. Yano, Y. Inagaki, H. Morodomi, T. Kawae, H. Sagayama, R. Kumai, Y. Murakami, K. Tomiyasu, A. Matsuo, and K. Kindo: Phys. Rev. Lett. **120**, (2018) 077201.
4. Magnetic Phase Diagrams and Magnetization Plateaus of the Spin-1/2 Antiferromagnetic Heisenberg Model on a Square-Kagome Lattice with Three Nonequivalent Exchange Interactions
   K. Morita and T. Tohyama: J. Phys. Soc. Jpn. **87**, (2018) 043704.

TOKIWA, Hiroaki [C class; 6500 (B)] (72)
— *Development & Application of Rational Drug Design using the Forth Innovation Methodology*

1. Molecular association model of PPARα and its new specific and efficient ligand, pemafibrate: Structural basis for SPPARMα
   Yuta Yamamoto, Kenta Takei, Sundaram Arulmozhiraja, Vladimir Sladek, Naoya Matsuo, Songiee Han, Takashi Matsuzaka, Motohiro Sekiya, Takaki Tokiwa, Mitsuo Shoji, Yasuteru Shigeta, Yoshimi Nakagawa, Hiroaki Tokiwa, Hitoshi Shiman: Biochem. Biophys. Res. Comm. (DOI: 10.1016/j.bbrc.2018.03.135) 499(2), 239-245 (2018).
2. Product release mechanism associated with structural changes in monomeric L-threonine 3-dehydrogenase
   Momoharu Motoyama, Shogo Nakano, Yuta Yamamoto, Hiroaki Tokiwa, Yasuhisa Asano, and Sohei Ito: Biochemistry (DOI: 10.1021/acs.biochem.7b00832) 56(43), 5758-5770 (2017)
3. 3-(Triflyloxy)benzynes Enable the Regiocontrolled Cycloaddition of Cyclic Ureas to Synthesize 1,4-Benzodiazepine Derivatives
   Hideki Kaneko, Takashi Ikawa, Yuta Yamamoto, Sundaram Arulmozhiraja, Hiroaki Tokiwa, Shuji Akai: Syn. Lett.(DOI: 10.1055/s-0036-1591924) 29(07) 943-948 (2018)
4. In silico analysis of interaction pattern switching in ligand - receptor binding in Golgi α-mannosidase II induced by inhibitors protonation state
   Yumiko Suzuki, Naoto Iwata, Kohei Dobashi, Ryo Takashima, Sundaram Arulmozhiraja, Erika Ishitsubo, Naoya Matsuo, Hiroaki Tokiwa: Tetrahedron (DOI: 10.1016/j.tet.2017.11.071) 74(3), 392-400 (2017).
5. Mechanistic Insight into Weak-Base-Catalyzed Generation of Carbon Monoxide from Phenyl Formate and Its Application to Catalytic Carbonylation at Room Temperature without Use of External Carbon Monoxide Gas
   Hideyuki Konishi,Mika Matsubara,Keisuke Mori,Takaki Tokiwa, Sundaram Arulmozhiraja,Yuta Yamamoto,Yoshinobu Ishikawa,Hiroshi Hashimoto,Yasuteru Shigeta,Hiroaki Tokiwa,and Kei Man-

abe: Adv. Synth. Catl. (DOI: 10.1002/adsc.201700751) 359, 3592-3601 (2017).

TONEGAWA, Takashi [B,C class; 1600 (B)] (285)
— *Numerical Study of the One-Dimensional Quantum Spin Systems with Spatial Structures*

1. Frustrated $S = 1/2$ Two-Leg Ladder with Different Leg Interactions
   T. Tonegawa, K. Okamoto, T. Hikihara, and T. Sakai: J. Phys.: Conf. Series **828**, 012003 (2017)
2. Exact Ground States of Frustrated Quantum Spin Systems Consisting of Spin-Dimer Units
   T. Hikihara, T. Tonegawa, K. Okamoto, and T. Sakai: J. Phys. Soc. Jpn. **86**, 054709 (2017)

TOYODA, Masayuki [B class; 600 (B)] (154)
— *Band-gap engineering by forming isotope superlattices and polytypic superlattices*

TSUNEYUKI, Shinji [C class; 7000 (B)] (67)
— *Development and application of a new method for material structure prediction supported by experimental data*

1. Quartic Anharmonicity of Rattlers and Its Effect on Lattice Thermal Conductivity of Clathrates from First Principles
   T. Tadano and S. Tsuneyuki, Phys. Rev. Lett. 120,105901 (2018)
2. First-Principles Lattice Dynamics Method for Strongly Anharmonic Crystals
   T. Tadano and S. Tsuneyuki, J. Phys. Soc. Japan 87,041015 (2018)
3. Universal two-dimensional characteristics in perovskite-type oxyhydrides ATiO2H (A = Li, Na, K, Rb, Cs)
   N. Sato, R. Akashi, and S. Tsuneyuki, Journal of Chem. Phys., 147,034507(2017)
4. Possible electronic entropy-driven mechanism for non-thermal ablation of metals
   Y. Tanaka and S. Tsuneyuki, App. Phys. Exp. 11, 046701 (2018)
5. Numerical investigation of triexciton stabilization in diamond with multiple valleys and bands
   H. Katow, J. Usukura, R. Akashi, K. Varga, and S. Tsuneyuki Phys. Rev. B 95, 125205 (2017)

TSURUTA, Kenji [C class; 2500 (B)] (120)
— *Ab-initio Study on Amorphization Dynamics and Ion Diffusion in Biogenous Iron Oxide*

UCHIDA, Takashi [B class; 500 (B)] (315)
— *Theory of the multiple spin density waves and the magnetic skyrmions in the triangular-lattice Hubbard model*

WAKABAYASHI, Daisuke [B class; 700 (B)] (306)
— *Large-scale molecular-dynamics simulation with ANN potentials: nm-scale domain structure in densified silica glass*

WATANABE, Hiroshi [C class; 5000 (B)] (254)
— *Molecular dynamics study of impurity effect on bubble nucleation*

1. Polymer effects on Karman Vortex: Molecular Dynamics Study
   Yuta Asano, Hiroshi Watanabe, Hiroshi Noguchi: J. Chem. Phys. **148**, 144901 (2018)
2. Failure of deterministic and stochastic thermostats to control temperature of molecular systems
   Hiroshi Watanabe: J. Phys. Soc. Jpn. **86**, 075004 (2017).

WATANABE, Hiroshi [B class; 400 (B)] (202)
— *Superconductivity, magnetism, and charge order in strongly correlated electron system with charge degree of freedom*

1. Random phase approximation for superconducting states in multi-orbital Hubbard models with spin-orbit coupling
   K. Nishiguchi, T. Shirakawa, H. Watanabe, and S. Yunoki: J. Phys.: Conf. Ser. **807** (2017) 052013.

WATANABE, Kazuyuki [C class; 10000 (B)] (51)
— *First-Principles Study of Excited Electron Dynamics and Optical Responses of Nanostructures*

1. Virtual substrate method for nanomaterials characterization
   B.D.J. Liu, M. Yamamoto, Y. Ueda, K. Watanabe, N.T. Cuong, S. Li, K. Tsukagoshi, H. Yoshikawa, H. Iwai, S. Tanuma, H. Guo, Z. Gao, X. Sun, and Z. Ding, Nat. Commun. **8**, 15629 (2017).
2. Plasmon excitation and electron emission of a carbon nanotube under a linearly polarized laser: A real-time first-principles study
   K. Uchida and K. Watanabe, Phys. Rev.B **96**, 125419 (2017).
3. Experimental and computational studies of positron-stimulated ion desorption from TiO2(110) surface
   T. Yamashita, S. Hagiwara, T. Tachibana, K. Watanabe and Y. Nagashima, Materials Research Express **4**, 116303 (2017).
4. Exact Time-Dependent Exchange-Correlation Potential in Electron Scattering Processes
   Y. Suzuki, L. Lacombe, K. Watanabe, N.T. Maitra, Phys. Rev. Lett. **119**, 263401 (2017).
5. Time-dependent first-principles study of angle-resolved secondary electron emission from atomic sheets
   Y. Ueda, Y. Suzuki, and K. Watanabe, Phys. Rev.B **97**,075406 (2018).

WATANABE, Satoshi [C class; 10000 (B)] (49)
— *Theoretical Analyses on Ionic Transport Properties, Electrical Properties and Interfacial Electronic States of Nanostructures*

1. Germanene and stanene on two-dimensional substrates: Dirac cone and Z_2 invariant
   Z. Ni, E. Minamitani, Y. Ando, and S. Watanabe: Phys. Rev. B **96** (2017) 075427.
2. Visualizing Type-II Weyl Points in Tungsten Ditelluride by Quasiparticle Interference
   C.-L. Lin, R. Arafune, R.-Y. Liu, M. Yoshimura, B. Feng, K. Kawahara, Z. Ni, E. Minamitani, S. Watanabe, Y. Shi, M. Kawai, T.-C. Chiang, I. Matsuda, and N. Takagi: ACS Nano **11** (2017) 11459.
3. Scanning tunneling spectroscopy of superconductivity on surfaces of $LiTi_2O_4(111)$ thin films
   Y. Okada, Y. Ando, R. Shimizu, E. Minamitani, S. Shiraki, S. Watanabe, and T. Hitosugi: Nat. Commun. **8** (2017) 15975.
4. Theoretical prediction of phonon-mediated superconductivity with Tc ≈25 K in Li-intercalated h-BN bilayer
   N. H. Shimada, E. Minamitani, and S. Watanabe: Appl. Phys. Express **10** (2017) 093101.
5. Cu diffusion in amorphous Ta_2O_5 studied with a simplified neural network potential
   W. Li, Y. Ando, and S. Watanabe: J. Phys. Soc. Jpn. **86** (2017) 104004.
6. Single-Molecule Quantum Dot as a Kondo Simulator
   R. Hiraoka, E. Minamitani, R. Arafune, N. Tsukahara, S. Watanabe, M. Kawai, and N. Takagi: Nat. Commun. **8** (2017) 16012.
7. Study of Li atom diffusion in amorphous Li_3PO_4 with neural network potential
   W. Li, Y. Ando, E. Minamitani, and S. Watanabe: J. Chem. Phys. **147** (2017) 214106.
8. Atomic-scale characterization of the interfacial phonon in graphene/SiC
   E. Minamitani, R. Arafune, T. Frederiksen, T. Suzuki, S.M.F. Shahed, T. Kobayashi, N. Endo, H. Fukidome, S. Watanabe, and T. Komeda: Phys. Rev. B **96** (2017) 155431.
9. ニューラルネットワークを用いたアモルファス物質中の原子拡散の研究
   安藤康伸, 李文文 and 渡邉 聡: 固体物理, 掲載決定.

YABANA, Kazuhiro [C class; 4000 (B)] (100)
— *First-principles calculation for surface electron dynamics*

YAMADA, Atsuo [C class; 5500 (B)] (81)
— *First-principles study on electrode materials for sodium ion batteries*

1. Charge Storage Mechanism of RuO_2/Water
   E. Watanabe, H. Ushiyama, K. Yamashita, Y. Morikawa, D. Asakura, M, Okubo and A. Yamada: J. Phys. Chem. C **121** (2017) 18975.

YAMADA, Atsushi [C class; 1500 (B)] (197)
— *Superconductivity and magnetic properties of the Hubbard model*

YAMAGUCHI, Shu [C class; 4500 (B)] (92)
— *Protonic Activity on the Hydrated Surface of Acidic and Basic Oxide Catalyst for CO2 Conversion Processes*

1. Effect of CO_2 Adsorption on Proton Migration on Hydrated ZrO_2 Surface: an *Ab Initio* Molecular Dynamic Study
   R. Sato, Y. Shibuta, F. Shimojo, S. Yamaguchi: Phys. Chem. Chem. Phys. **19** (2017) 20198.

YAMAJI, Youhei [E class; 16500 (B)] (13,212)
— *Numerical Studies on Excitation Spectra of Quantum Spin Liquids*

1. Ground-state properties of Na 2 IrO 3 determined from an ab initio Hamiltonian and its extensions containing Kitaev and extended Heisenberg interactions
   T. Okubo, K. Shinjo, Y. Yamaji, N. Kawashima, S. Sota, T. Tohyama, M. Imada: J. Phys. Soc. Jpn. **96** (2017) 054434.
2. Quantum lattice model solver HΦ
   M. Kawamura, K. Yoshimi, T. Misawa, Y. Yamaji, S. Todo, N. Kawashima: Computer Physics Communications **217** (2017) 180.
3. Restricted Boltzmann machine learning for solving strongly correlated quantum systems
   Y. Nomura, A. S. Darmawan, Y. Yamaji, M. Imada: Phys. Rev. B **96** (2017) 205152.
4. Quantum spin liquid signatures in Kitaev-like frustrated magnets
   M. Gohlke, G. Wachtel, Y. Yamaji, F. Pollmann, Y. B. Kim: Phys. Rev. B **97** (2017) 075126.
5. Finite-Temperature Signatures of Spin Liquids in Frustrated Hubbard Model
   T. Miasawa, Y. Yamaji: J. Phys. Soc. Jpn. **87** (2017) 023707.
6. Path to stable quantum spin liquids in spin-orbit coupled correlated materials
   A. Catuneanu, Y. Yamaji, G. Wachtel, Y. B. Kim, H.-Y. Kee: npj Qauntum Materials, in press; arXiv:1701.07837.
7. Numerical Algorithm for Exact Finite Temperature Spectra and Its Application to Frustrated Quantum Spin Systems
   Y. Yamaji, T. Suzuki, M. Kawamura: submitted to Phys. Rev. X; arXiv:1802.02854.
8. Classical and quantum spin dynamics of the honeycomb Γ model
   A. M. Samarakoon, G. Wachtel, Y. Yamaji, D. A. Tennant, C. D. Batista, Y. B. Kim: submitted to Phys. Rev. B; arXiv:1803.00601.

YAMASHITA, Koichi [C class; 5500 (B)] (79)
— *Large scale ab initio calculations on the fundamental processes of solar energy convergence devices and on designing principles for new materials*

1. Role of Quantum-Confinement in Anatase Nanosheets
   Daniele Varsano, Giacomo Giorgi, Koichi Yamashita and Maurizia Palummo: J. Phys. Chem. Lett. **8** (2017) 3867–3873.
2. Inorganic Lattice Fluctuation Induces Charge Separation in Lead Iodide Perovskites: Theoretical Insights
   H. Uratani and K. Yamashita: J. Phys. Chem. C **121** (2017) 26648–26654.
3. $MgTaO_2N$ Photocatalysts: Perovskite versus Ilmenite Structure. A Theoretical Investigation
   A. Kubo, G. Giorgi and K. Yamashita: J. Phys. Chem. C **121** (2017) 27813–27821.
4. Hybrid organic–inorganic $CH_3NH_3PbI_3$ perovskite building blocks: Revealing ultra-strong hydrogen bonding and mulliken inner complexes and their implications in materials design
   Arpita Varadwaj, Pradeep R. Varadwaj and Koichi Yamashita: J. Comput. Chem. **38** (2017) 2802–2818.
5. Revealing the Chemistry between Band Gap and Binding Energy for Lead-/Tin-Based Trihalide Perovskite Solar Cell Semiconductors
   A. Varadwaj, P. R. Varadwaj and K. Yamashita: ChemSusChem **11** (2018) 449–463.
6. Do surfaces of positive electrostatic potential on different halogen derivatives in molecules attract?

like attracting like!
A. Varadwaj, P. R. Varadwaj and K. Yamashita: J. Comput. Chem. **39** (2018) 343–350.

7. First-Principles Investigation of the Lewis Acid-Base Adduct Formation at the Methylammonium Lead Iodide Surface
   Giacomo Giorgi , Koichi Yamashita and Hiroshi Segawa: Phys. Chem. Chem. Phys. **20** (2018) 11183–11195.
8. Revealing Factors Influencing the Fluorine-Centered Non-Covalent Interactions in Some Fluorine-substituted Molecular Complexes: Insights from First-Principles Studies
   Arpita Varadwaj, Pradeep R. Varadwaj, Helder M. Marques and Koichi Yamashita: ChemPhysChem (2018) in press.
9. Halogen in materials design: Fluoroammonium lead triiodide (FNH_3PbI_3) perovskite as a newly discovered dynamical bandgap semiconductor in 3D
   Arpita Varadwaj, Pradeep R. Varadwaj and Koichi Yamashita: Int. J. Quantum Chem. (2018) in press.

YAMASHITA, Tomoki [C class; 4500 (B)] (91)
— *Development of crystal structure prediction method and search for magnet and spintronics materials*

1. Crystal structure prediction accelerated by Bayesian optimization
   T. Yamashita, N. Sato, H. Kino, T. Miyake, K. Tsuda, and T. Oguchi: Phys. Rev. Materials **2** (2018) 013803.

YAMAUCHI, Kunihiko [C class; 5500 (B)] (78)
— *First-Principles DFT Calculations for Transition-Metal Oxides*

1. Role of square planar coordination in the magnetic properties of Na4IrO4
   Xing Ming, Carmine Autieri, Kunihiko Yamauchi, and Silvia Picozzi: Phys. Rev. B 96, 205158 (2017).

YANAGISAWA, Susumu [C class; 3500 (B)] (111)
— *Theoretical investigation on electronic structure of organic semiconductor solids*

1. First-Principles Molecular Dynamics Analysis of Ligand-Free Suzuki-Miyaura Cross-Coupling in Water: Transmetalation and Reductive Elimination
   T. Hirakawa, Y. Uramoto, S. Yanagisawa, T. Ikeda, K. Inagaki and Y. Morikawa: J. Phys. Chem. C **121** (2017) 19904.
2. Theoretical determination of the ionization potential and the electron affinity of organic semiconductors
   S. Yanagisawa: AIP Conf. Proc. **1906** (2017) 030014.
3. A New Pentacene Polymorph Induced by Interaction with a Bi(0001) Substrate
   T. Shirasawa, S. Yanagisawa, S. Hatada, W. Voegeli, Y. Morikawa and T. Takahashi: J. Phys. Chem. C **122** (2018) 6240.
4. Experimental determination of electrostatic energy in organic thin films: Demonstration of orientation-dependent ionization energy and electron affinity
   K. Yamada, S. Yanagisawa, T. Koganezawa, K. Mase, N. Sato and H. Yoshida: submitted to Phys. Rev. B.

YANAGISAWA, Takashi [B class; 900 (B)] (200)
— *Optimized Monte Carlo method and first-principles calculations in strongly correlated electron systems*
— *Quantum Monte Carlo and first-principles study of strongly correlated electron systems*

1. One way to design a valence-skip compound
   I. Hase, T. Yanagisawa and K. Kawashima: Nanoscale Research Letters 12 (2017) 127.
2. Evolution of the CDW gap in valence skipper $RbTlX_3$ (X=F, Cl, Br): A first-principles study
   I. Hase, T. Yanagisawa and K. Kawashima: J. Phys. Conf. Ser. 871 (2017) 012030.
3. Crossover-induced spin fluctuation and electron pairing in strongly correlated electrons
   T. Yanagisawa, M. Miyazaki and K. Yamaji: J. Superconductivity and Novel Magnetism 31 (2017) 785.
4. Strongly correlated superconductivity

T. Yanagisawa, M. Miyazaki and K. Yamaji: Int. J. Mod. Phys. B32 (2018) 1840023.

5. Computational design of flat-band material
   I. Hase, T. Yanagisawa and K. Kawashima: Nanoscale Research Letters 13 (2018) 63.
6. Optimized wave function by kinetic renormalization effect in strongly correlated region of the three-band Hubbard model
   T. Yanagisawa, M. Miyazaki, I. Hase and K. Yamaji: J. Phys. Conf. Series (2018) in press.
7. Electronic structure of novel binary superconductor $SrGe_2$
   I. Hase, T. Yanagisawa, A. Iyo, H. Eisaki, Y. Yoshida and K. Kawashima: J. Phys. Conf. Series (2018) in press.
8. Possibility of flat-band ferromagnetism in hole doped pyrochlore oxide $Sn-2Nb-2O-7$ and $Sn-2Ta-2O-7$
   I. Hase, T. Yanagisawa, Y. Aiura and K. Kawashima: Physical Review Letters (2018) in press.
9. The Competition between CDW and the superconducting state in valence skip compounds
   I. Hase, T. Yanagisawa and K. Kawashima: Communications in Computational Physics 23 (2018) 773.

YASUDA, Chitoshi [C class; 8000 (B)] (223)

— *Randomness Effects on Quantum Spin Systems Coupled to Lattice Degrees of Freedom*

— *Randomness Effects on Quantum Spin Systems Coupled to Lattice Degrees of Freedom II*

1. Position of Effective Spins Induced by Dilution in Two-Dimensional Spin-Peierls Systems
   C. Yasuda and S. Miyara: J. Phys. Soc. Jpn. **87** (2018) 014704.
2. Notes on Ground-State Properties of Mixed Spin-1 and Spin-1/2 Lieb-Lattice Heisenberg Antiferromagnets
   Y. Hirose, S. Miura, C. Yasuda, and Y. Fukumoto: J. Phys. Soc. Jpn. **86** (2017) 083705.

YASUOKA, Kenji [C,D class; 7500 (B)] (63)

— *The Study on the Morphology Dependence of Anatase Nanocrystals*

— *The Study on the Stability of Excess Electrons in Anatase TiO2 Nanocrystals*

— *The study on the electronic state of reduced anatase TiO2 nanocrystal*

1. Density functional theory study of atomic and electronic properties of defects in reduced anatase TiO2 nanocrystals
   K. Morita, and K. Yasuoka: AIP Adv. **8** (2018) 035119.

YOSHIDA, Tsuneya [C class; 5500 (B)] (185)

— *Exotic phenomena induced by topology and strong correlations*

— *Exotic properties in strongly correlated topological systems*

1. Reduction of Z classification of a two-dimensional weak topological insulator: Real-space dynamical mean-field theory study
   Tsuneya Yoshida and Norio Kawakami:Phys. Rev. B 95, 045127
2. Fate of Majorana Modes in CeCoIn5/YbCoIn5 Superlattices: A Test Bed for the Reduction of Topological Classification
   Tsuneya Yoshida, Akito Daido, Youichi Yanase, and Norio Kawakami: Phys. Rev. Lett. 118, 147001

YOSHIDOME, Takashi [B,C class; 6300 (B)] (238,239)

— *Accurate computation of the free-energy change of apoplastocyanin using the end-points method*

— *Elucidation of binding and unbinding processes of a ligand to a protein using a hybrid of the manifold theory and the Markov state model*

1. An Accurate Computation of an Order Parameter with a Markov State Model Constructed using a Manifold-Learning Technique
   R. Ito and T. Yoshidome: Chem. Phys. Lett. **691** (2018) 22.

YOSHIZAWA, Kanako [C class; 3500 (B)] (110)

— *Hydrogen state in a rutile titanium dioxide by first-principles calculation*

□ SCCMS Projects

FUJITA, Takatoshi [3000 (B)] (333)
— *Excited-state calculations for molecular aggregates based on Green's function and fragmentation methods*

1. Development of the Fragment Molecular Orbital Method for Calculating Nonlocal Excitations in Large Molecular Systems
   T. Fujita, Y. Mochizuki, J. Phys. Chem. A **122** (2018) 3886.
2. Assessing the accuracy of integral equation theories for nano-sized hydrophobic solutes in water
   T. Fujita, Y. Yamamoto, J. Chem. Phys. **147** (2017) 014110.
3. Relating stacking structures and charge transport in crystal polymorphs of the pyrrole-based π-conjugated molecule
   T. Fujita, Y. Haketa, H. Maeda, T. Yamamoto, Org. Electron. **49** (2017) 53.

FUKUSHIMA, Tetsuya [5000 (B)] (335)
— *Materials design for energy-saving and energy-creation materials*

1. Structure of the high-entropy alloy AlxCrFeCoNi: fcc versus bcc
   M. Ogura, T. Fukushima, R. Zeller and P. H. Dederichs: J. Alloys Compd. **715** (2017) 454.
2. Theoretical investigation of phase separation in thermoelectric AgSbTe2
   H. Shinya, A. Masago, T. Fukushima and H. Katayama-Yoshida: Jpn. J. Appl. Phys. **56** (2017) 081201.
3. First-principles calculations on the origin of ferromagnetism in transition-metal doped Ge
   H. Shinya, T. Fukushima, A. Masago, K. Sato and H. Katayama-Yoshida: Phys. Rev. B **96** (2017) 104415.
4. Local Energies and Energy Fluctuations — Applied to the High Entropy Alloy CrFeCoNi
   T. Fukushima, H. Katayama-Yoshida, K. Sato, M. Ogura, R. Zeller and P. H. Dederichs: J. Phys. Soc. Jpn. **86** (2017) 114704.
5. Charge-density study on layered oxyarsenides (LaO)MAs (M = Mn, Fe, Ni, Zn)
   K. Takase, S. Hiramoto, T. Fukushima, K. Sato, C. Moriyoshi and Y. Kuroiwa: Appl. Phys. Express **10** (2017) 123001.
6. Anomalous Hall conductivity and electronic structures of Si-substituted Mn2CoAl epitaxial films
   K. Arima, F. Kuroda, S. Yamada, T. Fukushima, T. Oguchi and K. Hamaya: Phys. Rev. B **97** (2018) 054427.

GOHDA, Yoshihiro [5000 (B)] (342)
— *Structures and local magnetic properties of magnetic-material interfaces*

1. Prediction of ferromagnetism in MnB and MnC on nonmagnetic transition-metal surfaces studied by first-principles calculations
   S. Nakamura and Y. Gohda: Phys. Rev. B **96**, 245416 (2017).
2. Electron Theory on Grain-Boundary Structures and Local Magnetic Properties of Neodymium Magnets
   Y. Gohda, Y. Tatetsu, and S. Tsuneyuki: Mater. Trans. **59**, 332 (2018).
3. ネオジム磁石の粒界構造と局所磁性の電子論
   合田 義弘、立津 慶幸、常行 真司: 日本金属学会誌 **81**, 26 (2017).

IMADA, Masatoshi [25000 (B)] (323)
— *Studies on mechanisms of high-temperature superconductivity and search for principles that raise critical temperature*
— *Variational Fermi wave function combined with tensor network and machine learning for high-accuracy quantum lattice solver*

1. Quantum spin liquid signatures in Kitaev-like frustrated magnets
   Matthias Gohlke, Gideon Wachtel, Youhei Yamaji, Frank Pollmann, and Yong Baek Kim: Phys. Rev. B.**97** (2018) 075126

2. Finite-Temperature Signatures of Spin Liquids in Frustrated Hubbard Model
   Takahiro Misawa and Youhei Yamaji: J. Phys. Soc. Jpn. **87** (2018) 023707.
3. Competition among various charge-inhomogeneous states and d-wave superconducting state in Hubbard models on square lattices
   Kota Ido, Takahiro Ohgoe, and Masatoshi Imada: Phys. Rev. B. **97** (2017) 045138.
4. Competition among Superconducting, Antiferromagnetic, and Charge Orders with Intervention by Phase Separation in the 2D Holstein-Hubbard Model
   Takahiro Ohgoe and Masatoshi Imada: Phys. Rev. Lett. **119** (2017) 197001.
5. Restricted Boltzmann machine learning for solving strongly correlated quantum systems
   Yusuke Nomura, Andrew S. Darmawan, Youhei Yamaji, and Masatoshi Imada: Phys. Rev. B. **96** (2017) 205152.
6. Quantum lattice model solver H Phi
   Mitsuaki Kawamura, Kazuyoshi Yoshimi, Takahiro Misawa, Youhei Yamaji,Synge Todo, and Naoki Kawashima: Compt. Phys. Commun. **217**, (2017) 180.
7. Correlation-induced superconductivity dynamically stabilized and enhanced by laser irradiation
   Kota Ido, Takahiro Ohgoe, and Masatoshi Imada: Sci. Adv. **3** (2017) e1700718 .
8. Variational Monte Carlo method for fermionic models combined with tensor networks and applications to the hole-doped two-dimensional Hubbard model
   Hui-Hai Zhao, Kota Ido, Satoshi Morita, Masatoshi Imada: Phys. Rev. B. **96** (2017) 085103.
9. Low-energy effective Hamiltonians for correlated electron systems beyond density functional theory
   Motoaki Hirayama, Takashi Miyake, Masatoshi Imada, and Silke Biermann: Phys. Rev. B. **96** (2017) 075102.
10. Ground state properties of $\mathrm{Na_2IrO_3}$ determined from ab initio Hamiltonian and its extensions containing Kitaev and extended Heisenberg interactions
    Tsuyoshi Okubo, Kazuya Shinjo, Youhei Yamaji, Naoki Kawashima, Shigetoshi Sota, Takami Tohyama, and Masatoshi Imada: Phys. Rev. B. **96** (2017) 054434.

IITAKA, Toshiaki [15000 (B)] ()
— *Computational study of hydrous minerals using the path integral molecular dynamics method*

KAWAKATSU, Toshihiro [10000 (B)] ()
— *Numerical study of thermal transport on multiscale simulation*

1. Elongational viscosity of weakly entangled polymer melt via coarse-grained molecular dynamics simulation
   T. Murashima, K. Hagita, T. Kawakatsu: Nihon Reoroji Gakkaishi, submitted.
   http://arxiv.org/abs/1803.01517

KAWASHIMA, Naoki [25000 (B)] (329)
— *Application of Tensor Network Methods to Condensed Matter Physics*

1. Quantum lattice model solver HPhi
   Mitsuaki Kawamura, Kazuyoshi Yoshimi, Takahiro Misawa, Youhei Yamaji, Synge Todo, and Naoki Kawashima: Computer Physics Communications. **217**, 180-192.
2. Variational Monte Carlo method for fermionic models combined with tensor networks and applications to the hole-doped two-dimensional Hubbard model
   Hui-Hai Zhao, Kota Ido, Satoshi Morita, and Masatoshi Imada: Phys. Rev. B. **96**, 085103/1-16.
3. Ground state properties of Na2IrO3 determined from ab initio Hamiltonian and its extensions containing Kitaev and extended Heisenberg interactions
   Tsuyoshi Okubo, Kazuya Shinjo, Youhei Yamaji, Naoki Kawashima, Shigetoshi Sota, Takami Tohyama, and Masatoshi Imada: Phys. Rev. B. **96**, 054434/1-12.
4. Proposal of a spin-one chain model with competing dimer and trimer interactions
   Yun-Tak Oh, Hosho Katsura, Hyun-Yong Lee, and Jung Hoon Han: Phys. Rev. B. **96**, 165126/1-8.
5. Disordered quantum spin chains with long-range antiferromagnetic interactions
   N. Moure, Hyun-Yong Lee, S. Haas, R. N. Bhatt, and S. Kettemann: Phys. Rev. B. **97**, 014206/1-

6.

6. Tensor renormalization group with randomized singular value decomposition
   Satoshi Morita, Ryo Igarashi, Hui-Hai Zhao, and Naoki Kawashima: Phys. Rev. E. **97**, 033310/1-6.

KOHYAMA, Masanori [15000 (B)] (325)
— *First-Principles Phase Field Mapping*

1. A molecular heterojunction of zinc phthalocyanine and peanut-shaped fullerene polymer: A density functional study
   K. Tanikawa, K. Ohno, Y. Noda, S. Ono, R. Kuwahara, A. Takashima, M. Nakaya, and J. Onoe: Chem. Phys. Lett. **686** (2017) 68.
2. First-ptinciples study on the atomistic corrosion process of iron
   K.-H. Chew, R. Kuwahara, and K. Ohno: Phys. Chem. Chem. Phys. **20** (2018) 1653.
3. Extensive First-Principles Molecular Dynamics Study on the Li Encapsulation into C60 and Its Experimental Confirmation
   K. Ohno, A. Manjanath, Y. Kawazoe, R. Hatakeyama, F. Misaizu, E. Kwon, H. Fukumura, H. Ogasawara, Y. Yamada, C. Zhang, N. Sumi, T. Kamigaki, K. Kawachi, K. Yokoo, S. Ono, and Y. Kasama: Nanoscale **10** (2018) 1825.
4. Weakly spin-dependent band structures of antiferromagnetic perovskite LaMO3 (M = Cr, Mn, Fe)
   T. Okugawa, K. Ohno, Y. Noda, and S. Nakamura: J. Phys.: Condensed Mat. **30** (2018) 075502.
5. Hydrogenation reaction of carbon monoxide on ice surfaces
   K. Kuwahata and K. Ohno: ChemPhysChem. to be published.

MISAWA, Takahiro [12500 (B)] (174)
— *Finite-temperature calculations of* $YbMgGaO_4$ *using* $H\Phi$
— *Quantum transport phenomena in topological semimetals*

1. Quantum lattice model solver $H\Phi$
   M. Kawamura, K. Yoshimi, T. Misawa, *et al.*, Comp. Phys. Commun. **217**, 180-192 (2017).
2. 量子格子模型の汎用数値対角化パッケージ H Φ一スピン液体近傍の熱・スピン励起への適用一
   山地洋平・三澤貴宏・吉見一慶・河村光晶・藤堂眞治・川島直輝, 固体物理, Vol.52, No10 (2017).
3. ＜コラム＞mVMC 多変数変分モンテカルロ法のオープンソースソフトウェア
   三澤貴宏・今田正俊, 固体物理, Vol.52, No11 (2017).
4. Superconductivity Emerging from Excitonic Mott insulator - Theory of Alkaline Doped Fullerene
   T. Misawa and M. Imada, arXiv:1711.10205
5. mVMC - Open-source software for many-variable variational Monte Carlo method
   T. Misawa *et al.*, arXiv:1711.11418
6. Asymmetric melting of one-third plateau in kagome quantum antiferromagnets
   T. Misawa, Y. Motoyama and Y. Yamaji, arXiv:1801.07128.
7. Finite-Temperature Signatures of Spin Liquids in Frustrated Hubbard Model
   T. Misawa and Y. Yamaji, J. Phys. Soc. Jpn **87**, 023707 (2018).

MIYAKE, Takashi [5000 (B)] (339)
— *First-principles study of magnetic materials*

1. First-principles study of inter-site magnetic couplings and Curie temperature in $RFe_{12-x}Cr_x$ (R=Y, Nd, Sm)
   Taro Fukazawa, Hisazumi Akai, Yosuke Harashima and Takashi Miyake: J. Phys. Soc. Jpn. **87** (2018) 044706.
2. Crystal structure prediction accelerated by Bayesian optimization
   Tomoki Yamashita, Nobuya Sato, Hiori Kino, Takashi Miyake, Koji Tsuda, and Tamio Oguchi: Phys. Rev. Mat. **2** (2018) 013803.
3. First-principles investigation of magnetic compounds $NdFe_{12}$ and $NdFe_{12}X$ (X=B, C, N, O, F) and their inter-site magnetic couplings
   Taro Fukazawa, Hisazumi Akai, Yosuke Harashima, and Takashi Miyake: J. Appl. Phys. **122** (2017) 053901.

4. Quantum theory of rare-earth magnets
   Takashi Miyake and Hisazumi Akai: J. Phys. Soc. Jpn. **87** (2018) 041009.
5. Machine learning reveals orbital interaction in materials
   Tien Lam Pham, Hiori Kino, Kiyoyuki Terakura, Takashi Miyake, Ichigaku Takigawa, Koji Tsuda and Hieu Chi Dam: Sci. Technol. Adv. Mater. **18** (2017) 756.
6. Crystal-field effects in rare-earth-based hard magnets: an ab initio approach
   Pascal Delange, Silke Biermann, Takashi Miyake and Leonid Pourovskii: Phys. Rev. B **96** (2017) 155132.

MORITA, Akihiro [6000 (B)] (344)
— *Molecular simulation of ion transport and desolvation at electrode interface*

1. Microscopic Investigation of Ethylene Carbonate Interface: A Molecular Dynamics and Vibrational Spectroscopic Study
   Lin Wang, Liang Xin, Tatsuya Ishiyama, Qiling Peng, Shen Ye, and Akihiro Morita: Acta Phys. Chim. Sin., in press.
2. Hydrated Ion Clusters in Hydrophobic Liquid: Equilibrium Distribution, Kinetics and Implications
   Lingjian Wang, Nobuaki Kikkawa, and Akihiro Morita:J. Phys. Chem. B, in press.
3. Molecular Dynamics Study of Structure and Vibrational Spectra at Zwitterionoic Lipid/Aqueous KCl, NaCl, and $CaCl_2$ Solution Interfaces
   Tatsuya Ishiyama, Shinnosuke Shirai, Tomoaki Okumura, Akihiro Morita: J. Chem. Phys. **148** (2018) 222801.
4. Effect of Third-Order Susceptibility in Sum Frequency Generation Spectroscopy: Molecular Dynamics Study in Liquid Water
   Tatsuya Joutsuka, Tomonori Hirano, Michiel Sprik, and Akihiro Morita: Phys. Chem. Chem. Phys.**20** (2018) 3040-3053.
5. Structure at the Air/Water Interface in the Presence of Phenol: A Study using Heterodyne-Detected Vibrational Sum Frequency Generation and Molecular Dynamics Simulation
   Ryoji Kusaka, Tatsuya Ishiyama, Satoshi Nihonyanagi, Akihiro Morita, and Tahei Tahara: Phys. Chem. Chem. Phys.**20** (2018) 3002-3009.
6. Theoretical Investigation of C-H Vibrational Spectroscopy. 2. Unified Assignment Method of IR, Raman and SFG Spectra of Ethanol
   Lin Wang, Tatsuya Ishiyama, and Akihiro Morita: J. Phys. Chem. A**121** (2017) 6701-6712.
7. Theoretical Investigation of C-H Vibrational Spectroscopy. 1. Modeling of Methyl and Methylene Groups of Ethanol with Different Conformers
   Lin Wang, Tatsuya Ishiyama, and Akihiro Morita: J. Phys. Chem. A**121** (2017) 6687-6700.
8. A QM/MM Study on the Correlation between the Polarizations of π and σ Electrons in a Hydrated Benzene
   Daiki Suzuoka, Hideaki Takahashi, and Akihiro Morita: Mol. Sim.**43** (2017) 1209-1217.
9. Unveiling Subsurface Hydrogen-Bond Structure of Hexagonal Water Ice
   Yuji Otsuki, Toshiki Sugimoto, Tatsuya Ishiyama, Akihiro Morita, Kazuya Watanabe, and Yoshiyasu Matsumoto: Phys. Rev. B **96** (2017) 115405 (14 pages).
10. Computational Analysis of Vibrational Sum Frequency Generation Spectroscopy
    Tatsuya Ishiyama and Akihiro Morita: Annu. Rev. Phys. Chem. **68** (2017) 355-377.

NOBUSADA, Katsuyuki [10000 (B)] ()
— *Nano-optical response theory and computational design of unified photonic-electronic devices*

NOGUCHI, Hiroshi [12500 (B)] (217,219)
— *Molecular Dynamics Simulation of Complex Fluids*

1. Structure formation induced by two types of banana-shaped proteins adsorbed on lipid membranes
   H. Noguchi and J.-B. Fournier: Soft Matter **13**, 4099 (2017).
2. Acceleration and suppression of banana-shaped-protein-induced tubulation by addition of small membrane inclusions of isotropic spontaneous curvatures
   H. Noguchi: Soft Matter **13**, 7771 (2017).

3. Docosahexaenoic acid preserves visual function by maintaining correct disc morphology in retinal photoreceptor cells
H. Shindou, H. Koso, J. Sasaki, H. Nakanishi, H. Sagara, K. M. Nakagawa, Y. Takahashi, D. Hishikawa, Y. Iizuka-Hishikawa, F. Tokumasu, H. Noguchi, S. Watanabe, T. Sasaki, and T. Shimizu: J. Bio. Chem. **292**, 12054 (2017).
4. Bilayer sheet protrusions and budding from bilayer membranes induced by hydrolysis and condensation reactions
K. M. Nakagawa and H. Noguchi: Soft Matter **14**, 1397 (2018).
5. Polymer effects on Karman Vortex: Molecular Dynamics Study
Y. Asano, H. Watanabe, and H. Noguchi: J. Chem. Phys. **148**, 144901(2018).
6. 短距離古典分子動力学シミュレーションコードの GPGPU 化（１）
中川恒: 分子シミュレーション研究会会誌“アンサンブル”**19**, 267 (2017).
7. 短距離古典分子動力学シミュレーションコードの GPGPU 化（２）
中川恒: 分子シミュレーション研究会会誌“アンサンブル”**20**, 40 (2018).

OBA, Fumiyasu [12500 (B)] (337)
— *Exploration of novel semiconductors by first-principles screening*

1. Comparison of approximations in density functional theory calculations: Energetics and structure of binary oxides
Y. Hinuma, H. Hayashi, Y. Kumagai, I. Tanaka, and F. Oba, Phys. Rev. B 96, 094102-1-24 (2017).

OGATA, Shuji [12500 (B)] (330)
— *Simulation of organic-inorganic interfaces*

1. Large-Scale DFT Simulation of Li-atom Insertion and Extraction in QuinonsSWCNT Rechargeable Battery Cathodes
T. Tsuzuki, S. Ogata, and M. Uranagase: MRS Adv. (2018) 1-6., in press.
2. Smart MD-Sampling Method for Interfacial Free Energy between Polymer-Grafted Substrate and Liquid
M. Uranagase and S. Ogata: MRS Adv. **3** (2018) 519-524.

OKAZAKI, Susumu [5000 (B)] (332)
— *Conversion and storage of energy - Fuel cells and secondary batteries: Research and development of fundamental technologies of battery simulators*

1. Structural ordering of lipid bilayers induced by surfactant molecules with small hydrophilic head group
Y. Andoh, S. N. S. Mohamed, S. Kitou, S. Okazaki, Mol. Siml., 43, 1247-1255 (2017).
2. Molecular dynamics study of the aggregation rate for zwitterionic dodecyldimethylamine oxide and cationic dodecyltrimethylammonium chloride micelles
K. Fujimoto, Y. Kubo, S. Kawada, N. Yoshii, S. Okazaki., Mol. Simil., 43, 1331-1337 (2017).
3. Spherical harmonics analysis of surface density fluctuations of spherical ionic SDS and nonionic C12E8 micelles: A molecular dynamics study
N. Yoshii, Y. Nimura, K. Fujimoto, S. Okazaki, J. Chem. PHys., 147, 034906 (2017).
4. Molecular dynamics study of the potential of mean force of SDS aggregates
S. Kawada, K. Fujimoto, N. Yoshii, S. Okazaki, J. Chem. Phys., 147, 084903 (2017).
5. Transferable coarse-grained model for perfluorosulfonic acid polymer membranes
A. T. Kuo, S. Okazaki, W. Shinoda, J. Chem. Phys., 147, 094904 (2017).
6. Pressure tensor for electrostatic interaction calculated by fast multipole method with periodic boundary condition
N. Yoshii, Y. Andoh, S. Okazaki, J. Comput. Chem., in press
7. A thread-level parallelization of pairwise additive potential and force calculations suitable for current many-core architectures
Y. Andoh, S. Suzuki, S. Ohshima, T. Sakashita, M. Ogino, T. Katagiri, N. Yoshii, S. Okazaki, J. Supercomput., in press

ONO, Kanta [5000 (B)] (343)
— *Magnetization process of permanent magnets revealed by large-scale simulation*

OSHIYAMA, Atsushi [15000 (B)] (40)
— *Exploration of new-functionality and high-performance semiconductor devices*

1. First-principles study of lateral atom manipulation assisted by structural relaxation of a scanning tip apex
   B. Enkhtaivan, Y. Sugimoto and A. Oshiyama: Phys. Rev. B **96** (2017) 155417
2. A novel intrinsic interface state controlled by atomic stacking sequence at interface of SiC/SiO_2
   Y.-i. Matsushita and A. Oshiyama: Nano Letters **17** (2017) 6458
3. Mining single-electron spectra of the interface states from a supercell band structure of silicene on an Ag(111) substrate with band-unfolding methodology
   J.-I. Iwata, Y.-i. Matsushita, H. Nishi, Z.-X. Guo and A. Oshiyama: Phys. Rev. B **96** (2017) 235442
4. Unfolding energy spectra of double-periodicity two dimensional systems: twisted bilayer graphene and MoS_2 on graphene
   Y.-i. Matsushita, H. Nishi, J.-i. Iwata, T. Kosugi and A. Oshiyama: Phys. Rev. Materials **2** (2018) 010801(R)

SAITO, Susumu [7500 (B)] (340)
— *Materials design using B, C, and N for next-generation device*

1. Quasiparticle energies and dielectric functions of diamond polytypes
   M. Sakurai, J. R. Chelikowsky, S. G. Louie, and S. Saito: Phys. Rev. Materials **1**, 054603 (2017).
2. Energetics and Scanning Tunneling Microscopy Images of B and N Defects in Graphene Bilayer
   Y. Fujimoto and S. Saito: Springer Proceedings in Physics **186**, 107 (2017).
3. Alternative structure of TiO_2 with higher energy valence band edge
   S. Cho, P. Y. Yu, Y. Aoki, S. Saito, S. G. Louie, and M. L. Cohen: Phys. Rev. B **95**, 085422 (2017).
4. Probing a divergent van Hove singularity of graphene with a Ca_2N support: A layered electride as a solid-state dopant
   T. Inoshita, M. Tsukada, S. Saito, and H. Hosono: Phys. Rev. B **96**, 235404 (2017).

SHIBA, Hayato [12500 (B)] (328)
— *Study of frictional properties of dense polymer brushes by coarse-grained moleculer simulateon method*
— *Coarse-grained modeling approach to materials research on nanoscale dynamics of complex liquids*

1. 最近の研究から「２次元ガラスのダイナミクス – 無限対数ゆらぎと固有緩和」
   日本物理学会誌 **72**-10, 717 (2017).
2. Continuum limit of the vibrational properties of amorphous solids
   H. Mizuno, H. Shiba, and A. Ikeda: Proc. Natl. Acad. Sci. U.S.A. **114**, E9767 (2017).
3. Isolating long-wavelength fluctuation from structural relaxation in two-dimensional glass: cage-relative displacement
   H. Shiba, P. Keim, and T. Kawasaki: J. Phys: Cond. Matter **30**, 094004/1-9 (2018).
4. Molecular dynamics study of mesophase transitions upon annealing of imidazolium-based ionic liquids with long-alkyl chains
   H. Peng, M. Kubo, and H. Shiba: Phys. Chem. Chem. Phys. in press (2018).

SUGINO, Osamu [10000 (B)] (326)
— *Conversion and storage of energy - Fuel cells and secondary batteries: Research and development of fundamental technologies of battery simulators*

TAKETSUGU, Tetsuya [12500 (B)] (119)
— *Ab initio study on abundant nano-catalysts free from precious metals*

1. Optical readout of hydrogen storage in films of Au and Pd
   Y. Nishijima, S. Shimizu, K. Kurihara, Y. Hashimoto, H. Takahashi, A. Balcytis, G. Seniutinas, S. Okazakis, J. Juodkazyte, T. Iwasa, T. Taketsugu, Y. Tominaga, and S. Juodkazis: Opt. Express,

25 (2017) 24081.
2. Time-Dependent Density Functional Theory Study on Higher Low-Lying Excited States of $\mathrm{Au}_{25}(\mathrm{SR})_{18}^{-}$
M. Ebina, T. Iwasa, Y. Harabuchi, and T. Taketsugu: J. Phys. Chem. C, **122** (2018) 4097.

TOHYAMA, Takami [5000 (B)] (331)
— *Cooperation research with big experimental facilities*
1. Observation of Momentum-Dependent Charge Excitations in Hole-Doped Cuprates Using Resonant Inelastic X-Ray Scattering at the Oxygen K Edge
K. Ishii, T. Tohyama, S. Asano, K. Sato, M. Fujita, S. Wakimoto, K. Tustsui, S. Sota, J. Miyawaki, H. Niwa, Y. Harada, J. Pelliciari, Y. Huang, T. Schmitt, Y. Yamamoto, and J. Mizuki: Phys. Rev. B **96**, (2017) 115148.

YABANA, Kazuhiro [7500 (B)] (100)
— *Dynamics in nano-interface excited by high-intensity pulsed light*

YAMASHITA, Koichi [5000 (B)] (79)
— *Large scale calculations on the fundamental processes of organic and perovskite solar cells and their optimization in conversion efficiency*

YOSHIMI, Kazuyoshi [12500 (B)] (13)
— *Numerical study of two-dimensional electron gas system by using variational Monte Calro method*
— *Study of many-body correlation effects in quantum dots*

□ Doctor theses

1. **HIRAKAWA, Teruo**
   First-principles Molecular Dynamics (FPMD) Simulations of Chemical Reactions in Aqueous Solution and Improvement of Constant Temperature Order-N FPMD method
   Osaka University, 2018-03

2. **HORITA, Toshiki**
   Critical Phenomena of the Ising Model with Non-Integer Effective Dimensions - a Monte Carlo Study
   the University of Tokyo, 2018-03

3. **IDO, Kota**
   Superconductivity and spatial inhomogeneity induced by electron correlations in and out of equilibrium
   the University of Tokyo, 2018-03

4. **KATOW, Hiroki**
   A theoretical study on quantum state and optical trapping of excitons
   the University of Tokyo, 2018-03

5. **KIM, Jaehyun**
   Theoretical analysis of electronic structure of iron-sulfur clusters in hydrogenases
   University of Hyogo, 2018-03

6. **KUBO, Ayako**
   Theoretical investigations on controlling the properties of semiconductor photocatalysts by modifying structural factors
   The University of Tokyo, 2018-03

7. **KUBOTA, Dai**
   Numerical studies by dynamical mean-field theory on magnetism and superconductivity in strongly correlated electron systems
   the University of Tokyo, 2018-03

8. **LI, Han**
   Development of O(N) Ab-initio Molecular Dynamics that Exploits the Locality of Forces and its Acceleration through Machine Learning
   the University of Tokyo, 2018-03

9. **LI, Wenwen**
   Development of Neural Network Potentials to Study Atomic Diffusion Behaviors in Amorphous Materials
   the University of Tokyo, 2017-09

10. **MISAWA, Masaaki**
    First-principles study of the chemical reaction and phase transition mechanisms on oxide materials
    Kumamoto University, 2018-03

11. **MIZUTA, Yo Pierre**
    Thermoelectric Effects Driven by Nanoscale Magnetic Order: A Theoretical Study
    Kanazawa University, 2018-03

12. **MUTTAQIEN, Fahdzi**
    Chemistry of CO_2 Adsorption and Reaction on the Copper Surfaces
    Osaka University, 2017-09

13. **NAKAGAWA, Koh M.**
    Simulation studies of bilayer membranes: morphological changes induced by chemical reactions and pressure profile calculation method
    the University of Tokyo, 2018-03

14. **NI, Zeyuan**
    Theoretical investigation on surface/interface optimization and property analysis of novel 2D materials
    the University of Tokyo, 2017-09

15. **NISHIKAWA, Yoshihiko**
    Modern Monte Carlo approaches to classical spin systems: Irreversible algorithm and massive parallelization applied to chiral magnets
    the University of Tokyo, 2018-03

16. **TAKAHASHI, Jun**
    Quantum Annealing: Quantum Statistical Physics applied to Classical Computational Hardness
    the University of Tokyo, 2018-03

17. **TRAN Phuoc, Duy**
    Association and dissociation simulations of bio-molecular complex using parallel cascade selection molecular dynamics
    the University of Tokyo, 2018-03

□ Master Theses

1. **ASOU, Shogo**
   Coarse-grained molecular dynamics simulation of glassy polymer at high density
   Tohoku University, 2018-03

2. **BAN, Yusuke**
   Change in magnetization of ferromagnetic Pd(001) thin films induced by the strain effect of $BaTiO_3$
   Keio University, 2018-3

3. **FUJIKAKE, So**
   Machine Learning Potential Modeling for Theoretical Study on Heat Transport of Si-Ge Alloy
   the University of Tokyo, 2018-03

4. **FUJITA, Kazuhiro**
   Magnetoelectric couplings at Fe/BiFeO3(001) heterointerfaces studied by first-principles calculations
   Tokyo Institute of Technology, 2018-03

5. **FURUKAWA, Yoritaka**
   Quasi-particle energy spectra based on coupled-cluster Green's function: Applications to atoms and solids
   the University of Tokyo, 2018-03

6. **GOTO, Yuta**
   Study on metastable states in systems with multiple order parameters
   the University of Tokyo, 2018-03

7. **HASEGAWA, Shun**
   Adsorption and diffusion behaviors of a single metal atom on light-elemnt doped graphene
   Hokkaido University, 2018-03

8. **ISHIHARA, Takumi**
   First-principles calculation on the response of spin crossover molecule to electric fields
   the University of Tokyo, 2018-03

9. **ISHIKAWA, Fumihiro**
   Nonergodicity and localized mode in a classical harmonic chain bath model
   the University of Tokyo, 2018-03

10. **KANAGAWA, Tomosato**
    First-principles study on electric field effect of magnetic anisotropy in Fe/MgO-based interface systems
    Kanazawa University, 2018-03

11. **KISHI,Yuutaro**
    Crystal structure calculations of organic semiconductors by density functional theory
    University of Tsukuba, 2018-03

12. **KITANO, Shusuke**
    First-principles analysis of electronic state change of a MXene compound Ti_2CO_2 due to molecule adsorption
    the University of Tokyo, 2018-03

13. **KUBO, Akiho**
Electronic states of transition-metal dichalcogenide monolayers in asymmetrical structures
Ochanomizu University, 2018-03

14. **MAEDA, Yuto**
Canonical ensemble calculations of a spherical Kagome system by using the microcanonical thermal pure quantum state
The Tokyo University of Science, 2018-03

15. **MATSUGATANI, Akishi**
Topological Phases on the Magnetic Domain Wall of Pyrochlore Iridates
the University of Tokyo, 2018-03

16. **NAKAMURA, Shogo**
First-principles study of the electronic structure of manganese-compound ultrathin films on transition-metal surfaces
Tokyo Institute of Technology, 2018-03

17. **NGUYEN, Thi Phuong Thao**
First-principles calculation on perpendicular magnetocrystalline anisotropy in 3d transition-metal thin films
Osaka University, 2017-09

18. **OHSHIMA, Hiroyuki**
First-principles Molecular Dynamics Simulations of Decomposition Processes of HCOO on a Cu surface
Osaka University, 2018-03

19. **OKUMURA, Shun**
Numerical Study of a Chiral Soliton Lattice in Magnetic Conductors
the University of Tokyo, 2018-03

20. **SAKAKIBARA, Masaki**
First-principles Calculations of Oxygen Vacancies in Perovskite type $SrFeO_3$
Osaka University, 2018-03

21. **SANO, Ryoya**
Kitaev-Heisenberg Interactions in d7 Spin-Orbit Coupled Insulators
the University of Tokyo, 2018-03

22. **SATO, Shunsuke**
Molecular orbital interactions in phenacene crystals
University of Tsukuba, 2018-03

23. **SATONO, Yusuki**
Theoretical study of spin-spiral states in (Cr1—xFex)2O3
Saitama University, 2018-03

24. **SAWADA, Hiroyuki**
First-principles Calculations of Image Potential State of Pb-Phthalocyanine adsorbed Graphene
Osaka University, 2018-03

25. **SHIMADA, Noriaki**
    Numerical study of potential scattering problems in one-dimensional interacting electron systems
    the University of Tokyo, 2018-03

26. **SHIMIZU, Motoki**
    Quantum Monte Carlo Study of the Néel Temperature for the Quasi-One-Dimensional Antiferromagnetic Heisenberg Model Consisting of Bond-Alternated Chains
    University of the Ryukyus, 2018-03

27. **TANAKA, Tomonori**
    First-principles calculations of Bi adsorption on In/Si(111) pseudo-one-dimensional surface structures
    Tokyo Institute of Technology, 2017-09

28. **TANIMOTO, Kei**
    Structure analysis and STM simulation for Fe-adsorbed Si(111) surfaces and beta-FeSi2(100) nanocarpet using first-principles calculation
    Nara Institute of Science and Technology, 2018-03

29. **URA, Hiroyuki**
    Prediction of lattice thermal conductivity of layered nitrides by first-principles calculation based on perturbation theory
    the University of Tokyo, 2018-03

30. **WADA, Kazuma**
    Development of a New Meta-dynamics Method to Accelerate Calculations of Free-energy Surfaces
    Osaka University, 2018-03

31. **WATANABE, Akiei**
    Electronic states of Bi(110) ultrathin films studied by first-principles calculations
    Tokyo Institute of Technology, 2018-03

32. **WATANABE, Takahiro**
    Electronic Structure Calculation in Perovskite-Lead-Halide Mixed Crystals $CH_3NH_3Pb(I,Cl)_3$
    University of Fukui, 2018-03

33. **YAMAMOTO, Takuya**
    Tensor Network Renormalization for Non-uniform Classical Spin Systems
    the University of Tokyo, 2018-03

34. **YAMAZAKI, Syota**
    First-principles study of stability of metal clusters in SiO2 insulator films
    Chiba University, 2018-03

35. **YOSHIKAWA, Seiji**
    Structure search for sulfur hydride at high pressure based on imaginary phonon modes
    the University of Tokyo, 2018-03

36. **YOSHIZAWA, Toru**
    Large Deviation Analysis of Eigenstate Thermalization Hypothesis
    the University of Tokyo, 2018-03